frontiers | Research Topics

Experimental and numerical simulations of rock physics

Edited by
Huaimin Dong, Yihuai Zhang and Weichao Yan

Published in
Frontiers in Earth Science

ISSN 1664-8714
ISBN 978-2-8325-6662-6
DOI 10.3389/978-2-8325-6662-6

Generative AI statement
Any alternative text (Alt text) provided alongside figures in the articles in this ebook has been generated by Frontiers with the support of artificial intelligence and reasonable efforts have been made to ensure accuracy, including review by the authors wherever possible. If you identify any issues, please contact us.

About Frontiers

Frontiers is more than just an open access publisher of scholarly articles: it is a pioneering approach to the world of academia, radically improving the way scholarly research is managed. The grand vision of Frontiers is a world where all people have an equal opportunity to seek, share and generate knowledge. Frontiers provides immediate and permanent online open access to all its publications, but this alone is not enough to realize our grand goals.

Frontiers journal series

The Frontiers journal series is a multi-tier and interdisciplinary set of open-access, online journals, promising a paradigm shift from the current review, selection and dissemination processes in academic publishing. All Frontiers journals are driven by researchers for researchers; therefore, they constitute a service to the scholarly community. At the same time, the *Frontiers journal series* operates on a revolutionary invention, the tiered publishing system, initially addressing specific communities of scholars, and gradually climbing up to broader public understanding, thus serving the interests of the lay society, too.

Dedication to quality

Each Frontiers article is a landmark of the highest quality, thanks to genuinely collaborative interactions between authors and review editors, who include some of the world's best academicians. Research must be certified by peers before entering a stream of knowledge that may eventually reach the public - and shape society; therefore, Frontiers only applies the most rigorous and unbiased reviews. Frontiers revolutionizes research publishing by freely delivering the most outstanding research, evaluated with no bias from both the academic and social point of view. By applying the most advanced information technologies, Frontiers is catapulting scholarly publishing into a new generation.

What are Frontiers Research Topics?

Frontiers Research Topics are very popular trademarks of the *Frontiers journals series*: they are collections of at least ten articles, all centered on a particular subject. With their unique mix of varied contributions from Original Research to Review Articles, Frontiers Research Topics unify the most influential researchers, the latest key findings and historical advances in a hot research area.

Find out more on how to host your own Frontiers Research Topic or contribute to one as an author by contacting the Frontiers editorial office: frontiersin.org/about/contact

Experimental and numerical simulations of rock physics

Topic editors

Huaimin Dong — Chang'an University, China

Yihuai Zhang — University of Glasgow, United Kingdom

Weichao Yan — Ocean University of China, China

Citation

Dong, H., Zhang, Y., Yan, W., eds. (2025). *Experimental and numerical simulations of rock physics*. Lausanne: Frontiers Media SA. doi: 10.3389/978-2-8325-6662-6

Table of contents

frontiers | Frontiers in Earth Science

TYPE Original Research
PUBLISHED 16 August 2024
DOI 10.3389/feart.2024.1438185

OPEN ACCESS

EDITED BY
Yihuai Zhang,
University of Glasgow, United Kingdom

REVIEWED BY
Huaimin Dong,
Chang'an University, China
Amin Taghavinejad,
University of Glasgow, United Kingdom
Azibayam Amabogha,
University of Glasgow, United Kingdom

*CORRESPONDENCE
Sourav Kumar Sahoo,
s.sahoo@noc.ac.uk

RECEIVED 25 May 2024
ACCEPTED 29 July 2024
PUBLISHED 16 August 2024

CITATION
Khan SH, Sahoo SK, Falcon-Suarez IH, Marin-Moreno H, Sutiyoso H, Madhusudhan BN, Majumder CB, Arora A and Best AI (2024) Investigation of methane gas bubble dynamics and hydrate film growth during hydrate formation using 4-D time-lapse synchrotron X-ray computed tomography.
Front. Earth Sci. 12:1438185.
doi: 10.3389/feart.2024.1438185

Investigation of methane gas bubble dynamics and hydrate film growth during hydrate formation using 4-D time-lapse synchrotron X-ray computed tomography

Shadman H. Khan[1,2], Sourav Kumar Sahoo[1]*, Ismael Himar Falcon-Suarez[1], Hector Marin-Moreno[3], Hanif Sutiyoso[1], B. N. Madhusudhan[4], C. B. Majumder[2], Amit Arora[5,6] and Angus I. Best[1]

[1]National Oceanography Centre, Southampton, United Kingdom, [2]Department of Chemical Engineering, Indian Institute of Technology Roorkee, Roorkee, India, [3]School of Ocean and Earth Science, University of Southampton, Southampton, United Kingdom, [4]Faculty of Engineering and the Environment, University of Southampton, Southampton, United Kingdom, [5]Department of Chemical Engineering, National Institute of Technology, Hamirpur, Himachal Pradesh, India, [6]Department of Chemical Engineering, SBS State University Ferozepur, Punjab, India

We present a time-lapse 4-D high-resolution synchrotron imaging study of the morphological evolution of methane gas bubbles and hydrate film growth on these bubbles. Methane gas and partially water-saturated sand were used to form hydrate with a maximum hydrate saturation of 60%. We investigated the transient evolution of gas bubble size distribution during hydrate formation and observed three distinct stages: a) nucleation and hydrate film formation, b) rapid bubble break-up, c) gas bubble coalescence and hydrate framework formation. Our results show that the average gas bubble size distribution decreases from 34.17 μm (during hydrate nucleation) to 8.87 μm (during secondary bubble formation). The small-size methane bubble population (mean diameter below 10 μm) initially increases at the expense of the larger methane bubble population (mean diameter above 50 μm) due to breakage of the larger bubbles and coalescence of the smaller bubbles. We quantified that the average hydrate film thickness increases from 3.51 to 14.7 μm by tracking the evolution of a particular gas bubble. This thickness increase agrees with an analytical model with an average deviation error of 3.3%. This study provides insights into gas bubble distribution and hydrate film growth during hydrate formation, both of which impact the geophysical and mechanical properties of hydrate-bearing sediments.

KEYWORDS

hydrate film, XRCT, hydrate formation, methane hydrate, gas bubble dynamics

1 Introduction

Gas hydrates are ice-like polycrystalline compounds that host light guest molecules within the interlinked hydrogen-bonded cages (Sloan, 2003; You et al., 2023). Over the last few decades, hydrates have received worldwide attention due to their high development prospects. The scope of hydrate-based technology includes gas storage (e.g., Inkong et al., 2022), refrigeration (e.g., Wang et al., 2015), mixed gases separation (e.g., Babaee et al., 2021), carbon dioxide sequestration (e.g., Urych et al., 2022), desalination (e.g., Xu et al., 2018) and transportation of natural gas (e.g., Rajnauth et al., 2010). In recent years, offshore oil and gas exploration and exploitation have shifted towards deeper waters (e.g., Cordes et al., 2016) with lower seafloor temperatures and higher pressures. These conditions favor the hydrate formation both within the pipelines and the vicinity of the wellbore, posing a significant risk to pressure control and flow assurance (e.g., Cordes et al., 2016).

The kinetics of hydrate film growth conditions affect hydrate formation in oil-gas-water pipelines (Guimin et al., 2022), hydrate growth in the pore space and its effects on submarine slopes, and release of methane gas from hydrate deposits and water column seepage (Zhan et al., 2022). During methane seepage in the water column, hydrate films act as a protective layer, limiting gas dissolution (McGinnis et al., 2006). Recent experimental work has looked into co-existing methane gas and hydrate within the gas hydrate stability zone (Sahoo et al., 2018a; Sahoo et al., 2018b; Sahoo and Best, 2021; Madhusudhan et al., 2022). Hydrate films on gas bubbles may also have some effect on the geophysical properties and lead to uncertainties in remote geophysical quantification of hydrates (e.g., Marín-Moreno et al., 2017; Sahoo et al., 2019). So, there is a need to develop robust models for integrating the effect of a) gas distribution and b) hydrate film thickness on different geophysical and mechanical properties of hydrate-bearing sediments. Such modelling needs quantitative constraints obtained from image analysis of how the gas bubble distribution and size change and how the hydrate film evolves.

Conventional X-ray computed tomography (XRCT) and synchrotron CT (SXRCT) have recently contributed to improving our understanding of phase evolution and spatial redistribution during hydrate formation in porous media (Jin et al., 2006; Seol et al., 2006; Konno et al., 2013; Jin et al., 2014; Yang et al., 2015b; Ai et al., 2017; Li et al., 2024). In particular, SXRCT can provide nanometric resolution (e.g., 370 nm in Murshed et al. (2008)) and reveal information such as the morphology of voids, volume of discrete inclusions, surface area, topology of grain networks and crystallite information (Lei et al., 2019a; Lei et al., 2019b; Nikitin et al., 2020; Nikitin et al., 2021; Zhao et al., 2022). XRCT has been extensively used in various studies to investigate the microstructure of gas hydrate-bearing sediments, primarily under excess-gas conditions (Yang et al., 2015a; Zhao et al., 2015; Lei et al., 2019b). Le et al. (2020) explored methane hydrate (MH) morphologies and pore habits, as well as water migration, at both the pore and sample scales. Chen and Espinoza (2018) observed Ostwald ripening-type changes in the spatial distribution of xenon hydrate within the pore space of sediments, formed using the excess-gas method, via XRCT. Similarly, Lei et al. (2019a) reported water migration during the formation of carbon dioxide hydrate in sediments.

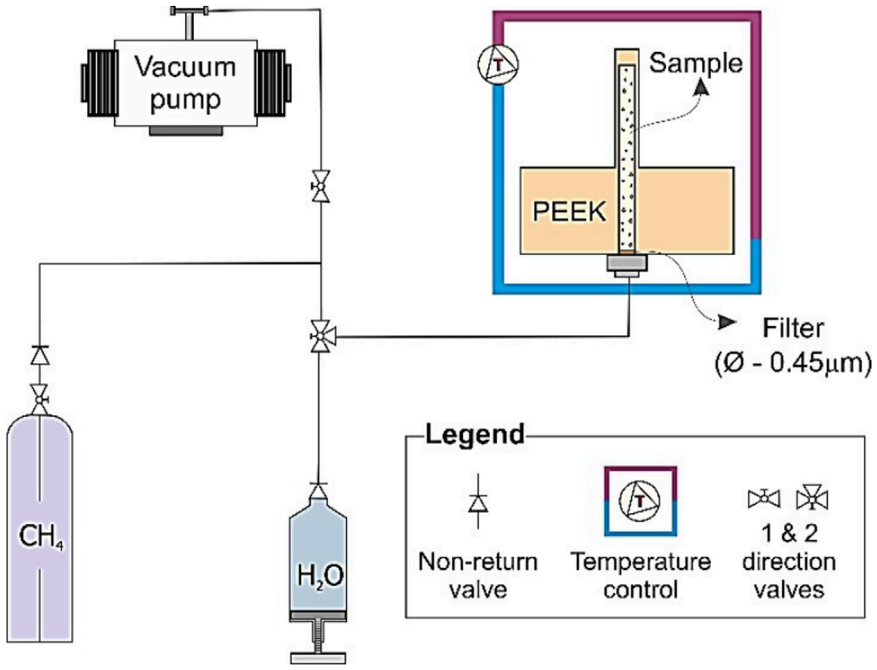

FIGURE 1
Schematic of the experimental setup for high resolution synchrotron imaging of methane hydrate formation from gas in water saturated sand after Sahoo et al. (2018a).

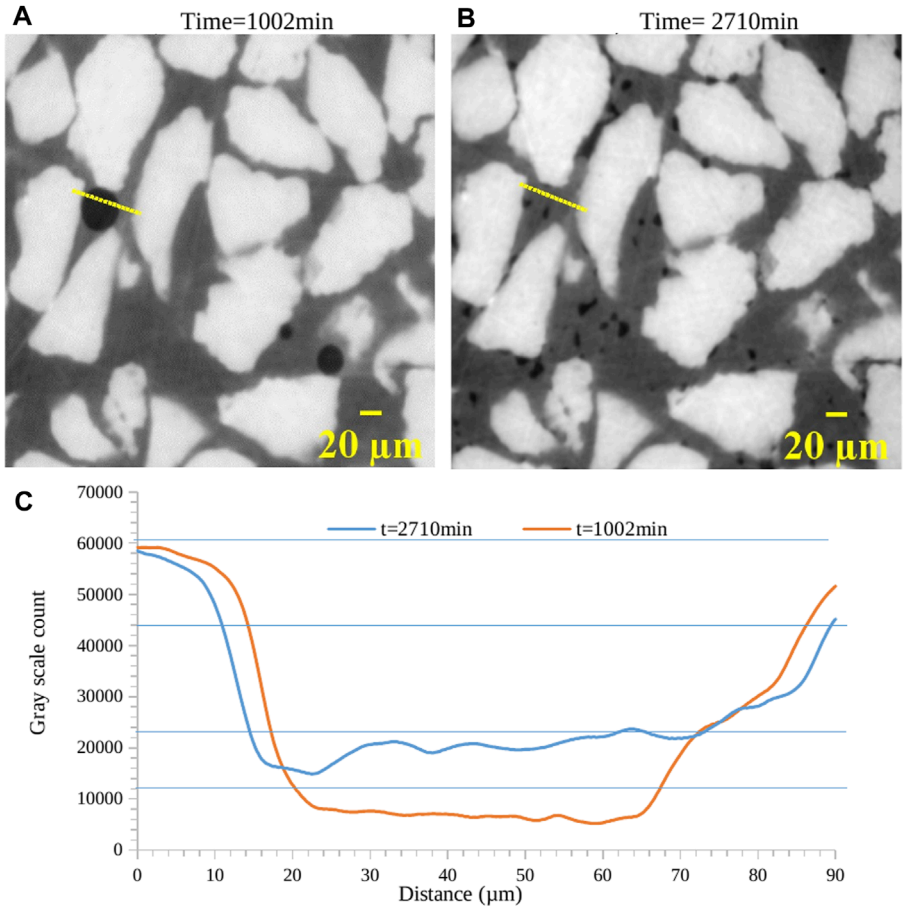

FIGURE 2
2D reconstructed tomography slices of the hydrate sample at different times **(A)** t = 1,002 min and **(B)** t = 2,710 min **(C)** Plot of gray levels of different phases, i.e., methane gas, methane hydrate, water and sand obtained during density normalization (details in section 3).

Recent studies by Lei et al. (2019a) have investigated methane hydrate morphologies and pore habits in sandy sediments under high-resolution imaging (approximately 2 µm). These studies initially used excess-gas conditions, followed by saline water injection, or directly used excess-water conditions. Kerkar et al. (2014) formed methane hydrate in saline water-saturated media (5 wt% $BaCl_2$) using the excess-water method and observed patchy methane hydrate distributions and heterogeneous hydrate accumulations via synchrotron radiation X-ray computed tomography (SXRCT). However, distinguishing between water and methane hydrate in XRCT images is indeed a challenge due to the poor contrast. The gray levels in XRCT images reflect the material's X-ray attenuation difference, primarily depending on the material's density and atomic number. To enhance XRCT/SXRCT image contrast, various methods have been employed, including the use of saline water solutions with heavy elements. For instance, Kerkar et al. (2014) used barium chloride ($BaCl_2$), Nikitin et al. (2020) used sodium bromide (NaBr), and Le et al. (2020) used potassium iodide (KI). These approaches significantly improve the ability to distinguish between different phases in the images.

Here, we use data from a 4D high-resolution synchrotron imaging experiment to visualize methane hydrate formation in partially water-saturated sand. The novelty of this work lies in our ability to track the dynamic behavior of methane gas bubbles and hydrate film growth across distinct hydrate formation stages.

2 Experimental procedure

We build on the experimental data from a high-resolution synchrotron imaging experiment presented in Sahoo et al. (2018a) to capture gas bubble dynamics during methane hydrate formation. Sahoo et al. (2018a) used time data for 805, 1,005, 1,410 and 2,710 min and investigated the overall distribution of the gas and hydrate. Here we use additional data for 1,045, 1,150, 1,270, and 1,605 min and reanalyzed the data to characterize gas bubble shape and size at each of these times and also measured thickness of the hydrate film. The present study incorporated all available and suitable time instants, in addition to those time instants analyzed in the previous study (Sahoo et al., 2018a). For example, in this paper we looked at all possible data where we could track a particular gas bubble and discuss its evolution. We also looked at tracking bubble size distribution at different time intervals.

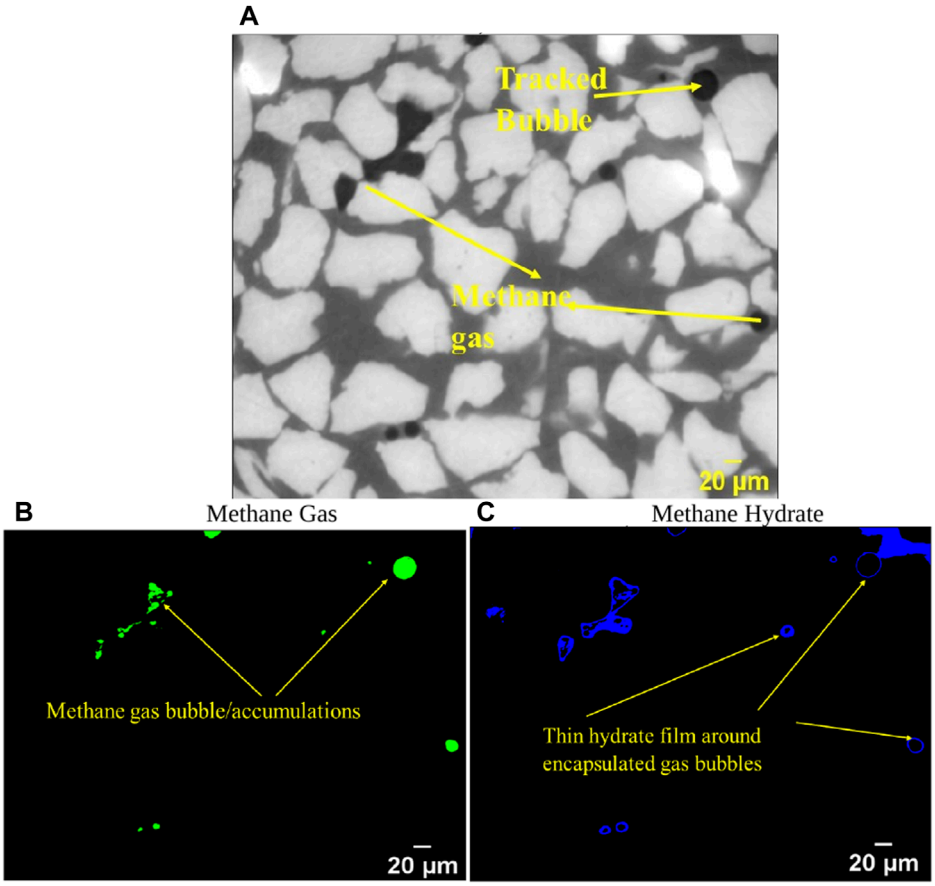

FIGURE 3
(A) Raw 2D image at time = 1,002 min. Methane gas distribution **(B)** and hydrate distribution **(C)** are depicted by green and blue color obtained using normalized density calibration (details in section 3).

The rig used in Sahoo et al. (2018a) consisted of a 0.8 mm wall thickness, 2 mm internal diameter, 10 mm height cylindrical holder made of polyether ether ketone (PEEK) to enhance the quality of the scanning, coupled to internal and external thermocouples for temperature control (Figure 1). The Leighton Buzzard sand (mean grain size d_{50} = 100 μm with an initial porosity of 35%) is a commonly available reservoir sand chosen as a non-reactive and clay free sediment based on commonly used gas hydrate modelling and experimental study of Priest et al. (2009), Best et al. (2013), Marín-Moreno et al. (2017), Sahoo et al. (2018a) The sample was initially dried, placed in the PEEK-holder, and subjected to vacuum. Then, the sample was partially (90%) saturated with a 35 gram/L NaCl solution (commonly accepted salinity of sea water) (Constable, 2013; Aladwani et al., 2024) and left for 3 days to ensure an effective pore fluid distribution by capillarity, which allows the excess water condition (Ellis, 2008; Priest et al., 2009). We have chosen an experimental condition to imitate those found in gas hydrate bearing sediments and also to compare with geophysical measurements done in another study by Sahoo et al. (2018a), Sahoo and Best (2021). The initial water saturation is chosen, so that we have enough volume occupied by gas based on the experiments. Thereafter, methane gas was injected into the holder at 10 MPa, and hydrates were formed by reducing the temperature to 2°C using a cryo jet stream connected to the rig. This setup simulates gas hydrate systems with localized gas flow such as those that may be found at the base of the gas hydrate stability zone (GHSZ) near gas chimneys (Ye et al., 2019).

A synchrotron source's monochromatic X-rays was used to image the formation of gas hydrate in the sand. The experiment was performed using a beam energy of 21 keV, 81-mm propagation distance and 200-ms exposure time (1,501 projections over 180° sample rotation), with 1.25×, 4×, and 10× objectives to obtain images at 1.625-, 0.625-, and 0.325-μm voxel size, respectively. The images were recorded using sensitive charged coupled device (CCD) cameras (2,560 × 2,160 pixels). The general scan frequency was around 30 min, with increased frequency to 15 min during rapid hydrate formation and reduced scan frequency during other times (1–3 h). We refer to Sahoo et al. (2018a) for further details.

3 Methodology

We obtained 2D slices using XRCT scans conducted at different times. These scans produce raw images that show the distribution of the different phases: sand grains, hydrate, water, and methane gas. The open-source software ImageJ was used to

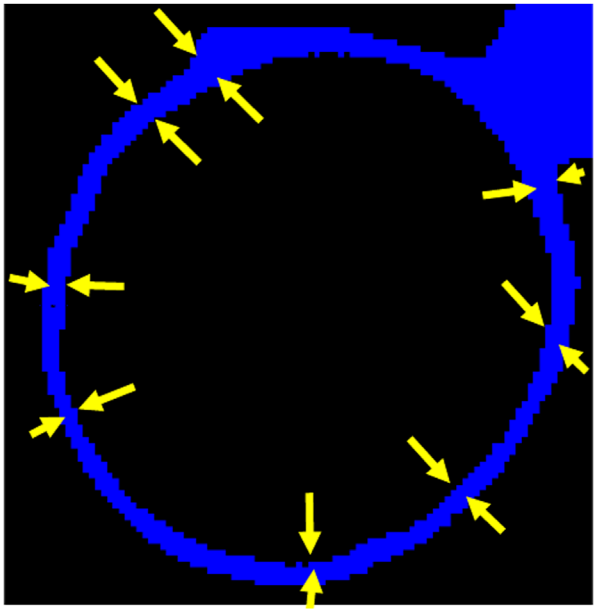

FIGURE 4
Representative hydrate film thickness measurement along the circumference at different points to determine average film thickness.

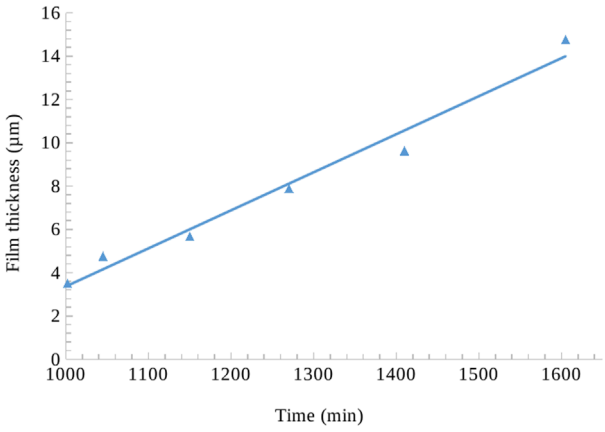

FIGURE 5
Evolution of hydrate film thickness over the course of the experiment.

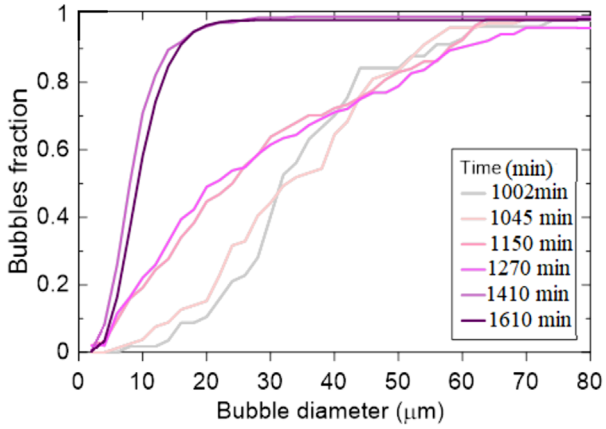

FIGURE 6
Cumulative size distribution plot of methane gas bubbles in the system at the different time instants.

process the image stacks. Figures 2A, B depict the original 2D slices obtained from synchrotron imaging for time instants, 1,002 min and 2,710 min. The yellow line in Figures 2A, B indicates approximately the same site at different times, and distance on the x axis in Figure 2C is the distance along this yellow line from left to right. Reconstruction of the distribution of the individual phases was done by measuring the grayscale count variation over the entire image area. The grayscale values of the CT images were calibrated to represent physical densities based on scans of the system without hydrate presence. This calibration follows the approach used in previous studies (Kneafsey et al., 2007; Iassonov et al., 2009) by correlating grayscale intensities to known density values for sand (2,650 kg/m^3), brine (1,025 kg/m^3), and methane gas (18 kg/m^3). The blue horizontal lines are boundary lines of grey scale count for each phase. After calibration, the grayscale values proportionally reflect the corresponding densities of these three components in regions without hydrate (Figure 2C). This establishes a relationship between grayscale intensity and density, allowing quantification of the hydrate formation and distribution from the CT data. A 5% confidence interval was used for the density-greyscale values (Sahoo et al., 2018a). For hydrate, we interpolated the grayscale value using a density of 925 kg/m^3. Methane hydrate and methane gas phases are distinctly identifiable in the 20–70 μm range. We obtained separate stacks of binary image files for sand, brine, hydrate, and methane gas by using the relationship between grayscale intensity and density.

In the initial stage of our investigation we measured the hydrate layer thickness surrounding a single gas bubble. We parsed through the 2D slices of methane gas (obtained from phase reconstruction) at different time instants. Figure 3 shows the distribution of methane gas and methane hydrate for the time of 1,002 min. In Figure 3A, grey area denotes brine, darker regions methane gas, and white regions are sand grains. Due to the similar density of brine and methane hydrate the former also appears grey. The methane gas bubble at the top-right corner is used to track hydrate film thickness variations over time. We chose one particular methane bubble for tracking the hydrate film thickness over time which could be seen at the next time instants without undergoing rupture or coalescence. It is evident that hydrate formation starts as a shell around a few methane gas bubbles (Figure 3C).

The hydrate film thickness around the gas bubble was meticulously measured by analyzing large datasets (file size around 6 GB for each time instant) using ImageJ software. To account for potential variations and eliminate localized errors, measurements were taken at multiple circumferential points along the bubble's periphery, as depicted in Figure 4. The straight-line tool was employed, carefully positioning lines perpendicular to the film's edge at regular intervals around the bubble. Multiple measurements were taken at each location to calculate an average representative thickness. This comprehensive approach was repeated for each

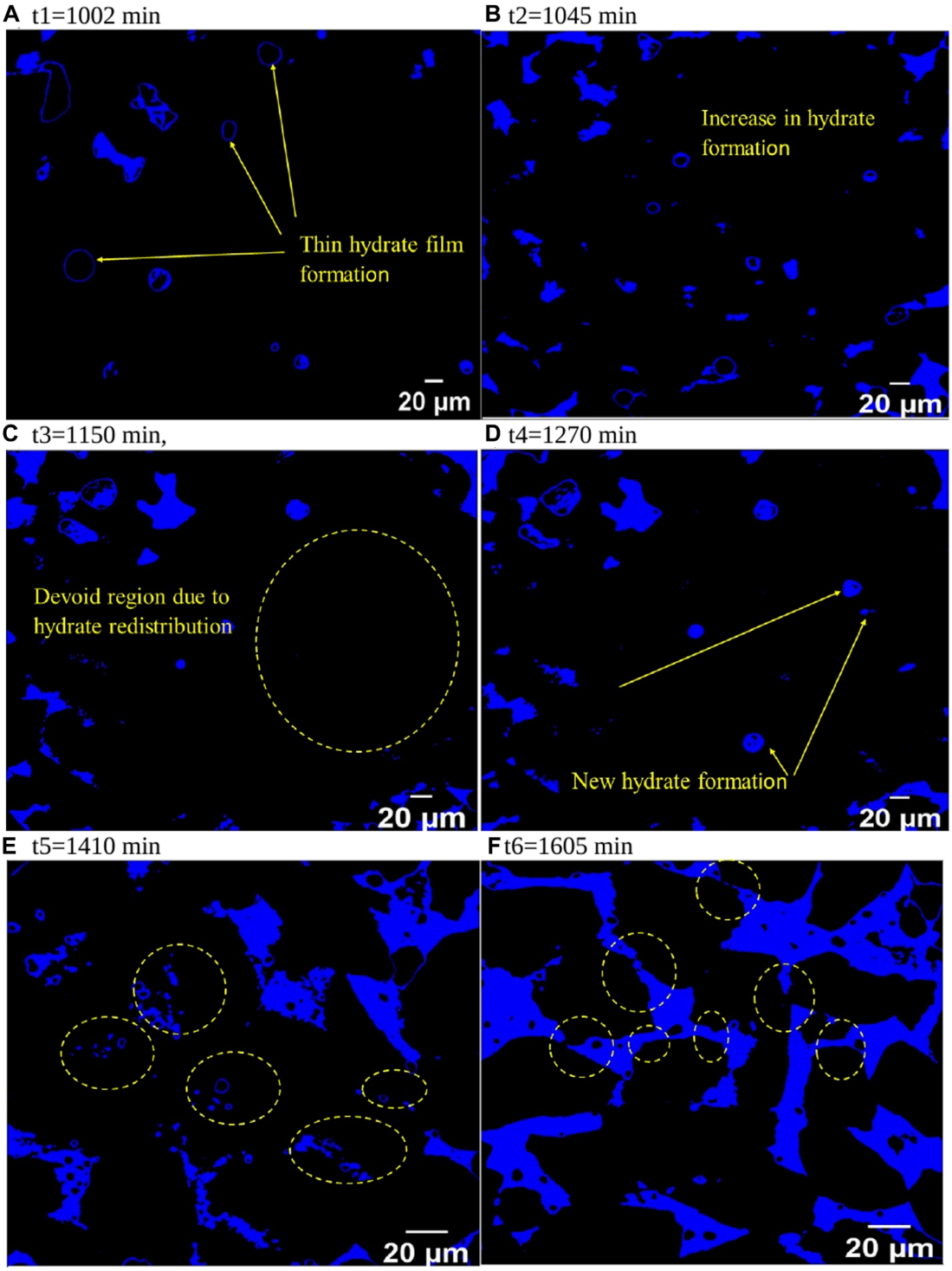

FIGURE 7
Methane hydrate growth (blue) in sediment pore space over time: **(A)** t1 = 1,002 min, initial hydrate film around methane bubbles; **(B)** t2 = 1,045 min, increased hydrate; **(C)** t3 = 1,150 min, hydrate-devoid region; **(D)** t4 = 1,270 min, new hydrate in devoid region; **(E)** t5 = 1,410 min, secondary hydrate formation; **(F)** t6 = 1,605 min, inter-pore hydrate bridges.

of the six distinct time instants (1,002, 1,045, 1,150, 1,270, 1,410, and 1,605 min) to monitor the evolution of film thickness during hydrate growth. The time frame selection was kept short due to the rapid hydrate formation during the initial stages. We used longer duration on the latter time instants to capture the slowing down phase of the hydrate formation when approaching full saturation. Henceforth, we adopt the widely used multiphase methodology of describing gas distribution as "bubbles" and "slugs"

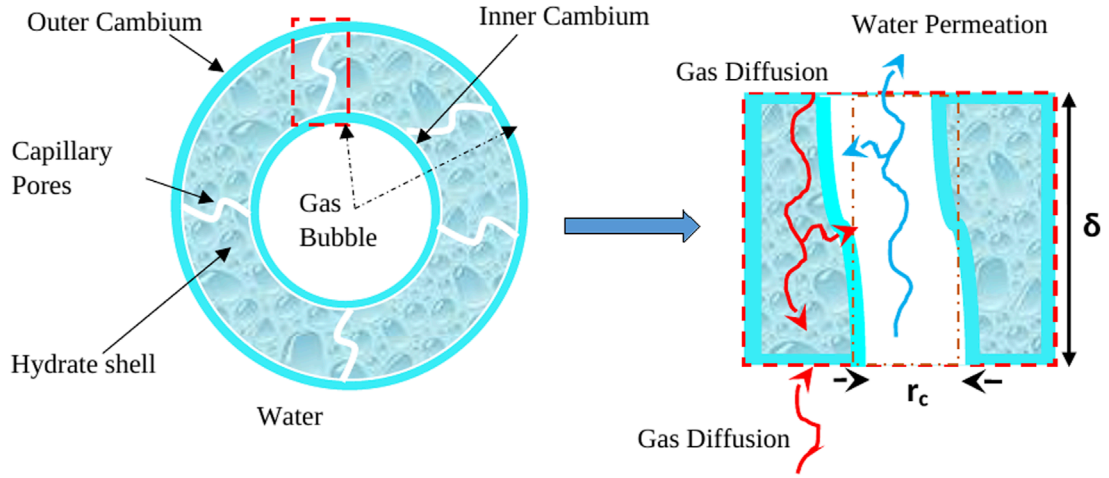

FIGURE 8
Hydrate shell growth with mass transfer pathways, adapted from Sun et al. (2019).

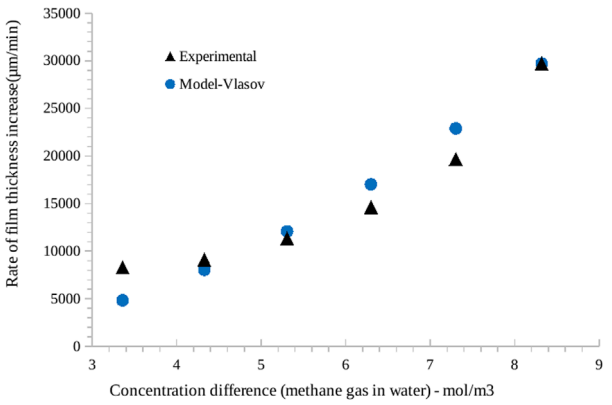

FIGURE 9
Comparison of rate of hydrate film thickness increase (as measured from synchrotron imaging) with theoretical model of Vlasov (2019). In x-axis, the concentration difference of methane gas in water at different temperatures is considered a driving force. Experimental data points are shown by black triangles (in case reader has b/w copy only), while blue dots show model prediction.

depending upon the classic spherical shape or distorted shape (Waltrich et al., 2013; Morgado et al., 2016).

4 Results and discussion

4.1 Experimental observations

Average hydrate film thickness of the tracked bubble increased by 320% during the experiment (Figure 5) in a span of 1605 min. Figure 6 shows a transition in gas bubble size distribution during hydrate formation, which suggests a general increase in bubble population of smaller bubbles with time. Furthermore, by grouping the gas distribution into three larger intervals with similar growing trends, i.e., t1 (1005 min)-t2 (1045 min), t3 (1150 min)-t4 (1270 min) and t5 (1410 min)-t6 (1605 min), we observe two major changes at ~1,170 min and ~1,410 min (Figure 6). We see distinct changes in gradient at these two times, indicating a decrease in the population of larger bubbles and an increase in the population of smaller bubbles.

Here we look at the distribution of gas and hydrate in the whole imaged area and how it varies with hydrate formation (Figure 7). Figure 7A shows bubbles or slugs of methane gas sparsely distributed and hydrate films around multiple gas bubbles following the first CT scan (t1 = 1002 min). These 2D slices only show the methane hydrate and the rest of the phases are set to black. Initially, hydrate forms as film around gas bubbles. Gas bubbles or slugs were preferentially distributed along the periphery, while fewer bubbles or slugs could be identified near the inner core, i.e., along the axis of the cylinder. Figures 7B–E shows the bubbles/slugs' size decreases with time while the hydrate film thickness increases. Hydrate formation appears uniformly distributed throughout the imaged area (Figure 7B). Figure 7C shows redistribution of hydrate formation the pore space, particularly around the cylinder's peripheral zone, and a significant increase of hydrate film thickness around the gas bubbles/slugs at t3 (1,150 min). At t4 (1,270 min), new hydrates appear around the sample's peripheral regions, which can originate by the partial rupture of the hydrate shells and methane release (Chen et al., 2014; Sahoo et al., 2018a; Sun et al., 2019) releasing multiple smaller gas bubbles. These gas bubbles/slugs then achieve thermodynamic equilibrium, forming smaller (secondary) hydrates. This explanation is supported by the observation of multiple smaller hydrates alongside a larger agglomerate of hydrates at t5 (1,410 min), with a more uniform distribution than at t3 (1,150 min).

In principle, hydrate film growth occurs from two sides, which can be described as inward and outward cambium growth (Liu et al., 2019; Sun et al., 2019). Figure 8 shows the multiple phenomena associated with the hydrate shell growth, including diffusion of free gas to the outer cambium, utilization of gas for hydrate formation within the pores, water permeation to the

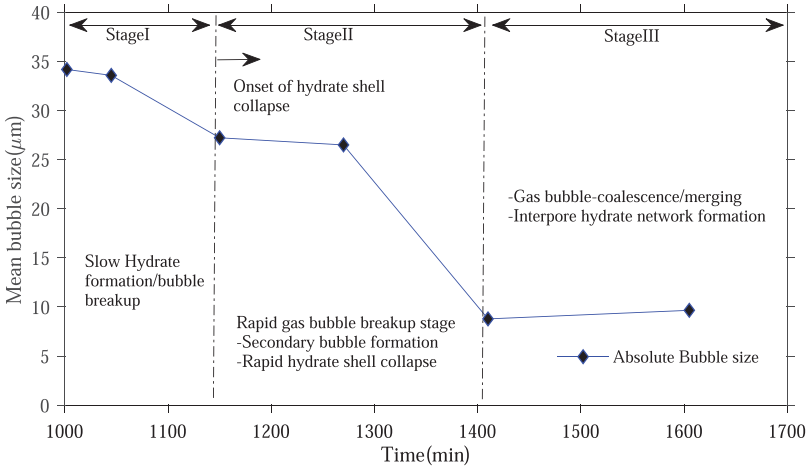

FIGURE 10
Different stages of hydrate growth depicting initial hydrate formation, onset of hydrate shell collapse, accelerated stage involving secondary gas bubbles formation and coalescence.

inner cambium through capillary pores, and gas diffusion from water to the outer cambium hydrate/water interface. However, when hydrate shell growth occurs without rupture, the diffusion limits the growing rate (Sun et al., 2018). When the hydrate shell ruptures, the gas contained within releases and forms smaller bubbles.

In our experiment, we think hydrate growth proceeds more from the outer shell and increases in thickness with the diffusion of gas from inside to outside through permeable channels. This is based on the evolving diameter of gas bubbles and increasing hydrate shell thickness. It is also expected that inner growth may occur, but our data cannot determine such growth.

4.2 Analytical validation of hydrate film growth

We compared our hydrate film thickness measurements with a model proposed by Vlasov (2019) to better understand the mechanisms controlling hydrate film growth and validate our measurements. The model assumes that the growth of the hydrate film along the gas-water interface depends on the movement of dissolved gas to the growing edge of the hydrate film. A hydrate film starts to grow along this gas-water interface. Hence, the rate of hydrate film growth depends on the balance between the diffusion velocity of dissolved methane and the kinetics of hydrate formation. The model considers two regimes for predicting the hydrate front propagation rate, i.e., kinetic and diffusion regimes. Both regimes operate in any given scenario, however, depending on the conditions, one of these regimes is the limiting factor for hydrate film growth. In the kinetic regime, the transport of dissolved gas to the hydrate formation front is faster than the hydrate formation reaction. In this case, the rate-limiting step is governed by the attachment to the hydrate crystal structure at the growth front, and the concentration of dissolved gas near the growth front stays close to the equilibrium solubility with the gas phase. In the diffusion regime, the hydrate formation reaction is faster than the transport of dissolved gas to the hydrate formation front. The kinetic reaction model assumes the concentration of dissolved gas (here methane) as the driving force for hydrate formation. The driving force is represented as $\Delta c = c_s - c_{eq}$, where c_s is the molar concentration of gas dissolved in water at liquid water-gas equilibrium and c_{eq} is the molar concentration at liquid water-hydrate-gas equilibrium.

The velocity of moving hydrate front data is determined using the procedure outlined in Freer et al. (2001) from the rate of film thickness increase with time. Figure 9 shows a good match between the model predictions and the experimentally measured hydrate film growth. Here we have run the model assuming a diffusion regime (all parameters are listed in Supplementary Material). The slight underprediction during the initial stages is indicative of the rapid hydrate formation kinetics, which progresses into diffusion-governed hydrate film growth during the later stages. We also run the model with kinetic regime, but the model results do not yield satisfactory agreement with experimental data. We calculate an average deviation error of 3.3% using Equation 1.

$$E(\%) = \frac{1}{N}\sum_{i=1}^{N}\frac{\left|R_{exp} - R_{model}\right|}{R_{exp}} \times 100 \quad (1)$$

Here, N is the total number of data points, and R_{exp}, R_{model} are the experimental and model rate of hydrate film growth, respectively. Overall, the model provides a decent prediction of experimentally measured hydrate film growth rate.

4.3 Insight and stages of hydrate growth

This section summarizes the different changes in gas bubble and hydrate morphology and distribution in sediments observed in our experimental study (Figure 10).

Stage I spans the initial hydrate nucleation and film formation phase, encompassing the first two times t1 (1,002 min) and t2 (1,045 min). Here, rapid initial hydrate film formation on gas bubbles occurs without significantly altering bubble size or distribution. Minimal dissolved gas transport limitations through the thin shell allows rapid hydrate film growth. Stage II captures the onset of hydrate shell instabilities and collapse, leading to secondary bubble formation. It includes time instants t3 (1,150 min) and t4 (1,270 min). Here, the hydrate film reaches a critical stability limit and partial rupture occurs, releasing new secondary bubbles that alter the bubble size distribution. The gas supply from breakdown leads to renewed localized hydrate film growth. Stage III incorporates the later phase of renewed bubble coalescence, pore-space redistribution, and the development of interpore hydrate frameworks. It spans time instants t5 (1,410 min) and t6 (1,605 min). Here, small bubbles coalesce and enable re-nucleation in small pores, exploiting residual water.

These three stages are represented by the significant change in the gradient of the lines in Figure 6B. The change in gradient clearly highlights how the distribution of gas bubbles changes with time. As the stages change from I to III, large bubbles are consumed by hydrate formation and smaller bubbles dominate the system. It seems there is a limit to the minimum gas bubble size, as depicted from the slight increase in average bubble size in t6 compared to t5 (Figure 10). Such observation is also shown in Figure 6B, where the curve hints at a minimum bubble size for the system. Our experiment was carried out for a limited time, and we should not conclude the minimum bubble size for natural systems is represented by our measured minimum size. However, we can indeed hypothesize that for laboratory studies forming hydrates from gas, there is likely a minimum gas bubble size limit.

5 Summary and conclusions

We employed 4D time-lapse synchrotron imaging of methane hydrate formation and focused on the evolution of free gas bubbles and hydrate film thickness over a duration of ~26 h. Initially, a thin hydrate film encapsulated gas bubbles, which later increased in thickness to undergo shrinking, wrinkling, and rupture due to internal gas consumption. The gas bubble size within the system varied widely with elapsed time. Initially, the mean gas bubble size was found to be 34.2 μm (t = 1002 min), while the final mean gas bubble size was reduced to 9.26 μm (t = 1605 min). We conclude:

1. The breakup of larger gas bubbles into smaller ones during hydrate formation indicates that there is a thermodynamic drive for the system to minimize gas bubble size.
2. The coalescence of the gas bubbles is limited by both hydrate film and the pore-hydrate framework. This allows the presence of discrete bubbles in the system.
3. Under the laboratory conditions of our study, the system transitions from a kinetic dominated regime to a diffusion dominated regime with increasing hydrate film growth.

Data availability statement

The raw data supporting the conclusions of this article will be made available by the authors, without undue reservation.

Author contributions

SK: Formal Analysis, Validation, Visualization, Writing–original draft, Writing–review and editing. SS: Conceptualization, Investigation, Methodology, Writing–original draft, Writing–review and editing. IF: Visualization, Writing–review and editing. HM-M: Formal Analysis, Writing–review and editing. HS: Formal Analysis, Writing–original draft. BM: Investigation, Writing–review and editing. CM: Funding acquisition, Writing–review and editing. AA: Funding acquisition, Writing–review and editing. AB: Funding acquisition, Supervision, Writing–review and editing.

Funding

The author(s) declare that financial support was received for the research, authorship, and/or publication of this article. The experimental work was funded NERC, UK grant NE/J020753/1. SK was funded by Newton Bhabha Fellowship grant 2021-22.

Acknowledgments

We thank the Swiss Light Source, SLS, Switzerland for funding the beam time to conduct the synchrotron imaging experiment. The authors are grateful to the editors and reviewers.

Conflict of interest

The authors declare that the research was conducted in the absence of any commercial or financial relationships that could be construed as a potential conflict of interest.

Publisher's note

Supplementary material

The Supplementary Material for this article can be found online at: https://www.frontiersin.org/articles/10.3389/feart.2024.1438185/full#supplementary-material

References

Ai, L., Zhao, J., Wang, J., and Song, Y. (2017). Analyzing permeability of the irregular porous media containing methane hydrate using pore network model combined with CT. *Energy Procedia* 105, 4802–4807. doi:10.1016/j.egypro.2017.03.950

Aladwani, N. S., North, L. J., Falcon-Suarez, I. H., and Best, A. I. (2024). Shale distribution effects on the joint elastic–electrical properties in reservoir sandstone. *Geophys. Prospect.* 72, 633–656. doi:10.1111/1365-2478.13331

Babaee, S., Hashemi, H., Naidoo, P., and Ramjugernath, D. (2021). Application of gas hydrates in the separation and purification of xenon from a mixture of xenon and argon. *J. Chem. Eng. Data* 66, 3815–3825. doi:10.1021/acs.jced.1c00435

Best, A. I., Priest, J. A., Clayton, C. R. I., and Rees, E. V. L. (2013). The effect of methane hydrate morphology and water saturation on seismic wave attenuation in sand under shallow sub-seafloor conditions. *Earth Planet. Sci. Lett.* 368, 78–87. doi:10.1016/j.epsl.2013.02.033

Chen, X., and Espinoza, D. N. (2018). Ostwald ripening changes the pore habit and spatial variability of clathrate hydrate. *Fuel* 214, 614–622. doi:10.1016/j.fuel.2017.11.065

Chen, L., Sloan, E. D., Koh, C. A., and Sum, A. K. (2014). Methane hydrate formation and dissociation on suspended gas bubbles in water. *J. Chem. Eng. Data* 59, 1045–1051. doi:10.1021/je400765a

Constable, S. (2013). Review paper: instrumentation for marine magnetotelluric and controlled source electromagnetic sounding. *Geophys. Prospect.* 61, 505–532. doi:10.1111/j.1365-2478.2012.01117.x

Cordes, E. E., Jones, D. O. B., Schlacher, T. A., Amon, D. J., Bernardino, A. F., Brooke, S., et al. (2016). Environmental impacts of the deep-water oil and gas industry: a review to guide management strategies. *Front. Environ. Sci.* 4. doi:10.3389/fenvs.2016.00058

Ellis, M. H. (2008). *Joint seismic and electrical measurements of gas hydrates in continental margin sediments*. Southam: University of Southampton. Available at: https://eprints.soton.ac.uk/63293/ (Doctoral Thesis, 284pp).

Freer, E. M., Sami Selim, M., and Dendy Sloan, E. (2001). Methane hydrate film growth kinetics. *Fluid Phase Equilib.* 185, 65–75. doi:10.1016/S0378-3812(01)00457-5

Guimin, Y., Hao, J., and Qingwen, K. (2022). Study on hydrate risk in the water drainage pipeline for offshore natural gas hydrate pilot production. *Front. Earth Sci.* 9. doi:10.3389/feart.2021.816873

Iassonov, P., Gebrenegus, T., and Tuller, M. (2009). Segmentation of X-ray computed tomography images of porous materials: a crucial step for characterization and quantitative analysis of pore structures. *Water Resour. Res.* 45. doi:10.1029/2009WR008087

Inkong, K., Yodpetch, V., Veluswamy, H. P., Kulprathipanja, S., Rangsunvigit, P., and Linga, P. (2022). Hydrate-based gas storage application using simulated seawater in the presence of a Co-promoter: morphology investigation. *Energy and Fuels* 36, 1100–1113. doi:10.1021/acs.energyfuels.1c03877

Jin, S., Nagao, J., Takeya, S., Jin, Y., Hayashi, J., Kamata, Y., et al. (2006). Structural investigation of methane hydrate sediments by microfocus X-ray computed tomography technique under high-pressure conditions. *Jpn. J. Appl. Phys.* 45, L714. doi:10.1143/JJAP.45.L714

Jin, Y., Konno, Y., and Nagao, J. (2014). Pressurized subsampling system for pressured gas-hydrate-bearing sediment: microscale imaging using X-ray computed tomography. *Rev. Sci. Instrum.* 85, 094502. doi:10.1063/1.4896354

Kerkar, P. B., Horvat, K., Jones, K. W., and Mahajan, D. (2014). Imaging methane hydrates growth dynamics in porous media using synchrotron X-ray computed microtomography. *Geochem. Geophys. Geosystems* 15, 4759–4768. doi:10.1002/2014gc005373

Kneafsey, T. J., Tomutsa, L., Moridis, G. J., Seol, Y., Freifeld, B. M., Taylor, C. E., et al. (2007). Methane hydrate formation and dissociation in a partially saturated core-scale sand sample. *J. Pet. Sci. Eng.* 56, 108–126. doi:10.1016/j.petrol.2006.02.002

Konno, Y., Jin, Y., Uchiumi, T., and Nagao, J. (2013). Multiple-pressure-tapped core holder combined with X-ray computed tomography scanning for gas-water permeability measurements of methane-hydrate-bearing sediments. *Rev. Sci. Instrum.* 84, 064501. doi:10.1063/1.4811379

Le, T.-X., Bornert, M., Aimedieu, P., Chabot, B., King, A., and Tang, A.-M. (2020). An experimental investigation on methane hydrate morphologies and pore habits in sandy sediment using synchrotron X-ray computed tomography. *Mar. Pet. Geol.* 122, 104646. doi:10.1016/j.marpetgeo.2020.104646

Lei, L., Liu, Z., Seol, Y., Boswell, R., and Dai, S. (2019a). An investigation of hydrate formation in unsaturated sediments using X-Ray computed tomography. *J. Geophys. Res. Solid Earth* 124, 3335–3349. doi:10.1029/2018jb016125

Lei, L., Seol, Y., Choi, J.-H., and Kneafsey, T. J. (2019b). Pore habit of methane hydrate and its evolution in sediment matrix–Laboratory visualization with phase-contrast micro-CT. *Mar. Pet. Geol.* 104, 451–467. doi:10.1016/j.marpetgeo.2019.04.004

Li, Y., Hao, Y., Wu, P., Hu, W., and Song, Y. (2024). Mechanical behavior of hydrate-bearing clayey-silty sediments in the south China sea: strain-rate dependency. *Energy and Fuels* 38, 5959–5973. doi:10.1021/acs.energyfuels.4c00399

Liu, Z., Sun, B., Wang, Z., and Chen, L. (2019). New mass-transfer model for predicting hydrate film thickness at the gas-liquid interface under different thermodynamics-hydrodynamics-saturation conditions. *J. Phys. Chem. C* 123, 20838–20852. doi:10.1021/acs.jpcc.9b03843

Madhusudhan, B. N., Sahoo, S. K., Alvarez-Borges, F., Ahmed, S., North, L. J., and Best, A. I. (2022). Gas bubble dynamics during methane hydrate formation and its influence on geophysical properties of sediment using high-resolution synchrotron imaging and rock physics modeling. *Front. Earth Sci.* 10, 877641. doi:10.3389/feart.2022.877641

Marín-Moreno, H., Sahoo, S. K., and Best, A. I. (2017). Theoretical modeling insights into elastic wave attenuation mechanisms in marine sediments with pore-filling methane hydrate. *J. Geophys. Res. Solid Earth* 122, 1835–1847. doi:10.1002/2016JB013577

McGinnis, D. F., Greinert, J., Artemov, Y., Beaubien, S. E., and Wüest, A. (2006). Fate of rising methane bubbles in stratified waters: how much methane reaches the atmosphere? *J. Geophys. Res. Ocean.* 111. doi:10.1029/2005JC003183

Morgado, A. O., Miranda, J. M., Araújo, J. D. P., and Campos, J. B. L. M. (2016). Review on vertical gas–liquid slug flow. *Int. J. Multiph. Flow.* 85, 348–368. doi:10.1016/j.ijmultiphaseflow.2016.07.002

Murshed, M. M., Klapp, S. A., Enzmann, F., Szeder, T., Huthwelker, T., Stampanoni, M., et al. (2008). Natural gas hydrate investigations by synchrotron radiation X-ray cryo-tomographic microscopy (SRXCTM). *Geophys. Res. Lett.* 35. doi:10.1029/2008GL035460

Nikitin, V. V., Dugarov, G. A., Duchkov, A. A., Fokin, M. I., Drobchik, A. N., Shevchenko, P. D., et al. (2020). Dynamic *in-situ* imaging of methane hydrate formation and self-preservation in porous media. *Mar. Pet. Geol.* 115, 104234. doi:10.1016/j.marpetgeo.2020.104234

Nikitin, V. V., Fokin, M. I., Dugarov, G. A., Drobchik, A. N., Andrade, V.De, Shevchenko, P. D., et al. (2021). Dynamic *in situ* imaging of methane hydrate formation in coal media. *Fuel* 298, 120699. doi:10.1016/j.fuel.2021.120699

Priest, J. A., Rees, E. V. L., and Clayton, C. R. I. (2009). Influence of gas hydrate morphology on the seismic velocities of sands. *J. Geophys. Res. Solid Earth* 114. doi:10.1029/2009JB006284

Rajnauth, J., Barrufet, M., and Falcone, G. (2010). "Potential industry applications using gas hydrate technology," in *Trinidad tobago energy resour. Conf.* SPE-133466-MS. doi:10.2118/133466-MS

Sahoo, S. K., and Best, A. I. (2021). The influence of gas hydrate morphology on reservoir permeability and geophysical shear wave remote sensing. *J. Geophys. Res. Solid Earth* 126, e2021JB022206. doi:10.1029/2021jb022206

Sahoo, Madhusudhan, B. N., Marín-Moreno, H., North, L. J., Ahmed, S., Falcon-Suarez, I. H., et al. (2018a). Laboratory insights into the effect of sediment-hosted methane hydrate morphology on elastic wave velocity from time-lapse 4-D synchrotron X-ray computed tomography. *Geochem. Geophys. Geosystems* 19, 4502–4521. doi:10.1029/2018GC007710

Sahoo, S. K., Marín-Moreno, H., North, L. J., Falcon-Suarez, I., Madhusudhan, B. N., Best, A. I., et al. (2018b). Presence and consequences of coexisting methane gas with hydrate under two phase water-hydrate stability conditions. *J. Geophys. Res. Solid Earth* 123, 3377–3390. doi:10.1029/2018JB015598

Sahoo, S. K., North, L. J., Marín-Moreno, H., Minshull, T. A., and Best, A. I. (2019). Laboratory observations of frequency-dependent ultrasonic P-wave velocity and attenuation during methane hydrate formation in Berea sandstone. *Geophys. J. Int.* 219, 713–723. doi:10.1093/gji/ggz311

Seol, Y., Kneafsey, T. J., Tomutsa, L., and Moridis, G. J. (2006). "Preliminary relative permeability estimates of methane hydrate-bearing sand," in *TOUGH symposium 2006* (Berkeley, California, USA: Lawrence Berkeley National Laboratory), 35–43. Available at: https://digital.library.unt.edu/ark:/67531/metadc882658/.

Sloan, E. D., Jr (2003). Fundamental principles and applications of natural gas hydrates. *Nature* 426, 353–359. doi:10.1038/nature02135

Sun, X., Wang, Z., Sun, B., Chen, L., and Zhang, J. (2018). Modeling of dynamic hydrate shell growth on bubble surface considering multiple factor interactions. *Chem. Eng. J.* 331, 221–233. doi:10.1016/j.cej.2017.08.105

Sun, B., Liu, Z., Wang, Z., Chen, L., Li, H., and Duan, W. (2019). Experimental and modeling investigations into hydrate shell growth on suspended bubbles considering pore updating and surface collapse. *Chem. Eng. Sci.* 207, 1–16. doi:10.1016/j.ces.2019.06.004

Urych, T., Chećko, J., Magdziarczyk, M., and Smoliński, A. (2022). Numerical simulations of carbon dioxide storage in selected geological structures in north-western Poland. *Front. Energy Res.* 10. doi:10.3389/fenrg.2022.827794

Vlasov, V. A. (2019). Diffusion-kinetic model of gas hydrate film growth along the gas–water interface. *Heat. Mass Transf.* 55, 3537–3545. doi:10.1007/s00231-019-02671-5

Waltrich, P. J., Falcone, G., and Barbosa, J. R. (2013). Axial development of annular, churn and slug flows in a long vertical tube. *Int. J. Multiph. Flow.* 57, 38–48. doi:10.1016/j.ijmultiphaseflow.2013.06.008

Wang, Z., Li, F., Fan, T., Xiong, W., and Yang, B. (2015). Research on the application of gas hydrate in cool storage air conditioning. *Procedia Eng.* 121, 1118–1125. doi:10.1016/j.proeng.2015.09.116

Xu, H., Khan, M. N., Peters, C. J., Sloan, E. D., and Koh, C. A. (2018). Hydrate-based desalination using cyclopentane hydrates at atmospheric pressure. *J. Chem. Eng. Data* 63, 1081–1087. doi:10.1021/acs.jced.7b00815

Yang, L., Zhao, J., Liu, W., Li, Y., Yang, M., and Song, Y. (2015a). Microstructure observations of natural gas hydrate occurrence in porous media using microfocus X-ray computed tomography. *Energy and Fuels* 29, 4835–4841. doi:10.1021/acs.energyfuels.5b00881

Yang, L., Zhao, J., Liu, W., Yang, M., and Song, Y. (2015b). Experimental study on the effective thermal conductivity of hydrate-bearing sediments. *Energy* 79, 203–211. doi:10.1016/j.energy.2014.11.008

Ye, J., Wei, J., Liang, J., Lu, J., Lu, H., and Zhang, W. (2019). Complex gas hydrate system in a gas chimney, South China Sea. *Mar. Pet. Geol.* 104, 29–39. doi:10.1016/j.marpetgeo.2019.03.023

You, Z., Hao, Y., Hu, W., Shen, S., Wu, P., and Li, Y. (2023). Strength analysis of hydrate-bearing sandy sediments in excess gas and excess water based on drained triaxial compression tests. *Eng. Geol.* 325, 107292. doi:10.1016/j.enggeo.2023.107292

Zhan, L., Liu, B., Zhang, Y., and Lu, H. (2022). Rock physics modeling of acoustic properties in gas hydrate-bearing sediment. *J. Mar. Sci. Eng.* 10, 1076. doi:10.3390/jmse10081076

Zhao, J., Yang, L., Liu, Y., and Song, Y. (2015). Microstructural characteristics of natural gas hydrates hosted in various sand sediments. *Phys. Chem. Chem. Phys.* 17, 22632–22641. doi:10.1039/c5cp03698d

Zhao, J., Liu, C., Li, C., Zhang, Y., Bu, Q., Wu, N., et al. (2022). Pore-scale investigation of the electrical property and saturation exponent of archie's law in hydrate-bearing sediments. *J. Mar. Sci. Eng.* 10, 111. doi:10.3390/jmse10010111

frontiers | Frontiers in Earth Science

TYPE Original Research
PUBLISHED 03 September 2024
DOI 10.3389/feart.2024.1437255

OPEN ACCESS

EDITED BY
Weichao Yan,
Ocean University of China, China

REVIEWED BY
Muhsan Ehsan,
Bahria University, Pakistan
Jianchao Wang,
Laoshan Laboratory, China

*CORRESPONDENCE
Yue Xiao,
xiaoyue0324@petrochina.com.cn

RECEIVED 23 May 2024
ACCEPTED 08 August 2024
PUBLISHED 03 September 2024

CITATION
Xiao Y, Jiang W and Liang C (2024) Data-driven multiscale geomechanical modeling of unconventional shale gas reservoirs: a case study of Duvernay Formation, Alberta, West Canadian Basin. *Front. Earth Sci.* 12:1437255. doi: 10.3389/feart.2024.1437255

Data-driven multiscale geomechanical modeling of unconventional shale gas reservoirs: a case study of Duvernay Formation, Alberta, West Canadian Basin

Yue Xiao*, Weidong Jiang and Chong Liang

Research Institute of Petroleum Exploration and Development (RIPED), Beijing, China

The Duvernay Formation in Canada is one of the major oil and gas source formations in the Western Canadian Sedimentary Basin, located at its deepest point. While it demonstrates promising development potential, challenges arise in the urgent need for integration of geology and engineering models, as well as in optimizing sweet spots, particularly as infill wells and pads become central operational objectives for the shale gas field. A lack of the geomechanical understanding of shale gas reservoirs presents a significant obstacle in addressing these challenges. To overcome this, we implemented data acquisition and prepared historical models and profiles, resulting in an extended high-resolution geological and reservoir property model with a fine grid system. Subsequently, a 3D full-field multi-scale geomechanical model was constructed for the main district by integrating seismic data (100 m), geological structures (km), routine logs (m), core data (cm), and borehole imaging (0.25 m), following a well-designed workflow. The predicted fracturability index (brittleness) ranges from 0.6 to 0.78, and a lower horizontal stress difference (STDIFF) is anticipated in the target formation, Upper Duvernay_D, making it a favorable candidate for hydraulic fracturing treatment. Post-analysis of the multi-disciplinary models and various data types provides guidelines for establishing a specific big database, which serves as the foundation for production performance analysis and aggregate sweet spot analysis. Fourteen geological and geomechanical candidate parameters are selected for the subsequent sweet spot analysis. This study highlights the effectiveness of multi-scale geomechanical modeling as a tool for the integration of multi-disciplinary data sources, providing a bridge between geological understanding and future field development decisions. The workflows also offer a data-driven framework for selecting parameters for sweet spot analysis and production dynamic analysis.

KEYWORDS

data-driven, nature fracture evaluation, multiscale geomechanical model, Duvernay Formation, unconventional shale gas

1 Introduction

The development of unconventional resources, such as shale gas and tight gas, presents one of the largest challenges for the oil and gas industry. While the fundamental logistics for characterizing and developing unconventional plays are similar to those for conventional resources, the process is complicated by the heterogeneous and anisotropic nature of the reservoirs, as well as the limited operational and dynamic timescales from development to depletion. The industry is currently navigating the complexities of an integrated cross-functional process, where the optimal development plan relies on a multi-scale and multi-disciplinary workflow.

Recent geomechanical studies on shale gas and oil development (Dusseault, 2013) (Rodriguez-Herrera et al., 2013) have focused on several aspects, including experimental mechanical studies that primarily address wellbore integrity and the mechanical parameters of physical models (Mehana et al., 2022). These studies also involve the prediction and calculation of geomechanical properties under experimental conditions (Bohn et al., 2020), the establishment of geomechanical models (Srinivasan et al., 2022)$^{-}$ (Ma et al., 2022), the design of refracturing operations (Zoback et al., 2022), and well pad development (Liu et al., 2022)$^{-}$ (Kuroda and Hayate, 2022). When designing and optimizing multiple-stage hydraulic fracturing, the primary factors influencing the stress field at the target well location include production history, interference among stages, and frac-hit occurrences between wells. Furthermore, in formations where natural fractures (NFs) are well-developed (Weng et al., 2011), it is important to consider the mechanisms and patterns of fault and NF development, as well as the interactions between natural fractures and hydraulic fractures. In China, there has been a detailed discussion and investigation into the establishment and application of geomechanical models during the geological–engineering integrated development of unconventional shale gas plays (Liang et al., 2016)$^{-}$ (Chen et al., 2017).

The success of operations during the Shale Revolution in North America can be attributed to several factors, including technological innovations, management reforms, and the establishment of comprehensive databases by both government and commercial platforms, which enhance data exchange efficiency. Prominent commercial database platforms in Canada, such as GeoSCOUT (GeoSCOUT, 2024) and Canada Discovery (Canadian Discovery, 2024), along with Enverus (Enverus, 2024) in the United States, have significantly contributed to this landscape. Once a permit is granted, access to state government databases can be readily obtained, as federal and state governments impose regulations on the reporting frequency of well data and the updating of field data (State public database in United States, 2024). These commercial databases play a crucial role in operators' decision-making processes. Even before the shale play boom of the 2010s, technological advancements led to the daily generation of substantial datasets in the oil and gas upstream and downstream sectors. Research indicates that over half of the time of engineers and geoscientists is spent searching for and consolidating data before initiating multi-disciplinary analysis (Brule et al., 2009). Furthermore, major oil companies are reassessing how data quality and density influence engineering decisions (Gaillot et al., 2020). It is essential for drilling and completion engineers to conduct rigorous quality checks on interpreted data provided by geologists and geophysicists prior to modeling activities. Reservoir properties and geomechanical parameters must be inter-validated across multiple data sources and scales; otherwise, the inherent uncertainty in models may lead to unreliable calculations and predictions.

The integration of multi-disciplinary and multi-scale data for informed decision-making necessitates several critical

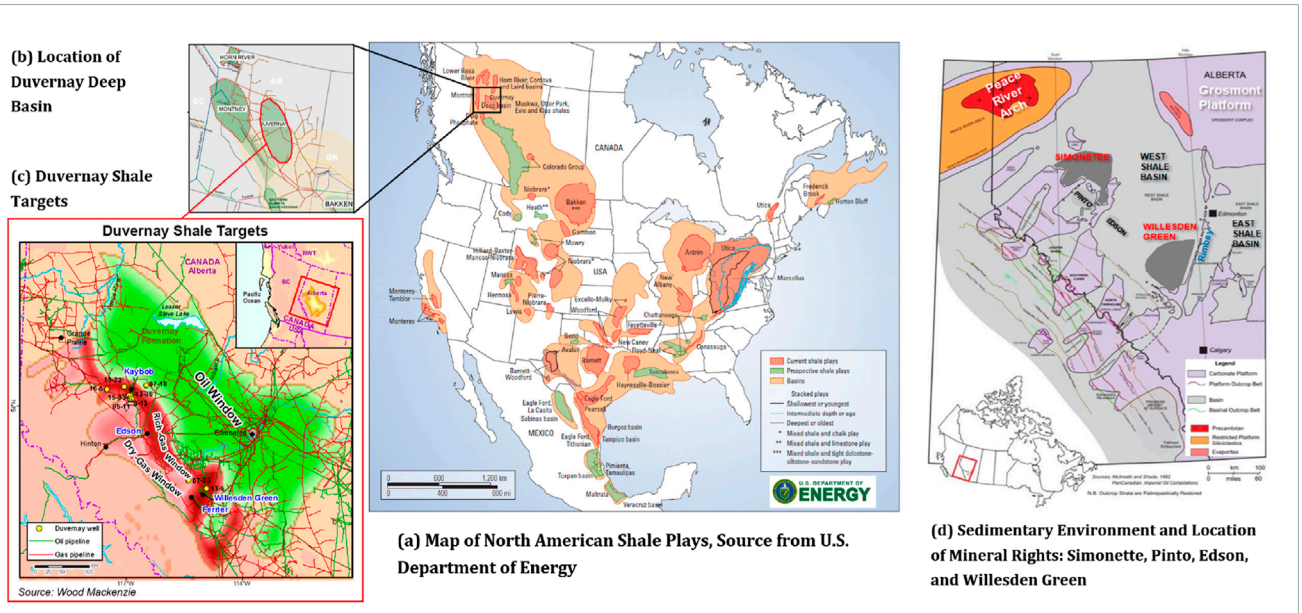

FIGURE 1
Overview of Duvernay Formation and project district: **(A)** distribution of shale plays in North America, source: U.S. Department of Energy (DOE); **(B)** location of Duvernay deep basin, source: U.S. Natural Gas Institute (NGI). **(C)** Duvernay shale target: Kaybob, Edson, Willesden Green, and Ferrier; well locations and oil–gas window, source: Wood Mackenzie. **(D)** Locations of mineral rights in Duvernay Formation and geological map of sedimentary basin (modified from Gilhooly et al., 2014) (Weissenberger et al., 2014).

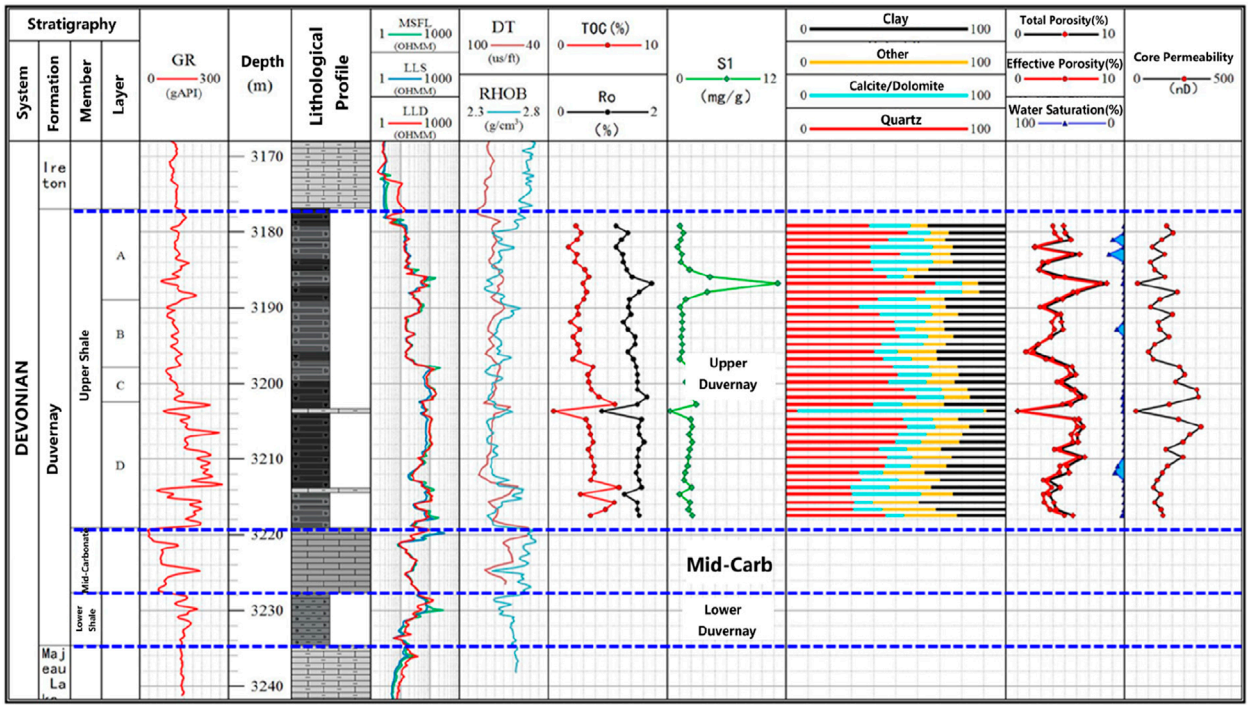

FIGURE 2
Duvernay composite stratigraphy of exploration well #1. Panel content in sequence: stratigraphy, gamma ray (GR), depth, resistivity logs (shallow, LLS; deep, LLD; medium, MSFL), sonic velocity and density logs (DT and RHOB), total organic carbon and maturity (TOC and Ro), absorbed gas Content (S1), lithological composition, log-interpreted porosity and water saturation, and core-based permeability.

TABLE 1 List of old data and model acquisition, data source, data type, and dataset details.

Source format	Data type	Details
3D seismic-interpreted results of the study area	3D seismic data volume	1
Well logging of the study area	Routine well logging data	40 vertical wells、314 horizontal wells
	Well logging interpretation	40 vertical wells
Stratigraphic information	Inter-well and separated layer logging data	Stratification at 40 vertical wells and 314 horizontal wells for Upper Duvernay-A, B, C, and D
	Structural map	Duvernay_Top and Duvernay_bottom
Production history of the study area	Accumulative production data (180–730 days)	Well count 260

components: 1) high-resolution geomodeling (Ehsan and Gu, 2020)⁻ (Amjad et al., 2023); 2) accurate interpretation of petrophysical and reservoir properties (Ehsan et al., 2024); and 3) robust computation and modeling of geomechanical parameters. Geomechanical modeling plays a pivotal role in bridging the gap between evaluation and design scenarios by incorporating geological complexity and addressing pre-existing mechanical discontinuities and anisotropic deformation, such as faults, bedding planes, and natural fractures (Eze and Hu, 2023), in conjunction with hydraulic fracturing systems. The development of a multi-scale geomechanical model facilitates the prediction of NFs across various scales and the upscaling of geomechanical parameters in three-dimensional distributions using advanced geostatistical methodologies.

By utilizing the geomechanical model, hydraulic fracturing simulations can optimize treatment designs for individual wells (Mariscal-Romero and Rodolfo, 2022) or across designated operational districts. This model effectively captures the evolution of *in situ* stresses induced by reservoir depletion, infill drilling, and refracturing interventions through iterative calculations, resulting in reliable production history matches (Xiao et al., 2022)⁻ (Pradhan et al., 2022) and accurate production forecasts, thereby

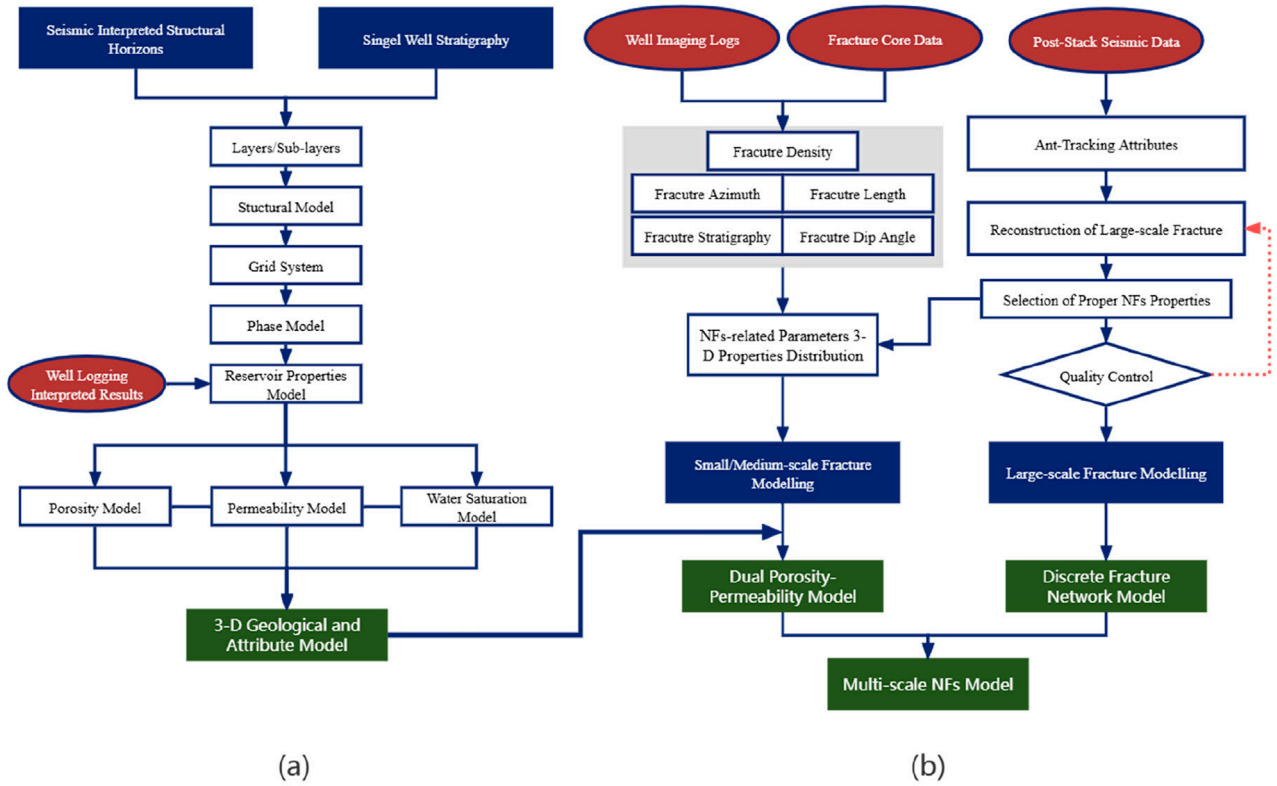

FIGURE 3
Integrated workflow of multi-scale geological modeling. **(A)** Flowchart adopted for reconstruction of the high-resolution geological model. **(B)** Workflow applied for multi-scale natural fracture (NF) prediction and evaluation.

TABLE 2 Simulation and calculation methodologies summary.

Modeling	Data preparation	Methodology
Attribute property modeling	Petrophysical analysis results from well log data	Sequential Gaussian simulation (SGS) (Verly, 1993)˙ (Sanei et al., 2023)
Multi-scale natural fractures evaluation	Seismic-interpreted ant-tracking body and borehole imaging data	Discrete fracture network (DFN) modeling
Natural fracture equivalent porosity and permeability calculation	Geological model and DFN model	Oda's method (Ghahfarokhi, 2017)
Missing DTs prediction	GR, RHOB, DTc	Artificial neural network (ANN) (Alameedy et al., 2022) (Eaton, 1972)
Overburden stress and pore pressure	Density logs	Eaton's method (Eaton, 1972)˙ (Legg, 2023)

enhancing the optimization of landing zone selections (Xiong, 2020). The Duvernay Formation, recognized as one of North America's most prominent unconventional shale plays (Kleiner, 2019) (Kleiner and Aniekew, 2019), offers an extensive array of case studies focusing on regional geomechanical assessments (Li et al., 2020)⁻ (Leshchyshyn and Thomson, 2016), optimization of hydraulic fracturing treatment parameters (Thomson et al., 2016)⁻ (Bowie, 2018), production prediction and enhancement (Hui et al., 2023), as well as seismic monitoring (Hui and Gu, 2023).

This article presents a case study on the integrated geological–engineering investigation of CNPC's Duvernay project in Simonette District, as submitted to the journal Frontiers in Earth Science. During the extensive data acquisition and processing phases, multi-disciplinary and multi-scale parameter calculations and modeling workflows for unconventional shale gas reservoirs were developed. First, the processing of multi-disciplinary input data and the related model assumptions are clarified and discussed in detail. Then, the workflows for the multi-scale geomechanical model

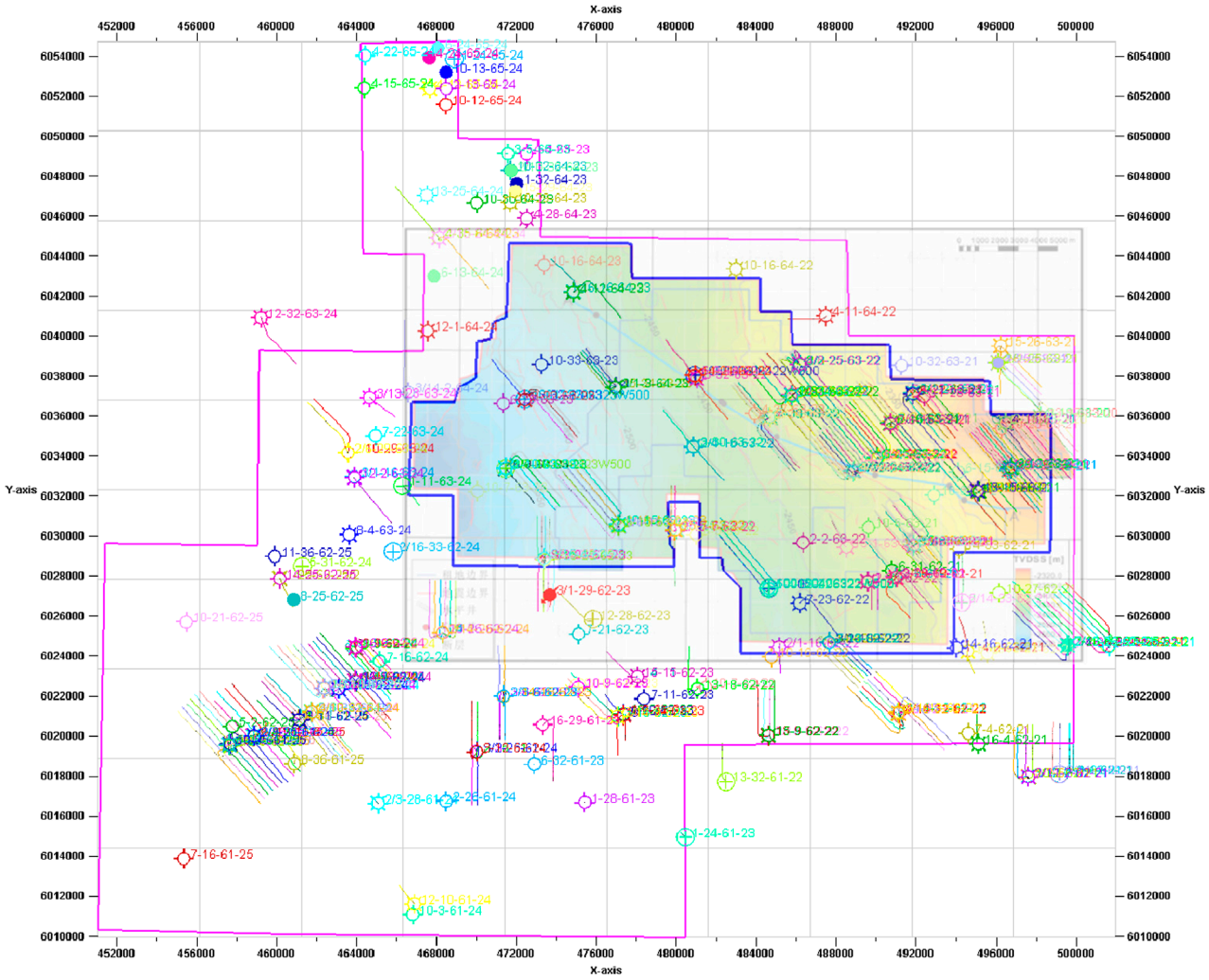

FIGURE 4
Comparison of old (navy blue) and new (magenta) study area with well locations in Duvernay Formation. The old one: 3D seismic interpreted structural tops of Duvernay Formation (early-stage geophysical data covered area).

and reservoir model are outlined, considering the data acquisition conditions established in the previous steps: 1) identification and modeling of NFs; 2) calculation of 1D geomechanical parameters for single wells; and 3) 3D geomechanical modeling and *in situ* stress predictions. Finally, the quality of the data is reassessed based on the multi-scale geomechanical model, and the controlling parameters for production performance are summarized for both geological and geomechanical candidates. This provides a foundation for the pre-construction of big data-based deep analysis. The development of a regional high-resolution reservoir attribute and geomechanical model offers valuable insights for parameter determination in sweet spot exploration and dynamic production analysis.

2 Project overview

The Duvernay Formation in Canada is a major oil and gas source formation located in the Western Canadian Sedimentary Basin, situated at the deepest point of the basin (Figures 1A, B). As a globally significant unconventional shale gas play, the formation has produced over 70 million barrels of equivalent gas from conventional reservoirs. The unconventional oil and gas zone spans an area of 6 million acres, contributing an estimated 110 to 190 billion barrels of equivalent oil resources. The target formation for the Duvernay project is the Devonian shale, which is rich in condensate oil.

The joint venture (JV) project began in 2012 with Encana (now Ovintiv), and the assets were segregated in 2020 when CNPC became the sole operator for the districts, including the studied area. The primary development area is Simonette, covering 254 km^2, which demonstrates strong development prospects for shale targets (Figure 1C). Dunn et al. (2012) illustrates a typical 3D sedimentary environment near Simonette, while Figure 1D marks the locations of other mineral rights within the Simonette region. The joint lands dip to the southwest. Over the past decade of full-scale development, the JV project has accelerated the iteration of unconventional resource

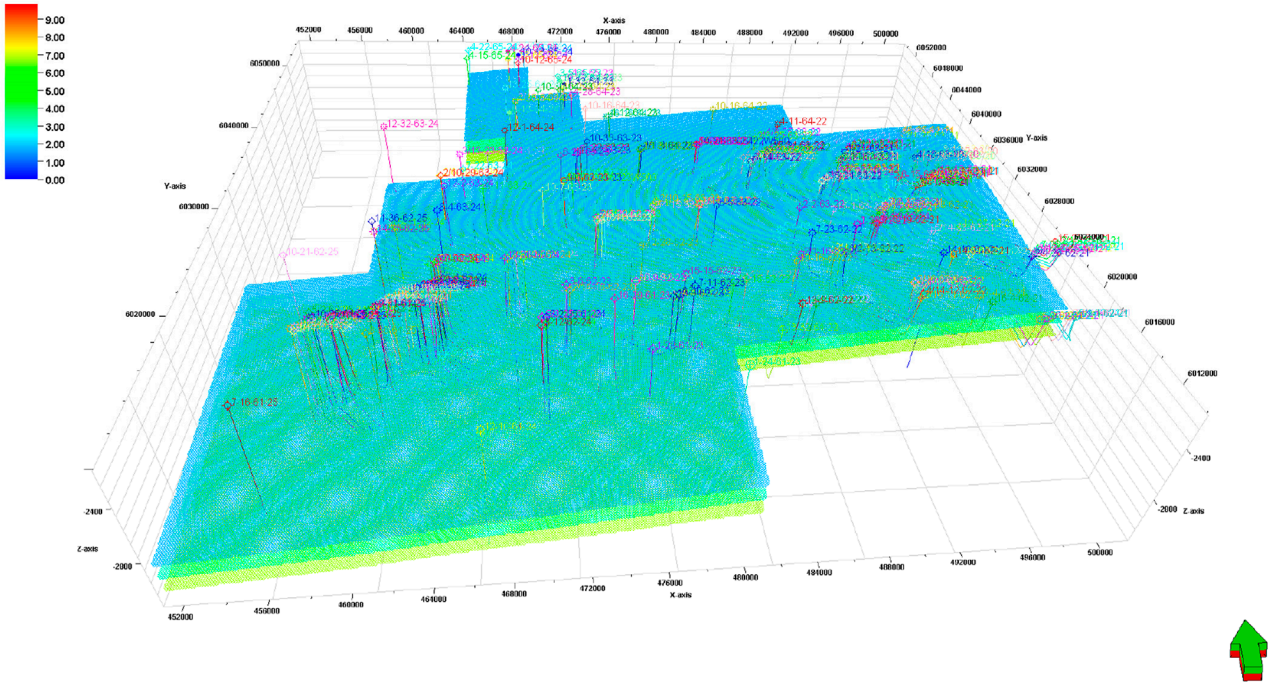

FIGURE 5
Geological grid system of the geological model in the studied area (layer Upper Duvernay_A with top, middle, and bottom geological grid).

TABLE 3 Grid system of all layers in the studied area, Resolution, and number count in the I * J * K direction of grids in each structural layer.

Layer/sublayer	Thickness (m)	Average H (m)	Horizontal grid resolution (m)	Vertical grid resolution (m)	I	J	K	Total grid count
A	2–19	12	100 × 100	0.23	498	565	50	14015400
B	2–13	6	100 × 100	0.13	498	565	50	14015400
C	0–11	4	100 × 100	0.1	498	565	50	14015400
D	0–25	14	100 × 100	0.27	498	565	50	14015400
Mid_Carb	3–25	9	100 × 100	0.17	498	565	50	14015400
Lower Duvernay	0–11	3	100 × 100	0.06	498	565	50	14015400
MLK	1–15	6	100 × 100	0.13	498	565	50	14015400
Total		54						98107800

development technologies, leading to a deeper understanding of the underground complexities and rock–liquid characteristics.

Petrophysical analyses were conducted on exploration wells as part of resource evaluation efforts during the early development stage. Although detailed discussions and consortium processes are beyond the scope of the current study, the results of the stratigraphical interpretation are presented in Figure 2. The Simonette Devonian formation features organic-rich shale with total organic carbon (TOC) levels ranging from 2% to 6%. It is vertically divided into three segments: Upper Duvernay shale, Middle Duvernay carbonate, and Lower Duvernay clay. The major production zone, the Upper Duvernay, is approximately 60 m thick and includes 10 m of limestone interlayers along with thin layers of clay limestone.

Characteristically, the Duvernay Formation is a classic high-resistivity shale reservoir with near-zero water saturation and interconnected organic porosity structures. Key coring and formation property observations confirm that permeable,

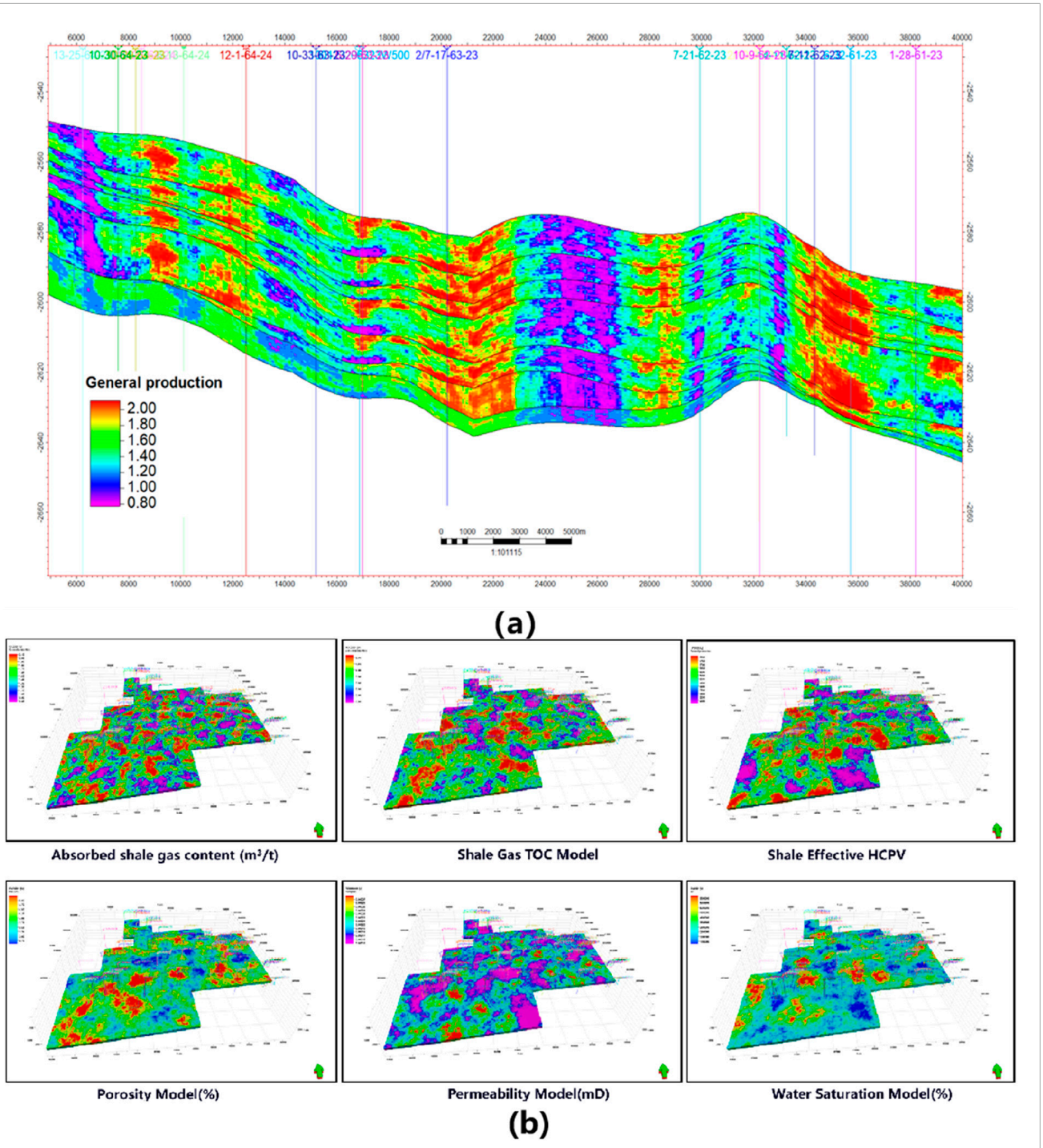

FIGURE 6
(A) Vertical profile of the absorbed shale gas content in the Duvernay Formation (m^3/t). **(B)** Reservoir parameter distribution in the 3D model. Absorbed shale gas content (m^3/t); shale gas total organic carbon (TOC); shale effective hydrocarbon pore volume (HCPV), porosity (%), permeability (mD), and water saturation (%).

interconnected effective porosity structures are accessible via highly connected, orthogonal fracture patterns. The Upper Duvernay is further subdivided into segments A, B, C, and D based on the TOC and lithological composition, with Upper Duvernay_D being identified as the most favorable landing zone due to its greater thickness and superior TOC performance.

We compare the reservoir properties of typical shale plays in North America with those of the Canadian Duvernay formation: Haynesville, Marcellus, Eagle Ford, and Barnett. Notably, unconventional plays in North America, such as Horn River, Bakken, and Marcellus, have achieved successful and economical production levels comparable to those found in the Duvernay Formation.

10.3389/feart.2024.1437255

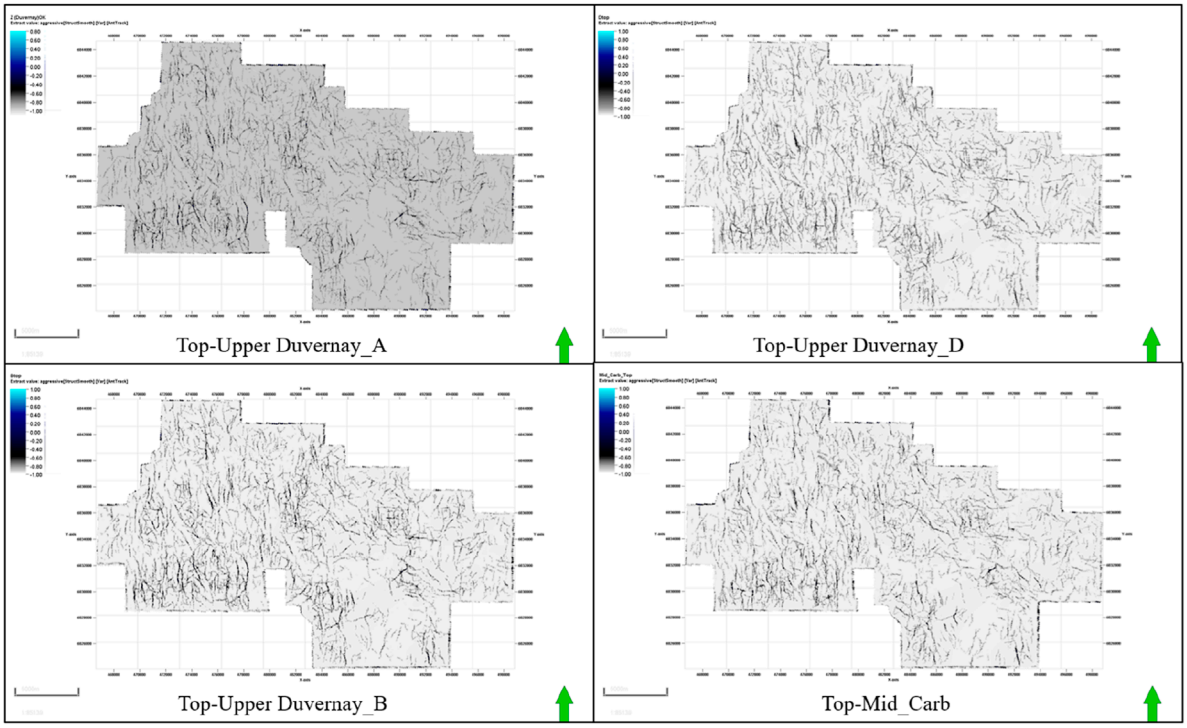

FIGURE 7
(A) Ant-tracking body model calculated from seismic interpretation along the eight structural surfaces across layers A to MLK of the Upper Duvernay. **(B)** Extraction of large-scale NFs from the ant-tracking attribute in the Duvernay Formation; NFs highly developed in Upper Duvernay_A, B, and D and Mid_Carb.

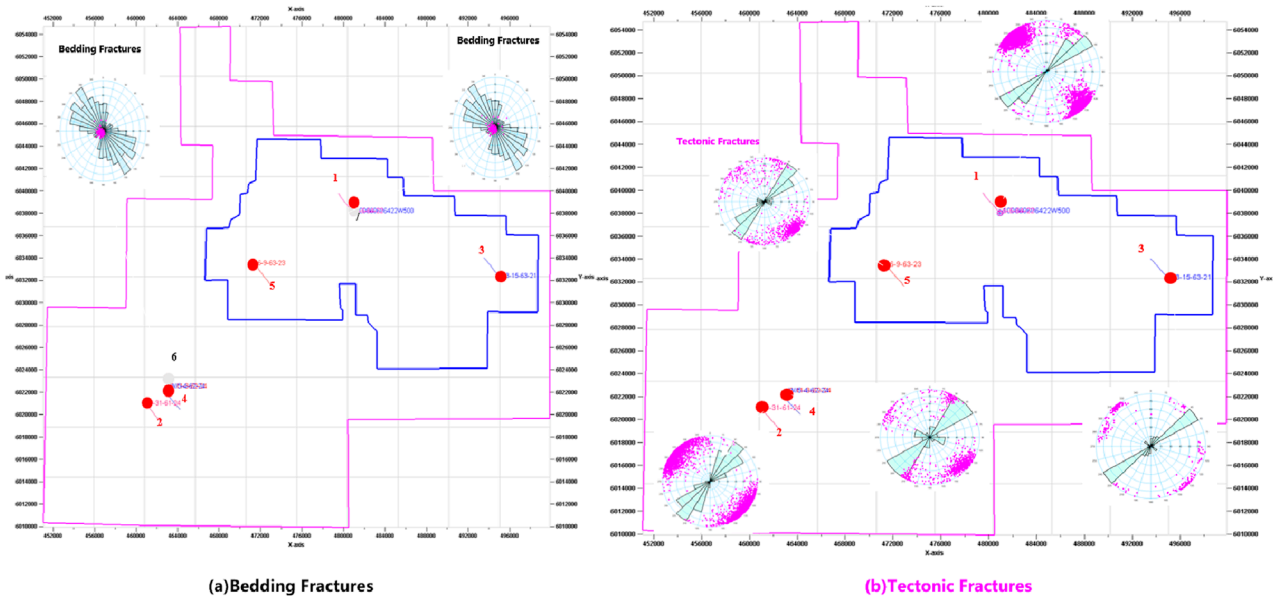

FIGURE 8
Well locations of **(A)** bedding fractures and **(B)** tectonic fractures in the study area, with the NF rosemap located in neighbor wells for well no. 1 to well No. 7.

3 Data acquisition and preparation

The primary task before undertaking multi-scale geomechanical modeling is the comprehensive assembly of data, which involves evaluating both the density and quantity of multi-source data within the studied area. Adequate data density is essential to ensure that sufficient effective data are available for most of the target district; this includes verifying the well count and ensuring that well data are sufficient to support the establishment of a foundational geological model, as insufficient data density can introduce significant uncertainty into the model from the outset. In terms of quantity, it is important to verify specific data types, such as reservoir pore pressure obtained from formation leak-off tests compared to measurements derived from diagnostic fracture injection tests; substantial discrepancies among these data sources can undermine their reliability and necessitate further investigation into their measurement processes and derivation methods. A summary of the current data acquisition efforts is provided in Table 1. Prior to any analysis or decision-making, integrating these data through various software tools from multiple vendors is critical for ensuring the robustness and accuracy of the subsequent analyses.

4 Problems and methodologies

Since the inception of the Joint Adventure Project in 2012, the targeted district has undergone significant changes, with infill drilling of wells and pads emerging as the predominant operational strategy during the middle-to-late stages of gas reservoir development. An analysis of current data acquisition along with historical models has identified several unresolved issues that impede future development.

i) 1) Absence of a discrete fracture network (DFN) model: the presence of horizontal beddings and well-developed high-angle natural fractures is advantageous for increasing the stimulated reservoir volume (SRV) and facilitating height-constrained fracture propagation. The lack of a DFN model poses substantial challenges to the development of a reliable reservoir depletion model and the optimization of the field development plan (FDP).
ii) 2) Lack of an integrated geological–engineering model: the existing geological model is limited to the original seismic explored area and does not incorporate geomechanical properties or *in situ* stress models. This limitation hinders the ability to conduct comprehensive reservoir and hydraulic fracturing simulations.
iii) 3) Ambiguity regarding dominant controlling factors: the primary factors influencing productivity and the enhancement of fracturing stimulation remain poorly defined.
iv) 4) Requirement for systematic sweet spot analysis: based on the current data acquisition efforts, improvement in data quality can be achieved by validating reservoir properties across multiple sources.

The concerns delineated in points iii) and iv) will extend beyond the scope of this study and will be addressed in subsequent publications. The reconstruction of a refined geological model and a multi-scale natural fracture DFN model will adhere to the integrated flowchart illustrated in Figures 3A, B. Furthermore, the prediction and calculation of the geomechanical model and three-dimensional stress distribution, as depicted in Figure 12, serve as critical inputs for optimizing hydraulic fracture design. These outputs,

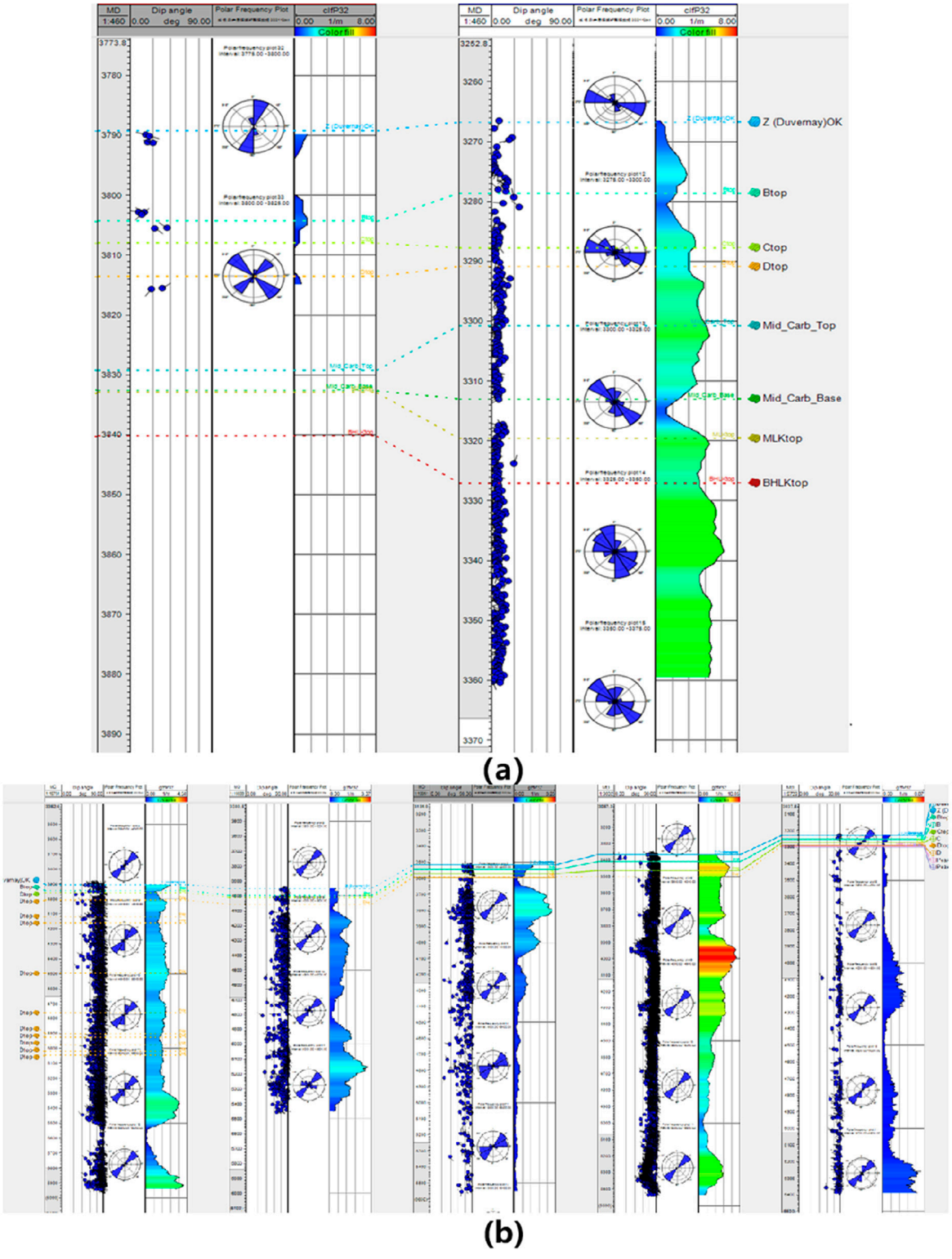

FIGURE 9
Cross-well plot for **(A)** bedding NF interpretation and **(B)**tectonic NF interpretation.

resulting from petrophysical analyses, highlight the geological complexity and anisotropy inherent in unconventional shale and tight gas reservoir developments. Advanced methodologies for hydraulic fracturing and flow simulation must account for multiple geological phenomena; failure to accurately capture fine-scale formation property inputs could lead to questionable

TABLE 4 Fracture strength prediction in borehole imaging logs.

NF prediction	Well no.	Fracture strength (P10)
Tectonic NFs	1	0.67
	2	1.76
	3	0.14
	4	4.59
	5	0.55
Bedding NFs	6	3.94
	7	0.47

predictions regarding hydraulic fracturing outcomes and effective SRV.

The methodologies utilized in establishing models and performing simulation upscaling are summarized in Table 2 and will be discussed in detail in the following sections.

5 Redefinition of geological models

The reconstruction of the multi-scale integrated geological model effectively utilizes all available data types, including drilling and completion data, well logging, seismic interpretation, sedimentary analysis, and reservoir characteristics. This process represents a fundamental workflow that requires meticulous processing and standardization of all data, whether in real-time or interpreted. The acquired drilling and completion data encompass wellhead locations, measured depth (MD), completion depths, and well trajectories. Well logging provides critical interpretations of lithology, reservoir properties, and stratigraphy derived from routine logs.

By integrating precise reservoir descriptions obtained from well log interpretations with seismic data, a three-dimensional geological structural model, geological grid system, and reservoir property model are constructed, as delineated in the flowchart given in Figure 3A, and detailed in Section 5.1, Section 5.2, and Section 5.3, respectively. The prediction and evaluation of NFs are detailed in Section 5.4, where the modeling of NFs builds upon the previously established geological and attribute models, resulting in a dual porosity–permeability model. Furthermore, as depicted in Figure 3B, medium and small NFs interpreted from borehole imaging and core data, combined with large-scale NFs extracted from ant-tracking data, contribute to the development of the multi-scale discrete fracture network (DFN) model, quantifying the strength and density of NFs.

In comparison to the original two-dimensional seismic exploration area, the current target model encompasses all production wells for PetroChina's Duvernay project in Simonette District, as depicted in Figure 4. The original geological model (navy-colored area) does not cover potential districts for infill pad or wells. Moreover, it dismisses more than half of the well information in the current mineral rights area. The new model (in magenta color) incorporates adequate well data while preserving an optimal level of data density, thereby mitigating the uncertainty associated with the model.

5.1 Geological structural modeling

During the process of structural modeling, seismic-interpreted layering positions are incorporated, utilizing constraints obtained from the layering at each well location. The workflow includes a quality control protocol for the structural layering model that encompasses 1) the conformity between well locations and the layering model, 2) conformity between the structural shape and the original structural map, and 3) accuracy of the layering contact relationships. The primary objective of these quality control measures is to achieve a strong correlation between the K elements related to layering and the initial findings from geophysical and geological studies, as well as to establish rational inter-layer contact relationships.

The final quality evaluation of the three-dimensional layering model indicates its effectiveness in accurately representing the overall structure of faults and sublayers, while also providing quantitative characteristics of minor structural changes within each layer and the outer geometry of the gas reservoir. Based on layer division data derived from drilling information, four series (Upper Duvernay, Mid_Carb, Lower Duvernay, and MLK) and eight structural surfaces have been established for seven geological layers and sublayers. Furthermore, the thickness distribution of each sublayer is calculated using a thickness contour map. The entire structural model extends from higher elevations in the west to lower elevations in the east in a monoclinic configuration, demonstrating reasonable structural inheritance in each layer with a gentle dip.

5.2 Geological grid system

The three-dimensional geological meshing constitutes the grid structure established on layering and faults, which is essential for supporting subsequent modeling and geomechanical analysis. The types, sizes, orientations, and magnitudes of the meshing collectively enhance the accuracy and reliability of the simulation results. A corner-point grid system is employed to capture the characteristics of discrete spatial locations through the coordination of eight hexahedral points. The undefined elemental lines are advantageous for reflecting the geological characteristics and geometry of the reservoir, particularly in complex gas reservoirs exhibiting well-developed natural fractures and structural variations.

The Petrel platform software is utilized to achieve this gridding objective, with the dimensions of the grid system primarily determined by well (pad) spacing, seismic trace spacing, and the computational capacity necessitated by the specific numerical model.

Meshing of the structural layering model results in a layering grid system comprising three horizontal components: top, middle,

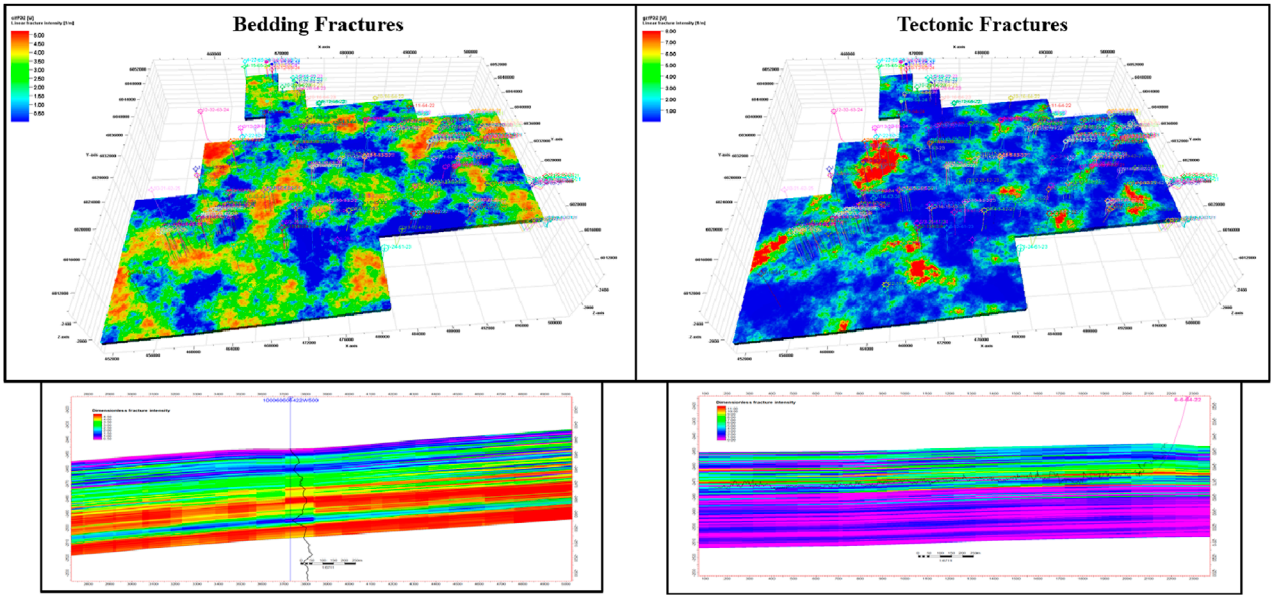

FIGURE 10
Strength attributes of medium-/small-scale NFs (interpreted bedding fractures and tectonic fractures), 3D model distribution in the top area and vertical profile in the bottom area.

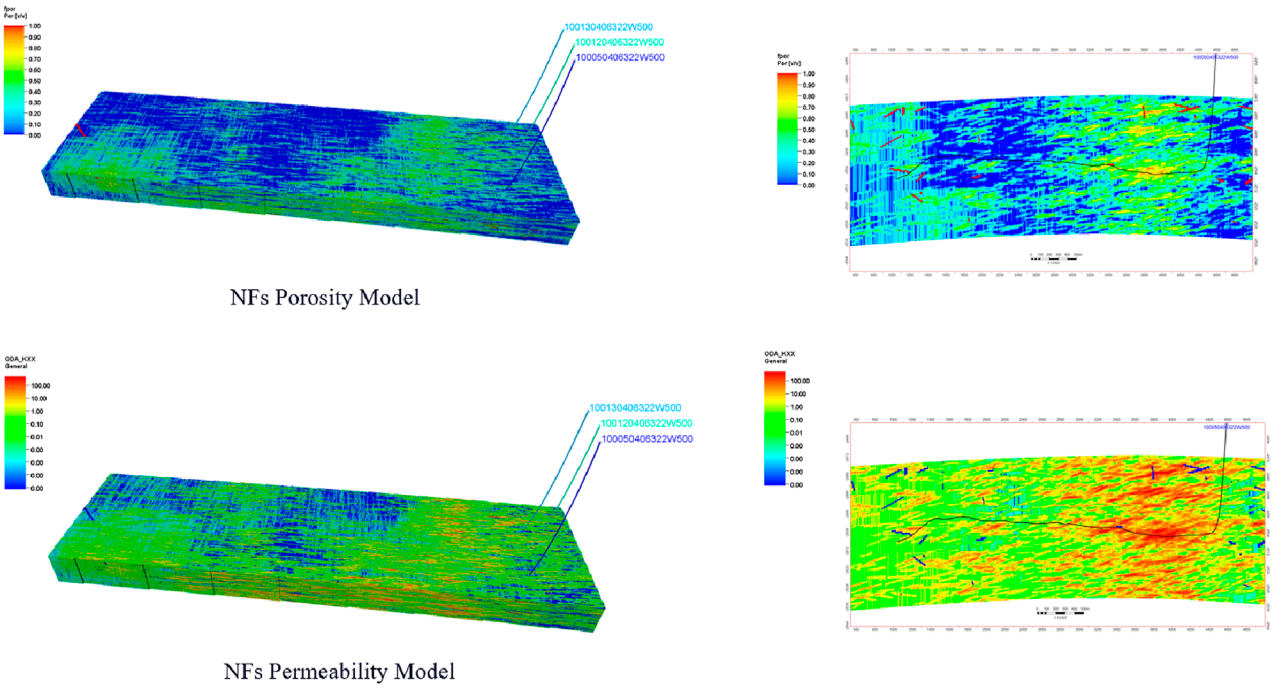

FIGURE 11
Porosity and permeability attributes of multi-scale NFs, 3D model, and vertical profile at the target well and pad location.

and base skeleton grids, which govern the overall construction of the three-dimensional model, as shown in Figure 5 the skeleton grids for Upper Duvernay_A. Quality control is also imperative to identify any abnormal twisting or folding of grids, particularly in proximity to faults, where a five-point key pillar gridding approach is applied; the location of the remaining two-point grids must be reconfirmed along the I and J directions. The new model builds upon geological and stratigraphical insights from previous analyses (as indicated in the workflow chart) and demonstrates a finer grid system, as detailed below.

10.3389/feart.2024.1437255

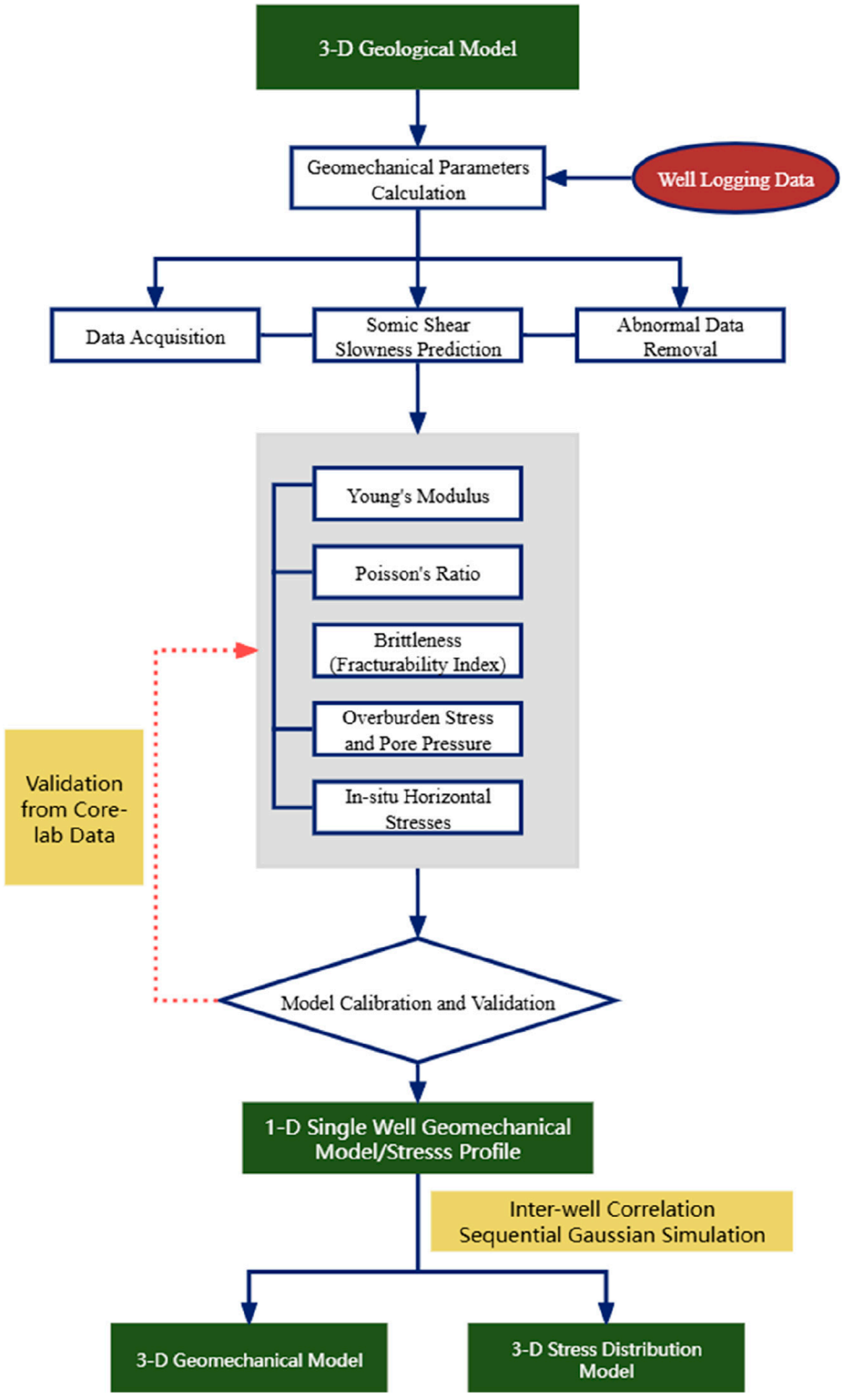

FIGURE 12
Flowchart for developing the multi-scale 3D geomechanical model, starts with results of reconstruction of the high-resolution 3D geological model in Figure 3.

i) The model encompasses an area of 1,321 km^2, integrating data from 40 vertical wells and 314 horizontal wells. The original seismic-interpreted area spans 414 km^2.

ii) Vertical layer distribution consists of Upper Duvernay, Mid_Carb, Lower Duvernay, and MLK sequentially, with Mid_Carb functioning as the carbonate inter-layer. The principal target

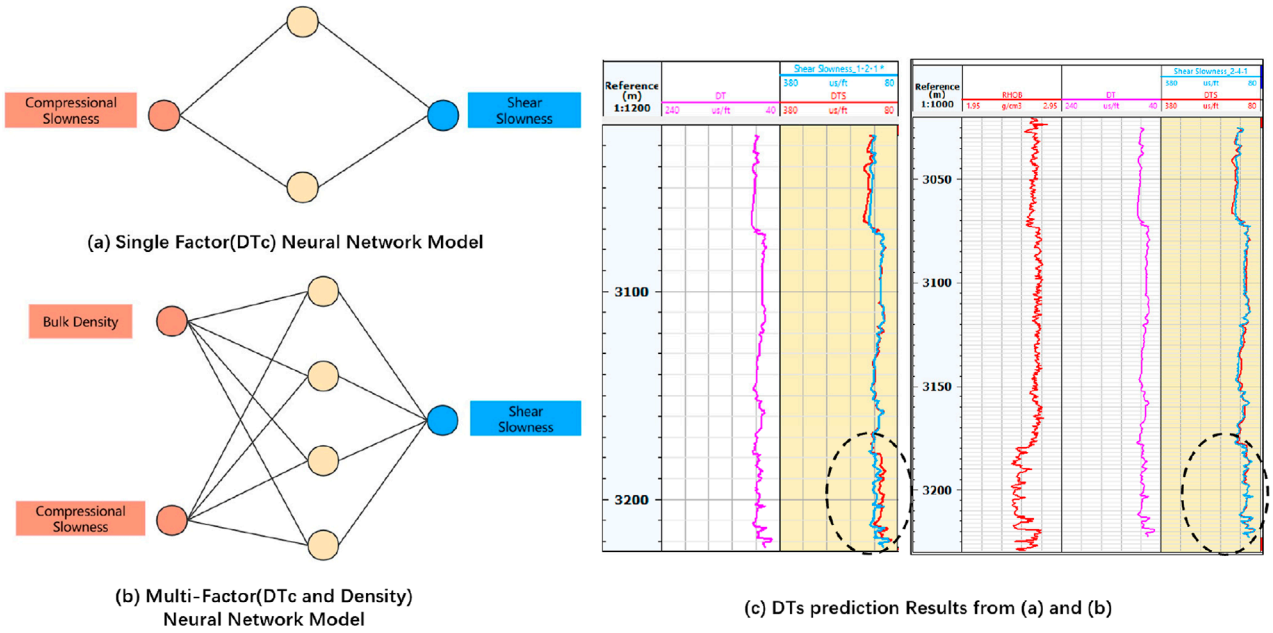

FIGURE 13
(A) Single-factor ANN model based only on DTc. **(B)** Multi-factor ANN based on both DTc and density. **(C)** Comparison of single-factor and multi-factor prediction on segment with real-time DTs.

layer, Upper Duvernay, is subdivided into A, B, C, and D sublayers.

iii) The structural layers of Upper Duvernay-A, Upper Duvernay-B, Upper Duvernay-C, Upper Duvernay-D, Mid_Carb, Lower Duvernay, and MLK exhibit an average thickness of approximately 13.7 m, with the most favorable layer being Upper Duvernay-D, which displays the greatest thickness of 25 m.

iv) The grid system of the geological model, within the target area of 1,321 km^2, features a horizontal distribution resolution of 100 × 100 m, resulting in a grid count of 498 × 565. The average grid thickness is 54 m, and vertical grid sizes range from 0.06 to 0.23 m, with each sublayer in Upper Duvernay divided into K = 50 sections. The total grid count for the high-resolution geological model exceeds 98 million (refer to Table 3 for details).

5.3 Attribute modeling

Petrophysical analysis is conducted for each well within the target area, and three-dimensional attributes are modeled using the sequential Gaussian simulation (SGS) methodology, upscaling petrophysical parameters at well locations for absorbed shale gas content (m^3/t), total organic carbon (TOC) (%), effective hydrocarbon pore volume (HCPV) (mg/g), porosity (%), permeability (mD), and water saturation (Sw) (%). Reservoir property models are assigned based on the geological model for each structural layer. Three-dimensional models illustrating absorbed shale gas content are presented in both vertical shown in Figure 6A and two-dimensional horizontal distribution profiles shown in Figure 6B. The average absorbed shale gas content ranges from 1.3 to 1.6 m^3/t, reaffirming Upper Duvernay-D as the most favorable sublayer, with maximum absorbed gas content reaching 2.2 m^3/t. Additional reservoir property models are depicted in Figure 6.

5.4 Natural fracture interpretation

The prediction and evaluation of multi-scale NFs are accomplished through the application of the discrete fracture network (DFN) technique. The flowchart illustrating DFN modeling for multi-scale NFs is presented in Figure 3B. The identification and classification of large-, medium-, and small-scale NFs are facilitated by results from seismic interpretation and borehole image logging data. Large-scale NFs, such as faults, are recognized based on pre-stack seismic interpretations, while medium- and small-scale NFs (including tectonic fractures, bedding fractures, and fissures) are recognized based on fracture strength attributes interpreted from borehole image logging data. The prediction of medium- and small-scale NFs is achieved by leveraging fracture density attributes referenced from fracture strength attributes.

The extraction of ant-tracking attributes from the eight structural surfaces across layers A to MLK is illustrated in Figure 7A. The planar configurations of ant-tracking attributes in each layer exhibit minimal variation with pronounced vertical inheritance. NFs are significantly more developed in the southwestern portion compared to other areas of the seismic exploration region. A total of seven large-scale NF systems have been extracted for layers A to MLK from the ant-tracking attributes, with the predominant NF direction orienting north–south, intersecting regionally across networks. Among the seven layers, large-scale NFs are more

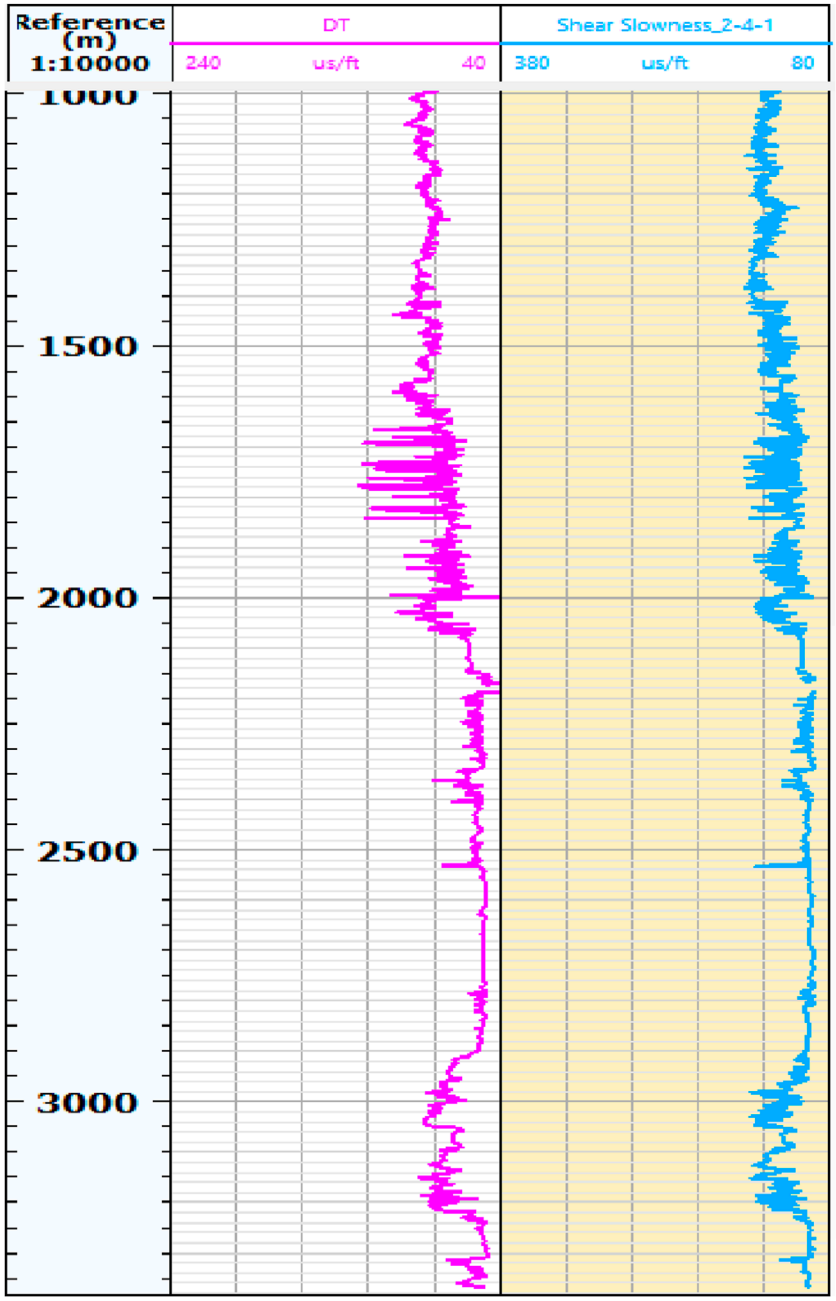

FIGURE 14
Prediction of DTs for missing segments lacking real-time data.

extensively developed in Upper Duvernay_A, B, D, and Mid-Carb, as shown in Figure 7B.

Figure 8 depicts the locations of wells with borehole imaging logs for bedding NF interpretation (Figure 8A) and tectonic NF interpretation (Figure 8B). A total of seven borehole imaging logs have been recorded and analyzed, with cross-well plots illustrating the tectonic fractures in two wells (Figure 9B) and bedding fractures in five wells (Figure 9A). In Figure 13, bedding fractures are notably more developed in Upper Duvernay, Mid_Carb, and MLK, with no indications present in Lower Duvernay. The interpretation of borehole imaging from these two wells predicts 382 bedding fractures, exhibiting dip angles ranging from 0° to 10°, with an average dip angle of 4° and northwest direction (142°). Tectonic NFs are estimated at a count of 15,503 with an average dip angle of 84° and a direction of northeast (45°). The predicted fracture strengths for the seven wells are summarized in Table 4.

The three-dimensional volumetric strengths of bedding fractures (Figure 10, left) and tectonic fractures (Figure 10, right) are upscaled from the interpreted results of well imaging logs in each well through interpolation. The vertical profiles of fracture strength at the wellbore plane correspond closely with the fracture

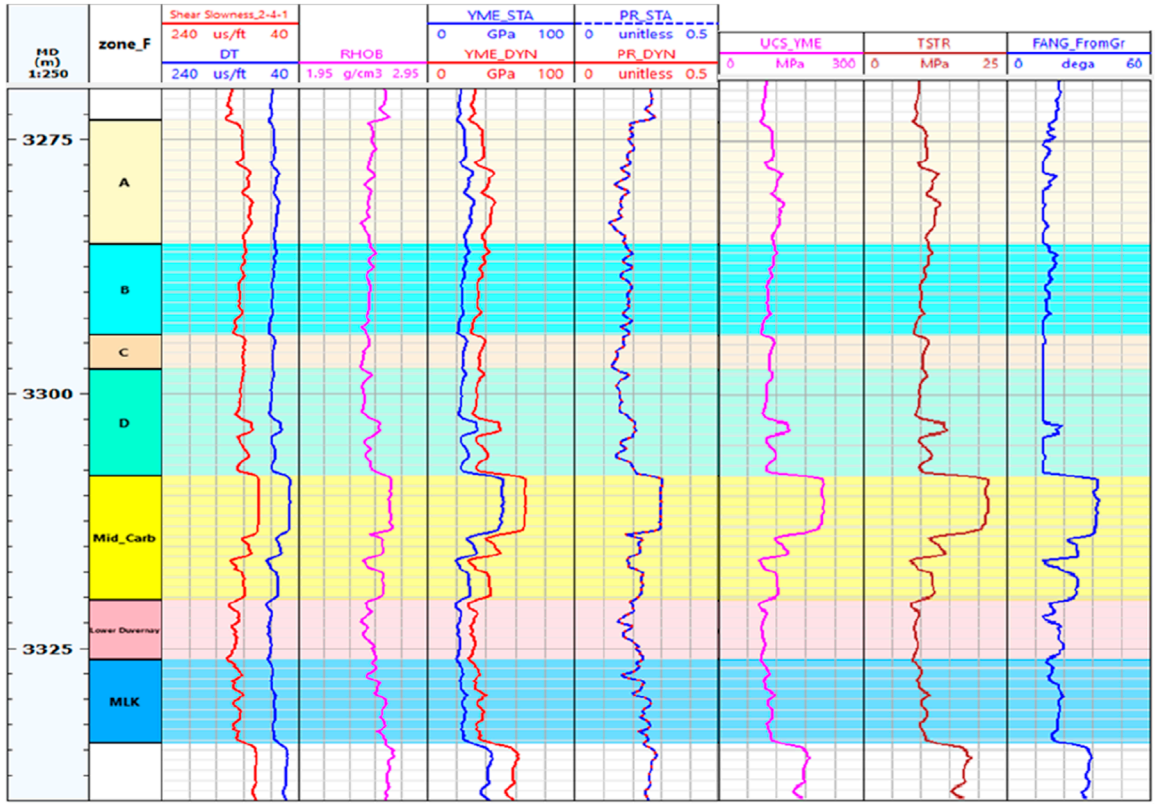

FIGURE 15
One-dimensional single-well geomechanical parameter calculation (real-time data: DTs and DTc; RHOB; dynamic and static Young's modulus, dynamic and static Poisson's ratio, UCS, TSTR, and frictional angle).

density curves for each well. The volumetric strength of fractures governs fracture development density, while the analysis of bedding fracture strike provides orientation insights. Consequently, the DFN (discrete fracture network) is established for the seven layers from A to MLK, comprising both bedding and tectonic fractures.

Employing Oda's approach, the fluid properties of the DFN model are upscaled for both macroscopic and microscopic fractures. The porosity and permeability attribute models are illustrated in Figure 11 at the target well pad location, in 3D view and vertical profile. The equivalent fracture porosity and fracture permeability are within the ranges of 0%–1% and 2–486 mD, respectively.

6 Multi-scale 3D geomechanical modeling

Utilizing the updated geological model grid system, a comprehensive geomechanical analysis is performed at each designated well location. Subsequently, the three-dimensional geomechanical parameters and stress distribution are simulated. Static mechanical parameters are derived from experimental rock mechanical measurements at specified depths, while continuous dynamic mechanical parameters are predicted from well logging data. To ensure accuracy in the modeling process, a conversion coefficient from dynamic to static parameters is applied. The foundational logic for developing a 1D single well geomechanical model is depicted in the accompanying flowchart (Figure 12). The 1D geomechanical model based on the single well location outputs both rock mechanical properties (Young's modulus, Poisson's ratio, and brittleness) and pressure–stress profile (overburden stress and pore pressure and *in situ* stresses).

6.1 Data quality check

The preliminary phase involves a comprehensive screening of well data, which encompasses laboratory core data, well logging data, and diagnostic fracture injection test (DFIT) data. A well is considered suitable for analysis only if all three data types are complete and have been cross-verified across multiple sources. By rigorously evaluating these real-time or derived datasets against established regional reservoir characteristics, particularly pore pressure, wells that exhibit anomalous values are excluded from the preliminary database. As a result, only 30 wells have successfully passed this initial screening.

Geomechanical parameter upscaling and calculations are commonly derived from specific logs, including gamma ray (GR), density log (RHOB), sonic compressional slowness (DTc), and sonic

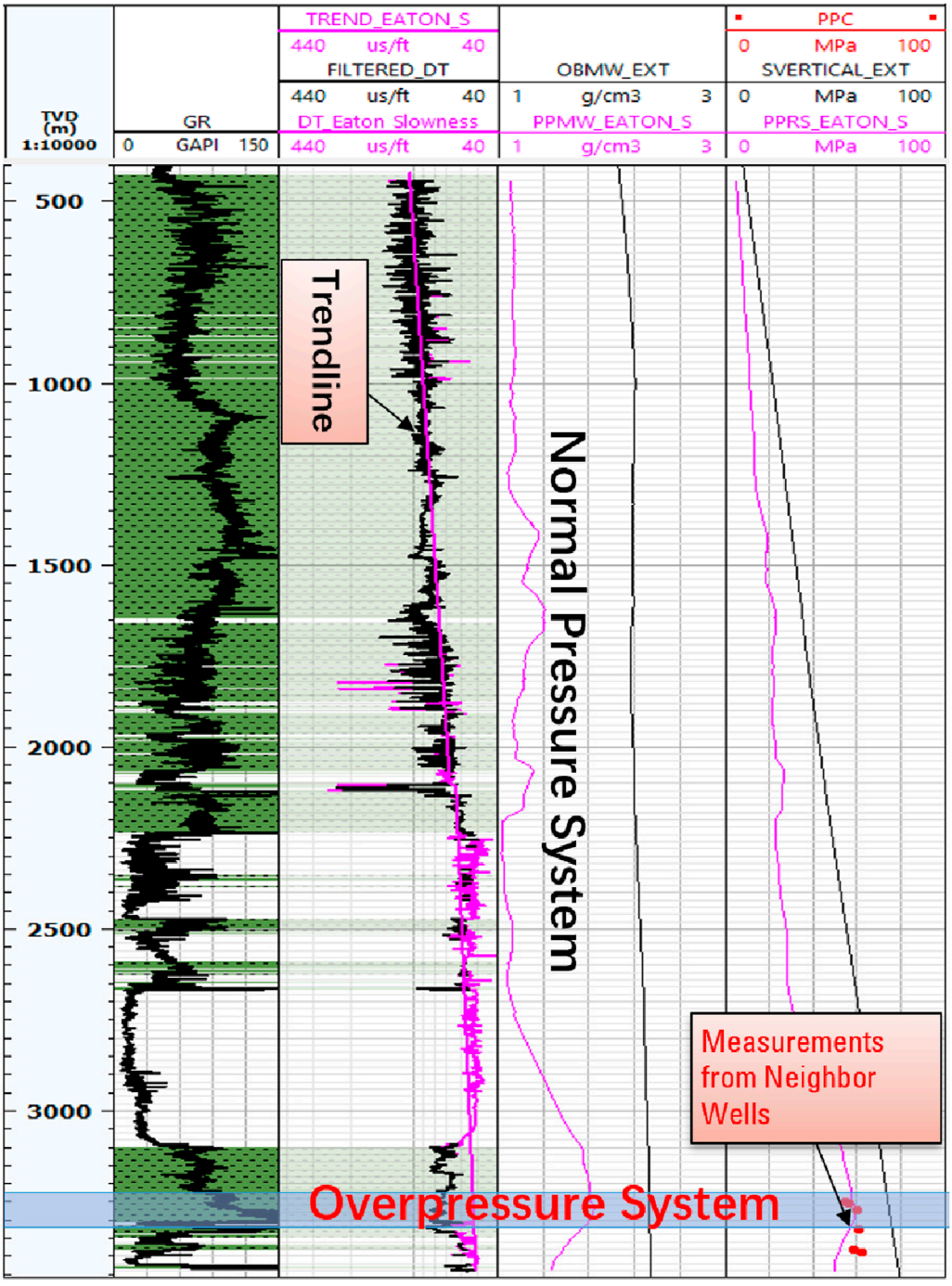

FIGURE 16
Analysis of overburden stress and reservoir pore pressure, with constraints from measurements of neighbor wells.

shear slowness (DTs). The current dataset comprises comprehensive well log information for only four wells; the remaining wells are deficient in sufficient number of DT segments. It is imperative to emphasize the vitality of DT data for accurately establishing single-well geomechanics; its absence or misinterpretation could substantially increase uncertainty in the geomechanical model. Given the interrelationships and predictive capacities of density, DTc, and DTs, a total of 13 wells—comprising exploratory and vertical wells—are selected as target wells for the development of the 1D geomechanical model. This selection process is critical to ensuring adequate spatial coverage within the study area, thereby enhancing the reliability of the final 3D model's distribution. The workflow for Sections 5.2 and 5.3 is illustrated in Figure 12.

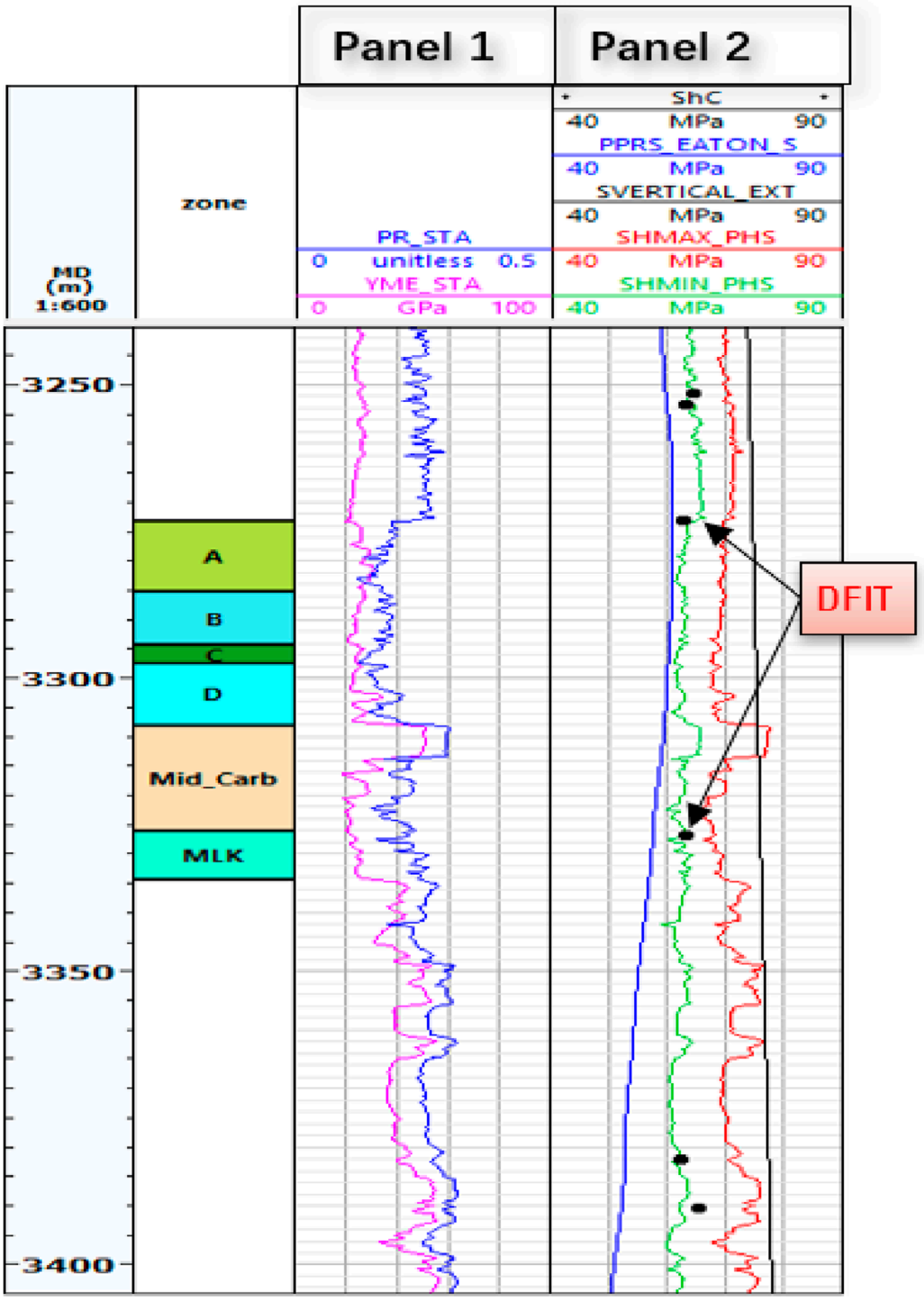

FIGURE 17
One-dimensional single-well-based *In situ* stress prediction: Panel 1 static Poisson's ratio and static Young's modulus. Panel 2 DFIT closure pressure (MPa), reservoir pore pressure (MPa), overburden stress (MPa), Sh, max (MPa), and Sh, min (MPa).

6.2 Single-well geomechanical parameter calculation

6.2.1 Sonic shear slowness match and prediction

The empirical correlations typically used for predicting DTs are primarily based on the theoretical equations as indicated below (Equation 1), where Δt_s represents sonic shear slowness, Δt_p is sonic compressional slowness, and ρ denotes density log values. The coefficients described in these equations may fall short in adequately capturing specific reservoir characteristics and variabilities, resulting in substantial deviations between predicted and actual data. To enhance the accuracy of DTs predictions, an

TABLE 5 Calculated brittleness of all layers in the studied area using BRIT and BI equations.

Layer/sublayer		BRIT		BI	
		Range	Ave.	Range	Ave.
Upper Duvernay	A	0.43–0.52	0.47	0.32–0.43	0.37
	B	0.41–0.47	0.44	0.30–0.40	0.36
	C	0.40–0.55	0.48	0.30–0.40	0.36
	D	0.41–0.52	0.46	0.31–0.40	0.36
Lower Duvernay	Mid_Carb	0.48–0.69	0.56	0.37–0.62	0.50
MLK		0.34–0.48	0.41	0.26–0.46	0.37

artificial neural network methodology is integrated into the current workflow. The artificial neural network (ANN) training function for DTs is constructed taking into consideration the two most influential variables: DTc and density (see Figure 13 for details). Both the single-factor ANN model and multi-factor ANN model are constructed, and the mechanisms are shown in Figures 13A, B, respectively. The multi-factor ANN model stands out with better prediction, see Figure 13C for details. The model is iteratively trained using real-time data from the four wells with complete data until the predicted DTs aligns with actual measurements. This validated model is then applied for predictions in wells or well segments lacking DTs data. Figure 14 demonstrates that the model successfully matches the real-time curves within an acceptable margin of error.

$$\Delta t_s = \Delta t_p \cdot \left[1 - \frac{1.15 \cdot (\rho^{-1} + \rho^{-3})}{e^{\frac{1}{\rho}}}\right]^{-1.5}. \quad (1)$$

6.2.2 Mechanical elastic-strength parameter calculation

Dynamic Young's modulus and Poisson's ratio are calculated from the following theoretical equations (Equations 2, 3):

$$\mathrm{YME} = \frac{\rho V_S^2 (3V_P^2 - 4V_S^2)}{(V_P^2 - V_S^2)}, \quad (2)$$

$$\mathrm{Pr} = \frac{(V_P^2 - 2V_S^2)}{2(V_P^2 - V_S^2)}, \quad (3)$$

where ρ represents the density log value, V_p is the sonic compressional velocity, and V_s is the sonic shear velocity obtained from logging. Due to the absence of valid core laboratory data for converting dynamic to static geomechanical parameters, an empirical conversion factor of 0.7 is applied to Young's modulus, while Poisson's ratio is fixed at 1. The unconfined compressive strength (UCS) is calculated based on static Young's modulus, and the tensile strength (TSTR) is derived from the UCS. The friction angle is determined from the GR values using the empirical relationship:

$$\mathrm{FANG-from\,GR} = 0.42 - 0.182 \times \mathrm{GR}$$

The outputs of the 1D geomechanical model are summarized. The average Young's modulus for the Upper Duvernay formation ranges from 25.3 to 27.3 GPa, accompanied by Poisson's ratios from 0.19 to 0.20. The Lower Duvernay formation exhibits an average Young's modulus of 31.7 GPa and a Poisson's ratio of 0.24. The results of the 1D geomechanical parameters are visually represented in Figure 15.

6.2.3 Density and reservoir pore pressure prediction

The overburden stress for the target formation is computed by integrating density logs along depth, represented as follows:

$$S_v = g\int_0^{TVD} \rho_b(z)dz.$$

The calculated values range from 80.6 to 81.8 MPa and increase with depth. For wells lacking real-time density logs, the trend line is extrapolated using reference points from neighboring wells. A total of 13 wells have been interpreted for overburden stress. Reservoir pore pressure is predicted for these wells using the Eaton method based on sonic data, shown in Equation 4. The resulting pore pressure for the Upper Duvernay_D target ranges from 58.8 to 63.2 MPa, corresponding to a pressure coefficient ranging from 1.79 to 1.91.

$$P_P = S - \left[(S - P_{NCT})\left(\frac{x_{NCT}}{x_{obs}}\right)^{3.0}\right], \quad (4)$$

where S is the overburden stress, P_{NCT} denotes the normal pressure, x_{NCT} represents the corresponding well logging response at normal pressure, and x_{obs} is the actual well logging response (specifically DTc for this study). The Upper Duvernay formation is identified as a typical over-pressurized formation with a pressure coefficient of approximately 1.8. Figure 16 provides an analysis of overburden stress and reservoir pore pressure calculations employing the Eaton method, validated against measured pore pressures from adjacent wells.

6.2.4 *In situ* stress predictions

By applying a pore-elastic isotropic model, the real-time closure pressure derived from DFIT can be equated to the minimum horizontal stress, facilitating the determination of regional tectonic coefficients. Direct field measurements do not provide evaluations for maximum horizontal stress, only its directional components. The following empirical equations (Equations 5, 6) offer methodologies for calculation, presuming a normal slip fault mechanism (where $S_V > S_{h,max} > S_{h,min}$). The calculated tectonic coefficients are as follows:

$$\varepsilon_x = -0.0001\, \varepsilon_y = 0.0003.$$

The predicted horizontal stress, given these assumptions, yields values of $S_{h,min}$ between 65.9 and 66.6 MPa and $S_{h,max}$ from 74.5 to 75.1 MPa for Upper Duvernay, while $S_{h,min}$ is 67.5 MPa and $S_{h,max}$ is 78.2 MPa for Lower Duvernay.

Investigation into the stress profile of the Duvernay Formation reveals a strike–slip fault mechanism, suggesting that $S_{h,min} > S_V > S_{h,max}$. Consequently, the tectonic coefficients are adjusted to correspond with the regional geological understanding and

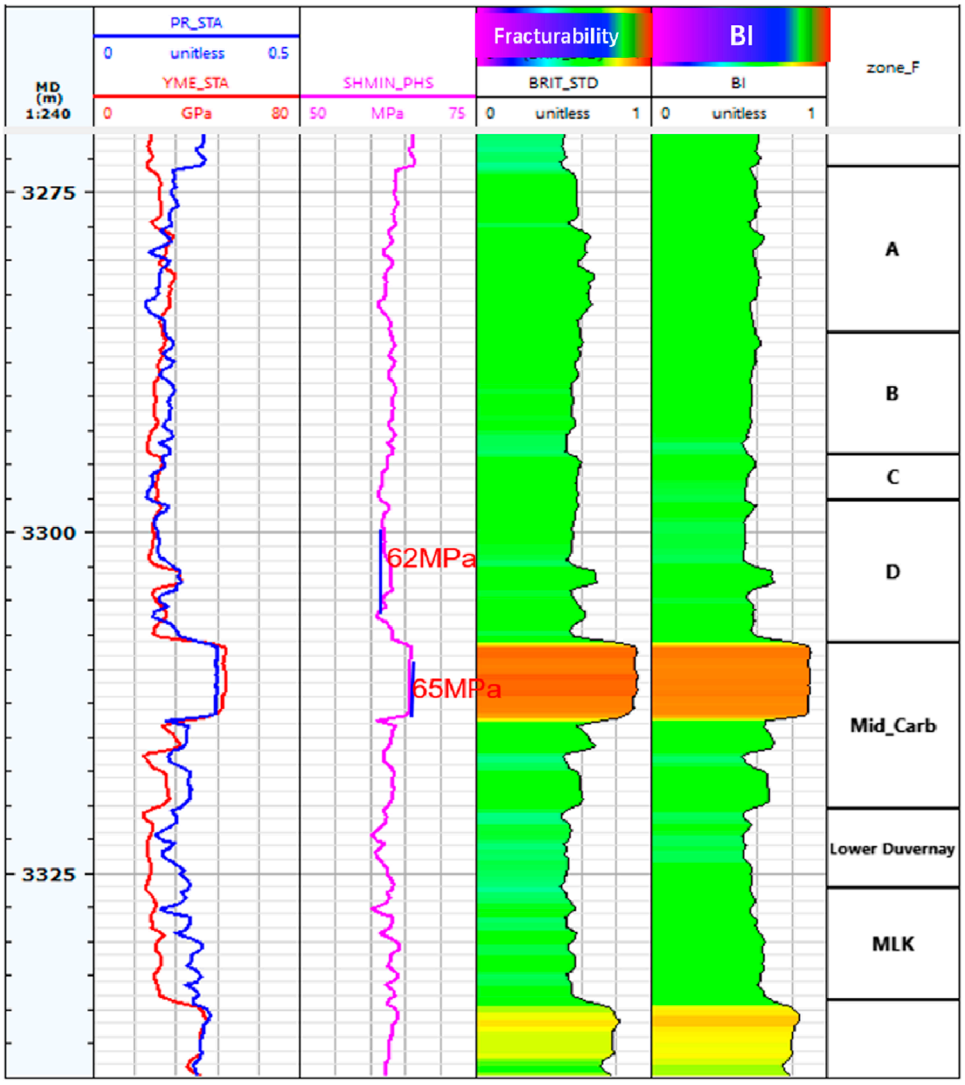

FIGURE 18
Brittleness Index calculated from two methods: BRIT and BI indicated segment in the target well.

focal mechanisms. The maximum horizontal stresses are thus regulated to $S_{h,max}$ values of 81.3–82.5 MPa for Upper Duvernay and approximately 81 MPa for Lower Duvernay. Figure 17 illustrates the 1D *in situ* stress predictions based on well data, utilizing real-time DFIT measurements as reference points.

$$S_{hmin} = \frac{v}{1-v}S_V + \frac{1-2v}{1-v}\alpha P_p + \frac{E}{1-v^2}\varepsilon_x + \frac{vE}{1-v^2}\varepsilon_y, \quad (5)$$

$$S_{Hmax} = \frac{v}{1-v}S_V + \frac{1-2v}{1-v}\alpha P_p + \frac{E}{1-v^2}\varepsilon_y + \frac{vE}{1-v^2}\varepsilon_x. \quad (6)$$

6.2.5 Formation brittleness (fracturability) prediction

Equations typically used for determining fracturability (BRIT) and the brittleness index (BI) are presented below in Equations 7, 8 and Poisson's Ratio in Equation 9, where YME and PR denote the dynamic Young's modulus and Poisson's ratio, respectively, while YME_{STA} and PR_{STA} signify the static estimates from core laboratory evaluations.

Table 5 summarizes the calculation results across each sublayer. Figure 18 compares the methodologies, revealing that results yield congruent indicators for the Upper Duvernay D layers and the Mid-Carb layer, with the minimum horizontal stress calculated at 62 MPa and 65 MPa, respectively.

$$\mathrm{BRIT} = \left(\frac{\mathrm{YME_{STA}}}{7} + \frac{\mathrm{PR_{STA}} - 0.4}{0.15 - 0.4}\right) \times 100\%, \quad (7)$$

$$\mathrm{BI} = \frac{\mathrm{YME} + \mathrm{PR}}{2\mathrm{YME}} = \frac{\mathrm{YME_{STA}} - \mathrm{YME\_STAmin}}{\mathrm{YME\_STAmax} - \mathrm{ME\_STAmin}} \times 100\%, \quad (8)$$

$$\mathrm{PR} = \frac{\mathrm{PR_{STA}} - \mathrm{PR\_STAmax}}{\mathrm{PR\_STAmin} - \mathrm{PR\_STAmax}} \times 100\%. \quad (9)$$

10.3389/feart.2024.1437255

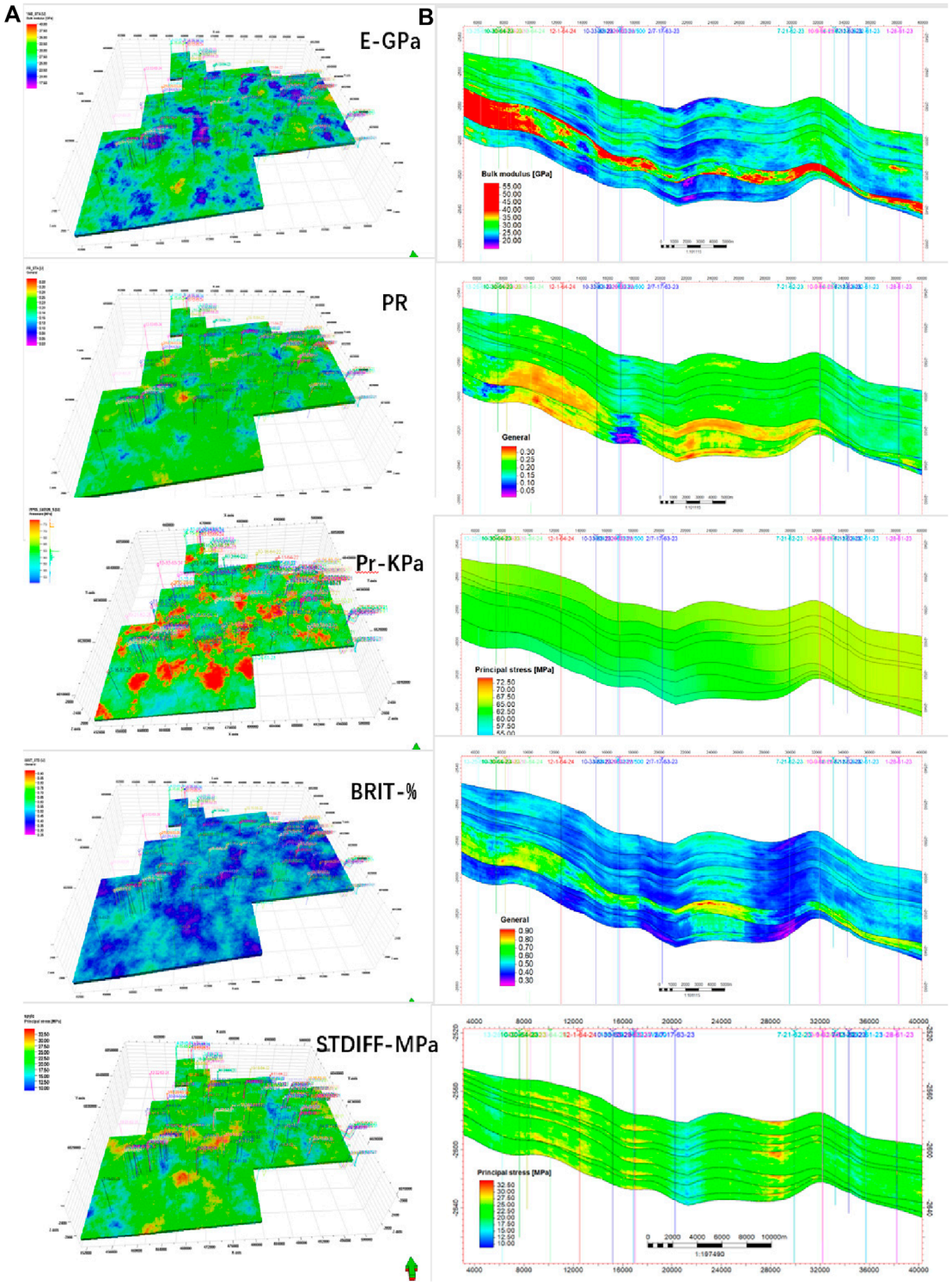

FIGURE 19
Three-dimensional geomechanical model **(A)** and vertical profile **(B)** for key parameters: Young's modulus (E-GPa), Poisson's ratio (PR), pore pressure (Pr-KPa), brittleness (%), and STDIFF (MPa).

TABLE 6 Summary of geological parameters, geomechanical parameters, and production history data.

Category	Candidate parameter	Number
Geological parameters	Porosity, permeability, gas saturation, TOC, adsorbed gas, fracture permeability, fracture density, and net pay thickness	7
Geomechanical parameters	Young's modulus, Poisson's ratio, brittleness, pore pressure, minimum horizontal stress, maximum horizontal stress, and overburden stress	7
Production data	Single-well equivalent gas production for 1 yr. and 2 yrs. (condensate oil–natural gas conversion ratio=1:1000)	2

6.3 Three-dimensional geomechanical modeling

The 1D geomechanical modeling calculates geomechanical parameters and *in situ* stresses at specific well locations. The subsequent step in the workflow involves performing inter-well correlations of these parameters and stress profiles across multiple planes. This process effectively upscales the geomechanical distribution from 1D to 3D by employing SGS for each geomechanical parameter, including Young's modulus, Poisson's ratio, pore pressure, brittleness, and fracturability.

As demonstrated in Figure 19, the average Young's modulus (E) ranges from 24 to 38.2 GPa, while Poisson's ratio (PR) varies between 0.19 and 0.25. Notably, the Mid_Carb formation exhibits a higher Young's modulus and a lower Poisson's ratio in comparison to both the Upper Duvernay and Lower Duvernay formations. This characteristic is advantageous for enhancing height containment during hydraulic fracture treatments, as it serves effectively as barrier bedding. Furthermore, the brittleness index falls within the range of 0.6–0.78, indicating a greater likelihood of developing complex fracture systems. It is also noteworthy that a lower stress differential (STDIFF) is observed in shale formations compared to carbonate formations, which serves as an additional critical indicator for the potential formation of complex fracture systems during hydraulic fracturing operations.

7 Post-analysis of models and data

In recent years, the significance of data analytics has expanded globally, with the oil and gas industry standing out as a critical sector in this regard. Big Data encompasses advanced technologies designed for the management and analysis of extensive datasets. The utilization of Big Data analytics serves as an effective method for deriving actionable insights from vast amounts of information, particularly concerning underground spatial data. However, the value of such extensive data is limited, unless it is systematically recognized, stored, analyzed, and refined for practical application.

A primary focus within the petroleum industry is to establish correlations between production performance and a multitude of variables within an integrated model that incorporates dynamic data, including production history and well treatment history. The multi-scale integrated geomechanical model provides a foundational framework for the development of a comprehensive database pertaining to the Duvernay Formation. Through the sequential implementation of data collection, data cleaning, model training, and predictive analytics, the foremost controlling factors influencing production performance can be prioritized, ultimately offering innovative solutions to facilitate highly efficient field development.

Previous sections also mark the preliminary construction of a Big Database. Based on the data collection and cleaning processes described in the previous section, where the multi-scale integrated model was established, the geological and engineering parameters identified for inclusion in the Big Data analysis are summarized in Table 6.

8 Conclusion and perspectives

This study focuses on Simonette District within the Canadian Duvernay shale play, establishing a complex and heterogeneous geomechanical model that incorporates a multi-scale natural fracture system through thorough analysis of the limited formation evaluation data from seismic interpretation, well logging, and well imaging. The model serves as a reliable foundation for simulating intricate hydraulic fracturing systems, optimizing hydraulic designs, and enhancing the productivity. Key achievements include the development of a fine-grid geological model that integrates geological, natural fracture, geomechanical, and stress models, alongside real-time fracturing treatment data and production history. The study also employs ANN methodologies to predict and estimate missing sonic shear slowness (DTs) data, significantly improving data quality through rigorous acquisition and preparation processes prior to analysis. Furthermore, post-analysis has identified 14 candidate parameters contributing to production performance, offering pathways for further sweet spot analysis based on the extensive database constructed.

Data availability statement

The original contributions presented in the study are included in the article/Supplementary Material, further inquiries can be directed to the corresponding author.

Author contributions

YX: data curation, formal analysis, project administration, software, supervision, writing–original draft, and writing–review and editing. WJ: conceptualization, investigation, writing–original

draft, and writing–review and editing. CL: data curation, methodology, validation, and writing–original draft.

Funding

The author(s) declare that financial support was received for the research, authorship, and/or publication of this article. The study is supported by the CNPC fundamental and perspective program, "Key Technologies for Canadian Shale Gas High-efficiency Development" (No. 2021DJ3303).

Acknowledgments

We thank CNPC (PetroChina) and RIPED (Research Institute of Petroleum Exploration and Development) for permission to publish this work. Opinions presented in this paper represent only the author's personal viewpoints. Contributions from WJ and CL are greatly acknowledged.

Conflict of interest

The authors declare that the research was conducted in the absence of any commercial or financial relationships that could be construed as a potential conflict of interest.

Publisher's note

Supplementary material

The Supplementary Material for this article can be found online at: https://www.frontiersin.org/articles/10.3389/feart.2024.1437255/full#supplementary-material

References

Alameedy, U., Alhaleem., A. A., Isah, A., Al-Yaseri, A., El-Husseiny, A., and Mahmoud, M. (2022). Predicting dynamic shear wave slowness from well logs using machine learning methods in the Mishrif Reservoir, Iraq. *J. Appl. Geophys.* 205, 104760. doi:10.1016/j.jappgeo.2022.104760

Amjad, M. R., Shakir, U., Hussain, M., Rasul, A., Mehmood, S., and Ehsan, M. (2023). Sembar Formation as an unconventional prospect: new insights in evaluating shale gas potential combined with deep learning. *Nat. Resour. Res.* 32 (6), 2655–2683. doi:10.1007/s11053-023-10244-x

Bohn, R., Hull, R., and Trujillo, K. (2020). "Learnings from the Marcellus shale Energy and environmental lab (MSEEL) using fiber optic tools and geomechanical modeling," in *URTec 2440, prepared for presentation at the unconventional resources technology conference held in austin, Texas, USA, 20-22 july 2020*.

Bowie, B. (2018). "Machine learning applied to optimize duvernay well performance," in Paper presented at the SPE Canada Unconventional Resources Conference, Calgary, Alberta, Canada, March 2018. doi:10.2118/189823-MS

Brule, M., Charalambous, Y., Crawford, M. L., and Crawley, C. (2009). Reducing the "data commute" heightens E& productivity. *J. Petroleum Technol.* 61 (09), 48–53. doi:10.2118/0909-0048-jpt

Calad, C., Rafiee, J., Sarma, P., Zhao, Y., and Dayanara, B. (2022). "Combining machine learning and reservoir simulation for robust optimization of completion design and well location of unconventional wells," in *Paper presented at the SPE/AAPG/SEG Unconventional Resources Technology Conference*. Houston, Texas, USA. doi:10.15530/urtec-2022-3723680

Canadian Discovery (2024). Canadian Discovery. Available at: https://cdl.canadiandiscovery.com/.

Chatterjee, A., Mondal, S., Basu, P., and Patel, B. K. (2012). "Pore pressure prediction using seismic velocities for deepwater high temperature- high pressure well in offshore krishna godavari basin, India," in *SPE oil and gas India conference and exhibition*, 153764.

Chen, S., Zhao, W. Z., Ouyang, Y. L., Zeng, Q., Yang, Q., Hou, H., et al. (2017). Prediction of sweet spots in shale reservoir based on geophysical well logging and 3D seismic data: a case study of Lower Silurian Longmaxi Formation in W4 block, Sichuan Basin, China. *China* 35 (2), P147–P171. doi:10.1177/0144598716679961

Dunn, L., Schmidt, G., Hammermaster, K., Brown, M., Bernard, R., Wen, E., et al. (2012). *The Duvernay formation (devonian): sedimentology and reservoir characterization of a shale gas/liquids play in alberta, Canada: CSPG conferences abstract archive, expanded abstracts*.

Dusseault, B. M. (2013). "Geomechanical aspects of shale gas development," in *Rock mechanics for resources, Energy and environment*, P39–P56.

Eaton, B. A. (1972). The effect of overburden stress on geopressure prediction from well logs. *J. Petroleum Technol.* 24 (8), 929–934. doi:10.2118/3719-pa

Eaton, B. A. (1975). "The equation for geopressure prediction from well logs," in *Fall meeting of the society of petroleum engineers of AIME*.

Ehsan, M., Chen, R., Latif, M. A. U., Abdelrahman, K., Ali, A., Ullah, J., et al. (2024). Unconventional reservoir characterization of patala formation, upper indus basin, Pakistan. *ACS Omega* 9 (13), 15573–15589. doi:10.1021/acsomega.4c00465

Ehsan, M., and Gu, H. (2020). An integrated approach for the identification of lithofacies and clay mineralogy through Neuro-Fuzzy, cross plot, and statistical analyses, from well log data. *J. Earth Syst. Sci.* 129 (1), 101. doi:10.1007/s12040-020-1365-5

Ehsan, M., Latif, M. A. U., Ali, A., Radwan, A. E., Amer, M. A., and Abdelrahman, K. (2023). Geocellular modeling of the cambrian to eocene multi-reservoirs, upper indus basin, Pakistan. *Nat. Resour. Res.* 32 (6), 2583–2607. doi:10.1007/s11053-023-10256-7

Enverus (Drilling Info) (2024). Enverus (Drilling Info). Available at: https://www.enverus.com/.

Eskandari, H., Rezaee, M. R., and Mohammadnia, M. (2004). Application of multiple regression and artificial neural network techniques to predict shear wave velocity from wireline log data fora carbonate reservoir, South-West Iran. *CSEG Rec.* 29 (7), 40–48.

Eze, P. C., and Hu, L. Y. (2023). "Natural fracture presence prediction in unconventional reservoirs using machine learning and geostatistical methods-workflow and HFTS1 case," in Paper presented at the SPE/AAPG/SEG Unconventional Resources Technology Conference, Houston, Texas, United States, June 2022. doi:10.15530/urtec-2022-3721712 no. urtec-2022-3721712.

Ferrer, G. G., Faskhoodi, M., Zhmodik, A., Li, Q., and Mukisa, H. (2020). "Completion optimization of child wells in a depleted environment, A Duvernay example," in *Prepared for presentation at the SPE Canada Unconventional Resources Conference originally scheduled to be held in Calgary, Alberta, Canada 18-19 March 2020. Due to COVID-19 the physical event was postponed until 29 September-2 October 2020 and was changed to a virtual event, SPE-200011-MS*.

Gaillot, P., Crawford, B., Liang, Y. M., and Alramahi, B. (2020). "Is my completions engineer provided with the correct petrophysical and geomechanical properties input," in *Presented at the abu dhabi international petroleum exhibition and conference, 9-12 november, abu dhabi, UAE, SPE-20337-MS*.

GeoSCOUT (2024). GeoSCOUT. Available at: https://www.geologic.com/geoscout/.

Ghahfarokhi, P. K. (2017). The structured gridding implications for upscaling model discrete fracture networks (DFN) using corrected Oda's method. *J. Petroleum Sci. Eng.* 153, 70–80. doi:10.1016/j.petrol.2017.03.027

Hui, G., Chen, Z., and Wang, H. (2023). "An integrated geology-engineering approach to Duvernay shale gas development: from geological modelling to reservoir simulation," in *SPE Canadian Energy technology conference and exhibition*.

Hui, G., and Gu, F. (2023). An integrated method to mitigate hazards from hydraulic fracturing–induced earthquakes in the Duvernay shale play. *SPE Reserv. Eval. and Eng.* 26 (02), 382–391. doi:10.2118/210287-pa

Kleiner, S., and Aniekew, O. (2019). "The Duvernay shale completion journey," in *Presented at the SPE Kuwait Oil&Gas conference and show held in mishref, Kuwait,13-16 october 2019, SPE-198070-MS*.

Kuroda, S., and Hayate, O. (2022). "Field measurement of the formation stress depletion and the pore pressure depletion in the Eagle Ford," in *Paper presented at the SPE/AAPG/SEG Unconventional Resources Technology Conference*. Houston, Texas, USA. doi:10.15530/urtec-2022-3708962

Legg, M. J. (2023). Predicting reservoir presence from seismic velocity mapping and pore pressure prediction. *Offshore Technol. Conf.*, 32393–ms. doi:10.4043/32393-MS

Leshchyshyn, T., and Thomson, J. (2016). "Duvernay proppant intensity production case study and frac fluid selection," in *Presented at the SPE annual technical conference and exhibition held in dubai, UAW, 26-28 september 2016, SPE-181687*.

Li, Q. G., Michi, O., and Boskovic, D. (2020). "Geomechanical Characterization and Modelling in the Montney fore Hydraulic Fracturing Optimization," in Paper presented at the SPE Canada Unconventional Resources Conference, Virtual, September 2020. doi:10.2118/199978-MS SPE-199978-MS

Liang, X., Xian, C., and Shu, H. (2016). "Three dimensional full-filed and pad geomechanics modelling assists effective shale gas field development, sichuan basin, China," in *Presented at the international petroleum technology conference held in bangkok, Thailand, 14-16 november 2016. IPTC-18984-MS*.

Liu, C., Wu, K., Wu, J., Chang, C., Yang, X., Gong, Y., et al. (2022). "An accurate and efficient fracture propagation model auto-calibration workflow for unconventional reservoirs," in *Paper presented at the SPE/AAPG/SEG Unconventional Resources Technology Conference*. Houston, Texas, USA. doi:10.15530/urtec-2022-3720957

Ma, W., Wu, K., Ge, J., and Yu, W. (2022). "Fracture performance evaluation from high-resolution distributed strain sensing measurement during production: insights for completion design optimization," in *Paper presented at the SPE/AAPG/SEG Unconventional Resources Technology Conference*. Houston, Texas, USA. doi:10.15530/urtec-2022-3723129

Mariscal-Romero, R. M., and Rodolfo, C. (2022). "Three-dimensional fractal model of hydraulically fractured horizontal wells in anisotropic naturally fractured reservoirs," in *Paper presented at the SPE/AAPG/SEG Unconventional Resources Technology Conference*. Houston, Texas, USA. doi:10.15530/urtec-2022-3724064

Mehana, M., Chen, B., and Rajesh, P. (2022). "Reduced-order models for wellbore leakage from depleted reservoirs," in *Paper presented at the SPE/AAPG/SEG Unconventional Resources Technology Conference*. Houston, Texas, USA. doi:10.15530/urtec-2022-3725868

Pradhan, Y., Lee, W. J., Lam, D., Hanna, K., Nguyen, T., and Andrew (Quang), T. (2022). "Forecasting well-to-well interference in the permian basin by applying neural networks on pre-run simulations," in *Paper presented at the SPE/AAPG/SEG Unconventional Resources Technology Conference*. Houston, Texas, USA. doi:10.15530/urtec-2022-3723394

Richards, G. J., Bere, A. T., Roberts, D. T., and Thomas, S. D. (2020). "Hydraulic fracturing in heterogenous reservoirs; modelling at petrophysical vs. Geomechanical resolution," in *ARMA 20-1842, prepared for presentation at the 54th US rock mechanics/geomechanics symposium held in golden, Colorado, USA, 28 june-1 july 2020*.

Rodriguez-Herrera, A. E., Suarez-Rivera, R., and Handwerger, D. (2013). "Field-scale geomechanical characterization of the Haynesville shale," in *Prepared for presentation at the 47th US rock mechanics/geomechanics symposium held in San Francisco, CA, USA, 23-26 june 2013*.

Sanei, M., Ramezanzadeh, A., and Asgari, A. (2023). Building 1D and 3D static reservoir geomechanical properties models in the oil field. *J. Petroleum Explor. Prod. Technol.* 13 (1), 329–351. doi:10.1007/s13202-022-01553-7

Shabelansky, A. H., Nihei, K. T., Fradelizio, G., Tracey, S., and Dimitri, B. (2022). "A numerical simulation of microseismic depletion delineation for duverney oilfield in Canada using a fast approach for a fully coupled 3D quasistatic poroelastic modeling," in *Paper presented at the SPE/AAPG/SEG Unconventional Resources Technology Conference*. Houston, Texas, USA. doi:10.15530/urtec-2022-3719909

Srinivasan, A., Liu, Y., Wu, K., Jin, G., and George, J. M. (2022). "Geomechanical modeling of fracture-induced vertical strain measured by distributed fiber optic strain sensing," in *Paper presented at the SPE/AAPG/SEG Unconventional Resources Technology Conference*. Houston, Texas, USA. doi:10.15530/urtec-2022-3722188

State public database in United States (2024). *State public database in United States*.

Tao Bai, P. T., and Tahmasebi, P. (2022). Sequential Gaussian simulation for geosystems modeling: a machine learning approach. *Geosci. Front.* 13 (1), 101258. doi:10.1016/j.gsf.2021.101258

Thomson, J., Zalslavsky, G., and Leshchyshyn, T. (2016). "Completion design production case study in the Duvernay shale formation," in *Presented at the SPE annual technical conference and exhibition held in dubai, UAW, 26-28 september 2016, SPE-181715-MS*.

Verly, G. (1993). *Sequential Gaussian simulation: a Monte Carlo method for generating models of porosity and permeability*. Berlin, Heidelberg: Springer Berlin Heidelberg, 345–356.

Weissenberger, J., Gilhooly, M., and Wong, P. (2014). "Regional frasnian stratigraphic framework, alberta outcrop and subsurface," in *Presented at the AAPG annual convention and exhibition*. Houston, Texas, United States. ndx_weissenberger.pdf (searchanddiscovery.com.

Weng, X., Kresse, O., and Cohen, C. (2011). "Modeling of hydraulic fracture network propagation in a naturally fractured formation," in *Presented at the SPE hydraulic fracturing technology conference and exhibition held in woodlands, Texas, USA*, 24–26. January 2011, SPE 140253.

Wilson, A. (2017). 3D full-field and pad geomechanics models aid shale gas field development in China. *J. Petroleum Technol.* 69 (10), P74–P76. doi:10.2118/1017-0074-jpt

Wüst, A. J. R., Ziarani, S. A., and Cui, X. A. (2020). "Interbedded carbonate and calcareous shales of the devonian Duvernay Formation of alberta, Canada: implications for completion due to high variability of geomechnical properties," in *Prepared for presentation at the SPE Canada Unconventional Resources Conference originally scheduled to be held in Calgary, Alberta, Canada 18-19 March 2020. Due to COVID-19 the physical event was postponed until 29 September-2 October 2020 and was changed to a virtual event, SPE-200011-MS*.

Xiao, Y., Liu, C., Yu, W., Sepehrnoori, K., and Zigler, C. (2022). "Robust uncertainty quantification of fracture geometries through automatic history matching with application in real shale gas," in *Paper presented at the SPE/AAPG/SEG Unconventional Resources Technology Conference*. Houston, Texas, USA. doi:10.15530/urtec-2022-3720381

Xie, J., Qiu, K. B., and Zhong, B. (2017). "Construction of a 3D geomechanical model for development of a shale gas reservoir in sichuan basin," in *Presented at the SPE Russian petroleum technology conference held in Moscow, Russia, 16-18 october 2017, SPE-187828-MS*.

Xiong, H. (2020). "Identify wellbore landing zones-the southern midland basin case study," in *Presented at the unconventional resources technology conference held in austin, Texas, USA, 20-22 july 2020, URTeC 2902624*.

Zoback, M., Ruths, T., McClure, M., Singh, A., Kohli, A., Hall, B., et al. (2022). "Lithologically-controlled variations of the least principal stress with depth and resultant frac fingerprints during multi-stage hydraulic fracturing," in *Paper presented at the SPE/AAPG/SEG Unconventional Resources Technology Conference*. Houston, Texas, USA. doi:10.15530/urtec-2022-3722883

frontiers | Frontiers in Earth Science

TYPE Original Research
PUBLISHED 18 October 2024
DOI 10.3389/feart.2024.1484021

OPEN ACCESS

EDITED BY
Huaimin Dong,
Chang'an University, China

REVIEWED BY
Xin Nie,
Yangtze University, China
Sheng-Qing Li,
China University of Petroleum (East China), China

*CORRESPONDENCE
Peiqiang Zhao,
pqzhao@cup.edu.cn

RECEIVED 21 August 2024
ACCEPTED 07 October 2024
PUBLISHED 18 October 2024

CITATION
Xin Y, Duan W, Han C, Bie K, Zhao X, Ai Y and Zhao P (2024) A method for calculating saturation in tight sandstone reservoirs based on the dual porosity model.
Front. Earth Sci. 12:1484021.
doi: 10.3389/feart.2024.1484021

A method for calculating saturation in tight sandstone reservoirs based on the dual porosity model

Yi Xin[1,2,3], Wei Duan[4], Chuang Han[1,2,3], Kang Bie[1,2,3], Xinjian Zhao[1,2,3], Yong Ai[1,2,3] and Peiqiang Zhao[4]*

[1]Tarim Oilfield Company, PetroChina, Korla, China, [2]R&D Center for Ultra-Deep Complex Reservoir Exploration and Development, China National Petroleum Corporation, Korla, China, [3]Engineering Research Center for Ultra-Deep Complex Reservoir Exploration and Development, Xinjiang Uygur Autonomous Region, Korla, China, [4]Beijing Key Laboratory of Earth Prospecting and Information Technology, China University of Petroleum, Beijing, China

Introduction: With the continuous development of exploration and development, tight sandstone reservoirs have become an essential field of oil and gas exploration. The tight sandstone reservoirs are characterized by complex lithology, poor pore structure, and strong heterogeneity, which bring great difficulties to formation evaluation by well logs. Especially, the accuracy of the Archie formula for calculating the water saturation of tight sandstone reservoirs containing fractures is not high, saturation evaluation faces greater challenges. Therefore, how to calculate the saturation of tight sandstone reservoirs more accurately is an urgent problem to be solved.

Methods: In this paper, the tight sandstone reservoirs of the Jurassic Ahe Formation in the Tarim Basin were taken as the research area. A saturation model that combines the effects of shale and fractures was proposed. Specifically, if the shale content is more than 20%, the Indonesian formula is used to calculate the saturation. If the shale content is less than 20%, the dual porosity model is adopted. Based on the rock resistivity and nuclear magnetic resonance (NMR) experiment results, the porosity and T_2 logarithmic mean values are selected as influencing factors to calculate the key parameters of the dual porosity model.

Results and Discussion: The saturation of tight sandstone reservoirs in the Jurassic Ahe Formation of the Tarim Basin is calculated through the method proposed in this paper. The case study shows that the accuracy of the proposed method is higher than that of the Archie model. The method proposed in this paper demonstrates excellent adaptability in the quantitative evaluation of saturation for tight sandstone reservoirs.

KEYWORDS

tight sandstone, dual porosity model, resistivity logs, water saturation calculation, rock resistivity experiment, nuclear magnetic resonance (NMR) experiment

1 Introduction

Tight sandstones generally refer to sandstones with a permeability of less than 0.1 mD and a porosity of less than 10% (Gao and Li, 2016). With the continuous development of exploration and development, tight sandstone reservoirs have become

an essential field of oil and gas exploration (Dai et al., 2012; Zou et al., 2012). Tight sandstone reservoirs are characterized by tight lithology, complex pore structure and firm heterogeneity (Rezaee et al., 2012; Desbbois et al., 2011; Lai et al., 2015). As a result, the accuracy of the Archie formula for calculating the water saturation of tight sandstone reservoirs is not high (Li et al., 2020; Hu et al., 2017; Feng et al., 2023). In addition, the Archie formula is not applicable to formations with high shale content (Zhang et al., 2023; Zhao et al., 2023; Vincent and wladyslaw, 2015). Therefore, how to calculate the saturation of tight sandstone reservoirs more accurately is an urgent problem to be solved.

Shale has a significant influence on the reservoir performance of tight sandstone reservoirs. When the reservoirs contain shale, the reservoirs' resistivity will be reduced, and the accuracy of the traditional method for calculating saturation will also decrease (Feng et al., 2021). There are many saturation models involving the influence of shale. The Simandoux formula (Simandoux, 1963) and the Indonesia formula (Leveaux and Poupon, 1971) apply to shale sandstones. With the development of the dual layer theory, the W-S model (Waxman and Smits, 1968) was developed for shaly sandstones or low-resistivity reservoirs. Clavier et al. (1984) proposed that clay water and free water in argillaceous sandstone conduct electricity in parallel, and they proposed the D-W model. Silva and Bassiouni (1986) investigated the influence of matrix and pore structure on shaly sandstone and proposed the S-B model. Given the internal sedimentary structure characteristics of thin interbedded sandstone and mudstone, Zhang et al. (2015) regarded the reservoir as a layered medium, and established a saturation calculation model of thin interbedded sandstone and mudstone.

The matrix porosity and permeability of tight sandstone reservoirs are low, and fractures are good channels and reservoir spaces for oil and gas migration (Luo, 2010; Zeng et al., 2013). Fractures affect the accurate calculation of tight sandstone saturation (Liu et al., 2018; Liao et al., 2024). The reservoir space of tight sandstone includes matrix pores and fractures. Aguilera and Aguilera (2003) considered the effects of matrix pores, fractures, and caves on the electrical conductivity of carbonate rocks and proposed the triple porosity model. Zhang (2010) established the saturation calculation model for fractured reservoirs based on the triple porosity model. Tang et al. (2018) calculated the saturation of Dabie Area, specifically when the fracture porosity is less than 0.055%, the equation based on conductive pore water is used for calculation. When the fracture porosity is more than 0.055%, the equation based on the theory of dual porosity media is deployed. Wang et al. (2022) established the tight sandstone saturation model using the fracture and matrix pore parallel conductivity model and digital core.

Additionally, the selection of the Archie parameters m and n is essential for saturation calculation. Many scholars have improved the accuracy of the Archie formula by adjusting the values of m and n. (Zhang and Shi, 2005; Yan et al., 2015; Xiao et al., 2013; Luo et al., 2014; Jiang, 2018; Li et al., 2020; Li et al., 2012; Wang et al., 2005; Zhang et al., 2006). In previous studies, there is a lack of a more comprehensive saturation model that combines the effects of shale and fractures. Additionally, the model parameters of tight sandstone are affected by pore structure (Li et al., 2020), and accurate calculation methods of the key parameters are difficult to establish. Therefore, the saturation calculation of tight sandstone needs to be further studied.

In this paper, the tight sandstone reservoirs of the Jurassic Ahe Formation in Tarim Basin were taken as the research area. This paper proposed a saturation model that combines the effects of shale and fractures. Specifically, when the shale content is more than 20%, the Indonesian formula is used to calculate the saturation. When the shale content is less than 20%, the dual porosity model of the matrix pore and fracture pore is adopted. The application to the tight sandstone reservoirs in Tarim Oilfield shows that the saturation calculation method proposed in this paper has less minor interpretation errors than the traditional calculation method. The saturation calculation method proposed in this paper improves the accuracy of saturation evaluation.

2 Geological setting

Kuqa Depression is a geological formation located in the northern Tarim Basin, which is adjacent to the Tianshan fold belt in the north. Tectonic units and location of Dibei gas field in Kuqa Depression are shown in Figure 1. Kuqa Depression is classified as a Mesozoic-Cenozoic foreland basin and is comprised of four thrust belts and three sags. The Northern Monocline, Kela, Yiqikelike, and Qiulitage thrust belts make up the four structural belts. The Baicheng, Yangxin, and Wushi sags are the main negative tectonic units (Zhao et al., 2022). The study area of this research is situated in the middle of the Yiqikelike thrust belt, specifically focusing on the DB 5 well as the primary research object.

The primary gas-bearing interval in the Dibei gas field is the Lower Jurassic Ahe Formation (Shi et al., 2018; Shi et al., 2024), which consists of braided river delta plain surface deposits characterized by low compositional maturity. The lithology of the Ahe Formation primarily comprises gravel, coarse sandstone, and medium sandstone. The sandstone reservoirs in this formation have an average thickness between 250 and 300 m. Dibei gas field is a typical tight sandstone gas reservoir, with the porosity of the Ahe Formation between 3.0% and 9.0%, with an average porosity of 5.94%. The permeability is between 0.1mD and 5.0mD, with an average air permeability of 0.818mD. According to the data from the drilling core, micro casting thin section, and scanning electron microscope, the tight sandstone reservoirs of Jurassic Ahe Formation in Tarim Basin are mainly pore-type reservoirs and pore-fracture-type reservoirs. The main reservoir space of pore reservoirs is matrix pores, such as argillaceous micropores and intergranular dissolved pores (see Figure 2).

The core observation results show that the fractures in the Ahe Formation are generally developed which are mainly high-angle structural fractures in the open or semi-closed state (Figure 3). Silicon and carbonate minerals can be seen in some fractures and corrosion traces of fillers can also be seen. The main reservoir space of a fracture-pore reservoir is matrix pore, and matrix rock is cut by various fractures with different occurrences. While providing part of the reservoir space, fractures mainly play the role of connecting matrix rocks and improving reservoir permeability.

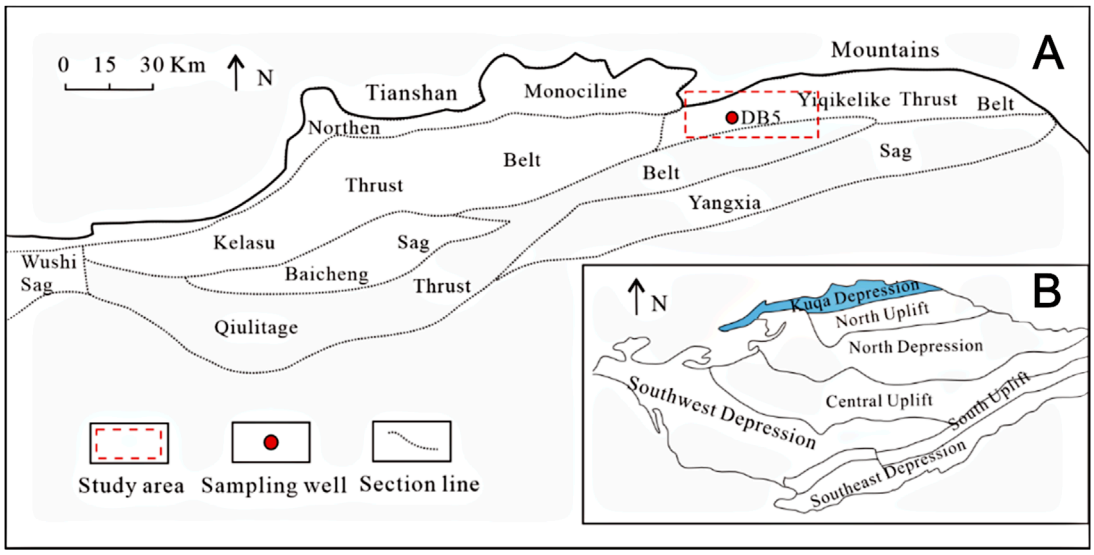

FIGURE 1
Tectonic units and location of Dibei gas field in Kuqa Depression. **(A)** Location of Kuqa Depression. **(B)** Sample well and structural outline of Dibei gas field in Kuqa Depression. (modified from Zhao et al., 2022).

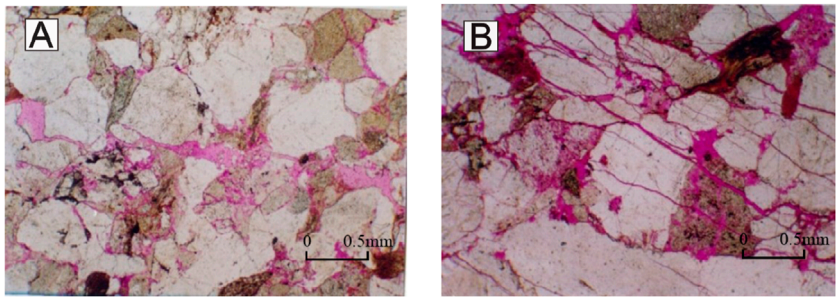

FIGURE 2
Reservoir space types of Jurassic Ahe Formation in Dibei area. **(A)** Shale micropores, a small amount of intragranular dissolved pores. **(B)** Structural fractures, potassium feldspar intragranular dissolved pores, matrix micropores.

3 Method for calculating saturation in tight sandstones

3.1 Dual porosity model

Aguilera and Aguilera (2003) published rigorous equations for dual porosity systems that were shown to be valid for all combinations of matrix and fractures or matrix and nonconnected pores. The model used in this paper is a combination of matrix and fractures, the model is composed of a rock skeleton, matrix pores, and fractures. The pore structure of rock determines the conductive path of rock, suppose the additional shale conductivity is not considered (core experiments of reservoirs in multiple research blocks show that the cation exchange capacity is minimal and can be ignored). In that case, the conductivity of matrix pores and fractured water is the same, but the conductive paths are different. Therefore, the rock is conductive in parallel through the matrix pore network and the fracture network. The model of the dual porosity reservoirs is shown in Figure 4, the matrix pores and fractures constitute a very complex fracture-pore system. Matrix porosity is the ratio of matrix pore volume to total volume which is calcuiated using Equation 1.

$$\phi_b = \frac{V_b}{V} \tag{1}$$

where ϕ_b is the matrix porosity (%); V_b is the volume of matrix pores (cm^3); V is the total volume of the composite system (cm^3).

Rock fracture porosity is the ratio of matrix pore volume to total volume which is calculated using Equation 2.

$$\phi_f = \frac{V_f}{V} \tag{2}$$

where ϕ_f is the fracture porosity (%); V_f is the volume of fracture (cm^3).

Total porosity of rock is calculated by Equation 3.

$$\phi = \frac{V_f + V_b}{V} \tag{3}$$

where ϕ is the total porosity (%).

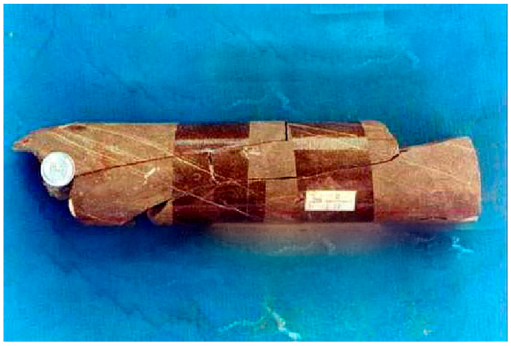

FIGURE 3
Characteristics of core fractures of Jurassic Ahe Formation in the Dibei area.

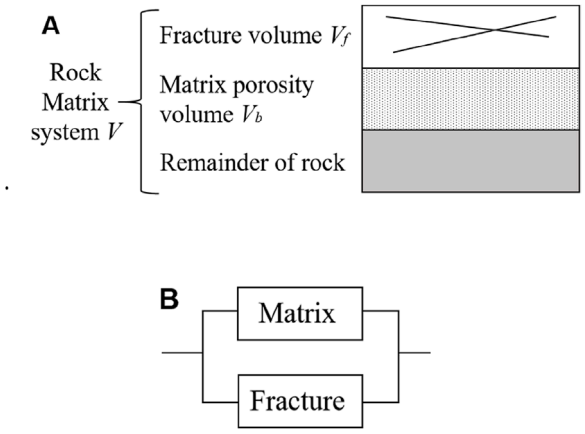

FIGURE 4
Schematic display of dual-porosity model. **(A)** Structure of rock dual porosity model. **(B)** Conductive path of rock dual porosity model (modified from Aguilera and Aguilera, 2004).

3.2 Calculation method of saturation

According to the theory of dual porosity medium, the pore space of a tight sandstone reservoir is divided into matrix pore space and fracture pore space. According to the definition of water saturation, the total water saturation can be expressed as Equation 4.

$$S_w = \frac{\phi_b S_{wb} + \phi_f S_{wf}}{\phi_b + \phi_f} \tag{4}$$

where ϕ_b is the matrix porosity (%); S_{wb} is the matrix water saturation (%); ϕ_f is fracture porosity (%); S_{wf} is fracture water saturation (%).

Under the background of fractures and non-connected pores, the physical properties of the matrix of the reservoir are relatively uniform. Therefore, when calculating the matrix pore saturation, we use the classical Archie formula (Archie, 1942), and the Archie formula is shown in Equation 5.

$$S_{wb} = \sqrt[n_b]{\frac{abR_w}{\phi_b^{mb} R_t}} \tag{5}$$

where R_w is the formation water resistivity ($\Omega \cdot$m); R_t is the formation resistivity ($\Omega \cdot$m); a, b, m_b, n_b are the rock electrical parameters of the matrix, which are determined by rock resistivity experiments. The rock samples contain virtually no fractures, so the m and n obtained from the rock resistivity experiment are regarded as the m_b and n_b of the rock matrix in this paper. Subsequently, this paper will enhance the calculation approach of rock electrical parameters in accordance with the actual circumstances of the reservoir, thereby enabling the saturation calculation to be more rational and precise.

According to the permeability characteristics of the dual porosity, Tang et al. (2018) and Wang (2020) calculated the water saturation of fracture using Equation 6.

$$S_{wf} = \sqrt[n_f]{\frac{1/R_t - 1/R_{xo} + \left(1/R_{mf}\right)\phi_f^{m_f}}{\left(1/R_w\right)\phi_f^{m_f}}} \tag{6}$$

where R_{xo} is the resistivity of the flushing zone ($\Omega \cdot$m); R_{mf} is the resistivity of mud filtrate ($\Omega \cdot$m); m_f and n_f are the electrical parameters of fractures.

Shale is dispersedly filled in the intergranular pore space of sandstone, which is conductive in parallel with the water of formation. When the reservoir contains shale, the resistivity of the reservoir will decrease, and the accuracy of the traditional method for calculating saturation will also decrease. There are many saturation models involving the influence of shale. The Indonesian formula is a famous formula in formation evaluation by well logs, as shown in Equation 7.

$$\frac{1}{S_w^n} = \left(\frac{V_{sh}^{cc}}{R_{sh}} + \frac{\phi}{\sqrt{aR_w}} \right)^2 R_t \tag{7}$$

where V_{sh} is the shale content (%); R_{sh} is the resistivity of the shale ($\Omega \cdot$m); cc = 1-V_{sh}/2. This formula is suitable for low-formation water salinity and shaly sandstone with V_{sh} less than 50%. This formula better solves the saturation calculation of shaly sandstone formation.

The research area belongs to fractured tight sandstone reservoirs. Fractures developed in rocks enhance the productivity of oil and gas reservoirs but also complicate the evaluation of oil and gas saturation. When calculating the oil and gas saturation of fractured tight sandstone reservoirs, factors such as physical properties, fractures, and lithology should be considered. For such reservoirs, this paper proposes a saturation evaluation method considering pore types and shale content (Figure 5). Specifically, when the shale content exceeds 20%, the Indonesian formula is used to calculate saturation. If the shale content is less than 20%, the dual porosity model is used to calculate saturation.

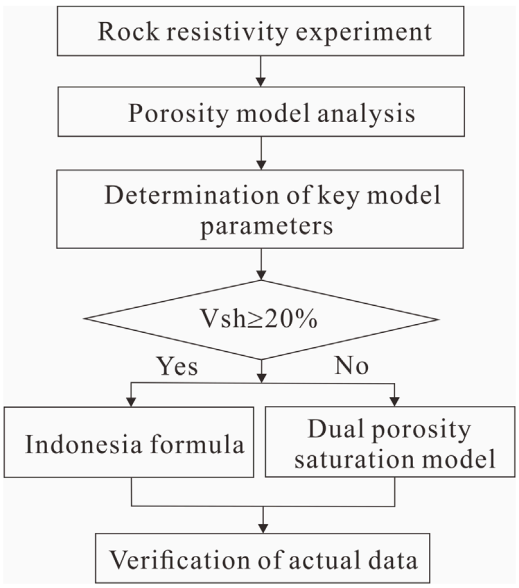

FIGURE 5
The calculation process of saturation.

4 Parameters of the dual porosity model

4.1 Porosity

Usually, intersection processing of multiple well logging methods is used to obtain accurate total porosity of the reservoirs. Compared with other well-logging methods, density and compensated neutron log responses are less affected by the heterogeneity of fractured reservoirs (Yong and Zhang, 1986). Therefore, we use the intersection of density and neutron logs to obtain the total porosity of the reservoir. The specific method is shown in Equations 8–10.

$$\phi = \sqrt{\frac{pordsc^2 + pornsc^2}{2}} \tag{8}$$

$$pordsc = \frac{\rho_b - \rho_{ma}}{\rho_f - \rho_{ma}} - V_{sh}\frac{\rho_{sh} - \rho_{ma}}{\rho_f - \rho_{ma}} \tag{9}$$

$$pornsc = \frac{\phi_N - \phi_{ma}}{\phi_{Nf} - \phi_{ma}} - V_{sh}\frac{\phi_{Nsh} - \phi_{ma}}{\phi_{Nf} - \phi_{ma}} \tag{10}$$

where ρ_{sh}, ρ_{ma}, ρ_f are the density logging values of mud, skeleton, and fluid, respectively (g/cm^3); ϕ_{sh}, ϕ_{ma}, ϕ_f are the neutron logging values of shale, rock matrix, and pore fluid, respectively (%).

Acoustic logging data basically do not reflect the fracture porosity but mainly reflect the matrix porosity of the rocks. The matrix porosity of the reservoirs is calculated by the acoustic volume model. The calculation formula is shown in Equation 11.

$$\phi_b = \frac{\Delta t - \Delta t_{ma}}{\Delta t_f - \Delta t_{ma}} - V_{sh}\frac{\Delta t_{sh} - \Delta t_{ma}}{\Delta t_f - \Delta t_{ma}} \tag{11}$$

where Δt_{sh}, Δt_{ma}, Δt_f are the acoustic time difference logging values of shale, rock matrix, and pore fluid, respectively (μs/ft).

In reservoir evaluation, imaging logging, and dual lateral logging data are usually used to calculate fracture porosity (Zhao et al., 2012). In this paper, the fractures are picked manually based on the intuitive interpretation of FMI (Formation Micro Scanner Image), and the electrical imaging data are calibrated using the optical scanning imaging data of the cores. Finally, the fracture parameters, such as fracture porosity, were calculated (Chen and Tan, 2003; Lai et al., 2015).

4.2 Determination of model parameters

Accurate model parameters m_b and n_b are the key to the quantitative evaluation of saturation. The porosity and the microscopic pore structure of the reservoirs affect the parameters of models (Ding et al., 2017). Capillary pressure measurement and nuclear magnetic resonance (NMR) measurement are the main methods to describe the microscopic pore structure of the reservoirs. In this paper, the standard NMR T_2 spectrum is selected to characterize the microscopic pore structure. Rock electrical and nuclear magnetic resonance experiments were carried out on 10 tight sandstone samples from Ahe Formation. The m_b value and n_b value of each core are obtained by rock electricity experiment, and the NMR T_2 spectrum of each core is obtained by the nuclear magnetic resonance experiment. Figure 6 shows the standard T_2 spectra of six tight sandstone samples. Six rock samples are saturated with NaCl solution, and the resistivity of NaCl solution is 0.138 Ω·m. The position and shape of the T_2 spectrum of the three rock samples are basically the same (Figure 6A), which indicates that the microscopic pore distributions of the three rock samples are similar. The amplitude and envelope area of the T_2 spectra of the three rock samples are different, which indicates that the porosity of the three rock samples is different. Under the condition that the formation water resistivity and micro-pore structure are basically the same, the parameters m_b and n_b are different when the porosity of the three rock samples is different. The results show that the change of porosity will lead to the change of m_b and n_b values. The position and shape of the T_2 spectra of the three rock samples are different, but the envelope area is the same (Figure 6B), indicating that the porosity of the three rock samples is the same, but the microscopic pore structure is different. Under the condition that formation water resistivity and porosity are basically the same, the parameters m_b and n_b are different if the microscopic pore structure of the three rock samples is different. The results show that the microscopic pore structure affects the values of m_b and n_b.

On the basis of determining the factors affecting the electrical properties of tight sandstone, it is necessary to determine the response relationship between the parameters and pore structure so as to provide a basis for the accurate calculation of saturation. Through the above analysis, it can be concluded that porosity and pore structure have a significant influence on the model parameters of rocks. The logarithmic mean of the NMR T_2 spectrum is usually used to describe the variation in the reservoir's microscopic pore structure (Zhang and Shi, 2005; Guo et al., 2022). The larger the

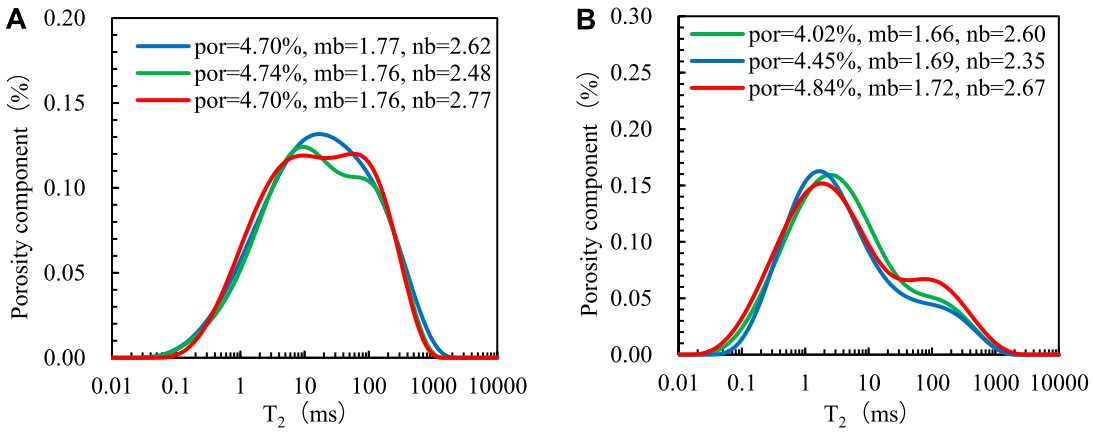

FIGURE 6
Standard T_2 distribution of different rock samples. **(A)** The effect of pore structure on model parameters. **(B)** The effect of porosity on model parameters.

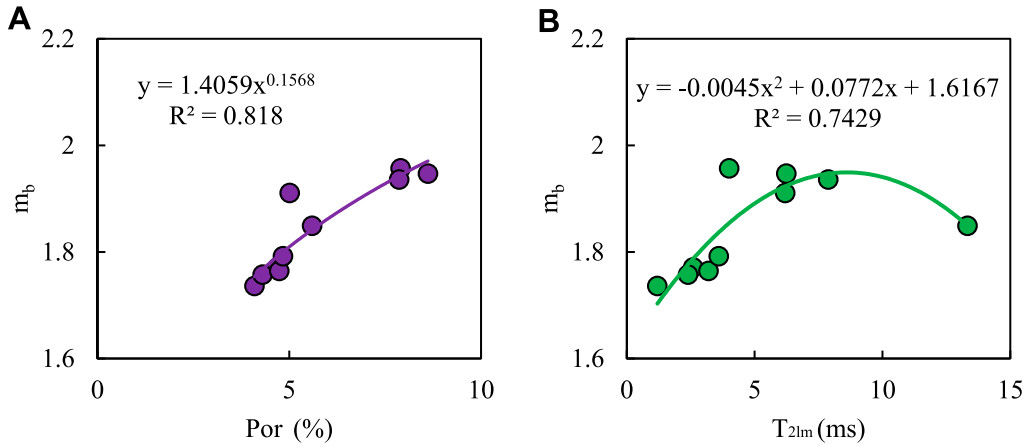

FIGURE 7
Analysis of influencing factors of m_b values. **(A)** Relationship between mb value and porosity. **(B)** Relationship between m_b value and T2 logarithmic mean value.

logarithmic mean value of T_2 (T_{2lm}), the larger the pore size of the reservoirs. And the smaller the T_{2lm}, the smaller the pore size of the reservoirs. Figure 7A shows the relationship between *mb* value and porosity ϕ of core analysis. It can be seen from the Figure that the m_b value and the porosity present a power function relationship, and the m_b value increases with the increases of porosity ϕ. Figure 7B shows the relationship between the m_b value of the core analysis and the T_{2lm} values. The statistical results show that the m_b value first increases with the increase of the T_{2lm} value, and then the m_b value decreases with the increase of the T_{2lm} value.

Figure 8A shows the relationship between the n_b value of core analysis and porosity ϕ. The value of n_b increases with the increase of the porosity ϕ and presents a power function relationship. Figure 8B shows the relationship between the n_b value of the core analysis and the T_{2lm} value. The statistical results show that as the T_{2lm} value increases, the n_b value decreases firstly, and then increases.

The experimental results show that the correlation between model parameters and any single factor is not particularly high. To reduce the error of single actor regression calculation, m_b and n_b values are calculated using the multi-factor fitting regression method. Multifactor regression considers the complex interaction between multiple parameters and reflects the actual properties of rocks more accurately. According to the results of the rock resistivity and nuclear magnetic resonance (NMR) experiment, porosity and T_2 logarithmic mean value are selected as influencing factors, and the calculation model of m_b value and n_b value is established by using multiple regression methods. The model is shown in Equations 12, 13.

$$m_b = 1.401\phi_b^{0.1524} - 0.0004826T_{2lm}^2 + 0.004525T_{2lm} \quad (12)$$

$$n_b = 4.447\phi_b^{-0.3701} + 0.0002246T_{2lm}^2 - 0.01689T_{2lm} \quad (13)$$

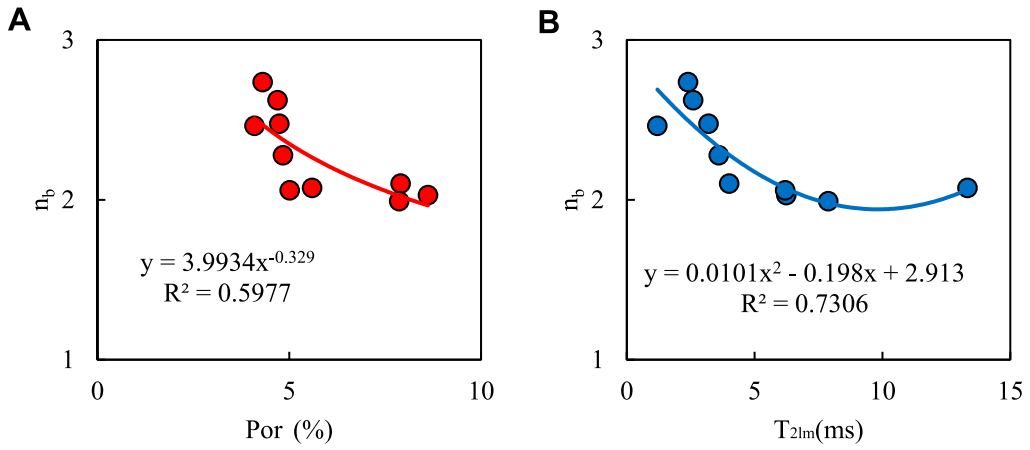

FIGURE 8
Analysis of influencing factors of n_b value. **(A)** The relationship between the value of n_b value and porosity. **(B)** The relationship between the value of nb and the T_2 logarithmic mean value.

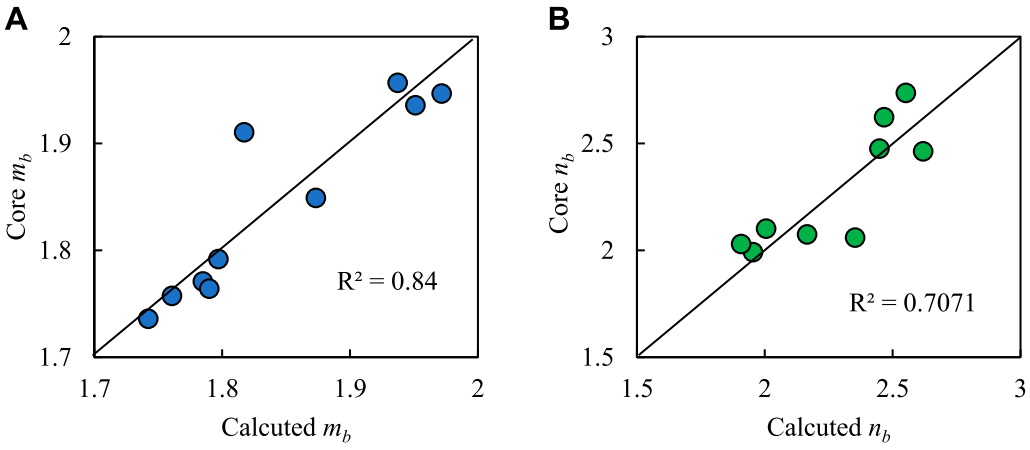

FIGURE 9
Cross plots of measured rock electrical parameter values and calculated rock electrical parameter values. **(A)** Cross plots of core analysis m_b and calculated m_b value. **(B)** Cross plots of core analysis n_b and calculated n_b values.

where m_b and n_b are the rock electrical parameters of the matrix; ϕ_b is the porosity of the matrix (%); T_{2lm} is the logarithmic mean of T_2 (ms).

Figure 9 shows the calculation results of the model. The m_b and n_b values calculated by the multiple linear regression method have a reasonable correlation with the m and n values measured by the experiment. The coefficient of determination for the m_b value is 0.8377, and for the n_b value is 0.7041, indicating that the calculation accuracy of this method is high, and porosity and pore structure are important factors affecting the model parameters of rocks.

In order to obtain electrical parameters for fractures, Tang et al. (2018) and Wang (2020) assume that the rock is a regular hexahedron with side length l, a diagonal fracture with angle β and width d_f passes through the rock, and a regular hexahedron hole with side length c develops inside the rock. According to the theory, the formula for calculating the parameters of fractured rock is shown in Equation 14.

$$m_f = -\frac{\log\left[l\left(\frac{1}{c+d_f} + \frac{l-c\cos\beta}{l\cos\beta d_f} + \frac{c}{(l-c)d_f}\right)\right]}{\log\left\{\left[\left(\frac{l^2}{\cos\beta} - c^2\right)d_f + c^3\right]/l^3\right\}} \tag{14}$$

where d_f is the fracture width (mm); β is the fracture angle (dega). Substituted into Equations 5, 6, the matrix saturation and fracture saturation are calculated, and the total water saturation of the reservoir is calculated by Equation 4.

For the n_f, there is still no method to determine it. We assume it is equal to n_b in this paper.

5 Results of saturation calculation

The saturation calculation method proposed in this paper was used to quantitatively evaluate the reservoir saturation of the

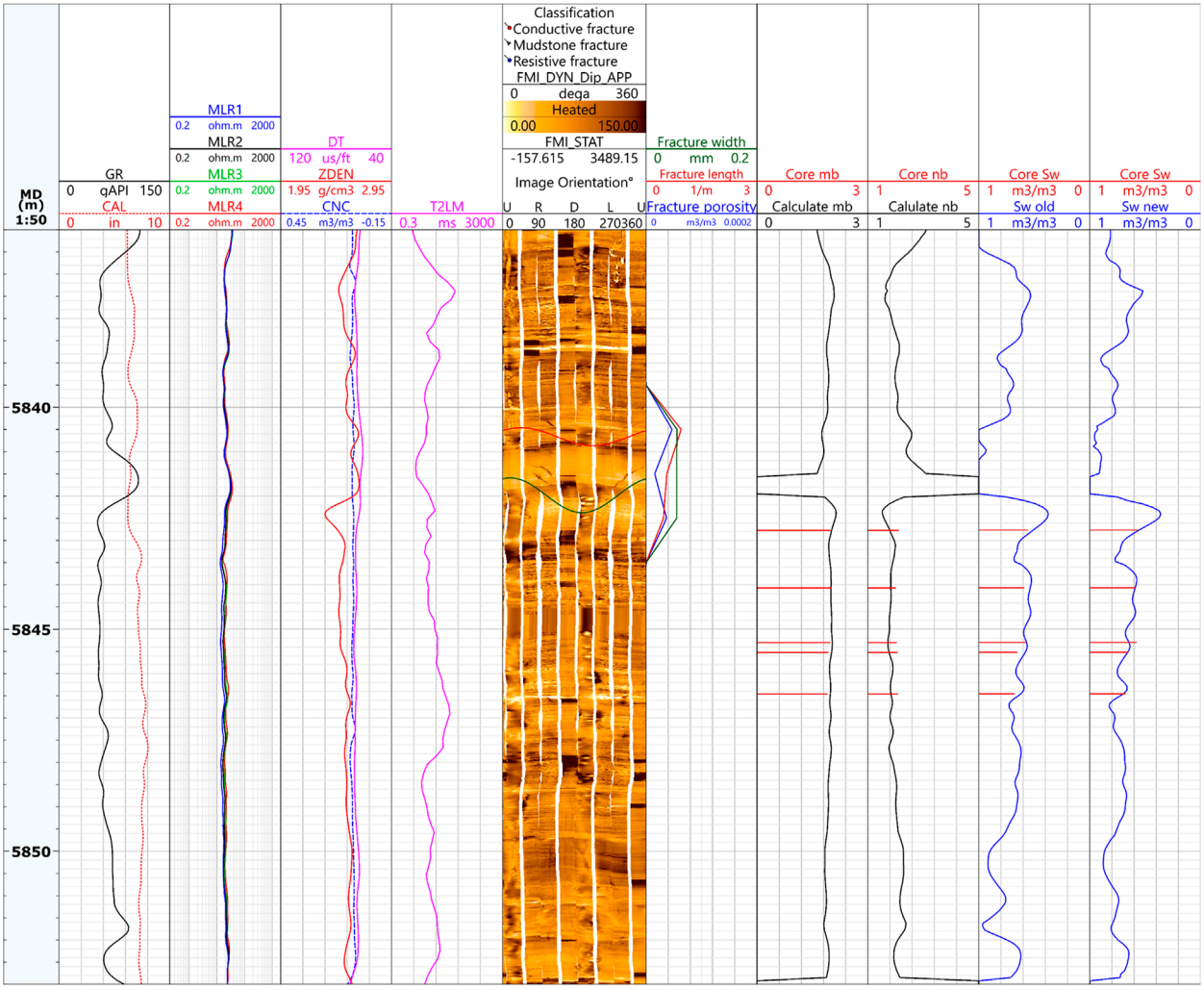

FIGURE 10
Saturation calculation results of the upper section of Ahe Formation in DB 5 Well, Dibei Gas Reservoir, Tarim Basin.

Jurassic Ahe Formation in Tarim Basin. The reservoir space types in the study area are mainly muddy micropores, intra-granular dissolved pores, intergranular dissolved pores, and micro-fractures, and the development degree of primary pores is low. Taking well DB5 as an example, the average core porosity is 5.67%, and the permeability is 0.52×10^{-3} μm^2. The Ahe Formation is a typical tight sandstone reservoir. Figures 10, 11 show the saturation calculation results. The sixth track is the processing result of the imaging logging. The seventh track is the fracture characteristic curves, which were calculated by using the imaging logging data. Fracture characteristic curves include fracture width, fracture length, and fracture porosity. The eighth track is the m_b value of multi-factor regression calculation and the m_b value of core analysis, and the ninth track is the n_b value of multi-factor regression calculation and the n_b value of core analysis. The m_b and n_b calculated by this method agree well with the m_b and n_b obtained by core analysis. The 10th track is the water saturation calculated by the Archie model, and the 11th track is the saturation calculated by the tight sandstone saturation calculation method proposed in this paper. As can be seen from Figures 10, 11, the water saturation calculated by the traditional Archie formula and the method proposed in this paper is in good agreement with the core analysis value.

In order to test the accuracy of the saturation calculation method more intuitively, we evaluate the accuracy of the saturation calculation by calculating the absolute error and the relative error. As can be seen from Table 1, the average relative error of saturation calculated by the traditional Archie formula is 5.88%. In comparison, the average relative error of the saturation calculation method proposed in this paper is 3.55%, which reduces the average relative error by 2.33%. Similarly, the average absolute error calculated by the traditional Archie formula is 9.87%. The average absolute error of the saturation calculation method proposed in this paper is only 6.11%, and the accuracy is improved by 3.76%. The results show that the saturation calculation method proposed in this paper meets the error requirement of reserve calculation and has higher accuracy than the traditional method.

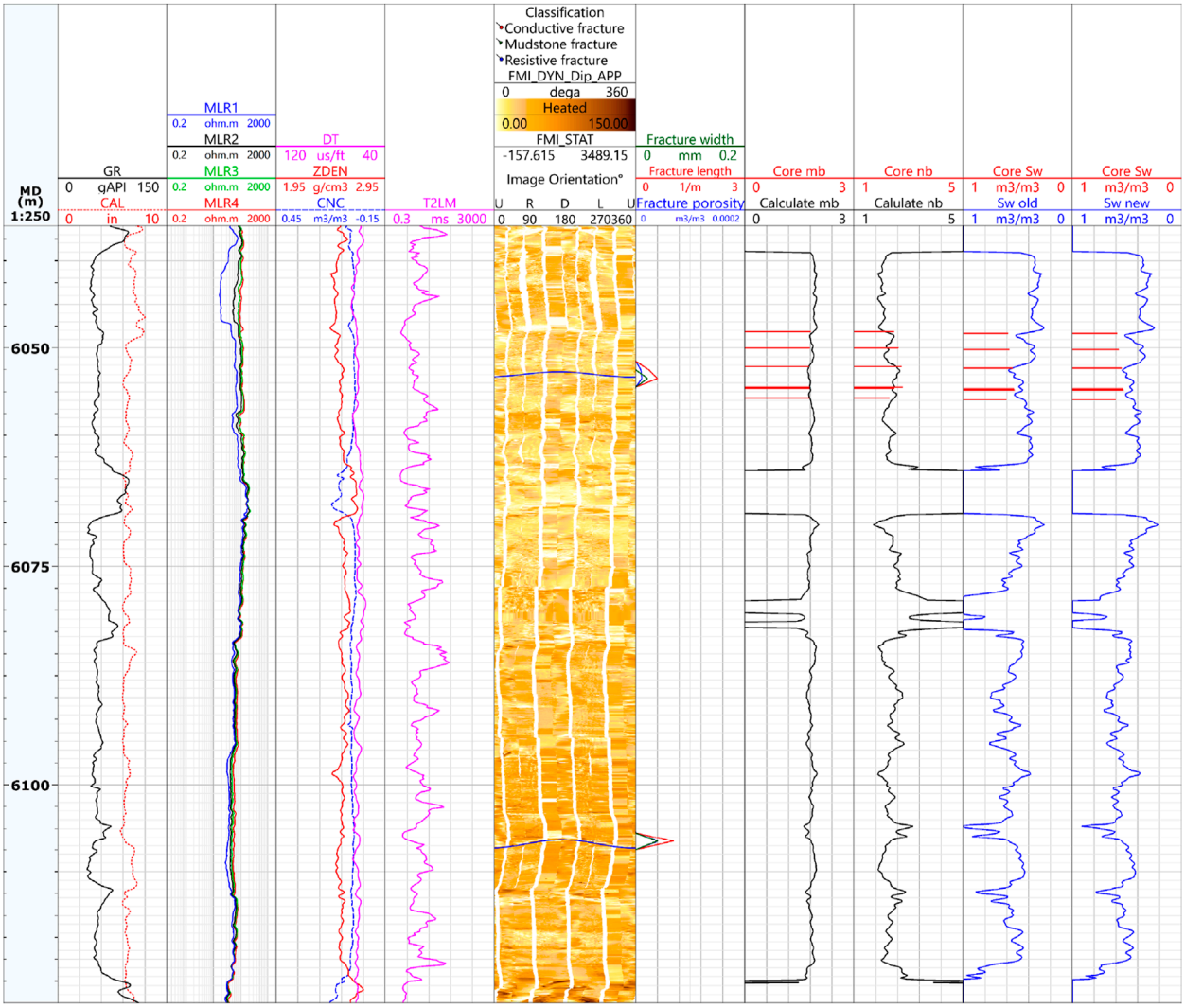

FIGURE 11
Saturation calculation results of the lower section of Ahe Formation in DB 5 Well, Dibei Gas Reservoir, Tarim Basin.

6 Discussion

Tight sandstone reservoirs are characterized by complex pore structure, high shale content, and developed fractures, but the Archie formula is applicable to pure sandstone reservoirs with favorable physical properties, and the accuracy of the Archie formula for calculating the water saturation of tight sandstone reservoirs is not high (Feng et al., 2023; Zhou et al., 2019). Different from the Archie formula, this paper adopts the dual porosity model for saturation calculation. The properties of the reservoir are influenced by its pore structure, and a precise understanding of the pore structure of the rock is the prerequisite for obtaining accurate saturation (Zhang, 2010). The fracture-matrix dual porosity model divides the rock pore system into two components: fracture porosity and matrix porosity. The fracture-matrix dual porosity model can independently consider the contribution of fracture and matrix porosity to the saturation, thus its calculation accuracy is high. In this paper, the precise parameters of the saturation model are determined by conducting the rock electricity and NMR experiments, further enhancing the calculation accuracy of the saturation model. The saturation calculation method proposed in this paper takes into account the multiple influences of lithology, physical properties, pore structure, and fractures on electrical properties. However, the Archie model merely considers the effects of physical properties and oil content on electrical properties (Hu et al., 2017). Therefore, the saturation calculated by this method is highly consistent with that of coring analysis and has high accuracy in the quantitative evaluation of hydrocarbon properties of tight sandstone reservoirs. Finally, when applying the saturation calculation method, it is necessary to carry out matching rock electricity and NMR measurement experiments to establish accurate model parameters.

TABLE 1 Comparative analysis table of saturation calculation error of Well Dibei 5 in Dibei Gas reservoir, Tarim Basin.

Depth (m)	Core analysis saturation (%)	Saturation calculated by archie formula (%)			Saturation calculated by the method in this paper (%)		
		Calculated value	Relative error	Absolute error	Calculated value	Absolute error	Relative error
5,842.73	56.28	52.10	4.18	7.43	57.06	0.78	1.38
5,844.04	59.49	53.76	5.73	9.62	59.24	0.25	0.42
5,845.27	57.98	56.81	1.17	2.02	64.38	6.40	11.04
5,845.49	65.51	58.33	7.18	10.96	66.03	0.52	0.79
5,846.43	68.12	61.70	6.42	9.42	69.09	0.97	1.42
6,048.12	59.22	53.21	6.01	10.14	57.75	1.47	2.48
6,049.98	57.81	41.97	15.84	27.40	43.73	14.08	24.36
6,052.1	54.97	59.65	4.68	8.51	60.37	5.4	9.82
6,054.49	53.84	52.28	1.56	2.90	54.31	0.47	0.87
6,054.63	53.11	51.55	1.56	2.95	53.59	0.48	0.90
6,055.73	60.55	50.13	10.42	17.21	52.25	8.30	13.71
Average	58.81	53.77	5.89	9.87	57.98	3.56	6.10

7 Conclusion

(1) Tight sandstone reservoirs are characterized by complex pore structure, high shale content, and developed fractures, which render the evaluation of saturation challenging. To address this issue, a method for calculating saturation in tight sandstone reservoirs is developed, comprehensively taking into account the influence of fractures, lithology, and other factors. If the shale content exceeds 20%, saturation is calculated using the Indonesian formula. Otherwise, the saturation is calculated using the double porosity model.

(2) The pore structure of rock constitutes one of the most crucial factors influencing the parameters of the saturation model. Based on the results of the rock resistivity and NMR experiments, porosity and the logarithmic mean value of T2 are chosen as input factors for calculating model parameters. Finally, the calculation model of m_b value and n_b value is established by the multiple regression method.

(3) The processing outcomes of logging data for tight sandstone reveal that the saturation calculation method proposed in this paper exhibits high precision in the saturation assessment of tight sandstone reservoirs. In contrast to the Archie model, this method considers the influences of lithology, pore structure, and fractures. Hence, the saturation evaluation results are more in line with the actual conditions of the reservoirs. The method proposed in this paper demonstrates excellent adaptability in the quantitative evaluation of saturation for tight sandstone reservoirs, and the saturation model suitable for other reservoirs will be further studied in the future.

Data availability statement

The datasets presented in this article are not readily available because exploratory research. Requests to access the datasets should be directed to PZ, pqzhao@cup.edu.cn.

Author contributions

YX: Conceptualization, Data curation, Formal Analysis, Investigation, Methodology, Software, Validation, Writing–original draft, Writing–review and editing. WD: Data curation, Formal Analysis, Methodology, Software, Validation, Writing–original draft, Writing–review and editing. CH: Validation, Writing–review and editing. KB: Validation, Writing–review and editing. XZ: Validation, Writing–review and editing. YA: Validation, Writing–review and editing. PZ: Supervision, Validation, Writing–review and editing.

Funding

The author(s) declare that no financial support was received for the research, authorship, and/or publication of this article.

Acknowledgments

The authors wish to appreciate the support provided by Tarim Oilfield Company and Beijing Key Laboratory of Earth Prospecting and Information Technology. The authors would also like to ackonwlege the editorial department and the reviewers for their comments on this paper.

Conflict of interest

Authors YX, CH, KB, XZ, and YA were employed by Tarim Oilfield Company and China National Petroleum Corporation.

The remaining authors declare that the research was conducted in the absence of any commercial or financial relationships that could be construed as a potential conflict of interest.

Publisher's note

All claims expressed in this article are solely those of the authors and do not necessarily represent those of their affiliated organizations, or those of the publisher, the editors and the reviewers. Any product that may be evaluated in this article, or claim that may be made by its manufacturer, is not guaranteed or endorsed by the publisher.

References

Aguilera, M. S., and Aguilera, R. (2003). Improved models for petrophysical analysis of dual porosity reservoirs. *Petrophysics - SPWLA J. Form. Eval. Reserv. Descr.* 44 (January), 21–35.

Aguilera, R. F., and Aguilera, R. (2004). A triple porosity model for petrophysical analysis of naturally fractured reservoirs. *Petrophysics - SPWLA J. Form. Eval. Reserv. Descr.* 45 (March), 157–166.

Archie, G. E. (1942). The electrical resistivity log as an aid in determining some reservoir characteristics. *Trans. Aime* 146 (01), 54–62. doi:10.2118/942054-G

Chen, Y., and Tan, M. J. (2003). Fracture detection and identification dsing logging techniques. *Well logging Technol.* 27 (S1), 11–14. doi:10.16489/j.issn.1004-1338.2003.s1.004

Clavier, C., Coates, G., and Dumanoir, J. (1984). Theoretical and experimental bases for the dual-water model for interpretation of shaly sands. *Soc. Petroleum Eng. J.* 24 (02), 153–168. doi:10.2118/6859-pa

Dai, J., Ni, Y., and Wu, X. (2012). Tight gas in China and its significance in exploration and exploitation. *Petroleum Explor. Dev.* 39 (3), 277–284. doi:10.1016/s1876-3804(12)60043-3

Desbois, G., Urai, J. L., Kukla, P. A., Konstanty, J., and Baerle, C. (2011). High-resolution 3D fabric and porosity model in a tight gas sandstone reservoir: a new approach to investigate microstructures from mm-to nm-scale combining argon beam cross-sectioning and SEM imaging. *J. Petroleum Sci. Eng.* 78, 243–257. doi:10.1016/j.petrol.2011.06.004

Ding, Y. J., Chai, X. Y., Shao, W. Z., Li, J. G., Han, Y., and Li, Q. H. (2017). Key parameters of water saturation based on concentration of T, spectrum distribution. *Well Logging Technol.* 41 (04), 405–411. doi:10.16489/j.issn.1004-1338.2017.04.005

Feng, S., Xie, R., Radwan, A. E., Wang, Y., Zhou, W., and Cai, W. (2023). Accurate determination of water saturation in tight sandstone gas reservoirs based on optimized Gaussian process regression. *Mar. Petroleum Geol.* 150, 106149. doi:10.1016/j.marpetgeo.2023.106149

Feng, S., Xie, R., Zhou, W., Yin, S., Chen, J., Zhang, M., et al. (2021). The new interpretation of the geological origin about differentiation phenomenon of resistivity in the tight sandstone reservoir. *Arabian J. Geosciences* 14 (20), 2074. doi:10.1007/s12517-021-08451-y

Gao, H., and Li, H. A. (2016). Pore structure characterization, permeability evaluation and enhanced gas recovery techniques of tight gas sandstones. *J. Nat. Gas Sci. Eng.* 28, 536–547. doi:10.1016/j.jngse.2015.12.018

Guo, Y., Pan, B., Zhang, L., Lei, J., Fan, Y., Ruhan, A., et al. (2022). A study on water saturation predictions in igneous reservoirs based on the relationship between the transverse relaxation time and the resistivity index. *J. Petroleum Sci. Eng.* 208, 109519. doi:10.1016/j.petrol.2021.109519

Hu, S. F., Zhou, C. C., Li, X., Li, C. L., and Zhang, S. Q. (2017). A tight sandstone trapezoidal pore oil saturation model. *Petroleum Explor. Dev.* 44 (5), 876–886. doi:10.1016/s1876-3804(17)30099-x

Jiang, H. (2018). *Experimental study of the conductivity model for tight oil rock in the Jurassic Systen of Sichuan Basin*. Beijing: China University of Petroleum. [dissertation/master's thesis]. [China (Beijing)].

Lai, J., Wang, G. W., Sun, S. M., Jiang, C., Zhou, L., Zheng, X. H., et al. (2015). Research advances in logging recognition and evaluation method of fractures in tight sandstone reservoirs. *Prog. Geophys. (in Chinese)* 30 (4), 1712–1724. doi:10.6038/pg20150426

Leveaux, J., and Poupon, A. (1971). Evaluation of water saturation in shaly formations. *The Log Analyst* 12 (04), 3–8.

Li, X., Li, C. L., Li, B., Liu, X. F., and Yuan, C. (2020). Response laws of electrical property and saturation evaluation method of tight sandstone. *Petroleum Exploration and Development* 47 (1), 202–212. doi:10.11698/PED.2020.01.20

Li, X., Zhao, W. Z., Zhou, C. C., Wang, T. S., and Li, C. L. (2012). Dual-porosity saturation model of low-porosity and low-permeability clastic reservoirs. *Petroleum Exploration and Development* 39 (01), 88–98. doi:10.1016/s1876-3804(12)60019-6

Liao, Q. Z., Wang, B., Chen, X., and Tan, P. (2024). Reservoir stimulation for unconventional oil and gas resources: recent advances and future perspectives. *Advances in Geo-Energy Research* 13 (1), 7–9. doi:10.46690/ager.2024.07.02

Liu, Z. Y., Zhang, C. G., Tang, J., and Xiao, C. G. (2018). Influence of fracture on rock resistivity and its application in saturation calculation. *Lithologic Reservoirs* 30 (02), 120–128. doi:10.12108/yxyqc.20180213

Luo, Q. (2010). Core observation and description of tight sandstone fractured reservoir an example from Wen ming zhai tight sandstone. *Xinjiang Petroleum Geology (in Chinese)* 31 (3), 229–231. doi:10.3724/SP.J.1077.2010.01195

Luo, S. C., Cheng, Z. G., Zhou, J. Y., Xi, H., and Wang, C. S. (2014). Research on saturation index n of tight sandstone reservoir. *Journal of Southwest Petroleum University Science and Technology Edition* 36 (04), 116–122. doi:10.11885/j.issn.1674-5086.2013.10.10.01.html

Rezaee, R., Saeedi, A., and Clennell, B. (2012). Tight gas sands permeability estimation from mercury injection capillary pressure and nuclear magnetic resonance data. *Journal of Petroleum Science and Engineering* 88–89, 92–99. doi:10.1016/j.petrol.2011.12.014

Shi, H., Luo, X. R., Lei, G. L., Wei, H. X., Zhang, L. Q., Zhang, L. K., et al. (2018). Effects of early oil emplacement on reservoir quality and gas migration in the Lower Jurassic tight sand reservoirs of Dibei gas field, Kuqa Depression, western China. *Journal of Natural Gas Science and Engineering* 50, 250–258. doi:10.1016/j.jngse.2017.12.004

Shi, P. Y., Shi, P. D., Bie, K., Han, C., Ni, X. W., Mao, Z. Q., et al. (2024). Prediction of permeability in a tight sandstone reservoir using a gated network stacking model driven by data and physical models. *Frontiers in Earth Science* 12. doi:10.3389/feart.2024.1364515

Silva, P. L., and Bassiouni, Z. (1986). Statistical evaluation of the S-b conductivity model for water-bearing shaly formations. *The log analyst* 27 (3), 9–19.

Simandoux, P. (1963). Dielectric measurements on porous media, application to the measurements of water saturation: study of behavior of argillaceous formations. *Revue de L' Institut Francais du Petrole.* 18 (S1), 193–215.

Tang, J., Xin, Y., Cai, D. Y., and Zhang, C. G. (2018). A method of calculating saturation for tight sandstone reservoirs: a case of tight sandstone reservoir in Dabie area of Kuqa depression in Tarim Basin of NW China. *Open Journal of Yangtze Oil and Gas* 03, 21–35. doi:10.4236/ojogas.2018.31003

Vincent, M., and Wladyslaw, A. (2015). Calculation of water saturation in low resistivity gas reservoirs and pay-zones of the Cretaceous Grudja Formation, onshore Mozambique basin. *Marine and Petroleum Geology* 67 (11), 249–261. doi:10.1016/j.marpetgeo.2015.05.016

Wang, L., Sun, B. D., Shen, A. X., and Wan, J. B. (2005). On application of rock electricity parameters of shaly sand reservoir with low-porosity and permeability, permeability, × field. *Well Logging Technology* 29 (02), 91–94+184. doi:10.16489/j.issn.1004-1338.2005.02.001

Wang, Q. (2020). *Study on saturation model and water cut evaluation method of tight sandstone*. China University of Geosciences. [dissertation/master's thesis]. [China(Beijing)].

Wang, Q., Tan, M. J., Xiao, C. W., Wang, S. Y., Han, C., and Zhang, L. T. (2022). Pore-scale electrical numerical simulation and new saturation model of fractured tight sandstone. *AAPG Bulletin* 106 (7), 1479–1497. doi:10.1306/04132220165

Waxman, M. H., and Smits, L. J. M. (1968). Electrical conductivities in oil-bearing shaly sands. *Society of Petroleum Engineers Journal* 8 (02), 107–122. doi:10.2118/1863-A

Xiao, L., Zou, C. C., Mao, Z. Q., Shi, Y. J., Liu, X. P., Jin, Y., et al. (2013). Estimation of water saturation from nuclear magnetic resonance (NMR) and conventional logs in low permeability sandstone reservoirs. *Journal of Petroleum Science and Engineering* 108 (August), 40–51. doi:10.1016/j.petrol.2013.05.009

Yan, J. P., Wen, D. N., Li, Z. Z., Gen, B., Liang, Q., and He, X. (2015). The influence of low permeable sandstone pore structure on rock electrical parameters and its applications. *Natural Gas Geoscience* 26 (12), 2227–2233. doi:10.11764/j.issn.1672-1926.2015.12.2227

Yong, S. H., and Zhang, C. M. (1986). *Logging data processing and comprehensive interpretation*. Beijing: China University of Petroleum Press.

Zeng, L. B., Su, H., Tang, X. M., Peng, Y. M., and Lei, G. (2013). Fractured tight sandstone oil and gas reservoirs: a new play type in the Dongpu depression. Bohai Bay basin, China. *AAPG Bulletin* 97 (3), 363–377. doi:10.1306/09121212057

Zhang, H. M. (2010). *Saturation interpretation model study on fractured reservoirs*. East China: China University of Petroleum. [dissertation/master's thesis]. [China(Qingdao)].

Zhang, J. Y., Liu, H. H., Liu, W., J. Sun, M., and Zhao, J. P. (2015). Thin sand and mudstone interbed saturation model based on a dual mudstone indicator. *Petroleum Drilling Techniques* 43 (02), 59–62. doi:10.11911/syztjs.201502011

Zhang, L. H., Zhou, C. C., Liu, G. Q., Xiu, L. J., Li, C. X., and Liu, Z. H. (2006). Influence of pore structures on electric properties and well logging evaluation in low porosity and permeability reservoirs. *Petroleum Exploration and Development* 33 (06), 671–676. doi:10.3321/j.issn:1000-0747.2006.06.006

Zhang, M. L., and Shi, Y. J. (2005). On archie's electrical parameters of sandstone reservoir with complicated pore structures. *Well Logging Technology* 29 (01), 21-23+28–12. doi:10.16489/j.issn.1004-1338.2005.05.016

Zhang, X., Li, Q. P., Li, L. X., Fan, Q., and Geng, J. H. (2023). Combination of sonic wave velocity, density and electrical resistivity for joint estimation of gas-hydrate reservoir parameters and their uncertainties. *Advances in Geo-Energy Research* 10 (2), 133–140. doi:10.46690/ager.2023.11.07

Zhao, G. J., Li, X. Q., Liu, M. C., Dong, C. Y., Chen, D. Y., and Zhang, J. (2022). Reservoir characteristics of tight sandstone and sweet spot prediction of Dibei gas field in eastern Kuqa depression, northwest China. *Energies* 15 (9), 3135. doi:10.3390/en15093135

Zhao, H., Shi, X., and SiMa, L. Q. (2012). Study on porosity exponent, saturation and fracture porosity for fractured reservoirs. *Progress in Geophysics. (in Chinese)* 27 (6), 2639–2645. doi:10.6038/j.issn.1004-2903.2012.06.043

Zhao, P. Q., Wang, Y. T., Li, G. R., Hu, C., Xie, J. R., Duan, W., et al. (2023). Joint inversion of saturation and qv in low-permeability sandstones using spontaneous potential and resistivity logs. *Petrophysics* 64, 741–752. doi:10.30632/PJV64N5-2023a8

Zhou, X. Q., Zhang, C., Zhang, Z. S., Zhang, R. F., Zhu, L. Q., and Zhang, C. M. (2019). A saturation evaluation method in tight gas sandstones based on diagenetic facies. *Marine and Petroleum Geology* 107, 310–325. doi:10.1016/j.marpetgeo.2019.05.022

Zou, C. N., Zhu, R. X., Liu, K. Y., Su, L., Bai, B. J., Zhang, X. X., et al. (2012). Tight gas sandstone reservoirs in China: characteristics and recognition criteria. *Journal of Petroleum Science and Engineering* 88 (89), 82–91. doi:10.1016/j.petrol.2012.02.001

frontiers | Frontiers in Earth Science

TYPE Original Research
PUBLISHED 21 October 2024
DOI 10.3389/feart.2024.1438930

OPEN ACCESS

EDITED BY
Huaimin Dong,
Chang'an University, China

REVIEWED BY
Suhaib Umer Ilyas,
Jeddah University, Saudi Arabia
Lin Zhang,
Hohai University, China

*CORRESPONDENCE
Jian Zhang,
zj451755562@gmail.com

RECEIVED 27 May 2024
ACCEPTED 30 September 2024
PUBLISHED 21 October 2024

CITATION
Du H, Zhang J, Zhao D, Wang S and Xu J (2024) Modeling the effect of dispersion and attenuation for frequency-dependent amplitude variation with offset.
Front. Earth Sci. 12:1438930.
doi: 10.3389/feart.2024.1438930

Modeling the effect of dispersion and attenuation for frequency-dependent amplitude variation with offset

Haoqi Du[1,2], Jian Zhang[1,2,3]*, Dongchang Zhao[4], Shuaiyang Wang[1,2] and Jiaqian Xu[1,2]

[1]The Faculty of Geosciences and Engineering, Southwest Jiaotong University, Chengdu, China, [2]Sichuan Province Engineering Technology Research Center of Ecological Mitigation of Geohazards in Tibet Plateau Transportation Corridors, Chengdu, China, [3]National Key Laboratory of Petroleum Resources and Engineering, China University of Petroleum, Beijing, China, [4]Sichuan Water Development Investigation, Design & Research Co., Ltd., Chengdu, China

As research in oil and gas exploration progresses, unconventional resources, such as shale gas, are increasingly becoming the focal point in the global pursuit of oil and gas resource. Shale gas reservoirs significantly differ from conventional sandstone reservoirs in aspects such as rock composition, pore type, occurrence mode, fluid, etc., thereby amplifying the challenges associated with geophysical modeling and the prediction of sweet spots. Since the formation and storage of shale gas are positively correlated with shale fracturing, a modeling approach based on Chapman theory is introduced to complete frequency-dependent petrophysical modeling. Additionally, the Frequency-dependent Amplitude Variation with Offset (FAVO) technique can estimate velocity dispersion by using the reflection coefficient information related to incidence angle and frequency. This method can more effectively identify fluids within shale reservoir. However, current FAVO forward modeling only considers the velocity dispersion and attenuation at the interface, neglecting the attenuation dispersion effects during interlayer propagation. To this end, we utilize Chapman-based petrophysical modeling as a foundation and conduct seismic forward modeling studies employing the compound matrix method. Through experimental analysis, we meticulously examine the attenuation dispersion effects at interfaces and within layers. Finally, we conduct FAVO simulations that vividly delineate the interplay between reservoir parameters and seismic responses.

KEYWORDS

frequency-dependent AVO, shale gas reservoirs, petrophysical modeling, attenuation dispersion effect, compound matrix algorithm

1 Introduction

Currently, the shortage of oil and gas resources has become a universal challenge faced by countries worldwide, leading to an increased focus on the development of unconventional oil and gas resources. Shale gas, as a typical unconventional oil and gas resource, is an important natural gas resource, accounting for about 50% of unconventional natural gas resources. It possesses immense exploration potential and utilization value (Zhen et al., 2013; Hou et al., 2023). Accurate petrophysical modeling of shale gas reservoir is an important step for seismic

exploration of shale gas. The equivalent theoretical model is an important tool for petrophysical research, which idealizes shale gas reservoir through certain assumptions, so as to establish the relationship between seismic response and the properties of shale gas reservoir. In shale gas reservoirs, the pore and crack system is the main storage and transportation channel for gas. Almost all oil and gas reservoirs are affected by natural cracks, which constitute one of the most significant factors affecting the capacity of unconventional shale gas reservoirs. Meanwhile, the presence of cracks complicates the physical properties of shale gas reservoirs, which are highly variable and show strong anisotropy in both vertical and horizontal directions. The traditional anisotropic equivalent medium theory for crack does not consider the effect of frequency on the elastic parameters of the model, leading to insensitivity of crack scale in such models (Hudson, 1980; Schoenberg, 1980; Hudson, 1981). For example, a few large horizontally arranged cracks developed in a homogeneous isotropic media can be equivalently represented by a larger number of small horizontally arranged cracks in the same medium. Subsequently, some scholars proposed an equivalent model based on the mechanism of attenuation and velocity dispersion produced by extrusion injection from small pores to large pores - the squirt-flow mechanism (i.e., fluid flow induced by seismic waves) (Dvorkin et al., 1995; Thomsen, 1995; Hudson et al., 1996; Pointer et al., 2000; Van Der Kolk et al., 2001; Ba et al., 2017; Zhang et al., 2021). However, these models cannot explain the frequency-dependent characteristics of seismic anisotropy across the full frequency range. Chapman, 2003; Chapman et al., 2006; Chapman et al., 2002) subsequently propose a dynamic equivalent petrophysical model, which incorporates the pore elasticity theory of particle squirt flows and combines a set of oriented mesoscopic cracks. The results show that the model can accurately predict attenuation and seismic dispersion effects within seismic frequency bands (Maultzsch et al., 2003; Liu et al., 2014). Therefore, the petrophysical model of shale gas reservoirs established based on Chapman theory effectively establishes the relationship between physical and seismic characteristics, providing a crucial foundation for the description and identification of shale gas reservoirs.

Reliable petrophysical models can serve frequency-dependent Amplitude Variation with Offset (FAVO) studies. FAVO technology is an organic combination of conventional AVO and frequency-dependent fluid identification techniques. It can make full use of the reflection coefficient's variation with incidence angle and frequency to estimate the amplitude attenuation and velocity dispersion characteristics of the reservoir within the seismic frequency band. Subsequently, combining these features with the physical mechanisms of attenuation dispersion can yield accurate petrophysical properties of the reservoir. Therefore, FAVO technology has become an important means to identify reservoir fluids (Wu, 2010; Cheng et al., 2012). In particular, the realization of accurate forward simulation of FAVO can more accurately establish the relationship between shale gas reservoir parameters and seismic response, which is essential for the identification of shale gas. In the study of FAVO, Zoeppritz (1919) gives a formula for calculating the reflection coefficient and transmission coefficients at an interface when a P-wave is incident, known as the "Zoeppritz equation". Many scholars have performed linear approximations of the Zoeppritz equation to reduce the computational complexity at the cost of accuracy (Bortfeld, 1961; Shuey, 1985; Smith and Gidlow, 1987; Hilterman, 1990). To ensure the accuracy of the results, many scholars have refined the Zoeppritz equation. Although these theories have succeeded in reducing computational complexity and improving the accuracy of the results, they typically only consider the influence of single interface conditions. It is shown that when the reservoir possesses a certain thickness, the interlayer effect can affect AVO characteristics, and its influence on the AVO response cannot be ignored. Therefore, building on this foundation, a large number of scholars have carried out studies based on full-wavefield forward modeling. Carcione et al., 2003 simulate the wave field in a patchy-saturated medium base on the finite-difference algorithm, wherein the elastic parameters were replaced with their corresponding complex elastic parameters. Moreover, they calculated and analyzed the seismic response corresponding to attenuation and velocity dispersion (Carcione et al., 2003; Wang et al., 2006). This wavefield numerical simulation method, while highly accurate, incurs extremely high computational costs. Utilizing a viscoelastic medium model to characterize the viscoelastic properties of fractured porous media can effectively reduce these computational costs, thereby enabling the simulation of seismic responses through wavefield modeling. Sidler et al. (2013) compare the seismic records formed by equivalent viscoelastic theory and pore theory, demonstrating that both have the same dispersion and attenuation characteristics. This method weakens the understanding of the physical mechanism involved in wavefield simulation. In contrast, obtaining the complex elastic parameters of a porous fractured medium through its physical attenuation mechanism is considered the most appropriate approach. Then, the viscoelastic wave equation is solved analytically to accurately obtain the corresponding seismic response while reducing the complexity of numerical simulation. Ren et al. (2009a, b) derive a formula for the frequently-dependent reflection coefficient at the interface between an elastic medium and a viscoelastic medium under conditions of vertical incidence. Liu et al. derive the frequency-varying reflection coefficient at the interface between non-dispersive and dispersive media under conditions of non-vertical incidence, based on the "Zoeppritz" equation (Liu et al., 2011). Zhao et al. (2014) provide a formula for the frequency-dependent reflection coefficient of scattered viscoelastic media. Guo et al. (2015) combine the rock physical model with seismic modeling and obtain the expression for the reflection coefficient based on propagation matrix theory. All the above studies are based on the assumption that the overlying layer is elastic, that is, only the attenuation and velocity dispersion effects of seismic waves at the interface are considered, while these effects between layers are not considered. Besides, there are some limitations to the propagation matrix theory in wavefield forward simulation. The method requires solving for the eigenvalues of the characteristic polynomials corresponding to the system matrix R when calculating the reflection coefficients for the comprehensive response of layered medium using the conventional matrix algorithm. In order to stabilize the final solution process, matrix product operations are required. It has been proved that as frequency increases, the matrix components gradually increase, leading to the loss of the effective value of the characteristic function. This leads to difficulties in obtaining accurate eigenvalues. And at greater depths, the eigenfunctions similarly lose important values under conditions of suitable frequency values. Due to the serious numerical ill-posed of analytic solutions of the propagation matrix

algorithm, three suitable solution methods have been derived (Sen and Roy, 2003), including recursive matrix algorithm (Kennett, 2009), compound matrix algorithm (Schmidt and Tango, 1986) and global large matrix algorithm (Phinney et al., 1987). The compound matrix algorithm is based on the compound rearrangement of the original propagation matrix solution system. The 4×4 matrices involved in the calculation are analytically rearranged into 6×6 matrices, and the analytical solution of the reflection coefficient is quickly obtained through a simple vectorization loop. The compound matrix algorithm is a generalized reflectivity method that is widely used in seismic exploration. Compared with the other two methods, it consumes less memory, runs faster, and has a simpler program implementation when the medium is isotropic. Therefore, it is a reasonable attempt to extend the compound matrix method to viscoelastic medium for wavefield forward modeling.

The principal contribution of this paper lies in constructing a model that precisely encapsulates the relationship between shale reservoir parameters and seismic response by integrating Chapman theory with the compound matrix method. The Chapman model is employed as an equivalent petrophysical model to investigate FAVO effects within shale gas reservoirs. Subsequently, the complex elasticity parameter (i.e., complex velocity) is utilized as input for wavefield forward modeling, thereby facilitating the simulation of seismic responses. The method takes into account the comprehensive propagation response, including attenuation dispersion effects, transmission losses, and converted waves at interfaces and between layers, thus more accurately simulating the seismic response of shale gas reservoirs. Considering the influence of propagation process, we re-establish the relationship between reservoir parameters, such as crack density, porosity, gas saturation, and crack aspect ratio and seismic response. Based the established model, we conduct a thorough analysis of the sensitivity of seismic response to the petrophysical parameters of shale gas reservoirs, thereby providing a foundation for the characterization and assessment of these reservoirs.

2 Methods

To accurately perform FAVO forward modeling of shale reservoir, we derive the relationship between a series of shale reservoir parameters and seismic response. We construct a petrophysical model of shale reservoir based on Chapman theory and use it as a bridge to establish the relationship between elastic parameters and FAVO response using the viscoelastic compound matrix algorithm.

2.1 Petrophysical modeling of shale reservoir based on chapman theory

Cracks are important for shale gas resource development and storage. Incorporating the physical properties of crack into the petrophysical modeling of shale gas reservoirs remains a key focus and challenge in current research. Chapman et al. 2002; Chapman et al. 2003 propose a micro-structure squirt flow theoretical model, which is consistent with Gassmann theory at low frequencies and squirt flow-related dispersion at high frequencies. Based on the squirt flow fluid model, an equivalent petrophysical model that considers mesoscale cracks, microscale pores and cracks is proposed. By inserting directional elliptic cracks and spherical pores into the isotropic medium, it is proved that the influence of micro-cracks is negligible. Therefore, only mesoscale and micro-scale cracks are considered, where the pores are interconnected, but the cracks are not, meaning one crack can be connected to multiple pores. Petrophysical modeling of shale reservoir using this model can take into account both mesoscale and microscopic scale fluid flows, providing a reasonable explanation of attenuation and velocity dispersion effects within seismic frequency bands. In order to accurately describe the equivalent model of shale reservoir, a series of parameters such as crack density, porosity, crack aspect ratio, fluid saturation, and time scale of shale reservoirs are needed. A schematic diagram of a multiscale model of a fracture-bearing porous medium for petrophysical modeling is shown in Figure 1.

For an equivalent dispersion model at different scales, the effective bulk modulus and effective shear modulus (Equations 1, 2) can be expressed as:

$$K_{eff} = \beta + \frac{2}{3}\mu - \frac{4eps\beta + \frac{4}{3}\mu^2(\beta+2\mu)}{3\mu(\beta+\mu)} - \frac{por\left(\beta+\frac{2}{3}\mu\right)(\beta+2\mu)}{4\mu} + eps\left(\frac{4\beta+\frac{4}{3}\mu^2(\beta+2\mu)}{3\mu(\beta+\mu)} + 4\pi r\left(\beta+\frac{2}{3}\mu\right)\right)A + \frac{9por(\beta+2\mu)\left(\beta+\frac{2}{3}\mu\right)B}{4\mu} \tag{1}$$

$$U_{eff} = \mu - \frac{16eps\mu(\beta+2\mu)\left(K_c+\frac{1}{1+i\omega\tau_m}\right)}{45(1+K_c)(3\beta+4\mu)} - \frac{32eps\mu(\beta+2\mu)}{45(3\beta+4\mu)} - \frac{15por\mu(\beta+2\mu)}{3\beta+4\mu} \tag{2}$$

where $\beta = v_{p_0}^2\rho - 2\mu$, $\mu = v_{s_0}^2\rho$. v_{P0} is the P-wave velocity when the shale reservoir is not cracked, and v_{S0} is the S-wave velocity when the shale reservoir is not cracked. *eps* is the crack density, *por* is the porosity; r is the crack aspect ratio, τ_m is the timescale parameter. K_p is the pore-space compressibility parameter, and K_c is the crack-space compressibility parameter, with the expressions (Equations 3, 4) being:

$$K_c = \frac{4\mu}{3K_f} \tag{3}$$

$$K_p = \frac{\pi\mu r(\beta+\mu)}{K_f(\beta+2\mu)} \tag{4}$$

where K_f is the fluid bulk modulus.

The expressions (Equations 5, 6) for the frequency-dependent parameters A and B are:

$$A = \frac{\frac{i\omega\tau_m}{3(1+K_c)} - \gamma' i\omega\tau_m + \left(\gamma' + \frac{1}{3(1+K_c)}\right)\left(\frac{1+i\omega\tau_m\gamma}{\gamma}\right)}{1 + i\omega\tau_m + \frac{1+i\omega\tau_m\gamma}{\gamma}} \tag{5}$$

$$B = \frac{(1+i\omega\tau_m)\left(\frac{1}{3(1+K_c)} + \gamma'\right) + i\omega\tau_m\left(\gamma' - \frac{1}{3(1+K_c)}\right)}{1 + i\omega\tau_m\gamma + \gamma(1+i\omega\tau_m)} \tag{6}$$

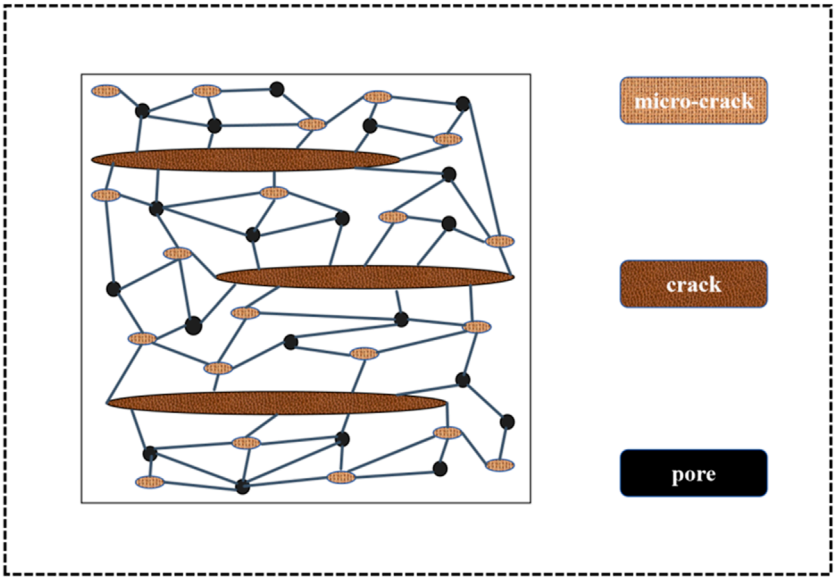

FIGURE 1
Schematic diagram of a multiscale model of a crack-bearing porous medium for petrophysical modeling, where the pores are interconnected, but the cracks are not.

TABLE 1 Numerical values used in the computations. Solid parameters of shale gas reservoir.

Solid parameter	V_{P0} (uncracked) (m/s)	V_{S0} (uncracked) (m/s)	Time scale parameter	Grain density (g/cm3)
	4,250	2,300	0.02	2.455

TABLE 2 Numerical values used in the computations. Fluid parameters of shale gas reservoirs, where fluid types include brine and gas.

Fluid parameter	Bulk modulus (MPa)	Density (g/cm3)
brine	2,800	1.09
gas	400	0.065

The expressions (Equations 7, 8) of non-dimensional parameters γ and γ' are:

$$\gamma' = \frac{\gamma(\beta + 2\mu)}{(3\beta + 2\mu)(1 + K_p)} \tag{7}$$

$$\gamma = \frac{9por(1 + K_p)(\beta + \mu)}{16eps(1 + K_c)(\beta + 2\mu)} \tag{8}$$

As a result, we can derive the effective bulk modulus and effective shear modulus of the shale reservoir, and thereby obtain the complex velocity of the vertical and horizontal waves. And the expressions are $v_{cp} = \sqrt{\frac{K_{eff} + \frac{4}{3}U_{eff}}{\rho}}$, $v_{cs} = \sqrt{\frac{U_{eff}}{\rho}}$. Finally, according to the obtained P-wave and S-wave complex velocity, the P-wave

TABLE 3 Numerical values used in the computations. Reservoir parameters of the constructed two-layer shale gas reservoir. Here, the thickness of the upper layer here is 1000 m.

Reservoir Parameter	Porosity	Crack density	Crack aspect ratio	Gas saturation
Upper layer	0.05	0.05	0.0001	0.5
Lower layer	0.15	0.10	0.00001	0.3

and S-wave quality factors can be determined using the following expressions (Equations 9, 10):

$$v_p = \left[\mathrm{Re}\left(\frac{1}{v_{cp}}\right)\right]^{-1}, v_s = \left[\mathrm{Re}\left(\frac{1}{v_{cs}}\right)\right]^{-1} \tag{9}$$

$$Q_p = \frac{\mathrm{Im}\left(v_{cp}^{\ 2}\right)}{\mathrm{Re}\left(v_{cp}^{\ 2}\right)}, Q_s = \frac{\mathrm{Im}\left(v_{cs}^{\ 2}\right)}{\mathrm{Re}\left(v_{cs}^{\ 2}\right)} \tag{10}$$

2.2 Forward simulation of viscoelastic compound matrix algorithm

In order to obtain seismic response based on rock physical modeling, we need to carry out forward seismic modeling researches. In this paper, in order to realize full wavefield simulation, the method of wave equation analytic solution (i.e., compound matrix algorithm) is proposed for seismic forward modeling. The compound matrix algorithm utilizes the second and third-order subdeterminant of the system matrix to transform

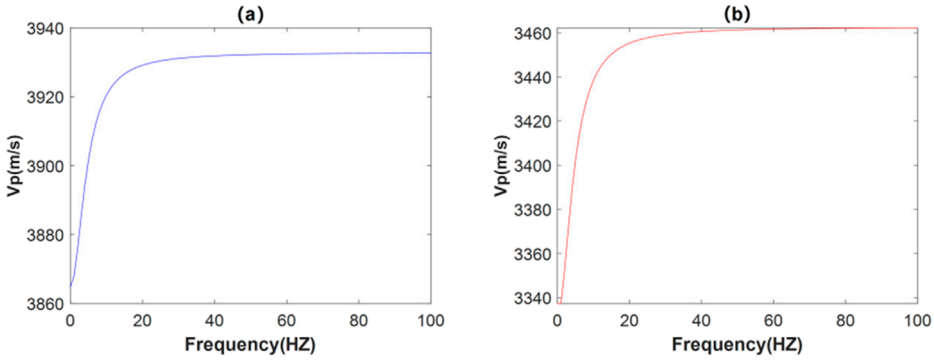

FIGURE 2
Variation of P-wave velocity with frequency for a two-layer shale gas reservoir model. **(A)** Upper layer. **(B)** Lower layer.

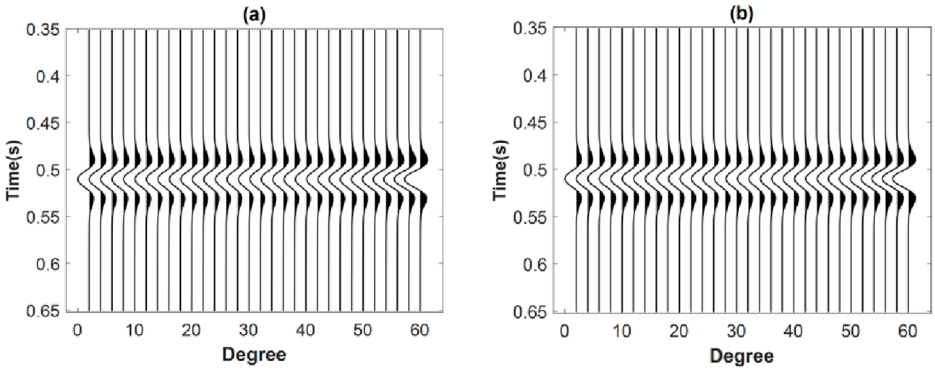

FIGURE 3
Comparison of angle gathers obtained from forward simulations for different media. **(A)** Two-layer cracked porous media. **(B)** Two-layer elastic medium.

the original system matrix into a new compound matrix. This approach ensures that the final computed analytical solution is free from numerical ill-posed. Moreover, vectorization operations not only reduce computational cost but also can quickly obtain high-precision seismic records. The specific steps for generalizing the compound matrix algorithm to viscoelastic media are as follows:

For a viscoelastic medium composed of N horizontally layers, the total reflection coefficient response can be obtained using the propagation vector (Equation 11):

$$v_i = \begin{bmatrix} \triangle & -R_{ps}\triangle & -R_{ss} & R_{pp}\triangle & R_{sp}\triangle & |R|\triangle \end{bmatrix}^T \tag{11}$$

The physical meaning of this formula refers to the propagation response from the lowest layer to the ith layer. Where Δ is the determinant of the system matrix, the value of which has no effect on the final calculation result. R_{pp}, R_{ss}, R_{ps} and R_{sp} represent the reflection coefficients of PP wave, SS wave, PS wave and SP wave, respectively. The determinant $|R| = \begin{vmatrix} R_{pp} & R_{ss} \\ R_{ps} & R_{sp} \end{vmatrix}$ in the formula has no physical meaning.

In order to calculate the total reflection coefficient of a layered viscoelastic medium, it is necessary to calculate the total propagation vector v_0 from the bottom up, i.e., from the Nth layer to the first layer (the surface). In order to effectively reduce the computational complexity, the layer propagation matrix G_i is defined by Equation 12:

$$v_i = G_i v_{i+1} \tag{12}$$

where G_i is the layer propagation matrix, the specific expression is shown in Appendix A.

Since the Nth layer is the lowest layer, it can be regarded as an infinite half-space viscoelastic medium with only reflections, and the propagation vector (Equation 13) of the Nth layer is:

$$v_N = \begin{bmatrix} 1 & 0 & 0 & 0 & 0 & 0 \end{bmatrix}^T \tag{13}$$

Finally, the total propagation vector v_0 can be calculated by the Equation 11. The reflection coefficient (Equation 14) of the attenuation effect can be obtained:

$$R_{\mathrm{pp}} = \frac{v_0(4)}{v_0(1)} = \frac{R_{pp}\triangle}{\triangle} \tag{14}$$

According to the conventional generalized reflectance method, the time-domain seismogram can be obtained by integrating

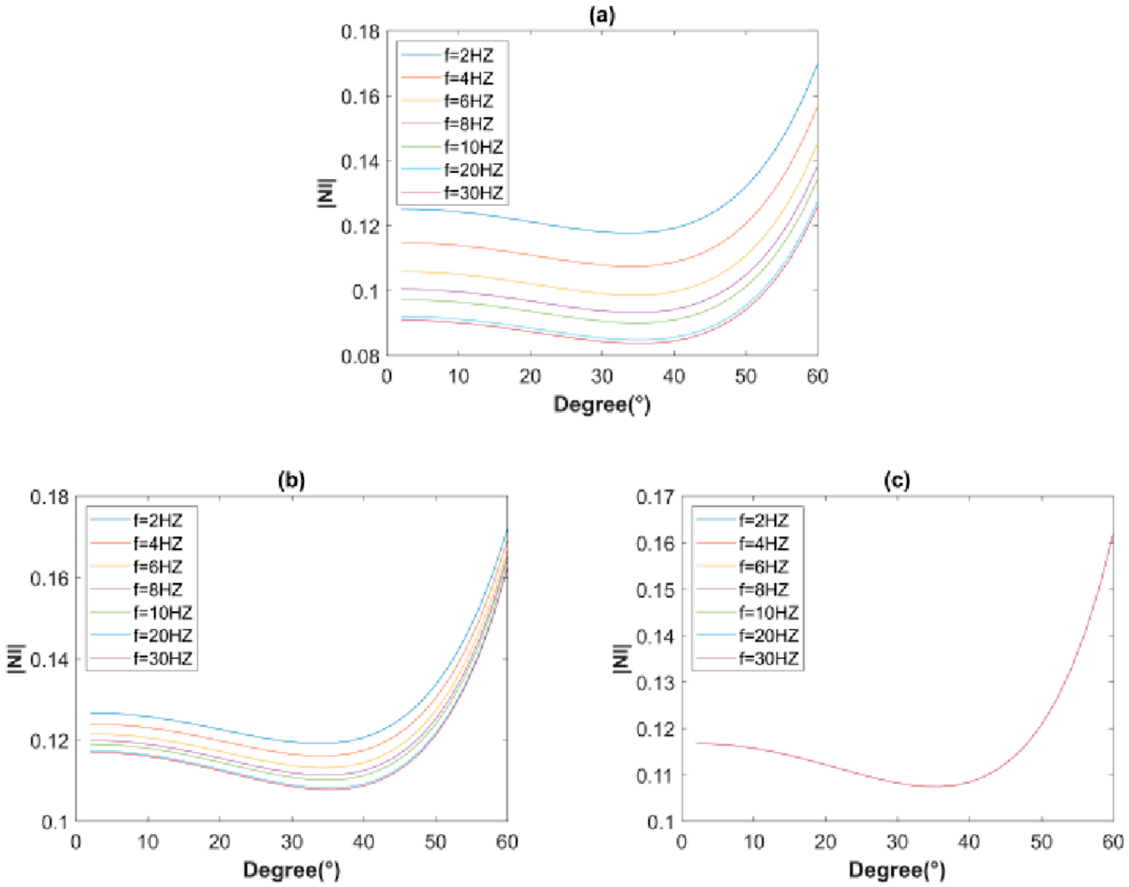

FIGURE 4
Variation of reflection coefficient with angle of incidence in the frequency range of 2–30 Hz for different medium models. **(A)** Two-layer cracked porous media. **(B)** The upper elastic medium and the lower cracked porous medium. **(C)** Two-layer elastic medium.

the frequency-slowness domain reflectance coefficient $R_{pp}(\omega,p)$, as follows (Equation 15):

$$G(t,x)=\frac{1}{2\pi}\int_{-\infty}^{\infty}\int_{-\infty}^{\infty}S(\omega)e^{j\omega t}\omega^2 pR_{pp}(\omega,p)J_0(\omega px)d\omega dp \qquad (15)$$

where $S(\omega)$ is the frequency-domain representation of the seismic wavelet, and $J_0(\omega px)$ is the 0-order form of the Bessel function.

3 Application

In order to establish the relationship between physical parameters of shale gas reservoir and seismic response, the Chapman model is selected as the petrophysical model to analyze the dispersion effects in shale gas reservoirs. FAVO forward analysis is carried out using the compound matrix algorithm, while considering the influence of attenuation and dispersion effects between layers and interfaces. Finally, the relationship between the petrophysical parameters of shale gas reservoir (e.g., crack density, porosity, crack aspect ratio, and gas saturation) and seismic response characteristics is experimentally analyzed.

3.1 Attenuation and velocity dispersion effect

Based on the actual physical properties of shale reservoirs from Eastern Sichuan Basin, a two-layer shale gas reservoir model is constructed for experiments. The corresponding crack pore medium parameters and the corresponding reservoir elastic and physical property parameters are shown in Tables 1–3. The set parameters are derived from actual data, while some of them refer to existing literature (Chapman et al., 2006; Pang and Stovas, 2020). The P-wave velocity *versus* frequency variation for the upper and lower layers is shown in Figure 2.

According to the slope of the curve, it can be seen that the dispersion of seismic waves initially increases with the rise in frequency, and then it progressively diminishes beyond a certain frequency threshold. Concurrently, as the frequency continues to increase, the P-wave velocity exhibits a gradual upward trend.

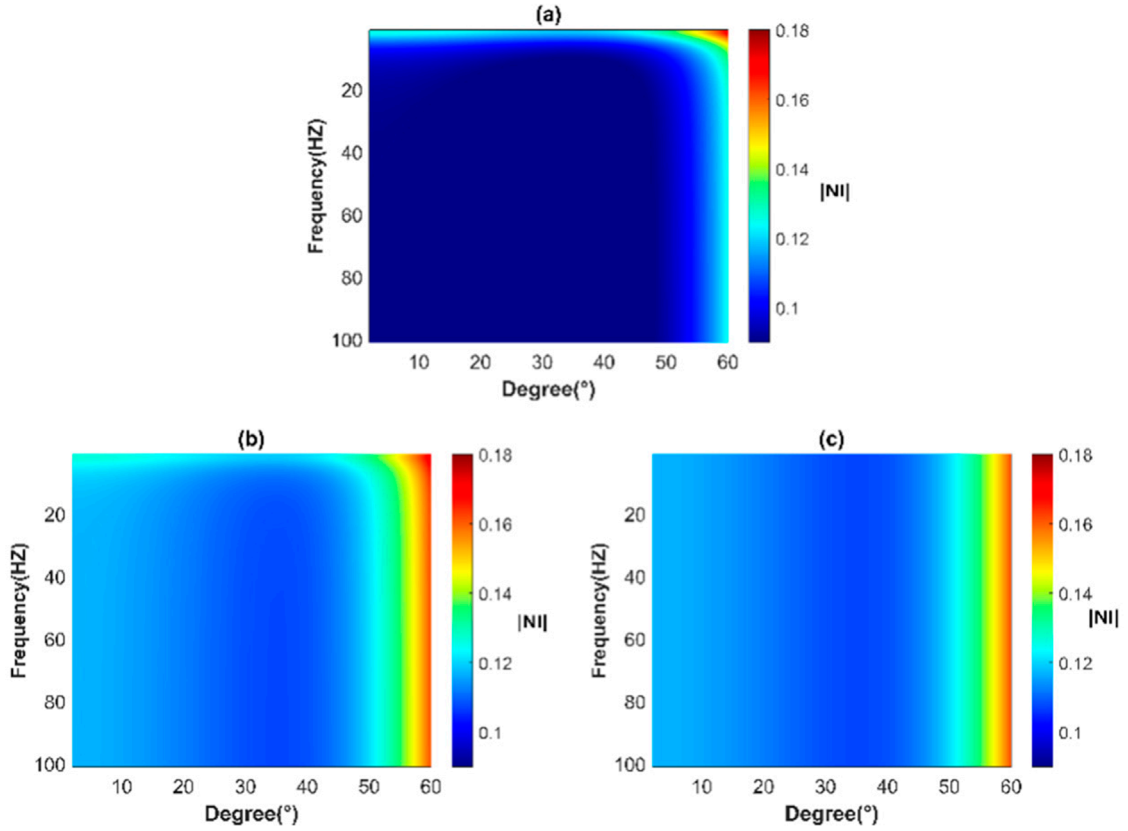

FIGURE 5
Frequency domain reflection coefficient *versus* frequency and incident angle for different medium models. **(A)** Two-layer cracked porous media. **(B)** The upper elastic medium and the lower cracked porous medium. **(C)** Two-layer elastic medium.

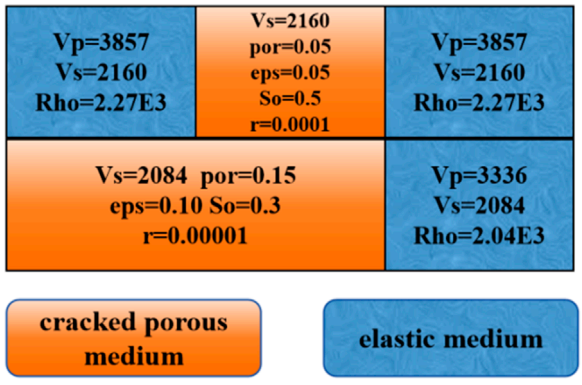

FIGURE 6
Schematic of a two-layer geological model used to test the effects of interlayer attenuation and dispersion on seismic response. The left part is a two-layer model considering only interface effects, the middle part is a two-layer model incorporating both interlayer and interface effects, and the right part is a two-layer elastic model.

3.2 FAVO analysis of interlayer decay and interface decay

Subsequently, the complex P-wave velocity calculated by the Chapman model, along with shear wave velocity and density given according to the actual situation, are incorporated into the forward calculation framework of the viscoelastic compound matrix algorithm. This integration facilitates the realization of the corresponding orthotropic analysis. The angle gathers of the two-layer cracked porous media and the two-layer elastic media are calculated, respectively, as shown in Figure 3. Figure 3A shows the seismic angle gathers for the two-layer cracked porous media. Figure 3B shows the seismic angle gathers for the two-layer elastic media. The comparison reveals that the seismic records obtained from the elastic media remain unchanged, while the waveforms of the seismic records obtained from the cracked porous media vary significantly with angle and exhibit obvious amplitude attenuation.

According to the linear time-invariant hypothesis, seismic waves in the convolution do not change over time. Based on this hypothesis, the attenuation and velocity dispersion of seismic waves in the reservoir are usually attributed to the reflection coefficient. When seismic waves propagate in cracked porous media, the corresponding reflection coefficient is closely related to frequency. Complex velocity is the key factor affecting the frequency dependence of the reflection coefficient. That is, the loss associated with seismic wave propagation, related to complex velocity, and the energy distribution involved in reflection and transmission at the medium interface, will lead to the frequency-dependent variation of the reflection coefficient.

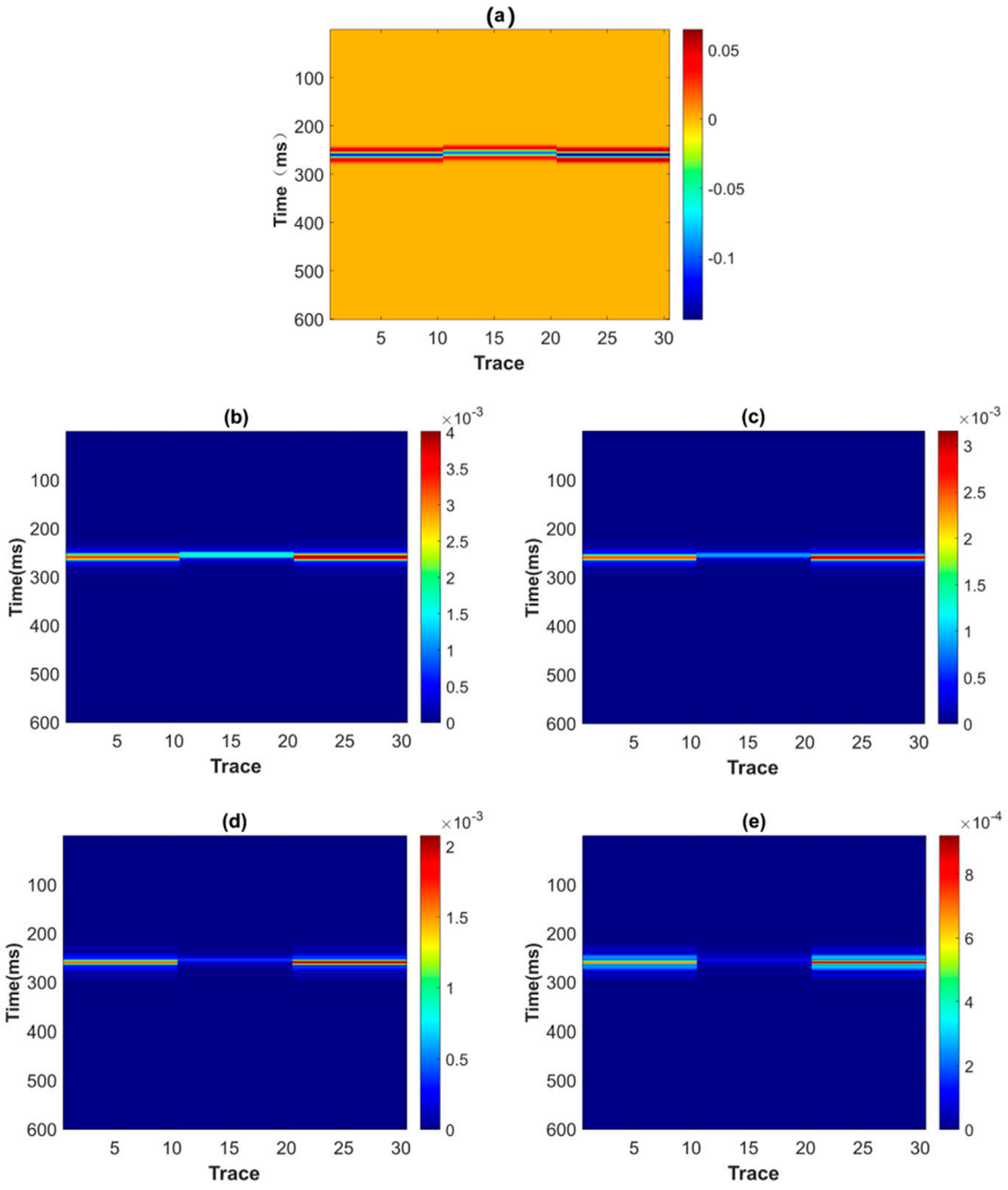

FIGURE 7
Seismic records computed using the compound matrix algorithm, along with their corresponding single-frequency profiles at different frequencies. **(A)** Self-transmitting and self-receiving profile. **(B)** 18 Hz frequency division profile. **(C)** 32 Hz frequency division profile. **(D)** 42 Hz frequency division profile. **(E)** 64 Hz frequency division profile.

We carry out experiments using the two-layer shale gas reservoir model shown in Tables 1–3 to analyze the influence of interlayer and interface attenuation on the FAVO response of shale reservoirs, and the results are shown in Figure 4. When both the upper and lower media are cracked porous media, the variation of the reflection coefficient with incident angle in the frequency range of 2–30 Hz is shown in Figure 4A. Since the upper layer is a cracked porous medium, the variation of the reflection coefficient response is affected by both the interlayer and the interface. As the frequency increases, the value of reflection coefficient decreases, but it keeps the same trend with the incidence angle across different frequencies. When the upper layer is an elastic medium and the lower layer is a cracked porous medium with constant parameters, the variation of the reflection coefficient with the incident angle in the frequency range of 2–30 Hz is shown in Figure 4B. Since the upper medium is elastic medium, that is, there is no interlayer influence on the change of reflection coefficient, thus, the change of reflection coefficient is only affected by the interface at this time. The value of the

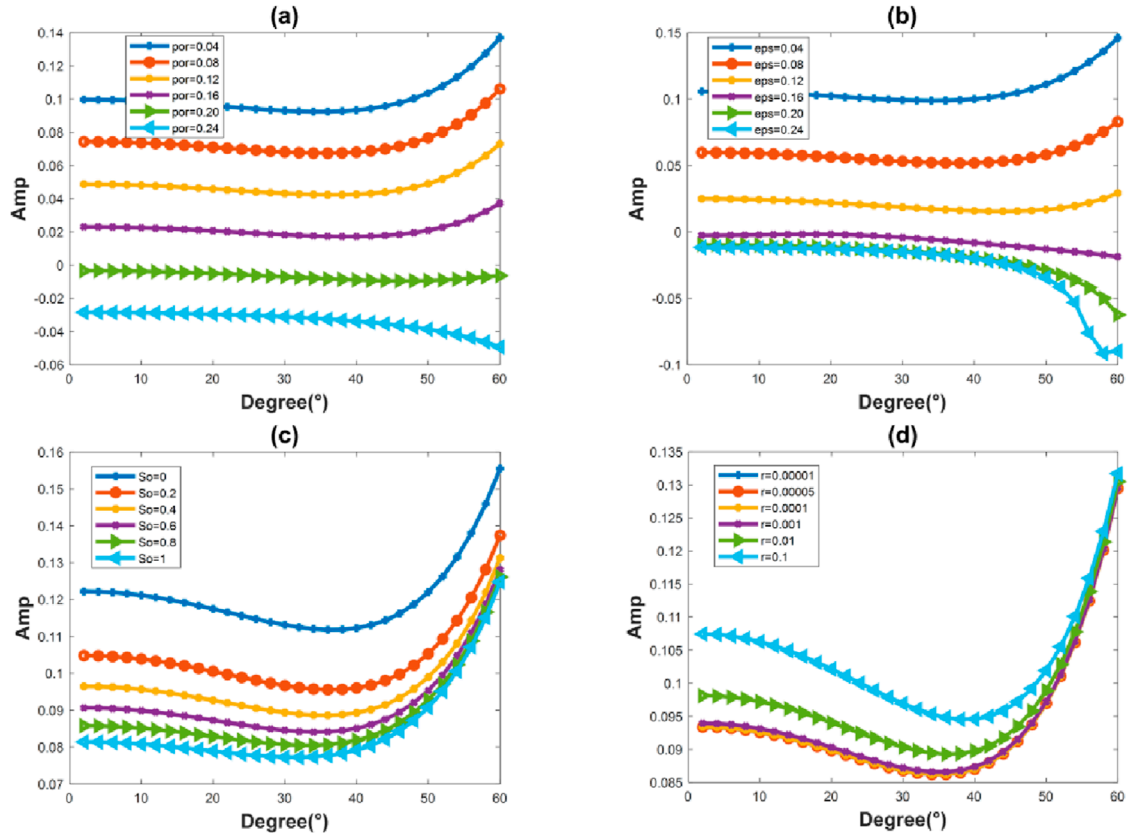

FIGURE 8
Variation of reflection coefficient with angle of incidence at 15 Hz for different **(A)** porosity, **(B)** crack density, **(C)** gas saturation, and **(D)** crack aspect ratio.

reflection coefficient decreases with increasing frequency, but these variations are significantly smaller compared to those observed in a two-layer cracked porous medium. The reflection coefficient at each frequency maintains the same trend with the variation of the incident angle. The variation of the reflection coefficient with the angle of incidence at 2–30Hz, when both the upper and lower media are elastic media, is shown in Figure 4C. Since both the upper and lower media are elastic layers, neither attenuation nor velocity dispersion occurs between the layers or at the interface, so the reflection coefficient does not change with frequency. In summary, it can be seen from Figures 4A–C that the interlayer attenuation dispersion effect has a great impact on the FAVO response of shale gas reservoirs compared to the attenuation dispersion effect at the interface.

Figures 5A–C show the complete frequency-domain reflection coefficients for the above three cases, respectively. When the seismic wave propagation process is affected by both interlayer and interface, the reflection coefficient varies greatly with frequency. The reflection coefficient varies little with frequency when only interface effects are present. The reflection coefficient of an elastic medium does not change with frequency, which is characterized by a white spectrum. That is, the effects of interlayer should not be ignored.

In order to further investigate the effect of interlayer attenuation and dispersion on seismic response, we designed the model shown in Figure 6. The geological model is equally divided into three parts: the left part is a two-layer model with cracked porous medium under an upper elastic medium, the middle part is a two-layer model with cracked porous medium both upper and lower, and the right part is a two-layer model with elastic medium both upper and lower. The corresponding parameters of the cracked porous medium are consistent with those listed in Tables 1–3.

The seismic records of the model are synthesized using compound matrix algorithm. Figure 7A shows the self-transmitting and self-receiving profile (vertical incidence) of the model. From the figure, it can be seen that the seismic records in the middle part are obviously different from those on the left and right sides, while those on the left and right sides are very similar. This indicates that the influence of the interface on the reflection coefficient in the seismic response is small. Given the simplicity of the model, we directly decompose its seismic records using the short-time Fourier transform. The corresponding frequency division profiles are shown in Figures 7B–E for frequencies of 18Hz, 32Hz, 48 Hz and 64Hz, respectively. The comparison reveals a low-frequency shadow phenomenon in the middle of the profile, and low-frequency shadow is an important means to identify fluid anomalies (Li et al., 2023). It is generally believed that the low-frequency shadow indicates the existence of an oil-bearing gas layer at its top. However, according to the above experimental settings, both the upper and lower layers are shale-bearing gas layers, indicating that the bottom of

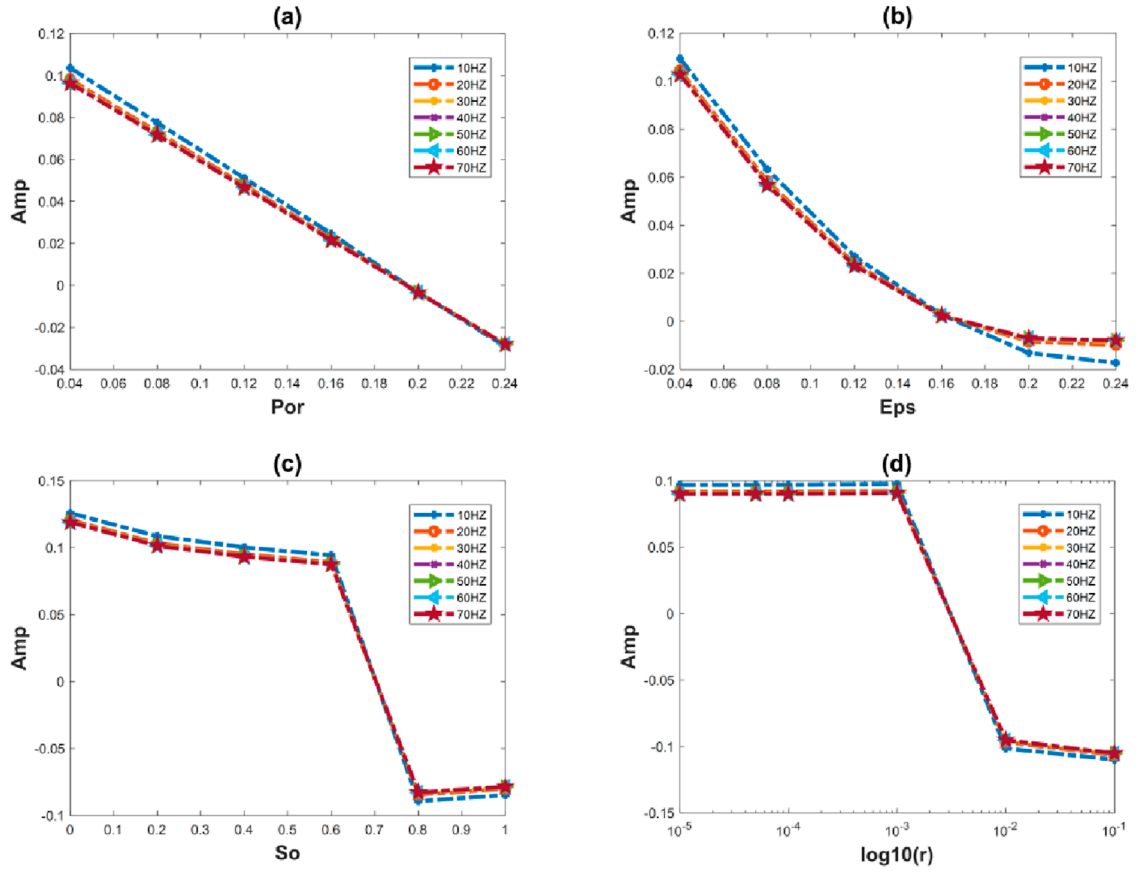

FIGURE 9
Variation of zero-angle reflection coefficients *versus* **(A)** porosity, **(B)** crack density, **(C)** gas saturation, and **(D)** crack aspect ratio at different frequencies.

the low-frequency shadow can also indicate the presence of an oil-bearing gas layer.

3.3 Relationship between petrophysical parameters of shale reservoir and seismic response

The above study proves that the effect of interlayer attenuation dispersion on the FAVO response of shale gas reservoir cannot be ignored. Therefore, we consider the dispersion effect of interlayer attenuation and use the Chapman model as a bridge to re-establish the relationship between petrophysical parameters of shale gas reservoirs and their seismic responses. As mentioned above, the Chapman model can be described using a series of parameters to establish the relationship between petrophysical and elastic parameters. Therefore, the influence of crack density, porosity, gas saturation, and crack aspect ratio on seismic response can be analyzed by numerical experiments, providing valuable guidance for the characterization of shale gas reservoirs.

We continue to use the two-layer cracked porous media model provided in Tables 1–3 for numerical experiments. The effects of crack density, porosity, gas saturation, and crack aspect ratio on seismic response are analyzed by changing one of these parameters in the upper medium while keeping the physical properties of the lower medium unchanged. Figure 8 shows the variation of the 15 Hz reflection coefficient with the incident angle for different porosity, crack density, gas saturation, and crack aspect ratio. It can be seen from the figure that the amplitude corresponding to the same incident angle changes with changes in porosity, and the corresponding AVO response also changes. During the process of increasing porosity, the corresponding AVO type changes when the porosity exceeds 0.20. Similar to the results observed with porosity variations, the amplitude corresponding to the same incidence angle also changes with variations in crack density, and the corresponding AVO response changes accordingly. During the process of increasing crack density, the corresponding AVO type changes when the crack density exceeds 0.12. The effect of changes in gas saturation on reflection amplitude is that the higher the gas saturation, the smaller the amplitude corresponding to the same angle of incidence. However, different from crack density and porosity, the corresponding AVO response is less affected by changes in gas saturation, and the AVO type remains consistent across different gas saturations. For the same incidence angle, the corresponding amplitude increases with an increasing crack aspect ratio, but the corresponding AVO response changes little, and the corresponding AVO types remain consistent across different crack aspect ratios.

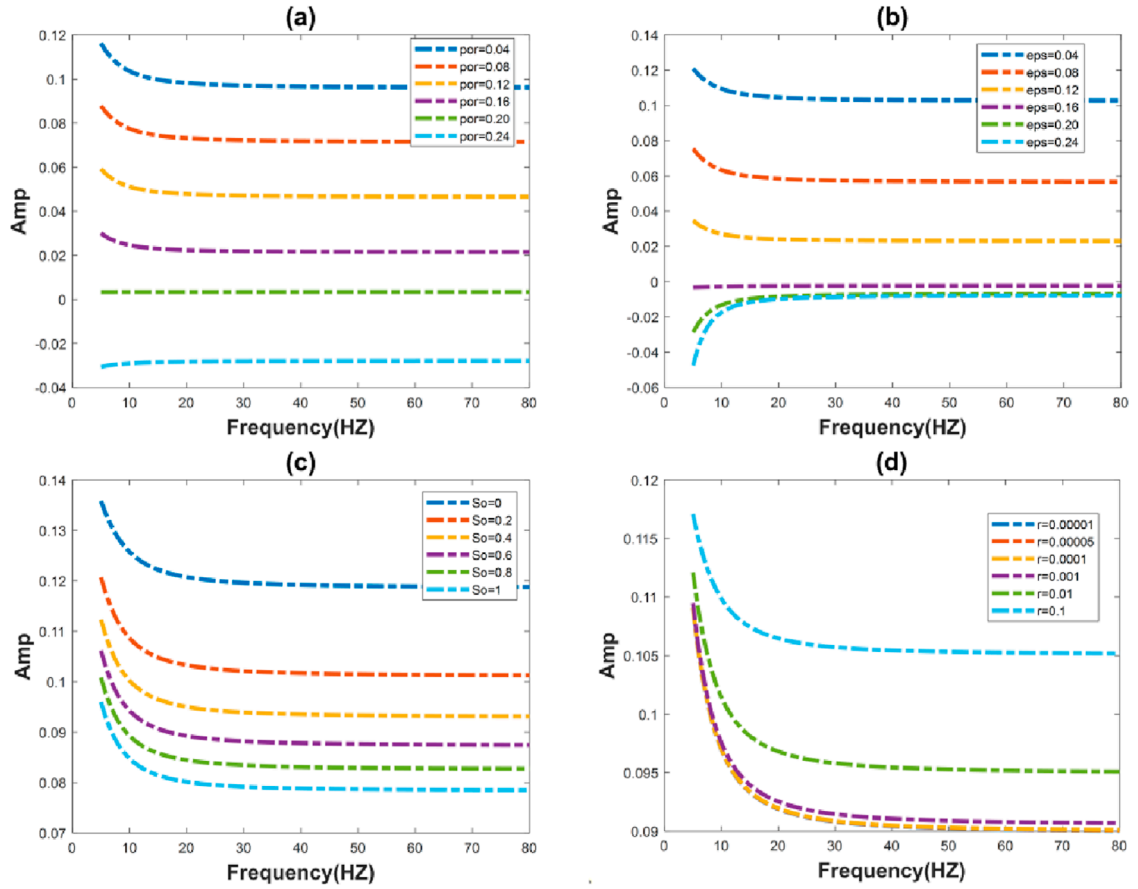

FIGURE 10
Variation of zero-angle reflection coefficient *versus* frequency for different **(A)** porosity, **(B)** crack density, **(C)** gas saturation, and **(D)** crack aspect ratio.

Figure 9 shows the changes of zero-angle reflection coefficients at different frequencies for varying porosity, crack density, gas saturation and crack aspect ratio. It can be seen from the figure that the attenuation of the reflection coefficients at each frequency remains consistent with changes in porosity, and dispersion is more pronounced in the low-frequency (10 HZ) region where porosity ranges from 0.04 to 0.16. The attenuation of the reflection coefficients at all frequencies is largely similar when affected by variations in crack density, and the frequency dispersion for both high and low crack densities is more pronounced in the low-frequency region. For the effect of changes in gas saturation, the attenuation of the reflection coefficient is essentially the same at all frequencies, and the dispersion in the low-frequency region is almost independent of the saturation. For the effect of crack aspect ratio variation, the attenuation of reflection coefficient at each frequency is basically the same. Similar to the effect of gas saturation, the dispersion in the low frequency region is almost not affected by the size of the crack aspect ratio.

Figure 10 shows the variation of the zero-angle reflection coefficient with frequency for different porosity, crack density, gas saturation, and crack aspect ratio. It can be seen from the figure that the amplitude corresponding to each frequency changes with porosity, and the dispersion is more pronounced in the low-frequency region. The amplitude corresponding to each frequency changes with crack density, and the dispersion effect is obvious at low frequencies (0-15HZ), with this effect being notably stronger than that observed with changes in porosity. The difference in the dispersion effect at low frequencies under different saturation is small. In the case of different aspect ratios of cracks, the dispersion effect in low-frequency bands is obvious, and it can be seen that the smaller the crack aspect ratio, the more obvious the dispersion effect. As the crack aspect ratio increases, the change curves basically overlap.

Figure 11 shows the self-transmitting and self-receiving seismic records for different porosity, crack density, gas saturation, and crack aspect ratio. It can be seen from the figure that changes in porosity significantly alter the elastic modulus of the crack pore medium, which leads to changes in travel time and reflection coefficients with frequency. When the porosity is small, the P-wave velocity of the upper medium is greater than that of the lower medium, resulting in a negative reflection coefficient. Conversely, when the porosity is large, the P-wave velocity of the upper medium is lower than that of the lower medium, leading to a positive reflection coefficient and a phase reversal in the wavelet. The effect of changes in crack density on the elastic modulus of the reservoir is largely consistent with that of changes in porosity, and the phenomenon of wavelet phase reversal is obvious. Different from the effects of porosity and crack density, the upper P-wave velocity is always greater than the

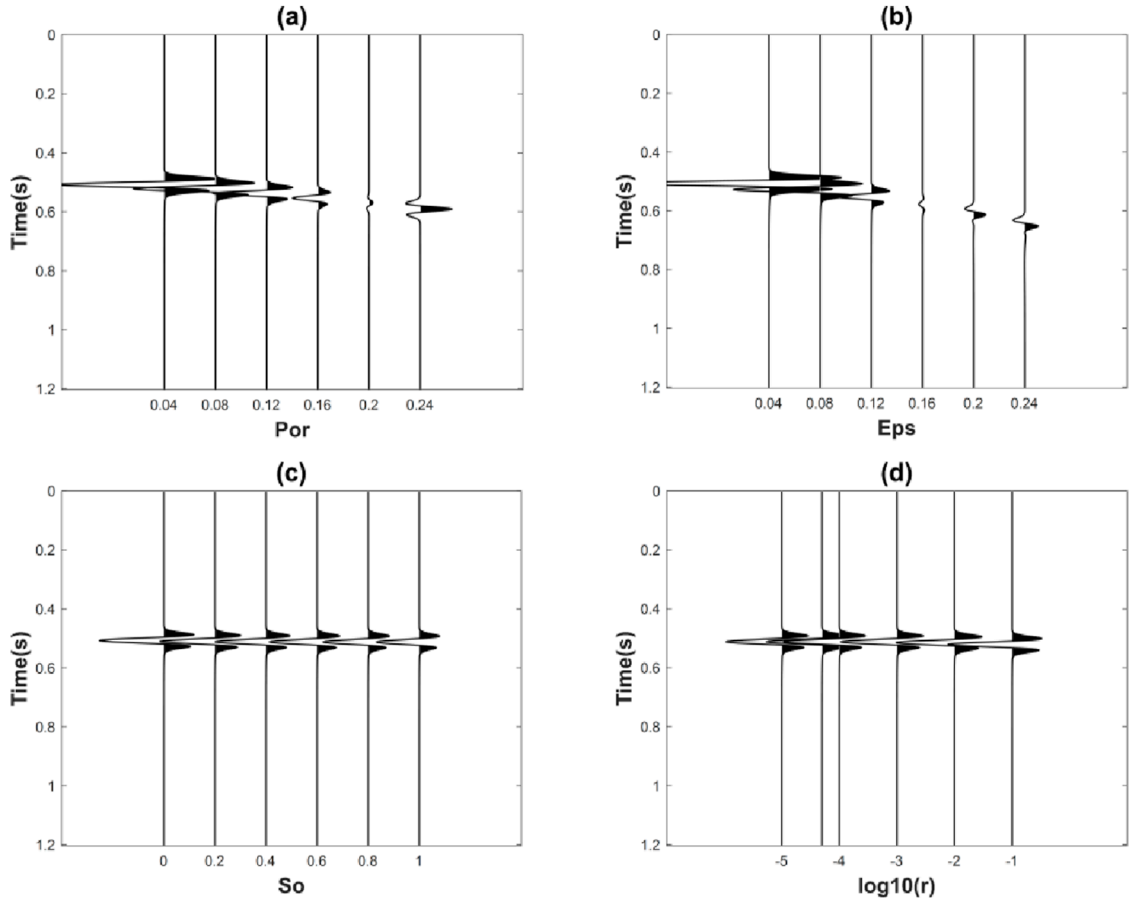

FIGURE 11
Self-transmitting and self-receiving seismogram corresponding to different **(A)** porosity, **(B)** crack density, **(C)** gas saturation, and **(D)** crack aspect ratio.

lower P-wave velocity, i.e., the reflection coefficient remains negative, regardless of the gas saturation and crack aspect ratio.

According to the above analysis, it is known that the seismic response is most sensitive to changes in crack density, which is reflected in travel time, AVO characteristics, and phase information. The seismic response is moderately sensitive to changes in porosity, exhibiting similar travel-time, AVO characteristics, and phase information as those observed with changes in crack density. The seismic response is the least sensitive to changes in gas saturation and crack aspect ratio, i.e., exhibiting small changes in AVO characteristics and insignificant phase changes. In summary, the sensitivity of the seismic response to changes in fracture density in shale gas reservoir media is the highest, followed by porosity, with gas saturation and crack aspect ratio showing the least sensitivity. Therefore, it is easier to obtain crack density and porosity from seismic records when characterizing shale gas reservoir parameters, compared to gas saturation and crack aspect ratio.

4 Discussion

The equivalent theoretical model is an important tool in petrophysical studies, which idealizes shale gas reservoir through certain assumptions to establish the relationship between seismic response and the properties of shale gas reservoir. In this paper, the Chapman model, a dynamic equivalent theoretical model, is selected as the petrophysical model and is combined with the compound matrix algorithm to adapt it to more complex reservoir scenarios. Meanwhile, we conduct a thorough analysis of the sensitivity of seismic response to the petrophysical parameters of shale gas reservoirs, thereby providing a foundation for the characterization and assessment of these reservoirs. Conventional FAVO forward modeling only considers the effect of the interface and ignores the more important effect of the interlayer, making it less applicable in practice. In contrast, we consider the effects of both the interface and interlayer simultaneously, which is crucial and has significant guiding importance for the identification of shale gas reservoirs and the characterization of shale gas fluids.

However, the petrophysical models used in this paper are still based on relatively ideal and simplified simple assumptions, such as fracture levels and no coupling between fractures. Considering multi-factor coupling can help us better characterize velocity dispersion and attenuation in rocks. In this paper, we have conducted a forward analysis to elucidate the relationship between reservoir parameters and seismic responses. A more critical task in reservoir characterization is to derive reservoir parameters from

known seismic records. The next step is to realize the inversion of shale reservoir parameters based on the model developed in this paper.

5 Conclusion

In this paper, we select the Chapman model as the petrophysical model and combine it with the compound matrix algorithm to analyze the FAVO effect in shale reservoirs in detail. The relationship between shale gas reservoir parameters (e.g., crack density, porosity, gas saturation, and crack aspect ratio) and seismic response is accurately established by FAVO forward simulation based on the compound matrix algorithm. The attenuation dispersion effects between interfaces and layers are considered and compared. The results show that the attenuation and velocity dispersion effects between layers of shale gas reservoir cannot be ignored, and their impact on seismic response is significantly larger than that of the attenuation and dispersion effects at the interface. The low-frequency shadow observed in the experiment proves the feasibility of indicating shale gas reservoir, and also proves that the low-frequency shadow can indicate the presence of shale gas reservoir not only at the top but also at the bottom. The experiments prove that the change of shale gas reservoir parameters (i.e., crack density, porosity, gas saturation and crack aspect ratio) affect the FAVO response, but to varying degrees. Specifically, the effect of crack density is greater than that of porosity, and greater than that of gas saturation and crack aspect ratio. This verifies the effectiveness of dispersion attributes for identifying gas in shale gas reservoir, and on this basis, the corresponding dispersion attributes extracted from seismic data will be considered for shale gas reservoir fluid identification.

Data availability statement

The raw data supporting the conclusions of this article will be made available by the authors, without undue reservation.

Author contributions

HD: Conceptualization, Writing–original draft. JZ: Conceptualization, Writing–original draft. DZ: Writing–review and editing. SW: Writing–review and editing. JX: Writing–review and editing.

Funding

The author(s) declare that financial support was received for the research, authorship, and/or publication of this article. This work was supported in part by the National Natural Science Foundation of China under Grant 42204108, in part by the Natural Science Foundation of Sichuan under Grant 2023NSFSC0768, in part by National Key Laboratory of Petroleum Resources and Engineering, China University of Petroleum, Beijing under Grant PRE/open-2305, in part by Research on Fine Exploration and Surrounding Rock Classification Technology for Deep Buried Long Tunnels Driven by Horizontal Directional Drilling and Magnetotelluric Methods Based on Deep Learning under Grant E202408010.

Conflict of interest

Author DZ was employed by Sichuan Water Development Investigation, Design & Research Co., Ltd.

The remaining authors declare that the research was conducted in the absence of any commercial or financial relationships that could be construed as a potential conflict of interest.

Publisher's note

References

Ba, J., Xu, W., Fu, L. Y., Carcione, J. M., and Zhang, L. (2017). Rock anelasticity due to patchy saturation and fabric heterogeneity: a double double-porosity model of wave propagation. *J. Geophys. Res. Solid Earth* 122 (3), 1949–1976. doi:10.1002/2016jb013882

Bortfeld, R. (1961). Approximations to the reflection and transmission coefficients of plane longitudinal and transverse waves. *Geophys. Prospect.* 9 (4), 485–502. doi:10.1111/j.1365-2478.1961.tb01670.x

Carcione, J. M., Helle, H. B., and Pham, N. H. (2003). White's model for wave propagation in partially saturated rocks: comparison with poroelastic numerical experiments. *Geophysics* 68 (4), 1389–1398. doi:10.1190/1.1598132

Chapman, M. (2003). Frequency-dependent anisotropy due to meso-scale fractures in the presence of equant porosity. *Geophys. Prospect.* 51 (5), 369–379. doi:10.1046/j.1365-2478.2003.00384.x

Chapman, M., Liu, E., and Li, X.-Y. (2006). The influence of fluid sensitive dispersion and attenuation on AVO analysis. *Geophys. J. Int.* 167 (1), 89–105. doi:10.1111/j.1365-246x.2006.02919.x

Chapman, M., Zatsepin, S. V., and Crampin, S. (2002). Derivation of a microstructural poroelastic model. *Geophys. J. Int.* 151 (2), 427–451. doi:10.1046/j.1365-246x.2002.01769.x

Cheng, B.-J., Xu, T.-J., and Li, S.-G. (2012). Research and application of frequency dependent AVO analysis for gas recognition. *Chin. J. Geophys.* 55 (2), 608–613. doi:10.6038/j.issn.0001-5733.2012.02.023

Dvorkin, J., Mavko, G., and Nur, A. (1995). Squirt flow in fully saturated rocks. *Geophysics* 60 (1), 97–107. doi:10.1190/1.1443767

Guo, Z.-Q., Liu, C., and Li, X.-Y. (2015). Seismic signatures of reservoir permeability based on the patchy-saturation model. *Appl. Geophys.* 12, 187–198. doi:10.1007/s11770-015-0480-6

Hilterman, F. (1990). Is AVO the seismic signature of lithology? A case history of Ship Shoal-South Addition. *Lead. Edge* 9 (6), 15–22. doi:10.1190/1.1439744

Hou, Z., Luo, J., Cao, C., and Ding, G. (2023). Development and contribution of natural gas industry under the goal of carbon neutrality in China. *Adv. Eng. Sci.* 55 (01), 243–252. doi:10.15961/j.jsuese.202200226

Hudson, J (1980). Overall properties of a cracked solid. *Cambridge University Press*, 371-384.

Hudson, J, Liu, E, and Crampin, S (1996). The mechanical properties of materials with interconnected cracks and pores. *Geophysical Journal International*, 124(1): 105-112.

Hudson, J A (1981). Wave speeds and attenuation of elastic waves in material containing cracks. *Geophysical Journal International*, 64(1): 133-150.

Kennett, B (2009). Seismic wave propagation in stratified media. *ANU Press*.

Li, Z., Chen, X., Pun, C.-M., and Cun, X. (2023). *High-resolution document shadow removal via A large-scale real-world dataset and A frequency-aware shadow erasing net*. IEEE, 12415–12424.

Liu, C., Li, B.-N., Zhao, X., Liu, Y., and Lu, Q. (2014). Fluid identification based on frequency-dependent AVO attribute inversion in multi-scale fracture media. *Appl. Geophys.* 11 (4), 384–394. doi:10.1007/s11770-014-0454-0

Liu, L., Cao, S., and Wang, L. (2011). Poroelastic analysis of frequency-dependent amplitude-versus-offset variations. *Geophysics* 76 (3), C31–C40. doi:10.1190/1.3552702

Maultzsch, S., Chapman, M., Liu, E., and Li, X. Y. (2003). Modelling frequency-dependent seismic anisotropy in fluid-saturated rock with aligned fractures: implication of fracture size estimation from anisotropic measurements. *Geophys. Prospect.* 51 (5), 381–392. doi:10.1046/j.1365-2478.2003.00386.x

Pang, S., and Stovas, A. (2020). Low-frequency anisotropy in fractured and layered media. *Geophys. Prospect.* 68 (2), 353–370. doi:10.1111/1365-2478.12833

Phinney, R. A., Odom, R. I., and Fryer, G. J. (1987). Rapid generation of synthetic seismograms in layered media by vectorization of the algorithm. *Bull. Seismol. Soc. Am.* 77 (6), 2218–2226. doi:10.1785/BSSA0770062218

Pointer, T., Liu, E., and Hudson, J. A. (2000). Seismic wave propagation in cracked porous media. *Geophys. J. Int.* 142 (1), 199–231. doi:10.1046/j.1365-246x.2000.00157.x

Ren, H., Goloshubin, G., and Hilterman, F. J. (2009a). Poroelastic analysis of amplitude-versus-frequency variations. *Geophysics* 74 (6), N41–N48. doi:10.1190/1.3207863

Ren, H., Goloshubin, G., and Hilterman, F. J. (2009b). Poroelastic analysis of permeability effects in thinly layered porous media. *Geophysics* 74 (6), N49–N54. doi:10.1190/1.3223185

Schmidt, H., and Tango, G. (1986). Efficient global matrix approach to the computation of synthetic seismograms. *Geophys. J. Int.* 84 (2), 331–359. doi:10.1111/j.1365-246x.1986.tb04359.x

Schoenberg, M. (1980). Elastic wave behavior across linear slip interfaces. *J. Acoust. Soc. Am.* 68 (5), 1516–1521. doi:10.1121/1.385077

Sen, M. K., and Roy, I. G. (2003). Computation of differential seismograms and iteration adaptive regularization in prestack waveform inversion. *Geophysics* 68 (6), 2026–2039. doi:10.1190/1.1635056

Shuey, R. (1985). A simplification of the Zoeppritz equations. *Geophysics* 50 (4), 609–614. doi:10.1190/1.1441936

Sidler, R., Rubino, J. G., and Holliger, K. (2013). Quantitative comparison between simulations of seismic wave propagation in heterogeneous poro-elastic media and equivalent visco-elastic solids for marine-type environments. *Geophys. J. Int.* 193 (1), 463–474. doi:10.1093/gji/ggs125

Smith, G., and Gidlow, P. (1987). Weighted stacking for rock property estimation and detection of gas. *Geophys. Prospect.* 35 (9), 993–1014. doi:10.1111/j.1365-2478.1987.tb00856.x

Thomsen, L. (1995). Elastic anisotropy due to aligned cracks in porous rock1. *Geophys. Prospect.* 43 (6), 805–829. doi:10.1111/j.1365-2478.1995.tb00282.x

Van Der Kolk, C., Guest, W., and Potters, J. (2001). The 3D shear experiment over the Natih field in Oman: the effect of fracture-filling fluids on shear propagation. *Geophys. Prospect.* 49 (2), 179–197. doi:10.1046/j.1365-2478.2001.00250.x

Wang, D., Zhang, H. L., and Wang, X. M. (2006). A numerical study of acoustic wave propagation in partially saturated poroelastic rock. *Chin. J. Geophys.* 49 (2), 465–473.

Wu, X. (2010). *Frequency dependent AVO inversion using spectral decomposition techniques*. Wuhan: China University of Geosciences.

Zhang, L., Ba, J., and Carcione, J. M. (2021). Wave propagation in infinituple-porosity media. *J. Geophys. Res. Solid Earth* 126 (4), e2020JB021266. doi:10.1029/2020jb021266

Zhao, H., Gao, J., and Liu, F. (2014). Frequency-dependent reflection coefficients in diffusive-viscous media. *Geophysics* 79 (3), T143–T155. doi:10.1190/geo2013-0038.1

Zhen, Q., Caineng, Z., Jianzhong, L., Qiulin, G., Xiaozhi, W., and Lianhua, H. (2013). Unconventional petroleum resources assessment: progress and future prospects. *Nat. Gas. Geosci.* 24 (2), 238–246.

Zoeppritz, K. (1919). On the reflection and propagation of seismic waves. *Gottinger Nachrichten* 1 (5), 66–84.

10.3389/feart.2024.1438930

Appendix A

The expression (Equation 16) of layer propagation matrix G_i is:

$$G_i = T_i^+ E_i T_i^- \tag{16}$$

where E_i is the phase time-shift matrix, T_i^+ and T_i^- represent the surface energy distribution matrix of down-going wave and up-going wave, respectively. The expressions (Equations 17, 18) are:

$$E_i = diag\left[e^{-j\omega d_i\left(q_p+q_s\right)} \quad 1 \quad e^{-j\omega d_i\left(q_p-q_s\right)} \quad e^{j\omega d_i\left(q_p-q_s\right)} \quad 1 \quad e^{j\omega d_i\left(q_p+q_s\right)}\right] \tag{17}$$

$$T_i^+ = \begin{bmatrix} \frac{-\left(p^2+q_p q_s\right)}{\mu} & \frac{-2pq_p}{\mu} & \frac{-\left(p^2-q_p q_s\right)}{\mu} & \frac{\left(p^2-q_p q_s\right)}{\mu} & \frac{-2pq_s}{\mu} & \frac{\left(p^2+q_p q_s\right)}{\mu} \\ \frac{jq_s}{\tilde{v}_{si}(\omega)^2} & 0 & \frac{-jq_s}{\tilde{v}_{si}(\omega)^2} & \frac{-jq_s}{\tilde{v}_{si}(\omega)^2} & 0 & \frac{jq_s}{\tilde{v}_{si}(\omega)^2} \\ -jp\left(\Gamma+2q_p q_s\right) & -4jp^2 q_p & -jp\left(\Gamma-2q_p q_s\right) & jp\left(\Gamma-2q_p q_s\right) & -2j\Gamma q_s & -jp\left(\Gamma+2q_p q_s\right) \\ -jp\left(\Gamma+2q_p q_s\right) & -2j\Gamma q_p & -jp\left(\Gamma-2q_p q_s\right) & jp\left(\Gamma-2q_p q_s\right) & -4jp^2 q_s & -jp\left(\Gamma+2q_p q_s\right) \\ \frac{-jq_p}{\tilde{v}_{si}(\omega)^2} & 0 & \frac{-jq_p}{\tilde{v}_{si}(\omega)^2} & \frac{-jq_p}{\tilde{v}_{si}(\omega)^2} & 0 & \frac{jq_p}{\tilde{v}_{si}(\omega)^2} \\ -\mu\left(\Gamma^2+4p^2 q_p q_s\right) & -4\mu\Gamma pq_p & -\mu\left(\Gamma^2-4p^2 q_p q_s\right) & \mu\left(\Gamma^2-4p^2 q_p q_s\right) & -4\mu\Gamma pq_s & -\mu\left(\Gamma^2+4p^2 q_p q_s\right) \end{bmatrix} \tag{18}$$

The up-going wave energy matrix T_i^- (Equation 19) can be represented by the elements of the down-going wave energy matrix T_i^+:

$$T_i^- = \begin{bmatrix} t_{61} & t_{51} & t_{31} & t_{31} & t_{21} & t_{11} \\ -t_{65} & 0 & -t_{45} & -t_{35} & 0 & -t_{15} \\ -t_{63} & -t_{51} & -t_{33} & -t_{33} & t_{12} & -t_{13} \\ t_{63} & -t_{51} & t_{33} & t_{33} & t_{21} & t_{13} \\ -t_{62} & 0 & -t_{42} & -t_{32} & 0 & -t_{12} \\ t_{61} & -t_{51} & t_{31} & t_{31} & -t_{21} & t_{11} \end{bmatrix} \tag{19}$$

where $\Gamma = 2p^2 - \frac{1}{\tilde{v}_{si}(\omega)^2}$, $\mu = \rho\tilde{v}_{si}(\omega)^2$, p represents horizontal slowness (also known as ray parameter), q_p and q_s represent P wave vertical slowness and S wave vertical slowness, respectively, the expressions (Equations 20, 21) are:

$$q_p = \sqrt{\frac{1}{\tilde{v}_{pi}(\omega)^2} - p^2} \tag{20}$$

$$q_s = \sqrt{\frac{1}{\tilde{v}_{si}(\omega)^2} - p^2} \tag{21}$$

where $\tilde{v}_{pi}(\omega)$ and $\tilde{v}_{si}(\omega)$ represent the frequency-dependent complex P-wave velocity and complex S-wave velocity of viscoelastic media, respectively.

frontiers | Frontiers in Earth Science

TYPE Original Research
PUBLISHED 28 October 2024
DOI 10.3389/feart.2024.1483285

OPEN ACCESS

EDITED BY
Huaimin Dong,
Chang'an University, China

REVIEWED BY
Pan Zhang,
China University of Petroleum Beijing, China
Jiaqi Xu,
Harbin Institute of Technology, China

*CORRESPONDENCE
Xiaoming Tang,
tangxiam@aliyun.com

RECEIVED 19 August 2024
ACCEPTED 07 October 2024
PUBLISHED 28 October 2024

CITATION
Li Y, Wang Z, Su Y and Tang X (2024) A theoretical analysis of the logging-while-drilling dipole acoustic reflection measurement.
Front. Earth Sci. 12:1483285.
doi: 10.3389/feart.2024.1483285

A theoretical analysis of the logging-while-drilling dipole acoustic reflection measurement

Yanghu Li[1,2], Zhenlin Wang[1,3], Yuanda Su[2] and Xiaoming Tang[2]*

[1]Research Institute of Petroleum Exploration and Development, Xinjiang Oilfield Company of Petro China, Karamay, China, [2]School of Geosciences, China University of petroleum (East China), Qingdao, China, [3]College of Petroleum Engineering, China University of Petroleum, Beijing, China

Post-drilling wireline acoustic single-well imaging technology can now detect geological structures tens of meters away from boreholes. Further development of this single-well imaging technology in the logging-while-drilling (LWD) environment will have significant values in real-time applications such as geosteering and reservoir navigation. Based on the wireline imaging application, we propose a new method for the LWD application. In wireline imaging, the four-component (4C) dipole acoustic data are azimuthally rotated to scan the reflectors around the borehole. In LWD, azimuthal scanning is achieved by drilling rotation such that the 4C dipole system in the wireline is replaced by a one-dipole-source and two-receiver LWD system, where the two receivers are mounted on opposite sides of the drill collar. For the LWD application, we first developed the theory for LWD dipole shear-wave reflection imaging and validated the theory using 3D finite-difference waveform modeling. Using the analytical solution, we analyzed the far-field radiation directivity of an acoustic LWD dipole source and the effect of drilling rotation on the shear-wave reflection imaging using the LWD acoustic system. The LWD analysis results show that, for fast formations, the SH-wave is the dominant component for imaging, whereas for slow formations, the P-wave becomes important and can be used for imaging. Our results also indicate that the reflection data acquired by the system are affected by the speed of drilling rotation. The take-off azimuth at the wave radiation may be different from the incident azimuth at the wave reception. Knowing the rotation speed, this azimuth difference can be corrected. A further advantage of using the oppositely mounted receivers is that the reflected wave arrives earlier (later) at the front (back)-side receiver; thus, the arrival time difference between the receivers can be used to eliminate the 180°-azimuth ambiguity of dipole acoustic imaging. For reflection imaging, using the proposed LWD system configuration, we tested its azimuth sensitivity and validated its 180°-ambiguity solution using synthetic LWD and field wireline dipole data. The results of this work, therefore, provide a theoretical foundation for the development of the LWD acoustic reflection imaging system.

KEYWORDS

borehole dipole reflection imaging, logging while drilling, azimuthal reception response, azimuth ambiguity, geosteering

Introduction

For oil and gas exploration and development in high-angle wells, it is necessary to develop the drilling and logging technology for the complex wells, especially in unconventional oil and gas exploration. The successful development of these complex wells relies on accurate geosteering technology to effectively track reservoir boundaries in real time. In this regard, borehole acoustic reflection imaging offers a promising tool for the geosteering application. In recent years, extensive research on borehole acoustic remote sensing technology has been carried out. Researchers have made significant progress in theoretical modeling, experimental validation, tool development, and field data analyses (e.g., Hornby, 1989; Tang, 2004; Tang and Patterson, 2009; Wei and Tang, 2012; Tang et al., 2014; Gong et al., 2015; Gong et al., 2018; Hirabayashi et al., 2017; Li and Yue, 2017; Bennett, 2019; Xu et al., 2019; Ben et al., 2020; Li et al., 2021a; Li et al., 2021b; Li et al., 2021c; Li et al., 2022a; Kong et al., 2023a; Kong et al., 2023b). The technology has been widely applied in wireline logging to delineate near-borehole geological structures such as formation interfaces, fractures, dissolution cavities, and faults (Bradley et al., 2011; Tang et al., 2016; Lee et al., 2019; Gu et al., 2021).

The wireline acoustic single-well imaging technology can now detect geological structures several tens of meters away from boreholes into the formation. This detection range is what is needed for the logging-while-drilling (LWD) geosteering application. For this reason, numerous researchers have carried out studies on the LWD acoustic reflection imaging technology (Nakken et al., 1996; Tang et al., 2007; Cao et al., 2016; Tan et al., 2016). The latest works (Li et al., 2022b; Tan et al., 2022; Rao et al., 2023) analyzed the radiation, scattering, and reception responses of an acoustic LWD dipole source. These studies, however, did not include the effect of drill collar rotation in the LWD environment. For the distance considered in the acoustic reflection imaging, the wave travel time in the formation usually takes several to tens of milliseconds. The wireline tool takes at least a few seconds to make one revolution such that the azimuth change during wave propagation in formation is negligible. In contrast, the LWD tool rotates with the drill bit, and the rotation speed can reach tens or even hundreds of revolutions per minute. In the case of high-speed rotation, one must analyze the effect on the received wavefield.

In the following sections, we first derive the far-field asymptotic solution for the wavefield of a LWD acoustic dipole source and study its radiation characteristics. Using the virtual source analogy, we further analyze the received wavefield for an acoustic reflection model containing a rotating LWD tool in the fluid-filled borehole. By using the cylindrical-wave expansion and the steepest–descent methods, we obtain the asymptotic solution for the LWD problem and validate the solution result using 3D finite-difference waveform modeling. Based on the solution result, we propose a one-dipole-source and two-receiver LWD acoustic reflection imaging system. We validate the feasibility of the system for geosteering applications using synthetic LWD and field wireline acoustic data examples.

Theoretical analysis

Radiation from a LWD dipole source inside the borehole

Figure 1 shows single-well reflection imaging using a LWD dipole tool. Compared with the wireline logging scenario, the drill collar occupies a large portion of the borehole and has substantial influence on the wavefield characteristics. The LWD borehole model consists of the fluid inside the drill collar, the drill collar, the fluid ring between the drill collar and the formation, and the formation, whose outer radii are r_1, r_2, r_3, and infinity, respectively. Assuming that the drill collar is in the center of the borehole, an annular dipole source is placed on the rim of the drill collar and pointed in the direction of the x-axis, with the radius of the source (modeled as a fluid ring) being the outer radius of the drill collar (i.e., $r_0 = r_2$), as shown in Figure 1B. The model shown in Figure 1 contains three fluid–solid boundaries at the inner and outer collar and the borehole–formation interfaces. The fluid–solid boundary condition requires the continuity of radial displacement and stress and vanishing of the azimuthal and axial shear stresses. The wave is actuated by assigning the radial displacement generated by the source to the drill collar at the source location. Combining the boundary conditions at the abovementioned interfaces yields a matrix equation with 12 unknown coefficients (Tang and Cheng, 2004):

$$\mathbf{H}\times\left[A^{fin},A^{dc},B^{dc},C^{dc},D^{dc},E^{dc},F^{dc},A^{fout},B^{fout},B^{fm},D^{fm},F^{fm}\right]^{T}=\mathbf{e}, \quad (1)$$

where $\mathbf{H}$ is a 12 × 12 matrix and $\mathbf{e}$ is a 12 × 1 vector, the latter resulting from the direct contribution of the dipole source (the detailed expressions of matrix $\mathbf{H}$ and vector $\mathbf{e}$ are given in Supplementary Appendix A1). The superscripts *fin*, *dc*, and *fout* correspond to the fluid inside the drill collar, the drill collar, and the fluid ring, respectively, and the respective coefficients govern the strength of the guided waves inside the borehole. The amplitude coefficients with superscript *fm* are related to the radiated waves for imaging geological structures in the formation. For far-field radiation, the asymptotic solutions of the displacement potential function of the radiated P-, SH-, and SV-waves from the LWD dipole source are (Tang and Wei, 2012).

$$\begin{cases}\phi^{fm}=-B^{fm}\left(\omega,k_{p0}^{t}\right)I_1\left(f_{p0}r_0\right)\cos\varphi\dfrac{e^{\mathrm{i}\omega R/\alpha_{fm}-\mathrm{i}\pi/4}}{4\pi R}\\ \chi^{fm}=-D^{fm}\left(\omega,k_{s0}^{t}\right)I_1\left(f_{s0}r_0\right)\sin\varphi\dfrac{e^{\mathrm{i}\omega R/\beta_{fm}-\mathrm{i}\pi/4}}{4\pi R}\\ \Gamma^{fm}=-F^{fm}\left(\omega,k_{s0}^{t}\right)I_1\left(f_{s0}r_0\right)\cos\varphi\dfrac{e^{\mathrm{i}\omega R/\beta_{fm}-\mathrm{i}\pi/4}}{4\pi R}\end{cases}, \quad (2)$$

where ω is the circular frequency; α_{fm} and β_{fm} are the formation P- and S-wave velocities, respectively; $k_{p0}^{t}=\left(\omega/\alpha_{fm}\right)\cos\theta_t$ and $k_{s0}^{t}=\left(\omega/\beta_{fm}\right)\cos\theta_t$ are the steepest–descent solutions of the radiated P- and S-wave wavenumbers, respectively; $f_{p0}=\sqrt{\left(k_{p0}^{t}\right)^2-\left(\omega/\alpha_f\right)^2}$ and $f_{s0}=\sqrt{\left(k_{s0}^{t}\right)^2-\left(\omega/\alpha_f\right)^2}$ denote the fluid radial wavenumbers calculated from k_{p0}^{t} and k_{s0}^{t}, respectively; α_f is the fluid velocity; I_1 represents the first kind of variant Bessel function with one order; θ_t is the angle between the radiated-wave direction and the borehole z-axis; φ is the angle between the projection of the

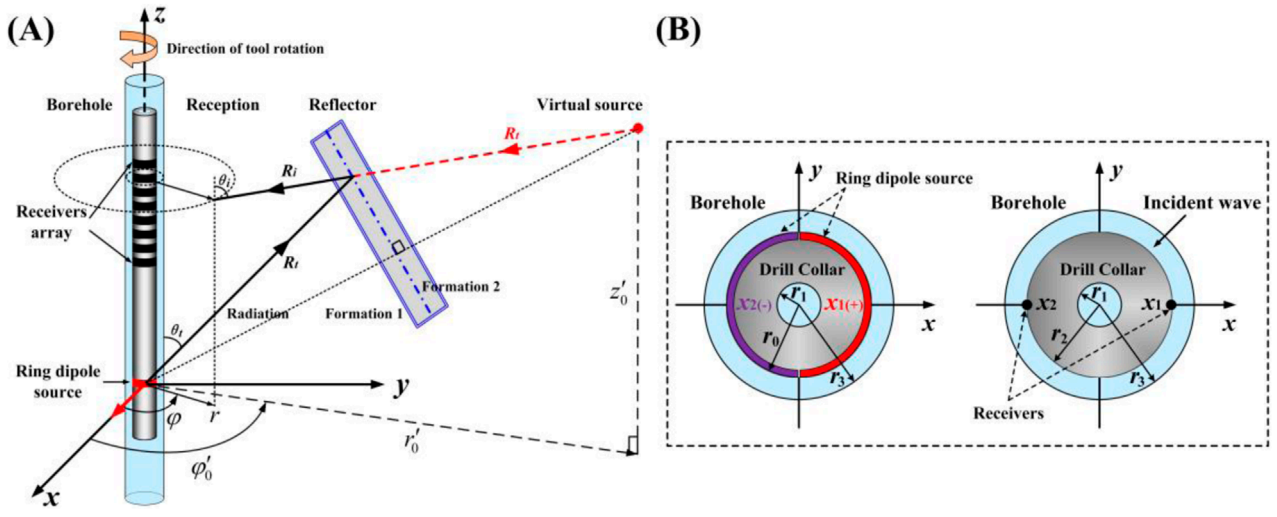

FIGURE 1
Configuration of LWD acoustic single-well reflection imaging **(A)** where the dipole source is oriented in the tool *x*-axis direction and **(B)** receivers are mounted at the opposite sides of the tool along the source orientation. The virtual source analogy is used to model the wave incidence to the borehole.

radiated-wave direction on the horizontal plane and the source orientation; and R stands for the distance from the source to the field point. The amplitude coefficients B^{fm}, D^{fm}, and F^{fm} are found by solving Equation 1.

Equation 2 shows that the radiated far-field wave is the product of two terms, one of which controls the spatial distribution of the wavefield and is called the radiation function of the borehole source:

$$\begin{cases} RD_P = B^{fm}\left(\omega, k_{p0}^t\right) I_1\left(f_{p0} r_0\right) \cos\varphi \\ RD_{SH} = D^{fm}\left(\omega, k_{s0}^t\right) I_1\left(f_{s0} r_0\right) \sin\varphi \\ RD_{SV} = F^{fm}\left(\omega, k_{s0}^t\right) I_1\left(f_{s0} r_0\right) \cos\varphi \end{cases}. \tag{3}$$

The common factor $-e^{-i\pi/4}/(4\pi)$ is omitted from Equation 3.

Another term of the radiated wavefield is the typical spherical wave propagation factor $e^{i\omega R/v}/R$, where v represents the formation S- or P-wave velocity. Consequently, the far-field P-, SH-, and SV-waves can be written as

$$\begin{cases} u_P = \left[-i\rho_{fm}\alpha_{fm}\omega B^{fm}\left(\omega, k_{p0}^t\right) I_1\left(f_{p0} r_0\right) \cos\varphi\right] \dfrac{e^{i\omega R/\alpha_{fm} - i\pi/4}}{4\pi\rho_{fm}\alpha_{fm}^2 R} \\ u_{SH} = \left[i\rho_{fm}\beta_{fm}\omega \sin\theta_t D^{fm}\left(\omega, k_{s0}^t\right) I_1\left(f_{s0} r_0\right) \sin\varphi\right] \dfrac{e^{i\omega R/\beta_{fm} - i\pi/4}}{4\pi\rho_{fm}\beta_{fm}^2 R} \\ u_{SV} = \left[\rho_{fm}\omega^2 \sin\theta_t F^{fm}\left(\omega, k_{s0}^t\right) I_1\left(f_{s0} r_0\right) \cos\varphi\right] \dfrac{e^{i\omega R/\beta_{fm} - i\pi/4}}{4\pi\rho_{fm}\beta_{fm}^2 R} \end{cases}, \tag{4}$$

where ρ_{fm} is the formation density. The expression in the square bracket of Equation 4 yields the far-field radiation directivity of the P-, SH-, and SV-waves, respectively, as

$$\begin{cases} \Re_P(\omega;\theta_t,\varphi) = -i\rho_{fm}\alpha_{fm}\omega B^{fm}\left(\omega, k_{p0}^t\right) I_1\left(f_{p0} r_0\right) \cos\varphi \\ \Re_{SH}(\omega;\theta_t,\varphi) = i\rho_{fm}\beta_{fm}\omega \sin\theta_t D^{fm}\left(\omega, k_{s0}^t\right) I_1\left(f_{s0} r_0\right) \sin\varphi \\ \Re_{SV}(\omega;\theta_t,\varphi) = \rho_{fm}\omega^2 \sin\theta_t F^{fm}\left(\omega, k_{s0}^t\right) I_1\left(f_{s0} r_0\right) \cos\varphi \end{cases}. \tag{5}$$

Reception response of a LWD tool inside the borehole

When the radiated waves represented by Equation 4 encounter a reflector in formation (assume that the reflector size is large compared to wavelength), they are reflected back and recorded by the receiver on the LWD tool (see Figure 1B). The received wave can generally be written as (Tang and Wei, 2012).

$$IWV(\omega) = S(\omega) \cdot RD(\omega) \cdot RF(\omega) \cdot \frac{e^{-\omega D/(2Qv)}}{4\pi\rho_{fm} v^2} \cdot \left[\frac{e^{i\omega D/v}}{D}\right], \tag{6}$$

where Q is the quality factor of the formation for the S- or P-waves; S is the source function; RD is the far-field radiation function given by Equation 3; RF denotes the reflection coefficient of the wave at the reflector, which can be calculated using the Zoeppritz equation (Aki and Richards, 1980). The form of RD and RF depends on the type of the incident wave considered (i.e., P-, SH-, or SV-waves); and $D = R_t + R_i$ is the total traveled distance from source to reflector and back to borehole, as shown in Figure 1A.

In the LWD measurement, however, it is important to note that the take-off azimuth at the wave radiation may be significantly different from the incident azimuth at the wave reception. For the model shown in Figure 1A, the azimuth of the reflector relative to the tool x-axis is φ'_0 at the wave takeoff; due to the tool rotation, the reflector azimuth changes to $(\varphi'_0 + \delta)$ when the wave is reflected back to the borehole, where δ is the offset angle of the tool during wave propagation in formation (assuming that tool rotation is clockwise). By treating the reflected wave incidence as spherical wave radiation from the virtual source located at the mirror point of the source on the reflector outside (see Figure 1A), the propagation distance D in Equation 6 is equated to a straight line linking the virtual source and borehole, as given by

$$D = \sqrt{r^2 + r'^2_0 - 2rr'_0 \cos\left(\varphi - \varphi'_0 - \delta\right) + \left(z - z'_0\right)^2}. \tag{7}$$

As a result, we can express the spherical wave propagation factor in Equation 6 as the summation of multipole cylindrical waves:

$$\frac{e^{i\omega D/v}}{D}=\frac{1}{\pi}\int_{-\infty}^{+\infty}\sum_{n=0}^{+\infty}\varepsilon_n I_n(k_v r)K_n(k_v r_0')\cos\{n[\varphi-(\varphi_0'+\delta)]\}e^{ik(z-z'_0)}dk, \quad (8)$$

where $k_v=\sqrt{k^2-\omega^2/v^2}$; I_n (K_n) is the n-order first (second)-kind modified Bessel function; and the Neumann factor ε_n is taken as 1 for $n=0$ and 2 for $n>0$. The substitution of Equation 8 into Equation 6 yields the displacement potential function for the incident P-, SH-, and SV-waves in the frequency–wavenumber domain:

$$\begin{cases}\phi^i=\dfrac{S(\omega)\cdot RD_P(\omega)\cdot RF_P(\omega)}{4\pi\rho_{fm}\alpha_{fm}^2}\displaystyle\sum_{n=0}^{+\infty}\varepsilon_n I_n(pr)K_n(pr_0')\begin{bmatrix}\cos n\varphi\cdot\cos n(\varphi_0'+\delta)\\+\sin n\varphi\cdot\sin n(\varphi_0'+\delta)\end{bmatrix}\\ \chi^i=\dfrac{S(\omega)\cdot RD_{SH}(\omega)\cdot RF_{SH}(\omega)}{4\pi\rho_{fm}\beta_{fm}^2}\displaystyle\sum_{n=0}^{+\infty}\varepsilon_n I_n(sr)K_n(sr_0')\begin{bmatrix}\cos n\varphi\cdot\cos n(\varphi_0'+\delta)\\+\sin n\varphi\cdot\sin n(\varphi_0'+\delta)\end{bmatrix}\\ \Gamma^i=\dfrac{S(\omega)\cdot RD_{SV}(\omega)\cdot RF_{SV}(\omega)}{4\pi\rho_{fm}\beta_{fm}^2}\displaystyle\sum_{n=0}^{+\infty}\varepsilon_n I_n(sr)K_n(sr_0')\begin{bmatrix}\cos n\varphi\cdot\cos n(\varphi_0'+\delta)\\+\sin n\varphi\cdot\sin n(\varphi_0'+\delta)\end{bmatrix}\end{cases}, \quad (9)$$

where the superscript i denotes the incident wave from the virtual source; the subscripts P, SH, and SV mean that the radiation function RD and reflection coefficient RF should correspond to the P-, SH-, and SV-waves, respectively. The common factor $e^{-\omega D/(2Qv)}$ is omitted from Equation 9.

The incident waves, in turn, will induce wave motions in and outside the borehole, and the induced wave displacement potential function of the P- and S-waves in the frequency–wavenumber domain has the same form as in Equation 8:

$$\begin{cases}\phi_f=\displaystyle\sum_{n=0}^{+\infty}\left\{\left[A_n^f\cos(n\varphi)+A'^f_n\sin(n\varphi)\right]I_n(fr)\right.\\ \qquad\left.+\left[B_n^f\cos(n\varphi)+B'^f_n\sin(n\varphi)\right]K_n(fr)\right\}K_n(k_v r_0'),\\ \phi=\displaystyle\sum_{n=0}^{+\infty}\{[A_n\cos(n\varphi)+A_n'\sin(n\varphi)]I_n(pr)\\ \qquad+[B_n\cos(n\varphi)+B_n'\sin(n\varphi)]K_n(pr)\}K_n(k_v r_0'),\\ \chi=\displaystyle\sum_{n=0}^{+\infty}\{[C_n\sin(n\varphi)-C_n'\cos(n\varphi)]I_n(sr)\\ \qquad+[D_n\sin(n\varphi)-D_n'\cos(n\varphi)]K_n(sr)\}K_n(k_v r_0'),\\ \Gamma=\displaystyle\sum_{n=0}^{+\infty}\{[E_n\cos(n\varphi)+E_n'\sin(n\varphi)]I_n(sr)\\ \qquad+[F_n\cos(n\varphi)+F_n'\sin(n\varphi)]K_n(sr)\}K_n(k_v r_0')\end{cases}, \quad (10)$$

where ϕ_f is the function of the fluid P-wave inside the drill collar or fluid ring; ϕ, χ, and Γ are for the P-, SH-, and SV-waves in the drill collar or formation; $f=\sqrt{k^2-\omega^2/\alpha_f^2}$, $p=\sqrt{k^2-\omega^2/\alpha^2}$, and $s=\sqrt{k^2-\omega^2/\beta^2}$ are the fluid P-, solid P-, and S-wave radial wavenumbers, respectively; α_f, α, and β denote fluid P-, solid P-, and S-wave velocities, respectively; and $A_n^f\sim F_n$ and $A'^f_n\sim F_n'$ are the amplitude coefficients of the respective waves. For the wavefield inside the collar (outside borehole), we must set the coefficients B_n^{fin} and B'^{fin}_n (A_n^{fm}, A'^{fm}_n, C_n^{fm}, C'^{fm}_n, E_n^{fm}, and E'^{fm}_n) to 0 to prevent the wavefield from going to infinity.

Combining Equations 9, 10 in conjunction with the boundary conditions for the three interfaces of the LWD model (see Figure 1), we obtain two matrix equations for the amplitude coefficients in the abovementioned equations

$$\text{and}\quad\begin{matrix}\mathbf{H}\times\left[A_n^{fin},A_n^{dc},B_n^{dc},C_n^{dc},D_n^{dc},E_n^{dc},F_n^{dc},A_n^{fout},B_n^{fout},B_n^{fm},D_n^{fm},F_n^{fm}\right]^T=\mathbf{e},\\ \mathbf{H}\times\left[A'^{fin}_n,A'^{dc}_n,B'^{dc}_n,C'^{dc}_n,D'^{dc}_n,E'^{dc}_n,F'^{dc}_n,A'^{fout}_n,B'^{fout}_n,B'^{fm}_n,D'^{fm}_n,F'^{fm}_n\right]^T=\mathbf{e}'\end{matrix}, \quad (11)$$

where the superscripts of the coefficient vectors have the same meaning as in Equation 1 and the matrix $\mathbf{H}$ is the same as in Equation 1. The vectors $\mathbf{e}$ and $\mathbf{e}'$ result from the P-, SH-, and SV-wave incidence from the virtual source. The detailed expressions of the vectors are given in Supplementary Appendix A2. Note that the tool rotation effect between wave radiation and incidence is included in the expressions.

The radial distance r_0' of the virtual source considered for the reflection imaging problem is generally large compared to wavelength such that the far-field condition $|k_v r_0'|\gg 1$ holds true, and the steepest-descent method can be used to calculate the wavenumber integral in Equation 10 (Tang and Patterson, 2009).

For the reflected wave reception in LWD, the receivers are located on the rim of the drill collar, having the same radius r_0 as that of the ring source. Therefore, the received wavefield corresponds to that of the borehole fluid at the drill collar interface.

For fluid pressure ($p=\rho_f\omega^2\phi_{fout}$),

$$p(\omega)=\frac{e^{i\omega D/v-i\pi/4}}{D}\sum_{n=0}^{+\infty}\left\{\left[A_n^{fout}\cos(n\varphi)+A'^{fout}_n\sin(n\varphi)\right]I_n(f_0r_0)\right.\\ \left.+\left[B_n^{fout}\cos(n\varphi)+B'^{fout}_n\sin(n\varphi)\right]K_n(f_0r_0)\right\}\rho_f\omega^2. \quad (12)$$

For radial fluid displacement ($u_r^f=\partial\phi_{fout}/\partial r$),

$$u_r^f(\omega)=\frac{e^{i\omega D/v-i\pi/4}}{D}\sum_{n=0}^{+\infty}\left\{\left[A_n^{fout}\cos(n\varphi)+A'^{fout}_n\sin(n\varphi)\right][nI_n(f_0r_0)/r_0+f_0I_{n+1}(f_0r_0)]\right.\\ \left.+\left[B_n^{fout}\cos(n\varphi)+B'^{fout}_n\sin(n\varphi)\right][nK_n(f_0r_0)/r_0-f_0K_{n+1}(f_0r_0)]\right\}, \quad (13)$$

where $f_0=\sqrt{\left(k_0^i\right)^2-\left(\omega/\alpha_f\right)^2}$ is the radial wavenumber of the fluid P-wave, $k_0^i=(\omega/v)\cos(\pi-\theta_i)$ is the steepest–descent solution of the wavenumber of the incident wave, and θ_i represents the angle between the incident direction of the wave and borehole axis; note that the wave travel distance D in Equations 6, 8 becomes $D=\sqrt{r'^2_0+(z-z'_0)^2}$ under the condition of $r\ll r_0'$. Fourier transform for Equations 12, 13 to the time domain yields the received waveform, which can be compared with waveform data from finite-difference numerical modeling.

Result verification

To validate the result from the abovementioned analytical solution, we carried out 3D finite-difference modeling (Wei and Tang, 2012) for the model given in Figure 1 (see model parameters in Table 1). The reflector is an interface between formations 1 and 2. The reflector has an azimuth angle of 0° and an inclination angle of 45°. The borehole is surrounded by a fast formation (see Table 1), and the borehole-to-virtual source distance is 10 m. Inside the borehole, the receivers are at a 1-m distance above the source and azimuthally spaced at 45°, as shown in Figure 2A. Tan et al. (2016) indicated that the dominant frequency band of LWD dipole shear-wave remote detection is 1,800 Hz–2,500 Hz. Therefore, a 2,500-Hz Ricker wavelet is used for the source excitation here. For this numerical validation modeling, the tool is stationary, i.e., the δ angle in Equation 9 is set to 0.

Figure 2B compares the numerical (dots) and analytical (curve) waveforms at the azimuthally distributed receivers

TABLE 1 Model parameters for LWD calculation.

	P-velocity ($m \cdot s^{-1}$)	S-velocity ($m \cdot s^{-1}$)	Density ($kg \cdot m^{-3}$)	Radii (m)
Fluid in the drill collar	1,500	—	1,000	0.027
Drill collar	5,860	3,130	7,850	0.090
Fluid ring	1,500	—	1,000	0.117
Fast formation	4,000	2,300	2,500	—
Slow formation	2,074	869	2,250	—
Formation 2	4,500	3,000	2,600	∞

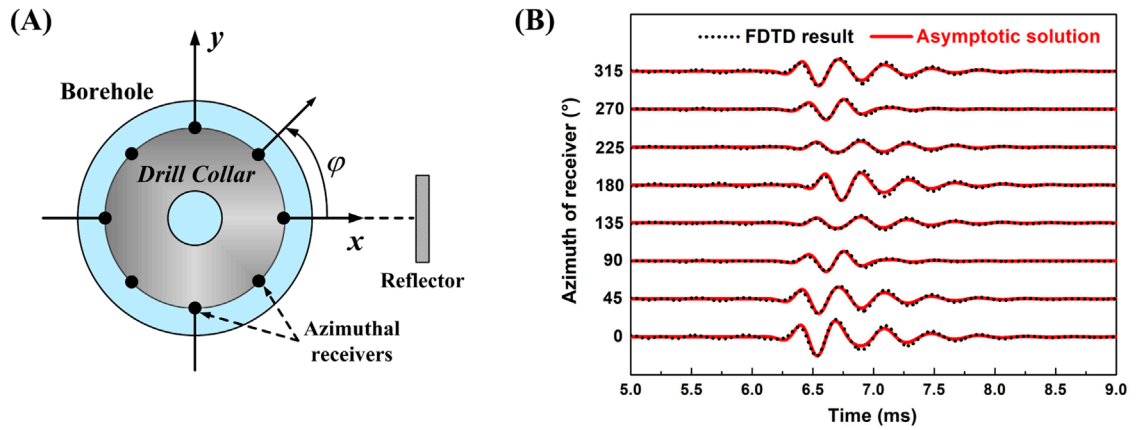

FIGURE 2
(A) Cross-section of LWD receiving configuration using azimuthally spaced receivers on the collar rim. **(B)** Comparison of the SV-wave reflection waves from the 3D finite-difference (dots) and the analytical solution (solid curves) calculations.

for the dipole source pointing to the x-axis direction. The comparison is in the time range from 5 ms to 9 ms, so that the waves traveling along the borehole, as shown in finite-difference modeling, are skipped, and only the reflected waves from the surrounding formation are compared. For validation purposes, Figure 2B shows only the comparison for the SV-waves for the inclined reflector model. The numerical and analytical waves agree very well, validating our asymptotic solution result.

Far-field radiation directivity of a LWD dipole source

Equation 5 allows us to investigate the radiation characteristics of a LWD dipole source inside the borehole. For the dipole source pointing to the x-axis (see Figure 1A), Figure 3 shows the far-field radiation patterns of the formation SH-, SV-, and P-waves for the 2,500-Hz source frequency. The radial scales mark the relative amplitude of the radiated waves for a source of unit intensity for the radiation angle in the $0° < \theta_t < 360°$ range. The SH (SV- and P-)-wave patterns are shown for the yoz (xoz) plane, where the azimuthal variation of the patterns attains maximum. The azimuthal variation in the SH (SV- and P-)-wave pattern is $\sin\varphi$ ($\cos\varphi$), as shown in Equation 5. When the formation reflector strikes in the direction parallel (perpendicular) to the dipole source orientation, the reflected SH-wave (SV- and P-waves) amplitude will be the largest. Notably, the borehole reception and radiation have the same directivity patterns because of reciprocity (Tang et al., 2014). The azimuthal variation characteristics of the dipole radiation are the basis for identifying the reflector azimuth in wireline dipole shear-wave reflection imaging, which also holds true for the LWD situation.

Figure 3 shows radiation patterns for both fast and slow formations (see Table 1). In the fast-formation case (Figure 3A), the P- and SH-wave patterns show the maximum strength in the horizontal direction, whereas the SV-wave pattern is null in this direction. This means that the P- and SH-waves, instead of the SV-wave, should be used to image reflectors that are inclined or parallel with the borehole. In the slow-formation case, the SH- and SV-wave patterns (Figure 3B) are more complex, and their radiation coverages decrease. In comparison, the P-wave radiation has the highest strength and coverage, meaning that the LWD dipole P-wave can be used for reflection imaging in slow formations.

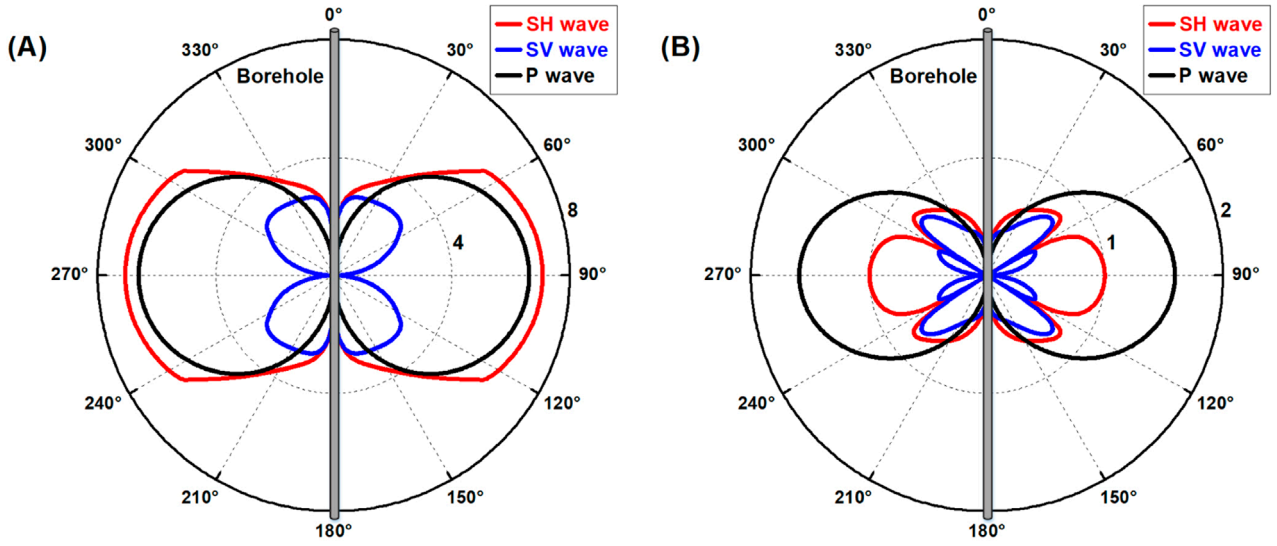

FIGURE 3
SH-, SV-, and P-wave radiation patterns of a 2,500-Hz LWD dipole source in **(A)** fast and **(B)** slow formations.

The one-dipole-source and two-receiver LWD measurement system

The wireline dipole acoustic reflection measurement acquires a four-component (4C) dataset (*xx*, *xy*, *yx*, and *yy*). The 4C data are mathematically rotated to scan a formation reflector in 360°. In the LWD case, azimuthal scanning is achieved by the drilling rotation, which allows us to use a one-dipole-source and two-receiver LWD system for the reflection measurement.

The principle of rotation imaging

The source–receiver configuration for the LWD measurement system is shown in Figure 1B, where the wave signals radiated from the dipole source are recorded by two receivers that are oppositely mounted on the collar rim along the dipole source direction. These two receivers form a receiving station, and the tool consists of eight or more such receiving stations. The receivers record two signals $xx_1^{(m)}$ and $xx_2^{(m)}$, where the first (second) letter denotes the source (receiver) orientation and the superscript m indicates the number of times of source excitation and data acquisition. It should be noted that the time interval between the two adjacent source excitations should be long enough to ensure that the first received signal is not affected by the second excitation. The LWD single-component dipole waveform is obtained by

$$xx^{(m)} = xx_1^{(m)} - xx_2^{(m)}. \tag{14}$$

For a centered tool in the borehole, Equation 14 produces a dipole signal as the $n = 1$ term is dominant the sum of the series of Equations 12, 13. The far-field wavefield of the centered annular dipole source is equivalent to that generated by a single force source on the well axis, and this simplified view is shown in Figure 4.

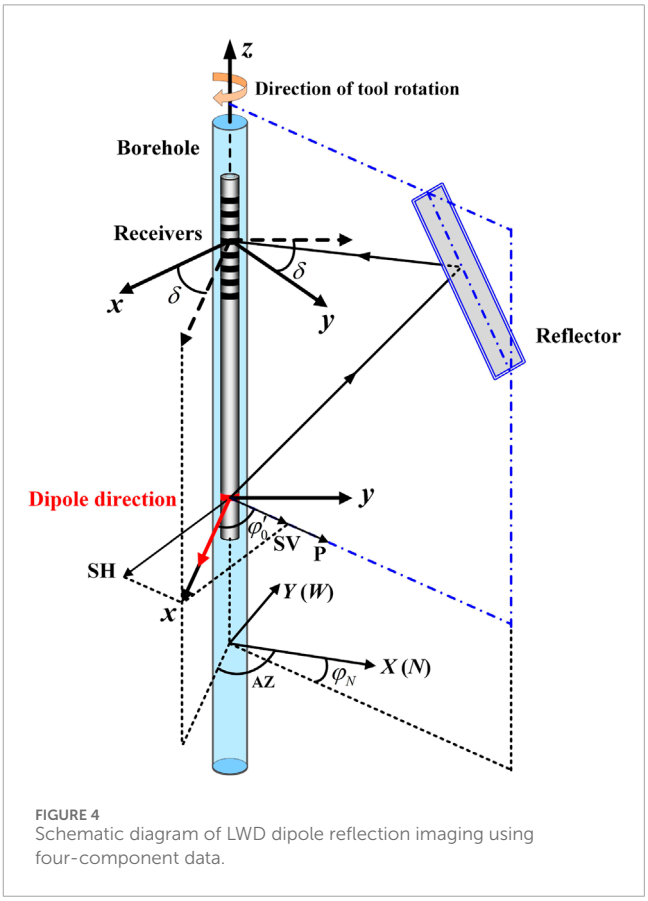

FIGURE 4
Schematic diagram of LWD dipole reflection imaging using four-component data.

Relative to the reflection azimuth, the dipole source vector can be projected onto two orthogonal directions perpendicular and parallel to the reflector, giving rise to the SV (and P) and SH components in the reflection data. We now record the data using

the x-oriented receivers of the measurement system. Considering the tool rotation, the recorded data are as follows:

$$\begin{cases} xx_S(\varphi_0') = SH \cdot \sin\varphi_0' \cdot \sin(\varphi_0' + \delta) + SV \cdot \cos\varphi_0' \cdot \cos(\varphi_0' + \delta), \\ xx_P(\varphi_0') = P \cdot \cos\varphi_0' \cdot \cos(\varphi_0' + \delta) \end{cases}, \tag{15}$$

where xx_S and xx_P are the dipole S- and P-wave components, respectively, the sum of which is the xx data in Equation 14. In field data processing, one transforms the rotation angle of the measured data from the tool coordinate system to the fixed coordinate system to eliminate the influence of tool rotation. In the field measurement, the angle between the x-axis of the tool coordinates and the x-axis of the earth coordinates (e.g., north) is always recorded, as shown in Figure 4. Using AZ, we obtain

$$\begin{cases} xx_S(AZ) = \left\{ \begin{array}{l} SH \cdot \sin(AZ - \varphi_N) \cdot \sin(AZ - \varphi_N + \delta) \\ +SV \cdot \cos(AZ - \varphi_N) \cdot \cos(AZ - \varphi_N + \delta) \end{array} \right\}, \\ xx_P(AZ) = P \cdot \cos(AZ - \varphi_N) \cdot \cos(AZ - \varphi_N + \delta) \end{cases} \tag{16}$$

where φ_N is the angle between the reflector azimuth and coordinate north. Using the triangle function property, Equation 16 can also be written as

$$\begin{cases} xx_S(AZ) = \dfrac{SV - SH}{2} \cdot \cos 2\left(AZ - \varphi_N + \dfrac{\delta}{2}\right) + \dfrac{SV + SH}{2} \cdot \cos\delta, \\ xx_P(AZ) = \dfrac{P}{2} \cdot \cos 2\left(AZ - \varphi_N + \dfrac{\delta}{2}\right) + \dfrac{P}{2} \cdot \cos\delta. \end{cases} \tag{17}$$

Equation 17 indicates that relative to the case of no tool rotation (i.e., $\delta = 0$), the reflector azimuth for a rotating tool, as determined from xx_S or xx_P, is offset by $\delta/2$ in the opposite direction of the tool rotation.

Using the analytical solution of Equation 12, the operation of the proposed one-dipole-source and two-receiver LWD measurement system can be accurately modeled and analyzed. In this modeling, we assume a 60°-dip reflector facing the north direction (i.e., $\varphi_N = 0$) and a borehole-to-virtual source distance of 20 m. The source-to-receiver distance is 3 m; a 2,500-Hz Ricker wavelet is used for the source excitation. Table 1 shows the simulation parameters of the borehole and formation (the fast formation is used for formation 1). Figures 5, 6 show the modeled xx_S and xx_P data, respectively, as calculated using Equation 14, for the azimuth AZ ranging from 0° to 360°, where the azimuthal labels represent the azimuth and the radial label represents the wave arrival time. In the respective figures, the stationary (A, $\delta = 0$) and rotating (B, $\delta = 20^o$) tool cases are modeled, and the variation patterns of the normalized wave amplitude $|xx_S(AZ)|$ and $|xx_P(AZ)|$ are compared in (C).

The results show the maximum of $|xx_S|$ and $|xx_P|$ points, respectively, toward the reflector strike and normal direction, as is the typical dipole characteristic. However, if the azimuth of the tool changes significantly during wave propagation in formation, the variation pattern of the $|xx_S|$ and $|xx_P|$ data will change accordingly. The modeling results given in Figures 5C, 6C indicate that the azimuth offset of $\delta = 20^o$ results in a 10° offset in the opposite direction of the tool rotation, which is consistent with Equation 17. Therefore, when using the amplitude information of dipole data $|xx|$ to determine the reflector azimuth, the result needs to be shifted $\delta/2$ toward the rotation direction of the tool to correct the rotation effect.

Based on the abovementioned analyses, the formula for determining the reflector azimuth using the LWD system is as follows.

For S-wave,

$$\varphi_N = \max\left[\left|xx_S(AZ)\right|\right] + \delta/2 \pm \pi/2. \tag{18}$$

For P-wave,

$$\varphi_N = \max\left[\left|xx_P(AZ)\right|\right] + \delta/2 + \pi/2 \cdot (1 \pm 1), \tag{19}$$

where the symbol max denotes seeking the value of AZ to maximize the function $|xx|$. The offset angle of the tool can be calculated from the rotation speed (revolutions per minute, RPM) and the arrival time (T_0) of the reflected signal as $\delta = RPM \cdot T_0$. The waveforms $xx^{(m)}$ in Equation 14 represent the recorded data at different times of source excitations, and the depth position of the source might change for different time stances. However, in the field logging scenario, the rate of penetration (ROP) of the bit is usually slow, which allows us to ignore the effect of the depth variation on the recorded data.

Elimination of azimuth ambiguity for the LWD system

The above mentioned analysis results also exhibit an inherent 180°-azimuth ambiguity of the dipole system, as apparent from Equations 16, 17 (and from Figures 5C, 6C). This ambiguity can be eliminated using the arrival time difference between the xx_1 and xx_2 data of the oppositely mounted receivers of the LWD system, as shown below.

For the case of $\delta = 0$ shown in Figures 5, 6, Figure 7 compares the waveforms xx_1 and xx_2 of the S- and P-waves (normalized by their maximum amplitude) for the tool azimuth AZ value of 30°. For this configuration, receiver x_1 (x_2) faces forward (backward) to the reflector such that xx_1 arrives earlier than xx_2 for both the S-wave (Figure 7A) and P-wave (Figure 7B) cases. For a closer look at the time difference, the S-waveform of xx_2 is flipped in Figure 7A (this flipping does not change the arrival time of the waveform). The arrival time difference between xx_1 and xx_2 can be utilized to provide a method for determining which side the reflector is at, front or back, thus eliminating the 180° ambiguity of the existing dipole acquisition system. It should be noted that AZ is the take-off azimuth of the tool at the source radiation. The tool azimuth at the data recording is $(AZ + \delta)$. Therefore, when using the arrival time difference between the reflected waves xx_1 and xx_2 to distinguish the reflector azimuth, it may be necessary to offset the tool azimuth by δ toward the rotation direction to compensate for the rotation-related arrival time changes.

Analysis of examples

Analysis of a synthetic LWD example

We now use the synthetic LWD dipole acoustic reflection data to test the applicability of the proposed LWD system and method for the drilling rotation condition. For the model shown in Figure 8, the reflector intersects the borehole with an angle of 30° in the middle of the 140-m-depth section, with the azimuth angles of the reflector in the lower and upper part of the intersection being 60° and 240°,

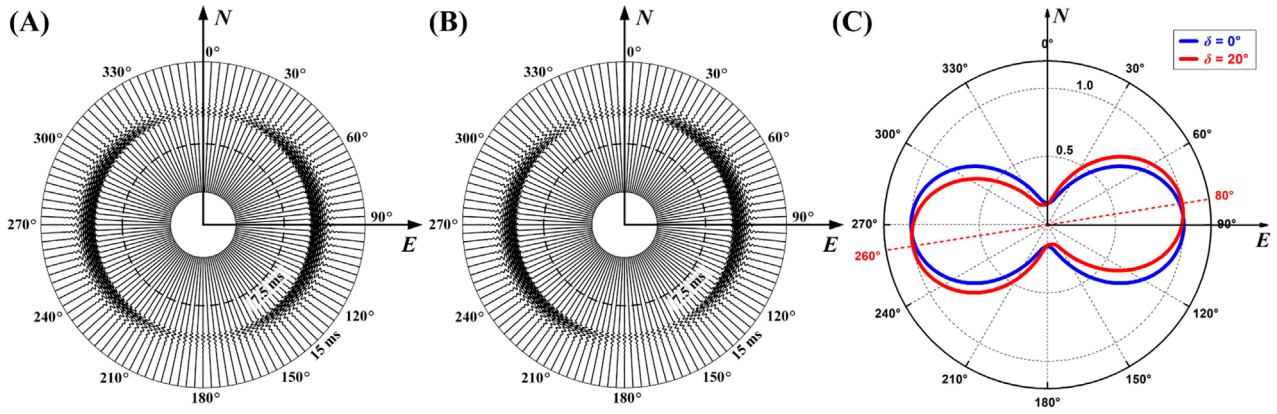

FIGURE 5
Azimuthal variation in the S-wave data from the LWD system. **(A)** Waveform *versus* azimuth for $\delta = 0°$. **(B)** Waveform *versus* azimuth for $\delta = 20°$. **(C)** Amplitude variation patterns of **(A)** and **(B)**; note that the pattern of **(B)** is rotated $\delta/2$ relative to that of **(A)**.

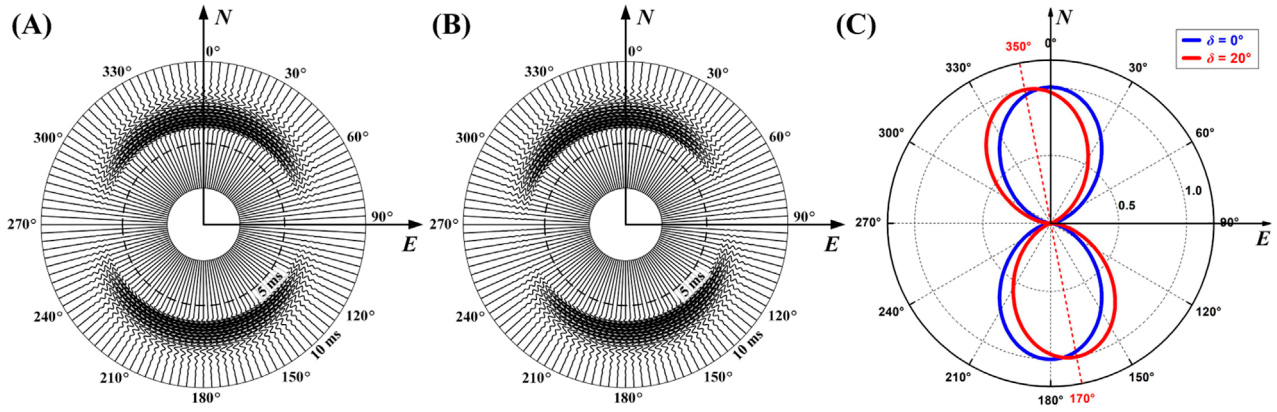

FIGURE 6
Azimuthal variation in the P-wave data from the LWD system. **(A)** Waveform *versus* azimuth for $\delta = 0°$. **(B)** Waveform *versus* azimuth for $\delta = 20°$. **(C)** Amplitude variation patterns of **(A)** and **(B)**; note that the pattern of **(B)** is rotated $\delta/2$ relative to that of **(A)**.

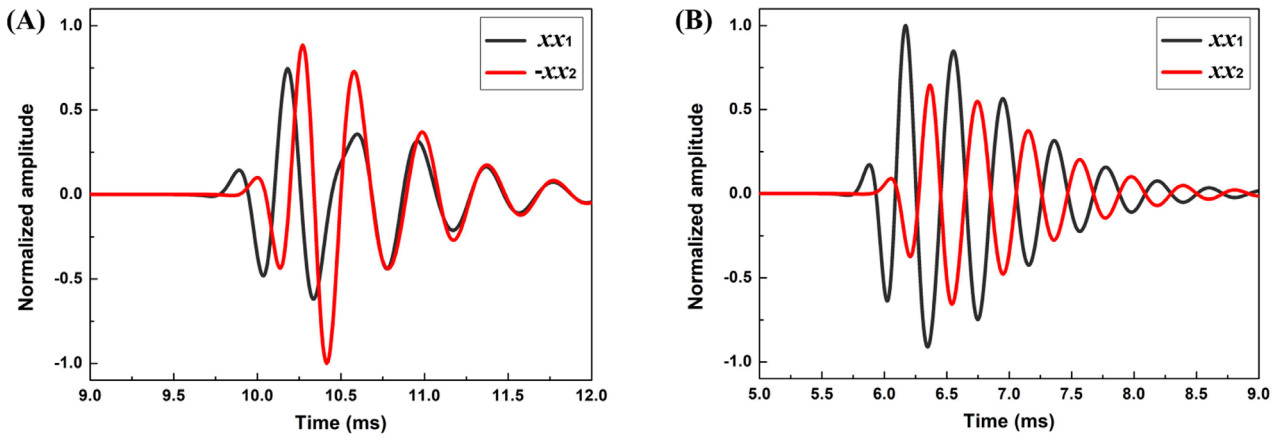

FIGURE 7
Comparison of xx_1 and xx_2 signals received at the opposite side of the tool (tool azimuth is 30° and $\delta = 0$). **(A)** and **(B)** are for S- and P-waves, respectively.

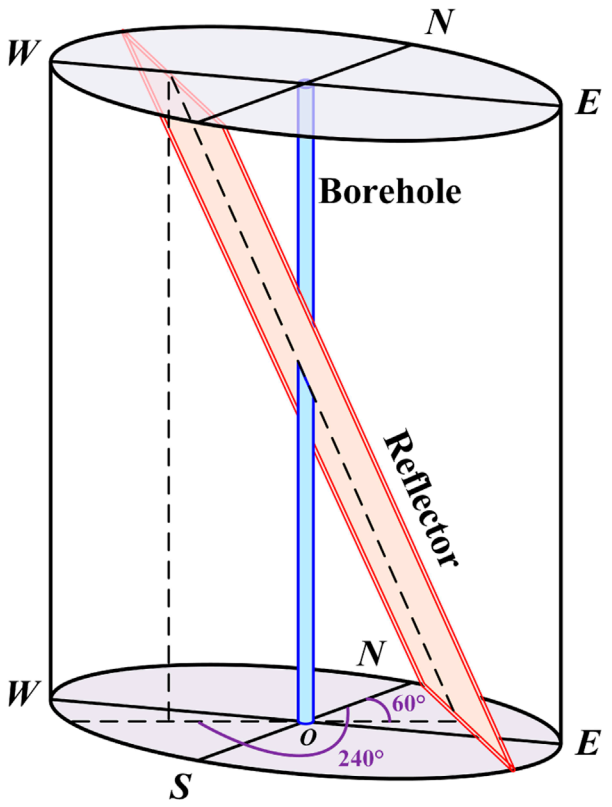

FIGURE 8
Borehole model with an inclined reflection interface.

respectively. The dipole S-wave detection method is used for data acquisition and processing, the results of which are given in Figure 9. It is assumed that the drilling has an RPM of 100 and an ROP of 10 m per hour. The time interval of the source excitation is 5 s. The time sampling interval and sampling points of the wavefield are 36 μs and 1,024, respectively. The dipole source is located 3 m below the receivers, and the source frequency is 2,500 Hz. The parameters of the borehole and formation and reflector are shown in Table 1, where fast formation 1 is used for the simulation.

Panel 1 of Figure 9 shows the azimuthal curve of the tool relative to north, indicating that the tool rotates rapidly for this while drilling simulation. Note that for a clearer view, the results of panels 1, 6, and 7 are displayed at intervals of 20 depth points. The computed xx_1 and xx_2 waveform data are displayed as variable density images in panels 2 and 3, respectively. For comparison, we also computed the borehole flexural waves traveling directly along the borehole, as indicated in the panels. For the data analysis, we first separate the xx_1 and xx_2 waves from the direct waves in the data and then compute the dipole data xx using Equation 14. Next, taking a moving depth window (about 41 adjacent depths, enough to cover several rotation cycles), the energy (squared amplitude) of the xx data *versus* the azimuth was computed for each depth within the window. Moving the window along the entire depth zone yields an energy image map *versus* tool azimuth in panel 4. The trend of the maximum energy delineates the reflector azimuth, as shown by the black line in panel 4, which shows that the reflector strike is approximately 140° ~ 150° or 320° ~ 330°. Therefore, the reflector azimuth is approximately 50° ~ 60° or 230° ~ 240°. Note that the delineated azimuth trend shows a drift from the borehole–reflector intersection toward the top or bottom of the well. This drift is the result of the tool azimuth offset between wave radiation and reception, as discussed before. From the wave travel time and RMP of the simulation, the offset angle $\delta = RPM \cdot T_0$ is calculated and plotted in panel 5. Correcting the data of panel 4 using the δ data of panel 5, we obtain the reflector azimuth in panel 6, as shown by the two data trends (markers) of approximately 60° and 240°. The result, however, shows the typical 180° ambiguity in the reflector azimuth. The final step of the analysis is to eliminate this ambiguity, and the time difference between the xx_1 and xx_2 waves is evaluated. The result is color-coded using the data of panel 6 (red: the time difference is positive; blue: the time difference is negative). The time-difference information allows us to choose the correct reflector azimuth. The azimuth data in panel 7 are consistent with the model shown in Figure 8, which shows that the up-dip and down-dip components of the reflector are on the opposite sides of the well, with azimuth angles of approximately 240° and 60°, respectively. Detailed time-difference and tool-rotation correction analyses are discussed in the following section.

To substantiate the abovementioned modeling and analysis results, we analyze the data at depths of 55.8464 m and 139.6063 m, which correspond to the up- and down-dip parts of the reflector, respectively. For the depth of 55.8464 m, 20 measurement points are selected above and below the depth, and the (normalized) amplitude of the wave $|xx|$ *versus* the azimuth is shown in Figure 10A for 41 depths (markers). The red curve given in Figure 10A is from the linear fitting of the data. The amplitude data peak at approximately 150° or 330°, indicating that the reflector strike is approximately 150° or 330° and the reflector azimuth is approximately 60° or 240°. Figure 10B compares the waveforms xx_1 and xx_2 for this depth point, where the tool azimuth is 300°. The figure shows that xx_1 is ahead of xx_2, which indicates that receiver x_1 (x_2) is at the same (opposite) side of the reflector. The true azimuth of the reflector is therefore 240°.

For the down-dip depth of 139.6063 m, Figure 11A shows that the amplitude data peak at approximately 140° or 320° and the reflector azimuth is approximately 50° or 230°. As shown in panel 5 of Figure 9, at this depth point, the tool rotation offset angle is 17.6°; after the rotation correction, the reflector azimuth is approximately 58.8° or 238.8°. The tool azimuth for this depth point is 173°. According to the rotation angle of the tool, the true tool azimuth at the data recording should be 190.6°. The waveforms measured at this depth show that xx_2 is ahead of xx_1 (Figure 11B), indicating that receiver x_2 (x_1) is at the same (opposite) side of the reflector. The true azimuth of the reflector is approximately 58.8°. We notice that the azimuth result at 55.8464 m is obtained without the tool rotation correction. This is because the reflector is close to the borehole at this depth, and the angle-offset value due to the rotation is small and can thus be ignored. This synthetic modeling example validates the concept of the LWD system and the analysis results.

Analysis of a field wireline example

Encouraged by the success of the synthetic LWD datatest and results, we use a dipole dataset from wireline logging for a

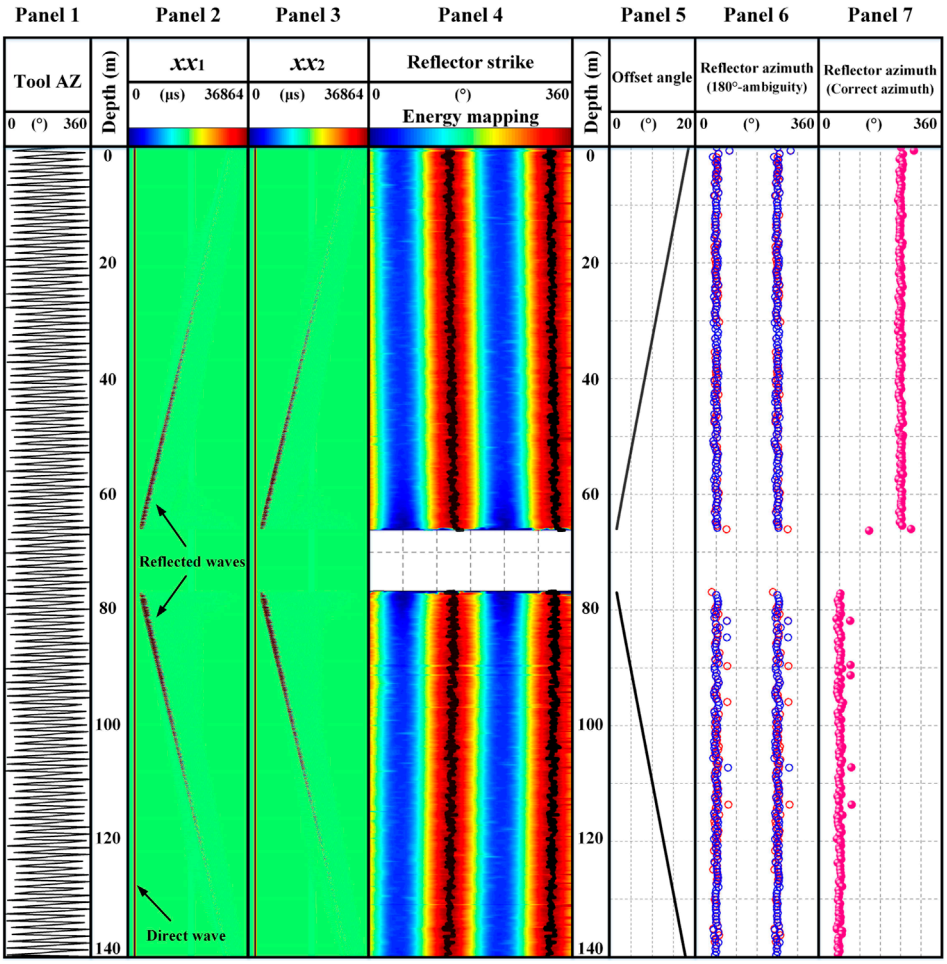

FIGURE 9
Synthetic data analysis example for delineating a formation reflector, simulating the drilling rotation of the LWD dipole system.

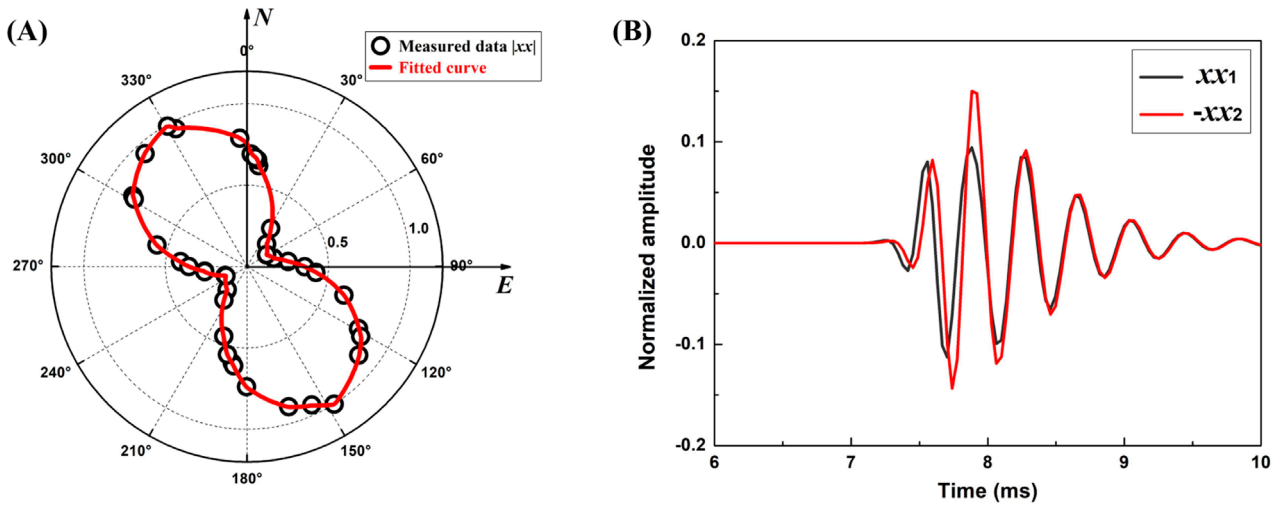

FIGURE 10
Reflector azimuth determination for the depth of 55.8464 m. **(A)** Data amplitude *versus* azimuth shows the 180° ambiguity. **(B)** Comparing the time difference of the opposite receivers resolves the ambiguity.

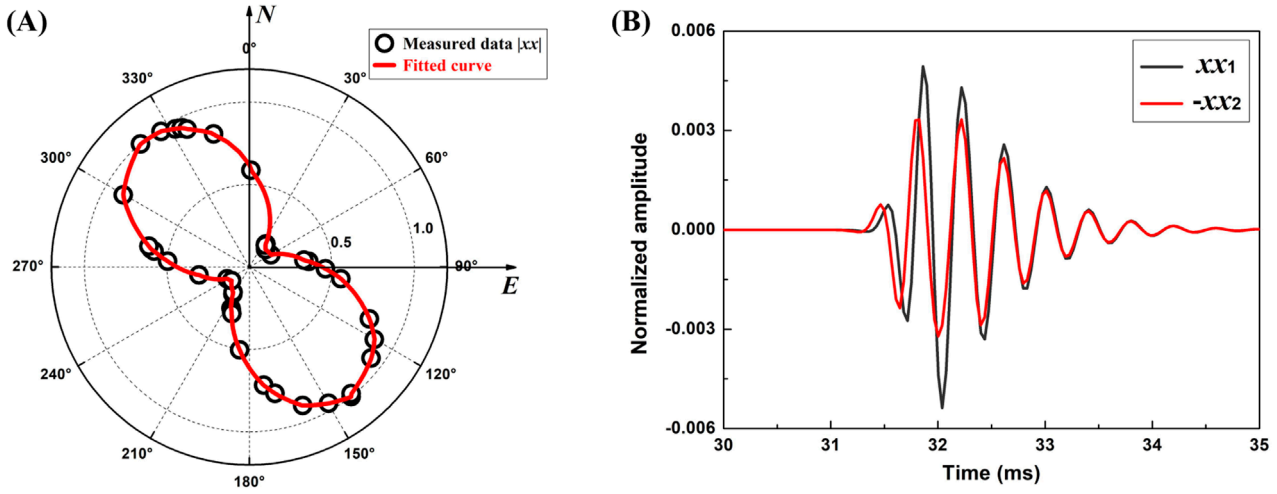

FIGURE 11
Reflector azimuth determination for the depth of 139.6063 m. **(A)** Data amplitude *versus* azimuth shows the 180° ambiguity. **(B)** Comparing the time difference of the opposite receivers resolves the ambiguity.

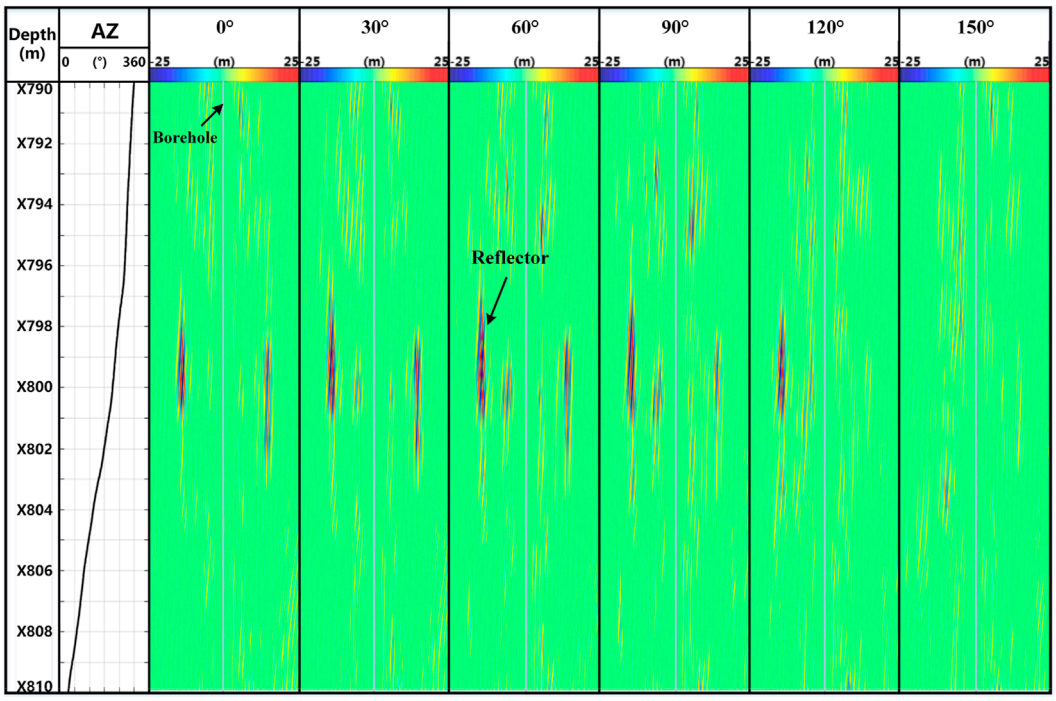

FIGURE 12
Azimuthal imaging result of wireline dipole shear-wave reflection data measured in an actual well.

further test. Figure 12 shows the azimuthal imaging results of dipole shear-wave measurement data within a 20-m interval of a well. The azimuth curve in panel 1 shows that the tool rotates continuously in this well section. First, the acquired four-component dipole data (*xx*, *xy*, *yx*, and *yy*) are processed through filtering, wavefield separation, and migration imaging, which yields the reflection signal from the reflector outside the borehole. In addition, the four-component reflection data are rotated to obtain the imaging of the well section in the 0°–150° azimuth (relative to the North Pole), as shown in panels 2–7. It can be seen that there is a high inclination angle reflector approximately 15 m away from the well, and the reflector is most clearly imaged in the 60° azimuth, whereas it is not imaged in the 150° azimuth, which indicates that the reflector strike is approximately 60° north by east (or 60° south by west).

Furthermore, only the *xx* component is used for azimuth recognition. For the depth of 799 m, 15 measurements are selected

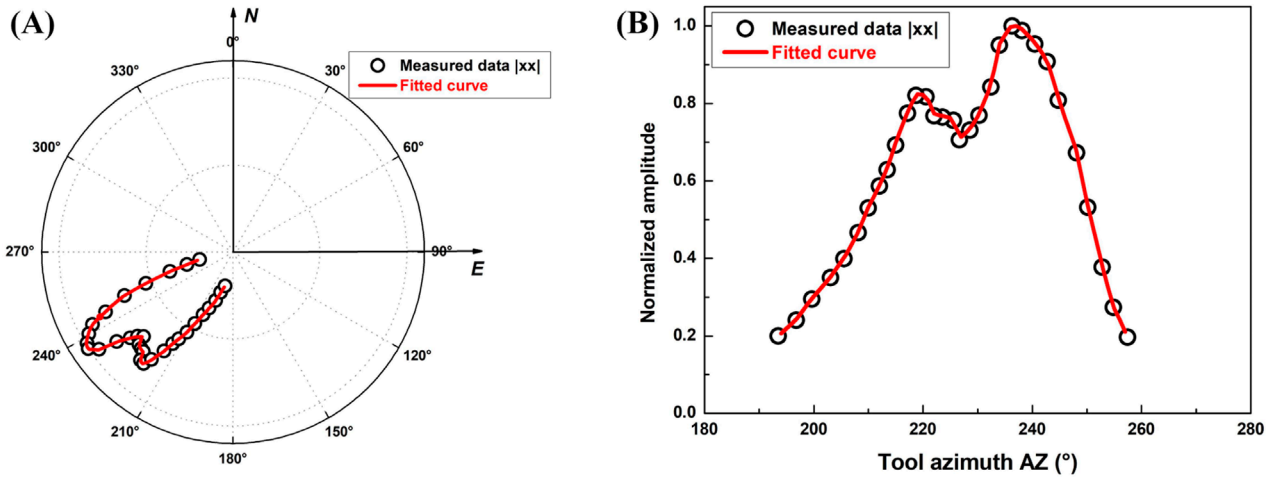

FIGURE 13
Azimuthal comparison result of wireline dipole shear-wave *xx*-component reflection data in the **(A)** polar and **(B)** Cartesian coordinate systems.

above and below the depth point, respectively. Figures 13A, B show the normalized azimuth amplitude results in the form of polar and Cartesian coordinate systems, respectively. The results show that at the depth range corresponding to these 31 measurement points, the tool rotated continuously by approximately 70°, and the signal amplitude reaches its maximum near 240°. Combined with the theoretical results shown in Figure 5, it is observed that the reflector strike is approximately 240° (i.e., 60° south by west), which is consistent with the orientation identification results obtained using the four-component rotation shown in Figure 12. The field example preliminarily confirms the practicability of the method proposed in this paper.

Discussion

The central result of this work is the analytical solutions of Equations 12, 13 for modeling the LWD tool reception responses in the borehole acoustic dipole reflection survey. The analytical solutions strictly consider the off-axis data acquisition configuration and the rotation effect of the drill collar, which has not been taken into account simultaneously in current studies. For example, Tan et al. (2016) and Tan et al. 2022 assumed an ideal on-axis data acquisition configuration and simulated the reception response for LWD dipole shear-wave reflection imaging using the elastic reciprocity theorem, while existing analyses (Tan et al., 2016; 2022; Li et al., 2022b; Rao et al., 2023) assumed that the drill collar is stationary, which is inconsistent with the actual situations. On this basis, a method for identifying the reflector azimuth using the LWD one-dipole-source and two-receiver measurement mode is proposed. Compared with the traditional wireline acoustic dipole remote sensing, the basic principles of the rotational imaging are the same. That is, the orientation of the maximum amplitude of the dipole S (P-)-waves recorded by the receivers located in different directions corresponds to the strike (azimuth) of the reflector, as shown by the blue curve with δ=0 in Figure 5C (Figure 6C). The difference is that the high-speed rotation of the drill collar will cause the above patterns to change, as shown by the red curves with δ=20° in Figures 5C, 6C. Therefore, the rotation effect of the tool should be considered when using LWD acoustic data for remote detection. In addition, in actual drilling, the drill collar often deviates from the well axis due to the weight and complex movement of the drill collar. The influence of drill collar eccentricity on the measurement mode proposed in this paper needs further study.

Conclusions

This paper developed a theoretical analysis to study the problem of borehole acoustic reflection imaging in the LWD environment. Particularly, we focused on determining the reflector azimuth in the presence of rapid drilling rotation. The drilling rotation has both benefits and a drawback in LWD reflector imaging. The major benefit is that the drilling rotation allows for using a one-dipole-source and two-receiver LWD dipole system to perform the azimuthal scanning of a formation reflector, whereas in wireline logging, four-component dipole data are required for the scanning. A further advantage is that, by mounting the two receivers on the opposite sides of the LWD tool, the reflection arrival time difference between the receivers can be used to eliminate the 180°-azimuth ambiguity of the dipole system. The drawback is that, due to the tool rotation, the take-off azimuth at wave radiation may be different from the incident azimuth at wave reception, thereby affecting the determination of reflector azimuth. Our analysis shows that this rotation-induced azimuth offset can be corrected using the wave reflection travel time and the RPM of the drilling operation. We tested the concept of the proposed LWD acoustic imaging system using synthetic LWD modeling and field wireline data. The theoretical analysis results, therefore, provide a foundation for the LWD system.

Data availability statement

The original contributions presented in the study are included in the article/Supplementary Material; further inquiries can be directed to the corresponding author.

Author contributions

YL: investigation, methodology, and writing–original draft. ZW: funding acquisition, investigation, and writing–original draft. YS: software, supervision, validation, and writing–review and editing. XT: methodology and writing–review and editing.

Funding

The author(s) declare that financial support was received for the research, authorship, and/or publication of this article. This work was supported by the National Natural Science Foundation of China (grant no. U21B2064), the Research and Application Projects of China National Petroleum Corporation (grant no. 2023ZZ15YJ02), and the Tianshan Talent Program of Xinjiang Autonomous Region (grant no. 2022TSYCJC0027).

Conflict of interest

Authors YL and ZW were employed by Xinjiang Oilfield Company of PetroChina.

The remaining authors declare that the research was conducted in the absence of any commercial or financial relationships that could be construed as a potential conflict of interest.

Publisher's note

All claims expressed in this article are solely those of the authors and do not necessarily represent those of their affiliated organizations, or those of the publisher, the editors, and the reviewers. Any product that may be evaluated in this article, or claim that may be made by its manufacturer, is not guaranteed or endorsed by the publisher.

Supplementary material

The Supplementary Material for this article can be found online at: https://www.frontiersin.org/articles/10.3389/feart.2024.1483285/full#supplementary-material

References

Aki, K., and Richards, P. (1980). *Quantitative seismology: theory and methods*. San Francisco: W. H. Freeman & Co.

Ben, J. L., Qiao, W. X., Che, X. H., Ju, X. D., Liu, J. Q., and Men, B. (2020). Experimental simulation of obtaining the reflector azimuth using azimuthal acoustic reflection tool in the underwater environment. *J. Petroleum Sci. Eng.* 195, 107649. doi:10.1016/j.petrol.2020.107649

Bennett, N. N. (2019). 3D slowness time coherence for sonic imaging. *Geophysics* 84 (5), D179–D189. doi:10.1190/geo2018-0077.1

Bradley, T., Patterson, D., and Tang, X. M. (2011). Applying a through-casing acoustic imaging technique to identify gas migration paths in a salt body. *First break* 29 (7), 75–84. doi:10.3997/1365-2397.29.7.51916

Cao, J. J., Tang, X. M., Su, Y. D., Wei, Z. T., and Zhuang, C. X. (2016). Radiation characteristics of the single well imaging field in while-drilling logging using an acoustic dipole source. *Chin. J. Geophys. (in Chinese)* 59 (9), 3503–3513. doi:10.6038/cjg20160932

Gong, H., Chen, H., He, X., Chang, S., Wang, X. M., Wang, B. C., et al. (2018). Modeling and inversions of acoustic reflection logging imaging using the combined monopole-dipole measurement mode. *Applied Geophysics* 15 (3-4), 393–400. doi:10.1007/s11770-018-0700-y

Gong, H., Chen, H., He, X., and Wang, X. M. (2015). Eliminating the azimuth ambiguity in single-well imaging using 3C sonic data. *Geophysics* 80 (1), A13–A17. doi:10.1190/GEO2014-0337.1

Gu, X. H., Tang, X. M., and Su, Y. D. (2021). Delineating a cased borehole in unconsolidated formations using dipole acoustic data from a nearby well. *Geophysics* 86 (5), D139–D147. doi:10.1190/geo2020-0570.1

Hirabayashi, N., Sakiyama, N., and Ikegami, T. (2017). Characteristics of waveforms recorded by azimuthally spaced hydrophones of sonic logging tool for incident plane waves. *Geophysics* 82 (6), D353–D368. doi:10.1190/GEO2017-0201.1

Hornby, B. E. (1989). Imaging of near-borehole structure using full-waveform sonic data. *Geophysics* 54 (6), 747–757. doi:10.1190/1.1442702

Kong, F. T., Xu, H. C., Gu, X. H., Luo, C. M., and Li, S. Q. (2023a). Segmentation of borehole acoustic reflection image using feature pyramid network and transfer learning. *Geoenergy Science and Engineering* 229, 212088. doi:10.1016/j.geoen.2023.212088

Kong, F. T., Xu, H. C., Gu, X. H., Luo, C. M., and Li, S. Q. (2023b). Denoising method of borehole acoustic reflection image using convolutional neural network. *Geoenergy Science and Engineering* 226, 211761. doi:10.1016/j.geoen.2023.211761

Lee, S. Q., Tang, X. M., and Su, Y. D. (2019). Shear wave imaging to determine near-borehole faults for ocean drilling exploration. *Geophysical Journal International* 217 (1), 288–293. doi:10.1093/gji/ggz023

Li, C., Chen, H., He, X., and Wang, X. M. (2021a). Identifying reflector azimuth from borehole multicomponent cross-dipole acoustic measurement. *Geophysics* 86 (6), D201–D214. doi:10.1190/GEO2020-0460.1

Li, C., and Yue, W. Z. (2017). High-resolution Radon transforms for improved dipole acoustic imaging. *Geophysical Prospecting* 65, 467–484. doi:10.1111/1365-2478.12434

Li, D., Qiao, W. X., Che, X. H., Ju, X. D., Yang, S. B., Lu, J. Q., et al. (2021b). Eliminating the azimuth ambiguity in reflected S-wave imaging logging based on the azimuthal receiver mode. *Journal of Petroleum Science and Engineering* 199, 108295. doi:10.1016/j.petrol.2020.108295

Li, Y. H., Tang, X. M., Li, H. R., and Lee, S. Q. (2021c). Characterizing the borehole response for single-well shear-wave reflection imaging. *Geophysics* 86 (1), D15–D26. doi:10.1190/GEO2020-0212.1

Li, Y. H., Tang, X. M., and Su, Y. D. (2022a). Borehole radiation and reception responses for azimuthal shear-wave reflection imaging with an off-centred dipole acoustic tool. *Journal of Geophysics and Engineering* 19, 1180–1195. doi:10.1093/jge/gxac077

Li, Z., Qi, Q. M., Hei, C., Jiang, C., and Wang, X. J. (2022b). Elastic-wave radiation, scattering, and reception of a dipole acoustic logging-while-drilling source in unconsolidated formations. *Frontiers in Earth Science* 10, 879345. doi:10.3389/feart.2022.879345

Nakken, E. I., Mjaaland, S., and Solstad, A. (1996). A new MVVD concept for geological positioning of horizontal wells. *Journal of Petroleum Technology* 48, 239–240. doi:10.2118/30454-MS

Rao, B., Su, Y. D., Li, S. Q., and Tang, X. M. (2023). Effects of collar eccentricity on azimuthal response characteristics for acoustic reflection measurement while drilling. *Geophysics* 88 (5), D325–D337. doi:10.1190/geo2022-0756.1

Tan, B. H., Tang, X. M., Wei, Z. T., Cao, J. J., and Su, Y. D. (2016). Dominant frequency band and reflected wave field of LWD dipole shear wave remote detection. *Acta petrolei Sincia* 37 (9), 1152–1158. doi:10.7623/syxb201609009

Tan, B. H., Zhang, K., Su, Y. D., Li, S. Q., and Zhang, L. J. (2022). Research on acoustic logging while drilling transmitting technologies. *Journal of Geophysics and Engineering* 19, 511–520. doi:10.1093/jge/gxac034

Tang, X. M. (2004). Imaging near-borehole structure using directional acoustic-wave measurement. *Geophysics* 69 (6), 1378–1386. doi:10.1190/1.1836812

Tang, X. M., Cao, J. J., Li, Z., and Su, Y. D. (2016). Detecting a fluid-filled borehole using elastic waves from a remote borehole. *The Journal of the Acoustical Society of America* 140 (2), EL211–EL217. doi:10.1121/1.4960143

Tang, X. M., Cao, J. J., and Wei, Z. T. (2014). Shear-wave radiation, reception, and reciprocity of a borehole dipole source: with application to modeling of shear-wave reflection survey. *Geophysics* 79 (2), T43–T50. doi:10.1190/geo2013-0096.1

Tang, X. M., and Cheng, C. H. (2004). *Quantitative borehole acoustic methods*. Elsevier Science Publishing.

Tang, X. M., and Patterson, D. J. (2009). Single-well S-wave imaging using multicomponent dipole acoustic-log data. *Geophysics* 74 (6), WCA211–WCA223. doi:10.1190/1.3227150

Tang, X. M., and Wei, Z. T. (2012). Single-well acoustic reflection imaging using far-field radiation characteristics of a borehole dipole source. *Chinese Journal of Geophysics (in Chinese)* 55 (8), 2798–2807. doi:10.6038/j.issn.001-5733

Tang, X. M., Zheng, Y. B., and Patterson, D. (2007). Processing array acoustic-logging data to image near-borehole geologic structures. *Geophysics* 72 (2), E87–E97. doi:10.1190/1.2435083

Wei, Z. T., and Tang, X. M. (2012). Numerical simulation of radiation, reflection, and reception of elastic waves from a borehole dipole source. *Geophysics* 77 (6), 1–5. doi:10.1190/segam2012-0014.1

Xu, J. Q., Hu, H. S., and Wang, Z. (2019). Asymptotic solution to a 3D dipole single-well imaging system with combined monopole and dipole receivers with an application in elimination of azimuth ambiguity. *Geophysics* 84 (5), D191–D207. doi:10.1190/geo2018-0658.1

frontiers | Frontiers in Earth Science

TYPE Original Research
PUBLISHED 20 December 2024
DOI 10.3389/feart.2024.1476891

OPEN ACCESS

EDITED BY
Jeroen van Hunen,
Durham University, United Kingdom

REVIEWED BY
Bin Gong,
Brunel University London, United Kingdom
Changtai Zhou,
City University of Hong Kong, Hong Kong SAR, China

*CORRESPONDENCE
Binwen Ma,
Binwen.ma@outlook.com

RECEIVED 06 August 2024
ACCEPTED 25 November 2024
PUBLISHED 20 December 2024

CITATION
Zhang X, Sun J, Chen Y, Wang C, Wang C, Ren W and Ma B (2024) Experimental study on the effects of rock mineral composition and loading rates on the acoustic emission and fracture characteristics in roof strata tensile fracture.
Front. Earth Sci. 12:1476891.
doi: 10.3389/feart.2024.1476891

Experimental study on the effects of rock mineral composition and loading rates on the acoustic emission and fracture characteristics in roof strata tensile fracture

Xiufeng Zhang[1], Jiaxin Sun[2], Yang Chen[1], Cunwen Wang[1], Chao Wang[1,3], Wentao Ren[4] and Binwen Ma[2,5]*

[1]Shandong Energy Group Co., Ltd., Jinan, Shandong, China, [2]Institute of Deep Earth Sciences and Green Energy, College of Civil and Transportation Engineering, Shenzhen University, Shenzhen, Guangdong, China, [3]Yanzhou Coal Industry Co., Ltd., Jining, Shandong, China, [4]Shandong Energy Group Luxi Mining Co., Ltd., Heze, Shandong, China, [5]School of Mechanics and Civil Engineering, China University of Mining and Technology, Beijing, China

The tensile fracture of the overlying strata in coal mines significantly affects the stability of the surrounding rock and the working face. This study investigates the effects of rock mineral composition and mining speed on roof strata fracture behavior through three-point bending tests under various mineral compositions and loading rates, simulating tensile fractures under different mining conditions. Fracture processes were monitored using an acoustic emission (AE) system and high-speed camera, with multifractal analysis and digital image correlation (DIC) applied to assess AE signal characteristics and crack propagation. Results indicated that siliceous sandstone (SS) exhibited more rapid and penetrating fractures compared to argillaceous sandstone (AS). Before reaching peak load, AS showed a broader multifractal spectrum width ($\Delta\alpha$) than SS, reflecting its more ductile fracture behavior, which also resulted in higher $\Delta\alpha$ values in the post-peak stage. Both $\Delta\alpha$ and multifractal spectrum difference ($\Delta f(\alpha)$) decreased with increasing loading rates for AS, indicating a weakening of the multifractal characteristics of the AE signals and a progressively dominant presence of strong signals. The fracture behavior in both rock types was dominated by tensile microcracks, along with tensile-shear composite and shear microcracks. Higher loading rates increased the proportion of tensile-shear composite and shear microcracks components in the AE signals, with the rate being lower in AS than SS. These findings provide a basis for predicting the characteristics of the tensile fracture of overlying strata in mined-out areas.

KEYWORDS

overlying roof strata, tensile fracture, acoustic emission monitoring, fracture characteristics, multiple fractals

1 Introduction

Coal mining is gradually shifting to deeper levels, with the mining depths exceeding 800 m. The complex deep geology environments lead to more severe dynamic disasters (Cui et al., 2022; Xie et al., 2023; Mahdi et al., 2022). As the working face advances, the periodic breaking of the overlying strata releases significant stored elastic energy in the mined-out area (Wang et al., 2021; Zhao et al., 2021), resulting in mining-induced seismicity (Zhu C. L. et al., 2022). Under the high static stress conditions of deep mining, these unpredictable seismic events easily induce the deformation of surrounding rocks, the ground vibration and the rockburst hazard (Guo et al., 2022; Ma et al., 2024). The tensile fracture behavior of overlying strata is significantly affected by the rock property and the mining speed. Studying the effects of the rock property and the mining speed on the fracture characteristics and patterns of the strata is of great significance for predicting and preventing disasters in deep resource extraction.

The tensile fracture of overlying strata, classified as type I fracture, is induced by the bending and subsidence of the goaf roof strata. Many studies have analyzed the energy release(Rakesh et al., 2022; Cheng et al., 2019; Li H. T. et al., 2022; Sun et al., 2019; Sun et al., 2020), fracture behavior, and breaking extent associated with the tensile fracture of overlying strata. Zhu J. B. et al. (2022) analyzed the damage characteristics and displacement changes of the overlying strata, and further investigated the influence of the strata tensile fracture on the stability of coal pillars. Yang et al. (2019) revealed the fracture mechanism of the goaf roof strata and analyzed the stress, deformation and stability of the roadway. Regarding the rock property effect, Zhang et al. (2020) studied the macroscopic crack propagation patterns and strength characteristics of mudstone, sandstone, and coal under three-point bending, demonstrating that the rock mesostructure significantly affects the macroscopic damage characteristics. Cai et al. (2022) analyzed the coupling evolution law of stress and energy in the overlying strata under mining activities using the methods of field experiments and fractal theory, revealing the breaking process of the roof strata and the disaster mechanisms. Moreover, the joint characteristics and anisotropy of rock significantly affect its mechanical behavior (Chen et al., 2022; Feng et al., 2023; Zhou et al., 2022; Zhu et al., 2024). Gong et al. (2024), based on simulations of the cross-scale failure processes in discontinuous rock masses, revealed the nonlinear mechanical behavior of rock. Qiu et al. (2023) and Yin et al. (2023) investigated the dynamic mechanical response of jointed rock masses under different strain rates and joint characteristics, highlighting their effects on strength and failure modes. These research results demonstrate that the tensile fracture of the overlying roof strata significantly affects the stability of the surrounding rock of roadways. However, few systematic studies have focused on the influence of the rock property and the mining speed on the fracture characteristics and patterns of the roof strata.

A great number of scholars have carried out three-point bending tests of rocks to simulate the tensile fracture of roof strata (Du et al., 2022; Li T. et al., 2018; Wei et al., 2021), with monitoring the damage process and acoustic emission signals using the acoustic emission (AE) system and the digital image correlation (DIC) techniques (Prikryl et al., 2003). Zhang et al. (2015) demonstrated that the AE system and DIC techniques can effectively monitor the initiation and propagation behavior of cracks in sandstone under three-point bending tests. Lin et al. (2019) investigated into the fracture process zone under three-point bending tests using AE and DIC techniques, validating that its energy changes conform to the linear softening law of the fracture process zone. Li X. L. et al. (2018) conducted three-point bending tests to reproduce the tensile fracture of roof strata and investigated the effect of mining speeds on the fracture characteristics of the overlying strata. It is found that the loading rate is exponentially positively correlated with the AE peak energy and peak load, and exponentially negatively correlated with the total AE count. Gao et al. (2021) studied the evolution processes of the surface deformation, crack propagation, and strain energy in coal samples under different stress paths using the AE system and DIC techniques.

The studies above demonstrate that the AE and DIC techniques effectively describe the damage characteristics of specimens under different rock properties and loading conditions. Some scholars have analyzed the AE signals associated with the damage processes of rock materials using fractal theory, which can describe irregular phenomena in nature and is widely used to study the damage characteristics of rock-like materials (Lei et al., 2023; Mao et al., 2020; Ghanbarian et al., 2019). Zhang et al. (2022) discovered that under three-point bending tests on granite at high temperatures, the multifractal spectrum width $\Delta\alpha$ gradually decreases and the ductile failure becomes dominant as the temperature of the rock samples increases. Lei et al. (2023) found that the decrease in $\Delta f(\alpha)$ indicates an increased proportion of large-scale shear fractures under uniaxial compression tests on sandstone with different crack distributions. Ou et al. (2023) applied the multifractal analysis method to the AE signals induced by rock brittle fracture, demonstrating that rock brittleness is positively correlated with the multifractal spectrum width $\Delta\alpha$ and negatively correlated with the difference between the two ends of the multifractal spectrum $\Delta f(\alpha)$. Sudden changes in these two parameters could serve as precursors to rock failure. These studies confirm that the fractal theory can effectively quantify the characteristics of AE signals induced by rock material damage. However, the AE signal characteristics for the tensile fracture of roof strata remain unclear, limiting early warning and prediction of the goaf roof strata breaking.

Based on the aforementioned research background and methods, a series of three-point bending tests were conducted under different rock properties and loading rates. The fracture strength, energy release, AE signals characteristics, and crack propagation associated with the tensile fracture of roof strata were obtained based on the AE monitoring systems, DIC technology, and high-speed cameras. Moreover, the fractal theory was applied to further analyze the fracture characteristics of roof strata under different rock properties and loading rates. The research findings will provide a basis for the early warning of the tensile fracture of overlying roof strata in mined-out areas.

2 Experimental Procedures

2.1 Specimens preparation

The sandstone layer dominates the overlying strata of underground coal resources, with its physical and mechanical properties influenced by various factors such as the size of clastic

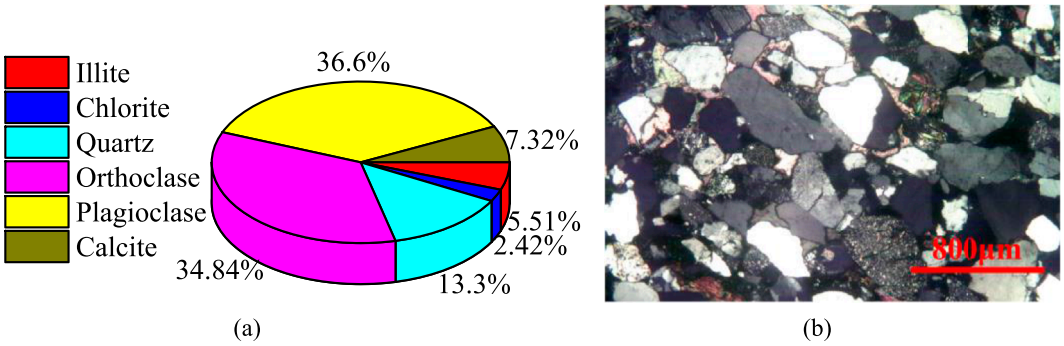

FIGURE 1
Image of argillaceous cemented sandstone main mineral components identification: **(A)** Main mineral composition proportions; **(B)** Mineral identification under a polarizing microscope.

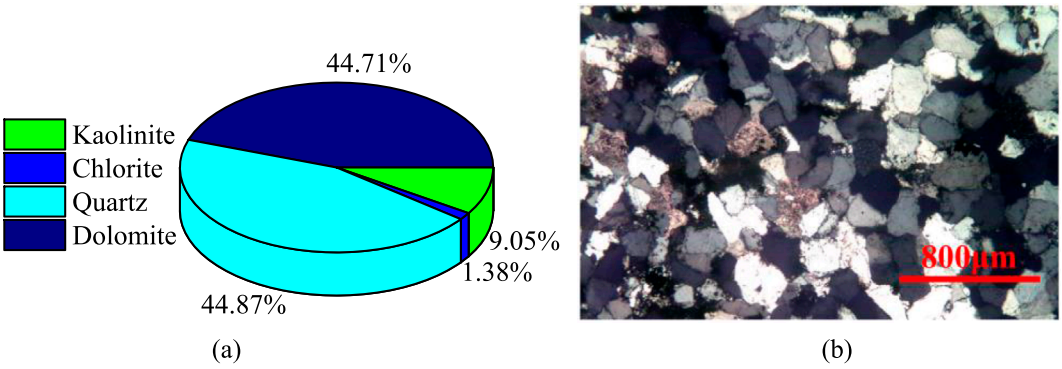

FIGURE 2
Image of siliceous cemented sandstone main mineral components identification: **(A)** Main mineral composition proportions; **(B)** Mineral identification under a polarizing microscope.

particles, composition, and types of cementing materials. Among these factors, the type of cementing material within the rock directly influences the bonding strength of the clastic particles, significantly affecting the overall mechanical performance of the sandstone (Gao and Kang, 2017). For sandstone materials, the most common types are argillaceous sandstone (AS) and siliceous sandstone (SS). Therefore, AS and SS were selected as test samples in this study, with the specimens sourced from a metal mine in Hunan and a coal mine in Shanxi. The primary mineral compositions of AS and SS are shown in Figures 1, 2, respectively. AS mainly comprises quartz lithic fragments, siliceous lithic fragments, argillaceous lithic fragments, and volcanic lithic fragments. The interstitial materials are primarily argillaceous, mica, chlorite, and carbonate minerals, with argillaceous materials mainly composed of clay mineral aggregates. In contrast, SS primarily consists of siliceous lithic fragments and quartz lithic fragments. The siliceous lithic fragments are composed of microcrystalline to cryptocrystalline siliceous aggregates, while the quartz lithic fragments are composed of granular quartz aggregates. The quartz particles exhibit serrated contacts. The interstitial materials in SS are mainly siliceous, carbonate minerals, and opaque minerals, with the siliceous materials mostly being secondary overgrowths of quartz surrounding the edges of the detrital particles.

According to the recommended methods of the International Society for Rock Mechanics and Rock Engineering, the basic physical and mechanical parameters of the two types of rock samples were measured, as shown in Table 1. Regarding P-wave velocity, AS exhibits stronger heterogeneity, while SS, with its higher density, is more homogeneous. Due to differences in material composition, there are significant distinctions in the strength parameters between the two types of rock. When preparing rock beam samples, the dimensions were uniformly processed to 250×30×50 mm (length×width×height). The prepared sandstone samples were free of prefabricated cracks and obvious joints, with the flatness error of the end faces controlled within 0.01 mm.

2.2 Experimental methods

Using the AGX-V material testing machine, three-point bending tests were conducted on rectangular sandstone specimens. The contact between the specimen and the upper loading end was linear, with a span of 200 mm between the lower support points, and the bottom of the testing machine was equipped with cylindrical supports. The specimens loading and the schematic of the

TABLE 1 The basic physical and mechanical parameters of two types of rock.

Rock properties	Rock type	
	AS	SS
Density ρ(kg/m^3)	2,308.60	2,648.12
P-wave velocity c(m/s)	2,940.40	4,335.67
Young's modulus E (GPa)	11.13	25.67
Poisson's ratio v	0.26	0.22
Static compressive strength σ_c (MPa)	72.14	217.78

Note. AS, argillaceous sandstone; SS, siliceous sandstone.

acoustic emission sensor arrangement are depicted in Figures 3A, B, respectively. Before the test, a preload of 10 N was applied. Loading tests were performed on both AS and SS specimens at loading rates of 0.05, 0.15, 0.5, 1.5, 5.0, and 15.0 mm/min, with each test group repeated five times.

During the tests, an acoustic emission (AE) monitoring system, digital image correlation (DIC) technology, and a high-speed camera were employed to capture real-time AE signals emanating from internal damage and failure of the specimens, as well as to monitor surface deformation. Simultaneously, the loading force and displacement at the loading end were recorded by the testing machine, with a data sampling frequency of 1 kHz. The tests were terminated when the loading force dropped below 0.3% of the peak value.

The experiment employed a PCI-2 Acoustic Emission (AE) system equipped with six Micro 30 sensors, which have a frequency response range of 150–400 kHz and a resonant frequency of 225 kHz. The system utilized preamplifiers with a gain of 40 dB, and all sensor signals were set with a trigger threshold of 45 dB. The sampling frequency was 5 MHz, with a sampling length of 2048.

To ensure accurate measurements, the surfaces of the rectangular sandstone specimens were polished, and the sensors were fixed in place with tape. High vacuum grease was applied to couple the sensors to the rock. As shown in Figure 3, sensors 1# to 3# were positioned on the left side of the specimen, while sensors 4# to 6# were on the right side. Each sensor was placed 70 mm from the specimen centre and equidistant from the top and bottom edges. Six sensors were chosen to ensure sufficient data collection and a balanced experimental setup. As shown in Figure 3, the experiment utilized a Phantom TMX 7510 high-speed camera along with two LED compensating light sources. The camera was strategically positioned in front of the specimen to monitor the deformation of the speckled area on the front surface and the failure process of the specimen. The speckle pattern, spanning a width of 50 mm, consisted of black spots on a white background, with spot sizes ranging from 0.1 to 1 mm. Just before the macroscopic fracture of the specimen, the high-speed camera was manually triggered to capture images at a frame rate of 20,000 fps.

3 Results and analysis

3.1 Load-displacement curves

The load-displacement curves of typical specimens from two lithologies subjected to different loading rates are depicted in Figure 4. It can be observed that the mechanical response trends of both types of sandstone are similar under various loading rates. Both types exhibit a nearly linear increase in load before the peak, followed by a sudden fracture after the peak, demonstrating clear brittle characteristics. However, the post-peak stress of AS does not drop to zero and retains some load-bearing capacity. By extracting the peak load of each specimen, the variation of the peak load with loading rate can be obtained, as shown in Figure 5. Within the loading rate range of 0.05–15 mm/min, both AS and SS show an increasing trend in peak load and failure strain. The peak load increments for AS are 0.3%, 2.0%, 6.8%, 7.0%, and 11.5%, while for SS they are 3.4%, 4.1%, 7.3%, 10.5%, and 13.1%. Due to the higher mineral content and cementation strength of SS, it has a stronger overall load-bearing capacity, with a slightly higher increase in peak load compared to AS.

3.2 Acoustic emission characteristic parameters

The complete waveform captured by the AE signal encapsulates a wealth of destructive information, enabling both direct and indirect assessments of the internal damage in the specimen (Zhang and Deng, 2020). AE parameters, such as AE counts and AE energy, play a pivotal role in elucidating the mechanisms of fracturing and damage in rock materials. AE counts measure the number of oscillations surpassing the threshold level of the signal, thereby indicating the rate of crack initiation and propagation. Concurrently, AE energy is calculated by integrating the waveforms recorded by the signal acquisition system, which facilitates an analysis of the energy dynamics associated with crack propagation and the overall severity of rock damage. Figure 6 illustrates the methods used to compute various AE characteristic parameters.

3.2.1 Time domain parameters

The failure process of rocks under load is essentially a process of energy transfer. This paper employs the AE energy parameters to characterize the failure features of sandstone. Under a three-point bending load, the typical time-domain images of sandstone at different loading rates are shown in Figure 7. To facilitate the quantitative analysis of the tensile fracture characteristics, the loading process is divided into three stages based on the load-time curves: Stage I. Tension and elastic stage ($0<\sigma \leq 0.9\ \sigma_{max}$), Stage II. Plastic failure stage ($0.9\ \sigma_{max}<\sigma \leq \sigma_{max}$), Stage III. Residual stage (After the peak load). Where σ and σ_{max} represent the stress and the peak failure stress of the sandstone specimen, respectively.

Stage I: Both AS and SS enter a tension phase characterized by the activation of pre-existing internal defects at the onset of loading. Initially, the load-time curve exhibits a gradual increase in slope over a short period (the first 10% of loading time), which then transitions into a sustained linear growth

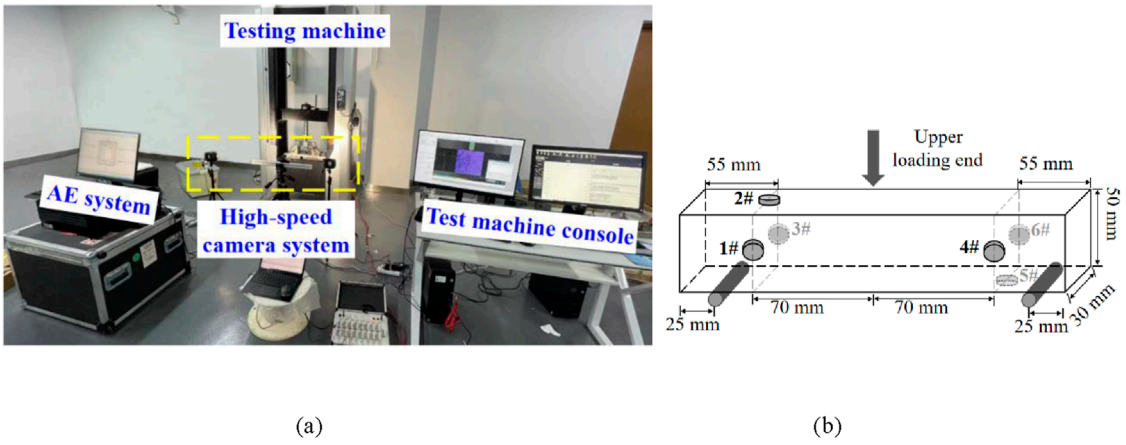

FIGURE 3
Schematic of test apparatus and set-up: **(A)** loading configuration of sample; **(B)** schematic of acoustic emission sensor arrangement.

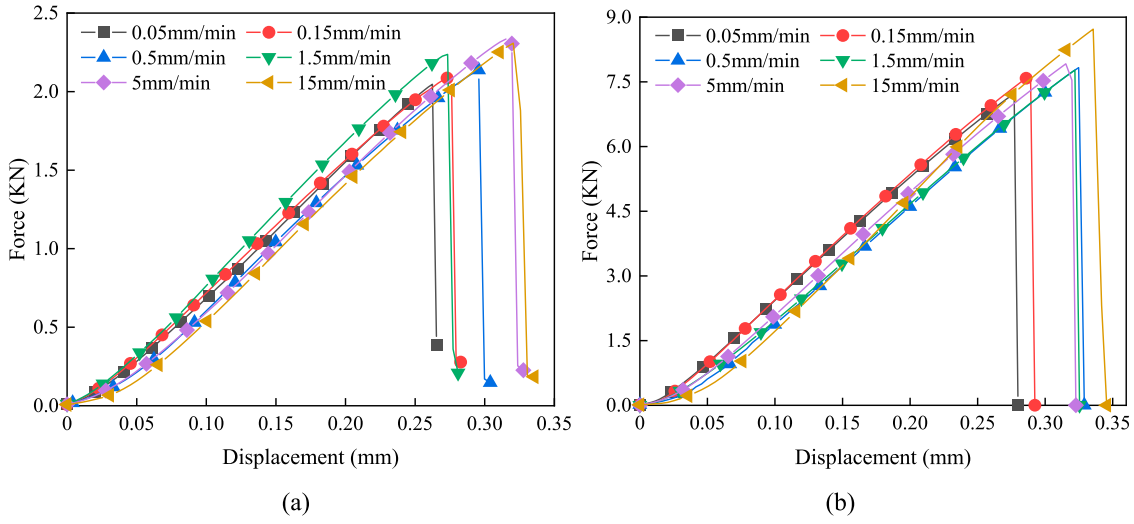

FIGURE 4
Force displacement diagram: **(A)** AS; **(B)** SS. AS= argillaceous sandstone; SS= siliceous sandstone. 0.05 mm/min denotes the experimental results for the specimen tested at a loading rate of 0.05 mm/min.

for the majority of the period (covering 80% of the loading time), signalling the elastic stage. During this phase, the AE energy characteristics of the AS and SS exhibit similar patterns, characterized by sporadic microcrack formation and low-intensity AE signals. The limited increase in cumulative AE energy indicates minimal elastic energy release, which contributes to preserving structural integrity by preventing the formation of larger fractures.

Stage II: As the loading force increases, approaching the peak load, micro-cracks progressively propagate and grow in scale. During this stage, the slope of the load-time curve gradually decreases until the peak load is reached, where the coalescence of previously accumulated cracks is observed, causing a sudden macroscopic fracture in the specimen. At this stage, individual AE signal energy peaks achieve the highest levels of the entire process, with a sharp increase in cumulative AE energy. As the loading rate increases, the peak energy of individual AE signals gradually rises, and the number of signals with higher energy significantly increases. The increased loading rate accelerates crack propagation, leading to a more concentrated release of stored energy. Compared to the AS, the SS exhibits higher individual energy peaks, greater increases, and a larger rise in cumulative energy, indicating a more abrupt and brittle fracture process

Stage III: After the peak load, macroscopic cracks traverse the specimen, causing a sudden drop in load-bearing capacity. The AS retains a certain residual strength after the peak drop, whereas the SS completely loses its load-bearing capacity. The AS continues to fail under the

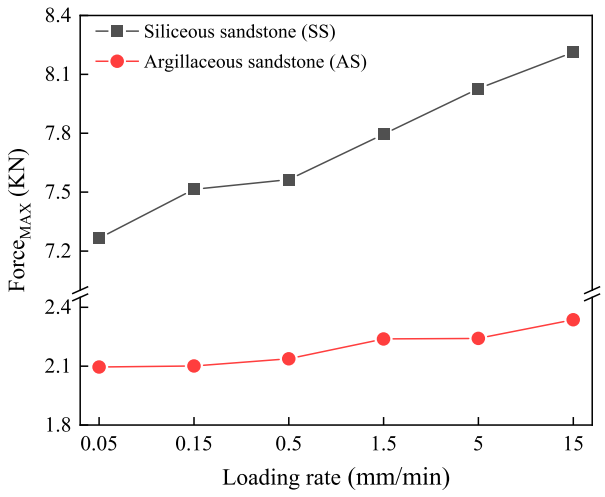

FIGURE 5
Image of the mean peak load.

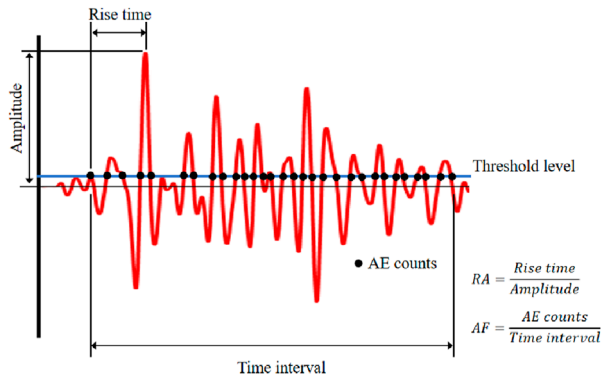

FIGURE 6
Graphical representations of AE characteristic parameters.

external force during this stage, with a significant post-peak residual phase, still generating notable AE energy signals. This ongoing AE activity suggests that microcrack development and crack bridging are still active. Thus, the cumulative AE energy continues to rise until the specimen is fully damaged. In contrast, the SS exhibits few significant AE energy signals at this stage, indicating a rapid fracture process with limited energy dissipation, further emphasizing that the AS has a markedly stronger ductile response than the SS.

3.2.2 Frequency domain parameters

Acoustic emission frequency domain characteristics can reflect the stress state and mechanical properties of rocks and provide a good representation of the overall spectral features (Kong et al., 2017; Liang et al., 2020). This study utilizes the fast flourier transform (FFT) to convert time-domain signals into the frequency domain, analyzing the distribution of dominant frequencies and the frequency structure. The typical frequency distribution images of sandstone are illustrated in Figure 8.

From the graph, the dominant frequencies for AS and SS throughout the entire three-point bending failure process primarily range between 100 and 300 kHz. In Stage I, both types of samples exhibit a low density of AE signals; however, the signal density significantly increases in Stages II and III. Particularly in Stage III, the residual stage, the propagation of internal cracks leads to the macroscopic fracture of the specimens, markedly increasing both the signal density and the amplitude of energy. During the early tension phase of Stage I, the SS shows a higher number of AE signals, but fewer during the elastic phase. The lower frequency and energy amplitude of AE signals before the formation of penetrating fractures indicate the sample's superior homogeneity and greater strength. Under varying loading rates, the AS consistently shows more AE signals in all loading stages compared to the SS, a phenomenon likely related to the lower strength and higher heterogeneity of the argillaceous sandstone samples, with each stage of continuous destruction accompanied by continuous AE signal release. The expansion of macroscopic cracks in AS and SS mainly occurs in Stage II, where there is a sudden increase in cumulative AE energy. As the loading rate increases, the onset of macroscopic cracks progressively advances. When the loading rate increases from 0.05 to 5 mm/min, the moments of a sharp increase in cumulative AE energy for the AS and SS respectively occur at 100, 97.8, 91.7% and 100, 98.5, 93.8% of the peak load.

To quantitatively describe the frequency distribution and the amplitude of dominant frequencies throughout the loading process of the AS and the SS, statistics on the dominant frequency distribution intervals were collected for loading rates of 0.05, 0.5, and 5 mm/min, with results presented in Table 2. Additionally, spectral graphs for the SS at loading rates of 0.05 and 5 mm/min were plotted, as shown in Figure 9. According to Table 2, the primary frequency distribution intervals for both AS and SS predominantly range between 200 and 250 kHz, accounting for 60%–80% and 30%–50% respectively, with fewer dominant frequencies below 100 kHz and above 250 kHz. For the AS, as the loading rate increases, the proportion of dominant frequencies in the 50–150 kHz range gradually increases, while the proportion in the 200–300 kHz range decreases. For the SS, with increasing loading rates, the proportion of dominant frequencies in the 50–100 kHz range gradually increases, whereas the proportion in the 200–250 kHz range decreases. It is evident that for both types of sandstone, the proportion of events at lower dominant frequencies increases with rising loading rates, while the proportion of events at higher dominant frequencies decreases.

Large-scale fractures in sandstone typically occur only after the load reaches a critical threshold, associated with AE signal events that exhibit lower dominant frequencies. These events, although less frequent, often feature larger signal amplitudes and contain higher energy, representing a smaller proportion of total events. In contrast, higher frequency events, indicative of small-scale damage, are more prevalent. The lower dominant frequencies observed in large-scale fracture events can be attributed to the longer wavelength of stress waves generated by the release of significant amounts of energy over larger fracture surfaces. With increasing loading rates, the destruction of sandstone samples accelerates, markedly

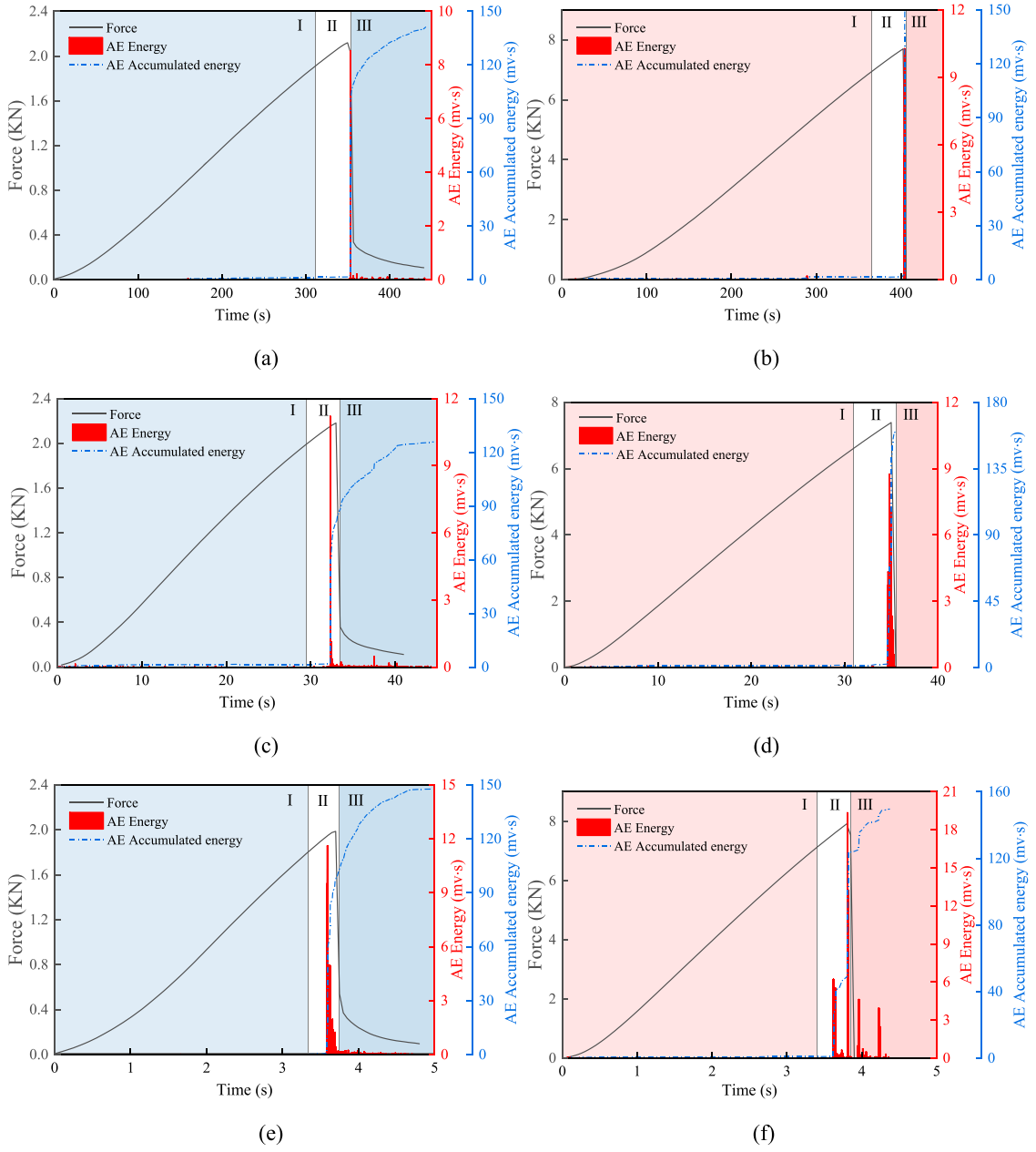

FIGURE 7
Typical sandstone time-domain image: **(A)** AS-0.05; **(B)** SS-0.05; **(C)** AS-0.5; **(D)** SS-0.5; **(E)** AS-5.0; **(F)** SS-5.0. AS= argillaceous sandstone; SS= siliceous sandstone; AS-0.05 denotes the experimental results for the AS specimen tested at a loading rate of 0.05 mm/min.

reducing the frequency of small-scale damage events, while the occurrence of large-scale fractures remains relatively stable or increases slightly. As a result, higher loading rates lead to a shift in the overall destruction pattern of the samples, increasing the proportion of low dominant frequency events and decreasing that of high dominant frequency events. Furthermore, the homogeneity of SS exceeds that of AS, leading to less variability in the proportion of dominant frequency ranges in SS compared to AS. As the loading rate increases, the spectral characteristics of both AS and SS transition from low to high frequencies while maintaining high amplitudes.

3.2.3 Multifractal characteristics of AE signals

Simple fractal dimensions sometimes fail to reflect local variations and the essential characteristics of signals. Therefore, this paper employs multifractal dimensions, which can describe the data structure across multiple scales (Li H. R. et al., 2022; Li X. L. et al., 2018), for processing and analyzing Acoustic Emission (AE) signals. The methodology involves constructing the fluctuation function $F_q(s)$ and the partition function $\chi_q(s)$ based on controlled time series. The generalized Hurst exponent $h(q)$ and the mass exponent $\chi_q(s)$ are then calculated (Miao et al., 2022; Niu et al., 2022). Subsequently, the fractal spectrum α-$f(\alpha)$ is plotted to analyze the nonlinear

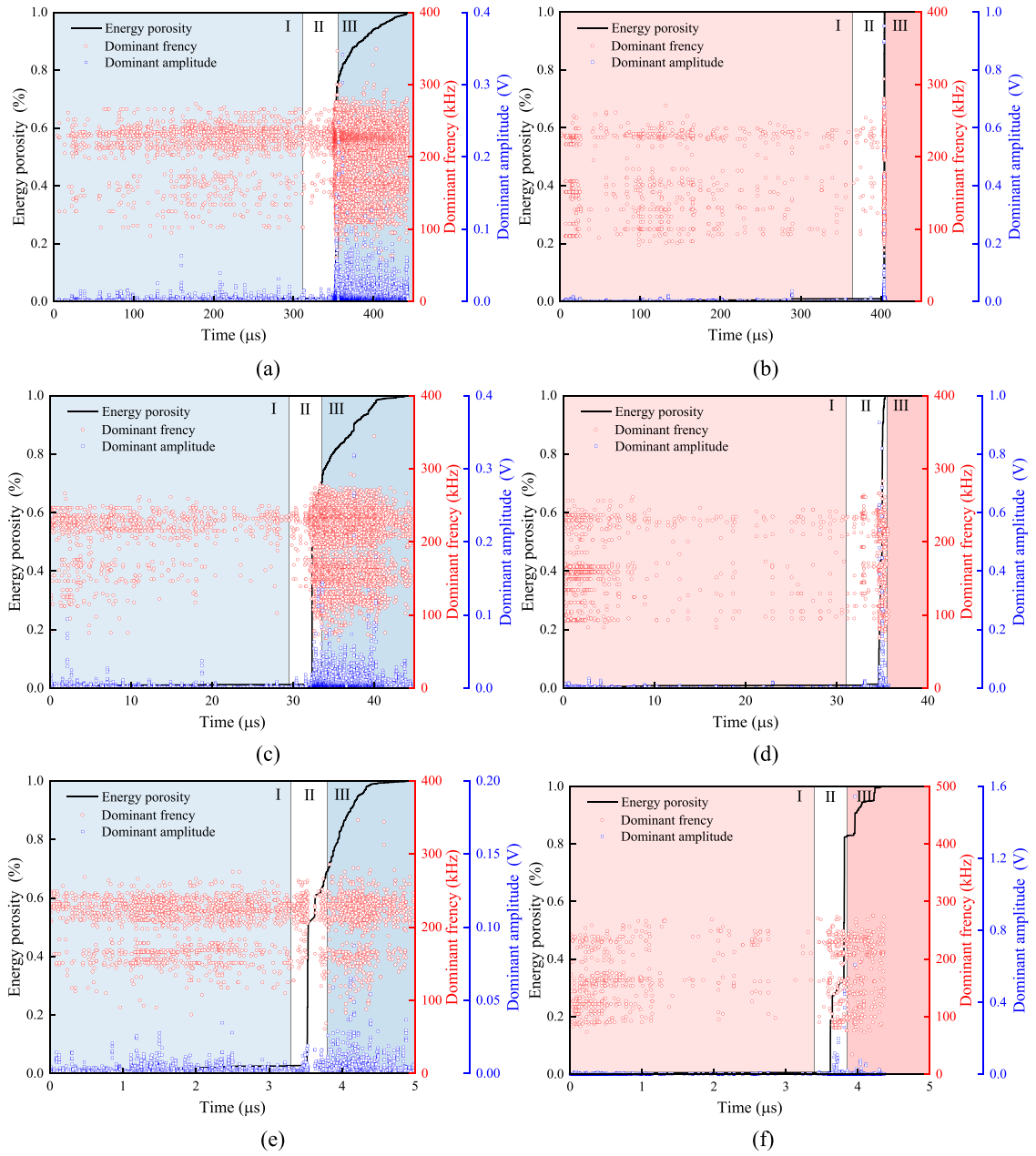

FIGURE 8
Typical sandstone dominant frequency distribution image: **(A)** AS-0.05; **(B)** SS-0.05; **(C)** AS-0.5; **(D)** SS-0.5; **(E)** AS-5.0; **(F)** SS-5.0. AS= argillaceous sandstone; SS= siliceous sandstone; AS-0.05 denotes the experimental results for the AS specimen tested at a loading rate of 0.05 mm/min.

characteristics, heterogeneity, and complexity of the AE signals, as well as the proportion of high-frequency and low-frequency signals. A typical example of AE signal calculations is illustrated in Figure 10.

The width of the multifractal spectrum, $\Delta\alpha=\alpha_{max}$ - α_{min}, indicates the level of heterogeneity in the Acoustic Emission (AE) energy data, with larger values suggesting more pronounced multifractal characteristics. The difference between the extremes of the multifractal spectrum, $\Delta f(\alpha) = f(\alpha_{max})$- $f(\alpha_{min})$, elucidates the frequency relationship between high-energy signals ($f(\alpha_{min})$) and low-energy signals ($f(\alpha_{max})$) (Hu et al., 2014; Ou et al., 2023; Zhang et al., 2022). A smaller value of $\Delta f(\alpha)$ (i.e., $f(\alpha_{max})$- $f(\alpha_{min}) < 0$) indicates that high-energy signals are more frequent and dominant. Conversely, if $f(\alpha_{max})$- $f(\alpha_{min}) > 0$, low-energy signals predominate. This analysis integrates the characteristics of the three destruction stages of AS and SS samples to evaluate their multifractal features. Focusing on the critical damage signals of each stage, the five sets of data with the highest amplitudes from each stage are selected for multifractal calculations, and their averages are computed. Figure 11 displays the change laws in the characteristic parameters of AE signals for the AS and SS under various loading rates.

TABLE 2 Distribution of the proportion of AE signals in different frequency intervals.

Specimen type		AS			SS		
Loading rate (mm/min)		0.05	0.5	5	0.05	0.5	5
Main frequency range	50–100 kHz	0.004	0.008	0.015	0.072	0.073	0.118
	100–150 kHz	0.078	0.093	0.148	0.254	0.252	0.250
	150–200 kHz	0.152	0.165	0.144	0.188	0.203	0.232
	200–250 kHz	0.724	0.698	0.660	0.452	0.420	0.362
	250–300 kHz	0.042	0.036	0.032	0.033	0.052	0.038
	300–350 kHz	0	0	0	0.001	0	0

Note. AS, argillaceous sandstone; SS, siliceous sandstone.

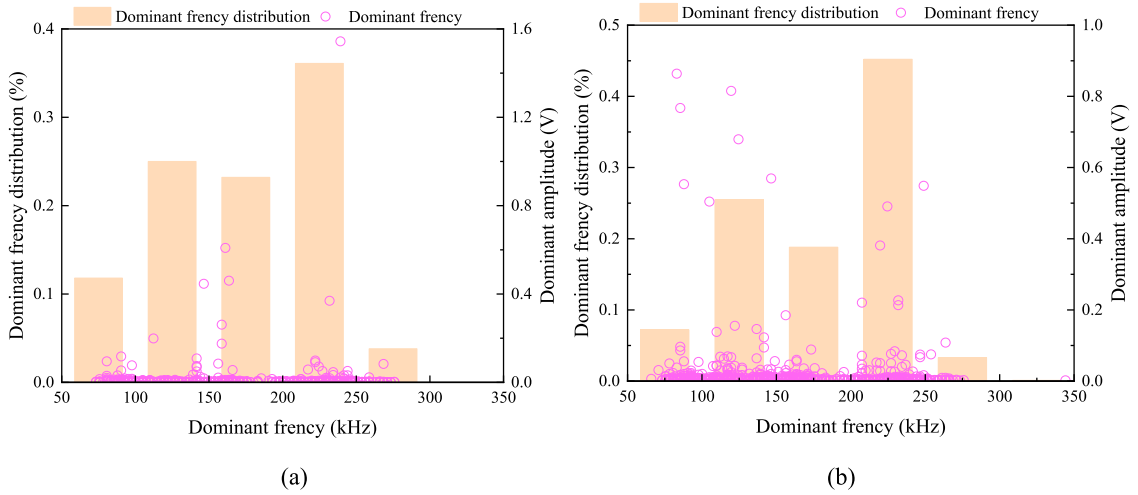

FIGURE 9
Typical sandstone spectral images: **(A)** SS-0.05; **(B)** SS-5.0. SS= siliceous sandstone; SS-0.05 denotes the experimental results for the SS specimen tested at a loading rate of 0.05 mm/min.

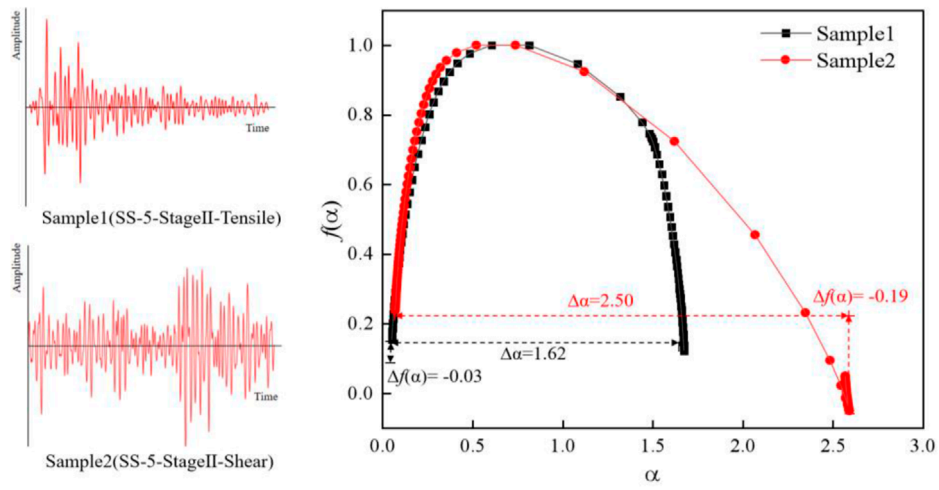

FIGURE 10
Multifractal spectrum and characteristic parameters. SS= siliceous sandstone; $\Delta\alpha$ denotes the width of the multifractal spectrum; $\Delta f(\alpha)$ denotes the difference between the extremes of the multifractal spectrum; Stage II= Plastic failure stage (Please refer to section 3.2.1 for specific phase description).

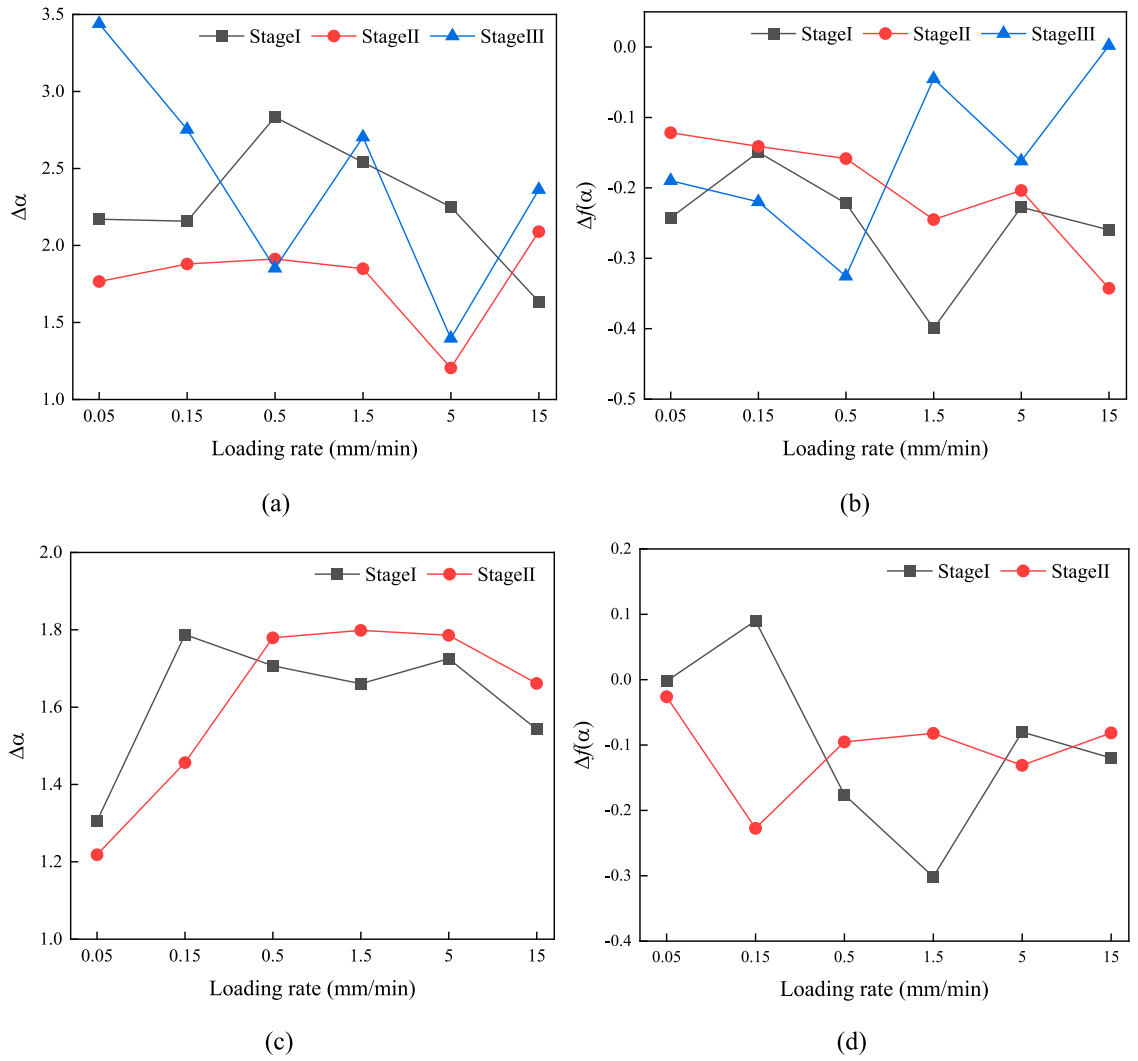

FIGURE 11
Change law of characteristic parameters for multifractal spectrum: **(A)** AS-Δα; **(B)** AS-Δ*f*(α); **(C)** SS-Δα; **(D)** SS-Δ*f*(α). AS= argillaceous sandstone; SS= siliceous sandstone; Δα denotes the width of the multifractal spectrum; Δ*f*(α) denotes the difference between the extremes of the multifractal spectrum.

The graph indicates that the characteristic parameters of AE signals for AS and SS vary under different loading rates. In the initial loading stages I and II, the absolute values of the difference between the extremes of the multifractal spectrum, $\Delta f(\alpha)$, for the AS and SS fluctuate and increase with the loading rate. Consequently, if the loading rate increases, the frequency of high-energy signal occurrences for both types of samples also rises, enhancing the heterogeneity of the released energy signals, and the damage signals in the argillaceous sandstone are more complex at the same loading rate. Additionally, the multifractal spectrum width $\Delta\alpha$ for the AS, which shows more pronounced ductile characteristics, is greater than for the SS, indicating that the AE signal's multifractal characteristics of post-load damage are more distinct in the AS. This could be linked to the stronger heterogeneity of its internal binders, with an increase in loading rate potentially leading to the expansion of more internal defects. For the SS, both $\Delta\alpha$ and the absolute value of $\Delta f(\alpha)$ fluctuate and increase with the loading rate. For this siliceous sandstone, the higher the loading rate, the more uneven the AE signal energy becomes in the first two stages, with the frequency of high-energy events increasing. In Stage III, both $\Delta\alpha$ and the absolute value of $\Delta f(\alpha)$ for the AS show a fluctuating downward trend with increasing loading rates. As the loading rate increases, the duration of the residual phase in AS shortens, and the frequency of high-energy signal release decreases. Additionally, an increased loading rate might cause high-energy damage to occur earlier.

3.3 Deformation and fracture characteristics

3.3.1 Fracture modes

The average frequency (AF) and rise angle (RA) of AE signals are commonly used to discriminate between tensile failure and shear

TABLE 3 Probability distribution of RA-AF events.

Specimen type		AS			SS		
Loading rate (mm/min)		0.05	0.5	5	0.05	0.5	5
Stage I	Tensile	0.998	0.998	0.973	1	0.993	0.981
	Shear	0.002	0.002	0.027	0	0.007	0.019
Stage II	Tensile	0.970	0.892	0.691	0.883	0.909	0.881
	Shear	0.030	0.108	0.309	0.117	0.091	0.119
Stage III	Tensile	0.997	0.973	0.900	0	0	0.894
	Shear	0.003	0.027	0.100	0	0	0.106

Note. AS, argillaceous sandstone; SS, siliceous sandstone; Stage I= Compaction and elastic stage; Stage II= Plastic failure stage; Stage III= Residual stage. (Please refer to Section 3.2.1 for specific phase description).

failure (or a mix of tensile and shear failure) (Niu et al., 2020; Zhang et al., 2020). The calculation formulas for the AF and RA are shown in Figure 6. The waveform of the tensile failure propagates as longitudinal waves, resulting in a smaller RA; while the shear failure waveforms propagate as shear waves, resulting in a larger RA. In this study, AF and RA were normalized (Zhao et al., 2022), and an AF/RA ratio greater than 1 was used to identify tensile failure, while a ratio of 1 or less indicated shear failure (or a mix of tensile and shear failure). This method was applied to analyze the failure modes of AS and SS at loading rates of 0.05, 0.5, and 5 mm/min. The calculation results are shown in Table 3, and the typical RA-AF distribution is shown in Figure 12.

As shown in Table 3, based on the AF/RA calculation results, the microcrack modes of both types of sandstone at different loading rates predominantly exhibit tensile fracture, with the AE signals of tensile fracture exceeding 60% at each stage. For various loading rates, the proportion of shear fracture in the plastic failure stage (Stage II) is higher than in the compaction and elastic stage (Stage I) and the residual stage (Stage III). The highest proportion of the tensile fracture occurs in Stage I for both types of sandstone, maintaining above 95%. The proportion of shear fracture in Stage I increases from 0.002% to 0.027% and from 0% to 0.019% for AS and SS as the loading rate increases. The highest proportion of the shear fractures occurs in Stage II. As the loading rate increases, the proportion increases for AS from 0.03% to 0.309%, whereas SS shows a relatively stable range of 9%–12%. The fracture mode variation in Stage III is similar to Stage I, with a slight increase in the proportion of shear fracture as the loading rate increases, while the proportion of tensile fracture remains above 85%. At lower loading rates, the amplitude of tensile fracture is higher, consuming more energy for small-scale fracture. The proportion of combined tensile and shear failures rises as the loading rate increases, indicating that the energy dissipated by the large-scale fracture is more than at lower loading rates.

The AS and SS exhibit predominantly tensile fracture under three points bending. In the initial loading stage, i.e., Stage I, the elastic energy is primarily stored as releasable energy, with a small amount of energy dissipated through the tensile micro-fracture. As the loading rate increases, the internal damage of rock accelerates and the structure becomes increasingly complex, with the tensile and shear mixed micro-fracture gradually increasing. The increased loading rate enhances the stress intensity around pre-existing micro-cracks, promoting their coalescence and leading to a more intricate fracture network. When the stored energy within the sample reaches its peak, the sample suddenly fails and the fracture mode largely exhibits the tensile fracture. In this stage, the mixed micro-fracture significantly increases and the proportion of it reaches a maximum in the whole loading process, indicating the complexity of the internal damage structure induced by the increased loading rate, as depicted in Figure 12. The sudden release of accumulated elastic energy contributes to the rapid propagation of tensile cracks, resulting in the dominant fracture mode being tensile. Numerous AE events are observed in the residual stage due to the ductility of the AS. However, the SS with poor ductility rapidly loses its load-bearing capacity after the peak load, leading to no significant residual stage. The SS exhibits a short residual stage at a high loading rate, with the predominantly dominant of tensile fracture.

3.3.2 Surface deformation

High-speed camera imaging combined with Digital Image Correlation (DIC) technology provides a precise capture of the evolution of surface cracks and strain fields in samples, thereby enhancing our understanding of AS and SS fracture characteristics. This study aims to facilitate the analysis of AS and SS fracture processes under various loading rates. To achieve this, the frame number when visible cracks first appear is defined as the crack initiation frame, and the frame when cracks penetrate the sample or result in a loss of load-bearing capacity is defined as the failure frame. The crack initiation and failure frames for AS and SS under different loading rates are summarized in Table 4, with the crack initiation frame designated as the 100th frame.

Table 4 demonstrates that as loading rates increase, the interval between crack initiation and failure frames decreases for both AS and SS, indicating accelerated fracture rates. However, at equivalent loading rates, AS exhibits slower fracture rates compared to SS. By employing DIC technology, we generated horizontal strain contour maps of the central surface area of samples, which are depicted in Figure 13. Due to space constraints, strain contour maps for loading rates of 0.05, 0.5, and 5 mm/min are presented in Figure 14.

Figure 14 presents images of the crack initiation frame, the second and fourth frames post-initiation, and the failure frames for both AS and SS. The overall fracture patterns indicate that under three-point bending, high strain zones initially manifest at the lower central part of the samples, where damage is most severe. Subsequently, stress concentration evolves into macroscopic cracks that progressively extend upward. In AS samples, cracks extend only halfway up the sample height at failure without developing through cracks. In contrast, SS exhibits more severe damage, with a rapid loss of load-bearing capacity upon macroscopic crack penetration. This higher fracture rate in SS is attributed to its greater elastic modulus, strength, and homogeneity,

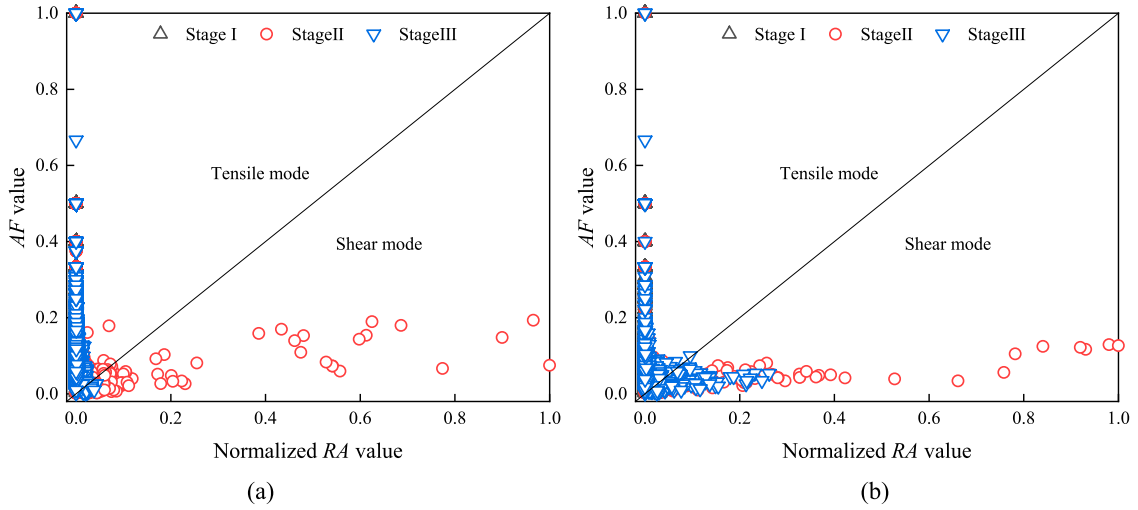

FIGURE 12
Distribution of the RA-AF values: **(A)** SS-0.05; **(B)** SS-5.0. SS= siliceous sandstone; SS-0.05 denotes the experimental results for the SS specimen tested at a loading rate of 0.05 mm/min.

TABLE 4 Frame rate parameters for sandstone failure under different conditions.

Loading rate (mm/min)		0.05	0.15	0.5	1.5	5	15
Crack initiation frame number		100	100	100	100	100	100
AS	Failure Frame Number	494	197	184	179	161	147
	Difference	394	97	84	79	61	47
SS	Failure Frame Number	168	166	150	132	112	110
	Difference	68	66	50	32	12	10

Note. AS, argillaceous sandstone; SS, siliceous sandstone.

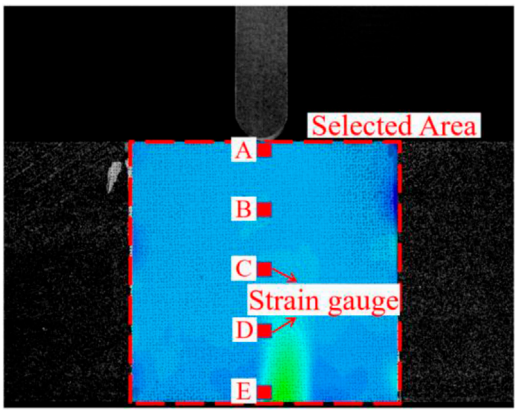

FIGURE 13
Regional division and strain gauge location.

which facilitate greater energy accumulation and release before failure.

Analysis of strain data indicates higher horizontal strain increase rates near the lower sections of both AS and SS under various loading rates. In AS, the midline consistently exhibits higher horizontal strain peaks in the lower section. SS shows a similar trend at loading rates below 5 mm/min; however, above this threshold, the horizontal strain peaks reverse (E < D < C < B < A), indicating lower strain in the lower tensile zone due to rapid crack penetration (less than 0.6 m), which limits pre-failure deformation.

Increasing loading rates accelerate crack propagation and intensify crack development, resulting in larger expansions upon loss of load-bearing capacity. Different sandstone types exhibit varying sensitivities to loading rates. As depicted in Table 4, as loading rates increase from 0.05 to 15 mm/min, AS and SS show significant increases in fracture rates by 75.1%, 78.7%, 79.9%, 84.5%, and 88.1% (with fracture duration decreasing from 19.7 m to 2.4 m) and 2.9%, 26.5%, 52.9%, 82.4%, and 85.3% (from 3.4 m to 0.5 m), respectively. For AS samples, fracture rate acceleration stabilizes when the loading rate exceeds 0.15 mm/min, whereas for SS samples, this stabilization occurs only when the loading rate exceeds 5 mm/min.

Considering factors such as crack deviation and strain variation intensity, this study placed five equidistant strain monitoring points along the central vertical line of AS and SS samples at loading rates of 0.05, 0.15, and 5 mm/min, as depicted in Figure 13. Surface strain data were extracted from 400 (50) frames before and 500 (100) frames after crack initiation for AS (SS), totalling 900 (100) frames. Due to the greater ductility of AS, 1,000 frames were extracted for AS-0.05, plotting horizontal strain variations in Figure 15.

Figure 15 illustrates that the horizontal strain slope at midline points of AS and SS increases as they approach the lower tensile zone, particularly at higher loading rates. Under bending loads, high-strain zones initially appear in the lower central part of the samples, releasing stored elastic energy as cracks propagate upward.

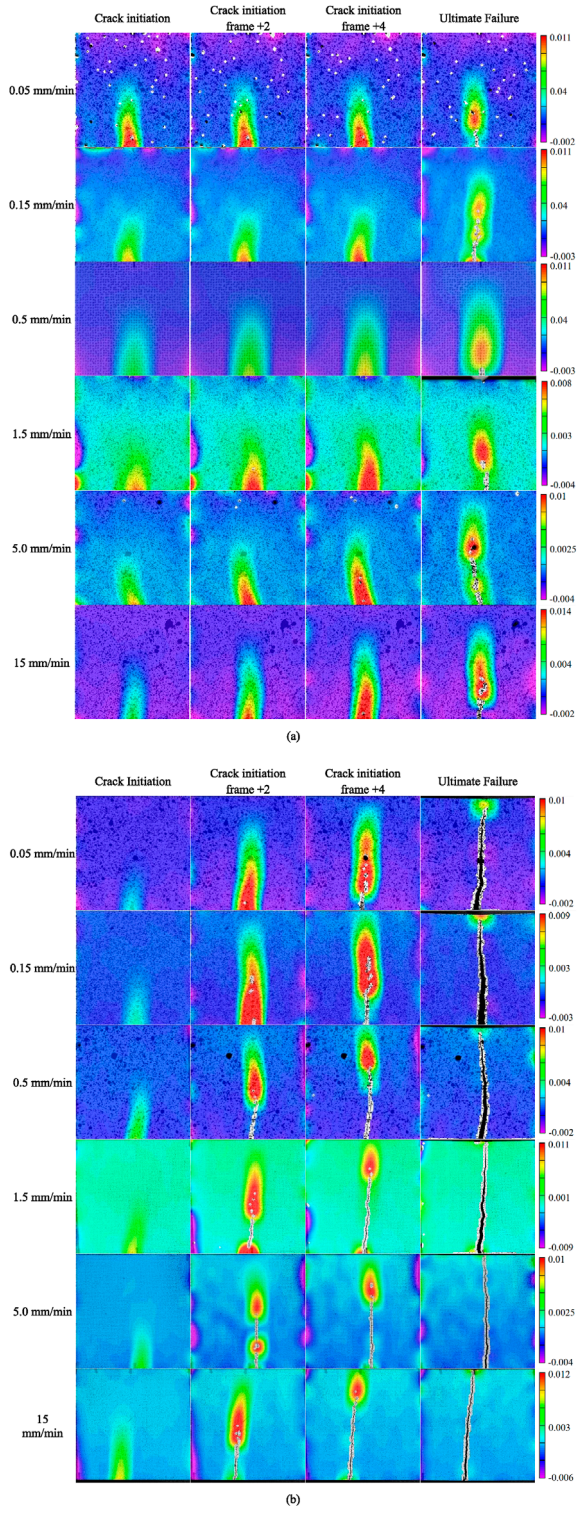

FIGURE 14
Horizontal strain cloud map of sandstone: **(A)** AS; **(B)** SS. AS= argillaceous sandstone; SS= siliceous sandstone; Crack Initiation denotes the moment when cracks appear in the specimen; Crack initiation frame +2 denotes the 0.1 m after the moment of crack initiation; Crack initiation frame +4 denotes the 0.2 m after the moment of crack initiation; 0.05 mm/min denotes that the specimen is subjected to a loading rate of 0.05 mm/min.

Consequently, both AS and SS exhibit higher strain rates in the lower section under varying loading rates. For AS, the midline exhibits a pattern of E > D > C > B > A, indicating higher strain nearer the lower tensile zone. SS shows a similar pattern at loading rates below 5 mm/min; however, at higher rates, the pattern reverses (E < D < C < B < A), reflecting lower strain in the lower tensile zone due to rapid fracture rates. The rapid fracture rate of SS at higher loading rates results in crack penetration within 12 frames, limiting pre-failure deformation and explaining the lower strain in the lower tensile zone. AS's ductility prevents this reversal even at loading rates up to 15 mm/min. Surface crack area increases with loading rate for both AS and SS, with AS exhibiting a decelerated increase due to differing fracture modes, while SS shows a continuously rising trend due to higher energy release at higher loading rates and faster-moving fracture fragments.

4 Discussion

The results and analysis presented reveal that the rock cement and loading rate play a significant role in the tensile fracture strength, energy release, and failure modes of rocks. Previous studies have shown that the rock cement can influence the failure characteristics of rock masses (Sergio et al., 2023; Shkuratnik et al., 2014). It can be found that the Acoustic Emission (AE) evolution law exhibits a clear correlation with the fracture stages and strength characteristics of rocks. This finding contributes to analyze the effects of rock property and mining speed on the tensile fracture of overlying rock layer in coal mines. Furthermore, this study demonstrates that the multifractal theory is an effective approach for identifying the micro-fracture characteristics of rocks. The real-time monitoring data, such as the amplitude, energy, event counts of AE, can be utilized to approximate the type and failure velocity of overlying rock layers. The stress level and fracture behavior of the overlying strata could be assessed, facilitating real-time adjustments to mining parameters. In comparison to argillaceous sandstone (AS), siliceous sandstone (SS) displayed more rapid and penetrative crack propagation, accompanied by a sharper elastic energy release and a higher disaster risk. Future research should be conducted to explore the variations of energy release associated with the rock type and mining speed under coal mining.

5 Conclusion

This study analyzes the influence of rock mineral composition and loading rate on the tensile fracture characteristics through the examination of Acoustic Emission (AE) signals and Digital Image Correlation (DIC) images. The main conclusions are as follows:

The tensile fracture of sandstone under three-point bending is categorized into the tension and elastic stage, the plastic failure stage, and the residual stage. The argillaceous rock shows a lower fracture strength than the siliceous rock. The tensile fracture of the argillaceous sandstone obviously displays the ductile characteristics. The tensile cracks of the siliceous sandstone rapidly propagate and through the specimen under varying

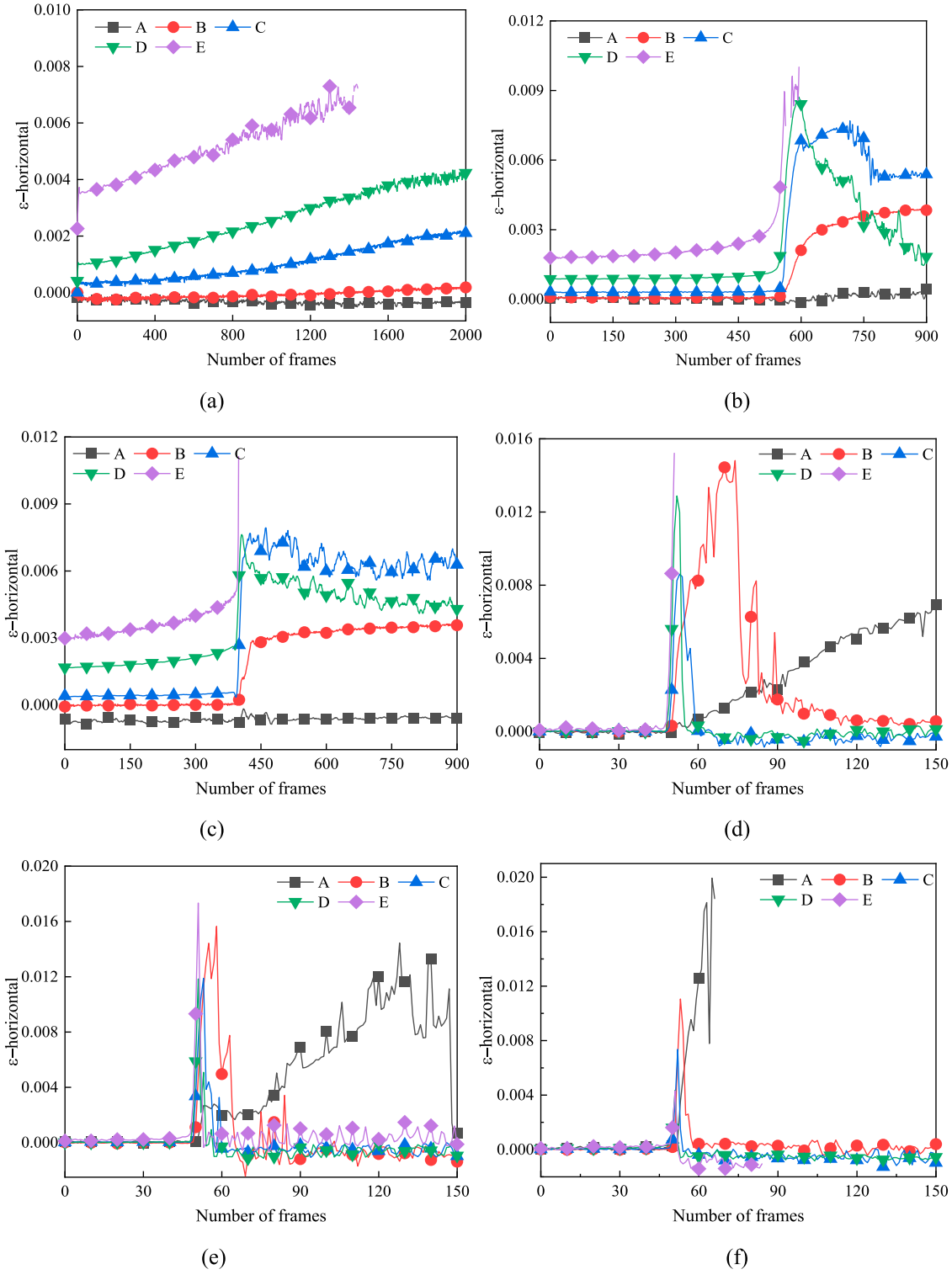

FIGURE 15
Strain gauge recording data: **(A)** AS-0.05; **(B)** AS-0.15; **(C)** AS-5.0; **(D)** SS-0.05; **(E)** SS-0.15; **(F)** SS-5.0. AS= argillaceous sandstone; SS= siliceous sandstone; AS-0.05 denotes the experimental results for the AS specimen tested at a loading rate of 0.05 mm/min.

loading rates, while no penetrating cracks are observed in the argillaceous rock.

The multifractal parameter Δα increases and fluctuates with the loading rate in both types of sandstone during Stages I and II. The argillaceous rock exhibits more distinct multifractal characteristics of AE signals. With an increase in loading rate, the proportion of tensile-shear mixed microcracks and large-scale shear microcracks increase, and small-scale tensile microcracks decrease.

The macroscopic crack propagation rate is slower in the argillaceous rock than that of the siliceous rock. The horizontal strain at the bottom center shows higher slope and peak values compared to the top. The peak strains in the bottom and top remain consistent at the loading rates below 5 mm/min, while the strain in the bottom is less than in the top at the loading rates above 5 mm/min.

Data availability statement

The original contributions presented in the study are included in the article/supplementary material, further inquiries can be directed to the corresponding author.

Author contributions

XZ: Writing–original draft. JS: Writing–original draft. YC: Writing–review and editing. CuW: Writing–review and editing. ChW: Writing–review and editing. WR: Writing–review and editing. BM: Methodology, Writing–original draft, Writing–review and editing.

Funding

The author(s) declare that financial support was received for the research, authorship, and/or publication of this article. This work is supported by the Taishan Industrial Experts Program (No. TSCX202408130), the Shandong Energy Group (No. SNKJ2022A01-R26), and the Open Fund of State Key Laboratory for Fine Exploration and Intelligent Development of Coal Resources (No. SKLCRSM21KFA01).

Conflict of interest

Authors XZ, YC, CuW, and ChW were employed by Shandong Energy Group Co., Ltd. Author ChW was employed by Yanzhou Coal Industry Co. Author WR was employed by Shandong Energy Group Luxi Mining Co.

The remaining authors declare that the research was conducted in the absence of any commercial or financial relationships that could be construed as a potential conflict of interest.

Publisher's note

References

Cai, J. J., Li, X. J., Guo, L. X., Xue, H. T., and Xu, B. Z. (2022). Fracture development and multifield coupling evolution law of soft overburden rock in a medium-thick coal seam mine. *Geofluids* 2022, 1–14. doi:10.1155/2022/6371887

Chen, B. P., Gong, B., Wang, S. Y., and Tang, C. A. (2022). Research on zonal disintegration characteristics and failure mechanisms of deep tunnel in jointed rock mass with strength reduction method. *Mathematics-Basel* 10, 922. doi:10.3390/math10060922

Cheng, Z. B., Pan, W. D., Li, X. Y., and Sun, W. B. (2019). Numerical simulation on strata behaviours of TCCWF influenced by coal-rock combined body. *Geomech. Eng.* 19, 269–282. doi:10.12989/gae.2019.19.3.255

Cui, J. F., Wang, W. J., and Yuan, C. (2022). Application of stability analysis in surrounding rock control and support model of deep roadway. *Int. J. Oil Gas. Coal T* 29, 1–192. doi:10.1504/ijogct.2021.10041466

Du, K., Sun, Y., Zhou, J., Khandelwal, M., and Gong, F. Q. (2022). Mineral composition and grain size effects on the fracture and acoustic emission (AE) characteristics of rocks under compressive and tensile stress. *Rock Mech. Rock Eng.* 55, 6445–6474. doi:10.1007/s00603-022-02980-y

Feng, X. H., Gong, B., Liang, Z. Z., Wang, S. Y., Tang, C. A., Li, H., et al. (2023). Study of the dynamic failure characteristics of anisotropic shales under impact Brazilian splitting. *Rock Mech. Rock Eng.* 57, 2213–2230. doi:10.1007/s00603-023-03673-w

Gao, F. Q., and Kang, H. P. (2017). Grain-based discrete-element modeling study on the effects of cementation on the mechanical behavior of low-porosity brittle rocks. *Int. J. Geomech.* 17, 04017061. doi:10.1061/(asce)gm.1943-5622.0000957

Gao, M. Z., Xie, J., Gao, Y. A., Wang, W. Y., Li, C., Yang, B. G., et al. (2021). Mechanical behavior of coal under different mining rates: a case study from laboratory experiments to field testing. *Int. J. Min. Sci. Techno* 31, 825–841. doi:10.1016/j.ijmst.2021.06.007

Ghanbarian, B., Perfect, E., and Liu, H. H. (2019). A Geometrical aperture-width relationship for rock fractures. *Fractals* 27, 1940002. doi:10.1142/s0218348x19400024

Gong, B., Zhao, T., Thusyanthan, I., and Tang, C. A. (2024). Modelling rock fracturing by a novel implicit continuous to discontinuous method. *Comput. Geotech.* 166, 106035. doi:10.1016/j.compgeo.2023.106035

Guo, Y., Lu, C. P., He, Z. L., and Song, J. F. (2022). Numerical and field investigations of tremors induced by thick-hard strata fracture. *Appl. Sci.* 12, 11151. doi:10.3390/app122111151

Hu, S. B., Wang, E. Y., Li, Z. H., Shen, R. X., and Liu, J. (2014). Time-varying multifractal characteristics and formation mechanism of loaded coal electromagnetic radiation. *Rock Mech. Rock Eng.* 47, 1821–1838. doi:10.1007/s00603-013-0501-9

Kong, B., Wang, E. Y., Li, Z. H., Wang, X. R., Niu, Y., and Kong, X. G. (2017). Acoustic emission signals frequency-amplitude characteristics of sandstone after thermal treated under uniaxial compression. *J. Appl. Geophys* 136, 190–197. doi:10.1016/j.jappgeo.2016.11.008

Lei, R. D., Tan, Y. L., Berto, F., Hu, C., and Qi, X. (2023). Temporal-frequency distribution and multi-fractal characterization of acoustic emission of rock materials containing two parallel pre-existing flaws. *Fatigue Fract. Eng. M.* 46, 2139–2155. doi:10.1111/ffe.13988

Li, H. R., Qiao, Y. F., Shen, R. X., and He, M. C. (2022a). Electromagnetic radiation signal monitoring and multi-fractal analysis during uniaxial compression of water-bearing sandstone. *Measurement* 196, 111245. doi:10.1016/j.measurement.2022.111245

Li, H. T., Qi, Q. X., Du, W. S., and Li, X. P. (2022b). A criterion of rockburst in coal mines considering the influence of working face mining velocity. *Geomech. Geophys Geo* 8, 37. doi:10.1007/s40948-021-00338-2

Li, T., Li, K. X., Pi, X. Y., and Fang, C. (2018a). Time-dependent behavior of acoustic emission feature parameters of sandstone under bending load. *J. China Coal Soc.* 43, 3115–3121. doi:10.13225/j.cnki.jccs.2018.0055

Li, X. L., Li, Z. H., Wang, E. Y., Liang, Y. P., Li, B. L., Chen, P., et al. (2018b). Pattern recognition of mine microseismic and blasting events based on wave fractal features. *Fractals* 26, 1850029. doi:10.1142/s0218348x18500299

Liang, Z. Z., Xue, R. X., Xu, N. W., and Li, W. R. (2020). Characterizing rockbursts and analysis on frequency-spectrum evolutionary law of rockburst precursor based on microseismic monitoring. *Tunn. Undergr. Sp. Tech. 105* 105, 103564. doi:10.1016/j.tust.2020.103564

Lin, Q., Wan, B., Wang, Y., Lu, Y. H., and Labuz, J. F. (2019). Unifying acoustic emission and digital imaging observations of quasi-brittle fracture. *Theor. Appl. Fract. Mec.* 103, 102301. doi:10.1016/j.tafmec.2019.102301

Ma, B. W., Xie, H. P., Zhou, C. T., Zhou, H. W., Gao, F., Cao, P. W., et al. (2024). Experimental investigation into influence of surrounding rock on strainburst: insight from failure process and energy partition. *Int. J. Rock Mech. Min. Sci.* 175, 105685. doi:10.1016/j.ijrmms.2024.105685

Mahdi, A., Ali, S., Alain, R., and Patrick, M. (2022). Rockburst in underground excavations: a review of mechanism, classification, and prediction methods. *Undergr. Space* 36, 255–270. doi:10.1016/j.undsp.2021.11.008

Mao, H. Y., Zhang, M., Jiang, R. C., Li, B., Xu, J., and Xu, N. W. (2020). Study on deformation pre-warning of rock slopes based on multi-fractal characteristics of microseismic signals. *Chin. J Rock Mech Eng* 39, 560–571. doi:10.13722/j.cnki.jrme.2019.1021

Miao, B., Wang, X. Y., and Li, H. R. (2022). Quantitative analysis of infrared thermal images in rock fractures based on multi-fractal theory. *Sustainability-Basel* 14, 6543. doi:10.3390/su14116543

Niu, Y., Li, Z. H., Wang, E. Y., Gao, F., Wang, F. C., Zhang, Z. Z., et al. (2022). An experimental study on precursor identification for gas-bearing coal failure from electric potential responses in the loading process. *Measurement* 196, 111229. doi:10.1016/j.measurement.2022.111229

Niu, Y., Zhou, X. P., and Berto, F. (2020). Evaluation of fracture mode classification in flawed red sandstone under uniaxial compression. *Theor. Appl. Fract. Mec.* 107, 102528. doi:10.1016/j.tafmec.2020.102528

Ou, J. C., Wang, E. Y., and Wang, X. Y. (2023). Time-frequency response of acoustic emission and its multi-fractal analysis for rocks with different brittleness under uniaxial compression. *Mathematics-Basel* 11, 4746. doi:10.3390/math11234746

Prikryl, R., Lokajicek, T., Li, C., and Rudajev, V. (2003). Acoustic emission characteristics and failure of uniaxially stressed granitic rocks: the effect of rock fabric. *Rock Mech. Rock Eng.* 36, 255–270. doi:10.1007/s00603-003-0051-7

Qiu, J. D., Zhou, C. T., Wang, Z. H., and Feng, F. (2023). Dynamic responses and failure behavior of jointed rock masses considering pre-existing joints using a hybrid BPM-DFN approach. *Comput. Geotech.* 155, 105237. doi:10.1016/j.compgeo.2022.105237

Rakesh, K., Arvind, K., Ashok, K., Arun, K., Sahendra, R., Amit, K., et al. (2022). Importance of fracturing hard and massive overlying strata for complete extraction of thick coal seam – case studies. *J. Geol. Soc. India* 98, 203–210. doi:10.1007/s12594-022-1960-y

Sergio, C., Annalisa, G., Alessandro, P., Andrea, R., and Constantino, T. (2023). Acoustic emissions in rock deformation and failure: new insights from Q-statistical analysis. *Entropy* 25, 701. doi:10.3390/e25040701

Shkuratnik, V. L., Novikov, E. A., and Oshkin, R. O. (2014). Experimental analysis of thermally stimulated acoustic emission in various-genotype rock specimens under uniaxial compression. *J. Min. Sci.* 50, 249–255. doi:10.1134/s1062739114020069

Sun, Y. J., Zuo, J. P., Karakus, M., and Wang, J. T. (2019). Investigation of movement and damage of integral overburden during shallow coal seam mining. *J. Rock Mech. Min. Sci.* 117, 63–75. doi:10.1016/j.ijrmms.2019.03.019

Sun, Y. J., Zuo, J. P., Karakus, M., and Wen, J. H. (2020). A novel method for predicting movement and damage of overburden caused by shallow coal mining. *Rock Mech. Rock Eng.* 53, 1545–1563. doi:10.1007/s00603-019-01988-1

Wang, Z. K., Li, W. P., Wang, Q. Q., Hu, Y. B., and Du, J. F. (2021). Monitoring the dynamic response of the overlying rock-soil composite structure to underground mining using BOTDR and FBG sensing technologies. *Rock Mech. Rock Eng.* 54, 5095–5116. doi:10.1007/s00603-021-02530-y

Wei, M. D., Dai, F., Liu, Y., Li, A., and Yan, Z. L. (2021). Influences of loading method and notch type on rock fracture toughness measurements: from the perspectives of T-stress and fracture process zone. *Rock Mech. Rock Eng.* 54, 4965–4986. doi:10.1007/s00603-021-02541-9

Xie, H. P., Zhang, R., Zhang, Z. T., Gao, M. Z., Li, C. B., He, Z. Q., et al. (2023). Reflections and explorations on deep earth science and deep earth engineering technology. *J. China Coal Soc.* 48, 3959–3978. doi:10.13225/j.cnki.jccs.2023.0989

Yang, H. Q., Han, C. L., Zhang, N., Sun, C. L., Pan, D. J., and Dong, M. H. (2019). Stability control of a goaf-side roadway under the mining disturbance of an adjacent coal working face in an underground mine. *Sustainability-Basel* 11, 6398. doi:10.3390/su11226398

Yin, X. H., Zhou, T., Zhou, C. T., Xie, H. P., and Zhu, J. B. (2023). Rate- and normal stress-dependent mechanical behavior of rock under direct shear loading based on a bonded-particle model (BPM). *Rock Mech. Rock Eng.* 56, 7959–7979. doi:10.1007/s00603-023-03486-x

Zhang, H., Fu, D. H., Song, H. P., Kang, Y. L., Huang, G. Y., Qi, G., et al. (2015). Damage and fracture investigation of three-point bending notched sandstone beams by DIC and AE techniques. *Rock Mech. Rock Eng.* 48, 1297–1303. doi:10.1007/s00603-014-0635-4

Zhang, N. B., Shan, R. L., Zhao, S. K., Sun, Z. X., Dong, Y. J., and Wang, Y. (2020). Investigation on cracking features of different rock under the bending load. *J. China Coal Soc.* 45, 671–681. doi:10.13225/j.cnki.jccs.2020.0580

Zhang, X., Li, Z. H., Wang, X. R., Wang, H., Li, B. L., and Niu, Y. (2022). Thermal effect on the fracture behavior of granite using acoustic emission and digital image correlation: an experimental investigation. *Theor. Appl. Fract. Mec.* 121, 103540. doi:10.1016/j.tafmec.2022.103540

Zhang, Z. H., and Deng, J. H. (2020). A new method for determining the crack classification criterion in acoustic emission parameter analysis. *J. Rock Mech. Min. Sci.* 130, 104323. doi:10.1016/j.ijrmms.2020.104323

Zhao, K., Ma, H. L., Yang, C. H., and Daemen, J. J. K. (2022). The role of prior creep duration on the acoustic emission characteristics of rock salt under cyclic loading. *J. Rock Mech. Min. Sci.* 157, 105166. doi:10.1016/j.ijrmms.2022.105166

Zhao, S. K., Sui, Q. R., Cao, C., Wang, X. C., Wang, C. L., Zhao, D. M., et al. (2021). Mechanical model of lateral fracture for the overlying hard rock strata along coal mine goaf. *Geomech. Eng.* 27, 75–85. doi:10.12989/gae.2021.27.1.077

Zhou, C. T., Xie, H. P., Zhu, J. B., Wang, Z. H., Li, C. B., and Wang, F. (2022). Mechanical and fracture behaviors of brittle material with a circular inclusion: insight from infilling composition. *Rock Mech. Rock Eng.* 55, 3331–3352. doi:10.1007/s00603-022-02799-7

Zhu, C. L., Zhang, J. X., He, Z. W., Wang, Y. Y., and Lan, Y. W. (2022). Effect mechanism of strata breakage evolution on stope deformation in extra-thick coal seams. *Alex Eng. J.* 61, 5003–5020. doi:10.1016/j.aej.2021.10.040

Zhu, J. B., Kong, J., Huang, Z. T., Sun, J. X., Lv, A. L., Zhang, K., et al. (2024). Experimental investigation of dynamic response of liquid-filled rock joints with horizontal inclination under stress wave loading. *J. China Coal Soc.* 49, 1873–1881. doi:10.13225/j.cnki.jccs.2023.1525

Zhu, J. B., Ma, B. W., Xie, H. P., Gao, F., Zhou, H. W., Zhou, C. T., et al. (2022). Differences and connections between mining seismicity and coal bursts in coal mines and preliminary study on coal bursts induced by mining seismicity. *J. China Coal Soc.* 47, 3396–3409. doi:10.13225/j.cnki.jccs.2021.1714

frontiers | Frontiers in Earth Science

TYPE Original Research
PUBLISHED 08 January 2025
DOI 10.3389/feart.2024.1518561

OPEN ACCESS

EDITED BY
Huaimin Dong,
Chang'an University, China

REVIEWED BY
Weichao Yan,
Ocean University of China, China
Haitao Wang,
Chongqing University of Science and Technology, China

*CORRESPONDENCE
Haiyan Wang,
haiyanwang7732@163.com

RECEIVED 28 October 2024
ACCEPTED 18 December 2024
PUBLISHED 08 January 2025

CITATION
Wang H, Yang X, Zhou C, Yan J, Yu J and Xie K (2025) Constructions of multi-scale 3D digital rocks by associated image segmentation method.
Front. Earth Sci. 12:1518561.
doi: 10.3389/feart.2024.1518561

Constructions of multi-scale 3D digital rocks by associated image segmentation method

Haiyan Wang*, Xuefeng Yang, Cong Zhou, Jingxu Yan, Jiaqi Yu and Kui Xie

PetroChina Daqing Oilfield Co., Ltd., Daqing, China

Digital rocks constructed from micro-CT image at a single-resolution face limitations in accurately identifying the entire pore space and mineral components of tight sandstones, due to their high content of nanoscale pores and clay. Consequently, the porosity values derived from such digital rocks are significantly lower compared to those obtained through laboratory measurements, resulting in discrepancies between the measured and calculated petrophysical properties. This study introduces a multi-scale digital rock modeling method by integrating three-dimensional micro-CT images acquired at two distinct resolutions and two-dimensional SEM images. Plunger-shaped core samples and their corresponding sub-samples were scanned at resolutions of 13.99 μm/voxel and 2.99 μm/voxel, respectively. The scale-invariant feature transform (SIFT) image registration technique was employed to accurately align the two sets of grayscale CT images. Correlation curves between the grayscale value in low-resolution CT images and various mineral contents were established based on the aligned regions, and utilized to construct multi-scale digital rock models. Intragranular pores, unresolvable by the micro-CT images, were identified using SEM imaging, enabling the incorporation of fine-scale features into the models. The resulting multi-scale digital rock models exhibited bulk porosity values that closely matched laboratory helium porosity measurements. Additionally, the elastic moduli calculated by the differential effective medium (DEM) model and the finite element method (FEM) demonstrated good correspondence with experimental results. These results validate the proposed multi-scale digital rock modeling method as an effective approach for accurately characterizing the porosity and mineral components of tight sandstone reservoirs.

KEYWORDS

digital rock, image registration, multi-scale, correlation segmentation, porosity, elastic modulus

1 Introduction

In modern society, the demand for fossil fuels continues to grow, while reserves of conventional oil and gas are gradually depleting. Consequently, the exploration and development of unconventional oil and gas resources have become increasingly important within the petroleum industry. In recent years, the production of oil and gas from unconventional resources has experienced significant growth (Tong et al., 2018; Wang et al., 2016). Among unconventional reservoirs, tight sandstone reservoirs are one of the major reservoirs for unconventional gas resources. Their pore structures and physical properties

are crucial for effective reservoir development (Guo et al., 2022; Li et al., 2017; Wang et al., 2017; Yin et al., 2017). However, tight sandstones are typically characterized by complex pore structures, a broad pore size distribution, and low porosity and permeability. These characteristics present significant challenges for conventional petrophysical experimental techniques when attempting to accurately determine their pore structure features and physical properties (Zhang et al., 2017).

Methods for measuring the porosity of low-permeability rock cores can be broadly classified into two categories: laboratory-based direct measurement techniques and indirect methods based on various downhole testing techniques. Laboratory techniques primarily include mercury intrusion porosimetry (MIP) and nitrogen gas adsorption (N2GA). MIP functions on the principle that mercury, as a non-wetting liquid, infiltrates pores under applied pressure (Abell et al., 1999). However, this method risks damaging the pore structure, particularly in smaller pores, as mercury infiltration requires higher pressures (Clarkson and Marc Bustin, 1996). In contrast, N2GA offers greater accuracy but is limited in its capacity to detect pores larger than 200 nm due to the experimental mechanism and sample size constraints. Indirect methods mainly predict core porosity from logging data, such as electrical imaging and sonic logging data (Alizadeh et al., 2015; Close et al., 2009; Newberry et al., 1996; Tixier et al., 1959; Yamada et al., 2013). Laboratory porosity measurements are not only time-consuming and costly but may also cause irreversible damage to the samples. Indirect methods are heavily dependent on the accuracy of the logging data and require a multitude of parameters. Variability in geological environments across different regions may further introduce uncertainties into these methods, affecting the reliability of these methods. Moreover, these traditional methods provide only average characteristics of the pore structure, lacking the capability to accurately delineate the microscopic features of the core pores. This limitation hampers their ability to comprehensively characterize the complexity of low-permeability rocks.

Digital rock technology, which digitizes actual rock cores using high-resolution imaging techniques such as X-ray computed tomography (CT) and scanning electron microscopy (SEM), offers an alternative approach. This technology provides detailed microscopic structural information at the pore scale, enabling the application of advanced numerical algorithms to simulate rock physics experiments. These simulations can effectively analyze the response of physical properties in rock samples. Digital rock technology simplifies the research process, reduces costs and time, enhances result repeatability, and avoids destructive testing of physical samples. It addresses challenges associated with measuring and quantitatively analyzing rock physical parameters, thereby overcoming the inherent limitations of conventional experimental techniques. In recent years, digital rock technology has become a pivotal tool for pore structure analysis and investigation of rock physical properties. Researchers have developed a variety of methods for constructing three-dimensional (3D) digital rock models, primarily focusing on direct modeling utilizing 3D CT images and reconstruction methods based on two-dimensional (2D) images (Bin et al., 2013; Hazlett, 1997; Liu et al., 2023; Liu et al., 2014; Quiblier, 1984; Wu et al., 2004; Yin et al., 2019; Zhao et al., 2007).

However, the unique characteristics of tight sandstones, such as low porosity, low permeability, wide pore size distribution, and high clay content, may lead to inaccuracies in structure modeling when utilizing digital rock technology based on single-resolution CT scanning. These limitations often lead to significant discrepancies between numerical simulation results and experimental data. To address this issue, this study presents a multi-scale digital rock modeling method that integrates 3D micro-CT images acquired at different resolutions with nanoscale 2D images obtained via SEM. Using the constructed multi-scale digital rock, we calculated the porosity and elastic moduli of tight sandstone samples. The calculated results exhibit good agreement with the laboratory measurements, suggesting that the multi-scale digital rock model provides an accurate depiction of the porosity and mineral components of actual tight sandstones.

2 Samples and experimental measurements

To evaluate the performance of the multi-scale digital rock modeling method proposed in this study, two tight sandstone cores from Changqing Oilfield were selected for digital rock construction and elastic moduli calculations. These core samples, which are plunger-shaped and labeled as N1 and N2, have a diameter of 24.5 mm and were initially subjected to low-resolution CT scanning. To facilitate the construction of a multi-scale digital rock, a cylindrical sub-sample with a diameter of 5 mm was extracted from each original core sample for higher-resolution CT scanning. Figure 1 presents a schematic diagram and photographs of the test sample, illustrating the extraction of the smaller cylindrical sub-sample from the larger core.

To assess the accuracy of the proposed multi-scale 3D digital rock modeling method, laboratory measurements were performed to characterize various properties of the core samples. Helium porosity measurements yielded values of 11.75% for the N1 core and 12.17% for the N2 core. Acoustic properties of the cores were also measured. When saturated with water, the longitudinal wave velocities were 4,217.6 m/s for the N1 core and 4,327.8 m/s for the N2 core, and the corresponding shear wave velocities were 2,551.8 m/s and 2,235.8 m/s, respectively. XRD experiments were conducted to analyze mineral contents, with the results presented in Table 1. These results indicate that the mineral components and their content of the two cores are similar, with the clay content in the N2 core being slightly higher than that in the N1 core, which is similar to the difference in porosities, demonstrating that the clay pores play a significant role in contributing the overall porosity.

3 Multi-scale 3D digital rock modeling method

3.1 Multi-resolution images

Imaging techniques used in digital rock modeling commonly include X-ray CT, SEM, focused ion beam scanning electron microscopy (FIB-SEM), etc. In this study, X-ray CT imaging was employed to construct 3D digital rock models. X-ray CT imaging is a non-destructive testing technology widely utilized in medical and

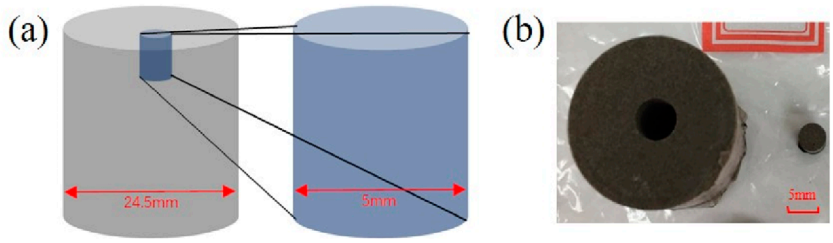

FIGURE 1
(A) Schematic diagram illustrating the extraction of a 5 mm diameter cylindrical subsample from a 24.5 mm diameter plunger core sample. **(B)** Photographs of the N1 core sample and its sub-samples.

TABLE 1 The contents of minerals in the core samples obtained from XRD experiments.

Sample	Quartz/%	Albite/%	Potash feldspar/%	Calcite/%	Dolomite/%	Siderite/%	Clay/%
N1	59	19	8	4	4	1	5
N2	59	20	9	1	3	1	7

industrial applications. The penetration of X-rays through an object causes attenuation, the extent of which depends on the material's properties, such as thickness and density. CT scans of cores taken from different angles generate attenuation maps (Dunsmuir et al., 1991), which are processed using reconstruction algorithms to produce 3D grayscale images. The grayscale values of pixels in these images correspond to the degree of X-ray attenuation, accurately reflecting the spatial distribution of different components.

Tight sandstone core samples and their sub-samples were imaged using CT scans of different resolutions. Initially, CT imaging with a resolution of 13.99 μm/voxel was performed on two original tight sandstone core samples. After extracting sub-samples from the original cores, high-resolution (2.99 μm/voxel) CT imaging was conducted on the small sub-samples. The 3D CT images had a resolution of 1,920 × 1,920 × 1,536 voxels. Figure 2 shows the CT scan slice images for both N1 and N2 samples at the different resolutions, highlighting the level of detail achieved at each scanning resolution. To identify micropores beyond the resolution limit of CT scanning, broad ion beam scanning electron microscopy (BIB-SEM) with a resolution of 5 nm/pixel was employed. Furthermore, to create a 2D image of the core surface with a large field of view, the MAPS image stitching technique was utilized. This technique involves combining multiple high-resolution SEM images to form a single, expansive image (Lemmens and Richards, 2013). The resulting MAPS image was of a considerable size, measuring 105,000 × 106,000 pixels, which provides a detailed and expansive view of the core's surface.

3.2 Image registration method

Image registration techniques aim to establish correspondence between corresponding positions in two different images through various operations such as rigid transformation, similarity transformation, affine transformation, projection transformation, and polynomial transformation. This technology is widely applied in medical image processing, image analysis, remote sensing fusion, and computer vision.

Image registration methods can be broadly categorized into information-based registration and feature-based registration. Grayscale-based registration methods, which rely on the grayscale features of two images, have been extensively studied. The principle of this approach involves using the grayscale value information at each position for alignment. Because images typically contain vast amounts of grayscale data, this method requires substantial computational resources and often results in prolonged registration times. Furthermore, because the two images may not be captured simultaneously or with the same equipment, variations in grayscale information can significantly reduce the success rate of registration. In contrast, feature-based image registration methods offer lower computational requirements and faster processing speeds, effectively enhancing both the efficiency and accuracy of registration. Algorithms such as the Harris corner detection, Moravec algorithm, and scale-invariant feature transform (SIFT) have been developed to support feature-based image registration.

In this study, the SIFT algorithm was employed for image registration, a method based on feature points. This method was first introduced by Lowe at the International Conference on Computer Vision in 1999 (Lowe, 1999). SIFT algorithm is based on the scale space and ensures invariance to image translation, rotation, scaling, and even affine transformations. The algorithm represents image information across various scales using a Difference of Gaussian (DOG) pyramid and identifies key points by detecting extrema in the DOG images. The precise locations and scales of these key points are determined using an optimization algorithm, which also eliminates points with poor responses or edge responses, thereby yielding the image's feature points. By calculating the magnitude and orientation of gradients around the feature points, an orientation is assigned, ensuring the feature points remain invariant to scale and rotation. Local image information around each feature point

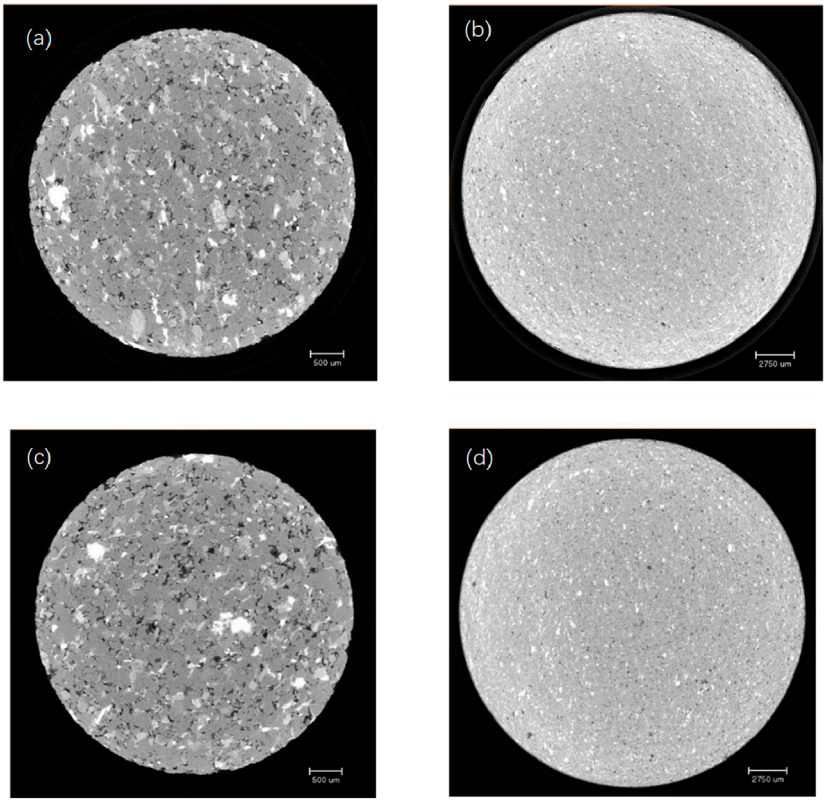

FIGURE 2
High-resolution (2.99 μm/voxel) CT scan slice images of the **(A)** N1 and **(C)** N2 sub-samples. Low-resolution (13.99 μm/voxel) CT images of the **(B)** N1 and **(D)** N2 origin samples.

is then used to generate distinctive descriptors, further enhancing the accuracy of feature matching. The positional information of matching feature points allows the calculation of the matching region between two images. Corresponding sections of images with varying resolutions can be aligned through operations such as rotation and cropping. These functions can be implemented using the open-source program "siftdemoV4" developed by Lowe (1999), Lowe (2004). Figure 3 illustrates the flowchart of the image registration process, detailing each step in the procedure.

3.3 Microporosity of mineral component

Based on the geometry of pores in the core samples, pore spaces can be categorized into intergranular pores, intragranular pores, intercrystalline pores, and cracks. CT imaging is capable of identifying large pores located between particles of various components in the core. However, it cannot resolve micropores due to its resolution limitation (Liu and Ostadhassan, 2017). Therefore, incorporating microporosity associated with different mineral components reflects the objective reality, thereby enabling a more accurate estimation of core porosity.

Nano-resolution 2D MAPS imaging enables identifying pore types and their spatial locations. Small pore clusters within the feldspar, quartz or calcite grains are classified as dissolved pores, while larger pore clusters located between quartz, albite, and feldspar grains are categorized as intercrystalline pores. Clusters of small pores surrounded by clay minerals are identified as clay-dominated micropores. Statistical analysis of various pore types observed in the MAPS image facilitates the calculation of microporosity with each mineral component. The corresponding data are presented in Table 2.

3.4 Associated image segmentation

Coarse-scale digital rocks feature lower resolution, with each voxel potentially representing multiple mineral components. In contrast, fine-scale digital rocks offer more precise information but may lack broader representativeness due to their limited sample size. Consequently, an effective strategy for rock physics research involves integrating digital rocks at both scales and performing upscaling operations to bridge the discrepancies between scales.

Based on the scale relationship between the two resolutions in CT imaging, each voxel in the coarse-scale digital rock corresponds to a $5 \times 5 \times 5$ voxel grid in the fine-scale digital rock. Utilizing this relationship, the proportions of mineral components within each voxel can be extracted. By statistically analyzing all voxels with the same grayscale value in the coarse-scale digital rock, the average content of each mineral component can be determined, enabling the calculation of the mineral component proportions represented by that grayscale value. By using a program to perform

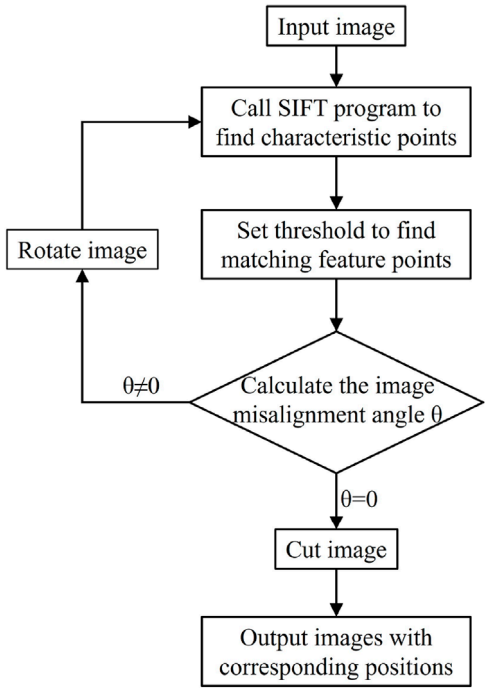

FIGURE 3
Flowchart of the image registration procedure based on SIFT algorithm.

traversal statistics, a correlation curve between grayscale values and the mineral component proportions in the coarse-scale digital rock was generated (Figure 4). This curve establishes a direct mapping between image grayscale information and mineral component proportions.

The porosity of each voxel in the coarse-scale digital rock is calculated using the formula:

$$\emptyset_i = \sum_k f_k(g_i) \times \varphi_k \quad (1)$$

where $\emptyset_i$ is the porosity of the ith voxel, g_i is the grayscale value of the ith voxel, $f_k(g_i)$ is the proportion of the kth component corresponding to the grayscale value g_i which can be obtained from the correlation curves (Figure 4), and φ_k is the microporosity of the kth component (see Table 2). After calculating the porosity of all voxels within the coarse-scale image using Equation 1, the total porosity of the entire core sample is obtained by averaging all voxel porosities.

3.5 Elastic modulus calculation

The complexity of multi-component tight sandstone digital rocks, coupled with the inclusion of microporosity, makes the conventional single-mineral-component method for calculating the elastic modulus no longer applicable. To address this limitation, we developed an integrated approach that combines the differential effective medium (DEM) model with the finite element method (FEM). Figure 5 illustrates the step-by-step flowchart of the proposed calculation methodology.

In this study, CT imaging was utilized to segment the core into five distinct components: pores, clay, quartz (albite), potash feldspar, and dolomite. This segmentation is crucial for accurately modeling the rock's physical properties. The coarse-scale digital rock is represented by an 8-bit grayscale image consisting of 256 distinct grayscale values. The equivalent elastic modulus for each of these grayscale values was obtained using two-step DEM calculation process. In the first DEM step, each mineral component, assumed to be in its pure solid state, was designated as the matrix, with micropores incorporated to compute the component's equivalent elastic modulus (Berryman, 1980). The elastic moduli for pure mineral component were determined using the data in Table 3. Additionally, since the sound velocity measurements were conducted under water-saturated conditions, the elastic properties of water were considered during the addition of the pores. In the second DEM step, different components were sequentially added based on the correlation curve, enabling the calculation of the equivalent elastic modulus corresponding to each grayscale value, which represents different mineral mixtures. Following the DEM calculations, the FEM was applied to compute the overall elastic moduli of the coarse-scale digital rock. The employed FEM program is developed by Garboczi (1998). This program uses a hexahedral mesh with voxels as elements and has been validated for accuracy in multiple studies (Arns et al., 2005; Arns et al., 2002).

4 Results and discussions

4.1 Image registration

Figure 6 displays the registration images for CT images at varying resolutions, generated using the SIFT registration program. The figure reveals both correctly matched points and instances of mismatched points. These mismatched points can be corrected through manual intervention.

Once accurate registration information is obtained, the 3D images are adjusted through rotation, and corresponding cube images at different resolutions are extracted. Figures 7A, B present 3D comparison images of the N1 and N2 cores, respectively. The double arrows in these figures indicate corresponding feature points, demonstrating the precise alignment of the images across different resolutions.

4.2 Porosities

Core porosity is a crucial parameter for estimating reservoir oil and gas reserves as well as productivity. It represents one of the most important petrophysical characteristic in oilfield exploration and development. Generally, higher porosity in the reservoir cores correlates with greater oil and gas reserves and easier extraction. Enhancing the precision of core porosity calculations provides valuable guidance for the exploitation and development of oil and gas fields.

Table 4 presents the calculated porosity for the different digital rock models. For the single-scale N1 digital rock, porosities are 1.5% at 13.99 μm/voxel resolution and 5.7% at 2.99 μm/voxel

TABLE 2 Microporosity of the mineral component in the tight sandstone samples.

Component	Pore	Clay	Quartz	Feldspar	Siderite
Microporosity φ	1	0.3	0.03	0.1	0

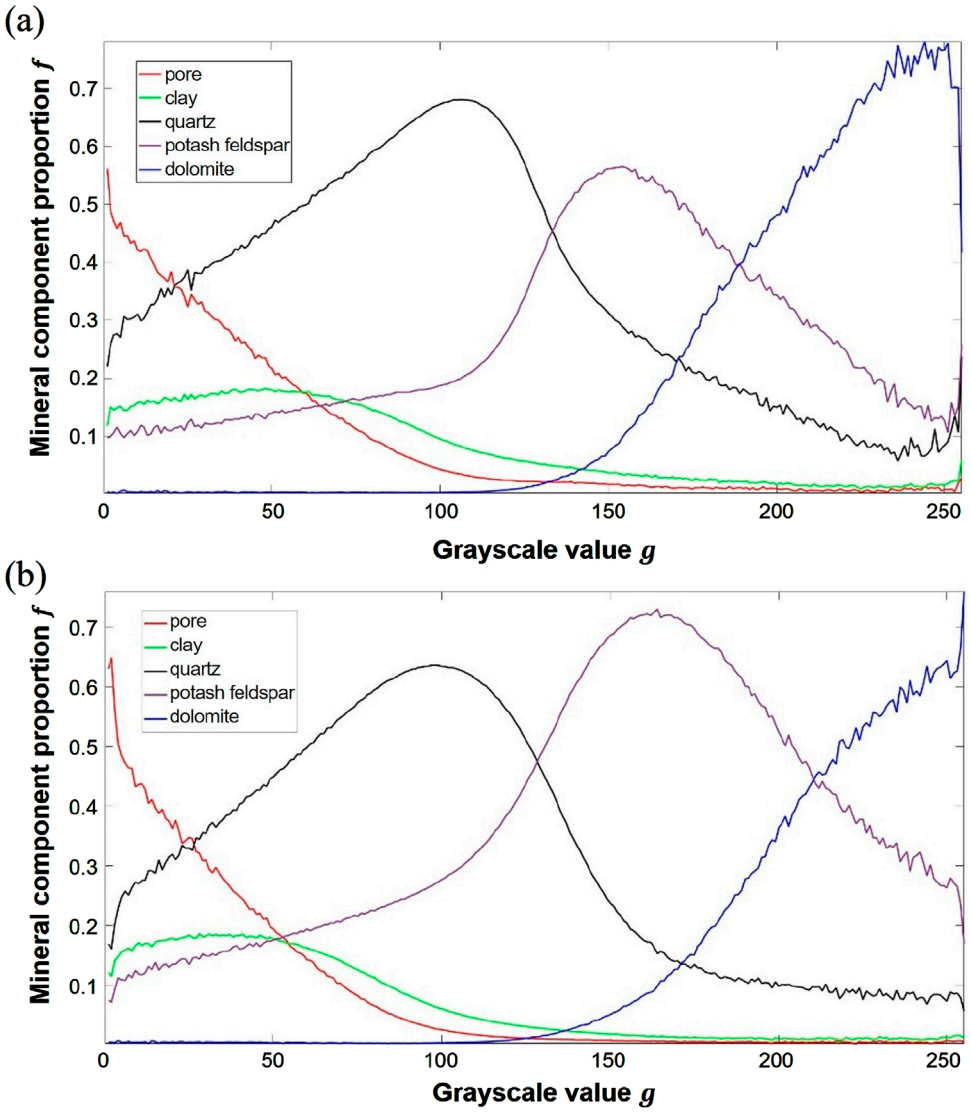

FIGURE 4
The correlation curves between grayscale value and mineral component proportion in the coarse-scale digital rocks of **(A)** N1 and **(B)** N2 based on low resolution CT grayscale images.

resolution, while for the N2 core, the corresponding values are 0.5% and 2.3%, respectively. In the multi-scale and multi-component models, incorporating microporosity results in porosities of 11.13% for N1 and 12.94% for N2, compared to 3.43% and 5.11% without considering microporosity. These results suggest that porosities derived from single-scale resolutions deviate significantly from experimental measurements, highlighting the limitations of such calculations in fully characterizing the pore structures of core samples.

Significantly, incorporating the microporosity of mineral components produces porosity estimates that closely match experimental gas porosities. The calculated porosity errors for the N1 and N2 rock cores are 5.28% and 6.33%, respectively, compared to experimental porosities. This highlights the substantial contribution of micropores to total porosity in tight sandstone cores. The use of multi-scale digital rocks for porosity calculations demonstrates improved accuracy, thereby enhancing the reliability of the results.

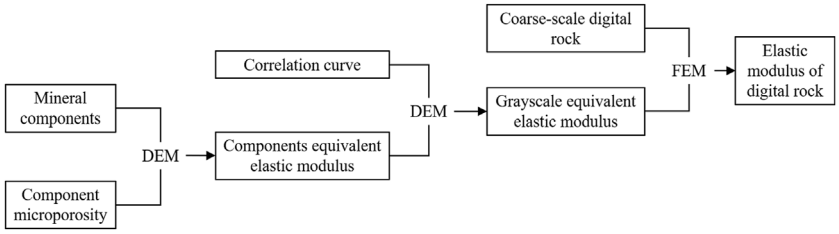

FIGURE 5
Flowchart of elastic modulus calculation method for upscaled digital rock based on the combination of DEM and FEM.

TABLE 3 The elastic moduli for each component when it is in a pure phase state.

Component	Bulk modulus/GPa	Shear modulus/GPa
Water	2.18	0
Clay	37.9	14.8
Quartz	37.7	44.5
Albite	55.1	29.7
Potash feldspar	56.2	29.3
Dolomite	95.5	11.4

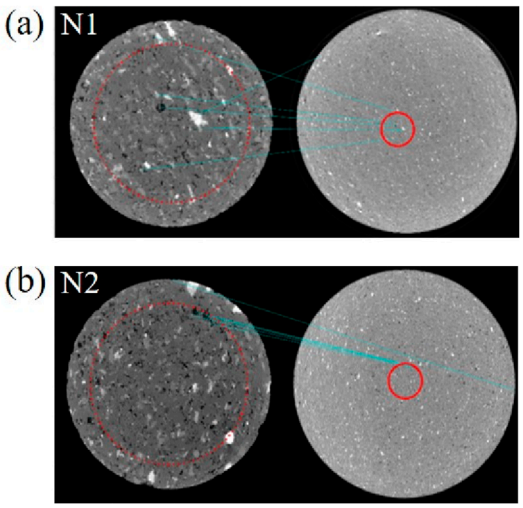

FIGURE 6
Registration images of and core samples **(A)** N1 and **(B)** N2 at different resolutions, with high-resolution images on the left and corresponding low-resolution images on the right. The blue line indicates the matching points.

Jin et al. (2018) constructed a digital rock model using CT images with a resolution of 0.7 μm/voxel and introduced component microporosity to calculate core porosity, achieving an error margin

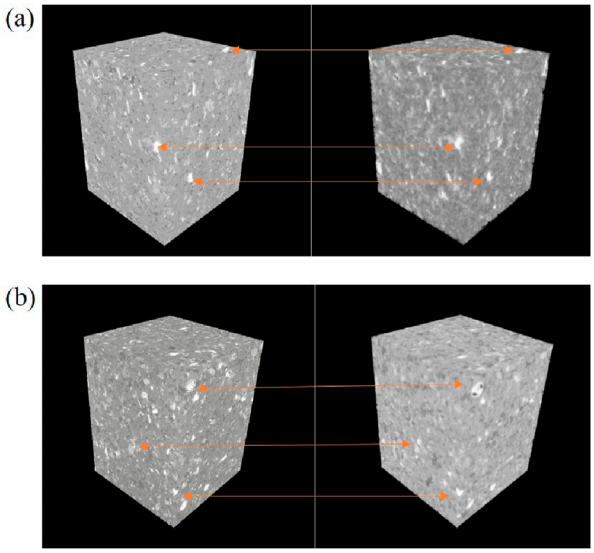

FIGURE 7
3D images of and core samples **(A)** N1 and **(B)** N2 at different resolutions, with high-resolution images on the left and corresponding low-resolution images on the right. The double arrows indicate corresponding feature points.

within 5.20%. The accuracy of porosity calculations at a single-resolution digital rock depends on image resolution, with higher-resolution images yielding more precise results. In our study, despite using a maximum CT image resolution of 2.99 μm/voxel, which is significantly lower than the 0.7 μm/voxel used by Jin et al., the maximum calculation error is 6.33%, comparable to the reported 5.20%. This result suggests that establishing an upscaled digital rock model effectively reduces the resolution requirements while maintaining high calculation accuracy.

4.3 Elastic moduli

Based on the constructed multi-scale digital rock, the proportions of various mineral components in the low-resolution images can be accurately quantified. Table 5 provides a comparative analysis of the N2 core's XRD experimental data and the corresponding statistical results derived from the multi-scale digital rock model. Since the differentiation of components in X-ray CT

TABLE 4 Porosities from lab measurements and digital rock samples at different scales.

Sample	Porosity calculated by digital rock/%				Helium porosity/%
	Single-scale digital rock		Multi-scale digital rock	Multi-scale digital rock with microporosity	
	13.99 μm	2.99 μm			
N1	1.5	5.7	3.43	11.13	11.75
N2	0.5	2.3	5.11	12.94	12.17

TABLE 5 Mineral components and contents of the N2 core sample from XRD measurements and the digital rock method.

Method	Clay/%	Quartz (plagioclase)/%	Potash feldspar (calcite)/%	Dolomite (siderite)/%
XRD	7.00	79.00	10.00	4.00
Digital rock	7.67	81.68	9.19	1.46

TABLE 6 Results of elastic moduli from the simulation based on the multi-scale digital rock method and the experimental measurements.

Sample	Multi-scale digital rock		Experimental measurements	
	Bulk modulus/Gpa	Shear modulus/Gpa	Bulk modulus/Gpa	Shear modulus/Gpa
N1	21.67	18.29	22.5	16.1
N2	27.85	13.56	29.7	12.3

images relies on variations in voxel grayscale values, minerals that exhibit minimal differences in grayscale value may be aggregated into a single phase, even though they represent distinct components.

Table 5 demonstrates that the mineral component analysis derived from correlation-based segmentation closely aligns with the XRD experimental data, although a notable disparity exists between the measurements for dolomite and siderite. This disparity is primarily attributed to misalignment during the image registration process, which disproportionately affects minerals with low abundance that are primarily distributed as discrete points within the core, rendering them more sensitive to registration inaccuracies.

Table 6 presents the elastic moduli results from the simulations based on the multi-scale digital rocks compared with the experimental measurements. The calculated elastic moduli exhibit good agreement with the experimental data, validating the accuracy of the multi-scale digital rock model. These results confirm that the constructed model effectively captures the distribution characteristics of minerals and pores within the core, providing a reliable modeling method for further digital rock physics research.

In unconventional oil and gas reservoirs, such as tight sandstones and shales, the reservoir rocks often exhibit a high degree of heterogeneity. Traditional digital rock technology, which relies on single-resolution imaging, faces challenges in balancing field of view and image resolution. In recent years, multi-scale digital rock technology, which employs various resolutions and imaging techniques, has made significant progress. Walls et al. (2017) compared multi-scale digital rocks using SEM imaging at different resolutions, demonstrating that multi-resolution imaging significantly improves pore identification accuracy. Islam et al. (2019) conducted multi-scale imaging and numerical simulations on the permeability of heterogeneous carbonate rocks, establishing porosity-permeability curves and analyzing resolution impacts on porosity calculations. Liu et al. (2017) explored the pore characteristics of rock samples through fractal theory, revealing that pore complexity and fractal dimensions increase with magnification.

In the multi-scale digital rock techniques, upscaling methods have been developed to correlate data across scales effectively, enabling comprehensive analysis of core properties. These methods include the overlay method, representative elementary volume (REV), and integration of multiple computational approaches. The overlay method allows for the refinement of images and is commonly used in the upscaling construction of pore models. Yao et al. (2015) constructed multi-scale pore network models using different resolution SEM images and the Markov Chain-Monte Carlo method. The REV method involves partitioning the core to ensure that each section has similar properties, thus achieving upscaling from high to low resolution. Sun et al. (2019) proposed an upscaling porosity method using REV selection across CT-scanned samples. Suhrer et al. (2020) obtained multiple REVs based on

image complexity to achieve upscaling modeling. The integration of multiple computational methods utilizes the differences in scale between different computational methods. Ning et al. (2016) combined molecular dynamics (MD) and lattice Boltzmann methods to achieve nanoscale-to-microscale fluid transport simulations.

In this study, a two-step upscaling process was used to calculate the equivalent elastic moduli for the FEM simulations. Nano-resolution SEM data provided micro-porosity insights, integrated into mineral components. The precise registrations of high- and low-resolution CT images provide the relationship between mineral component proportions and grayscale value in the coarse-scale digital rocks, thereby obtaining the equivalent elastic moduli of each voxel. This approach maintains computational accuracy while significantly improving efficiency. It is noteworthy that due to the high sensitivity of the elastic modulus to porosity and mineral components, this upscaling method is particularly suitable for elastic modulus calculations. However, for flow characteristics and electrical properties, which depend on pore connectivity, fine-scale structural information loss during upscaling may impact the result accuracy, warranting further investigation.

5 Conclusion

This study introduces a method for constructing multi-scale digital rocks by integrating 3D micro-CT images at two different resolutions and 2D SEM-MAPS images. SIFT image registration was applied to align high- and low-resolution CT images, establishing a correlation curve between grayscale values in low-resolution images and mineral component proportions. To capture the microporosity of mineral components not identified by micro-CT, nanoscale SEM-MAPS scanning was employed. Using the correlation curve, microporosity of mineral components and low-resolution CT images, the multi-scale digital rocks were constructed. This multi-scale modeling method successfully produced digital rock models that accurately represent the porosity and minerals' content of tight sandstones. An upscaling method by calculating the equivalent elastic moduli of voxels of different greyscale value based on DEM theory was utilized and the FEM simulation was deployed to calculate the elastic moduli of the cores. The porosities and simulated elastic moduli of the multi-scale digital rocks exhibited good agreement the experimental data. These results confirm that the constructed model effectively captures the distribution characteristics of minerals and pores within the core, which helps to improve the efficiency and accuracy of subsequent rock physics simulation researches.

Data availability statement

The original contributions presented in the study are included in the article/supplementary material, further inquiries can be directed to the corresponding author.

Author contributions

HW: Conceptualization, Data curation, Formal Analysis, Investigation, Methodology, Resources, Supervision, Validation, Visualization, Writing–original draft, Writing–review and editing. XY: Conceptualization, Data curation, Methodology, Writing–review and editing. CZ: Supervision, Validation, Visualization, Writing–review and editing. JXY: Data curation, Methodology, Investigation, Writing–review and editing. JQY: Supervision, Validation, Visualization, Writing–review and editing. KX: Supervision, Visualization, Writing–review and editing.

Funding

The author(s) declare that no financial support was received for the research, authorship, and/or publication of this article.

Conflict of interest

Authors HW, XY, CZ, JnY, JaY, and KX were employed by PetroChina Daqing Oilfield Co., Ltd.

Generative AI statement

The author(s) declare that no Generative AI was used in the creation of this manuscript.

Publisher's note

References

Abell, A. B., Willis, K. L., and Lange, D. A. (1999). Mercury intrusion porosimetry and image analysis of cement-based materials. *J. Colloid Interface Sci.* 211, 39–44. doi:10.1006/jcis.1998.5986

Alizadeh, M., Movahed, Z., and Junin, R. B. (2015). Porosity analysis using image logs. *Environ. Sci.* 10, 326–337. doi:10.1016/S1876-3804(13)60042-7

Arns, C., Bauget, F., Sakellariou, A., Senden, T. J., Sheppard, A. P., Sok, R. M., et al. (2005). Digital core laboratory: petrophysical analysis from 3D imaging of reservoir core fragments. *Petrophysics-The SPWLA J. Form. Eval. Reserv. Descr.* 46, 260–277.

Arns, C. H., Knackstedt, M. A., Pinczewski, W. V., and Garboczi, E. J. (2002). Computation of linear elastic properties from microtomographic images: methodology and agreement between theory and experiment. *Geophysics* 67 (5), 1396–1405. doi:10.1190/1.1512785

Berryman, J. G. (1980). Long-wavelength propagation in composite elastic media II: ellipsoidal inclusions. *J. Acoust. Soc. Am.* 86, 1820–1831. doi:10.1121/1.385172

Bin, B., Rukai, Z., Songtao, W., Wenjing, Y., Gelb, J., Gu, A., et al. (2013). Multi-scale method of Nano (Micro)-CT study on microscopic pore structure of tight

sandstone of Yanchang Formation, Ordos Basin. *Petroleum Explor. Dev.* 40, 354–358. doi:10.1016/S1876-3804(13)60042-7

Clarkson, C. R., and Marc Bustin, R. (1996). Variation in micropore capacity and size distribution with composition in bituminous coal of the Western Canadian Sedimentary Basin: implications for coalbed methane potential. *Fuel* 75, 1483–1498. doi:10.1016/0016-2361(96)00142-1

Close, D., Cho, D., Horn, F., and Edmundson, H. (2009). The sound of sonic: a historical perspective and introduction to acoustic logging. *CSEG Rec.* 34, 34–43.

Dunsmuir, J. H., Ferguson, S. R., D'Amico, K. L., and Stokes, J. P. (1991). X-ray microtomography: a new tool for the characterization of porous media. *SPE Annu. Tech. Conf. Exhib.* SPE-22860. doi:10.2118/22860-MS

Garboczi, E. J. (1998). *Finite element and finite difference programs for computing the linear electric and elastic properties of digital images of random materials*. Gaithersburg: National Institute of Standards and Technology.

Guo, W., Dong, C., Lin, C., Wu, Y., Zhang, X., and Liu, J. (2022). Rock physical modeling of tight sandstones based on digital rocks and reservoir porosity prediction from seismic data. *Front. Earth Sci.* 10, 932929. doi:10.3389/feart.2022.932929

Hazlett, R. (1997). Statistical characterization and stochastic modeling of pore networks in relation to fluid flow. *Math. Geol.* 29, 801–822. doi:10.1007/BF02768903

Islam, A., Faisal, T. F., Chevalier, S., Jouini, M. S., and Sassi, M. (2019). Multi-scale experimental and numerical simulation workflow of absolute permeability in heterogeneous carbonates. *J. Petroleum Sci. Eng.* 173, 326–338. doi:10.1016/j.petrol.2018.10.031

Jin, Z., Wang, F., Guo, C., He, Z. L., and Wang, X. L. (2018). A calculation method for the effective electrical properties of rocks based on digital core technology. *Geophys. Geochem. Explor.* 42, 1280–1288. doi:10.11720/wtyht.2018.0175

Lemmens, H., and Richards, D. (2013). 4 Multiscale imaging of shale samples in the scanning electron Microscope. *Am. Assoc. Petroleum Geol. Mem.* 102, 27–35. Electron Microscopy of Shale Hydrocarbon Reservoirs. doi:10.1306/13391702M1023582

Li, D., Wei, J., Di, B., Ding, P., and Shuai, D. (2017). The effect of fluid saturation on the dynamic shear modulus of tight sandstones. *J. Geophys. Eng.* 14, 1072–1086. doi:10.1088/1742-2140/aa7179

Liu, K., and Ostadhassan, M. (2017). Multi-scale fractal analysis of pores in shale rocks. *J. Appl. Geophys.* 140, 1–10. doi:10.1016/j.jappgeo.2017.02.028

Liu, L., Yao, J., Imani, G., Sun, H., Zhang, L., Yang, Y., et al. (2023). Reconstruction of 3D multi-mineral shale digital rock from a 2D image based on multi-point statistics. *Front. Earth Sci.* 10, 1104401. doi:10.3389/feart.2022.1104401

Liu, X., Wang, J., Ge, L., Hu, F., Li, C., Li, X., et al. (2017). Pore-scale characterization of tight sandstone in Yanchang Formation Ordos Basin China using micro-CT and SEM imaging from nm-to cm-scale. *Fuel* 209, 254–264. doi:10.1016/j.fuel.2017.07.068

Liu, X., Zhu, H., and Liang, X. (2014). Digital rock physics of sandstone based on micro-CT technology. *Chin. J. Geophys.* 57, 1133–1140. doi:10.6038/cjg20140411

Lowe, D. G. (1999). "Object recognition from local scale-invariant features," in Proceedings of the Seventh IEEE International Conference on Computer Vision, Kerkyra, Greece, 20-27 September 1999, 1150–1157 vol.2. doi:10.1109/ICCV.1999.790410

Lowe, D. G. (2004). Distinctive image features from scale-invariant keypoints. *Int. J. Comput. Vis.* 60, 91–110. doi:10.1023/B:VISI.0000029664.99615.94

Newberry, B., Grace, L., and Stief, D. (1996). Analysis of carbonate dual porosity systems from borehole electrical images. *Permian Basin oil and gas recovery Conf.*, 123–129. doi:10.2118/35158-MS

Ning, Y., He, S., Liu, H., Wang, H., and Qin, G. (2016). "Upscaling in numerical simulation of shale transport properties by coupling molecular dynamics simulation with lattice Boltzmann method," in *SPE/AAPG/SEG unconventional resources technology conference* (San Antonio, TX: URTec). URTEC-2459219. doi:10.15530/URTEC-2016-2459219

Quiblier, J. (1984). A new three-dimensional modeling technique for studying porous media. *J. Colloid Interface Sci.* 98, 84–102. doi:10.1016/0021-9797(84)90481-8

Suhrer, M., Nie, X., Toelke, J., and Ma, S. (2020). "Upscaling method for obtaining primary drainage capillary pressure and resistivity index with digital rock physics," in *International petroleum technology conference* (Dhahran, Saudi Arabia: IPTC). doi:10.2523/IPTC-20035-ABSTRACT

Sun, H., Belhaj, H., Tao, G., Vega, S., and Liu, L. (2019). Rock properties evaluation for carbonate reservoir characterization with multi-scale digital rock images. *J. Petroleum Sci. Eng.* 175, 654–664. doi:10.1016/j.petrol.2018.12.075

Tixier, M., Alger, R., and Doh, C. (1959). Sonic logging. *Trans. AIME* 216, 106–114. doi:10.2118/1115-G

Tong, X., Zhang, G., Wang, Z., Wen, Z., Tian, Z., Wang, H., et al. (2018). Distribution and potential of global oil and gas resources. *Petroleum Explor. Dev.* 45, 779–789. doi:10.1016/S1876-3804(18)30081-8

Walls, J., Davalos, G., and Weinreich, M. (2017). "Integration and comparison of multi-scale digital rock analysis with bulk rock porosity and LECO TOC within multiple Appalachian basin formations," in *SPE/AAPG/SEG unconventional resources technology conference* (Austin, TX: URTEC). (pp. URTEC-2697890). doi:10.15530/urtec-2017-2697890

Wang, H., Ma, F., Tong, X., Liu, Z., Zhang, X., Wu, Z., et al. (2016). Assessment of global unconventional oil and gas resources. *Petroleum Explor. Dev.* 43, 925–940. doi:10.1016/S1876-3804(16)30111-2

Wang, Y., Agostini, F., Skoczylas, F., Jeannin, L., and Portier, É. (2017). Experimental study of the gas permeability and bulk modulus of tight sandstone and changes in its pore structure. *Int. J. Rock Mech. Min. Sci.* 91, 203–209. doi:10.1016/j.ijrmms.2016.11.022

Wu, K., Nunan, N., Crawford, J. W., Young, I. M., and Ritz, K. (2004). An efficient Markov chain model for the simulation of heterogeneous soil structure. *Soil Sci. Soc. Am. J.* 68, 346–351. doi:10.2136/sssaj2004.3460

Yamada, T., Quesada, D., Etchecopar, A., Le Nir, I., Delhomme, J.-P., Russel-Houston, J., et al. (2013). Revisiting porosity analysis from electrical borehole images: integration of advanced texture and porosity analysis. *SPWLA Annu. Logging Symp*.

Yao, J., Hu, R., Wang, C., and Yang, Y. (2015). Multiscale pore structure analysis in carbonate rocks. *Int. J. Multiscale Comput. Eng.* 13 (1), 1–9. doi:10.1615/IntJMultCompEng.2014010500

Yin, H., Zhao, J., Tang, G., Zhao, L., Ma, X., and Wang, S. (2017). Pressure and fluid effect on frequency-dependent elastic moduli in fully saturated tight sandstone. *J. Geophys. Res. Solid Earth* 122, 8925–8942. doi:10.1002/2017JB014244

Yin, X., Zheng, Y., Zong, Z., and Lin, L. (2019). Estimation of reservoir properties with inverse digital rock physics modeling approach. *Chin. J. Geophys.* 62 (2), 720–729. doi:10.6038/cjg2019L0385

Zhang, L., Lu, S., Xiao, D., and Li, B. (2017). Pore structure characteristics of tight sandstones in the northern Songliao Basin, China. *Mar. Petroleum Geol.* 88, 170–180. doi:10.1016/j.marpetgeo.2017.08.005

Zhao, X., Yao, J., and Yi, Y. (2007). A new stochastic method of reconstructing porous media. *Transp. Porous Media* 69, 1–11. doi:10.1007/s11242-006-9052-9

frontiers | Frontiers in Earth Science

TYPE Original Research
PUBLISHED 22 January 2025
DOI 10.3389/feart.2025.1506238

OPEN ACCESS

EDITED BY
Huaimin Dong,
Chang'an University, China

REVIEWED BY
Wang Song,
China University of Petroleum, China
Naixing Feng,
Anhui University, China

*CORRESPONDENCE
Shaogui Deng,
dengshg@upc.edu.cn

RECEIVED 04 October 2024
ACCEPTED 02 January 2025
PUBLISHED 22 January 2025

CITATION
Zhang P, Deng S, Yuan X, Liu F and Xie W (2025) Fast forward modeling and response analysis of extra-deep azimuthal resistivity measurements in complex model.
Front. Earth Sci. 13:1506238.
doi: 10.3389/feart.2025.1506238

Fast forward modeling and response analysis of extra-deep azimuthal resistivity measurements in complex model

Pan Zhang[1], Shaogui Deng[2]*, Xiyong Yuan[3], Fen Liu[1] and Weibiao Xie[1]

[1]Petroleum Institute, China University of Petroleum-Beijing at Karamay, Karamay, China, [2]School of Geosciences, China University of Petroleum, Qingdao, China, [3]Sinopec Matrix Corporation, Qingdao, China

The Extra-Deep Azimuthal Resistivity Measurements (EDARM) tool, as an emerging technology, can effectively identify geological interfaces within a range of several tens of meters around the borehole, providing geological structures for directional drilling, and effectively improving reservoir encounter rates and enhancing oil and gas recovery rates. However, the signal is jointly affected by interfaces located both ahead of the drill bit and around the borehole, making it impossible to directly obtain the interface position from the signal. Considering the increased detection range of EDARM and the requirements for computational efficiency, this paper presents a 2.5-dimensional (2.5D) finite element method (FEM). By leveraging the symmetry of simulated signals in the spectral domain, the algorithm reduces computation time by 50%, significantly enhancing computational efficiency while preserving accuracy. During the geosteering process, fault and wedge models were simulated, and various feature parameters were extracted to assess their impact on the simulation outcomes of EDARM. The results show that both Look-around and Look-ahead modes exhibit sensitivity to changes in the angle of the geological interface. Crossplot analysis allows for effective identification of interface inclinations and the distances between the instrument and the geological interface. This recognition method is quick, intuitive, and yields reliable results.

KEYWORDS

extra-deep azimuthal resistivity measurement, 2.5D finite element method, logging while drilling, boundary detection, complex model

1 Introduction

Geosteering is a critical technology for minimizing development costs and optimizing the extraction of complex oil and gas resources. It directs the drilling trajectory of instruments in high-angle and horizontal wells (Li et al., 2005; Li et al., 2014; Wu et al., 2020; Omeragic et al., 2005; Bittar and Aki, 2015; Bell et al., 2006). Over the past several decades, geosteering technology has evolved from post-drilling track adjustments to active steering (Bittar et al., 2009; Li et al., 2014; Hu and Fan, 2018; Wang and Fan, 2019). The detection range has expanded from a few meters to several tens of meters, significantly reducing the risks associated with drilling operations and

enhancing the overall success rate (Iverson et al., 2004; Dupuis and Denichou, 2015). Currently, oil service companies have developed proprietary extra-deep azimuthal resistivity measurement (EDARM) instruments that effectively detect geological anomalies over distances of several tens of meters and identify interfaces ahead of the drill bit, thereby providing geological guidance on a reservoir scale (Hartman et al., 2014; Li and Zhou, 2017).

The Geosphere, developed by Schlumberger, is the first commercially available EDARM instrument capable of detecting resistivity, anisotropy, interfaces, and dipping angles (Seydoux et al., 2014; Thiel et al., 2018). Recent research has focused on the physical aspects, detection performance, and sensitivity of EDARM (Larsen et al., 2015; Wu et al., 2018; Wang et al., 2019a; Zhang et al., 2021; Wang et al., 2015). Investigations primarily center on its ability to detect interfaces around the instrument within layered media, aiming to ascertain the positional relationship between the instrument and these interfaces (Xia et al., 2019; Wang et al., 2019b; Lu et al., 2019). In specific geological structures, such as fault and wedge models, interfaces may be located ahead of the drill bit. While some researchers have evaluated the Look-ahead capability of the instrument (Constable et al., 2016; Hagiwara, 2018; Lu et al., 2019; Liang et al. 2023), few have explored the relationship between Look-around and Look-ahead modes. Understanding this relationship is essential for accurately determining the distance and angle between the instrument and the interface. Further investigation is needed to elucidate the detection characteristics of EDARM, thereby providing precise and reliable information about adjacent boundaries and formation structures.

The current limitations in the application of EDARM primarily stem from two factors: First, the extended detection range leads to a more complex formation model, which in turn reduces the efficiency of forward modeling; second, the logging response is influenced by interfaces at varying orientations, complicating the inversion process. To address the issue of forward modeling efficiency, the prevalent approach is to apply equivalent dimensionality reduction methods tailored to the characteristics of the while-drilling measurement environment. This involves solving the 3D electromagnetic field using a 2D model, commonly referred to as the 2.5D algorithm. The 2.5D algorithm for while-drilling electromagnetic wave logging was first proposed by Rozas and Pardo in 2016, with a systematic explanation provided in 2018 (Rodríguez-Rozas and Pardo, 2016 and Rodríguez-Rozas et al. 2018). In 2018, Zeng et al. introduced a 2.5D finite difference method (FDM) that simultaneously resolves electric and magnetic field components, enabling more intuitive and implementable modeling of fully anisotropic media. Wu et al. (2019) then applied the 2.5D FDM to logging-while-drilling (LWD), achieving fast and accurate electromagnetic field calculations. Their team later optimized the algorithm with a novel near-optimal quadrature (2022) and Lebedev grid discretization methods (2023) (Wu et al., 2023), reducing the single-point computation time to 7.6 s and further enhancing the 2.5D algorithm's performance. For EDARM inversion, current efforts have focused on reducing the number of inversion parameters by classifying formation models. Noh et al. (2021) developed a deep learning method to improve inversion efficiency, incorporating a classification module to distinguish between cases with and without fault planes. Wu et al. (2022) used the 2.5D FDM to simulate signal responses under different fault, curved boundary, and unconformity conditions, analyzing variations in the instrument's maximum detection range. Zhao et al. (2024) applied a coupled physics-driven and data-driven approach to tackle the 2.5D inversion problem, enabling the retrieval of formation parameters under varying dip angles and fault conditions. Overall, while significant progress has been made, further improvements in the computational efficiency of the 2.5D algorithm are necessary, along with a clearer understanding of the response patterns of boundary conditions under different geological scenarios, to fully realize the potential of ultra-deep geosteering.

In this paper, we developed a fast forward algorithm and analyzed the calculation results for various detection modes. The first section discusses the investigation characteristics of the Look-around and Look-ahead modes. In the second section, we propose the 2.5-dimensional finite element method (2.5D FEM) to calculate the responses of complex models. Next, we investigate the detection performance of the Look-around and Look-ahead modes in both fault and wedge models. Additionally, we generated crossplots to determine the vertical distance and angle between the instrument and the interface. Based on the findings from the previous sections, a brief conclusion is presented in the final section.

2 Method

Efficiently and rapidly simulating geological structures, such as faults, folds, and unconformities that frequently occur around the wellbore during drilling, is crucial. Currently, two primary approaches address this issue. One method employs a sliding window processing strategy, treating complex geological structures as equivalent layered models for calculation. However, this approach is suitable only for structurally simple and gradually changing formations and does not guarantee precision (Bakr et al., 2017; Pardo and Torres-Verdín, 2015; Hu et al., 2018). The alternative method utilizes 3D numerical algorithms to simulate geological models in detail, achieving high-precision results (Davydycheva et al., 2003; Jahani et al., 2023; Davydycheva et al., 2023). However, the substantial computational workload and resource consumption lead to reduced computational efficiency, making it inadequate for the real-time demands of logging while drilling.

2.1 Governing equation

In the calculation of electromagnetic wave logging, a magnetic dipole is employed as a source during simulation to address the substantial difference between the spacing and the size of the coils, allowing for the solution of the spatial electromagnetic field. Assuming the time factor is e^{-iwt}, in the quasi-steady-state situation, the Maxwell's equations can be expressed as:

$$\nabla \times \boldsymbol{E} - i\omega\boldsymbol{\mu}\boldsymbol{H} = -\boldsymbol{M}_i$$

$$\nabla \times \boldsymbol{H} - \boldsymbol{\sigma}\boldsymbol{E} = \boldsymbol{J}_i$$

where $\boldsymbol{E}$ and $\boldsymbol{H}$ represent electric fields and magnetic fields, the $\boldsymbol{\mu}$ and $\boldsymbol{\sigma}$ represent the magneto conductivity and conductivity, the $\boldsymbol{J}_i$ and $\boldsymbol{M}_i$ represent the current density and the magnetic current density.

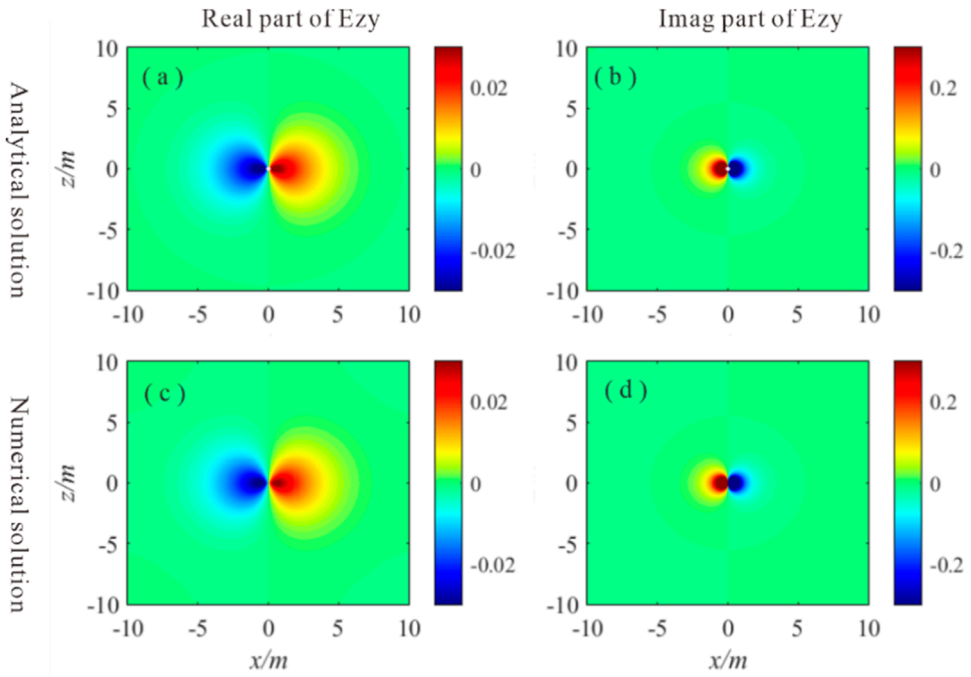

FIGURE 1
Electromagnetic field distribution of Ezy. **(A, B)** are the real parts and imaginary of Ezy calculated using the analytical method; **(C, D)** are the real parts and imaginary of Ezy calculated using the numerical method.

The instrument detects signals during the drilling process, remaining unaffected by borehole invasion and mud interference. Typically, the properties of the formation remain stable and unchanged along a certain direction during actual detection, assuming characteristic alignment along the y-axis. To leverage this stability, the spatial Fourier transform can replace solving problems in the 3D spatial domain with a series of 2D spectral domain problems, effectively reducing the dimensionality of the computational model. Based on the frequency domain differential properties of the spatial Fourier transform, the following Equation can be obtained:

$$\hat{F}\left[\frac{\partial f}{\partial y}\right] = \int_{-\infty}^{\infty} \frac{\partial f(x,y,z)}{\partial y} e^{-ik_y y} dy = ik_y \int_{-\infty}^{\infty} f(x,y,z) e^{-ik_y y} dy$$
$$= ik_y \hat{F}\left(x,k_y,z\right)$$

where $\hat{F}$ represent the spatial Fourier transform. By using the above equation, we can obtain the expression of the magnetic field in the x and z directions in the spectral domain.

$$\hat{H}_x = -\frac{ik_y}{\gamma_z^2}\frac{\partial \hat{H}_y}{\partial x} + \frac{\sigma_z}{\gamma_z^2}\frac{\partial \hat{E}_y}{\partial z} - \frac{\sigma_z}{\gamma_z^2} M_{s,x}\delta(A)$$

$$\hat{H}_z = -\frac{ik_y}{\gamma_x^2}\frac{\partial \hat{H}_y}{\partial z} - \frac{\sigma_x}{\gamma_x^2}\frac{\partial \hat{E}_y}{\partial x} - \frac{\sigma_x}{\gamma_x^2} M_{s,z}\delta(A)$$

and the electrical field in x and z directions is

$$\hat{E}_x = \frac{i\omega\mu_0}{\gamma_x^2}\frac{\partial \hat{H}_y}{\partial z} - \frac{ik_y}{\gamma_x^2}\frac{\partial \hat{E}_y}{\partial x} - \frac{ik_y}{\gamma_x^2} M_{s,z}\delta(A)$$

$$\hat{E}_z = -\frac{i\omega\mu_0}{\gamma_z^2}\frac{\partial \hat{H}_y}{\partial x} - \frac{ik_y}{\gamma_z^2}\frac{\partial \hat{E}_y}{\partial z} + \frac{ik_y}{\gamma_z^2} M_{s,x}\delta(A)$$

where the $\hat{H}_x$ and $\widehat{E}_x$ represent the magnetic field and electrical field in spectral domain, respectively. $\gamma_z^2 = k_y^2 - i\omega\mu_0\sigma_z$ and $\gamma_x^2 = k_y^2 - i\omega\mu_0\sigma_x$.

2.2 Grid meshing and resistivity assignment

In finite element algorithms, the accuracy of simulation results is influenced by the density of the discretized mesh. Finer mesh refinement enhances simulation accuracy but results in a significant decline in computational efficiency. Therefore, it is crucial to partition the geological model judiciously. Given that the geological models targeted by multi-component electromagnetic logging exhibit relatively gentle undulations, structured meshes can be utilized within a specific precision range to effectively reduce the size of the solution matrix and enhance computational efficiency. This algorithm employs non-uniform mesh partitioning to balance computational accuracy and efficiency. The mesh partitioning strategy is outlined as follows: (1) To ensure the stability of the signal source and the accuracy of multi-component field solutions, uniform sampling is required between the transmitting and receiving antennas; (2) The mesh length gradually increases from the coil system to the boundary of the solution, with the mesh length increment factor maintained within the range of 1–1.1; (3) Due to the skin effect, the electromagnetic field decays exponentially with distance from the source. Since the signal source is always at the origin, the solution boundary is set at four times the skin depth from the source.

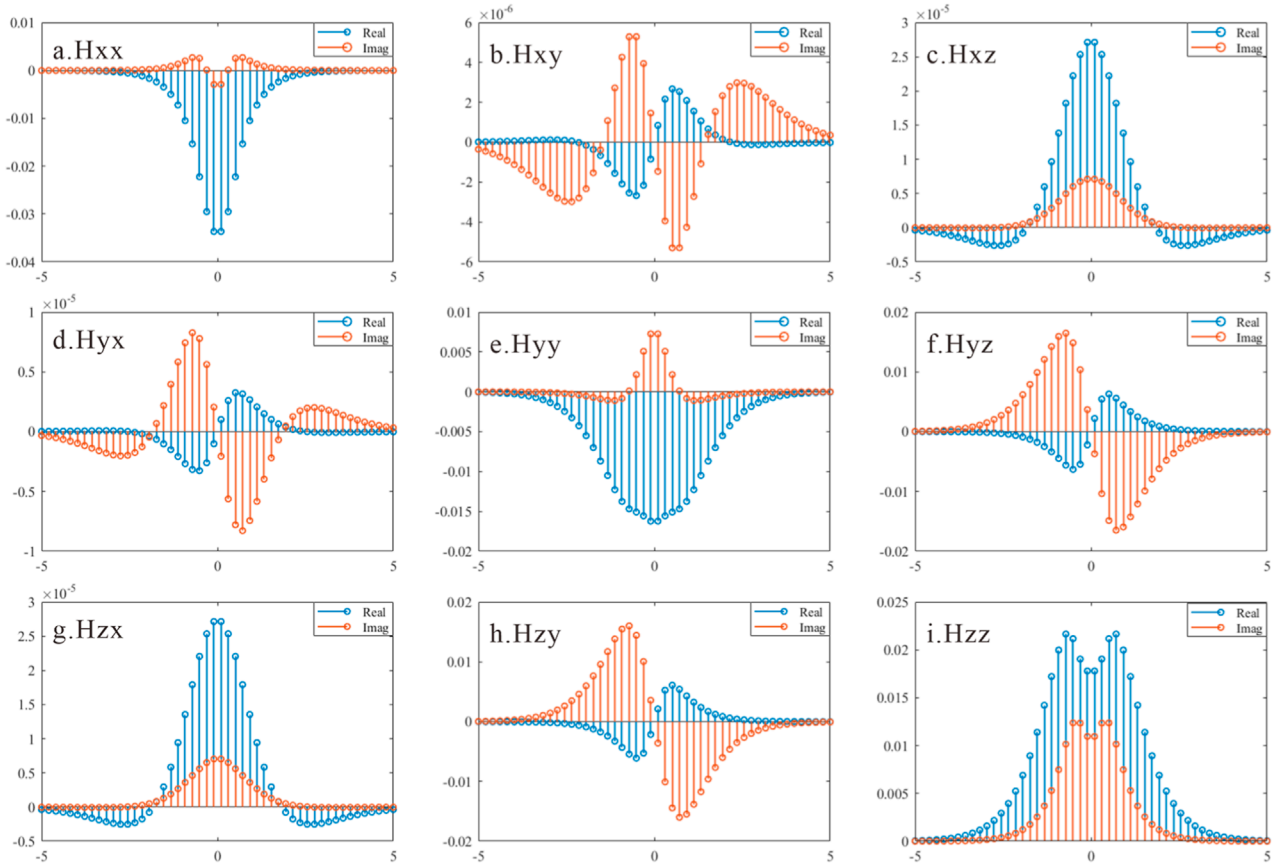

FIGURE 2
Magnetic dipole response of different components in the spectral domain. **(A-C)** are the Hxx, Hxy and Hxz signals; **(D-F)** are the Hyx, Hyy and Hyz signals; **(G-I)** are the Hzx, Hzy and Hzz signals. The blue lines and red lines represent the real part and the imaginary part of response.

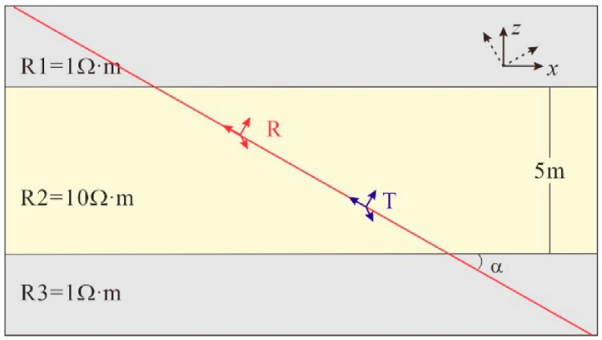

FIGURE 3
The model of the 1D formation. The red line represent the wellbore trajectory.

2.3 Singularity of signal source

Setting up multiple-component field sources in 2.5D FEM presents several challenges, which are primarily addressed by two approaches: the pseudo-Dirac source method and the application of a background field with spectral domain solutions. The pseudo-Dirac source method, introduced by Herrmann in 1979 and widely employed in electromagnetic exploration as well as marine-controlled source electromagnetic methods, offers computational simplicity but exhibits reduced accuracy near source points. In contrast, the background field method provides higher accuracy but is more complex and less efficient. Given the importance of computational efficiency in multi-component drilling well logging, where only field values at receiving antennas are required, this paper adopts the pseudo-Dirac source method for simulation verification. The signal source utilized in this study, exemplified for the x-direction, is as follows:

$$M_{s,x}(x-x_0) = \frac{1}{2\tau}\begin{cases} 0 & (x-x_0) \le -2\tau \\ (x-x_0+2\tau)/\tau^2/2 & -2\tau(x-x_0) \le -\tau \\ -(x-x_0+2\tau)/\tau^2/2+2(x-x_0+2\tau)/\tau-1 & -\tau(x-x_0) \le \tau \\ (x-x_0+2\tau)/\tau^2/2-4(x-x_0+2\tau)/\tau+8 & \tau(x-x_0) \le 2\tau \\ 0 & 2\tau(x-x_0) \end{cases}$$

where x_0 is the source point coordinates, τ is the length of the unit grid near the signal source.

We evaluated the accuracy of the pseudo-Dirac source method by comparing its field distribution with that obtained from an

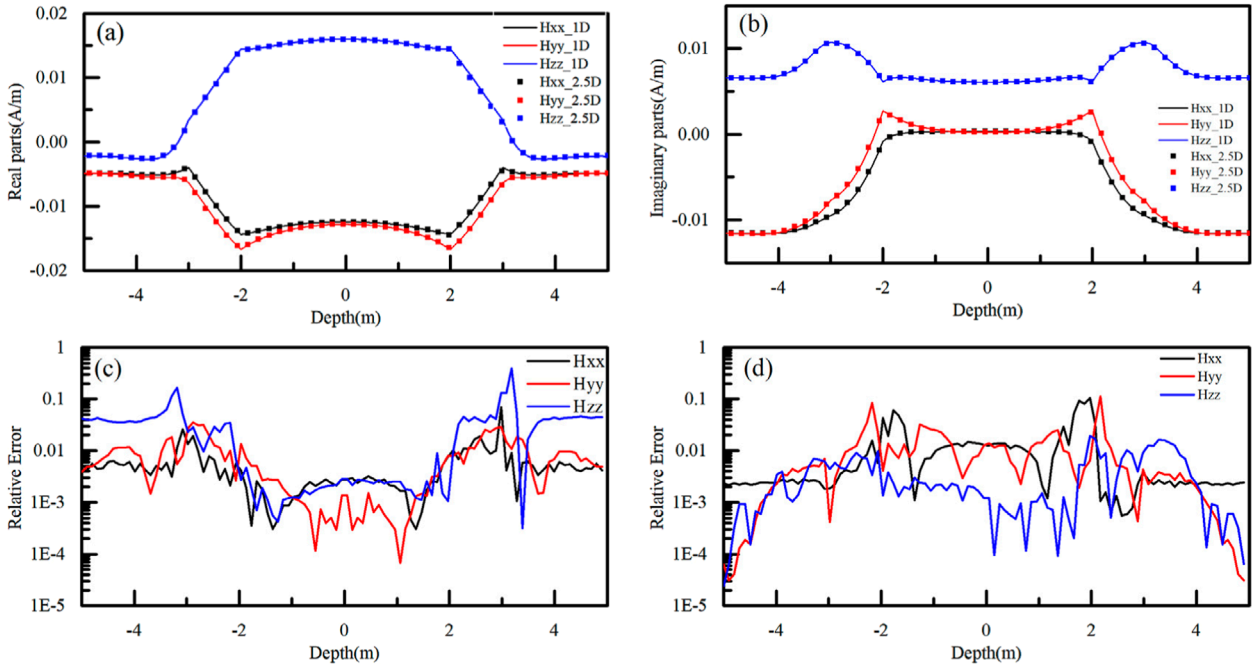

FIGURE 4
Validation of coplanar an coaxial signals in a 1D layered model. **(A, B)** are the real parts and imaginary parts of signal, the curves and the scatters are from the analytical solutions and the 2.5D algorithm. **(C, D)** are the relative errors of real and imaginary parts between the analytical solutions and the 2.5D algorithm.

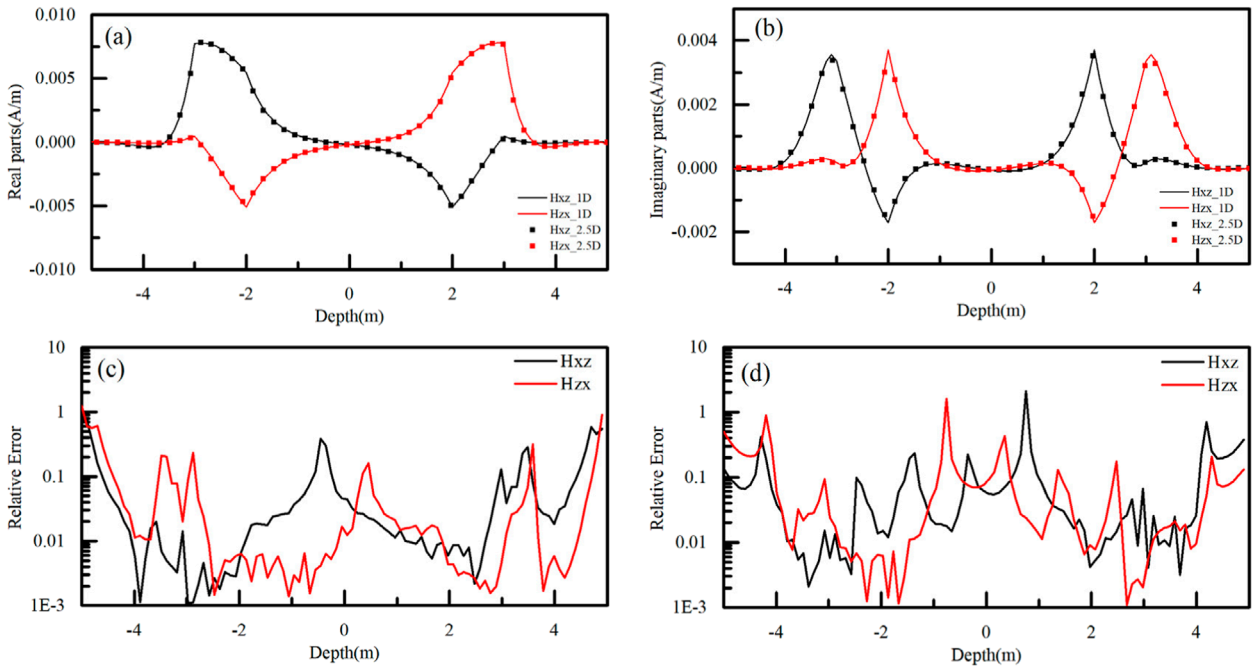

FIGURE 5
Validation of orthogonal signals in a 1D layered model. **(A, B)** are the real parts and imaginary parts of signal, the curves and the scatters are from the analytical solutions and the 2.5D algorithm. **(C, D)** are the relative errors of real and imaginary parts between the analytical solutions and the 2.5D algorithm.

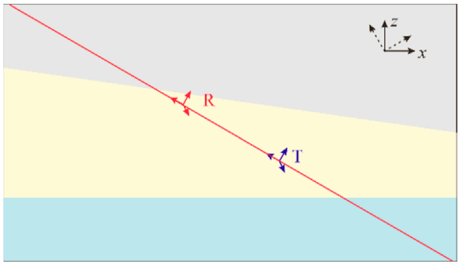

FIGURE 6
The model of the 2D formation. The red line represents the wellbore trajectory. T and R are the transmitter and receiver.

analytical approach. In a uniform formation with a resistivity of 10 Ω·m and a signal frequency of 400 kHz, we examined the spatial distribution of the electromagnetic field generated by a magnetic dipole oriented in the z-direction. Under these conditions, the magnetic field component H_{zy} is zero, leaving only the electric field component E_{zy}. Figures 1A–D illustrate the real and imaginary parts of analytical solution and numerical solution, respectively. The results demonstrate that the pseudo-Dirac source method produces outcomes consistent with the analytical solution.

2.4 Spectral domain field characteristics study

In solving for the spatial domain electromagnetic field, the calculation of the spectral domain electromagnetic field is crucial. To investigate this matter, we examined the response characteristics of multi-component signals in the spectral domain under conditions of a uniform medium. In this study, the medium resistivity is set to 10 Ω·m, the signal frequency is 400 kHz, and the spacing is 2 m. The spectral domain responses of the magnetic field signals generated by magnetic dipoles oriented in the x, y, and z directions under these conditions are illustrated in Figure 2. As depicted in this figure, it is evident that the real and imaginary parts of the signals Hxx, Hxz, Hyy, Hxz, and Hzz are even functions in the spectral domain, while Hxy, Hyx, Hyz, and Hzy are odd functions in the spectral domain. Based on this characteristic, the following approximation can be made: The equations should be inserted in editable format from the equation editor.

$$H_*(x, y = y_0, z) = \frac{1}{\pi}\int_{k_y=0}^{\infty} \hat{H}_* e^{-ik_y y_0} dk_y$$

where * represent xx, xz, yy, zx, zz and $\hat{H}$ represent the signal in the spectral domain.

$$H_*(x, y = y_0, z) = 0$$

where * represent xy, yx, yz, zy.

3 Algorithm validation

3.1 1D layered model

As a first example, we establish a three-layer model in Figure 3 to validate the computational accuracy of 2.5D-FEM method. The formation resistivities from top to bottom are 1 Ω·m, 10 Ω·m, 1 Ω·m. The upper and the lower layers are semi-infinite, and the middle layer is 5 m thick. The instrument has drilled from bottom to top with a relative dip angle of 60°. Simulate the induced magnetic field signals with 400 KHz frequency and 2 m spacing.

The simulated results and relative error are shown in Figures 4, 5, validated with the results computed using an analytical solution. It can be observed that the results of analytical solution and 2.5 FEM are almost equivalent, which indicates the 2.5D FEM is accurate. In addition, the relative errors of the real and imaginary parts of coplanar and coaxial signals are generally less than 1%. A slight increase in error occurs when the instrument passes through the interface, which is attributed to the difference between the equivalent resistivity at the boundary and the actual resistivity. For the orthogonal signals, the mean relative error is close to 1%, with larger errors occurring only when the signal amplitude approaches zero. However, in practical calculations, this does not impact the amplitude ratio or phase difference signals.

3.2 2D model

To further demonstrate the computational efficiency of the 2.5D FEM, we established a 2D model in Figure 6. The resistivity of formation from top to bottom are 1 Ω·m, 10 Ω·m, 3 Ω·m. Keep the instrument parameters consistent with the previous section, and the corresponding simulation results are shown in Figure 7. This figure compares the results obtained using the 2.5D finite element method with those from the commercial software COMSOL. It can be seen that both methods show good consistency, demonstrating that the 2.5D finite element algorithm can be used to solve the electromagnetic field distribution of 2D models.

The computation based on the current mesh discretization took a total of 20.23 s. The number of unknowns to be solved is 22,320, with the corresponding matrix size being 22,320 × 22,320, and the number of non-zero elements is 261,764. Additionally, the 2.5D finite element algorithm is based on solving a series of spectral domain 2D problems, with each 2D solution process being independent and non-interfering. This perfectly aligns with the need for parallel computing. Therefore, parallel computation methods can be employed to solve these problems. On a laptop [Intel(R) Core (TM) I7-1360P with 2.20 GHz speed; RAM is 32 GB]. When the number of computation kernel involved in parallel computation is increased from 1 to 12, the computation time per logging point is significantly reduced from 20.23 s to 5.81 s, with the corresponding results shown in Table 1. In contrast, COMSOL requires 362 s, highlighting the significant difference in computational efficiency and fully demonstrating the effectiveness of this method. Moreover, compared to similar 2.5D algorithms (Li et al., 2022), this method has significantly improved computational efficiency. From the table, we can observe that as the number of computation kernel increases,

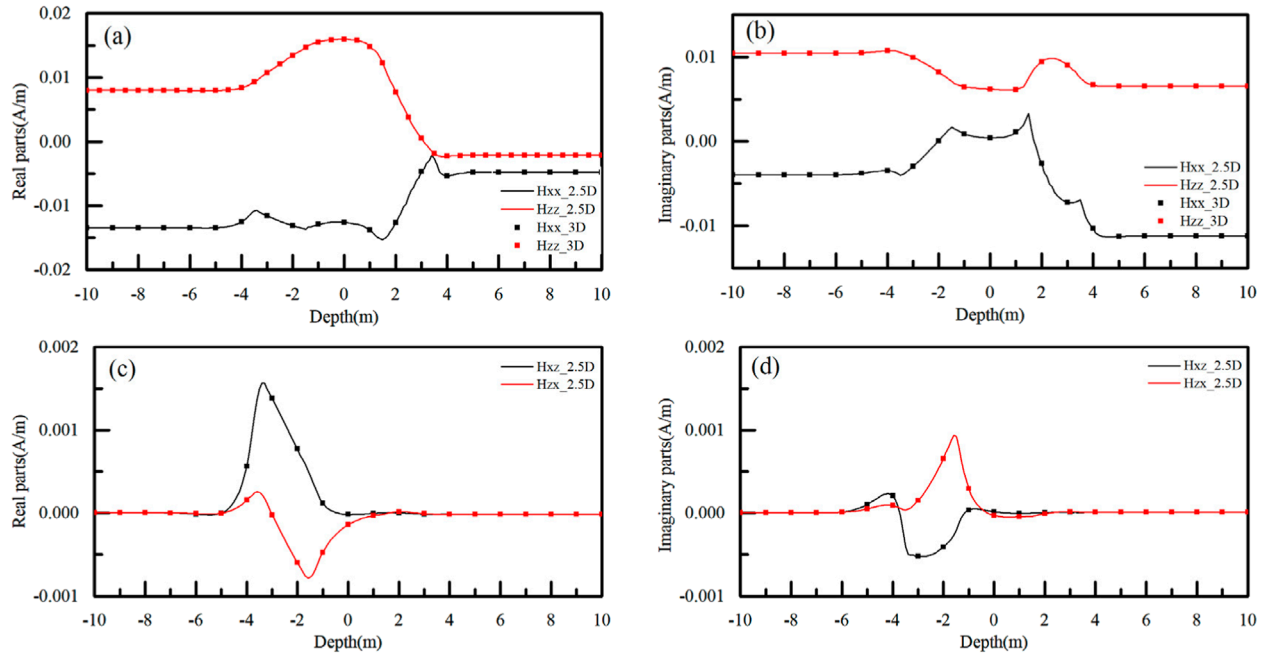

FIGURE 7
Validation of 2.5D FEM in a 2D model. **(A, B)** are the real parts and imaginary parts of Hxx and Hzz signals, the curves and the scatters are from the analytical solutions and the 2.5D algorithm. **(C, D)** are the real parts and imaginary parts of Hxz and Hzx signals. the curves and the scatters are from the analytical solutions and the 2.5D algorithm.

TABLE 1 The parallel computing efficiency under different computation kernel.

Number of computation kernel	1	2	4	6	8	10	12
Computation time/s	20.23	15.13	6.54	6.08	5.98	5.88	5.81
Speedup ratio	1	1.34	3.09	3.33	3.38	3.44	3.48

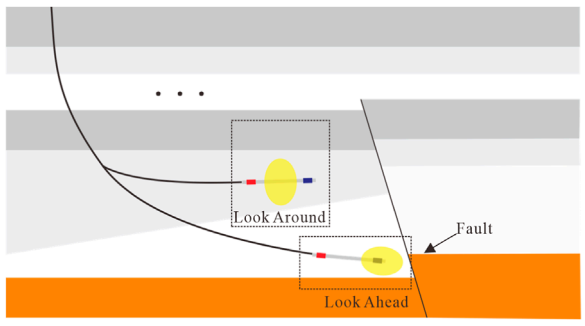

FIGURE 8
The formation model of EDARM. The black line represents the wellbore trajectory. The Look-around and Look-ahead measurement scenarios have been shown in this Figure.

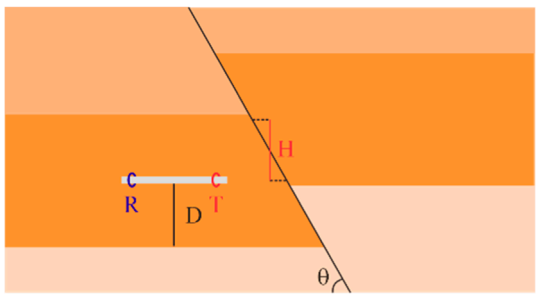

FIGURE 9
The fault model and parameters.

4 Analysis of responses in complex model

the computational efficiency of this method improves significantly. However, when the number of computation kernel exceeds 6, the acceleration effect on the algorithm becomes less noticeable.

EDARM is defined through the combination of multi-component signals. In addition to its capability to obtain formation resistivity and anisotropy, it can also detect the interface around

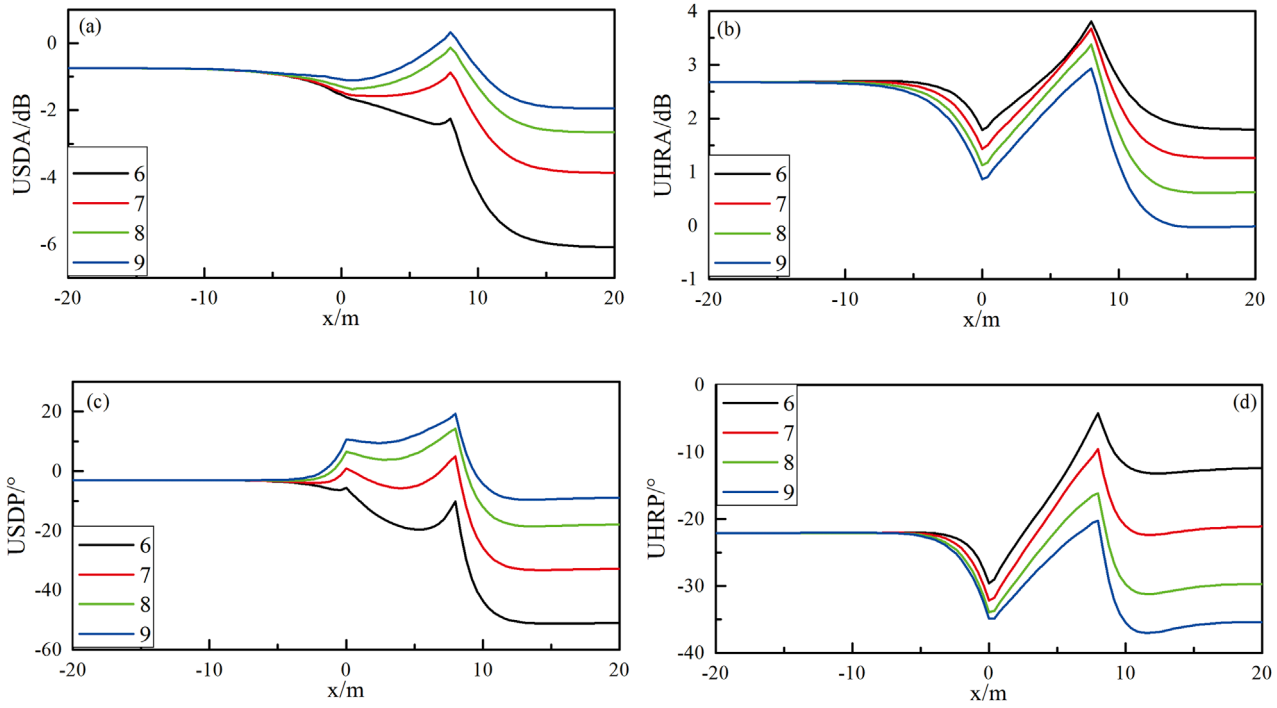

FIGURE 10
The responses of fault model under different H. **(A, C)** represent the ATT and PS signals of Look-around mode; **(B, D)** represent the ATT and PS signals of Look-ahead mode.

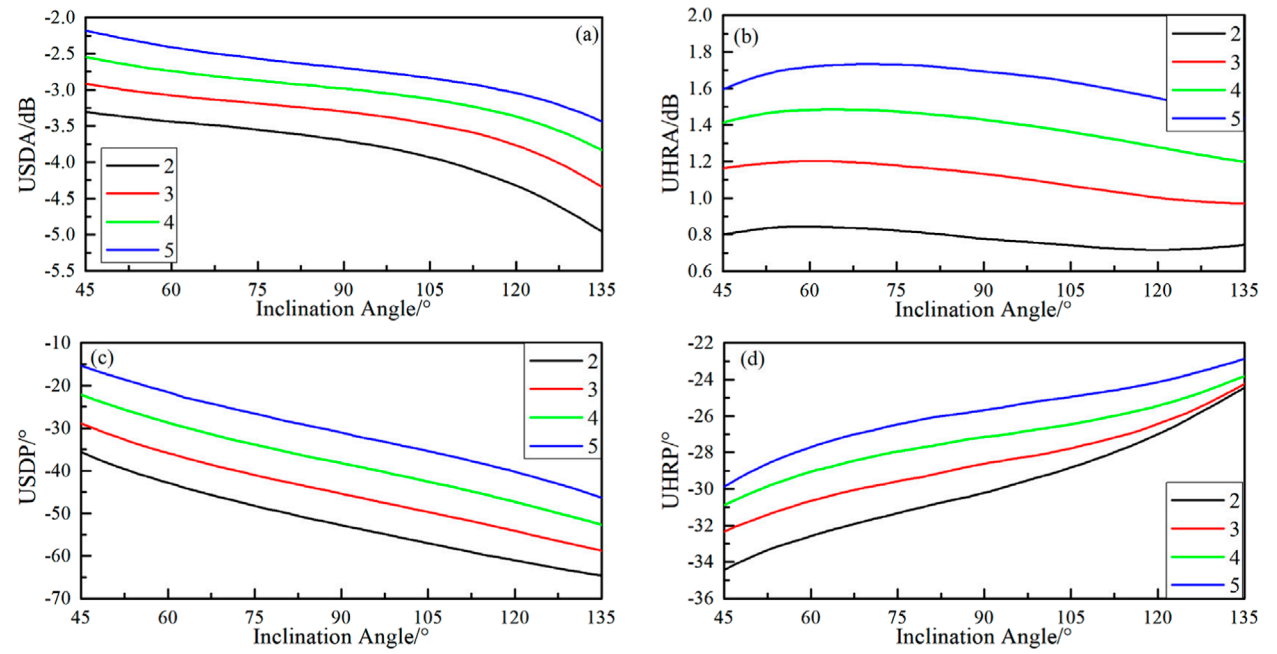

FIGURE 11
The responses of fault model under different angle. **(A, C)** represents the ATT and PS signals of Look-around mode; **(B, D)** represents the ATT and PS signals of Look-ahead mode.

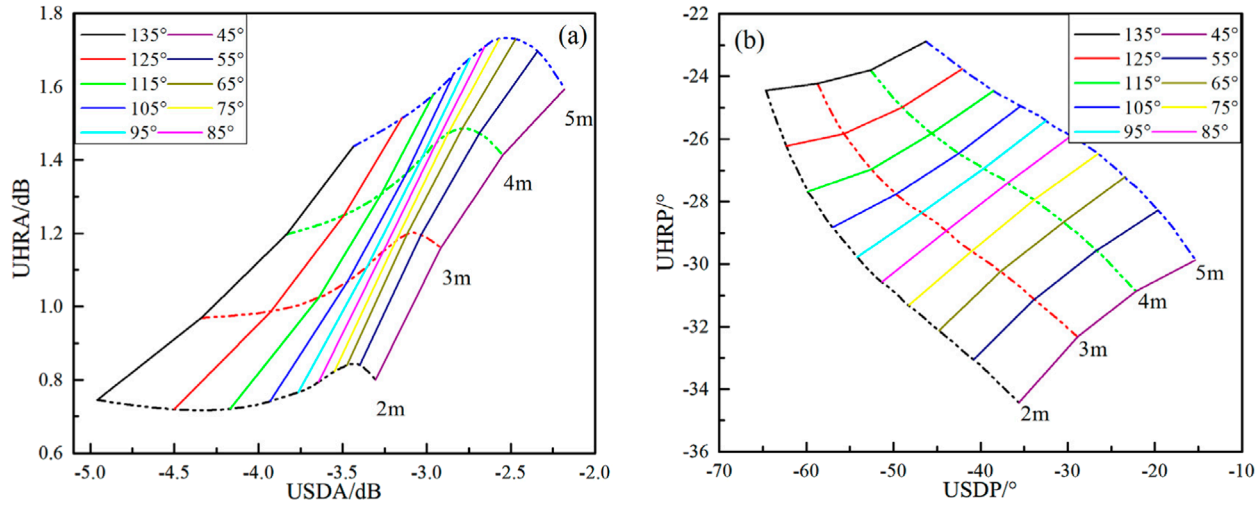

FIGURE 12
The crossplots of Look-around and Look-ahead signals in fault model. **(A, B)** are the crossplots of ATT and PS signals. The solid lines represent the inclination angle, the dashed lines represent the distance between the instrument and boundary.

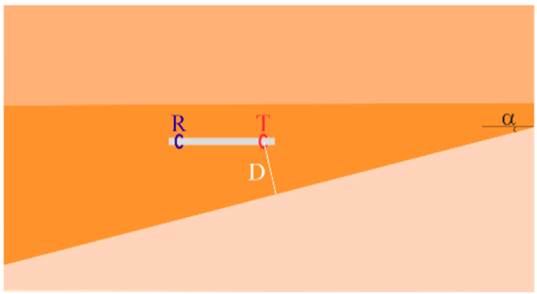

FIGURE 13
The wedge model and parameters.

and ahead of the instrument, greatly enhancing its geosteering ability. The definition of EDARM for boundary detection as follow:

$$USDA = 20\log_{10}\left|\frac{V_{zz}-V_{zx}}{V_{zz}+V_{zx}}\cdot\frac{V_{zz}+V_{xz}}{V_{zz}-V_{xz}}\right|$$

$$USDP = -angle\left(\frac{V_{zz}-V_{zx}}{V_{zz}+V_{zx}}\cdot\frac{V_{zz}+V_{xz}}{V_{zz}-V_{xz}}\right)$$

$$UHRA = 20\log_{10}\left|\frac{2V_{zz}}{V_{xx}+V_{yy}}\right| \quad UHRP = -angle\left(\frac{2V_{zz}}{V_{xx}+V_{yy}}\right)$$

where the USDA and USDP represent the attenuation (ATT) and phase shift (PS) of Look-around mode, the UHRA and UHRP represent the ATT and PS of Look-ahead mode.

To facilitate the explanation of the detection characteristics of Geosphere under different formation model, we adopt the fault and wedge models, which are commonly encountered in actual drilling scenarios (as shown in Figure 8).

4.1 Fault model

Faults play a crucial role in the migration and accumulation of oil and gas, presenting a significant challenge in geosteering. Accurately identifying the location of the interface ahead of the instrument is essential to prevent the drill bit from penetrating the reservoir. To investigate the impact of fault structures on logging responses, a model, as shown in Figure 9, has been developed. Three structural parameters are defined to characterize fault variations: the relative vertical displacement (H) between the upper and lower fault blocks, the distance (D) from the instrument to the fault boundary, and the angle (θ) between the fault plane and the formation interface. Assuming an instrument spacing of 8 m, a signal frequency of 24 kHz, and formation resistivities of 4 Ω·m, 20 Ω·m, and 2 Ω·m (from top to bottom), with a 10 m thick middle layer, the instrument is drilled horizontally from left to right.

4.1.1 Relative vertical displacement

Assuming the distance (D) from the instrument to the boundary is set at 5 m, and the angle between the fault plane and the formation interface is fixed at 30°, the responses of the Look-ahead and Look-around modes were simulated for various relative vertical displacements (H) ranging from 6 m to 9 m. The simulation results are shown in Figure 10, where the x-axis represents the horizontal position of the transmitter, with the fault plane located at x = 0 m. As illustrated in the figure, when the instrument approaches the fault plane at a fixed distance from the upper and lower interfaces (x < 0 m), the Look-around mode signals remain constant, exhibiting no significant abnormalities. However, once the instrument drills through the fault plane (x > 0 m), a noticeable anomaly appears, with the signal difference becoming more pronounced as the instrument nears the interface. In contrast, the Look-ahead mode signals show a clear declining trend as the instrument approaches the fault plane. The signal difference becomes more pronounced as the H value

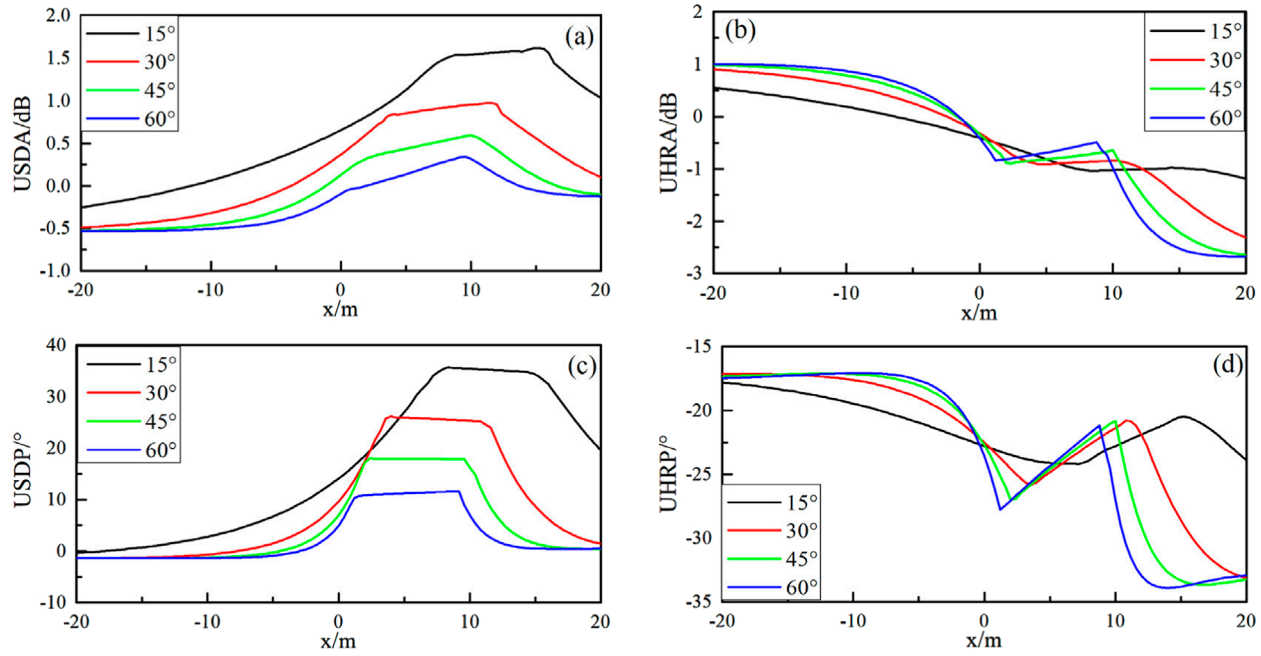

FIGURE 14
The responses of wedge model under different angle. **(A, C)** represents the ATT and PS signals of Look-around mode; **(B, D)** represents the ATT and PS signals of Look-ahead mode.

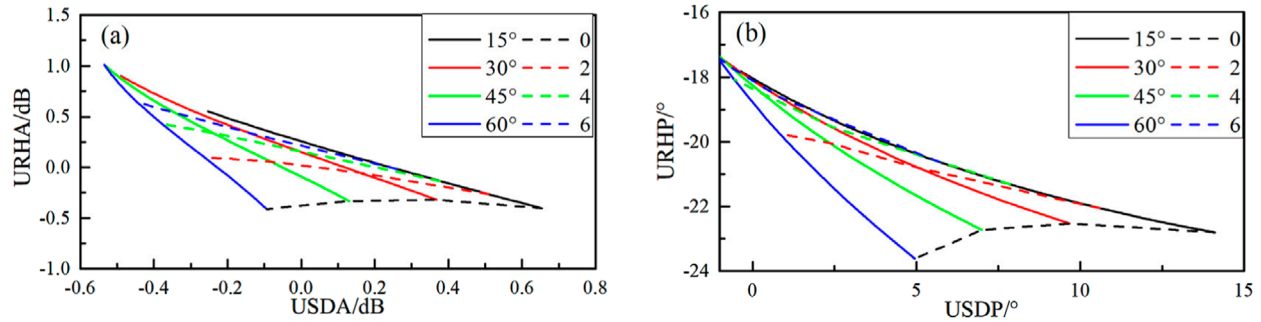

FIGURE 15
The crossplots of Look-around and Look-ahead signals in wedge model. **(A, B)** are the crossplots of ATT and PS signals. The solid lines represent the inclination angle, the dashed lines represent the distance between the instrument and boundary.

increases. Specifically, at H = 9 m, the UHRA and UHRP signals are able to identify the fault plane at distances of 4.6 m and 3.45 m ahead, respectively. Overall, circumferential measurement signals are primarily influenced by the borehole wall interface and are unable to effectively represent the interface ahead of the instrument. In contrast, the signals of Look-around can accurately identify the interface ahead of the drill bit.

4.1.2 Inclination angle

The previous analysis revealed that the Look-around and Look-ahead modes exhibit distinct response patterns to the fault plane. To further investigate the relationship between the measurement signals and the instrument's position relative to the interface, additional simulations were conducted. In these simulations, the instrument parameters were held constant, with the DTB fixed at 1 m and H at 5 m. The distance from the instrument to the fault plane (x) was varied from 2 m to 5 m, while the inclination angle (θ) was considered within a range of 45°–135°. The instrument's position was fixed, and the responses were simulated across varying inclination angles (θ). The results are presented in Figure 11.

The simulations show that both the Look-ahead and Look-around signals exhibit regular variations with changes in the fault plane's inclination angle. Specifically, the Look-around signal decreases as the inclination angle increases, demonstrating a

negative correlation. In contrast, the Look-ahead signal displays more complex behavior with changes in the inclination angle. Among the Look-ahead signals, the amplitude ratio signal (UHRA) is relatively insensitive to the inclination angle, while the phase difference signal (UHRP) shows a strong positive correlation. Overall, both Look-ahead and Look-around measurement signals exhibit clear and consistent trends with respect to the inclination angle, indicating a discernible relationship that warrants further exploration.

The Look-around and Look-ahead detection mode signals were combined under identical geological model conditions to generate crossplots, as shown in Figure 12. In these plots, the x-axis represents the signals of Look-around detection mode, while the y-axis represents the signal of Look-ahead detection mode. The dashed line indicates the distance from the instrument to the fault plane, and the solid line represents the fault plane's inclination angle. The crossplots clearly show that the solid and dashed lines intersect, dividing the plot into distinct zones. During the geosteering process, resistivity characteristics often vary due to the inherent properties of the rock. These resistivity values can be derived using inversion algorithms. Based on this, the corresponding intersection chart can be selected, and the position of the measured data points on the chart can be used to approximate both the distance and the angle between the instrument and the fault plane. Furthermore, a comparison of the two crossplots reveals that, when the fault plane's dip angle is small, the amplitude ratio crossplot is confined to a smaller region, indicating lower signal sensitivity. In contrast, the phase difference signal distribution is more evenly spread across regions, making it easier to detect changes in both the fault dip angle and the distance from the instrument to the fault plane.

4.2 Wedge model

The angles of the upper and lower formation interfaces differ are commonly occur in geosteering study. The wedge model, as shown in Figure 13, is used to investigate the impact of interface dip angle changes on measurement signals. In this model, the instrument is assumed to be parallel to the upper interface and forms an angle α with the lower interface. With the instrument fixed at a distance of 8 m from the upper interface, and maintaining constant instrument parameters and formation resistivity, simulations were conducted for both Look-around and Look-ahead responses under varying α values, as shown in Figure 14.

The figures clearly demonstrate that as the angle α increases, the strength of the Look-around detection signal gradually decreases, while the strength of the Look-ahead detection signal increases. Similar to the earlier analysis of fault structures, a noticeable separation between the curves is observed at different angles. This behavior suggests that a crossplot can be used to assess the relative position of the instrument in relation to the formation interface.

Figure 15 presents a crossplot of the Look-around and Look-ahead signals. The axes of this plot are consistent with those in Figure 15, where the solid line represents the angle between the instrument and the formation interface, and the dashed line indicates the perpendicular distance from the transmitting antenna to the interface. The plot clearly shows that the curves intersect, dividing the plot into several regions. Notably, when the angle is larger and the distance to the interface is shorter, the occupied area expands, making it easier to extract the corresponding values from the crossplot.

5 Discussion

This study introduces a novel 2.5D FEM fast forward algorithm, along with simulations tailored for specific drilling geological orientation scenarios, which offer new insights into signal processing and interface identification. The new algorithm significantly improves computational efficiency by using a pseudo-Dirac function for the signal source equivalence and signal spectrum domain analysis. With the integration of parallel computing, the computation time for a single point is reduced to under 6 s, offering improved efficiency compared to other algorithms. In addition, for specific fault model and wedge model analysis, a fast identification method for interface position and angle is proposed for the first time. This method is applicable to most scenarios in drilling geological orientation. The fast and efficient forward algorithm, along with the simple interface identification method, provides algorithmic support and initial value optimization for the inversion of formation interfaces. This approach effectively addresses the issue of low processing efficiency in existing ultra-deep geological orientation.

Data availability statement

The original contributions presented in the study are included in the article/Supplementary Material, further inquiries can be directed to the corresponding author.

Author contributions

PZ: Conceptualization, Data curation, Formal Analysis, Funding acquisition, Investigation, Methodology, Resources, Supervision, Validation, Visualization, Writing–original draft, Writing–review and editing. SD: Funding acquisition, Methodology, Resources, Validation, Writing–original draft. XY: Formal Analysis, Methodology, Visualization, Writing–review and editing. FL: Data curation, Funding acquisition, Validation, Writing–review and editing. WX: Data curation, Supervision, Validation, Visualization, Writing–review and editing.

Funding

The author(s) declare that financial support was received for the research, authorship, and/or publication of this article. This research was funded by Natural Science Foundation of Xinjiang Uygur Autonomous Region (2022D01B140 and 2021D01E22), Research Foundation of China University of Petroleum-Beijing at Karamay (XQZX20230009), National Natural Science Foundation of China (42204121), Research project of the Tianchi Talent Introduction Plan in Xinjiang Uygur Autonomous Region and

Karamay Science and Technology Plan Project (Innovative Talents) 20232023hjcxrc0052.

Conflict of interest

Author XY was employed by Sinopec Matrix Corporation.

The remaining authors declare that the research was conducted in the absence of any commercial or financial relationships that could be construed as a potential conflict of interest.

Generative AI statement

The author(s) declare that no Generative AI was used in the creation of this manuscript.

Publisher's note

Supplementary material

The Supplementary Material for this article can be found online at: https://www.frontiersin.org/articles/10.3389/feart.2025.1506238/full#supplementary-material

References

Bakr, S. A., Pardo, D., and Torres-Verdín, C. (2017). Fast inversion of logging-while-drilling resistivity measurements acquired in multiple wells. *Geophysics* 82 (3), E111–E120. doi:10.1190/geo2016-0292.1

Bell, C., Hampson, J., Eadsforth, P., Chemali, R., Helgesen, T., Meyer, H., et al. (2006). "Navigating and imaging in complex geology with azimuthal propagation resistivity while drilling," in *SPE annual technical conference and exhibition*, SPE–102637.

Bittar, M., and Aki, A. (2015). Advancement and economic benefit of geosteering and well-placement technology. *Lead. Edge* 34 (4), 524–528. doi:10.1190/tle34050524.1

Bittar, M., Klein, J., Beste, R., Hu, G., Wu, M., Pitcher, J., et al. (2009). A new azimuthal deep-reading resistivity tool for geosteering and advanced formation evaluation. *SPE Reserv. Eval. & Eng.* 12 (02), 270–279. doi:10.2118/109971-pa

Constable, M. V., Antonsen, F., Stalheim, S. O., Olsen, P. A., Fjell, Ø. Z., Dray, N., et al. (2016). "Looking ahead of the bit while drilling: from vision to reality," in *SPWLA 57th annual logging symposium*.

Davydycheva, S., Druskin, V., and Habashy, T. (2003). An efficient finite-difference scheme for electromagnetic logging in 3D anisotropic inhomogeneous media. *Geophysics* 68 (5), 1525–1536. doi:10.1190/1.1620626

Davydycheva, S., Torres-Verdín, C., Hou, J., Saputra, W., Rabinovich, M., Antonsen, F., et al. (2023). "3D electromagnetic modeling and quality control of ultradeep borehole azimuthal resistivity measurements," in *SPWLA annual logging symposium* (Lake Conroe, Texas, USA: SPWLA), D041S013R002.

Dupuis, C., and Denichou, J. M. (2015). Automatic inversion of deep-directional-resistivity measurements for well placement and reservoir description. *Lead. Edge* 34 (5), 504–512. doi:10.1190/tle34050504.1

Hagiwara, T. (2018). "Detection sensitivity and new concept of deep reading look-ahead look-around geosteering tool," in *SEG international exposition and annual meeting* (Anaheim, California, USA: October).

Hartmann, A., Vianna, A., Maurer, H. M., Sviridov, M., Martakov, S., Lautenschläger, U., et al. (2014). "Verification testing of a new extra-deep azimuthal resistivity measurement," in *SPWLA annual logging symposium*.

Hu, X., and Fan, Y. (2018). Huber inversion for logging-while-drilling resistivity measurements in high angle and horizontal wells. *Geophysics* 83 (4), D113–D125. doi:10.1190/geo2017-0459.1

Hu, X. F., Fan, Y. R., Wu, F., Lei, W., and XiYong, Y. (2018). Fast multiple parameter inversion of azimuthal LWD electromagnetic measurement. *Chin. J. Geophys.* 61 (11), 4690–4701. doi:10.6038/cjg2018L0746

Iverson, M., Fejerskov, M., Skjerdingstad, A., Clark, A. J., Denichou, J. M., Ortenzi, L., et al. (2004). Geosteering using ultradeep resistivity on the Grane field, Norwegian North Sea. *Petrophysics* 45 (3), 232–240.

Jahani, N., Torres-Verdín, C., and Hou, J. (2023). Limits of three-dimensional target detectability of logging while drilling deep-sensing electromagnetic measurements from numerical modelling. *Geophys. Prospect.* 72, 1146–1162. doi:10.1111/1365-2478.13451

Larsen, D. S., Hartmann, A., Luxey, P., Martakov, S., Skillings, J., Tosi, G., et al. (2015). "Extra-deep azimuthal resistivity for enhanced reservoir navigation in a complex reservoir in the Barents Sea," in *SPE annual technical conference and exhibition. September*.

Li, H., Wu, Z., and Yue, X. (2022). A near-optimal quadrature for 2.5 D EM logging-while-drilling tool modeling. *J. Appl. Geophys.* 207, 104841. doi:10.1016/j.jappgeo.2022.104841

Li, H., and Zhou, J. (2017). "Distance of detection for LWD deep and ultra-deep azimuthal resistivity tools," in *SPWLA annual logging symposium* (Oklahoma City, Oklahoma, USA: SPWLA. June), D053S013R009.

Li, Q., Omeragic, D., and Chou, L. E. F. (2005). "New directional electromagnetic tool for proactive geosteering and accurate formation evaluation while drilling," in *SPWLA annual logging symposium* (SPWLA). SPWLA-2005-UU.

Li, S., Chen, J., and Binford, J. R. (2014). "Using new LWD measurements to evaluate formation resistivity anisotropy at any dip angle," in *SPWLA annual logging symposium* (Abu Dhabi, United Arab Emirates: SPWLA). SPWLA-2014-EEEE.

Liang, P., Di, Q., Chen, W., Zhang, W., Liu, R., and Li, X. (2023). An EM LWD tool for deep reading looking-ahead. *IEEE Access* 11, 142601–142610. doi:10.1109/access.2023.3339777

Lu, H., Shen, Q., Chen, J., Wu, X., and Fu, X. (2019). Parallel multiple-chain DRAM MCMC for large-scale geosteering inversion and uncertainty quantification. *J. Petroleum Sci. Eng.* 174, 189–200. doi:10.1016/j.petrol.2018.11.011

Noh, K., Pardo, D., and Torres-Verdín, C. (2021). 2.5-D deep learning inversion of LWD and deep-sensing EM measurements across formations with dipping faults[J]. *IEEE Geoscience Remote Sens. Lett.* 19, 1–5. doi:10.1109/lgrs.2021.3128965

Omeragic, D., Li, Q., Chou, L., Yang, L., Duong, K., Smits, J. W., et al. (2005). *Deep directional electromagnetic measurements for optimal well placement*. Dallas, Texas, USA: SPE Annual Technical Conference and Exhibition.

Pardo, D., and Torres-Verdín, C. (2015). Fast 1D inversion of logging-while-drilling resistivity measurements for improved estimation of formation resistivity in high-angle and horizontal wells. *Geophysics* 80 (2), E111–E124. doi:10.1190/geo2014-0211.1

Rodríguez-Rozas, Á., and Pardo, D. (2016). *A priori* Fourier analysis for 2.5 D finite elements simulations of logging-while-drilling (LWD) resistivity measurements. *Procedia Comput. Sci.* 80, 782–791. doi:10.1016/j.procs.2016.05.368

Rodríguez-Rozas, Á., Pardo, D., and Torres-Verdín, C. (2018). Fast 2.5 D finite element simulations of borehole resistivity measurements. *Comput. Geosci.* 22, 1271–1281. doi:10.1007/s10596-018-9751-7

Seydoux, J., Legendre, E., Mirto, E., Dupuis, C., Jean-Michel, D., Bennett, N., et al. (2014). Full 3D deep directional resistivity measurements optimize well placement and provide reservoir-scale imaging while drilling. In *SPWLA annual logging symposium* Abu Dhabi, United Arab Emirates: SPWLA-2014.

Thiel, M., Bower, M., and Omeragic, D. (2018). 2D reservoir imaging using deep directional resistivity measurements. *Petrophysics* 59 (02), 218–233. doi:10.30632/pjv59n2-2018a7

Wang, L., Deng, S., Zhang, P., Cao, Y. C., Fan, Y. R., and Yuan, X. Y. (2019a). Detection performance and inversion processing of logging-while-drilling extra-deep azimuthal resistivity measurements. *Petroleum Sci.* 16 (5), 1015–1027. doi:10.1007/s12182-019-00374-4

Wang, L., and Fan, Y. (2019). Fast inversion of logging-while-drilling azimuthal resistivity measurements for geosteering and formation evaluation. *J. Petroleum Sci. Eng.* 176, 342–351. doi:10.1016/j.petrol.2019.01.067

Wang, L., Fan, Y. R., Huang, R., Yu-Jiao, H., Zhen-Guan, W., Dong-Hui, X., et al. (2015). Three dimensional Born geometrical factor of multi-component induction logging in anisotropic media. *Acta Phys. Sin.* 64 (23), 239301. doi:10.7498/aps.64.239301

Wang, L., Li, H., and Fan, Y. R. (2019b). Bayesian inversion of logging-while-drilling extra-deep directional resistivity measurements using parallel tempering Markov chain Monte Carlo sampling. *IEEE Trans. Geoscience Remote Sens.* 57 (10), 8026–8036. doi:10.1109/tgrs.2019.2917839

Wu, H. H., Golla, C., Parker, T., Clegg, N., and Monteilhet, L. (2018). "A new ultra-deep azimuthal electromagnetic LWD sensor for reservoir insight," in *SPWLA annual logging symposium* (London, UK: SPWLA).

Wu, Z., Fan, Y., Wang, J., Zhang, R., and Liu, Q. H. (2019). Application of 2.5-D finite difference method in logging-while-drilling electromagnetic measurements for complex scenarios. *IEEE Geoscience Remote Sens. Lett.* 17(4): 577–581. doi:10.1109/lgrs.2019.2926740

Wu, Z., Li, H., Han, Y., Zhang, R., Zhao, J., and Lai, Q. (2022). Effects of formation structure on directional electromagnetic logging while drilling measurements. *J. Petroleum Sci. Eng.* 211, 110118. doi:10.1016/j.petrol.2022.110118

Wu, Z. G., Li, H., and Yue, X. Z. (2023). 2.5-Dimensional modeling of EM logging-while-drilling tool in anisotropic medium on a Lebedev grid. *Petroleum Sci.* 20(1): 249–260. doi:10.1016/j.petsci.2022.09.010

Wu, Z. G., Wang, L., Fan, Y. R., Deng, S. G., Huang, R., and Xing, T. (2020). Detection performance of azimuthal electromagnetic logging while drilling tool in anisotropic media. *Appl. Geophys.* 17 (1), 1–12. doi:10.1007/s11770-020-0804-z

Xia, X., Persello, C., and Koeva, M. (2019). Deep fully convolutional networks for cadastral boundary detection from UAV images. *Remote Sens.* 11 (14), 1725. doi:10.3390/rs11141725

Zhang, P., Deng, S., Hu, X., et al. (2021). Detection performance and inversion processing of logging-while-drilling extra-deep azimuthal resistivity measurements. *Chin. J. Geophys.* 64 (6), 2210–2219.

Zhao, N., Li, N., Xiao, Z., Wang, X., and Qin, C. (2024). Physics-driven deep learning pixel-based inversion of logging-while-drilling in anisotropic formation. *IEEE Trans. Geoscience Remote Sens.* 62, 1–12. doi:10.1109/tgrs.2024.3355463

frontiers | Frontiers in Earth Science

TYPE Original Research
PUBLISHED 22 January 2025
DOI 10.3389/feart.2024.1520486

OPEN ACCESS

EDITED BY
Weichao Yan,
Ocean University of China, China

REVIEWED BY
Lin Zhang,
Hohai University, China
Xin Nie,
Yangtze University, China
Yuhang Guo,
Jilin University, China

*CORRESPONDENCE
Fei Wang,
wangfei@chd.edu.cn
YaFeng Li,
liyafqh@petrochina.com.cn

RECEIVED 31 October 2024
ACCEPTED 24 December 2024
PUBLISHED 22 January 2025

CITATION
Zhang D, Li Y, Guo Y, Xia H, Liu Y, Yan J, Wang F and Wu Y (2025) Research on shale dynamic and static elastic modulus and anisotropy based on pressurization history. *Front. Earth Sci.* 12:1520486. doi: 10.3389/feart.2024.1520486

Research on shale dynamic and static elastic modulus and anisotropy based on pressurization history

Di Zhang[1,2], YaFeng Li[1,2]*, YaNan Guo[1,2], HanLin Xia[1,2], YanXin Liu[1,2], JiaShen Yan[1,2], Fei Wang[3]* and YinTing Wu[3]

[1]Exploration and Development Research Institute, Qinghai Oilfeld Company, PetroChina, Dunhuang, China, [2]Qinghai Provincial Key Laboratory of Plateau Saline - Lacustrine Basinal Oil & Gas Geology, Dunhuang, China, [3]College of Geological Engineering and Mapping, Chang'an University, Xi'an, China

The dynamic and static elastic parameters of rocks exhibit differences. It is of great practical significance to carry out experiments on dynamic and static elastic parameters of rocks under reservoir conditions and determine the conversion relationship between dynamic and static elastic parameters. In this study, shale oil samples from the second member of Kongdong sag in Dagang Oilfield were analyzed by triaxial compression experiments at different bedding angles and longitudinal and shear wave velocity tests. Dynamic and static stiffness coefficient, elastic modulus and acoustic wave velocity change under different directions of pressure and pressure relief. The results indicate that the P-wave velocity, fast shear wave velocity, slow shear wave velocity, dynamic and static Young's modulus exhibit an increase as the confining pressure rises, and the parameters are greater during the unloading process than during loading process. At identical confining pressures, the dynamic Young's modulus measured by cores with parallel bedding plane is greater than that measured by cores with vertical bedding plane. The dynamic and static elastic mechanical parameters of different bedding angles can be transformed under varying pressures, and the dynamic elastic mechanical parameters measured under varying levels of confining pressure can be transformed into static elastic mechanical parameters under equivalent confining pressures, which offer fundamental parameters for examining rock mechanics properties and serving as a reference for developing fracturing construction plans for oil and gas reservoirs.

KEYWORDS

shale, elastic modulus, anisotropy, rock physics, rock mechanics

1 Introduction

Because of tight lithology and low natural productivity, most shale oil reservoirs necessitate fracturing techniques to achieve economically viable output. The mechanical properties of the reservoir rocks serve as the fundamental basis for the design of fracturing operations. Methods to quantify the elastic parameters of rocks include both static and dynamic approaches (Cheng and Johnston, 1981; Fjær, 2019; Bian et al., 2015; Gong et al., 2019; Wang et al., 2020a), the determination of static elastic mechanical parameters involves measuring the deformation of rock samples subjected to static

loading conditions, whereas the dynamic parameters are derived through calculations based on the velocity of sound waves propagating within those rock samples. Given the distinctive features of underground engineering, it is advisable to adopt the static elastic parameters of rock in practical engineering applications. Nevertheless, acquiring these static elastic parameters involves extracting cores from underground locations and conducting laboratory tests, a process that is both time-consuming and costly. To obtain accurate static elastic parameters under actual reservoir conditions, it is essential to replicate the temperature and pressure conditions within the reservoir, a more expensive process that often necessitates a substantial amount of core experimental data to precisely characterize the reservoir's mechanical properties. Consequently, in real-world engineering scenarios, dynamic methods such as logging and seismic exploration are commonly employed to assess the mechanical properties of reservoirs. These dynamic techniques enable the acquisition of elastic parameters under authentic reservoir conditions that extend continuously throughout the depth, effectively addressing certain limitations associated with static methods.

As early as 1933, Zisman highlighted the differences that exist between the dynamic and static elastic parameters associated with rocks. After that, many researchers at home and abroad have studied the correlation existing between dynamic elastic parameters (Young's modulus and Poisson's ratio) and static elastic constants of rocks for various lithology (Eissa and Kazi, 1988; Ameen M S et al., 2009; Wang et al., 2020b). However, the connection between the dynamic and static Poisson's ratios is less apparent. The static elastic parameters of rocks are interconnected with the dynamic elastic parameters, and there are some differences. The causes of the variance in the dynamic and static elastic parameters of shale are intricate. The external reasons are mainly the pressurization mode, pressurization conditions, temperature and testing frequency (Gordon and Davis, 1968; Li et al., 2019); The internal reasons are mainly anisotropy of shale, mineral composition, argillaceous content, development of pores and micro-fractures, pore fluid, *etc.* (Hornby et al., 1994; Rickman et al., 2008; Sone and Zoback, 2013; Ghafoori et al., 2018).

Researchers from both national and international backgrounds have performed comprehensive studies on the elements that affect the dynamic and static elastic characteristics of rocks. In terms of temperature, it is considered that the longitudinal and shear wave velocities of rocks decrease as temperature rises, the dynamic Young's modulus decreases with increasing temperature, and the static Young's modulus increases with temperature rise. In terms of pressure, the velocities of longitudinal and transverse waves and the dynamic and static Young's modulus of rock increase with the increase of hydrostatic pressure (Asef and Farrokhrouz, 2010; 2017; Bian et al., 2019; Zhang L et al., 2021). In shale samples perpendicular to the bedding plane, the impact of temperature and pressure on the acoustic and mechanical properties of rocks is similar to that of sandstone (Vernik and Liu, 1997; Sayers, 1999; Wang et al., 2020a; Zhang L et al., 2022), but shale is heterogeneous, and the acoustic and mechanical properties of rocks vary significantly in different directions.

When measuring rock mechanics and acoustic parameters, in addition to the effects of temperature and pressure, the pressurization mode and pressurization history should also be considered. The research shows that the influence of cracks in rock on Young's modulus is different during the compression and decompression stages. Different strain amplitudes will lead to different dynamic and static elastic parameters. The strain amplitude ranges from 10 to 5 to 10–3 in rock mechanics test, and the rock deformation caused by sound waves is about 10–6 in acoustic test. Different dynamic and static load responses lead to different dynamic and static elastic parameters (Tutuncu et al., 1998; Batzle et al., 2006). Fjar (1999) divided the deformation caused by stress into elastic deformation, inelastic deformation caused by normal compression and inelastic deformation caused by shear deformation, and developed a mathematical model to elucidate the distinction between dynamic and static modulus. Wang et al. (2020b) analyzed how sandstone samples exhibit axial and radial strain in response to external stress, and they examined the distinctions between the dynamic and static elastic properties of sandstone through the stress-strain curve. Therefore, when analyzing the response law of various influencing factors to the difference of dynamic and static elastic properties of shale, we must fully consider the influence of pressurization methods and conditions.

In this study, shale oil samples sourced from the second member of Cangdong Sag in Dagang Oilfield served as the focus of the investigation. This study examined the dynamic and static elastic parameters of the rocks from various angles, analyzing the dynamic and static stiffness coefficients, elastic modulus, and acoustic wave velocity of shale under pressurization and depressurization conditions across different directions. The dynamic and static elastic modulus transformation model of rock under different confining pressures is established, which can provide basic parameters for the study of rock mechanics properties under reservoir conditions and provide reference for the formulation of fracturing construction scheme for oil and gas reservoirs.

2 Geological background

Cangdong Sag is positioned on the southern flank of Huanghua Sag in the Bohai Bay Basin, nestled between the Cangxian Uplift, Xuhei Uplift, and Kongdian Uplift. This region constitutes a Cenozoic continental rift lake basin formed amid regional extension, covering an exploration area of approximately 1,760 square kilometers. During the Paleogene period, the geological layers in this region comprise various formations, including the Kongdian Formation, Shahejie Formation, and Dongying Formation, listed in order from the lowest to the highest. The primary exploration horizon for shale oil is the second member of the Kongdian Formation, deposited during a flooding period and exhibiting a thickness ranging from 400 to 600 m. The lithology of the second member of the Konger Formation primarily comprises gray-black to black shale with limited light gray silty sandstone content. The shale found in the second member of the Kongdian Formation is distinguished by its considerable thickness, advantageous parent material for hydrocarbon generation, elevated organic matter content, and high conversion efficiency. On average, the organic matter content surpasses 2.00%, with a mean value of 3.61% and a maximum reaching 11.92%. Additionally, the average potential for

TABLE 1 Basic parameters of shale oil samples in the second member of Kongdong sag.

Sample number	Length/cm	Diameter/cm	Porosity/%	Bulk density/g/cm^3	Total organic carbon (%)	Maturity (%)
A-0°	4.978	2.489	1.3	2.32	6.19	0.11
A-45°	5.142	2.481	1.5	2.37	6.19	0.11
A-90°	5.189	2.490	1.2	2.36	6.19	0.11

hydrocarbon generation is recorded at 22.18 mg/g, while the highest value is 73.00 mg/g.

3 Samples and experimental scheme

3.1 Sample description

3.1.1 Porosity and permeability characteristics of samples

The porosity, permeability and bulk density of shale oil samples with different bedding angles in the second member of Congdong sag were tested by AP-608 overburden porosimeter. The outcomes of the test are presented in Table 1. As can be observed in Table 1 that the porosity of this batch of shale oil samples is between 1.3% and 1.5%, the permeability is 0.01 mD, and the bulk density measurements range from 2.32 to 2.37 g/cm^3, and the basic parameters of samples with different bedding angles are slightly different. The analysis of the sample revealed a total organic carbon content of 6.19% and a maturity level of 0.11%. With both high total organic carbon content and maturity levels, the sample exhibited excellent hydrocarbon generation potential.

3.1.2 Geochemical parameters of shale oil samples

The whole rock analysis and clay content test of different stratified shale oil samples were carried out by using X-ray diffraction, based on this analysis (see Table 2), it is evident that the brittle composition of the various stratified shale oil samples in the second section of the Cangdong Depression hole is relatively high, in which the content of quartz and feldspar brittle minerals is around 60%, the content of dolomite minerals is around 35%, and the content of clay minerals is around 5%. Analysis of the clay mineral content shows (see Figure 1) that the clay minerals consist of illite and ilmenite/montmorillonite layers, with 79% illite and 21% ilmenite/montmorillonite. The ilmenite layer is 35% and the illite layer is 65% of the ilmenite/montmixed layer.

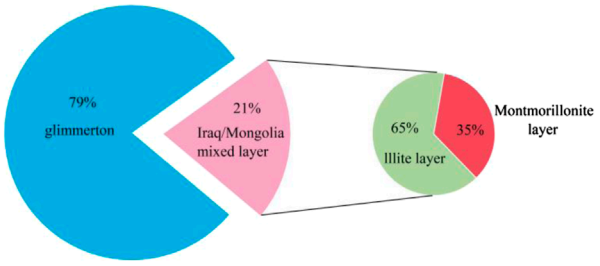

FIGURE 1
Analysis of clay mineral content, total organic carbon content and maturity.

3.2 Experimental equipment and experimental process

3.2.1 Sample preparation

In order to study anisotropy of bedding shale, a plunger sample measuring 2.5 cm in diameter and 5.0 cm in length was extracted from the rock at angles of 0°, 45° and 90° between the bedding plane and the end face of the rock sample by diamond wire cutting, as shown in Figure 2.

In Figure 2, V_p (0°) denotes the longitudinal wave propagating parallel to the symmetry axis, with its vibration direction aligned with the propagation direction. V_p (45°) represents the longitudinal wave propagating at a 45° angle to the symmetry axis, with its vibration direction coinciding with the propagation direction. V_p (90°) indicates the longitudinal wave propagating perpendicular to the symmetry axis, where the propagation and vibration directions are aligned. V_{sh} (0°) describes the shear wave traveling parallel to the symmetry axis, with the vibration direction parallel to the bedding plane. V_{sh} (45°) refers to the shear wave propagating at a 45° angle to the symmetry axis, with the vibration direction perpendicular to the propagation direction. V_{sh} (90°) illustrates the shear wave propagating perpendicular to the symmetry axis, with the vibration direction parallel to the bedding plane. V_{sv} (0°) denotes the shear wave propagating parallel to the symmetry axis, with the vibration direction parallel to the bedding plane. V_{sv} (45°) represents the shear wave propagating at a 45° angle to the symmetry axis, with the vibration direction perpendicular to the propagation direction. V_{sv} (90°) indicates the shear wave propagating perpendicular to the symmetry axis, with the vibration direction perpendicular to the bedding plane.

3.2.2 Experimental device

This study needs to test the acoustic and mechanical characteristics of rocks at the same time. The instrument in question is a multifunctional rock acoustic and mechanical

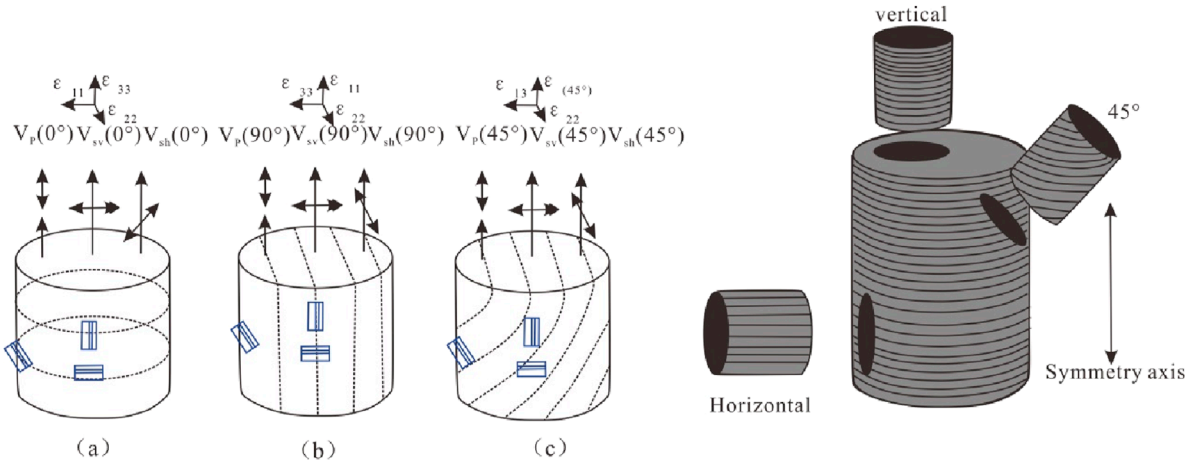

FIGURE 2
Shale coring azimuth diagram at different angles.

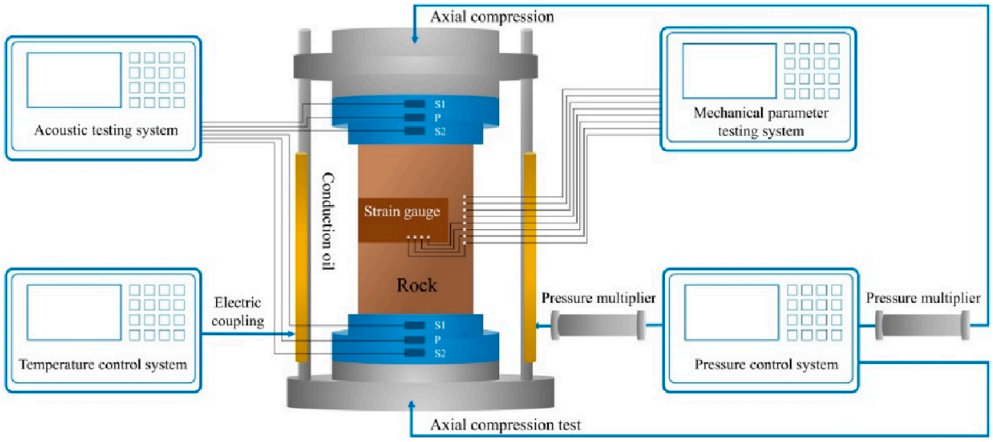

FIGURE 3
Joint measurement system of rock sample acoustics and mechanics.

parameter measuring system (Figure 3), this system is engineered to conduct acoustic and triaxial mechanical experiments on rock samples under reservoir conditions, with temperatures reaching as high as 150°C and pressures up to 68 MPa. When measuring mechanical parameters, apart from pore pressure and confining pressure, it can also produce axial pressure of about 820 kN at most; There are two ways to measure strain: strain gauge or LVDT. The equipment can be operated by manual control, software control and script control, and can be automatically measured. To enhance the precision of radial strain measurement, this test intends to utilize a strain gauge for measuring shale strain.

The acoustic probe integrates a pair of longitudinal wave transducers and two pairs of orthogonally polarized shear wave transducers, with central frequencies of 0.8 and 0.45 MHz, respectively.

3.2.3 Experimental process

The confining pressure is kept at 30 MPa, and the deviatoric stress is controlled from 0 to carry out nine continuous pressurization/depressurization cycles. Each cycle involves a 5 MPa increase in the maximum deviatoric stress, culminating in a final cycle with a maximum deviatoric stress of 45 MPa. The acoustic and mechanical parameters of rock were measured during the whole experiment, as shown in Figure 4.

Response analysis of anisotropy to shale's dynamic and static elastic properties under cyclic pressure. The variation laws of axial strain, radial strain and volume strain of shale at different angles under different pressurization cycles are analyzed, and the response laws of anisotropy to the nonlinear lag evolution characteristics of rocks are discussed, and the effects of anisotropy on the dynamic and static elastic properties of shale subjected to cyclic pressurization are analyzed in detail.

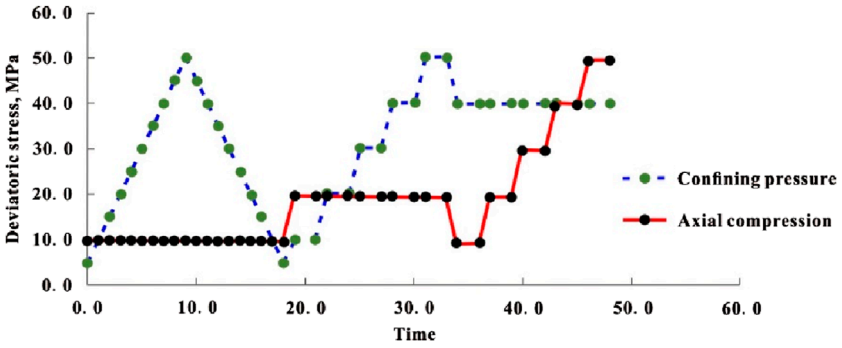

FIGURE 4
Schematic diagram of rock stress loading path and dynamic and static elastic parameters test.

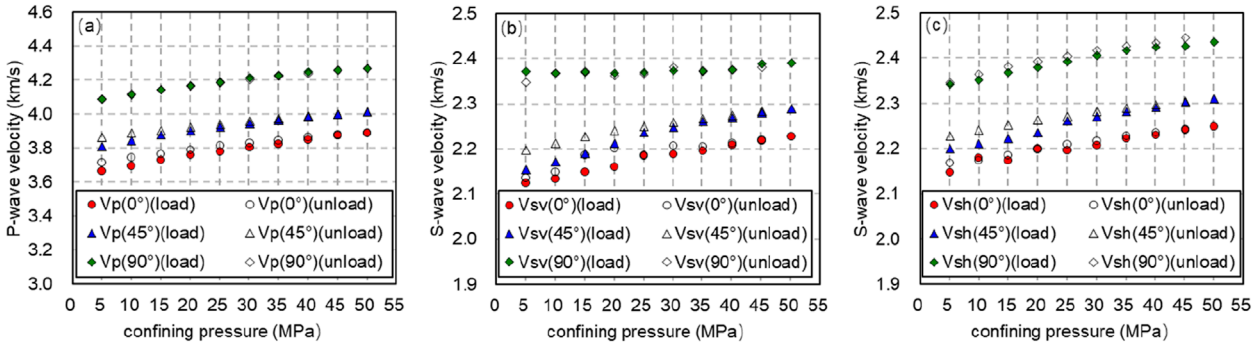

FIGURE 5
The longitudinal and transverse wave velocities during confining pressure loading (solid line) and unloading (dotted line). **(A)** The longitudinal wave velocities during confining pressure loading (solid line) and unloading (dotted line). **(B)** The fast transverse wave velocities during confining pressure loading (solid line) and unloading (dotted line). **(C)** The slow transverse wave velocities during confining pressure loading (solid line) and unloading (dotted line).

4 Dynamic elastic parameters and its anisotropy

4.1 Ultrasonic velocity and its anisotropy

Keep the deviatoric stress at 10 MPa, and compare and analyze the P-wave velocity, fast and slow shear wave velocity of rocks at different angles when the confining pressures are 0, 5, 10, 15, 20, 25, 30,35, 40, 45 and 50 MPa, respectively (Figure 5).

Comparing the velocities of shale samples in different directions, it is found that the velocity of shale satisfies the TI medium $V_p(90^\circ) > V_p(45^\circ) > V_p(0^\circ)$ inequality, $V_{sv}(90^\circ) > V_{sv}(45^\circ) > V_{sv}(0^\circ)$ and, $V_{sh}(90^\circ) > V_{sh}(45^\circ) > V_{sh}(0^\circ)$ which is consistent with the velocity relationship of natural gas shale in different directions in other literatures (Gong et al., 2020). As confining pressure rises, the velocities of P-waves, fast shear waves, and slow shear waves in various bedding orientations also increase. This phenomenon occurs mainly due to the closure of micro-cracks and flexible pores in the shale, leading to enhanced rock stiffness and resulting in faster sound wave propagation.

Comparing the velocities during loading and unloading, it is found that there is a difference between the two processes, that is, the unloading process exhibits a higher acoustic velocity than the loading process. Taking the rock under axial compression of 10 MPa and confining pressure of 50 MPa as an example, during loading, $V_p(0^\circ)$, $V_p(45^\circ)$, and $V_p(90^\circ)$ are 3.7777, 3.9225 and 4.1835 km/s respectively; When the pressure is released, the sum is 3.8111, 3.9381 and 4.1902 km/s, respectively, which is consistent with previous studies on the loading and unloading process of shale (Gong F et al., 2019; Wang et al., 2020b). The primary cause of this situation is the irreversible change of rock microstructure. Inelastic pores and micro-cracks are closed during the loading process, and these inelastic pores and micro-cracks cannot be completely recovered during the unloading process, which leads to the difference of acoustic wave velocity during the loading or unloading process.

In the loading phase, as the confining pressure rises from 5 to 50 MPa, $V_p(0^\circ)$ increases by 0.224 km/s, $V_p(45^\circ)$ and $V_p(90^\circ)$ increase by 0.2038 and 0.182 km/s. The research findings indicate that there are differences in the growth rates of acoustic velocity across different bedding directions, with the increase in acoustic velocity along the symmetry axis being notably greater than that observed perpendicular to the symmetry axis. And the growth rate of longitudinal wave velocity surpasses that of shear wave velocity.

10.3389/feart.2024.1520486

TABLE 2 Analysis of rock mineral composition and clay content by XRD.

Sample number	Quartz rock	Potassium feldspar	Plagioclase	Calcite	Dolomite	Pyrite	Siderite	Ankerite	Plaster	Clinoptilolite	Clay mineral
A-0°	15	11	24	11	1	0	0	34	0	0	4
A-45°	12	11	22	14	1	0	2	31	0	3	4
A-90°	12	4	25	13	0	1	0	38	1	0	6

During the pressurization process, with the confining pressure increasing from 10 to 50 MPa, the P-wave and S-wave velocities of the rock are measured at axial pressures of 10 and 20 MPa, respectively. The results of these tests are illustrated in Figure 6.

In Figure 6, the solid line corresponds to an axial compression of 10 MPa, whereas the dashed line indicates an axial pressure of 20 MPa. It is evident that, under the same confining and axial pressures, rocks exhibiting various bedding angles show differences in both P-wave and S-wave velocities. $V_p(90°) > V_p(45°) > V_p(0°)$ $V_{sv}(90°) > V_{sv}(45°) > V_{sv}(0°)$ and $V_{sh}(90°) > V_{sh}(45°) > V_{sh}(0°)$ when the axial pressure is constant, both the P-wave velocity and S-wave velocity increase in different bedding directions as the confining pressure rises. The primary cause lies in the increase of confining pressure or axial pressure, micro-cracks and flexible pores in shale are closed, rock stiffness increases and sound wave propagation becomes faster. The acoustic velocity measured along the symmetry axis is notably greater than the rate of increase observed in the direction perpendicular to the symmetry axis, while the growth rate of longitudinal wave velocity surpasses that of transverse wave velocity.

4.2 Dynamic elastic modulus and anisotropy

For VTI media, especially horizontal layered shale, the stress-strain relationship adheres to the generalized Hooke's law, as shown in Formula 1, Auld (1973).

$$\sigma_{ij} = C_{ijkl} \cdot \varepsilon_{kl} \tag{1}$$

where is σ_{ij} the stress component; Is ε_{kl} the strain component; Is C_{ijkl} the stiffness coefficient matrix, and the specific form is Formula 2.

$$\begin{bmatrix} \sigma_{11} \\ \sigma_{22} \\ \sigma_{33} \\ \sigma_{23} \\ \sigma_{13} \\ \sigma_{12} \end{bmatrix} = \begin{bmatrix} C_{11} & C_{12} & C_{13} & 0 & 0 & 0 \\ C_{12} & C_{11} & C_{13} & 0 & 0 & 0 \\ C_{13} & C_{13} & C_{33} & 0 & 0 & 0 \\ 0 & 0 & 0 & C_{44} & 0 & 0 \\ 0 & 0 & 0 & 0 & C_{44} & 0 \\ 0 & 0 & 0 & 0 & 0 & C_{66} \end{bmatrix} \begin{bmatrix} \varepsilon_{11} \\ \varepsilon_{22} \\ \varepsilon_{33} \\ 2\varepsilon_{23} \\ 2\varepsilon_{13} \\ 2\varepsilon_{12} \end{bmatrix} \tag{2}$$

The stiffness coefficient matrix of transversely isotropic strata contains five independent stiffness coefficients, namely, C_{11}, C_{33}, C_{44}, C_{66}, and C_{13}. Stiffness coefficient C_{12} is not an independent parameter, it is closely related to $C_{12} = C_{11} - 2C_{66}$ and. These five stiffness coefficients are closely related to formation density and P-wave velocity.

The dynamic stiffness coefficients C_{11d}, C_{33d}, C_{44d}, C_{66d}, C_{12d}, and C_{13d} (Cheadle et al., 1991; Mah and Schmidt. 2001), the specific formula is as follows.

$$C_{11d} = \rho_b V_p^2(90°) \tag{3}$$

$$C_{33d} = \rho_b V_p^2(0°) \tag{4}$$

$$C_{66d} = \rho_b V_{sh}^2(90°) \tag{5}$$

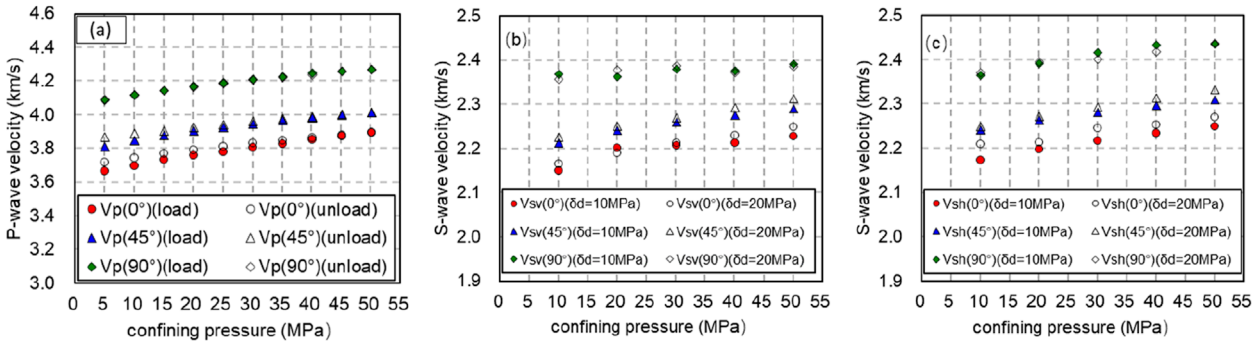

FIGURE 6
The velocity changes of longitudinal wave and transverse wave in the process of confining pressure. **(A)** The longitudinal velocity changes of longitudinal wave and transverse wave in the process of confining pressure. **(B)** The slow transverse wave velocity changes of longitudinal wave and transverse wave in the process of confining pressure. **(C)** The fast transverse wavevelocity changes of longitudinal wave and transverse wave in the process of confining pressure.

$$C_{44d} = \rho_b V_{sv}^2(0°) \tag{6}$$

$$C_{12d} = C_{11d} - 2\rho_b V_{sh}^2(90°) \tag{7}$$

$$C_{13d} = -C_{44d} + \sqrt{4\rho_b^2 V_p^4(45°) - 2\rho_b V_p^2(45°)(C_{11d} + C_{33d} + 2C_{44d}) + (C_{11d} + C_{44d})(C_{33d} + C_{44d})} \tag{8}$$

where the longitudinal $V_p(0°)$ wave traveling along the symmetry axis, the direction of vibration aligns with the direction of propagation. For the longitudinal wave $V_p(45°)$, which propagates at a 45-degree angle to the symmetry axis, the vibration direction also corresponds to the propagation direction. In the case of the longitudinal wave $V_p(90°)$, propagating perpendicularly to the symmetry axis, the propagation direction matches the vibration direction. Shear wave $V_{sh}(0°)$, which propagates parallel to the symmetry axis, has a vibration direction that runs parallel to the bedding plane. The transverse wave $V_{sh}(45°)$, oriented at a 45-degree angle with respect to the symmetry axis, exhibits a vibration direction that is perpendicular to the propagation path. For the transverse wave $V_{sh}(90°)$, which moves perpendicular to the symmetry axis, the vibration direction is aligned with the internal layer structure. The $V_{sv}(0°)$ transverse wave, propagating parallel to the symmetry axis, also has a vibration direction that is parallel to the interior of the layer. The transverse wave $V_{sv}(45°)$, moving at a 45-degree angle to the symmetry axis, has its vibration direction perpendicular to that of the propagation. Finally, the transverse wave $V_{sv}(90°)$, traveling perpendicular to the symmetry axis, features a vibration direction that is also perpendicular to the internal layer

According to this, the dynamic Young's Modulus E_{11d} and E_{33d} and the dynamic Poisson's ratios μ_{12d}, μ_{31d} and μ_{13d} of shale in different directions can be obtained (Christensen and Zywicz, 1990; Gautam and Wong, 2006):

$$E_{11d} = C_{11d} + \frac{C_{13d}^2(-C_{11d} + C_{12d}) + C_{12d}(-C_{33d}C_{12d} + C_{13d}^2)}{C_{33d}C_{11d} - C_{13d}^2} \tag{9}$$

$$E_{33d} = \frac{C_{11d}^2 C_{33d} + 2C_{13d}^2 C_{12d} - 2C_{11d}C_{13d}^2 - C_{33d}C_{12d}^2}{C_{11d}^2 - C_{12d}^2} \tag{10}$$

$$\mu_{12d} = \frac{C_{33d}C_{12d} - C_{13d}^2}{C_{33d}C_{11d} - C_{13d}^2} \tag{11}$$

$$\mu_{31d} = \frac{C_{13d}}{C_{11d} + C_{12d}} \tag{12}$$

$$\mu_{13d} = \frac{C_{13d}(C_{11d} - C_{12d})}{C_{33d}C_{11d} - C_{13d}^2} \tag{13}$$

where: is E_{11d} the dynamic Young's modulus measured by cores with parallel bedding planes; In order E_{33d} to use the dynamic Young's modulus measured by the vertical bedding plane core; μ_{12d}, μ_{13d},is the dynamic Poisson's ratio measured by cores with parallel bedding planes; μ_{31d} To utilize the dynamic Poisson's ratio obtained from cores taken along the vertical bedding plane.

The dynamic stiffness coefficient of rock can be obtained from Formulas 3–8. Figure 7 shows the dynamic stiffness coefficient of rock obtained during pressurization or depressurization when the axial pressure is 10 MPa and the confining pressure changes from 5 to 50 MPa.

From Figure 7, it is evident that when the axial pressure remains constant, the dynamic stiffness coefficients C_{11d}, C_{33d}, C_{44d}, C_{66d}, C_{12d} and C_{13d} of rock all increase with the rise of confining pressure during loading or unloading; Under the same confining pressure, the dynamic stiffness coefficient obtained in unloading process is greater than that obtained in loading process.

In the process of pressurization, the axial pressure is controlled to be 10 and 20 MPa, and the confining pressure is raised from 10 to 50 MPa. With the axial pressure held constant, the dynamic stiffness coefficient increases as confining pressure rises. Additionally, at the same confining pressure, the dynamic stiffness coefficient observed with 20 MPa of axial compression is higher than that seen with 10 MPa of axial compression, as illustrated in Figure 8.

From Formulas 9–13, the dynamic Young's modulus, dynamic Poisson's ratio and dynamic stiffness coefficient in different bedding directions can be calculated. Figure 9 depicts the changing trend of dynamic Young's modulus and dynamic Poisson's ratio with

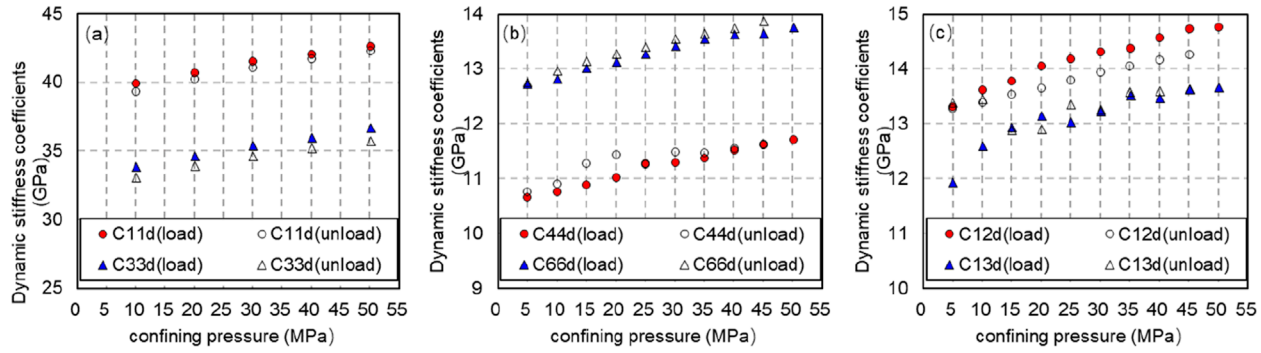

FIGURE 7
Variation of dynamic stiffness coefficient with confining pressure (axial pressure is 10 MPa, solid line is pressurization process, and dotted line is decompression process). **(A)** Variation of dynamic stiffness coefficient C11d and C33d with confining pressure (axial pressure is 10 MPa, solid line is pressurization process, and dotted line is decompression process). **(B)** Variation of dynamic stiffness coefficient C44d and C66d with confining pressure (axial pressure is 10 MPa, solid line is pressurization process, and dotted line is decompression process). **(C)** Variation of dynamic stiffness coefficient C12d and C13d with confining pressure (axial pressure is 10 MPa, solid line is pressurization process, and dotted line is decompression process).

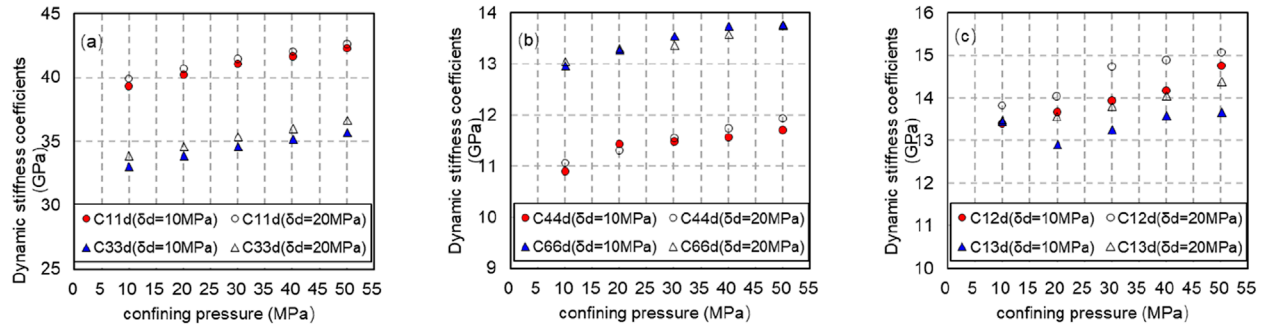

FIGURE 8
Variation of dynamic stiffness coefficient with confining pressure (solid line shows axial compression of 10 MPa, and dotted line shows axial compression of 20 MPa during pressure relief).**(A)** Variation of dynamic stiffness coefficient C11d and C33d with confining pressure (solid line shows axial compression of 10 MPa, and dotted line shows axial compression of 20 MPa during pressure relief). **(B)** Variation of dynamic stiffness coefficient C44d and C66d with confining pressure (solid line shows axial compression of 10 MPa, and dotted line shows axial compression of 20 MPa during pressure relief). **(C)** Variation of dynamic stiffness coefficient C12d and C13d with confining pressure (solid line shows axial compression of 10 MPa, and dotted line shows axial compression of 20 MPa during pressure relief).

confining pressure at different bedding angles when the axial pressure is 10 MPa and the confining pressure is increased from 5 to 50 MPa. Figure 9 exhibits Young's modulus at different bedding angles increases with the increase of confining pressure when the axial pressure is constant. Under the same confining pressure, the dynamic Young's modulus measured by cores with parallel bedding plane is greater than that measured by cores with vertical bedding plane. At the same bedding angle, the dynamic Young's modulus obtained during pressure relief is greater than that obtained during pressure increase.

According to the anisotropy parameter proposed by Thomsen (1986), the anisotropy of shale can be expressed ε by γ three δ independent parameters, sum, as shown in Equations 14–18.

$$\alpha = \sqrt{C_{33}/\rho} \tag{14}$$

$$\beta = \sqrt{C_{44}} \tag{15}$$

$$\varepsilon = \frac{C_{11} - C_{33}}{2C_{33}} \tag{16}$$

$$\gamma = \frac{C_{66} - C_{44}}{2C_{44}} \tag{17}$$

$$\delta = \frac{(C_{13} + C_{44})^2 - (C_{33} - C_{44})^2}{2C_{33}(C_{33} - C_{44})} \tag{18}$$

where: ε *is* anisotropy of longitudinal wave velocity, γ *is* anisotropy of shear wave velocity, and δ is coefficient of variation of longitudinal wave, which indicates the speed of change of anisotropy of longitudinal wave in vertical direction.

From Figure 10, when the axial pressure remains constant, α the β dynamic ε anisotropy γ coefficients δ of rock, and exhibit varying patterns in response to the confining pressure under loading or unloading conditions. When maintaining constant axial pressure, it rises with α the β elevation of confining pressure under loading or ε unloading, γ and δ diminishes with escalating confining pressure.

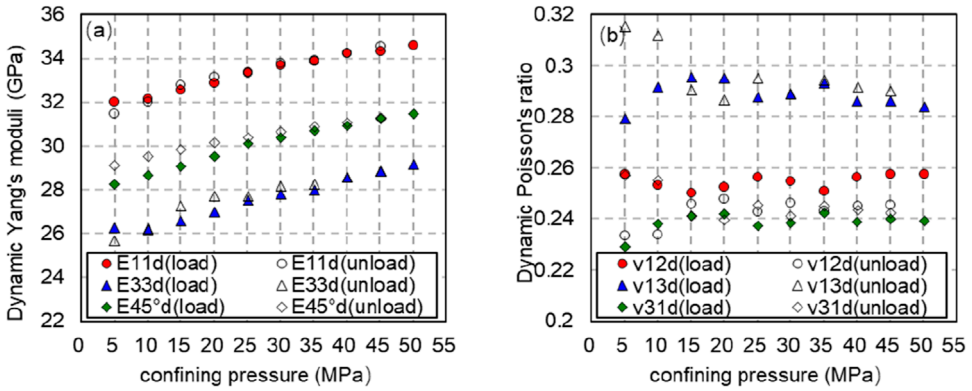

FIGURE 9
Dynamic Young's modulus and Poisson's ratio with confining pressure at different bedding angles. Variation law (solid line is pressurization process, dotted line is depressurization process). **(A)** Dynamic Young's modulus with confining pressure at different bedding angles. Variation law (solid line is pressurization process, dotted line is depressurization process). **(B)** Dynamic Poisson's ratio with confining pressure at different bedding angles. Variation law (solid line is pressurization process, dotted line is depressurization process).

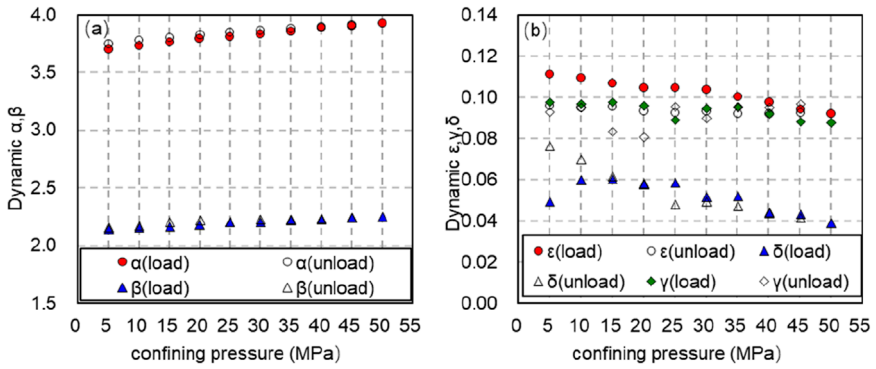

FIGURE 10
Variation law of dynamic anisotropy coefficient with confining pressure (solid line shows pressurization process and dotted line shows depressurization process). **(A)** Variation law of dynamic anisotropy coefficient α, β with confining pressure (solid line shows pressurization process and dotted line shows depressurization process). **(B)** Variation law of dynamic anisotropy coefficient ε, γ and δ with confining pressure (solid line shows pressurization process and dotted line shows depressurization process).

At an equal confining pressure, are α basically β the ε same during loading and unloading, and the value γ of, δ during loading is greater than that during unloading.

In the process of pressurization, the axial pressure is controlled to be 10 and 20 MPa, and the confining pressure is increased from 10 to 50 MPa. Under the same axial pressure, the dynamic anisotropy α coefficient β rises with the escalation of confining pressure, and decreases ε with γ the δ increase of confining pressure. Under the same confining pressure, the anisotropy coefficient under the axial compression of 20 MPa is smaller than the dynamic anisotropy coefficient under the axial compression of 10 MPa, as shown in Figure 11.

In the process of increasing pressure, there are at least three mechanisms that will affect the anisotropy of the sample. When the oriented arrangement of clay minerals is enhanced, the corresponding compaction process will reduce the porosity of the sample. The increase of oriented arrangement of clay minerals will increase the anisotropy of the sample velocity, but the decrease of porosity will decrease the anisotropy of the sample, which is due to the size and shape of mineral particles. Under the same stress, larger particles are more likely to be broken than smaller ones. In the process of compaction, "hard" pores may be transformed into "soft" pores arranged neatly, consequently resulting in the escalation of velocity anisotropy. Hence, these mechanisms ought to be taken into account during the shale compaction process.

5 Static elastic parameters and its anisotropy

5.1 Stress-strain curve

The rock samples underwent triaxial compression experiments. The triaxial compression measurement is shown in Figure 12. The three curves in the Fig represent axial strain, radial strain and axial pressure respectively. One static elastic constant measurement

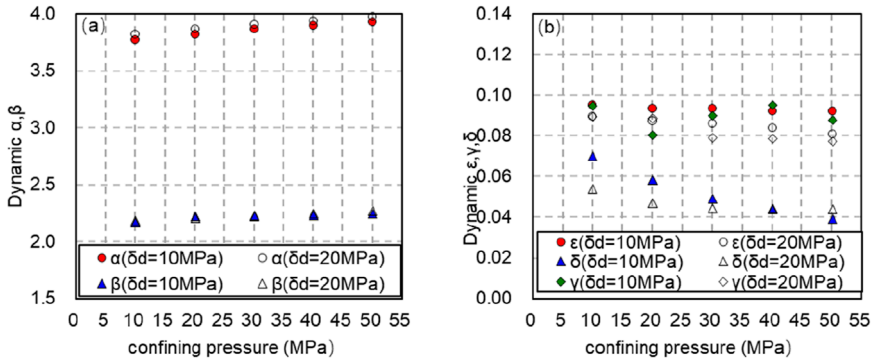

FIGURE 11
Variation of dynamic anisotropy coefficient with confining pressure (solid line is axial compression of 10 MPa, dashed line is axial compression of 20 MPa). **(A)** Variation of dynamic anisotropy coefficient α, β with confining pressure (solid line is axial compression of 10 MPa, dashed line is axial compression of 20 MPa). **(B)** Variation of dynamic anisotropy coefficient t ε, γ and δ with confining pressure (solid line is axial compression of 10 MPa, dashed line is axial compression of 20 MPa).

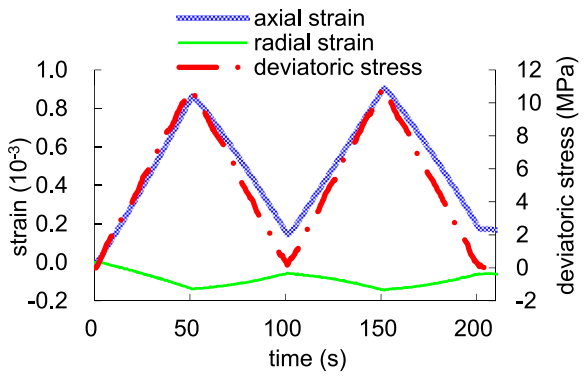

FIGURE 12
Static elastic parameter measurement process.

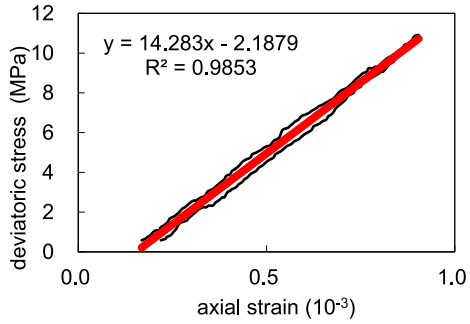

FIGURE 13
Calculation diagram of static elastic mechanical parameters.

is carried out for three pressurization cycles-the axial pressure increases by 15 MPa at a uniform speed, and then decreases to the initial pressure. For three cycles, the axial pressure and axial and radial strains are collected and the static elastic constant of rock samples is calculated, as shown in Figure 13.

5.2 Static elastic modulus and anisotropy

5.2.1 Static elastic modulus calculation of rock

According to the stress-strain measurement results, the static Young's modulus E_{11s} and E_{33s} of shale and the static Poisson's ratios μ_{12s}, μ_{31s} and μ_{13s} can be calculated (Cheadle et al., 1991; Mah and Schmitt, 2001; Miller et al., 2013):

$$E_{11s} = \partial\sigma_{11}/\partial\varepsilon_{11} \tag{19}$$

$$E_{33s} = \partial\sigma_{33}/\partial\varepsilon_{33} \tag{20}$$

$$E_s(45°) = \partial\sigma(45°)/\partial\varepsilon(45°) \tag{21}$$

$$\mu_{12s} = -\partial\varepsilon_{22}/\partial\varepsilon_{11} \tag{22}$$

$$\mu_{31s} = -\partial\varepsilon_{11}/\partial\varepsilon_{33} \tag{23}$$

$$\mu_{13s} = -\partial\varepsilon_{33}/\partial\varepsilon_{11} \tag{24}$$

where: E_{11s} is the dynamic Young's modulus obtained through measurement by cores with parallel bedding planes; For the purpose of using the dynamic Young's modulus of the E_{33s} direction, which is measured by the vertical bedding plane core; μ_{12s}, μ_{13s} is the dynamic Poisson's ratio measured by cores with parallel bedding planes; μ_{31s} To utilize the dynamic Poisson's ratio measured from vertical bedding plane cores. In the pressurization-depressurization cycle, the axial pressure is controlled to be 0~10 MPa. With the increase of the confining pressure from 10 to 50 MPa, the sum of static Young's modulus of different bedding angles obtained in both the E_{11s} pressurization E_{33s} process $E(45°)$ and the depressurization process intensifies with the rise in confining pressure. Like the dynamic Young's modulus, in the depressurization process, the static Young's modulus of different bedding angles is greater than

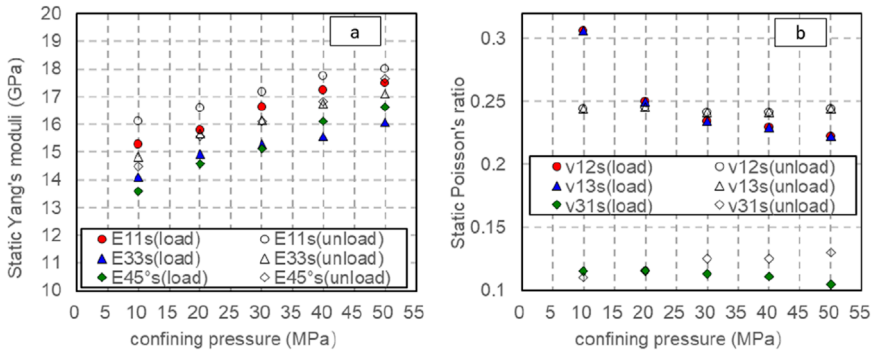

FIGURE 14
Changes of static elastic parameters with confining pressure at different bedding angles (axial pressure is 0–10 MPa). **(A)** Changes of static Young's modulus with confining pressure at different bedding angles (axial pressure is 0–10 MPa). **(B)** Changes of static Poisson's ratio with confining pressure at different bedding angles (axial pressure is 0–10 MPa).

that in the pressurization process. The change of static Poisson's ratio with confining pressure at different bedding angles is more complicated, ν_{12s} but ν_{31s} it is not obvious with the increase of ν_{13s} confining pressure, and it decreases significantly with the increase of confining pressure during pressurization or depressurization, as shown in Figure 14.

5.2.2 Determination of static stiffness coefficient of rock

The stress-strain method can be utilized to ascertain the static elastic modulus of rock. For VTI medium, the static stiffness coefficients C_{11s}, C_{33s}, C_{44s}, C_{66s}, C_{12s} and C_{13s} of shale can be further calculated. The specific formulas are as follows (Wang et al., 2020a):

$$C_{11s} = \frac{E_{11s}(1+\mu_{13s}\mu_{31s})}{(1-\mu_{12s}-2\mu_{13s}\mu_{31s})(1+\mu_{12s})} \tag{25}$$

$$C_{33s} = \frac{E_{33s}(1-\mu_{12s}^2)}{(1-\mu_{12s}-2\mu_{13s}\mu_{31s})(1+\mu_{12s})} \tag{26}$$

$$C_{44s} = \left[\frac{4}{E_s(45°)} - \frac{1}{E_{11s}} - \frac{1-2\mu_{31s}}{E_{33s}}\right]^{-1} \tag{27}$$

$$C_{66s} = \frac{E_{11s}}{2(1+\mu_{12s})} \tag{28}$$

$$C_{12s} = \frac{E_{11s}(\mu_{12s}+\mu_{13s}\mu_{31s})}{(1-\mu_{12s}-2\mu_{13s}\mu_{31s})(1+\mu_{12s})} \tag{29}$$

$$C_{13s} = \frac{E_{11s}\mu_{31s}}{1-\mu_{12s}-2\mu_{13s}\mu_{31s}} \tag{30}$$

The static stiffness coefficient of rock can be obtained from Formulas 25–30. Figure 15 shows the static stiffness coefficient of rock obtained during pressurization or depressurization when the axial pressure is 0–10 MPa and the confining pressure changes from 5 to 50 MPa.

Figure 15 illustrates that the static stiffness coefficients C_{11s}, C_{33s}, C_{44s}, C_{66s}, C_{12s} and C_{13s} of rock exhibit an increment as the confining pressure rises during loading or unloading; Under the same confining pressure, the static stiffness coefficient obtained in unloading process is greater than that obtained in loading process. The static stiffness coefficients C_{44s} and C_{66s}, exhibit significant variations with the escalating confining pressure during pressurization or depressurization, whereas C_{11s}, C_{33s} and C_{13s} remain unaffected by the changing confining pressure levels. During pressurization, C_{12s} declines as the confining pressure rises, while during depressurization, it escalates alongside the increasing confining pressure.

Equations 14–18 offer a method for computing the static anisotropy characteristics of shale oil specimens. Observation from Figure 16 reveals that the anisotropy parameter obtained during the pressure relief process is greater than that obtained during the pressurization process. ε With γ the increase of confining pressure, anisotropy value decreases slightly, and the parameters obtained in pressurization stage and decompression stage have no obvious change law with confining pressure.

6 Comparative analysis of dynamic and static elastic parameters

Contrast and analyze the dynamic Young's modulus and static Young's modulus measured during loading or unloading under the experimental conditions of confining pressure of 1–50 MPa and eccentric stress of 10 MPa (Figure 17). From Figure 7, it is observable that the dynamic and static Young's moduli increase as the confining pressure rises. The Young's modulus in different directions is higher than that in the pressurized state, given the same confining pressure. Taking into account the impact of confining pressure, the model for converting dynamic and static Young's Modulus in various orientations (Table 3) reveals a notable relationship between the static Young's Modulus in distinct directions and the dynamic Young's Modulus in the corresponding direction post pressure adjustment. Through the model conversion outlined in Table 3, the application domain can be extended to vertical, horizontal, and high-angle wells, thereby enabling the accurate determination of the static mechanical parameters of rocks under various well-logging conditions.

Considering the dynamic and static elastic modulus conversion model in different directions (see Figure 18), the static Young's modulus that has been calculated correlates well with the

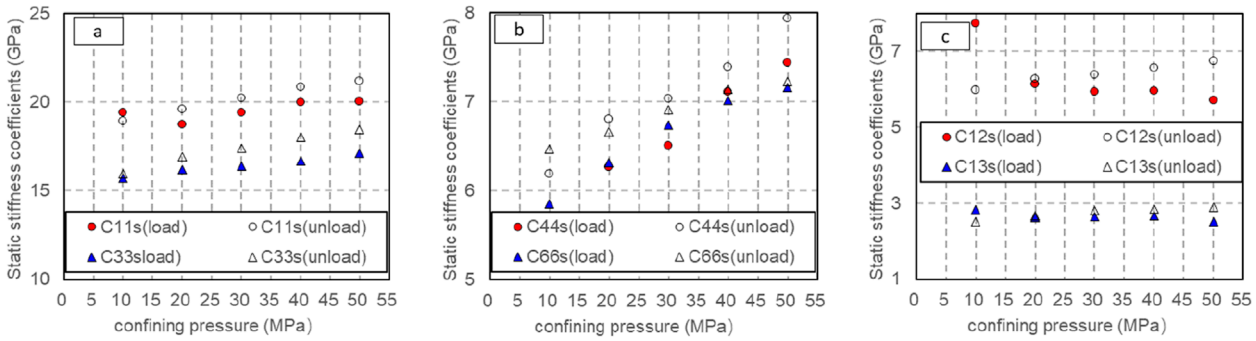

FIGURE 15
Variation of static stiffness coefficient with confining pressure (solid line pressurization process, dotted line decompression process). **(A)** Variation of static stiffness coefficient C11s, C33s with confining pressure (solid line pressurization process, dotted line decompression process). **(B)** Variation of static stiffness coefficient C44s, C66s with confining pressure (solid line pressurization process, dotted line decompression process). **(C)** Variation of static stiffness coefficient C12s, C13s with confining pressure (solid line pressurization process, dotted line decompression process).

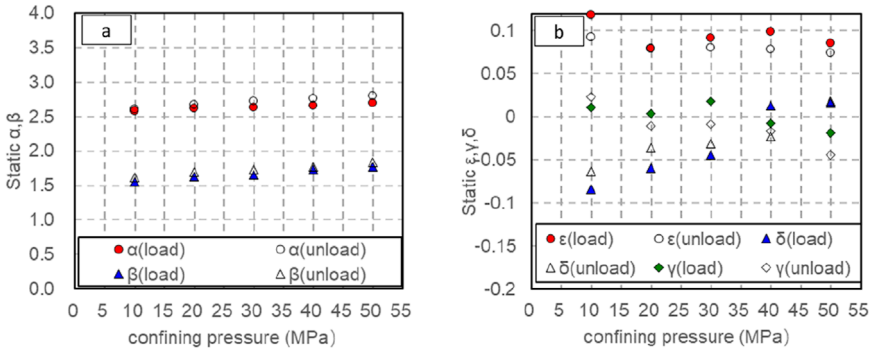

FIGURE 16
Variation of static anisotropy coefficient α, β with confining pressure (solid line shows pressurization process and dotted line shows depressurization process). **(A)** Variation of static anisotropy coefficient α, β with confining pressure (solid line shows pressurization process and dotted line shows depressurization process). **(B)** Variation of static anisotropy coefficient ε, γ and δ with confining pressure (solid line shows pressurization process and dotted line shows depressurization process).

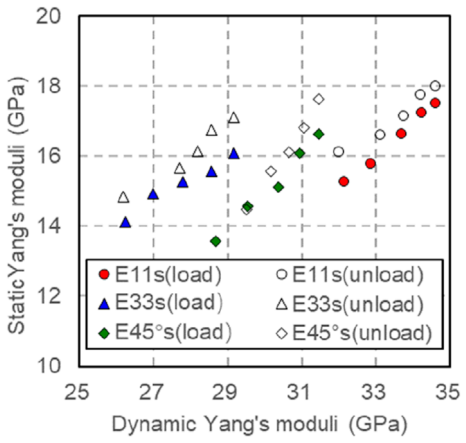

FIGURE 17
Dynamic and Static elastic modulus under different confinement pressure and pressure.

measured static Young's modulus, and the correlation coefficient is 0.9268 (see Fig 18). Using this conversion model, the static Young's modulus of rocks in different directions can be predicted under arbitrary pressure.

The dynamic Poisson's ratio and Poisson's ratio are measured during loading or unloading under the experimental conditions of confining pressure of 10–50 MPa and eccentric stress of 10 MPa (Figure 19). Upon examining Figure 19, it becomes evident that under pressure relief, the change in ν_{12s} with respect to confining pressure is not significant, whereas under pressure, ν_{12s} decreases as the confining pressure increases. Under the pressure ν_{31s} relief condition, the change of confining pressure is not obvious, but ν_{31s} it decreases with the increase of confining ν_{13s} pressure under the pressure condition. It is insensitive to the relationship with confining pressure under the condition of pressurization or depressurization. Considering the influence of confining pressure, as seen in Table 1, the dynamic and static Poisson's ratio conversion models in different directions (Table 4) show that the static Poisson's ratio in different directions after pressure correction has significant

TABLE 3 Dynamic and static Young's modulus conversion models in different directions.

Elastic parameter	Model expression	Correlation coefficient (R2)
E_{11s}	1.14Ln (P/P0) + 0.22E_{11d} + 8.29	0.85
$E_{45^\circ s}$	−0.31Ln (P/P0) + 1.48E_{45d} − 29.0641	0.92
E_{33s}	−0.76 ln (P/P0) + 1.14E_{33d} − 15.40	0.79

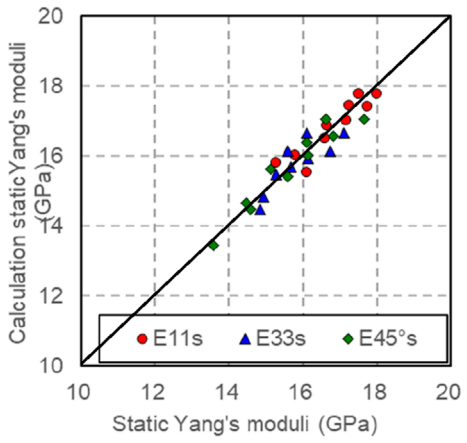

FIGURE 18
Dynamic and static Young's relief conditions modulus conversion model.

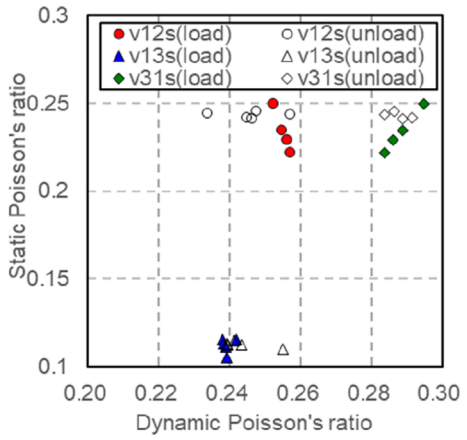

FIGURE 19
Dynamic and static Poisson's ratio under different confining pressures and pressure relief conditions.

correlation with the dynamic Poisson's ratio in the corresponding direction. Using this conversion model, the static Poisson's ratio of rocks in different directions under arbitrary pressure can be predicted, as shown in Figure 20.

7 Discussion

Static elastic mechanics parameters is a key parameter in shale oil and gas extraction and water injection fracturing engineering, and different pressurization methods and pressurization conditions have an important influence on the dynamic and static elastic characteristics of shale, so exploring the main controlling factors of the dynamic and static elastic characteristics under different temperature and pressure conditions is a key scientific problem that needs to be solved urgently in shale oil and gas extraction and water injection fracturing engineering.

The acoustic-mechanical coupling system of rock samples was used to analyze the effects of dynamic and static elastic properties of shale at different angles under triaxial pressurization conditions. In order to explore the anisotropy of laminated shale, diamond wire cutting was utilized to cut the rock into three angle samples with the angles of 0 o, 45o and 90 o between the laminated surface and the end face of the rock samples, and the longitudinal wave velocity, as well as the fast and slow transverse wave velocities, were tested for each sample under different temperatures and pressures respectively, and the stress-strain curves of the rock were tested at the same time. Calculation of dynamic stiffness coefficients C11d, C33d, C44d, C66d, C12d, and C13d for different test conditions based on Hooke's law for VTI media and based on Equations 3–8, and the elastic moduli E11d , E33d, μ12d, μ31d and μ13d were calculated based on the elasticity of different laminar angles based on Equations 9–13. Strain curves, the static modulus of elasticity E11s, E33s, μ12s, μ31s, μ13s are calculated for different lamination angles based on Equations 19–24, based on which the static stiffness coefficients C11s, C33s, C44s, C66s, C12s and C13s can be further calculated.

When calculating the dynamic elasticity parameters, the effects of temperature and pressure need to be taken into account. The dynamic Young's modulus and static Young's modulus of shale oil with different stratigraphic angles increase with the increase of pressure, and increase quickly with the pressure when the pressure is lower, and with the continuous increase of pressure, the increase of Young's modulus slows down and tends to a stable value. The dynamic and static Young's modulus of shale oil with different stratification angles are linearly related, and the dynamic Young's modulus is larger than the static Young's modulus, and the correlation between the dynamic and static Poisson's ratio is poor, and the dynamic Poisson's ratio of shale oil is larger than the static Poisson's ratio in general. There is a strong dependence between the shale oil stiffness coefficient and the perimeter pressure, and the elastic stiffness coefficient shows a trend of increasing with the increase of the perimeter pressure under both dynamic

TABLE 4 Dynamic and static Poisson's ratio conversion models in different directions.

Elastic parameter	Model expression	Correlation coefficient (R^2)
v_{12s}	−0.03718 ln (P/P0) + 1.559857 v_{12d} −0.1091	0.65
v_{13s}	−0.04477 ln (P/P0) − 1.87251 v_{13d} + 0.833521	0.69
v_{31s}	−0.00296 ln (P/P0) − 0.28712 v_{31d} + 0.184471	0.28

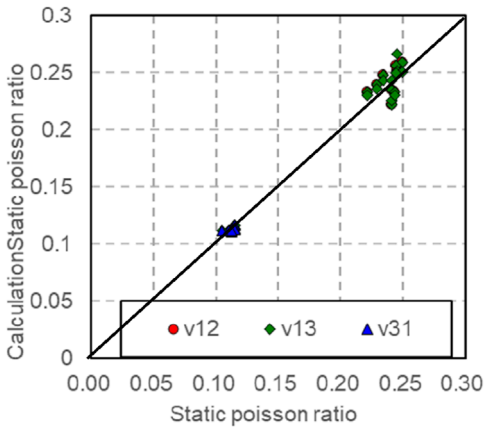

FIGURE 20
Dynamic and static Poisson's ratio conversion model.

and static test conditions, and the elastic parameters related to longitudinal waves (C11, C33) are more obvious than the elastic parameters related to transverse waves (C44, C66) with the change of pressure. Whether static or dynamic elastic modulus, there are some differences in Young's modulus and Poisson's ratio between vertical and horizontal directions, and generally the elastic modulus is larger in the direction of horizontal strata. The Poisson's ratio/Young's modulus ratio on different stratigraphy have high correlation, and the Poisson's ratio/Young's modulus ratio obtained by acoustic wave test has higher correlation.

The conversion models of Young's modulus and Poisson's ratio for different laminar angles were established respectively, which can be applied in vertical wells in vertical wells respectively, and can obtain continuous static elastic mechanical parameters, which extends the adaptability of static rock mechanical parameters.

8 Conclusion and suggestions

Taking the shale oil sample of lacustrine facies in the second member of Kongdong sag in Bohai Bay Basin as the research object, dynamic and static rock acoustics and mechanics were jointly measured in various directions, subsequent examination of the experimental findings culminates in the following deductions:

(1) Under identical confining and axial pressure, the P-wave velocity and S-wave velocity of rocks vary with different bedding angles, and when $V_p(90^\circ) > V_p(45^\circ) > V_p(0^\circ)$ the $V_{sv}(90^\circ) > V_{sv}(45^\circ) > V_{sv}(0^\circ)$ axial $V_{sh}(90^\circ) > V_{sh}(45^\circ) > V_{sh}(0^\circ)$ pressure is constant, the P-wave velocity and S-wave velocity elevate as the confining pressure escalates across different bedding orientations; When the confining pressure remains constant, the velocities of longitudinal and transverse waves in different bedding directions increase with its escalation; The primary factor is that As the confining pressure or axial stress rises, micro-cracks and flexible pores within shale close, rock stiffness increases and sound wave propagation becomes faster. The acoustic velocity aligned with the symmetry axis shows a significantly higher growth rate compared to the velocity observed perpendicular to it, and the growth rate of longitudinal wave velocity exceeds that of transverse wave velocity.

(2) There are differences in dynamic and static Young's modulus, Poisson's ratio and stiffness properties in different bedding directions. When maintaining constant axial pressure, the dynamic and static Young's modulus of different bedding angles rise proportionally with increasing confining pressure. Under the same confining pressure, the dynamic Young's modulus measured by cores with parallel bedding plane is greater than that measured by cores with vertical bedding plane. At the same bedding angle, the dynamic Young's modulus recorded during pressure release surpasses that obtained during pressure augmentation. The static young's modulus and sum of E_{11s} different E_{33s} bedding $E(45^\circ)$ angles increase with rising confining pressure. Like the dynamic young's modulus, the static young's modulus of different bedding angles exceeds that of the pressurized one during the process of pressure relief. The alteration of static Poisson's ratio with varying confining stress across distinct bedding angles presents a more intricate scenario, v_{12s} but v_{31s} it is not obvious with rising v_{13s} confining pressure, and it decreases significantly during both pressurization and depressurization.

(3) The dynamic and static electromechanical properties of different stratigraphic angles can be converted under different pressures, and the dynamic electromechanical parameters measured under different peripheral pressures can be converted into static electromechanical parameters under the corresponding peripheral pressures, which can serve as the foundation for examining the mechanical characteristics of rocks under reservoir conditions, and provide the reference basis for developing a hydraulic fracturing construction program of oil and gas reservoirs.

Data availability statement

The original contributions presented in the study are included in the article/supplementary material, further inquiries can be directed to the corresponding author.

Author contributions

DZ: Writing–review and editing. YL: Data curation, Formal analysis, Writing–review and editing. YG: Investigation, Writing–review and editing. HX: Data curation, Software, Writing–review and editing. YL: Methodology, Supervision, Writing–review and editing. JY: Conceptualization, Investigation, Writing–review and editing. FW: Writing–original draft, Writing–review and editing. YW: Validation, Investigation, Funding acquisition, Writing–review and editing.

Funding

The author(s) declare that financial support was received for the research, authorship, and/or publication of this article. This study was supported by Natural Science Foundation of Shaanxi Provincial Department of Education Upper Level Fund Project (2022JM-139).

Conflict of interest

Authors DZ, YL, YG, HX, YL and JY were employed by Qinghai Oilfeld Company, PetroChina.

The remaining authors declare that the research was conducted in the absence of any commercial or financial relationships that could be construed as a potential conflict of interest.

Generative AI statement

The author(s) declare that no Generative AI was used in the creation of this manuscript.

Publisher's note

All claims expressed in this article are solely those of the authors and do not necessarily represent those of their affiliated organizations, or those of the publisher, the editors and the reviewers. Any product that may be evaluated in this article, or claim that may be made by its manufacturer, is not guaranteed or endorsed by the publisher.

References

Ameen, M. S., Smart, B. G. D., Somerville, J. M., Hammilton, S., and Naji, N. A. (2009). Predicting rock mechanical properties of carbonates from wireline logs (A case study: arab-D reservoir, Ghawar field, Saudi Arabia). *Mar. and Petroleum Geol.* 26 (4), 430–444. doi:10.1016/j.marpetgeo.2009.01.017

Asef, M. R., and Farrokhrouz, M. (2010). Governing parameters for approximation of carbonates UCS. *Electron J. Geotech. Eng.* 15, 1581–1592.

Asef, M. R., and Farrokhrouz, M. (2017). A semi-empirical relation between static and dynamic elastic modulus. *J. Petroleum Sci. Eng.* 157 (2017), 359–363. doi:10.1016/j.petrol.2017.06.055

Auld, B. A. (1973). Acoustic fields and waves in solids. *John Wiley and Sons* I. doi:10.1063/1.3128926

Batzle, M. L., Han, D. H., and Hofmann, R. (2006). Fluid mobility and frequency-dependent seismic velocity—direct measurements. *Geophysics* 71 (1), N1–N9. doi:10.1190/1.2159053

Bian, H. Y., Wang, F., Zhang, C. E., Gao, X. H., ZhangY, H., Duan, C. W., et al. (2019). A new model between dynamic and static elastic parameters of shale based on experimental studies. *Arabian J. Geosciences* 12 (20), 609. doi:10.1007/s12517-019-4777-2

Bian, H. Y., Wang, F., Zhang, Y. H., and Yue, C. W. (2015). Experimental study of dynamic and static elastic parameters of tight sandstones under reservoir conditions. *Chin. J. Rock Mechan. Enginee.* 34 (S1), 3045–3054. doi:10.13722/j.cnki.jrme.2014.1109

Cheadle, S. P., Brown, R. J., and Lawton, D. C. (1991). Orthorhombic anisotropy: a physical seismic modeling study. *Geophysics* 56 (10), 1603–1613. doi:10.1190/1.1442971

Cheng, C. H., and Johnston, D. H. (1981). Dynamic and static moduli. *Geophys. Res. Lett.* 8 (1), 39–42. doi:10.1029/GL008i001p00039

Christensen, R. M., and Zywicz, E. (1990). A three-dimensional constitutive theory for fiber composite laminated media. *J. Appl. Mech.* 57, 948–955. doi:10.1115/1.2897666

Eissa, E. A., and Kazi, A. (1988). Relation between static and dynamic young's moduli of rocks. *Int. J. Rock Mech. Min. Sci. and Geomechanics Abstr.* 25 (6), 479–482. doi:10.1016/0148-9062(88)90987-4

Fjær, E. (2019). Relations between static and dynamic moduli of sedimentary rocks. *Geophys. Prospect.* 67 (1), 128–139. doi:10.1111/1365-2478.12711

Gautam, R., and Wong, R. C. K. (2006). Transversely isotropic stiffness parameters and their measurement in Colorado shale. *Can. Geotechnical J.* 43 (12), 1290–1305. doi:10.1139/T06-083

Ghafoori, M., Rastegarnia, A., and Lashkaripour, G. R. (2018). Estimation of static parameters based on dynamical and physical properties in limestone rocks. *J. Afr. Earth Sci.* 137 (2018), 22–31. doi:10.1016/j.jafrearsci.2017.09.008

Gong, F., Di, B., Wei, J., Ding, P., Tian, H., and Han, J. (2019). A study of the anisotropic static and dynamic elastic properties of transversely isotropic rocks. *Geophysics* 84 (6), C281–C293. doi:10.1190/geo2018-0590.1

Gordon, R. B., and Davis, L. A. (1968). Velocity and attenuation of seismic waves in imperfectly elastic rock. *J. Geophys. Res.* 73 (12), 3917–3935. doi:10.1029/jb073i012p03917

Hornby, B. E., Schwartz, L. M., and Hudson, J. A. (1994). Anisotropic effective-medium modeling of the elastic properties of shales. *Geophysics* 59 (10), 1570–1583. doi:10.1190/1.1443546

Li, H., Han, D. H., Gao, J., Yuan, H., and Wang, Y. (2019). Pressure loading histories and clay fraction effects on the static and dynamic elastic properties of sand-clay synthetic sediments. *Powder Technol.* 345, 804–814. doi:10.1016/j.powtec.2019.01.033

Mah, M., and Schmitt, D. R. (2001). Experimental determination of the elastic coefficients of an orthorhombic material. *Geophysics* 66 (4), 1217–1225. doi:10.1190/1.1487068

Miller, D., Plumb, R., and Boitnott, G. (2013). Compressive strength and elastic properties of a transversely isotropic calcareous mudstone. *Geophys. Prospect.* 61, 315–328. doi:10.1111/1365-2478.12031

Rickman, R., Mullen, M. J., Petre, J. E., Grieser, B., and Kundert, D. (2008). A practical use of shale petrophysics for stimulation design optimization: all shale plays are not clones of the Barnett Shale. *SPE Annu. Tech. Conf. Exhib.* doi:10.2118/115258-MS

Sayers, C. M. (1999). Stress-dependent seismic anisotropy of shales. *Geophysics* 64 (1), 93–98. doi:10.1190/1.1444535

Sone, H., and Zoback, M. D. (2013). Mechanical properties of shale-gas reservoir rocks—Part 1: static and dynamic elastic properties and anisotropy. *Geophysics* 78 (5), D381–D392. doi:10.1190/geo2013-0050.1

Thomsen, L. (1986). Weak elastic anisotropy. *Geophysics* 51 (10), 1954–1966. doi:10.1190/1.1442051

Tutuncu, A. N., Podio, A. L., and Sharma, M. M. (1998). Nonlinear viscoelastic behavior of sedimentary rocks, Part II: hysteresis effects and influence of type of fluid on elastic moduli. *Geophysics* 63 (1), 195–203. doi:10.1190/1.1444313

Vernik, L., and Liu, X. (1997). Velocity anisotropy in shales: a petrophysical study. *Geophysics* 62 (2), 521–532. doi:10.1190/1.1444162

Wang, Y., Han, D. H., Li, H., Zhao, L., Ren, J., and Zhang, Y. (2020a). A comparative study of the stress-dependence of dynamic and static moduli for sandstones. *Geophysics* 85 (4), MR179–MR190. doi:10.1190/geo2019-0335.1

Wang, Y., Zhao, L., Han, D. H., Mitra, A., Li, H., and Aldin, S. (2020b). Anisotropic dynamic and static mechanical properties of organic-rich shale: the influence of stress. *Geophysics* 86 (2), C51–C63. doi:10.1190/geo2020-0010.1

Zhang, L., Ba, J., and Carcione, J. M. (2021). Wave propagation in infinituple-porosity media. *J. Geophys. Res. Solid Earth* 126 (4), e2020JB021266. doi:10.1029/2020jb021266

Zhang, L., Ba, J., Li, C., Carcione, J., and Zhou, F. (2022). Joint inversion of the unified pore geometry of tight sandstones based on elastic and electrical properties. *J. Petroleum Sci. Eng.* 219, 111109. doi:10.1016/j.petrol.2022.111109

frontiers | Frontiers in Earth Science

TYPE Original Research
PUBLISHED 11 February 2025
DOI 10.3389/feart.2025.1508283

OPEN ACCESS

EDITED BY
Weichao Yan,
Ocean University of China, China

REVIEWED BY
Suhaib Umer Ilyas,
Jeddah University, Saudi Arabia
Li Dan,
CNOOC Research Institute Ltd, China
Wang Song,
China University of Petroleum, China

*CORRESPONDENCE
Weibiao Xie,
gareth123@126.com
Qiuli Yin,
2023591301@cupk.edu.cn

RECEIVED 09 October 2024
ACCEPTED 09 January 2025
PUBLISHED 11 February 2025

CITATION
Xie W, Yin Q, Dai X, Fan Y and Zhang P (2025) The relationship between water production rate and resistivity in sand-based porous materials under two-phase fluid flow and its application.
Front. Earth Sci. 13:1508283.
doi: 10.3389/feart.2025.1508283

The relationship between water production rate and resistivity in sand-based porous materials under two-phase fluid flow and its application

Weibiao Xie[1,2]*, Qiuli Yin[1,2]*, Xueping Dai[1,2], Yang Fan[3] and Pan Zhang[1,2]

[1]School of Petroleum, China University of Petroleum (Beijing) at Karamay, Karamay, China, [2]State Key Laboratory of Petroleum Resources and Prospecting, China University of Petroleum (Beijing), Beijing, China, [3]China Petroleum Logging Co., Ltd., Xian, Shanxi, China

Accurately predicting the water production rate of multiple-phase fluid flows through porous rock is important for many engineering and geological applications. Taking into account irreducible water and capillary tortuosity, the equivalent rock element model from previous studies has been improved. Based on the improved capillary equivalent rock element model, this study proposes a relationship model between the water production rate in two-phase fluid systems and the resistivity index. The relationship model is verified using rock samples, and the result shows that the water production rate calculated by the new model closely matches experimental values, improving parameter calculation accuracy. In addition, applications of the new model to well logging data show that the calculated water production rate is consistent with the actual production situation. This approach is more efficient and accurate in reservoir evaluation. The new model provides a new idea for studying the seepage characteristics of rocks with multiple-phase fluids.

KEYWORDS

pore structure, resistivity index, water production rate, two-phase fluid, sand-based porous material

1 Introduction

The seepage characteristics of porous media with multiple-phase fluids are a research hot spot (Chen and Yao, 2017; Behrang et al., 2016). Understanding the seepage characteristics of rocks in oil–water two-phase flow and oil–gas–water three-phase flow is fundamental for reservoir development planning, production forecasting, and reservoir evaluation (Tiab and Donaldson, 2024; McKenna et al., 2020; Yushu Wu, 2015).

The water production rate, defined as the water volume ratio during reservoir exploitation, is an important seepage characteristic parameter and serves as a dynamic indicator for evaluating the reservoir's oil-bearing properties. The theoretical results show that there is a clear functional relationship between water production rate

and relative permeability (Schön, 2011). In order to accurately calculate the water production rate, several researchers have developed methods for relative permeability. Honarpour et al. derived a relationship model between water production rate and water saturation based on the empirical relative permeability model proposed by Honarpour (2018), Kasha et al. (2023), and Corey (1954). This model is one of the most widely used models, but it only considers the general relationship between water production rate and water saturation, and the accuracy is low in low porosity and low permeability reservoirs (Bear, 2013; Rutqvist et al., 2002). Chima et al. (2010) analyzed the relationship between water production rate and relative permeability during natural gas exploitation in a fractured reservoir. Clarkson described the variation in the water production rate during coal-bed gas exploitation using relative permeability analysis (Clarkson et al., 2011). A theoretical model of gas–water relative permeability in gas hydrate reservoirs is established by Lei et al. (2020). These models can accurately predict the water production rate in fractured formations, coal-bed gas formations, and gas hydrate reservoirs, but their application range is limited. Schlachter et al. examined the water production rate using Modular Dynamics Tester (MDT) testing and logging (Schlachter, 2007; Whittle et al., 2003; Wu and Zhang, 2018). Wang et al. used machine learning and deep learning to predict relative permeability and the oil content ratio during reservoir exploitation, achieving good results (Wang et al., 2022; Zhong et al., 2021).

Previous studies have shown that relative permeability is a key parameter in determining the water production rate, and relative permeability itself is a function of water saturation (Iscan, 2021; Xu et al., 2014). Therefore, the relationship between water production rate and water saturation plays a crucial role in determining the water production rate (Pius and Olamigoke, 2020). Water saturation is a static parameter describing the oil-bearing properties of a reservoir. A common method for determining water saturation is using rock electrical properties, with widely used existing models such as the Archie model and the three-water model (Archie, 1942; Rangelov and Nassiri, 2018; Xie et al., 2023; Jin et al., 2020). The equivalent rock element model (EREM), which incorporates the impact of the pore structure on rock resistivity, is also extensively utilized in the investigation of rock seepage (Shang et al., 2003; Shang et al. 2004; Shang et al. 2008). Consequently, using rock electrical properties to determine the water production rate proves to be a valuable approach. However, research on this topic is limited.

Research has shown that the seepage characteristics and electrical properties of rocks are closely related to the pore structure (Yin et al., 2020; Smirnov et al., 2019; Reza-E-Rabbi et al., 2020). Xie et al. (2020) proposed a relationship model between relative permeability and rock electrical properties, considering the effect of the pore structure. Xu P et al. developed a relative permeability model based on the fractal theory (Peng et al., 2013; Wang et al., 2019). The pore structure is an essential factor in establishing the relationship model between water production rate and rock electrical properties. Taking into account the effect of the pore structure, this paper has improved the EREM, and a relationship model between water production rate and resistivity index is proposed. Seven rock samples with different pore structure types were used to validate the new model, and the average relative error between the water production rate calculated by the new model and the experimental data is 5%. The results of both verification and application show that the new model can directly calculate the water production rate from the resistivity index and accurately predict the water production rate of rocks with different pore structures. The novel model incorporates pore structure characterization parameters to mitigate the impact of the pore structure on the water production rate, thereby enhancing the precision of water production rates. In addition, the new model provides a new idea for studying the seepage characteristics of rocks and enriches the data foundation for guiding reservoir development planning, production forecasting, and reservoir evaluation.

2 Relationship between water production rate and electrical resistivity in two-phase fluid flows

2.1 Improved capillary equivalent rock element model

According to the EREM (Shang et al., 2003; Shang et al. 2004; Shang et al. 2008), we obtain

$$\begin{cases} \phi = \phi_b + \phi_s \\ p = \phi_b / \phi_s \end{cases}, \tag{1}$$

where in Equation 1, ϕ (v/v) is the total porosity, ϕ_b (v/v) is the macropore porosity, ϕ_s (v/v) is the throat-pore porosity, and p (dimensionless) is the ratio of ϕ_b to ϕ_s. Obviously, p is closely related to the pore structure. Figure 1 shows the equivalent rock element model of the porous media. Figure 1A shows the pore distribution of the porous media. Figure 1B shows the equivalent rock element model of the porous media.

In Figure 1, ϕ is the total porosity, ϕ_b is the macropore porosity, ϕ_s is the throat-pore porosity, and V_{ma} is the matrix volume.

Generally, the flow characteristics are mainly featured by throat pores. Figure 2 shows the flow model of the pore fluids. The equivalent capillary porosity can be expressed as

$$\phi_m = \frac{\phi}{1 + p(1-\phi)}, \tag{2}$$

where in Equation 2, ϕ_m (v/v) is the equivalent capillary porosity.

In Figure 2, ϕ_m is the equivalent capillary porosity and V_{ma} is the matrix volume.

Actually, water-wetted rocks contain irreducible water. The effective flow porosity ϕ_{em} (v/v) is expressed as

$$\phi_{em} = \phi_m(1 - S_{mirr}), \tag{3}$$

where S_{mirr} (v/v) is the equivalent capillary irreducible water saturation (the ratio of irreducible water porosity to equivalent capillary porosity). ϕ_{wi} (v/v) is the bound water volume. The equivalent capillary irreducible water saturation can be calculated as follows:

$$S_{mirr} = S_{irr}[1 + p(1-\phi)], \tag{4}$$

where S_{irr} (v/v) is the total irreducible saturation (the ratio of total irreducible water to total porosity).

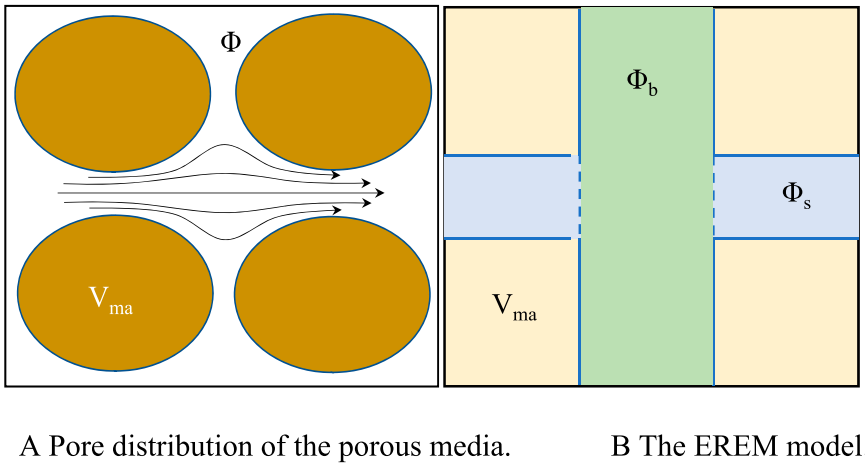

FIGURE 1
Equivalent rock element model of the porous media. **(A)** Pore distribution of the porous media. **(B)** EREM.

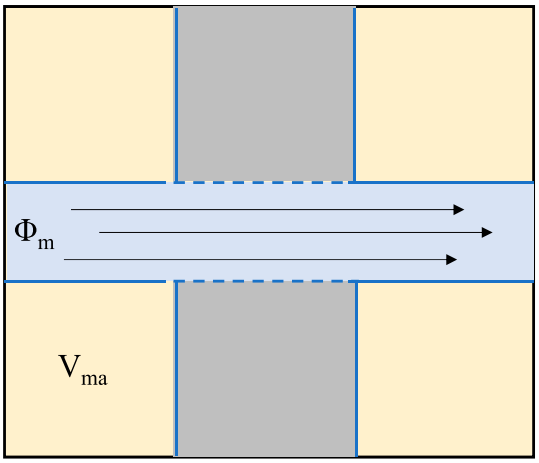

FIGURE 2
Flow model of the pore fluids.

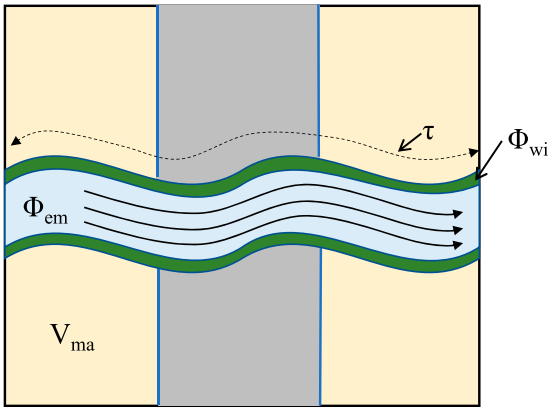

FIGURE 3
ICEREM.

By substituting Equation 4 into Equation 3, the effective porosity of flow fluids is expressed as

$$\phi_{em} = \frac{\phi}{1 + p(1-\phi)} - \phi S_{irr}. \tag{5}$$

The equivalent rock element model assumes that the effective flow pores are straight capillaries. However, studies have shown that the flow of pore fluids in porous media is a complex process (Cai et al., 2019). In order to simulate the actual flow of pore fluids, the effective flow pores are assumed to be curved capillaries. Figure 3 shows the improved capillary equivalent rock element model (ICEREM), where τ is the tortuosity. The ICEREM introduces the volume of bound water, which is more consistent with the microscopic pore characteristics of the rock, and its pore structure characterization accuracy is further improved than that of the EREM model.

In Figure 3, ϕ_{em} is the effective flow porosity, τ is the equivalent tortuosity per unit volume of the rock, ϕ_{wi} is the bound water volume, and V_{ma} is the matrix volume.

2.2 Relationship between water production rate and electrical resistivity in two-phase fluid flows

According to Darcy's law and Poiseuille equation (Darcy, 1856; Song R et al., 2019), the water flow through the rock section can be expressed as

$$Q_0 = \frac{K\Delta p}{\mu_w}\frac{\phi_{em}}{\tau^2}, \tag{6}$$

where Q_0 (m3) is the water flow, K (md) is the permeability, Δp (Pa) is the pressure difference in the rock section, μ_w (s) is the water viscosity, and τ (dimensionless) is the equivalent tortuosity per unit volume of the rock.

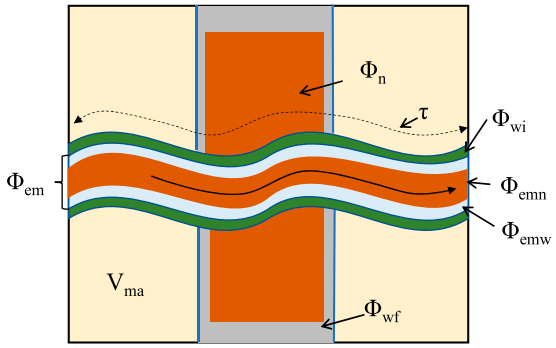

FIGURE 4
Distribution of the two-phase fluid flows in the capillary pores.

From Equation 6, it is assumed that fluids flow only in the effective flow pores, as shown in Figure 3.

As the non-wetting phase fluid entered the pores, it was mainly distributed in the central part of the capillary pores. Figure 4 shows the distribution of the two-phase flow fluids in the capillary pores.

In Figure 4, ϕ_{em} is the effective flow porosity, τ is the equivalent tortuosity per unit volume of the rock, ϕ_{wi} is the bound water volume, ϕ_{emn} is the oil porosity in the effective flow porosity, ϕ_{emw} is the water porosity in the effective flow porosity, ϕ_n is the oil porosity in the macropore porosity, ϕ_{wf} is the water porosity in the macropore porosity, and V_{ma} is the matrix volume.

The water flow and non-wetting phase fluid flow across the rock section can be expressed as

$$\begin{cases} Q_w = \dfrac{K\Delta p}{\mu_w}\dfrac{\phi_{em}S_{wem}}{{\tau_{tw}}^2} \\ Q_n = \dfrac{K\Delta p}{\mu_n}\dfrac{\phi_{em}(1-S_{wem})}{{\tau_{tn}}^2} \end{cases}, \tag{7}$$

where Q_w (m3) is the water flow, Q_n (m3) is the non-wetting phase fluid flow, μ_n (s) is the non-wetting phase fluid viscosity, S_{wem} (v/v) is the water saturation of the effective flow porosity, τ_{tw} is the equivalent tortuosity of the water flow in the effective flow capillary pores, and τ_{tn} (dimensionless) is the equivalent tortuosity of the non-wetting phase fluid flow in the effective flow capillary pores.

According to Equation 7, the water production rate of a two-phase fluid flow can be calculated as follows:

$$F_w = \frac{Q_w}{Q_w+Q_n} = \frac{1}{\left[1+\frac{(1-S_{wem})}{S_{wem}}\frac{{\tau_{tw}}^2}{{\tau_{tn}}^2}\frac{\mu_w}{\mu_n}\right]}. \tag{8}$$

Rock conductivity is the parallel conductance between equivalent capillary porosity and the invalid flow part (invalid flow capillary porosity and the rock matrix). The conductivity of the invalid flow part is assumed to be 0, and the conductivities of water-saturated and partially saturated rock can be obtained as follows:

$$\begin{cases} \sigma_0 = \sigma_c\left(\dfrac{\phi_{em}}{\tau^2}+\dfrac{\phi_m S_{mirr}}{{\tau_r}^2}\right) \\ \sigma_t = \sigma_c\left(\dfrac{\phi_{em}S_{wem}}{{\tau_{tw}}^2}+\dfrac{\phi_m S_{mirr}}{{\tau_r}^2}\right)+\sigma_n\dfrac{\phi_{em}(1-S_{wem})}{{\tau_{tn}}^2} \end{cases}. \tag{9}$$

In Equation 9, σ_0 (S/M) is the water-saturated rock conductivity, σ_t (S/M) is the partially saturated rock conductivity, σ_c (S/M) is the water conductivity, σ_n (S/M) is the non-wetting phase fluid conductivity, τ_r (dimensionless) is the equivalent tortuosity of the irreducible water, and σ_{ma} (S/M) is the conductivity of the rock matrix.

The three-water model considers rock conductivity as a parallel conductance among shaly irreducible water, micropore irreducible water, and free water, and each conductance component follows the Archie model (Zhang and Pan, 2010; Mo et al., 2001). According to the three-water model, the conductivity of water-saturated and partially saturated rock can be further revised as follows:

$$\begin{cases} \sigma_0 = \sigma_c\left[{\phi_{em}}^{m1}+(\phi_m S_{mirr})^{m2}\right] \\ \sigma_t = \sigma_c{\phi_{em}}^{m1}{S_{wem}}^{n1}+\sigma_c(\phi_m S_{mirr})^{m2}+\sigma_n{\phi_{em}}^{m1}(1-S_{wem})^{n2} \end{cases}. \tag{10}$$

In Equation 10, both shaly irreducible water and micropore irreducible water are treated as irreducible water and are assumed to have the same conductivity. $m1$ and $n1$ (dimensionless) are the cementation exponent and saturation exponent of the equivalent capillary pores, respectively. $m2$ and $n2$ represent the cementation exponent and saturation exponent of the irreducible water pores, respectively.

By comparing Equation 9 with Equation 10, we can derive the equivalent tortuosity for the water flow in effective flow capillary pores τ_{tw} (dimensionless) and non-wetting phase fluid flow in the same effective flow capillary pores τ_{tn} (dimensionless):

$$\begin{cases} {\tau_{tw}}^2 = {S_{wem}}^{1-n1}\tau^2 \\ {\tau_{tn}}^2 = \dfrac{1-S_{wem}}{(1-S_{wem})^{n2}}\tau^2 \end{cases}. \tag{11}$$

In addition, when the non-wetting phase fluid conductivity equals the pore water conductivity, according to Equations 9, 10, τ_{tn} can be written as follows:

$${\tau_{tn}}^2 = \frac{1-S_{wem}}{1-{S_{wem}}^{n1}}\tau^2. \tag{12}$$

However, the difference between actual non-wetting phase fluid conductivity and wetting phase fluid conductivity may cause a variation in τ_{tn}. To eliminate the difference, according to Equations 11, 12, τ_{tn} is defined as

$${\tau_{tn}}^2 = \frac{1-S_{wem}}{(1-{S_{wem}}^{n1})^{n2}}\tau^2. \tag{13}$$

By substituting Equations 4, 5, 11, 13 into Equation 8, the water production rate F_w (v/v) of the two-phase fluid flow can be simplified as

$$F_w = \frac{1}{\left[1+\frac{\mu_w}{\mu_n}{S_{wem}}^{-n1}(1-{S_{wem}}^{n1})^{n2}\right]}. \tag{14}$$

According to Equations 9, 10, the relationship between S_{wem} and the resistivity index is as follows:

$$\begin{cases} {S_{wem}}^{n1}+\dfrac{\sigma_n}{\sigma_c}\left(1-{S_{wem}}^{n1}\right)^{n2} = \dfrac{1+H}{RI}-H \\ H = \dfrac{\phi^{m2-m1}{S_{irr}}^{m2}}{\{[1+p(1-\phi)]^{-1}-S_{irr}\}^{m1}} \end{cases}, \tag{15}$$

where RI (dimensionless) is the resistivity index and $RI = \frac{\sigma_0}{\sigma_t}$. Generally, the conductivity of the non-wetting phase fluid (usually oil, gas, or kerosene) is much lower than that of pore water. So, we can assume that $\frac{\sigma_n}{\sigma_c}(1 - {S_{wem}}^{n1})^{n2} \to 0$. Then, Equation 15 can be simplified as

$$\begin{cases} {S_{wem}}^{n1} = \dfrac{1+H}{RI} - H \\ H = \dfrac{\phi^{\alpha 1} {S_{irr}}^{\alpha 2}}{\{[1+p(1-\phi)]^{-1} - S_{irr}\}^{\alpha 3}} \end{cases}, \tag{16}$$

where $\alpha 1$, $\alpha 2$, and $\alpha 3$ (dimensionless) are the exponents (functions of $m1$, $n1$, $m2$, and $n2$).

By comparing Equation 16 with Equation 14, the relationship between the resistivity index and water production rate F_w can be obtained.

$$F_w = \frac{1}{\left\{1 + \frac{\mu_w}{\mu_n}\left(\frac{1+H}{RI} - H\right)^{-\alpha 4}\left[1 - \left(\frac{1+H}{RI} - H\right)^{\alpha 5}\right]^{\alpha 6}\right\}}. \tag{17}$$

In Equation 17, $\alpha 4$, $\alpha 5$, and $\alpha 6$ are introduced to account for the difference between the equivalent tortuosity of pore fluids and that of the electrical current. Generally, $\alpha 1$, $\alpha 2$, $\alpha 3$, $\alpha 4$, $\alpha 5$, and $\alpha 6$ are regional coefficients, which can be calculated using the least squares method.

In Equations 16, 17, pore structure characterization parameters p and S_{irr} are innovatively introduced, which can accurately characterize the seepage law of the two-phase fluid in rocks with different pore structure characteristics.

3 Verification

To verify the model in this paper, the selected rock samples have the same sedimentary environment and lithology, ensuring that the resistivity and seepage capacity of the samples are mainly affected by the pore structure while minimizing the influence of other factors, such as clay content. Seven rock samples selected from the Dongying Formation, Nanpu Sag, are used to verify the relationship model between the RI and water production rate. The porosity ranges from 0.19 to 0.255 (v/v), the permeability ranges from 6.09 to 292 (md), and the irreducible water content ranges from 0.518 to 0.861 (v/v). The rock samples are tested using nuclear magnetic resonance (NMR) experiments and combined tests of resistivity and water–oil two-phase seepage. The seven rock samples, with low clay content, are selected to minimize the influence of shale on resistivity. Table 1 presents the characteristic parameters of the seven rock samples.

Figure 5 shows the T_2 spectrum of rock samples; the variation in the distribution of the T_2 spectra and the position of T_2 peak values indicate differences in pore structures. For example, sample No. 1 shows a double-peak right-skew type with the highest peak position of 100 ms; sample No. 2 shows a double-peak balanced type with the highest peak position of 10 ms; sample No. 3 shows a double-peak left-skew type with the highest peak position of 3 ms; sample No. 4 shows a double-peak right-skew type with the highest peak position of 30 ms; sample No. 5 shows a medium peak with the peak position of 10 ms; sample No. 6 shows a single-peak left-skew type with the peak position of 2 ms; and sample No. 7 shows a single-peak left-handed type with the peak position of 3 ms.

Figures 6–8 show the relationship among RI (resistivity index), F_w (water production rate), and S_w (water saturation). Figure 6 shows the relationship between resistivity and water saturation for the seven rock samples, which exhibit non-Archie phenomenon, and the Archie saturation index n ranges from 1.14–3.1.

It can be observed that $S_w - F_w$ data and $RI - F_w$ data for the seven rock samples in Figures 7, 8 are highly dispersed, which is primarily caused by differences in pore structures. This means that significant errors in the water production rate can occur without considering the pore structure (Honarpour, 2018; Purcell 1949; Burdine 1953; Corey, 1954).

In Equation 16, parameter p is related to the pore structure and is used to calculate the water production rate. In this section, mercury injection capillary pressure (MICP) and NMR experimental data are used to determine macropores and throat pores.

The Swanson parameter (inflexion point) of the mercury injection curve is used to distinguish large and small pores (throat pores) in rock samples (Swanson, 1981; Zhang and Weller, 2021; Xiao et al., 2017). The integral curve of the NMR T_2 spectrum corresponds well with the mercury injection curve. According to the definition of the Swanson parameter, T_2 time at the inflexion point between macropore and small pores is determined, and then parameter p is determined. In this paper, T_2 time at the inflexion point is 110 ms, determined by averaging data from 25 rock samples. Figure 9 shows the classification of macropores and throat pores.

In Figure 9, the NMR T_2 spectra of the core sample (red line) and the pore size distribution of the core sample derived from the MICP experimental data (blue dash-dotted line) are presented. T_2 (ms) is the transverse relaxation time. S (T_2) (%) is the T_2 pore component. ra (μm) is the pore radius. S (ra) (%) is the pore component derived from MICP experimental data. Demarcation T_2 time (ms) is the inflexion point between macropores and throat pores, which is 110 ms in this part.

Regional coefficients $\alpha 1$, $\alpha 2$, $\alpha 3$, $\alpha 4$, $\alpha 5$, and $\alpha 6$ are calculated using porosity, irreducible water saturation, p, and water production rate through the least squares method: $\alpha 1 = 0.005721$, $\alpha 2 = 1.221832$, $\alpha 3 = 0.32887$, $\alpha 4 = 1.72147$, $\alpha 5 = 0.82583$, and $\alpha 6 = 6.14863$.

In order to compare with previous research results, the water production rate is expressed as

$$F_w = 1/\left[1 + \frac{\mu_w}{\mu_n}\frac{k_{rn}}{k_{rw}}\right], \tag{18}$$

where the relative permeability of oil and water phases in the Equation 18 can be calculated according to the model proposed by Wang and Cardenas (2018).

$$\begin{cases} k_{rw} = \left(\dfrac{S_w - S_{irr}}{1 - S_{irr} - S_{or}}\right)^a \\ k_{rn} = 1 - \left(\dfrac{S_w}{1 - S_{or}}\right)^b \end{cases}, \tag{19}$$

where in Equation 19, S_w is water saturation, S_{irr} is bound water saturation, S_{or} is residual oil saturation, k_{rw} is water phase relative permeability, and k_{rn} is oil phase relative permeability. a and b are regional experience indexes, and $a = 1.8104$ and $b = 3.1182$ in this region. The calculation results are shown in Figure 10.

TABLE 1 Characteristic parameters of rock samples.

NO.	Shale content v/v	Porosity v/v	Permeability md	Formation factor	Irreducible water saturation v/v	p
1	0.017	0.241	46.811	12.131	0.544	0.239
2	0.044	0.250	24.400	9.072	0.566	0.075
3	0.025	0.242	55.473	10.512	0.642	0.140
4	0.029	0.194	45.400	15.274	0.518	0.039
5	0.022	0.255	292.000	8.015	0.533	0.095
6	0.037	0.199	6.090	10.641	0.861	0.033
7	0.038	0.216	102.000	6.971	0.536	0.005
Range average value	0.017–0.044 0.03	0.19–0.255 0.23	6.09–292 81.7	6.97–15.3 10.37	0.518–0.861 0.6	0.005–0.24 0.089

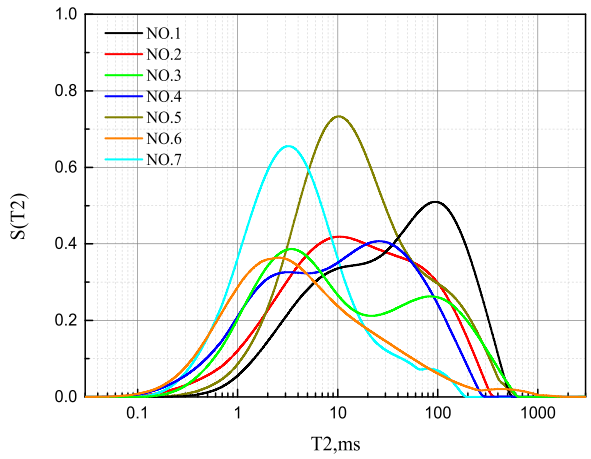

FIGURE 5
T_2 spectrum of the seven rock samples.

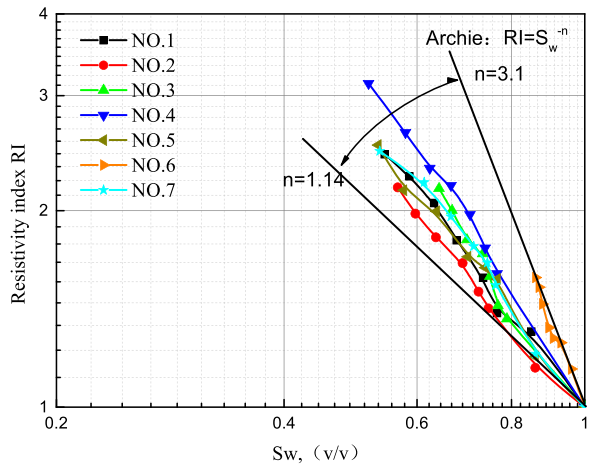

FIGURE 6
Relationship between *RI* and S_w.

The water production rate can be calculated using Equation 17 and Wang and Cardenas model. Figure 10 shows the comparison between the calculated water production rate using Equation 17 and experimental data (the red point in Figure 10), where the goodness of fit is 0.97945, and the average relative error is 5%. Figure 10 shows the comparison between the calculated water production rate by the Wang and Cardenas model and experimental data, where the goodness of fit is 0.7995 and the average relative error is 23%. The result indicates a strong agreement between the calculated water production rate and experimental data.

4 Application in well logging data

The new method is applied to Well NPX49 in Nanpu Sag, Huanghua depression, China. The NMR logging measurement mode of Well NPX49 is D9TWE3. Specific parameter areas are as follows: for Group A, TW_1 = 12.988 s, TEs = 0.9 ms, and the echo number is 500; for Group B, TWs = 1 s, TEs = 0.9 ms, and the echo number is 500; for Group C, TWc = 0.02s, TEc = 0.6 ms, and the echo number is 20; for Group D, TW_1 = 12.988 s, TE_1 = 3.6 ms, and the echo number is 125; and for Group E, TWs = 1 s, TE_1 = 3.6 ms, and the echo number is 125. Drilling mud resistivity is 2.26 OHMM/18°C.

Figure 11 shows the evaluation result of Well NPX49 (layers 1–3) using the new method. The reservoir parameters and water production rate of the produced fluid from layers 1–3 are shown in Table 2.

In Figure 11, tracks from left to right include tracks 1–4: natural gamma-ray logging (GR: GAPI)/spontaneous potential logging (SP: MV), depth (meters), apparent resistivity logs (RLLD/RLLS: OHMM), acoustic-wave slowness logs (AC: us/m), bulk density (DEN: g/cm3), and neutron porosity (CNL:%). Track 5: NMR

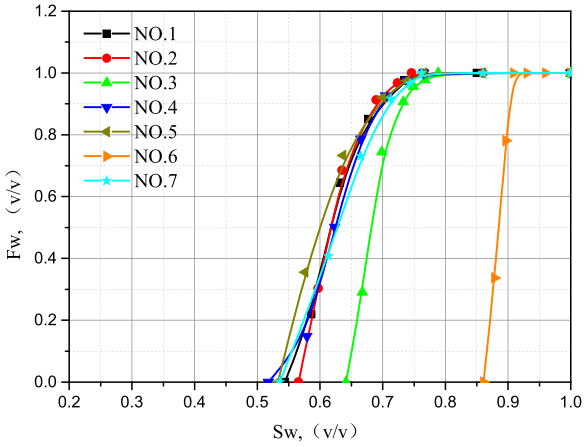

FIGURE 7
Relationship between S_w and F_w.

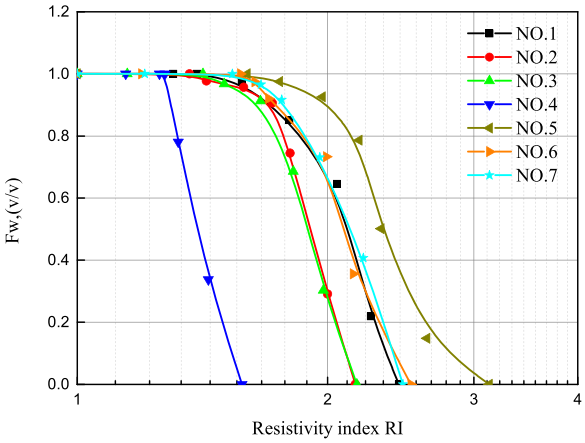

FIGURE 8
Relationship between RI and F_w.

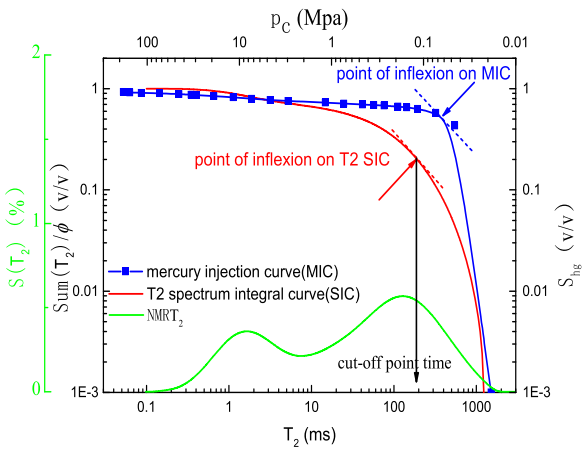

FIGURE 9
Classification of macropores and throat pores.

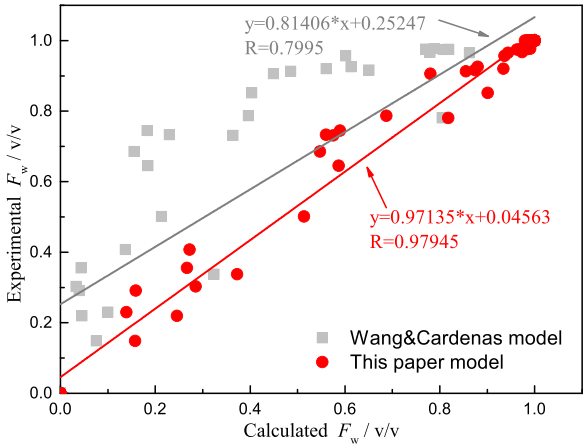

FIGURE 10
Comparison between calculated F_w and experimental data.

logging T_2 spectra measured with parameters TE = 0.9 ms and TW=12988 ms (NMR.TA:ms). Track 6: NMR logging T_2 spectra measured with parameters TE = 3.6 ms and TW=12988 ms (NMR.TB: ms). Track 7: clay-bound water porosity (PWC: V/V)/ capillary-bound water porosity (PWI: V/V)/ movable water porosity (POR: V/V) computed from NMR logging. Track 8: permeability calculated from NMR logging (NMR.PERM: MD). Track 9: water saturation by the Archie model (ARCHIE.SW: V/V)/ irreducible water saturation from NMR (NMR.SIRR: V/V). Track 9: the new method calculated the water production rate of percolating fluid (FW: V/V). Track 10: the number of the layer.

In layers 1–3, the low natural gamma-ray logging values present the characteristics of sandstone with low clay content. The resistivity of layer 1 is high, with a value of 39 Ω·m. The distribution of NMR T_2 spectra for both short-TE and long-TE is broad. The calculated water saturation is 40.3%, and the bound water saturation calculated based on NMR is 38%, demonstrating excellent oil-bearing characteristics. The daily oil production of layer 1 is 14 m^3 with no water (the water production rate F_w of layer 1 is 0, as shown in Table 2; F_w represents the volume ratio of water in the produced liquid volume). This indicates that pore water in layer 1 is in a bound state and cannot flow. The resistivity of layers 2 and 3 is low, with values of 22 and 27 Ω·m, respectively. The distribution of NMR T_2 spectra for short-TE and long-TE is also broad. The calculated water saturation is 65.8% and 61.7% for layers 2 and 3, respectively, indicating the oil-bearing characteristics of layers 2 and 3.

The distribution of long-TE T_2 spectra and short-TE T_2 spectra narrows from layer 1 to layer 3. The oil saturations of layers 1–3 are 59.7%, 34.2%, and 38.3%, respectively. The calculated water saturation reduced from layer 1 to layer 3, indicating that layer 1 is more oil-rich than layers 2 and 3. The calculated results of layers 2 and 3 show some differences. However, the daily oil production of layer 2 is 0.2 m^3, with a water production rate of 95.6%. The daily oil production of layer 3 is 3.2 m^3, with a water production rate of 60.4%. The main reason for the difference between layers 2 and 3 is the difference in the pore structure; for instance, the NMR T_2 spectrum in layer 2 shows obvious bimodal right-skew characteristics, while in layer 3, it shows single-modal left-skew characteristics. The application results show

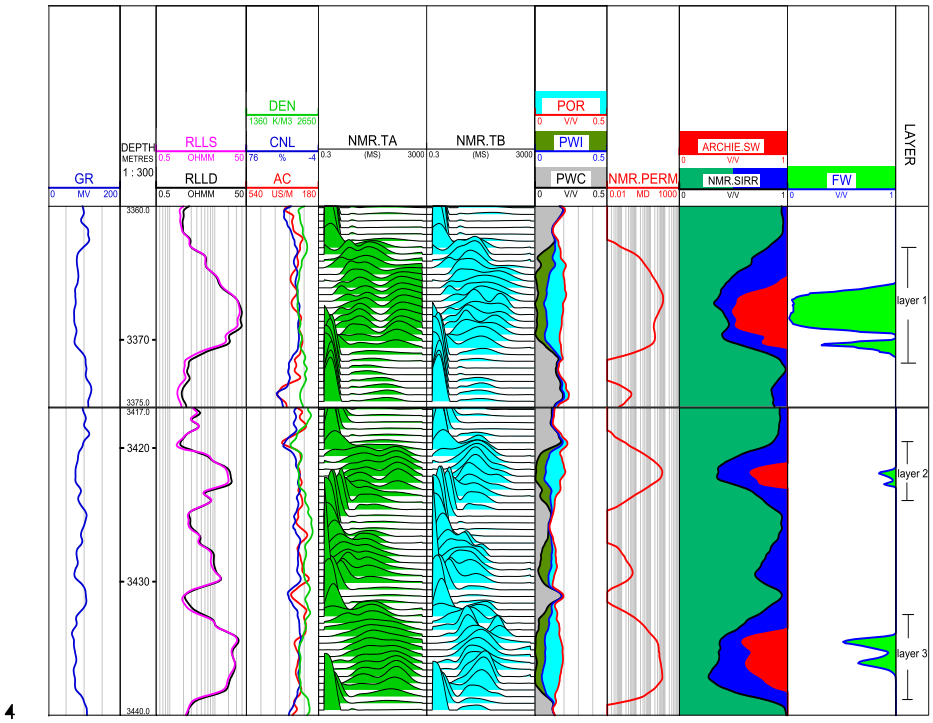

FIGURE 11
Application to well NPX49 (layers 1–3).

TABLE 2 Reservoir parameters.

No.	Rt ohm.m	POR %	PERM md	SIRR %	Sw_Archie %	Calculated F_w %	Production F_w %
Layer 1	39	21	75	38	40.3	5.5	0
Layer 2	22	20	55	36	65.8	87.1	95.6
Layer 3	27	18	52	33	61.7	67.5	60.4

that oil saturation does not reflect actual oil production. The water production rate calculated by the new model is consistent with the actual production situation.

5 Discussion and future work

(1) Accurately estimating the pore structure is a crucial factor in improving the accuracy of water production rate prediction models. The new model can directly calculate the water production rate from the resistivity index, avoiding errors introduced by water saturation calculation in previous $S_w - F_w$ relationship models. On one hand, the new model incorporates pore structure characterization methods, and its accuracy has been verified through experimental data and practical engineering applications. On the other hand, compared with the Wang and Cardenas model, which requires sequential calculations of water saturation, bound water saturation, and residual oil saturation before determining the water production rate, the new model leverages pore structure models and the similarity between current conduction and seepage flow patterns, directly estimating the water production rate based on rock resistivity. This approach is straightforward and minimizes intermediate error propagation.

(2) The new model can accurately predict the water production rate of rocks with different pore structures with the introduction of a pore structure-related parameter p. The pore structure-related parameter p should be obtained from the NMR T_2 spectrum. Therefore, resistivity and nuclear magnetic resonance logging data need to be obtained and applied to actual logging data.

(3) The error in the water production rate calculated by the new model may be caused by the following factors: ①pore structure differences between the actual model and the ICEREM, ② flow path differences between the electrical and fluid flows, ③measurement errors in experimental data, and ④ the presence of additional conductive minerals in the rock skeleton.

(4) Since the ICEREM model mainly considers irreducible water and capillary tortuosity, other pore structure parameters, such as wettability and shaly content, are assumed to be uniform; the accuracy of the new model can be further improved by classifying pore structures and redefining the empirical parameters in Equations 16, 17 of each pore structure type.
(5) The wetting phase saturation value in a reservoir does not accurately reflect the wetting phase ratio of the output fluid volume in two-phase fluid seepage, so the calculated water saturation/oil saturation is not consistent with the actual water/oil ratio, as shown in Figure 11. However, the water production rate calculated by the new model is consistent with the actual production situation, indicating that the model can be used to guide reservoir production or the application of two-fluid seepage in a porous material.

Further research directions concerning the electrical properties of sand-based porous materials and the conductivity equation of rocks may include the following aspects:

a. A new equation should be established for rock resistivity based on sandstone pore structure characteristics. However, in carbonate, volcanic rocks, and other types of rock, the pore characteristics differ from those of sandstone, such as fractures and caves in carbonate and high- and low-angle fractures in volcanic rocks (Xie et al., 2024a). The new model's adaptability needs further validation, and model parameters must be determined by sample experiments.
b. The model in this paper does not consider skeleton conductivity, but some mineral skeletons in rock samples are conductive, such as wet clay and pyrite. Considering the influence of conductive minerals on rock conductivity is the next step to improve the accuracy of the model.
c. The conductivity models of rock are widely used in well logging research, reservoir evaluation, reservoir research, and geological research (Xie et al., 2024b). One of the next steps is to extend the new model in this paper and apply it to these research areas.
d. The conductivity theory of sandstone in this paper can be extended and applied to cement, coal, and other types of porous materials, but it needs to be verified and analyzed by conducting experiments on different types of porous media.

6 Conclusion

(1) Pore structure significantly influences rock electrical properties and seepage characteristics. The EREM has been improved by considering irreducible water and capillary tortuosity.
(2) Based on the ICEREM, the relationship model between the water production rate and resistivity index has been proposed.
(3) Compared to the previous water production rate models ($S_w - F_w$ relationship models), the new model, on one hand, avoids errors caused by water saturation calculation; on the other hand, it introduces a pore structure-related parameter p to address the effect of the pore structure on rock seepage characteristics and electrical properties.
(4) The results of verification and application have shown that the water production rate calculated by the new model is in accordance with experimental values and the actual water production rate.
(5) The new model can predict the water production rate based on electrical properties, dynamically enhance reservoir evaluation, and strengthen the database for reservoir development planning, production forecasting, and reservoir evaluation.

Data availability statement

The raw data supporting the conclusions of this article will be made available by the authors, without undue reservation.

Author contributions

WX: conceptualization, methodology, writing–original draft, and writing–review and editing. QY: conceptualization, methodology, and writing–review and editing. XD: writing–review and editing. YF: data curation, validation, and writing–review and editing. PZ: writing–review and editing.

Funding

The author(s) declare that financial support was received for the research, authorship, and/or publication of this article. This article was supported by the Research Foundation of Karamay, China (2024hjcxrc0075), the Research Foundation of the China University of Petroleum-Beijing at Karamay (No. XQZX20230012), "Tianchi Talent" Introduction Plan Foundation of Xinjiang, and the Natural Science Foundation of Xinjiang (No. 2021D01E22).

Conflict of interest

Author YF was employed by China Petroleum Logging Co., Ltd.
The remaining authors declare that the research was conducted in the absence of any commercial or financial relationships that could be construed as a potential conflict of interest.

Generative AI statement

The author(s) declare that no Generative AI was used in the creation of this manuscript.

Publisher's note

References

Archie, G. E. (1942). The electrical resistivity log as an aid in determining some reservoir characteristics. *Trans. AIME* 146 (01), 54–62. doi:10.2118/942054-g

Bear, J. (2013). Dynamics of fluids in porous media. *Cour. Corp.*

Behrang, A., Mohammadmoradi, P., Taheri, S., and Kantzas, A. (2016). A theoretical study on the permeability of tight media; effects of slippage and condensation. *Fuel* 181, 610–617. doi:10.1016/j.fuel.2016.05.048

Burdine, N. T. (1953). Relative permeability calculations from pore size distribution data. *Petr.trans.am Inst.mining Metall.eng.* 98 (3), 71–78.

Cai, J., Lin, D., Singh, H., Zhou, S., Meng, Q., and Zhang, Q. (2019). A simple permeability model for shale gas and key insights on relative importance of various transport mechanisms. *Fuel* 252, 210–219. doi:10.1016/j.fuel.2019.04.054

Chen, X., and Yao, G. (2017). An improved model for permeability estimation in low permeable porous media based on fractal geometry and modified Hagen-Poiseuille flow. *Fuel* 210, 748–757. doi:10.1016/j.fuel.2017.08.101

Chimá, A., Chávez, E. A., and Calderón, Z. (2010). "An equation to predict two-phase relative permeability curves in fractures," in *SPE Latin American and Caribbean petroleum engineering conference* (Society of Petroleum Engineers). doi:10.2118/138282-MS

Clarkson, C. R., Rahmanian, M., Kantzas, A., and Morad, K. (2011). Relative permeability of CBM reservoirs: controls on curve shape. *Int. J. Coal Geol.* 88 (4), 204–217. doi:10.1016/j.coal.2011.10.003

Corey, A. T. (1954). The interrelation between gas and oil relative permeabilities. *Prod. Mon.* 19 (1), 38–41.

Darcy, H. (1856). *Les Fontaines Publiques de la Ville de Dijon*. Paris: Dalmont.

Honarpour, M. M. (2018). *Relative permeability of petroleum reservoirs*. CRC Press.

Iscan, A. G. (2021). Water saturation calculation using fractional flow and production logging data in a Caspian region sandstone petroleum reservoir. *J. Petroleum Sci. Eng.* 200, 108355. doi:10.1016/j.petrol.2021.108355

Jin, Y., Li, S., and Yang, D. (2020). Experimental and theoretical quantification of the relationship between electrical resistivity and hydrate saturation in porous media. *Fuel* 269, 117378–378. doi:10.1016/j.fuel.2020.117378

Kasha, A., Myers, M., Hathon, L., Sakhaee-Pour, A., Sadooni, F., Nasser, M., et al. (2023). Integrated approach for closure correction of mercury injection capillary pressure measurements. *Geoenergy Sci. Eng.* 230, 212245. doi:10.1016/j.geoen.2023.212245

Lei, G., Liao, Q., Lin, Q., Zhang, L., Xue, L., and Chen, W. (2020). Stress dependent gas-water relative permeability in gas hydrates: a theoretical model. *Adv. Geo-Energy Res.* 4 (3), 326–338. doi:10.46690/ager.2020.03.10

McKenna, S. A., Akhriev, A., Ciaurri, D. E., and Zhuk, S. (2020). Efficient uncertainty quantification of reservoir properties for parameter estimation and production forecasting. *Math. Geosci.* 52 (2), 233–251. doi:10.1007/s11004-019-09810-y

Mo, X. W., He, D. H., Li, Z.Bo, Wen, X. C., and Li, G. R. (2001). The application of three-water conduction model in the interpretation of low-resistivity reservoir. *J. Changchun Univ. ence Technol* (01), 92–95. doi:10.13278/j.cnki.jjuese.2001.01.019

Peng, Xu, Qiu, S., Yu, B., and Jiang, Z. (2013). Prediction of relative permeability in unsaturated porous media with a fractal approach. *Int. J. Heat Mass Transf.* 64, 829–837. doi:10.1016/j.ijheatmasstransfer.2013.05.003

Pius, T. O., and Olamigoke, O. (2020). "Investigating the correlation between water saturation obtained from cased-hole saturation tool measurements and produced water cut in strong water drive reservoirs," in *SPE Nigeria annual international conference and exhibition*, D013S018R002.

Purcell, W. R. (1949). Capillary pressures - their measurement using mercury and the calculation of permeability therefrom *J. Pet. Technol.* 1 (02), 39–48.

Rangelov, M., and Nassiri, S. (2018). Empirical time-dependent tortuosity relations for hydrating mortar mixtures based on modified archie's law. *Constr. Build. Mater.* 171, 825–838. doi:10.1016/j.conbuildmat.2018.03.173

Reza-E-Rabbi, S., Ahmmed, S. F., Arifuzzaman, S. M., Sarkar, T., and Khan, M. S. (2020). Computational modelling of multiphase fluid flow behaviour over a stretching sheet in the presence of nanoparticles. *Eng. Sci. Technol. Int. J.* 23 (3), 605–617. doi:10.1016/j.jestch.2019.07.006

Rutqvist, J., Wu, Y. S., Tsang, C. F., and Bodvarsson, G. (2002). A modeling approach for analysis of coupled multiphase fluid flow, heat transfer, and deformation in fractured porous rock. *Int. J. Rock Mech. Min. Sci.* 39 (4), 429–442. doi:10.1016/s1365-1609(02)00022-9

Schlachter, G. (2007). "Using wireline formation evaluation tools to characterize coalbed methane formations," in *Eastern regional meeting* (Society of Petroleum Engineers). doi:10.2118/111213-ms

Schön, J. (2011). *Physical properties of rocks: a workbook*, 8. Elsevier.

Shang, B. Z., Hamman, J. G., and Caldwell, D. H. (2003). "A physical model to explain the first Archie relationship and beyond," in *SPE annual technical conference and exhibition* (Society of Petroleum Engineers). doi:10.2118/84300-MS

Shang, B. Z., Hamman, J. G., and Caldwell, D. H. (2004). "Water saturation estimation using equivalent rock element model," in *SPE annual technical conference and exhibition* (Society of Petroleum Engineers). doi:10.2118/90143-MS

Shang, B. Z., Hamman, J. G., and Caldwell, D. H. (2008). "Improved water saturation estimation using equivalent rock element model and applications to different rock types," in *Europec/EAGE conference and exhibition* (Society of Petroleum Engineers). doi:10.2118/113342-MS

Smirnov, N. N., Nikitin, V. F., and Skryleva, E. I. (2019). Microgravity investigation of seepage flows in porous media. *Microgravity Sci. Technol.* 31 (1), 629–639. doi:10.1007/s12217-019-09733-7

Song, R., Wang, Y., Liu, J., Cui, M., and Lei, Y. (2019). Comparative analysis on pore-scale permeability prediction on micro-ct images of rock using numerical and empirical approaches. *Energy ence and Eng.* 7 (2), 2842–2854. doi:10.1002/ese3.465

Swanson, B. F. (1981). A simple correlation between permeabilities and mercury capillary pressures. *J. Petroleum Technol.* 33 (12), 2498–2504. doi:10.2118/8234-pa

Tiab, D., and Donaldson, E. C. (2024). *Petrophysics: theory and practice of measuring reservoir rock and fluid transport properties*. Elsevier.

Wang, F., Jiao, L., Zhao, J., and Cai, J. (2019). A more generalized model for relative permeability prediction in unsaturated fractal porous media. *J. Nat. Gas Sci. Eng.* 67, 82–92. doi:10.1016/j.jngse.2019.04.019

Wang, L., and Cardenas, M. B. (2018). Connecting pressure-saturation and relative permeability models to fracture properties: the case of capillary-dominated flow of supercritical CO2 and brine. *Water Resour. Res.* 54 (9), 6965–6982. doi:10.1029/2018wr023526

Wang, Y., Li, H., Xu, J., Liu, S., and Wang, X. (2022). Machine learning assisted relative permeability upscaling for uncertainty quantification. *Energy* 245, 123284. doi:10.1016/j.energy.2022.123284

Whittle, T. M., Lee, J., and Gringarten, A. C. (2003). "Will wireline formation tests replace well tests?," in *SPE annual technical conference and exhibition* (Society of Petroleum Engineers). doi:10.2118/84086-MS

Wu, Y., Zhang, H., Yang, D., Zhang, H., and Yuan, W. (2018). Oil-gas breakthrough time and water content predict or mdt pump in low permeability reservoir. *Well logging Technol.* 42 (5), 557–561. doi:10.16489/j.issn.1004-1338.2018.05.012

Xiao, L., Liu, D., Wang, H., Li, J., Lu, J., and Zou, C. (2017). The applicability analysis of models for permeability prediction using mercury injection capillary pressure (MICP) data. *J. Petroleum Sci. Eng.* 156, 589–593. doi:10.1016/j.petrol.2017.06.042

Xie, W., Yin, Q., Guan, W., Wang, G., and Lai, J. (2020). Estimating the relative permeability from the electrical parameters of sandstone with a complex pore structure. *Energy&Fuels* 34, 14124–14131. doi:10.1021/acs.energyfuels.0c03218

Xie, W., Yin, Q., Wu, L., Yang, F., Zhao, J., and Wang, G. (2024b). A new nuclear magnetic resonance-based permeability model based on two pore structure characterization methods for complex pore structure rocks: permeability assessment in Nanpu Sag, China. *Geophysics* 89 (1), MR43–MR51. doi:10.1190/geo2023-0026.1

Xie, W., Yin, Q., Zeng, J., Wang, G., Feng, C., and Zhang, P. (2023). Fractal-based approaches to pore structure investigation and water saturation prediction from NMR measurements: a case study of the gas-bearing tight sandstone reservoir in Nanpu sag. *Fractal Fract.* 7, 273. doi:10.3390/fractalfract7030273

Xie, W., Yin, Q., Zeng, J., Yang, F., Zhang, P., and Yan, B. (2024a). An improved rock resistivity model based on multi-fractal characterization method for sandstone micro-pore structure using capillary pressure. *Fractal Fract.* 8, 118. doi:10.3390/fractalfract8020118

Xu, F., Mu, L., Wu, X., Sun, T., Ding, Y., Tian, X., et al. (2014). New expression of oil/water relative permeability ratio vs. water saturation and its application in water flooding curve. *Energy Explor. and exploitation* 32 (5), 817–830. doi:10.1260/0144-5987.32.5.817

Yin, X., Jiang, S., YanLu, L., Wei, G., Jungang, L., Peng, W., et al. (2020). Impact of pore structure and clay content on the water-gas relative permeability curve within tight sandstones: a case study from the ls block, eastern ordos basin, China. *J. Nat. Gas ence Eng.* 81, 103418. doi:10.1016/j.jngse.2020.103418

Yushu Wu (2015). *Multiphase fluid flow in porous and fractured reservoirs*. Houston: Gulf professional publishing.

Zhang, L., Pan, B., Li, Z., Mo, X., Xia, Z., and Xu, W. (2010). New three-water conduction model and its application in evaluation of low porosity and low permeability reservoir. *Oil Geophys. Prospect.* 45 (3), 431–435. doi:10.13810/j.cnki.issn.1000-7210.2010.03.025

Zhang, Z., and Weller, A. (2021). A comparative study of permeability prediction for Eocene sandstones—Part 1: application of modified Swanson models to mercury injection capillary pressure and nuclear magnetic resonance data. *Geophysics* 86 (6), M233–M243. doi:10.1190/geo2021-0194.1

Zhong, Z., Sun, A. Y., Ren, B., and Wang, Y. (2021). A deep-learning-based approach for reservoir production forecast under uncertainty. *SPE J.* 26 (03), 1314–1340. doi:10.2118/205000-pa

frontiers | Frontiers in Earth Science

TYPE Original Research
PUBLISHED 12 February 2025
DOI 10.3389/feart.2025.1499748

OPEN ACCESS

EDITED BY
Weichao Yan,
Ocean University of China, China

REVIEWED BY
Huachuan Wang,
University of Strathclyde, United Kingdom
Jiaqi Xu,
Harbin Institute of Technology, China

*CORRESPONDENCE
Zhuwen Wang,
wangzw@jlu.edu.cn

RECEIVED 21 September 2024
ACCEPTED 02 January 2025
PUBLISHED 12 February 2025

CITATION
Qi X, Wang S, Wei Y and Wang Z (2025) Numerical simulation study on coal seam response characteristics of shallow three-electrode laterolog.
Front. Earth Sci. 13:1499748.
doi: 10.3389/feart.2025.1499748

Numerical simulation study on coal seam response characteristics of shallow three-electrode laterolog

Xinghua Qi[1,2], Shimao Wang[2], Yuxuan Wei[2] and Zhuwen Wang[1]*

[1]College of Geo-Exploration Science and Technology, Jilin University, Changchun, China, [2]School of Mining Engineering and Geology, Xinjiang Institute of Engineering, Urumqi, China

Shallow three-electrode laterolog is widely used in the field of coal field logging because of its strong economy. Coal seams in Xinjiang region have the characteristics of large thickness variation, high dip angle, easy diameter enlargement and fracture development, but the law of these characteristics in the three-electrode laterolog curve is not clear. In this paper, through the finite element simulation software COMSOL Multiphysics, 2D and 3D models are constructed based on shallow three-electrode laterolog, and the characteristics of using shallow three-electrode laterolog in coal field logging are studied. The results show that the electrode system coefficient of shallow three-electrode laterolog instrument should be 0.94 times of the theoretical electrode system coefficient. The discrimination ability of shallow three-electrode laterolog to coal seams is about 0.3 m. There is a power function relationship between the determination coefficient of coal seam boundary and the ratio of coal seam-surrounding rock resistivity ratio. An increase in the dip angle of the coal seam leads to an increase in the apparent thickness of the coal seam following a quadratic function relationship, while an increase in the wellbore radius results in a quadratic function decrease in the apparent resistivity of the coal seam. An increase in both the width and length of the fractures leads to a decrease in apparent resistivity following a power function relationship. The research results provide a more accurate reference standard for the analysis and evaluation of coal seams using shallow three-electrode laterolog.

KEYWORDS

shallow three-electrode laterolog, numerical simulation, fractured coal seam, stratification and thickness determination, boundary of coal seam, wellbore enlargement

1 Introduction

Laterolog was developed in the 1950s in order to reduce the diversion effect of drilling fluid and the influence of low-resistance surrounding rock during logging, so as to obtain more accurate apparent resistivity curves (Doll, 1951). The laterolog enhances the longitudinal resolution of the main electrode through the transverse shielding and longitudinal extension of the current, thereby improving the accuracy of the stratification and thickness determination of the reservoir. The technique is widely used in saltwater drilling fluid Wells, high-resistance thin layer zones, and carbonate zones.

Three-electrode laterolog is a kind of laterolog, which is widely used in coal exploration because of its advantages of economic benefits, simple structure, convenient use and low maintenance cost. Tang (1985), Huang (2010), and Xu (1988) applied the three-electrode laterolog to the actual quantitative interpretation of coal quality, stratification and thickness determination and mud intrusion analysis, and achieved remarkable results. In addition, Chen et al. (2013) designed a new three-electrode laterolog instrument STM32 for the acquisition of different probe signals. However, three-electrode laterolog failed to achieve the expected results in some coal fields in Xinjiang.

Coal seams in Xinjiang have the geological characteristics of large dip angle and large thickness variation. In addition, there are obvious differences in fracture propagation and fracture morphology between the coal seam and other areas (Lan, 2024; Lu et al., 2021). At the same time, the coal seams in Xinjiang also show the characteristics of large thickness variation, widespread distribution of fractured reservoirs and obvious drilling enlargement. Due to these factors, the corresponding relationship between the three-electrode laterolog response characteristics and the coal seam spatial characteristics and electrical characteristics is not clear, so it is urgent to carry out relevant research.

The corresponding laws and characteristics of laterolog instruments can be studied by forward modeling. Many researchers use forward modeling to study the control factors and build correction charts or conduct studies of complex reservoirs. In the research field of dual laterolog, Zhang et al. (2002), Fan and Lu (2005), and Deng et al. (2009) used the forward model to study the response characteristics of double dual laterolog of layer thickness, surrounding rock and well, and established the corresponding map; Zhang et al. (2014), Ge et al. (2019), Wu et al. (2022), and Hu et al. (2019) studied the logging response characteristics of fractured reservoirs in different fracture spatial locations, geometric shapes and fluid conductivity based on the forward model, and established the relationship between fracture parameters and dual laterolog response; Liu et al. (2012a), Liu et al. (2012b), Deng et al. (2012), and Pan et al. (2022) constructed dual laterolog forward models for unconventional reservoirs such as carbonate reservoirs, sand-mudstone interbeds, fracture-cavity reservoirs, and dissolved vuggy fractured reservoirs to study the controlling factors of their logging responses; Mohammed et al. (2021), Shalaby and Islam (2017), and Wiersberg et al. (2020), and others, utilized logging data that includes Dual Laterolog (DLL), QLGA data, and seismic data to determine the characteristics of oil and gas reservoir profiles, assess gas flow and the development of fractures, thereby guiding the interpretation and development of oil and gas reservoirs; Saboorian-Jooybari et al. (2016), Xue et al. (2022), and Wang et al. (2023) used measured data and a dual laterolog forward model for fracture identification and evaluation. In the research field of array laterolog, Feng et al. (2018) and Ni et al. (2018) studied the apparent resistivity characteristics of well inclination, layer thickness, surrounding rock and eccentricity distance based on the forward model of directional and horizontal Wells, and established the corresponding layer thick-surrounding rock correction charts and surrounding rock correction charts; Liang et al. (2021) established wellbore correction charts and surrounding rock correction charts through forward modeling to compare measured data and analyze the performance of logging instruments; Wu et al. (2008) and Pan et al. (2013) studied the controlling factors of logging curves based on Robin boundary conditions and different measurement modes, and Hu et al. (2019) realized fast inversion of logging data by adding Windows; Sushant et al. (2017) established a 3D model with vertical fractures to explain the unusual curve separation issues in array lateral logging in shale gas reservoirs; Ni et al. (2017) and Si et al. (2020) studied the log response characteristics of complex reservoirs using the mud intrusion anisotropy model and the fractured reservoir model of horizontal Wells. At the same time, Huo and Li (1990) and Szijártó et al. (2017) utilized the finite element method to establish a shallow three-electrode laterolog model, investigating the impact of various geometric and electrical parameters on the lateral curves. However, the conditions were complex, not systematic, and no specific functional patterns were derived (Huo and Li, 1990; Szijártó et al., 2017).

Therefore, this paper uses the finite element software COMSOL Multiphysics to establish the shallow three-electrode laterolog model of coal seam, and systematically studies the influence of coal seam thickness, coal seam-surrounding rock resistivity ratio, coal seam dip angle, coal seam wellbore enlargement and coal seam fracture on the apparent resistivity curve. The purpose of this paper is to provide a useful reference for coal seam identification and evaluation of shallow three-electrode laterolog in coal field.

2 Technical road

This study is based on the principles of shallow three-electrode laterolog and finite element theory, utilizing COMSOL Multiphysics software to establish a constant voltage shallow three-electrode laterolog model, in order to investigate the response characteristics of shallow three-electrode laterolog in coal seams. Under the premise of identical parameters, the study compares the differences in apparent resistivity curves between 2D and 3D models, ensuring the consistency of forward modeling results. Analyzing the ratio of apparent resistivity to true resistivity obtained from empirical formulas in an ideal state, the study corrects the electrode system coefficients to enhance the accuracy of the results. Subsequently, by altering parameters such as coal seam thickness, coal seam-surrounding rock resistivity ratio, coal seam wellbore enlargement and coal seam fracture in the 2D model, and coal seam dip angle in the 3D model, the study analyzes the characteristics of the apparent resistivity curves and summarizes the response patterns.

3 Principle of three-electrode laterolog

Shallow three-electrode laterolog (LL3), namely, three-electrode laterolog, can be divided into shallow three-electrode laterolog and deep three-electrode laterolog according to the different lateral exploration depth (in order to avoid occupying the paper's space, this paper only takes shallow three-electrode laterolog as an example to study its response characteristics). The electrode system of shallow three-electrode laterolog consists of five cylindrical metal electrodes, in which the main electrode (A_0) is located in the middle, and a shield electrode (A_1, A_2) and a loop electrode (B_1, B_2) are symmetrically arranged on both sides. The electrode spacing

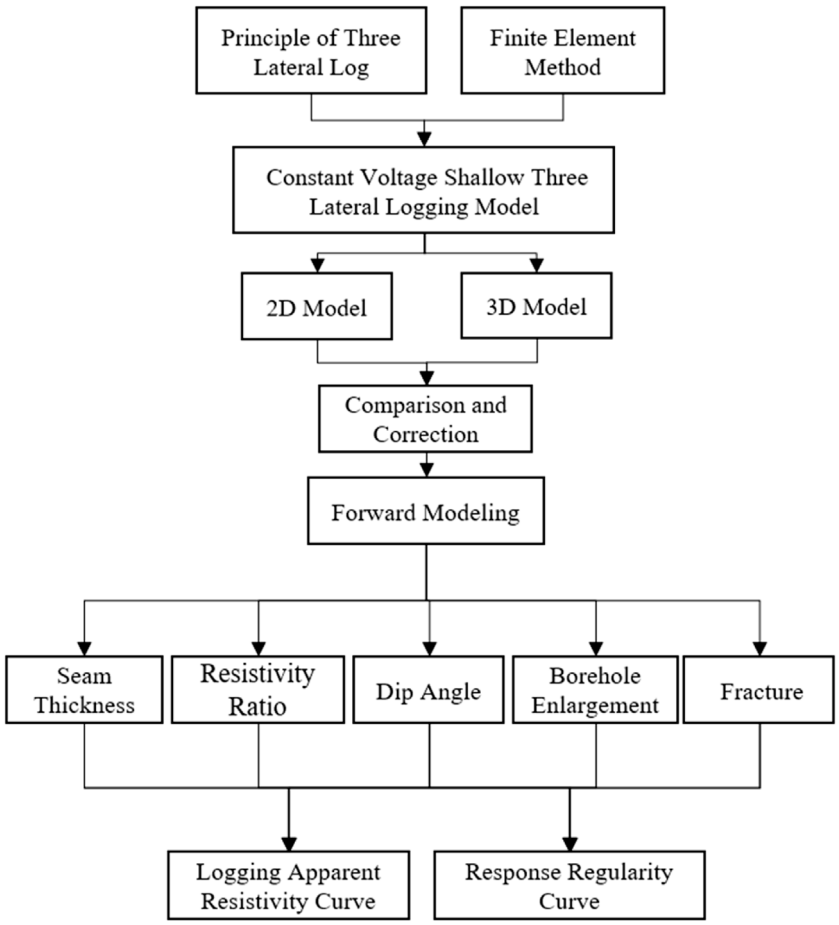

FIGURE 1
Technology roadmap.

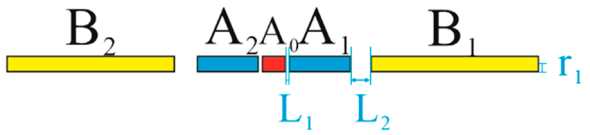

FIGURE 2
Shallow three-electrode laterolog parameters.

between the main electrode and the shield electrode (L_1) and the shield electrode and the loop electrode (L_2) are respectively. As shown in Figure 2.

In the logging process, the main electrode and the shielding electrode are passed with the same polarity of current I_0 and I_s, and I_0 is kept constant. The method of automatic control of I_s is adopted to make the potential on the main electrode (A_0) and the two shielding electrodes (A_1 and A_2) tend to be equal, and the potential gradient along the electrode or the shaft is zero ($\partial U/\partial z = 0$). Thus, it is ensured that the current flowing from the main electrode does not flow along the well axis. The main current I_0 is roughly squeezed into a disc-shaped laminar flow. The thickness of this disk layer, or main current layer, is approximately equal to the length of the main electrode plus half the distance between the main electrode and each shield electrode, and it remains essentially constant for a certain radial distance. This characteristic of the main current layer makes the shallow three-electrode laterolog curve have high longitudinal stratification ability.

The apparent resistivity R_a can be expressed as follows:

$$R_a = K\frac{U}{I_0} \tag{1}$$

Where: R_a is the apparent resistivity in Ω·m; U is the surface potential of the electrode in V; I_0 represents the main current intensity in A.

According to the empirical formula, the coefficient K of electrode system in shallow three-electrode laterolog can be approximated as follows:

$$K = \frac{2\pi A_0}{\lg \frac{2(A_0+A_1+L_1)}{r_0}} \tag{2}$$

Where, K is the coefficient of shallow three-electrode laterolog electrode system; A_0 is the length of the main electrode; A_1 represents the length of the shielding electrode 1, and it is equal

in length to the shielding electrode 2 (i.e., A_2), L_1 is the distance between the upper and lower shielding electrodes and the main electrode, and r_0 is the radius of the electrode. Their units are all meters (m).

4 Three-electrode laterolog finite element modeling

4.1 Basic theory of electric field simulation

Numerical simulation is a basic and economic research means. In this paper, COMSOL Multiphysics numerical simulation software is used to construct a shallow three-electrode laterolog model to explore the corresponding characteristics of coal seam shallow three-electrode laterolog under different conditions.

When constructing the model, the current module in COMSOL Multiphysics software is used, and the physical field related law is mainly reflected in the Gaussian electric field law. Its expression is:

$$-\nabla \cdot V = E \tag{3}$$

$$\nabla \cdot D = \rho_V \tag{4}$$

The linear relationship between the current density J_c and the electric field E is as follows:

$$J_c = \sigma \cdot E \tag{5}$$

In electrical conductors, the current density is proportional to the electric field strength, and the proportionality factor is the conductivity σ.

Where: U is voltage, unit is V; E is the electric field strength in V/m; D is the electric displacement vector, also known as the electric flux density, in C/m^2. ρ_v is the charge density in C/m^3; J_c is the conductive current density vector in A/m^2; σ is the conductive capacity of the material in S/m.

4.2 Model and parameter setting

Considering that the calculation time of 2D model is short, and only 3D model can effectively study the characteristics of inclined strata, this paper constructs 2D model and 3D model at the same time. The 2D model is used to study the response characteristics of coal seam thickness, coal seam-surrounding rock resistivity ratio, coal seam wellbore enlargement and coal seam fracture, and the 3D model is used to study the response characteristics of coal seam dip angle. To save computing resources and time cost, the model is shown in Figure 3.

In Figure 3, both the 2D and 3D models are composed of simulated strata and electrode systems. The 2D model is 2 m wide and 15 m high, and the 3D model has a radius of 2 m and 15 m high. Second, the lithology of the 2D and 3D models are the same, the middle is coal seam, the upper surrounding rock is sandstone, and the lower surrounding rock is limestone. The electrodes were attached to the left wellbore of the 2D model and the middle wellbore of the 3D model. Parametric scanning was performed from 2.5 m to 12.5 m for the 2D model and from −2.5 m to 7.5 m for the 3D model, and the apparent resistivity of a point was measured at an interval of 0.125 m.

The measurement method of the model is constant voltage shallow three-electrode laterolog, and the lithology of the formation is sandstone-coal-limestone interbed. The specific model parameters are shown in Table 1.

5 Model comparison and correction

5.1 Model comparison of 2D and 3D models

In theory, the difference between 2D and 3D models is solely due to the dimensions, which affect the computation time and the precision of the results. Under the same conditions, both models should yield roughly the same outcomes. Based on this, this section conducts a consistency test of the models to demonstrate the consistency between the 2D and 3D models, as shown in Figure 4.

From Figure 4, it can be observed that between 2.5 m and 12.5 m of the parametric scan, the apparent resistivity curve distinctly reflects the electrical property differences of different geological bodies and the changes at their boundaries. The coal seam, located between 5 m and 10 m, exhibits an apparent resistivity that is higher in the middle and lower on both sides; moreover, the boundary areas where the upper surrounding rock (limestone) and the lower surrounding rock (sandstone) approach the coal seam also show symmetrical resistivity fluctuation characteristics. Due to the homogeneous model constructed in this paper, there is a significant resistivity difference at the coal-rock boundary, and the resistivity does not transition gradually, hence minor fluctuations, known as boundary effects, appear at the boundary. Notably, due to the different levels of mesh discretization in the 2D and 3D models, the apparent resistivity curves exhibit variations in fluctuation and smoothness outside the boundaries (2.5–4 m, 6–9 m, 11–12.5 m). This has a minor impact on the study of the response characteristics of shallow three-electrode laterolog and can be neglected.

Based on this, the computational results from the 2D and 3D models do not differ significantly, thus allowing for the separate execution of both models to perform the corresponding calculations.

5.2 Electrode system coefficient correction

In order to calculate the apparent resistivity more accurately, the coefficient of the electrode system is corrected. Because Equation 2 is a simplified calculation of the electrode system coefficient, the obtained electrode system coefficient is the theoretical electrode system coefficient, which will lead to a certain error between the measured apparent resistivity and the true resistivity. Since the voltage and current are not changed in the model, the difference of apparent resistivity is caused by the difference of electrode system coefficients.

When the external environment is completely consistent (i.e., the resistivity of wellbore water, sandstone, coal seam, and limestone are all 1,000 Ω·m), the apparent resistivity should be infinitely close

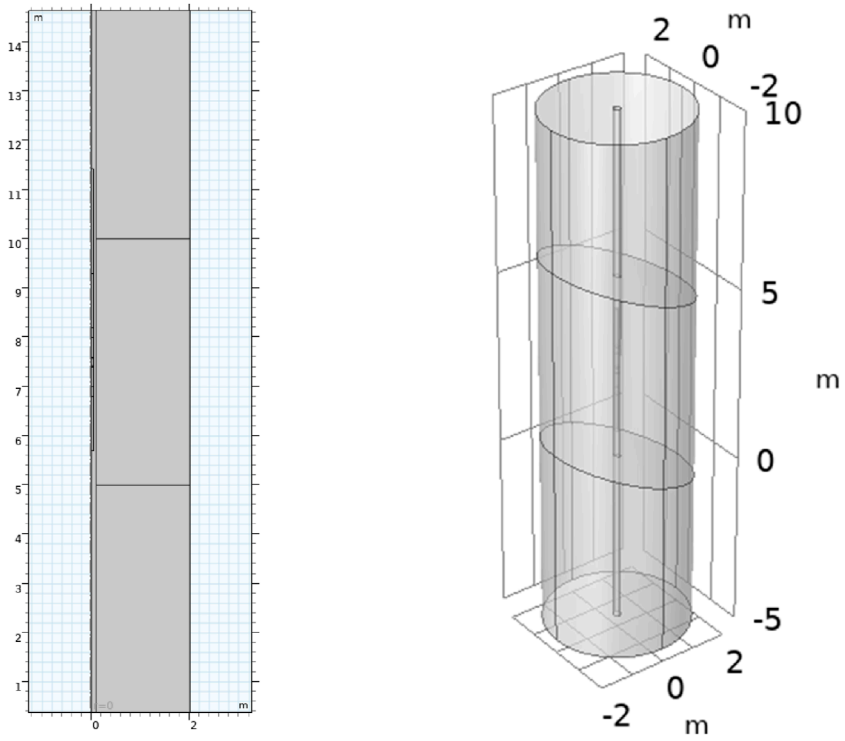

FIGURE 3
2D model and 3D model diagram.

TABLE 1 Parameters of the model.

Parameter	Numerical value	Description
H_0	15 m	Formation height (coal seam, sandstone and limestone 5 m each)
L_0	2 m	Formation width
ρ_s	100 Ω·m	Sandstone resistivity
ρ_c	1,000 Ω·m	Coal seam resistivity
ρ_l	10 Ω·m	Limestone resistivity
r_0	0.1 m	Wellbore radius
r_1	0.0 5 m	Electrode radius
A_0	0.15 m	Main electrode length
A_1, A_2	0.2 m	Length of upper and lower shielding electrodes
B_1, B_2	1.1 m	Upper and lower loop electrode lengths
L_1	0.025 m	Distance between the upper and lower main electrodes and the shielding electrode
L_2	0.2 m	Distance between upper and lower main electrode and loop electrode
U	10 V	On-load voltage

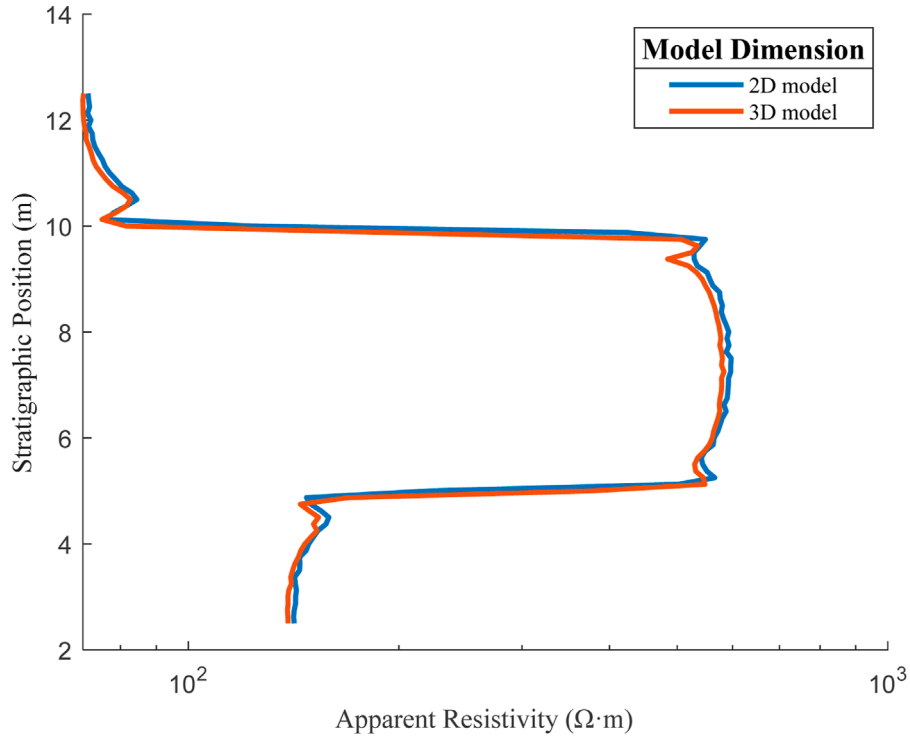

FIGURE 4
Comparison of apparent resistivity curves of 2D and 3D model Stratum.

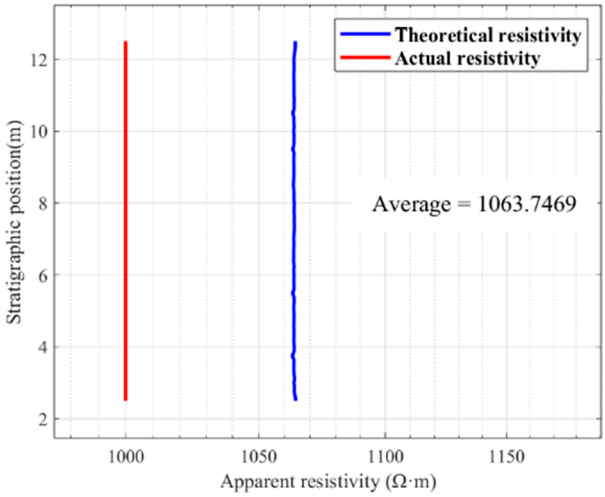

FIGURE 5
Comparison of theoretical and actual resistivity.

to the true resistivity, and the corresponding error can be analyzed by comparing the theoretical resistivity with the actual resistivity, as shown in Figure 5.

Figure 5 shows that the theoretical electrode system coefficient calculated according to Formula 2 is 1.0637,469 times that of the actual electrode system coefficient. This means that in the actual logging process, the measured apparent resistivity should be multiplied by the inverse of 1.0637,469, that is, about 0.94, so that the measured apparent resistivity is closer to the true resistivity.

6 Simulation results

6.1 Coal seam thickness

The change of coal seam thickness can be reflected in the apparent resistivity curve, so it is necessary to explore its longitudinal resolution ability by changing the thickness of the seam. Under the initial condition of the 2D model, the thickness of the coal seam was gradually reduced, and the thickness of the coal seam was set to 5 m, 3 m, 1 m, 0.5 m and 0.3 m, respectively, to obtain the apparent resistivity curves under different seam thicknesses, as shown in Figure 6.

From Figure 6, it can be observed that there is a logarithmic function relationship between seam thickness and apparent resistivity: $Y = 405.8770 \ln(x) + 93.3621$, with the correlation coefficient R^2 between the fitting formula and the curve reaching as high as 0.9903. As the coal seam thickness decreases, the resistivity of the coal seam contracts accordingly, and the apparent resistivity of the coal seam also declines. It is noteworthy that at a seam thickness of 0.3 m, the apparent resistivity curve only shows an abnormal protrusion, and the characteristics of the coal seam are no longer distinct, indicating that the stratification capability of the coal seam thickness has reached its limit. Therefore, it is judged that the stratification and thickness determination capability of shallow three-electrode laterolog is around 0.3 m, and when the coal seam

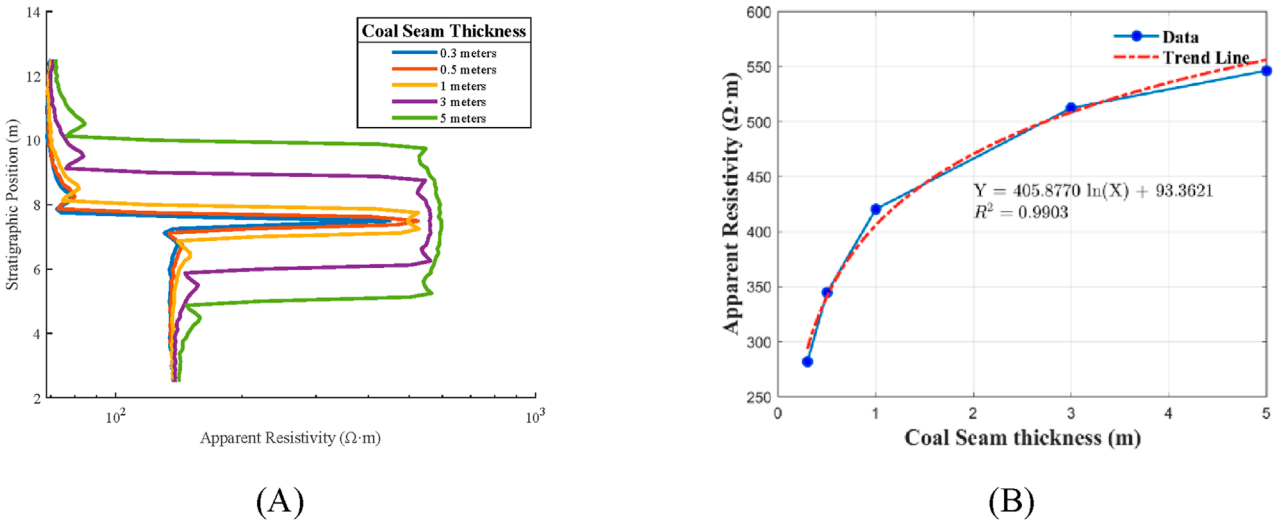

FIGURE 6
Apparent resistivity curves of stratum with different coal seam thicknesses and the response pattern of average apparent resistivity of coal seams.

thickness is less than 0.3 m, it is necessary to perform coal seam correction to identify the coal seam.

6.2 Coal seam-surrounding rock resistivity ratio

In the initial condition of the 2D model, the resistivity of the upper and lower surrounding rock is set to be the same, and there is a certain multiple relationship between the resistivity value and the resistivity of the coal seam (the resistivity of the coal seam remains unchanged). By setting the coal-rock resistivity ratio from 10/9 to 10, the partial apparent resistivity curve is shown in Figure 7A. Subsequently, the corresponding coal seam boundary determination coefficient is calculated according to Equation 6, and the correction plate is drawn, as shown in Figure 7B.

The formula for determining coefficient of coal seam boundary can be expressed as follows:

$$A = \frac{\ln \rho_b - \ln \rho_{min}}{\ln \rho_{max} - \ln \rho_{min}} \quad (6)$$

Where, A is the determination coefficient of coal seam boundary, which is dimensionless; ρ_b is the apparent resistivity value at the coal seam boundary in Ω·m, and ρ_{max} is the maximum apparent resistivity value at the apparent resistivity mutation in Ω·m. ρ_{min} is the minimum apparent resistivity value in Ω·m at the abrupt change in apparent resistivity.

Figure 7B shows that there is a power function relationship between the coal-rock resistivity ratio and the determination coefficient of coal seam boundary: $Y = 0.5235x^{-0.3343}$, and the correlation coefficient R^2 between the fitting formula and the curve is as high as 0.9989. This indicates that the correction map obtained by forward modeling can be effectively applied to the boundary determination and thickness determination of coal seam in actual shallow three-electrode laterolog.

6.3 Coal seam dip angle

The 2D model can only simulate the logging environment in the axisymmetric case. When the dip angle of the ground lseam changes, it can be clearly seen from the geometry of the model, and it can no longer be numerically simulated by the 2D model, so it must be numerically simulated by the 3D model.

In the initial condition of the 3D model, the dip angle of the coal seam is set as 0°, 15°, 30°, 45° and 60° respectively (keep the bottom of the coal seam unchanged, with the increase of the dip angle, the coal seam extends upward; When the dip angle is 60°, in order to ensure a complete apparent resistivity curve, the length of the model is increased to 20 m), and the apparent resistivity curves under different dip angles are obtained, as shown in Figure 8A. According to the formula in Figure 8B, the apparent thickness of the coal seam on the apparent resistivity curve is determined, as shown in Figure 8B.

The results (Figure 8B) of determining the apparent thickness of the coal seam based on the formula in Figure 7B are generally consistent with the results obtained using trigonometric functions geometrically to calculate the apparent thickness. This indicates that the shallow three-electrode laterolog apparent resistivity curve is also effective in determining the apparent thickness of inclined coal seams. At the same time, it can be seen from Figure 8B that there is a quadratic functional relationship between the dip angle of coal seam and the apparent thickness of coal seam: $Y = 0.0020x^2 - 0.0390x + 5.1391$, and the correlation coefficient R^2 between the fitting formula and the curve can reach 0.9857.

6.4 Wellbore enlargement in coal seam

Under the initial condition of the 2D model, the enlargement degree of the coal seam wellbore is gradually expanded (Initial wellbore radius is 0.1 m), and the enlargement radius of the coal

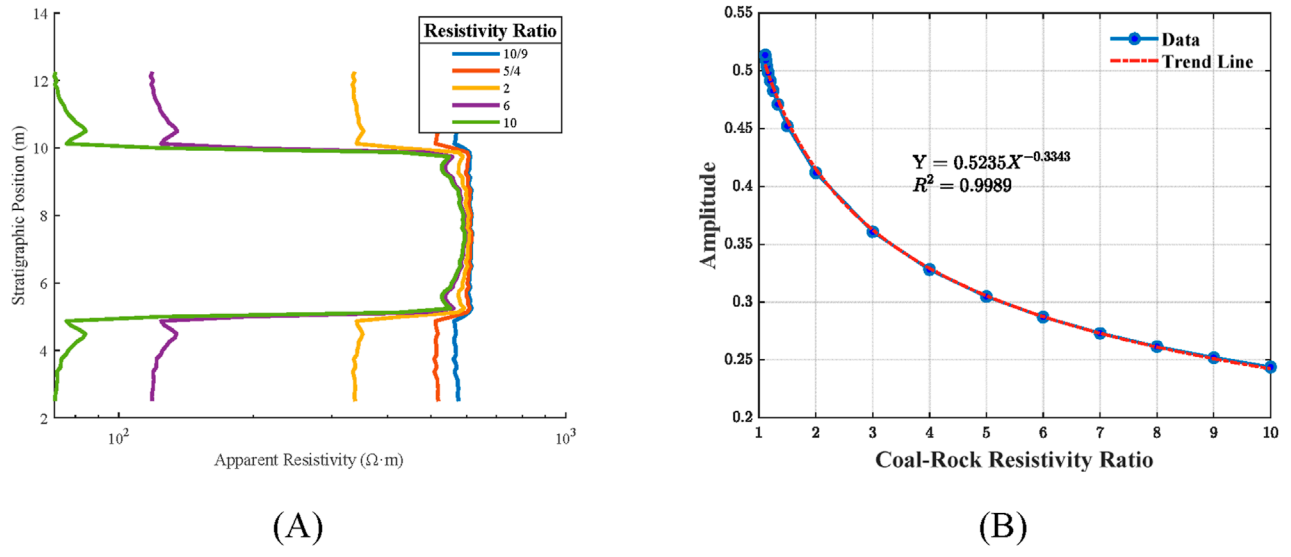

FIGURE 7
Apparent resistivity curves of stratum with different coal seam thicknesses and the response pattern of boundary amplitude.

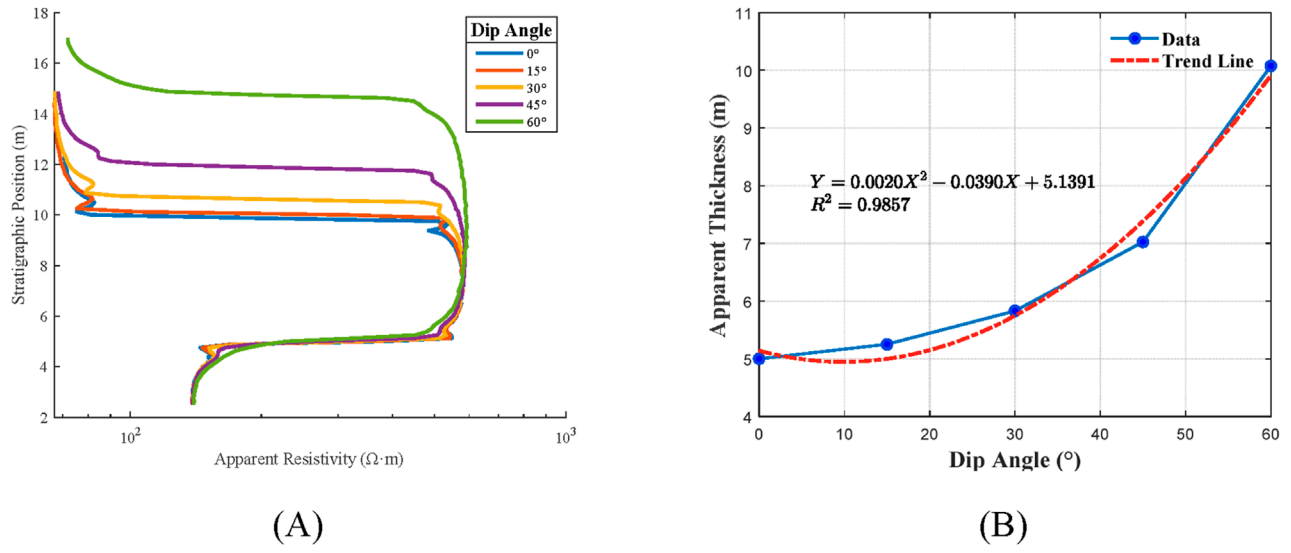

FIGURE 8
Apparent resistivity curves of stratum with different coal seam dip angles and the response pattern of apparent thickness of coal seams.

seam wellbore is set to 0 cm, 1 cm, 2 cm, 3 cm, 4 cm and 5 cm respectively. As a result, the apparent resistivity curves of different coal seam wellbore enlargement radius are obtained, as shown in Figure 9A, and the corresponding average resistivity of coal seam is calculated, and the results are shown in Figure 9B.

As can be seen from Figure 9, there is a quadratic functional relationship between coal seam wellbore enlargement and coal seam apparent resistivity: $Y = 32.7840x^2 - 264.5293x + 525.4810$, and the correlation coefficient R^2 between the fitting formula and the curve is as high as 0.9930. The distance between the electrode and the coal seam increases due to the enlargement of the wellbore, which makes the current more trapped in the wellbore mud and increased by the influence of the low resistivity of the mud, so it is difficult to accurately measure the resistivity of the coal seam. Therefore, it is very necessary to carry out well correction.

6.5 Fracture

Under the initial condition of the 2D model, three additional coal seam fractures were added, and the positions on the z-axis were 6.452–6.453 m, 6.953–6.954 m and 7.454–7.455 m, respectively. The fracture spacing was 0.5 m, the fracture width was 1 mm, and the fracture length was 2 m.

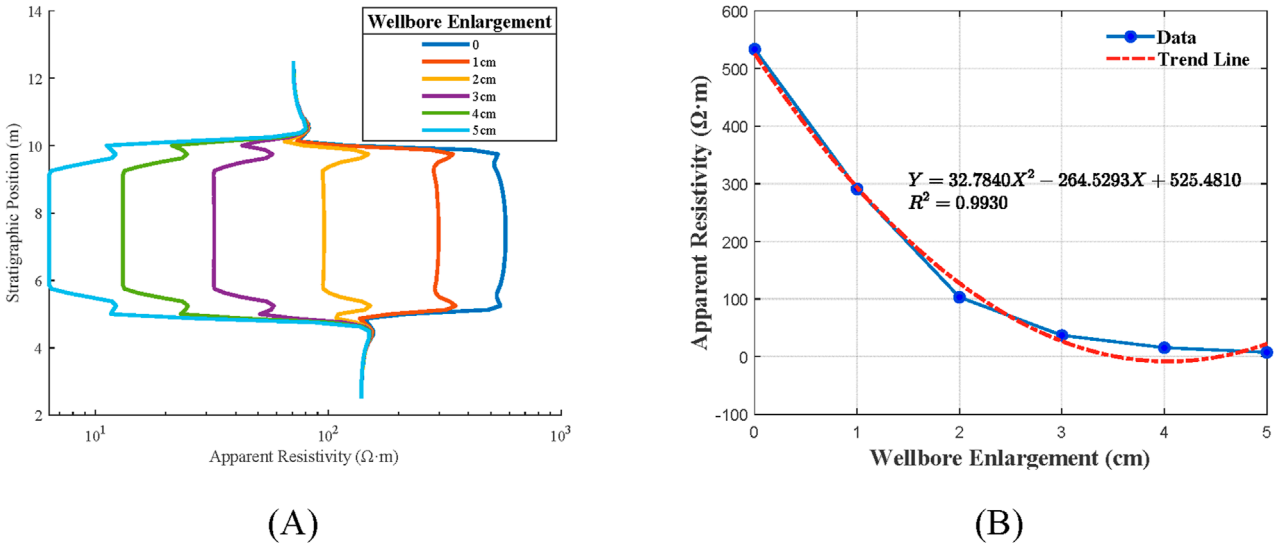

FIGURE 9
Apparent resistivity curves of stratum with different coal seam wellbore enlargements and the response pattern of average apparent resistivity of coal seams.

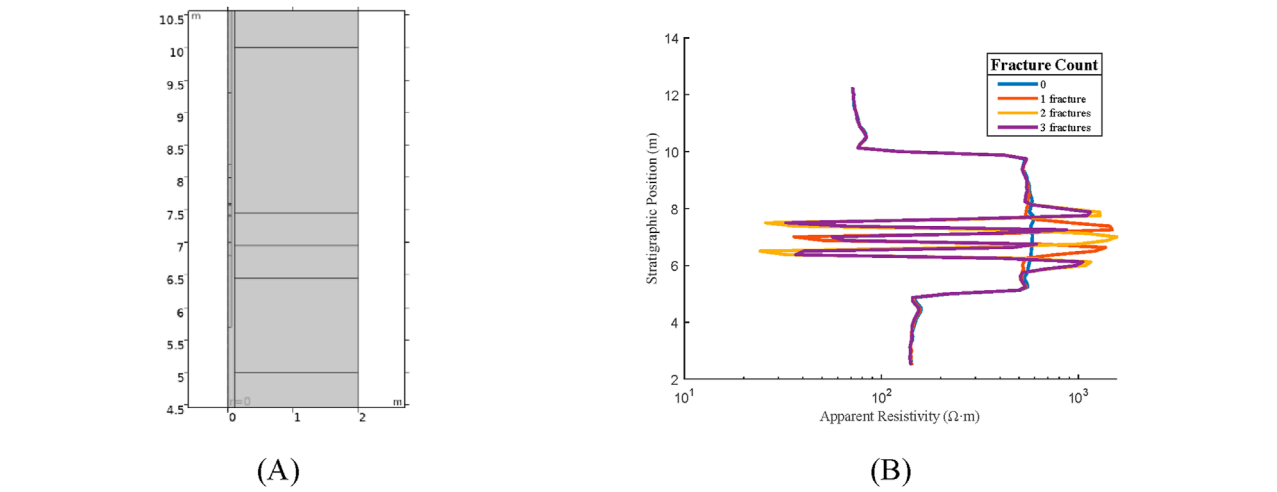

FIGURE 10
Fracture locations and apparent resistivity curves of stratum with different fracture count.

6.5.1 Fracture count

Under the condition of adding fractures in the 2D model, the number of fractures is set to 0, 1, 2, and 3, respectively, (when there is 1 fracture, the position is at 6.953–6.954 m; when there are 2 fractures, the positions are at 6.452–6.453 m and 7.454–7.455 m respectively; when there are 3 fractures, the positions are at 6.452–6.453 m, 6.953–6.954 m, and 7.454–7.455 m respectively) to obtain the apparent resistivity curves under different number of fractures, as shown in Figure 10. The results indicate that the addition of fractures leads to the minimum value of resistivity at the fracture, and the boundary effect generated by fractures leads to the increase of the apparent resistivity of the nearby coal seam.

6.5.2 Fracture width

Under the condition of adding fractures in the 2D model, the fracture widths were set as 0.1 mm, 0.25 mm, 0.5 mm, 0.75 mm, 1 mm and 2mm, respectively, to obtain the apparent resistivity curves under different fracture widths, as shown in Figure 11. This suggests that there is a power function relationship between the fracture width and the apparent resistivity of coal seam: $Y = 51.0479x^{-0.2693}$, and the correlation coefficient R^2 between the fitting formula and the curve can reach 0.9391.

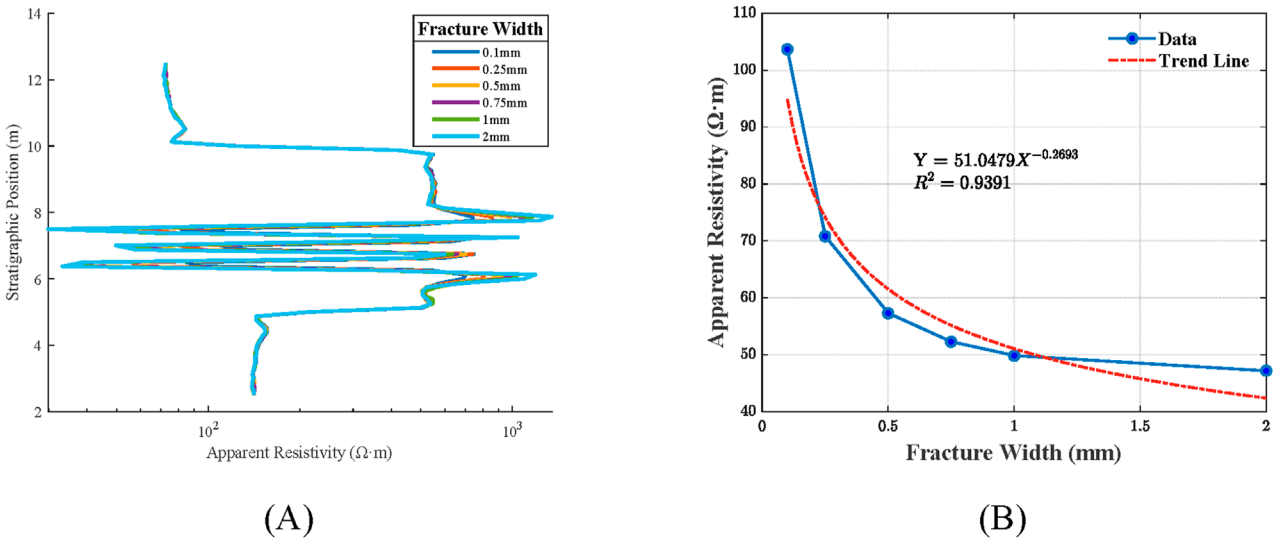

FIGURE 11
Apparent resistivity curves of stratum with different coal seam fracture widths and the response pattern of average apparent resistivity of fluids within fractures.

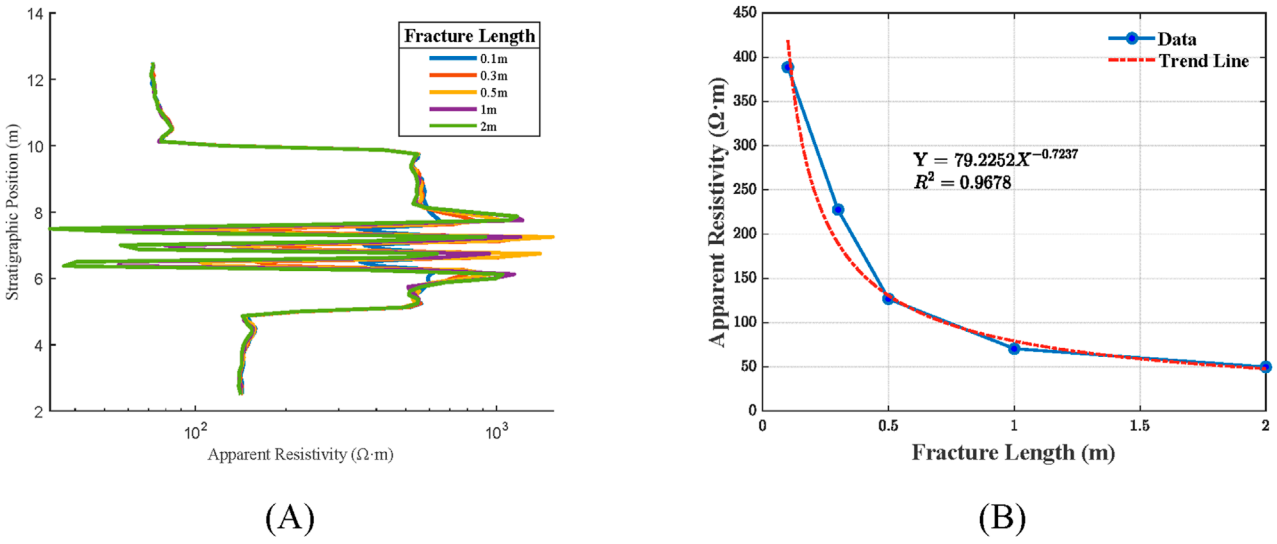

FIGURE 12
Apparent resistivity curves of stratum with different coal seam fracture lengths and the response pattern of average apparent resistivity of fluids within fractures.

6.5.3 Fracture length

Under the condition of adding fractures in the 2D model, the lengths of the fractures are set to 0.1 m, 0.3 m, 0.5 m, 1 m, and 2 m, respectively, to obtain the apparent resistivity curves under different fracture lengths, as shown in Figure 12. The findings reveal that the increase in fracture length leads to a decrease in the apparent resistivity of the fluid within the fracture, and there exists a power function relationship between the two, given by $Y = 79.2252x^{-0.7237}$, with the correlation coefficient R^2 between the fitting formula and the curve can reach 0.9678.

7 Discussion

This paper, based on 2D and 3D models, investigates the influence of geometric and electrical parameters such as coal seam thickness, coal-rock resistivity ratio, the dip angle of the coal seam, wellbore enlargement in the coal seam, fractures count, fracture width and fracture length, by adjusting these parameters within the models. By analyzing the response characteristics of shallow three-electrode laterolog, the study summarizes the related patterns, with results presented in Table 2.

TABLE 2 Response characteristics of shallow three-electrode laterolog under different parameters.

Parameter	Variation range	Correlation	Fitting formula	R^2
Seam thickness	0.3–5 (m)	Positive	$Y = 405.8770 \ln(x) + 93.3621$	0.9903
Resistivity ratio	10/9–10	Negative	$Y = 0.5235x^{-0.3343}$	0.9989
Dip angle	0–60 (°)	Positive	$Y = 0.0020x^2 - 0.0390x + 5.1391$	0.9857
Wellbore	0.1–0.15 (m)	Negative	$Y = 32.7840x^2 - 264.5293x + 525.4810$	0.9930
Fracture count	0–3 (count)	—	—	—
Fracture width	0.1–2 (mm)	Negative	$Y = 51.0479x^{-0.2693}$	0.9391
Fracture length	0.1–2 (m)	Negative	$Y = 79.2252x^{-0.7237}$	0.9678

The coal seam thickness is positively correlated with resistivity, and when the coal seam is at 0.3 m, the apparent resistivity is significantly lower than the true resistivity, indicating that the stratification capability has reached its limit. This phenomenon is consistent with the research of Szijártó et al. (2017). The coal-rock resistivity ratio is negatively correlated with the amplitude at the coal-rock boundary, with a high correlation coefficient of 0.9989, which is the highest among all parameters. This study further refines the research of Huo and Li (1990) in this area, resulting in specific functional patterns. An increase in the dip angle of the coal seam leads to an increase in the apparent thickness of the coal seam, which is also reflected in the apparent resistivity curve. This result is generally consistent with the research of Huo and Li (1990). The wellbore enlargement in the coal seam is negatively correlated with the apparent resistivity of the coal seam, and changes rapidly within 1 cm of wellbore enlargement. This study further supplements the research of Szijártó et al. (2017) on the variation of well diameter over the entire well section. The addition of fractures causes the coal seam to increase abnormally due to boundary effects, and both the increase in fracture width and length lead to a power function decrease in the electrical conductivity of the fluid within the fractures.

Building on the coal seam thickness depicted in Figure 6B of Section 6.1, two corresponding seam thickness correction curves can be derived through further processing. This paper, considering the length and necessity of the article, did not proceed with further research. Additionally, in Section 6.5 regarding fractures, it would be possible to investigate the response characteristics of fluid resistivity changes within the fractures. However, this is essentially similar to Section 6.2 on the coal-rock resistivity ratio, and the paper did not conduct further research on this aspect either. Future work will be committed to studying heterogeneous formation models and further validating the models with actual measured data to assist in the evaluation of complex reservoirs.

8 Conclusion

In this paper, COMSOL Multiphysics is used to construct the model of coal seam apparent resistivity measurement by shallow three-electrode laterolog, and the effects of coal seam thickness, coal seam-surrounding rock resistivity ratio, coal seam dip angle, coal seam wellbore enlargement and coal seam fracture on apparent resistivity curve are studied. This paper draws the following conclusions:

(1) The coal seam thickness has a positively correlated logarithmic function relationship with the apparent resistivity of the coal seam, while the coal-rock resistivity ratio has a negatively correlated power function relationship with the coal-rock boundary determination coefficient. Forward modeling simulations indicate that the stratification and thickness determination capability of shallow three-electrode laterolog for coal seams is approximately 0.3m; when the seam thickness is less than this value, it is necessary to correct the coal seam thickness to accurately obtain the coal seam resistivity; the correlation coefficient between the coal-rock resistivity ratio and the coal-rock boundary determination coefficient is as high as 0.9989, and the correction chart in this paper can effectively determine the coal-rock boundary.

(2) The relationship between coal seam dip angle and apparent thickness of the coal seam, as well as the relationship between borehole enlargement in the coal seam and apparent resistivity of the coal seam, are both quadratic function relationships. The coal seam dip angle is positively correlated with the apparent thickness of the coal seam, and with the knowledge of the formation dip angle, the true thickness of the strata can be obtained through the results of shallow three-lateral logging. The enlargement of the wellbore in the coal seam is negatively correlated with the apparent resistivity of the coal seam. Wellbore enlargement hinders the lateral extension of the electric current, which can easily lead to distortion of the coal seam resistivity, and wellbore correction is necessary in certain situations.

(3) The addition of fractures leads to an abnormal increase in the coal seam due to boundary effects. Moreover, both the fracture width and length exhibit a negative correlation with the resistivity of the fluid within the fractures, following a power function relationship. Therefore, shallow three-electrode laterolog can be utilized to explore the development state of fractures. Future work will be dedicated to the development of heterogeneous formation models, and combining actual measured data to further validate the models, assisting in the evaluation of complex reservoirs.

Data availability statement

The original contributions presented in the study are included in the article/supplementary material, further inquiries can be directed to the corresponding author.

Author contributions

XQ: Conceptualization, Methodology, Writing–review and editing. SW: Formal Analysis, Writing–review and editing, Writing–original draft. YW: Data curation, Software, Writing–review and editing. ZW: Supervision, Funding acquisition, Writing–review and editing.

Funding

The author(s) declare that financial support was received for the research, authorship, and/or publication of this article. Zhuwen Wang: National Natural Science Foundation of China: 41790453 and 41874135; Xinghua Qi: Xinjiang backbone talent training program: 2024; Shimao Wang: College Students' Innovative Entrepreneurial Training Plan Program: 202310994008.

Conflict of interest

The authors declare that the research was conducted in the absence of any commercial or financial relationships that could be construed as a potential conflict of interest.

Publisher's note

All claims expressed in this article are solely those of the authors and do not necessarily represent those of their affiliated organizations, or those of the publisher, the editors and the reviewers. Any product that may be evaluated in this article, or claim that may be made by its manufacturer, is not guaranteed or endorsed by the publisher.

References

Chen, X., Zeng, W., Yuan, P., and Wang, Y. (2013). Design of a new three-lateral logging collector based on STM32. *Electron. Prod.* (No.6), 30–31. doi:10.16589/j.cnki.cn11-3571/tn.2013.06.009

Deng, S., Li, Z., and Li, Z. (2009). Response of dual laterolog and fast correction for layer thickness and shoulder bed in horizontal wells. *Petroleum Explor. And Dev.* 36 (No.6), 725–729. doi:10.1016/s1876-3804(10)60005-5

Deng, S., Mo, X., Lu, C., Zhang, Y., and Liu, L. (2012). Numerical simulation of the dual laterolog response to fractures and caves in fractured-cavernous formation. *Petroleum Explor. And Dev.* 39 (No.6), 751–757. doi:10.1016/s1876-3804(12)60100-1

Doll, H. G. (1951). The laterolog: a new resistivity logging method with electrodes using an automatic focusing system. *J. Petroleum Technol.* 3 (11), 305–316. doi:10.2118/951305-g

Fan, X., and Lu, L. (2005). Investigation on influence factors of laterolog curve form. *Glob. Geol.* 24 (No.4), 396–401.

Feng, J., Liu, D., Nin, X., Xu, G., Ao, X., and Xu, S. (2018). Impact analysis and rapid correction of layer thickness-shoulder bed for the response of array lateral logging in directional wells. *Fault-Block Oil and Gas Field* 25 (No.5), 593–597.

Ge, X., Fan, Y., Li, J., Tan, B., Wang, L., Wu, Z., et al. (2019). Expermental studies and investigations on the dual lateral log response of near borehole fractures. *Chin. J. Geophys.* 62 (No.1), 354–360. doi:10.6038/cjg2018L0128

Hu, S., Chen, L., and Wang, J. (2019). Fast inversion of array laterolog measurements in an axisymmetric medium. *Appl. Geophys.* 16 (No.4), 539–548. doi:10.1007/s11770-019-0767-0

Huang, M. (2010). Effect of mud intrusion on three lateral apparent resistivity logging and gamma logging: a case study of Nuheting uranium deposit. *J. henan polytechinc Univ. Nat. Sci.* 29 (No.A1), 72–74. doi:10.16186/j.cnki.1673-9787.2010.s1.008

Huo, Q., and Li, D. (1990). 3D finite element forward simulation of array laterolog curves in dipping formations. *Coal Geol. China* (2), 60–69.

Lan, Z. (2024). Discussion on coalbed methane mining mode of large dip coal seam in Xinjiang. *China Petroleum Chem. Stand. Qual.* 44 (No.17), 93–95.

Liang, Y., Tian, F., and Li, F. (2021). Design of borehole and surrounding rock correction program for array lateral logging based on COMSOL. *Instrum. Tech.* (No.5), 27–30. doi:10.19432/j.cnki.issn1006-2394.2021.05.008

Liu, D., Xia, P., Wan, W., Yan, L., and Zhao, J. (2012a). Response characteristics of dual laterolog in fractured carbonate reservoirs in horizontal Wells. *Lithol. oil-gas Reserv.* 24 (No.3), 1–4.

Liu, D., Yan, L., Xia, P., Wan, W., and Dong, D. (2012b). Response of dual lateral logging on interbeded sand-shale in horizontal well. *J. Southwest Petroleum University:Science and Technol. Ed.* 34 (No.3), 78–82. doi:10.3863/j.issn.1674-5086.2012.03.011

Lu, H., Wang, Y., Zhang, J., Zhong, J., Jiang, W., Wang, J., et al. (2021). Research on multi fracture and effective supporting fracturing technology in large dip coal seam of Xinjiang. *China Energy Environ. Prot.* 43 (No.3), 70–74. doi:10.19389/j.cnki.1003-0506.2021.03.014

Mohammed, S., Ahmed, F., Khalid, M., Fouad, S., Alsrory, A. S. A. E., and Mohammed, M. (2021). Structural and stratigraphic study of the Sharyoof oil field, Block 53, in Say'un-Masilah basin using seismic reflection and well logging methods, Yemen. *Arabian J. Geosciences*, Vol.14(14): 10. doi:10.1007/s12517-021-07672-5

Ni, X., Xu, G., Bie, K., Ao, X., Xu, S., and Liu, D. (2017). Influencing factors of array laterolog forword response for fractured reservoir based on horizontal well. *Fault-Block Oil and Gas Field*, Vol.24(No.6), 788–792. doi:10.6056/dkyqt201706012

Ni, X., Xu, G., Bie, K., Feng, J., Xu, S., and Liu, D. (2018). Array laterolog response and rapid correction of the surrounding rock/layer thickness influence for highly deviated/horizontal wells. *Petroleum Geol. Oilfield Dev. Daqing* 37 (No.2), 144–151. doi:10.19597/j.Issn.1000-3754.201705058

Pan, K., Wang, W., Tang, J., and Tan, Y. (2013). Mathematical model and fast finite element modeling of high resolution array lateral logging. *Chin. J.Gephys.in Chin.* 56 (No.9), 3197–3211. doi:10.6038/cjg20130932

Pan, W., Wu, F., and Meng, F. (2022). Numerical simulation of dual lateral logging resistivity of carbonate solution-vuggy reservoir. *Sci. Technol. Eng.* 22 (No.23), 10022–10033.

Saboorian-Jooybari, H., Dejam, M., Chen, Z., and Pourafshary, P. (2016). Comprehensive evaluation of fracture parameters by dual laterolog data. *J. Appl. Geophys.* 131, 214–221. doi:10.1016/j.jappgeo.2016.06.005

Shalaby, M. R., and Islam, M. A. (2017). Fracture detection using conventional well logging in carbonate Matulla Formation, Geisum oil field, southern Gulf of Suez, Egypt. *J. Petroleum Explor. Prod. Technol.* 7 (4), 977–989. doi:10.1007/s13202-017-0343-1

Si, Z., Deng, S., Lin, F., Yuan, X., Li, H., and Tian, C. (2020). Numerical simulation of laterolog response of mud intrusion anisotropic formation array. *Geophys. Prospect. petroleum* 55 (No.1), 187–196. doi:10.13810/j.cnki.issn.1000-7210.2020.01.022

Sushant, M., Fei, L., Alexandre, B., Arcady, R., and Ra, M. (2017). Modeling tools for drilling, reservoir navigation, and formation evaluation. *J. Syst. Cybern. Inf.* 3, 81–87.

Szijártó, M., Balázs, L., Drahos, D., and Galsa, A. (2017). Numerical sensitivity test of three-electrode laterolog borehole tool. *Acta Geophys.* 65 (4), 701–712. doi:10.1007/s11600-017-0063-4

Tang, G. (1985). Application effect of three-lateral logging instrument in coal geological exploration. *Well logging Technol.* 9 (No.4), 75–77. doi:10.16489/j.issn.1004-1338.1985.04.013

Wang, N., Wang, N., Wang, N., Li, K., Sun, J., Wang, D., et al. (2023). Research on dual lateral log simulation of shale bedding fractures under different influencing conditions. *Front. Energy Res.* 11, 1249985. doi:10.3389/fenrg.2023.1249985

Wiersberg, T., Pierdominici, S., Lorenz, H., Almqvist, B., and Klonowska, I. (2020). Identification of gas inflow zones in the COSC-1 borehole (Jämtland, central Sweden) by drilling mud gas monitoring, downhole geophysical logging and drill core analysis. *Appl. Geochem.* 114, 104513. doi:10.1016/j.apgeochem.2019.104513

Wu, J., Chen, M., Xu, W., Cun, D., Yang, D., and Ynag, H. (2022). Numerical model of dual laterolog intrusion response in tight fractured reservoir. *Unconv. Oil and Gas* 9 (No.4), 32–36. doi:10.19901/j.fcgyq.2022.04.05

Wu, J., Xie, W., Xie, X., Zhang, J., and Xu, X. (2008). Forward response analysis of array lateral logging tool. *J. Xi Shiyou Univ. Nat. Sci. Ed.* 23 (No.1), 73–76+80+113-114.

Xu, Y. (1988). Application of three-lateral logging method in stratified fixed thickness interpretation. *Coal Geol. Explor.* (3), 65–67.

Xue, Y., Wang, L., Zhao, X., and Tian, H. (2022). The fractured model study of low-permeability reservoir in xinli oil field. *Front. Earth Sci.* 10, 841456. doi:10.3389/feart.2022.841456

Zhang, Y., Wei, B., and Yang, H. (2002). Numerical analysis of response of dual laterolog instruments. *Procress Geophys.* 17 (No.4), 671–676.

Zhang, Z., Gao, C., and Gao, Y. (2014). A study of the controlling factors on the resistivity of fractured reservoir using the numerical simulation. *Nat. Gas. Geosci.* 25 (No.2), 252–258. doi:10.11764/j.issn.1672-1926.2014.02.0252

frontiers | Frontiers in Earth Science

TYPE Original Research
PUBLISHED 04 March 2025
DOI 10.3389/feart.2025.1524301

OPEN ACCESS

EDITED BY
Huaimin Dong,
Chang'an University, China

REVIEWED BY
Delu Li,
Xi'an University of Science and Technology, China
Yuhang Guo,
Jilin University, China

*CORRESPONDENCE
Jiejun Zhu,
450950734@qq.com

RECEIVED 07 November 2024
ACCEPTED 07 February 2025
PUBLISHED 04 March 2025

CITATION
Zhu J, Peng J, Lv Z and Chen S (2025) Reservoir type classification and water yield prediction based on petrophysical conversion models.
Front. Earth Sci. 13:1524301.
doi: 10.3389/feart.2025.1524301

Reservoir type classification and water yield prediction based on petrophysical conversion models

Jiejun Zhu[1,2,3]*, Jian Peng[1,2,3], Zhibin Lv[1,2,3] and Shuangquan Chen[1]

[1]College of Geophysics, China University of Petroleum (Beijing), Beijing, China, [2]Qaidam Comprehensive Geological and Mineral Exploration Institute of Qinghai Province, Golmud, China, [3]Qinghai Provincial Key Laboratory of Salt Lake Resources Exploration and Research in Qaidam Basin, Golmud, China

In the Chaixi region of the Qaidam Basin's Qigequan tectonic zone, the compact sandstones are characterized by their low porosity and permeability, featuring intricate pore-throat formations, varied lithologies, assorted clay minerals, and pronounced unevenness among the reservoirs. There's a weak link between reservoir metrics and logging reactions, making it challenging to assess these reservoir parameters. The microscopic pore structure of the reservoir can be illustrated through both the nuclear magnetic resonance relaxation time distribution and the capillary pressure curve. By using fractal dimensions to classify the reservoir, a conversion model between the transverse relaxation time in nuclear magnetic resonance logging and the capillary pressure in the mercury injection curve is established, enabling the conversion of pseudo-capillary pressure curves. Key elements of the pseudo-capillary pressure curve, specifically discharge and drive pressure, median pressure, and sorting coefficient, were analyzed and integrated with the generalized regression neural network for accurate reservoir type classification. An efficient categorization of reservoir types was accomplished by isolating three key elements from the pseudo capillary pressure curve—displacement pressure, median pressure, and sorting coefficient—and integrating them with the generalized regression neural network. Utilizing a rock physics framework, a correlation between transverse relaxation time of nuclear magnetic resonance and relative permeability conversion was formulated to accurately forecast the rate of water generation in the reservoirs of the western Qaidam Basin. The anticipated outcomes demonstrated a strong link with the real rate of water production. This technique presents an innovative method to forecast the comparative permeability of oil-water stages and the rates of water generation in compact sandstone reservoirs.

KEYWORDS

dense sandstone reservoir, T_2-Pc Modelling, fractal dimension, T_2-Kr Modelling, projected water yield

1 Introduction

Assessing the structure of pores plays a crucial role in evaluating reservoirs. The dimensions and arrangement of pores and throats play crucial roles in determining the reservoir's capacity for storage and its permeability (Lai et al., 2018). Widely adopted techniques for analyzing the architecture of rock pores encompass techniques like thin-section identification, mercury compression,

TABLE 1 Parameters of mercury compression for different reservoir types.

Rock type	Class I	Class II
Permeability ($10^{-3}\mu m^2$)	0.299	0.001 ~ 0.470
Porosity (%)	4.114	3.652 ~ 7.964
Displacement Pressure (MPa)	1.011	6.869 ~ 24.105
Median Pore Radius (μm)	0.063	0.010 ~ 0.023
Median mercury Saturation Pressure (MPa)	11.709	31.498 ~ 75.202
Maximum Mercury Saturation (%)	84.063	38.829 ~ 73.919
Peak Penetration Distribution (%)	45.333	32.759 ~ 50.417
Peak Pore Size Distribution (%)	12.699	11.853 ~ 21.423

nuclear magnetic resonance (NMR), and scanning electron microscopy (SEM). However, it is often difficult to systematically characterise the complex pore space information within the rock by a single pore structure characteristic parameter (Tian et al., 2018).

During the initial years of the 1990s, core NMR techniques were utilized in petrophysical experiments, revealing that both the T2 distribution and capillary pressure curve are indicative of the distribution of the pore size (Wang et al., 2018; Dong et al., 2023). Numerous researchers, aiming to perpetually assess reservoir characteristics and formation depth using logging curves, employed NMR for inverting capillary pressure curves (Xie et al., 2021; Jin et al., 2024), thereby determining the correlation between these pressure points and the period of transverse relaxation. Utilizing various transformation techniques, one can derive the pseudo-capillary pressure curve (Xiao et al., 2016; Zhang et al., 2020; Gray et al., 2021), and a power function correlation exists between the relaxation time at T2 and the size of pores in throat radius, altering across different sizes of pores (Guo et al., 2019; Zhou et al., 2022; Li et al., 2023). Oil and water phases' relative permeability varies dynamically with alterations in pore configuration and water saturation levels, with the relative permeability curve mirroring the fundamental flow law of oil and water phases in oil and water seepage (Su et al., 2020; Ji et al., 2022; Pei et al., 2022; Moodie and McPherson, 2024).

Many researchers have devoted themselves to exploring the application of different methods in reservoir water yield prediction, including the determination of theoretical water yield curves through seepage theory and the correction of relative permeability curves through nonlinear optimisation algorithms, which are analysed based on production and core experimental data (Peng, 2020; Wu et al., 2024). A relative permeability calculation model considering the non-Darcy effect is established, and the effects of different non-Darcy coefficients on the phase permeability curve and reservoir production are analysed by phase permeability experiments and numerical simulations. There are also studies proposing the use of neural networks to construct a prediction model, as well as the development of a calculation model based on nuclear magnetic resonance and conventional logging data, etc., in order to better carry out the calculation and quantitative evaluation of water production rate (Azim and Aljehani, 2022; Mo et al., 2024). In addition, some researchers not only analysed the influence of phase permeability experiments and numerical simulations, but also introduced new parameters such as bound water saturation and tortuosity, aiming to improve the accuracy of water production rate prediction (Parvazdavani et al., 2022; Yi et al., 2024).

This research initially identifies the link between the NMR T2 spectrum and capillary pressure curve in the study area's uneven strata, derived from petrophysical studies, and categorizes this connection with the capillary pressure curve, subsequently integrating it with the GRNN neural network for effective reservoir classification. In the case of various reservoir types, NMR T2 to relative permeability graphs were developed, leading to the computation of the reservoir's water production rate, which closely aligns with the real production figures.

2 Geological profile of the study area

2.1 Geological background

Situated in the Qinghai-Tibetan Plateau's northeastern region, the Qaidam Basin, a diamond-shaped desert basin between mountains, ranks among China's top ten inland sedimentary basins. It spans approximately 850 km from east to west and 150–300 km from north to south, spanning roughly 121,000 km^2. Its elevation ranges between 2,600 and 3,700 m, with elevated areas in the west and low in the east, and wide in the west and narrow in the east (Figure 1). Currently, the basin comprises five main tectonic segments and 25 auxiliary tectonic segments; it features 13 stratigraphic formations spanning from the Paleozoic to the Cenozoic, with confirmed oil and gas reserves scattered across the Jurassic, Paleocene, Neocene, and Quaternary periods (Li X. et al., 2024).

In the western region of Qaidam, the structure features a total backslope in its superficial section and a fractured nose in its deeper area, with the Qigequan Oilfield forming multiple layers of oil layers ranging from shallow to deep at the backslope's heart. Presently, evidence supports the existence of seven distinct stratigraphic layers, specifically the Shishigou Formation (N_3^2 uncapped), the Upper Youshashanshan Formation (N_2^2), the Lower Youshashanshan Formation (N_1^2·), the Shangchaigou Formation (N_1·), the upper segment of the Lower Ganzhaigou (E_2^3·), the lower segment of the Lower Ganzhaigou (E_1^3·), and the Luluehe Formation (E_{1+2}·). The tight sandstone reservoirs in Chaixi area are mainly developed in lacustrine sedimentary environments. The upper section of the Shanqiaogou Formation ($E2^3$) is a lacustrine basal fine-grained detrital structure, with sediments mainly consisting of fine-grained mudstone and sandstone. The depositional depth ranges from 300 to 1,000 m, with gray sandstone and conglomerate dominating in the basin margins and brownish red mudstone predominating in the northwest section, concentrated in the sandstone-gravel and muddy sedimentary environments near the lake edge and in the center of the lake, showing obvious heterogeneity characteristics (Hao et al., 2020; Wenjie and Ye, 2024).

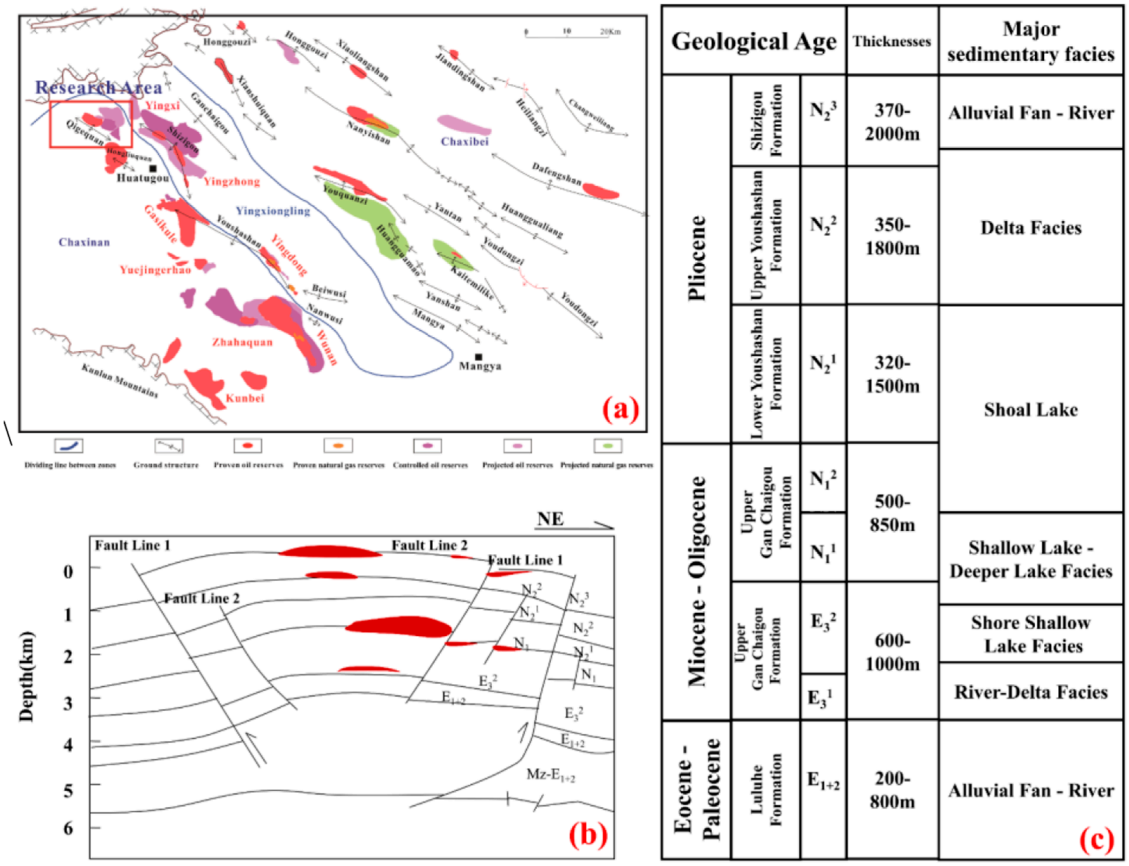

FIGURE 1
Allocation of key oil and gas reserves and the positioning of the Qigequan Oilfield in the Qaidam Basin's western region **(A)**, along with the hydrocarbon reservoir's profile **(B)** and the stratigraphic lithological profile **(C)**.

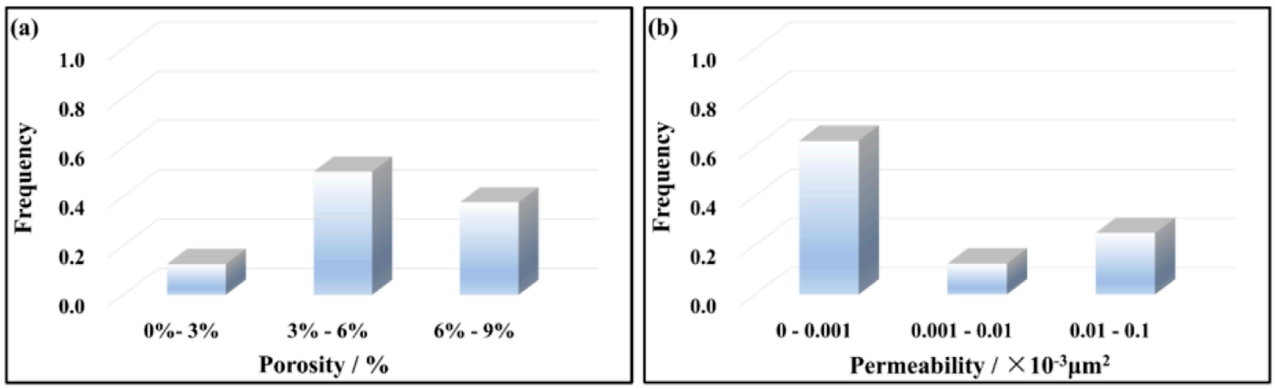

FIGURE 2
Histogram of porosity analysis **(A)**, histogram of permeability analysis **(B)**.

2.2 Tight sandstone reservoir characteristics

2.2.1 Reservoir physical characteristics

The examination of the core's physical data reveals a wide range of physical characteristics in the Lower Ganchaigou Formation's reservoir from the Oligocene, with the porosity of the eight core samples varying between 3.65% and 7.96%, averaging at 5.77%. Permeability ranges from 0.0007 to 0.47 × 10^{-3} μm^2, with an average of approximately 1 × 10^{-3} μm^2, categorized under low porosity and ultra-low permeability (Figure 2).

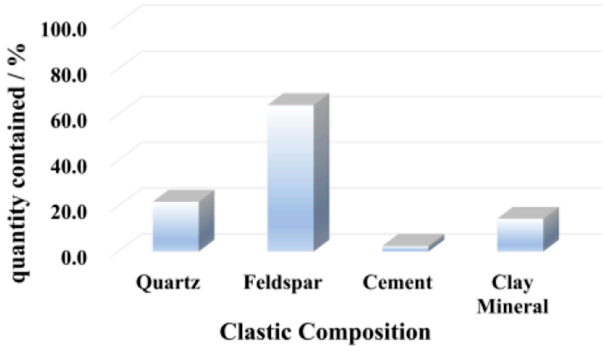

FIGURE 3
Statistical diagram of rock chip composition analysis.

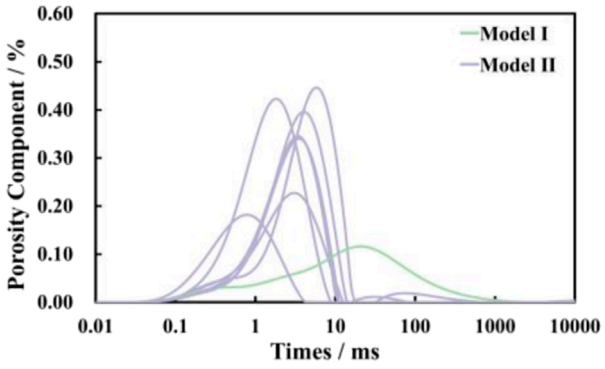

FIGURE 4
NMR T_2 distribution of core samples from Qigequan Oilfield.

2.2.2 Clastic composition

The rock chip composition of the samples is quartz, clasts, clay minerals and other colluvium (Figure 3). By analyzing the thickness of the casts, feldspar is clearly more abundant than quartz in content, and the colluvium is dominated by carbonates (calcite, dolomite, aragonite and rhodochrosite).

3 Characterization of reservoir microporous structure

3.1 Characterization of pore structure by NMR T_2 spectroscopy

Nuclear magnetic resonance (NMR) denotes the interplay between atomic nuclei and a magnetic field (Wei et al., 2019). The three main types of NMR relaxation are surface relaxation, fluid volume relaxation, and diffusion relaxation in a gradient field. Consequently, the complete relaxation of NMR in porous materials is characterized by this mathematical equation:

$$\frac{1}{T_2} = \frac{1}{T_{2B}} + \rho\left(\frac{S}{V}\right) + \frac{D(\gamma G T_E)^2}{12} \quad (1)$$

Where: T_2 is the total relaxation time, ms; T_{2B} is the volume fluid lateral relaxation time, ms; ρ is the surface relaxation strength; S is the pore surface area, cm^2; V is the pore volume, cm^3; G is the magnetic field strength, 10^{-4}T/cm; γ is the rotational magnetism ratio of the hydrogen proton, $(T \cdot s)^{-1}$; T_E is the echo spacing, ms; D is the apparent diffusion spacing of the pore fluid, cm^2/s.

In single-phase pore fluid, the water's volume relaxation time (2-3 s) is much longer than T_2, making T_{2B} negligible for total relaxation. When the magnetic field gradient G is very small, the echo interval T_E is particularly short, and the diffusive relaxation is negligible.

Relaxation at the surface of rock particles happens due to energy reduction, a result of ongoing interactions between fluid molecules in the pore space and the surface of the particles. Surface relaxation depends on the rock's relaxation intensity and surface area. Bigger pores exhibit lower S/V ratios, reduced particle collisions, and extended relaxation periods; conversely, smaller pores display higher S/V ratios and briefer relaxation durations. Consequently, the T2 spectrum observed in saturated water rocks essentially mirrors the interplay between the fluid within the pores and the surface of these pores. Equation Simplification of Equation 1 is possible as:

$$\frac{1}{T_2} = \rho\left(\frac{S}{V}\right) \quad (2)$$

The S/V of spherical pores is $3/r$, and the S/V of tubular throats is $2/r$, r being the radius of the ball. Therefore, Equation 2 can be expressed in the form of Equation 3:

$$\frac{1}{T_2} = \frac{F\rho}{r} \quad (3)$$

Where: F is the shape factor. The distribution of NMR T_2 spectra reflects the distribution of rock pore sizes, with large pore sizes corresponding to large lateral relaxation times and small pore sizes corresponding to smaller lateral relaxation times.

The NMR T_2 spectra of the core samples drilled from the reservoir of the Lower Paleocene Ganchaigou Formation were measured (Figure 4). The main peak (the peak with the largest amplitude) of the T_2 spectrum of the core samples with Class I pore structure is located between 10 and 100 ms, and the amplitude of the main peak is lower than that of Class II, which indicates that there are more macropores; the main peak of the T_2 spectrum of the core samples with Class II pore structure is located between 0 and 10 ms, which indicates that there are more micropores.

3.2 Capillary pressure curves characterize pore structure

The capillary pressure curve delineates the correlation between capillary pressure and pore size in rock pores, derived from experimental data under specific circumstances. The term "capillary pressure" denotes the force exerted in a capillary tube by capillary movements, linked to aspects like the size of the pores and their ability to wet. The contour and features of the capillary pressure curve are indicative of the rock's pore configuration and moisture-absorbing attributes, crucial for evaluating the reservoir's water and fluid retention abilities (Zhao et al., 2021).

The capillary pressure curve in these experiments is primarily examined using the mercuric pressure technique. Given the relative

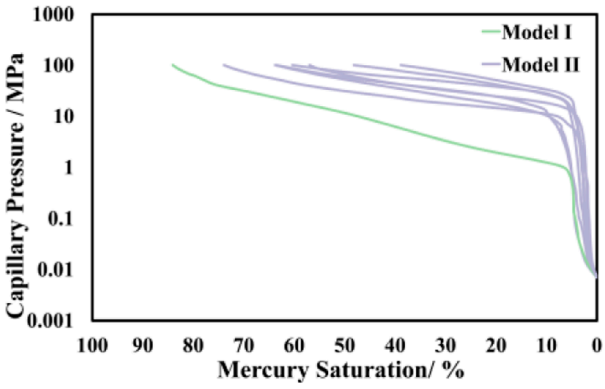

FIGURE 5
Capillary pressure curves of core samples from Qigequan Oilfield.

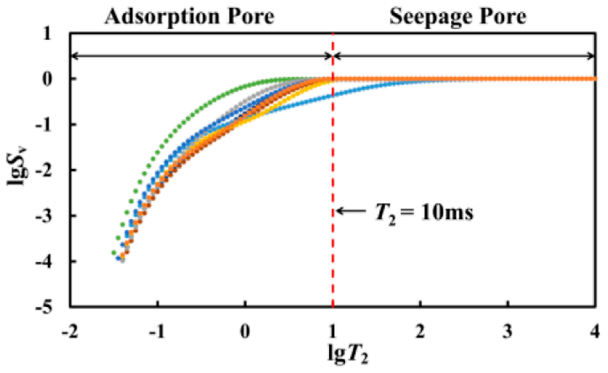

FIGURE 6
Relationship between T_2 and Sv of rock samples from the reservoir of the Lower Paleocene Lower Ganchigou Formation.

stability of mercury's surface tension and wetting contact angle, the capillary pressure curve, as recorded by the mercuric pressure meter, is frequently employed to adjust the size and distribution of pores. Under the presumption that the pore structure consists of cylindrical capillary clusters varying in thickness, Equation 4 illustrates the correlation between capillary pressure and the size of the pores.

$$P_c = \frac{2\sigma \cos\theta}{r_c} \tag{4}$$

Where: Pc is capillary pressure (absolute pressure), MPa; σ is surface tension, N/m; θ is wetting contact angle, °; r_c is capillary radius, μm.

Under laboratory conditions, $\sigma = \frac{0.48N}{m}$, $\theta = 140°$, then there are:

$$P_c = \frac{0.735}{r_c} \tag{5}$$

The capillary pressure curve is converted to an orifice throat size and distribution curve according to Equation 5.

A graph depicting the mercury injection curve for the core sample was created. Based on the curve's morphological features and mercury injection's experimental variables, the core's pore structures can be categorized into two groups (Figure 5). The parameter characteristics of the two types of reservoirs are shown in Table 1. A lesser drainage pressure results in a greater pore diameter. An increase in displacement pressure results in a reduction of the pore diameter. The characteristics of Class I pores are favorable, with the mercury entry curve being slanted, minimal drainage pressure, clear platform intervals, minimal drainage and median pressure, a larger pore throat ratio, the capillary pressure curve's gentler section being parallel, the gentler section lower, and a well-maintained reservoir. Class II rock samples exhibit a less favorable pore structure compared to class I rock samples. When subjected to a specific increase in external pressure, the saturation point of pore displacement in high-pressure rocks is minimal, the average pressure is high, and the curve for capillary pressure is sharp. This indicates subpar organization of the reservoir, uneven fracture patterns, and a minor distortion in its coarseness.

3.3 Principle of nuclear magnetic rotation pseudo-capillary pressure curve

3.3.1 Fractal dimension theory

Assuming that the reservoir pore size distribution obeys the fractal theory (Cheng et al., 2024), there are N pores with pore sizes larger than r to satisfy the power law relationship as follows:

$$N(>r) = \int_r^{r_{max}} P(r)dr = ar^{-D} \tag{6}$$

where a is the constant of proportionality, D is the fractal dimension, N is the number of pores, r_{max} is the maximum pore radius in the reservoir, and P(r) is the pore size distribution density function.

$$P(r) = \frac{dN(>r)}{dr} = a' r^{-D-1} \tag{7}$$

where $a' = -Da$ is a constant of proportionality.

The cumulative pore volume for pores with sizes smaller than r is obtained by integrating $P(r)$ over the pore volume formula, yielding:

$$V(<r) = a''\left(r^{3-D} - r_{min}^{3-D}\right) \tag{8}$$

Therefore, the total pore volume is calculated by setting $r = r_{max}$:

$$V_s = V(<r_{min}) = a''\left(r^{3-D} - r_{min}^{3-D}\right) \tag{9}$$

By taking the ratio of V $(<r)$ to V_s, the cumulative pore volume fraction S_v is expressed. Assuming $r_{min} << r_{max}$, this simplifies to:

$$S_v = \frac{r^{3-D}}{r_{max}^{3-D}} \tag{10}$$

The above equation is called the fractal geometry equation for reservoir pore size distribution.

Since: T_2 is proportional to the pore size r, therefore:

$$S_v = \left(\frac{T_{2\,max}}{T_2}\right)^{D-3} \tag{11}$$

where Sv represents the proportion of the overall pore volume represented by the aggregate volume of pores exhibiting transverse relaxation times shorter than T_2. At this juncture, a rough fractal geometry equation for the NMR T_2 spectrum is derived.

According to the derivation of Equations 6–11, Taking logarithms on both sides has:

$$S_v = (3-D)\lg(T_2) + (D-3)\lg(T_{2\,\max}) \tag{12}$$

Derived from Equation 12 A linear correlation exists between saturation and T2 distribution time within the double logarithmic coordinate framework, suggesting a fractal nature of T_2 distribution time.

3.3.2 NMR fractal dimension calculation

The T_2 cutoff value (T_{2_cutoff}) is the corresponding T_2 value when the cumulative saturation is maximum and tends to be stable at different T_2 times after centrifugation. It is the dividing line between movable fluid and bound fluid. Movable fluid generally exists in large pores and is easy to be dislodged under a certain external pressure. Some bound fluids remain in small pores and cannot be dislodged. For compact sandstone deposits characterized by minimal porosity and permeability, the traditional T_2_cutoff value for logging data processing (33 ms) has become inapplicable (Zhang et al., 2023).

Upon approximately setting 10 ms as the limit, significant alterations in the core samples' slopes were observed on both sides of T_2 = 10 ms (Figure 6). Consequently, the test samples were confined within the T_2 threshold value, and the fractal dimension Ds for the percolating pores were determined for the segment of $T_2 \geq T_2$_cutoff value, while the fractal dimension Da for the absorbed pores was computed for the segment of $T_2 < T_2$_cutoff (Figure 7). The results of the calculation of the fractal dimension of the sample are shown in Table 2.

3.3.3 NMR pseudo-capillary pressure

Currently, the study of pore structure is mostly applied to core laboratory analysis, which mainly includes core CT, mercury pressure experiment and NMR experiment. However, the laboratory tests are expensive, the period is long, and the test results cannot represent the actual situation of the whole target stratigraphic section. Therefore, it is very necessary to use logging data to analyze the micro pore structure of the reservoir.

The time distribution spectrum of NMR T_2, derived from aligning with NMR logging data, more accurately represents the size of rock pores. Currently, the lab predominantly utilizes compressed mercury data for assessing rock pore configurations, a method that fails to consistently represent the entire well section's pore structure and is subject to certain constraints. Nonetheless, NMR data is capable of capturing the long-term details of the formation throughout the entire well section, and the T_2 distribution of NMR is closely linked to the pore structure and maintains strong continuity, aiding in the rapid identification and classification of reservoirs in the continuous depth. Compared to measurements of capillary pressure profiles, NMR assessments are rapid and non-invasive. The methods for converting pseudo-capillary pressure curves using T_2 distribution are: linear and power function methods (Li S. J. et al., 2024).

It was found that the capillary pressure Pc has a power exponential relationship with the transverse relaxation time T_2 (Equation 13):

$$p_c = m\left(\frac{1}{T_2}\right)^n \tag{13}$$

where m and n are transformation parameters and are dimensionless.

The case where the T_2 spectrum is bimodal requires a segmented power function to construct the pseudo-capillary pressure curve (Equations 14, 15), where:

At the large aperture

$$p_{c1} = m_1\left(\frac{1}{T_2}\right)^{n_1} \tag{14}$$

At the small aperture

$$p_{c2} = m_2\left(\frac{1}{T_2}\right)^{n_2} \tag{15}$$

where: P_{c1}, P_{c2} is the capillary pressure, MPa; T_2 is the distribution time of the NMR T_2 spectrum, ms; m_1, m_2, n_1, n_2 are the pending conversion parameters.

The core samples were subjected to NMR to pseudo-hairpipe pressure using the above equation, and the fit is shown (Figure 8).

Based on the categorization of the pressure mercury curve and the outcomes of the NMR fractal dimension analysis, along with the impact of the samples in aligning with the capillary pressure curve, two distinct conversion models have been formulated (Equations 16–19):

Model I: when Ds ≥ 2.9

$$P_c = 62.044\frac{1}{T_2^{1.612}}\left(T_2 < T_{2\_cutoff}\right) \tag{16}$$

$$P_c = 0.5943\frac{1}{T_2^{1.058}}\left(T_2 \geq T_{2\_cutoff}\right) \tag{17}$$

Model II: When Ds < 2.9

$$P_c = 140.79\frac{1}{T_2^{1.005}}\left(T_2 < T_{2\_cutoff}\right) \tag{18}$$

$$P_c = 3901.4\frac{1}{T_2^{1.891}}\left(T_2 \geq T_{2\_cutoff}\right) \tag{19}$$

4 Conversion of pseudo-capillary pressure curves and classification of reservoir types for the whole well section

Utilizing the segmented power function technique, the relationship between lateral relaxation time T2 and capillary pressure Pc in the piezomercury curve is determined. This model, tailored to various reservoirs, transforms the NMR T_2 spectra of the entire well section into depth-dependent pseudo-capillary pressure curves. The characteristics of these pseudo-capillary pressure curves serve to qualitatively categorize the reservoirs directly. Utilizing the previously mentioned technique, a machine learning algorithm has been developed to handle the logging data for the entire well section.

4.1 GRNN principles of neural network methods

The concept of the General Regression Neural Network (GRNN) was introduced by Dr. D. F. Specht. The foundation lies in the

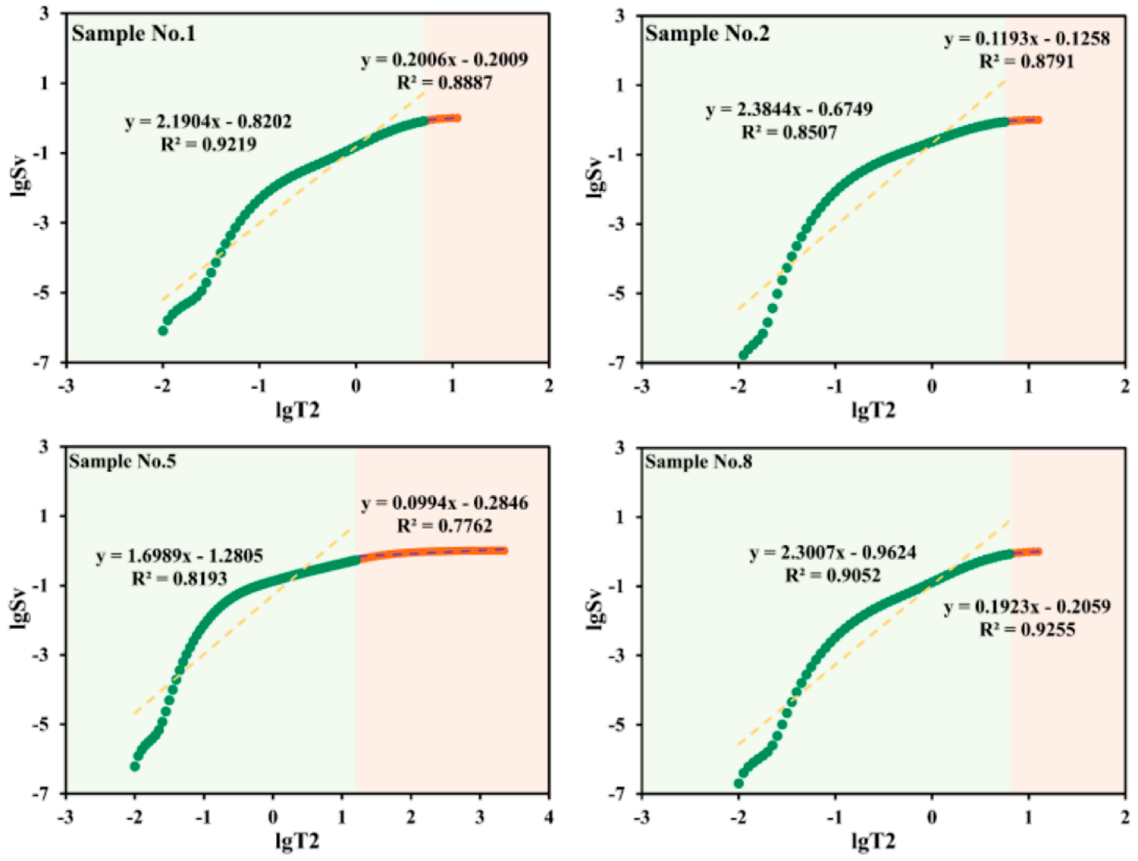

FIGURE 7
Calculation of the dimensionality of the nuclear magnetic fractal.

Radial Basis Function (RBF) network framework, lacking a distinct structure, and relies on the probability density function (PDF) linking independent and dependent variables in the sample data, rather than the intrinsic equation format. The Probability Density Function (PDF) is used to compare the independent and dependent variables in the sample data, rather than using the intrinsic equation format. Estimation of the function occurs via a Parzen window, employing the sample data as initial conditions, conducting nonparametric estimations, and determining the regression value of the dependent variable against the independent variable. The learning speed is fast, the nonlinear approximation is good, and it has strong robustness and fault tolerance. It also achieves good classification results with a small number of samples (Al-Dousari et al., 2022).

4.2 Classification of reservoir types

Pseudo-capillary pressures at continuous depths are obtained using T_2-Pc conversion models for different reservoir types. The spectral peaks are forward and the double peaks are not obvious, the T_2 distribution time is small, and the high discharge pressure corresponds to microporosity. As the T_2 time increases, the spectral peaks are backward and the double peaks are obvious, and the small discharge-driven pressure corresponds to large pores.

For the training samples, the trio of capillary pressure curve parameters (Discharge Drive pressure, Median Pressure, and Sorting Coefficient) were chosen, capable of categorizing the type of reservoir throughout the entire well section (Figure 9).

Figure 9 shows the classification results of the 2,910 ~ 2,960 m well section, and combined with standard logging data for comprehensive analysis. According to the NMR T2 spectrum and the characteristics of the proposed capillary pressure curve, two different reservoir sections, 2,915 ~ 2,917 m (Class i) and 2,937 ~ 2,939 m (Class ii), are classified in this section.

The reservoir is located at 2,915 ~ 2,917 m, which is a Class I reservoir with clear double peaks of NMR T_2 inverse spectrum. This is typical of reservoirs with well-defined microporosity in which bound water dominates. In this profile, the middle part of the proposed capillary pressure curve is mostly parallel, and the pore size distribution is relatively uniform. The low replacement pressure, median pressure, and sorting coefficient indicate that the reservoir fluid flow resistance is low and the reservoir porosity is relatively uniform. These characteristics indicate that the reservoir has moderate to high permeability, which usually supports efficient hydrocarbon flow and makes it more favorable for production.

On the other hand, the forward NMR T_2 spectrum of the Class II reservoir located at 2,937 ~ 2,939 m has a less pronounced peak compared to that of the Class I reservoir, which may indicate a different distribution of pore sizes or a higher degree

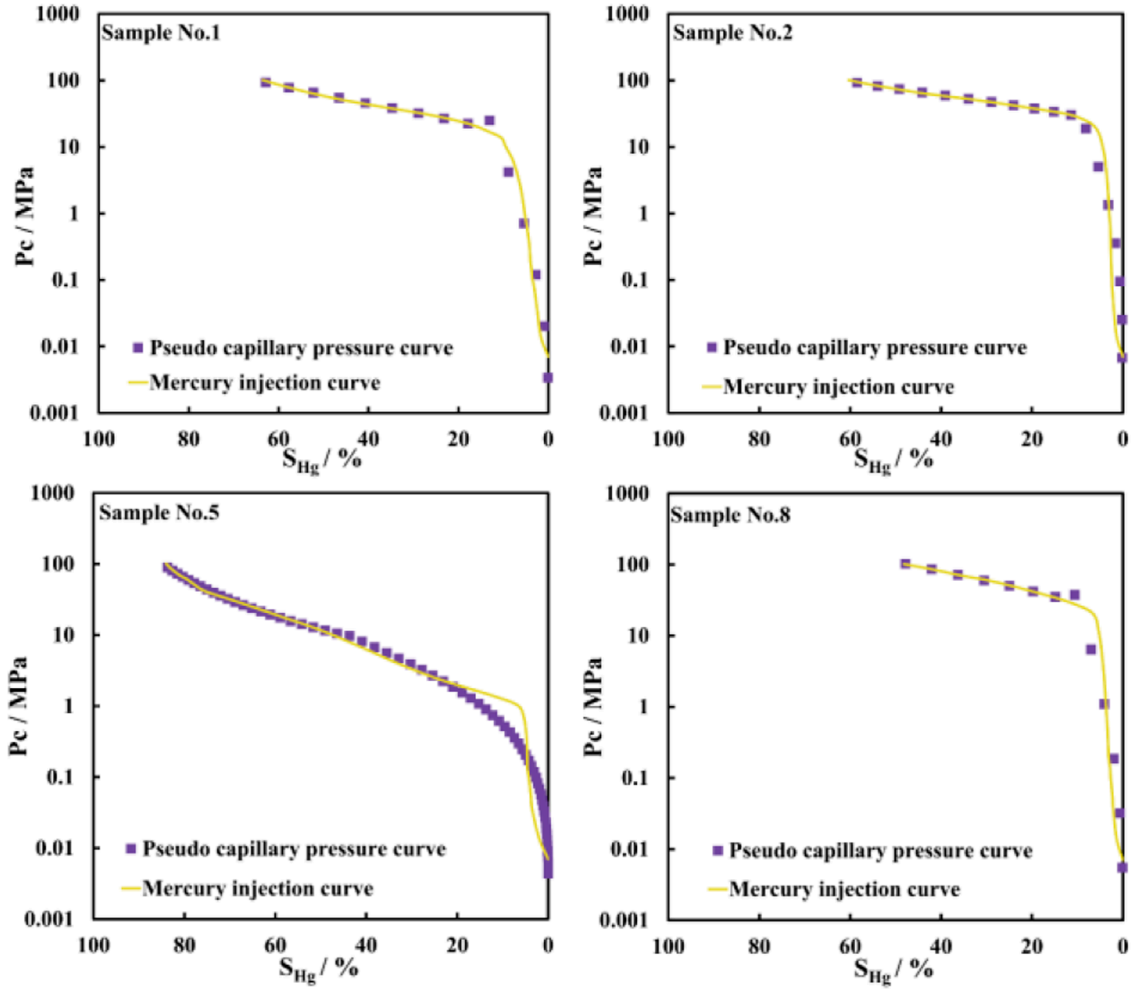

FIGURE 8
Nuclear magnetic conversion pseudo-capillary pressure curve.

of presence of larger pores. The middle section of the pseudo-capillary pressure curve is basically parallel, but there is some distortion at the end. This indicates that the pore structure of this reservoir is more complex or non-homogeneous than that of class I reservoirs. The driving pressure, median pressure and sorting coefficient of this profile are higher than that of class I reservoir, indicating that the fluid flow resistance of this reservoir is greater, the pore structure is more non-homogeneous, the permeability is lower, and the fluid transportation is more difficult. This is characteristic of the reservoir and may require additional production enhancement or enhanced recovery techniques to optimize production. The results of this reservoir classification correspond to the classification of core samples, which demonstrates the feasibility of this method.

To further verify the effectiveness of the GRNN model in the reservoir type classification task, the model results were quantitatively analyzed using standard classification performance indicators, including accuracy (Accuracy), recall (Recall), and F1 score (F1-Score). In addition, the confusion matrix (Confusion Matrix) was used to visualize the classification effects of the model on different reservoir categories (Class I and Class II).

The classification performance of the GRNN model is shown in Table 3. On the Class I reservoir, the recall rate and F1 score are 91.5% and 92.4%, respectively, indicating that the model can accurately identify the Class I reservoir and has a good balance in classification results. On the Class II reservoir, the recall rate and F1 score are 88.7% and 87.5%, respectively, which are slightly lower than those of Class I, but still indicate that the model has good classification ability. The overall accuracy rate is 94.2%, indicating that the model has high accuracy in classifying the samples as a whole.

5 Reservoir oil-water permeability and water production rate

5.1 Oil-water permeability and water yield

Within dense sandstone regions, subpar relative permeability calculations result in imprecise water production rate estimations, prompting the creation of a T_2-Kr conversion model to predict continuous strata's water production rates.

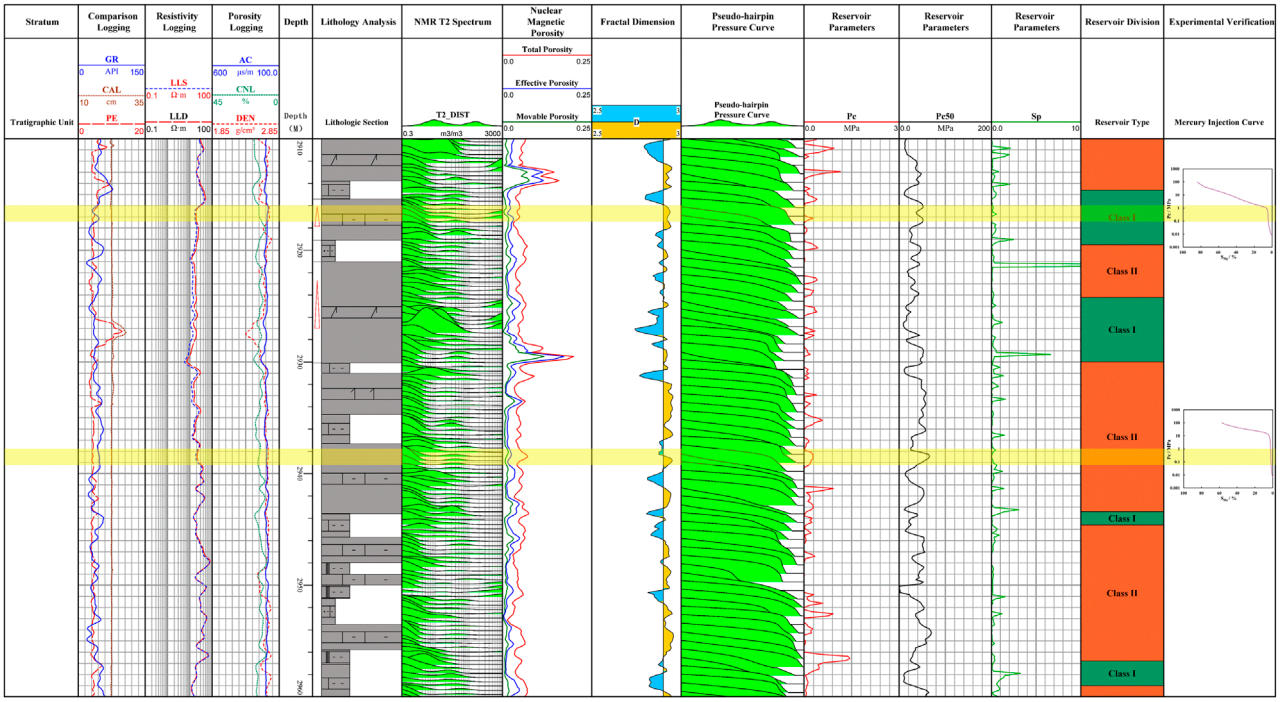

FIGURE 9
Effectiveness of NMR pseudo-capillary pressure in predicting reservoir category.

TABLE 2 Results of NMR fractal dimension calculation for rock samples.

Sample number	Permeability ($10^{-3}\mu m^2$)	Porosity (%)	D_a ($T_2 < T_{2\_cutoff}$)	D_s ($T_2 \geq T_{2\_cutoff}$)
No. 1	0.0014	5.815	0.8096	2.7994
No. 2	0.0011	4.506	0.6156	2.8807
No. 3	0.4700	7.964	—	2.7686
No. 4	0.0190	7.296	1.0083	2.7255
No. 5	0.0090	3.652	1.3011	2.9006
No. 6	0.0019	5.880	0.1633	2.8783
No. 7	0.0007	6.911	0.5808	2.8403
No. 8	0.299	4.114	0.6993	2.8077

The curve of relative permeability comprehensively mirrors the flow dynamics of oil and water phases. The rate of water production represents the proportion of water output to the overall liquid output when oil and water are combined.

$$f_w = \frac{Q_w}{Q_w + Q_o} = \frac{K_w/\mu_w}{K_w/\mu_w + K_o/\mu_o} = \frac{1}{1 + \left(\frac{K_{ro}}{K_{rw}}\right)\left(\frac{\mu_w}{\mu_o}\right)} \quad (20)$$

The same reservoir has a constant viscosity ratio μ_w/μ_o The water production rate at this point is related to the relative permeability ratio of oil and water. This equation is known as the divergence equation.

5.2 T_2-*Kr* conversion model

In the area of dense sandstone, the relative permeability is poorly calculated, resulting in inaccurate calculation of water production rate. To address the challenge of interpreting logging due to the intricate nature of Qigequan Oilfield's reservoir pores, the T_2-Kr conversion model was developed for rock samples of various

TABLE 3 Performance indicators of GRNN classification model.

Indicators	Values (%)
Accuracy	94.2
Recall (Class I)	91.5
Recall (Class II)	88.7
F1-Score (Class I)	92.4
F1-Score (Class II)	87.5

reservoir types (Guo et al., 2023; Wei et al., 2024), factoring in the intricacies of pore structures in dense sandstone reservoirs and the impact of meander curvature, to forecast the rate of water production in the continuous layer. According to Posenille's law, the flow rate of fluid through a single capillary pore:

$$q = \frac{\pi r^4 \Delta p}{8\mu L} \tag{21}$$

Let the pore volume of a single capillary tube be $V = \pi r^2 L$, The capillary pressure is $P_c = \frac{2\sigma \cos\theta}{r}$.

Assuming that the number of capillaries that make up the rock is n, the total flow rate through the rock per unit cross sectional volume is:

$$Q = \frac{(\sigma \cos\theta)^2 \Delta p}{2\mu L^2} \sum_{i=1}^{n} \frac{V_i}{P_{ci}^2} \tag{22}$$

Equation 23 can be obtained by combining Darcy's formula, which is used to calculate the absolute permeability:

$$K = \frac{(\sigma \cos\theta)^2}{2} \varphi\lambda \sum_{i=1}^{n} \frac{S_i}{P_{ci}^2} \tag{23}$$

Under the assumption of ongoing changes in the capillary radius, a correction factor is implemented to account for the discrepancy between the theoretical rock state and the actual rock (Equations 24, 25):

$$K = \frac{(\sigma \cos\theta)^2}{2} \varphi\lambda \sum_{S=0}^{S=1} \frac{dS}{P_c^2} \tag{24}$$

$$K_{rw} = \frac{K_w}{K} = \frac{\int_0^{S_i} \frac{dS}{P_c^2}}{\int_0^1 \frac{dS}{P_c^2}} \tag{25}$$

T_2-Pc conversion model based on Bianhuiyuan's derivation, as shown in Equation 26.

$$K_{rw} = \frac{\int_{T_{2c}}^{T_2} dT_2^c}{\int_{T_{2c}}^{T_{2\max}} dT_2^c} \tag{26}$$

where T_{2c} is the T_2 cutoff corresponding to bound water, ms; c is an index related to pore structure, decimal.

Formula 27 is the calculation formula of oil phase relative permeability:

$$K_{ro} = (1 - S_w^*)^2 (1 - K_{rw}) \tag{27}$$

Substituting Equations 21, 22 into Equation 20 yields the water yield equation for the new T_2-Pc conversion model.

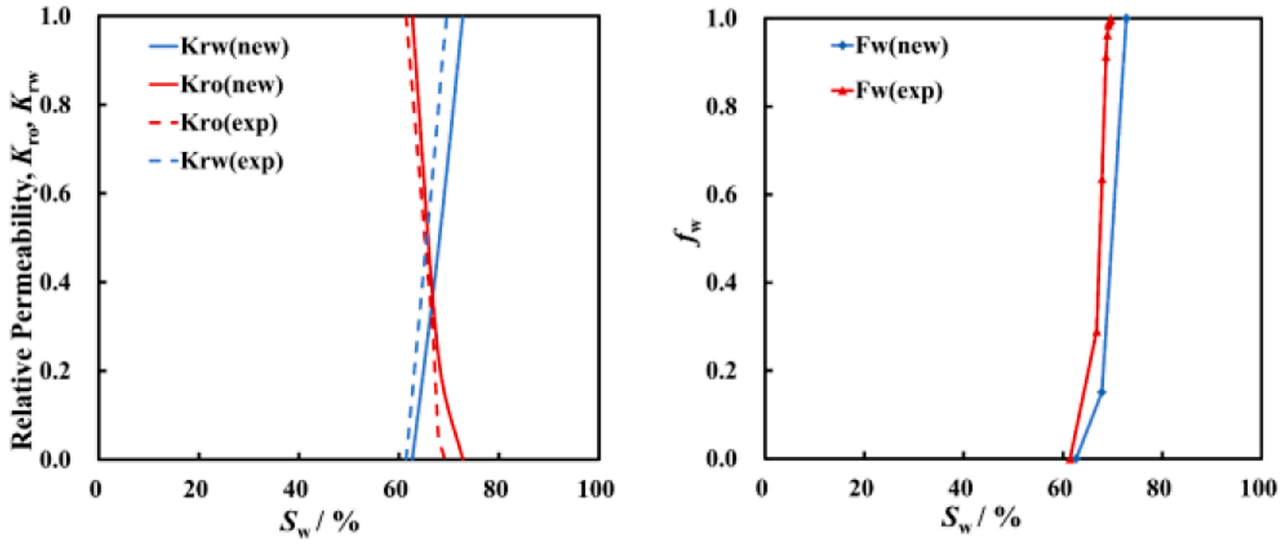

FIGURE 10
Comparison of calculated oil-water two-phase permeability and water yield curves of Class I rock samples with experimental analyses.

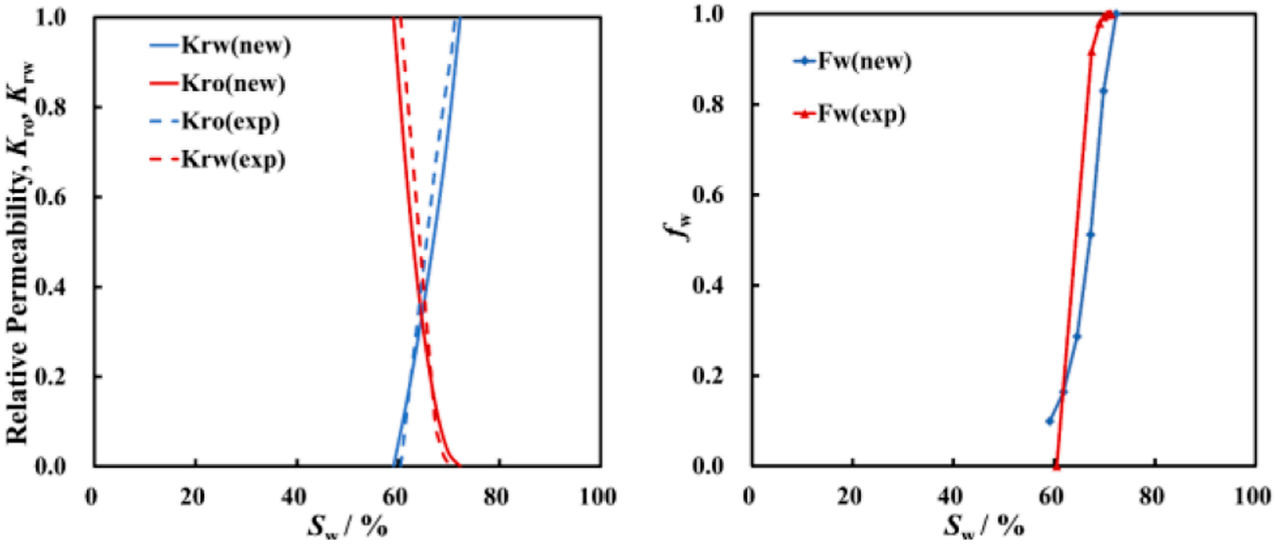

FIGURE 11
Comparison of calculated oil-water permeability and water yield curves of Class II rock samples with experimental analyses.

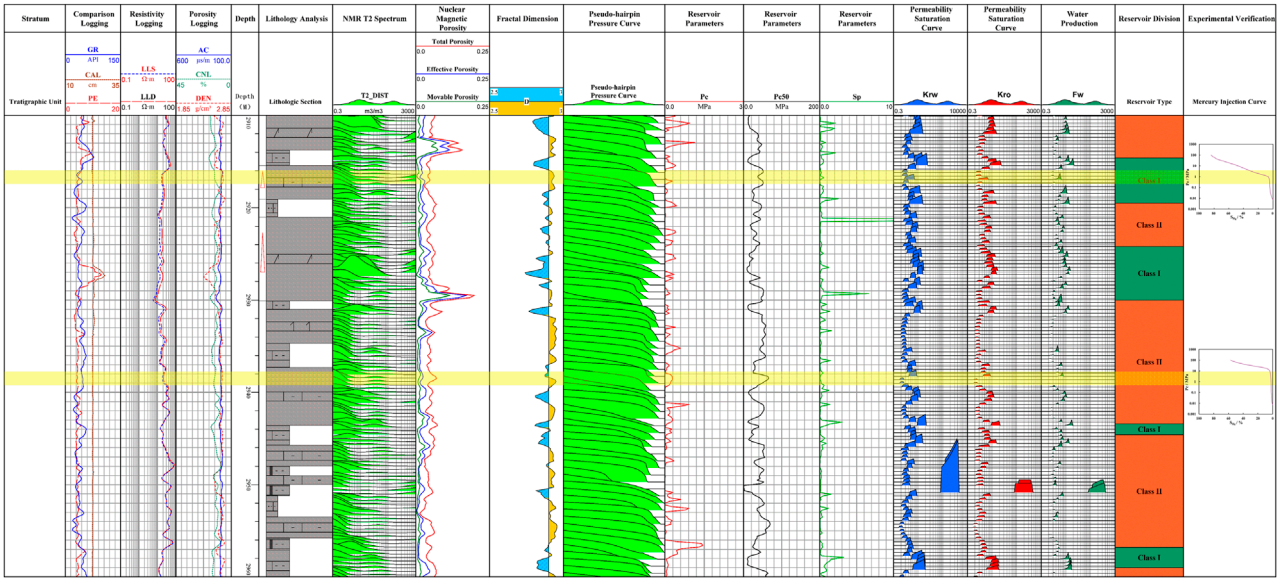

FIGURE 12
Reservoir quality and capacity treatment results for well X.

5.3 Reservoir phase infiltration and water yield calculations using nuclear magnetic logging

A good linear relationship between the pore structure index c and lg (T_{2max}/T_{2s}) was found (Equation 28).

$$c = -1.0493 \lg\left(\frac{T_{2\,\max}}{T_{2s}}\right) + 1.8054 \tag{28}$$

From Figures 10, 11 it can be shown that the predictions fit well with the experimentally measured results and the conversion model is feasible.

For each depth point in NMR logging, data undergo processing to ascertain normalized water saturation. Subsequently, the pore index is computed, determining the remaining oil saturation in the bound water. The relative permeability of oil and water, along with the pseudo-productivity curve at various depths, are ascertained. Following this, the water saturation from standard logging is utilized to project the water saturation onto the pseudo-productivity curve within the respective depth range, enabling the determination of the well section's water productivity range. The ultimate outcome of transforming the entire well section is achieved (Figure 12).

Standard logging figures for well X indicate a water saturation span of 29%–49%, equating to a pseudo water production rate of

79%–90.06%. The well's daily oil output stands at 5.89 m^3, and its water content is 88%, based on the well test outcomes from 3,240 to 3,242 m, aligning with both forecasted and actual test results.

As depicted in Figure 12, the T_2-Kr conversion model can determine the comparative permeability of oil and water in compact sandstone and the rate of water generation. Two varieties of reservoir rocks were chosen for this model, demonstrating a favorable conversion outcome. The entire well section underwent conversion to achieve the research objective of forecasting the comparative permeability of oil and water in Chaiwai's tight sandstone reservoirs and the rate of water production.

6 Discussion

The experimental data of this study mainly come from the tight sandstone reservoirs in the Chaixi area. However, the adopted method has strong regional applicability and can be extended to different reservoir types and tectonic environments. Compared with the common linear transformation method and power function transformation method, the piecewise power function method used in this paper can depict the details more precisely when converting the nuclear magnetic transverse relaxation time to the capillary pressure curve, laying a foundation for the accuracy of parameter extraction in reservoir type classification. Meanwhile, in the conventional reservoir type classification, the unified model parameters are usually applied throughout the entire well section. In this paper, the fractal dimension is used to conduct the basic classification of pore structure for complex strata, and different model parameters are fitted for different pore types, providing higher accuracy for reservoir type classification. Future research can integrate more regional data to further verify and expand the applicability of the model. Additionally, although this study uses fractal dimension and machine learning methods for reservoir classification and permeability prediction, future research can explore the integration of more advanced technologies, such as deep learning, to further enhance the accuracy and universality of the model.

7 Conclusions and recommendations

In this research zone, the compact sandstone deposits are characterized by their low porosity and permeability, exhibiting significant non-uniformity. Utilizing the fractal dimension aids in categorizing reservoirs, and a model linking the lateral relaxation time T_2 in NMR logging to the capillary pressure Pc in the piezomercury curve has been developed for classifying reservoir types throughout the well section. The T_2-Kr conversion model was developed to fulfill the research objective of forecasting the comparative permeability of oil, water, and the rate of water production in Chaixi's dense sandstone reservoirs, with the thesis's primary research findings being.

(1) By applying fundamental concepts from capillary pressure curves and NMR T2 spectra, we categorize rock specimens, utilizing the fractal dimension to confirm the precision of these classifications.

(2) Utilizing the reciprocal conversion dynamics of petrophysical factors, determine the segmented power function link between the lateral relaxation time T_2 in NMR and the capillary pressure Pc in the piezomercury graph, and implement the related T_2-Pc conversion model derived from the fractal dimension outcomes of the reservoir categorization, applied to the case and demonstrating the effectiveness of the conversion technique.

(3) Utilizing various conversion models for transforming NMR T_2 spectra into pseudo-capillary pressure graphs, three principal capillary pressure parameters are chosen for calculation, these parameters are picked as the training set, and the GRNN neural network processes the entire well section's formation data to forecast the type of reservoir. Findings indicate the technique's suitability for categorizing dense sandstone deposits, with a positive classification impact.

(4) Utilizing the T_2-Kr conversion model to forecast the relative permeability and rate of water generation in oil-water rock samples from various reservoir types, aiming to fulfill the research objective of estimating the relative permeability and production rate of water in tight sandstone reservoirs around Chaixi.

Data availability statement

The original contributions presented in the study are included in the article/supplementary material, further inquiries can be directed to the corresponding author.

Author contributions

JZ: Data curation, Resources, Validation, Writing–original draft. JP: Software, Writing–original draft. ZL: Formal Analysis, Investigation, Writing–original draft. SC: Formal Analysis, Writing–review and editing.

Funding

The author(s) declare that no financial support was received for the research, authorship, and/or publication of this article.

Conflict of interest

The authors declare that the research was conducted in the absence of any commercial or financial relationships that could be construed as a potential conflict of interest.

Generative AI statement

The author(s) declare that no Generative AI was used in the creation of this manuscript.

Publisher's note

References

Al-Dousari, M., Almudhhi, S., and Garrouch, A. A. (2022). Predicting the flow zone indicator of carbonate reservoirs using NMR echo transforms and routine open-hole log measurements: insights from a field case study spanning extreme microstructure properties. *J. Eng. Res.* 10 (1A), 330–346. doi:10.36909/jer.13185

Azim, R. A., and Aljehani, A. (2022). Neural network model for permeability prediction from reservoir well logs. *Processes* 10 (12), 2587. doi:10.3390/pr10122587

Cheng, Y. Y., Luo, X., Zhuo, Q. G., Gong, Y. J., and Liang, L. (2024). Description of pore structure of carbonate reservoirs based on fractal dimension. *Processes* 12 (4), 825. doi:10.3390/pr12040825

Dong, J., Huang, Z. L., Chen, J. L., Li, T. J., Zhao, J., Pan, Y. S., et al. (2023). Pore structure and fractal characteristics of tight sandstone: a case study for huagang formation in the xihu sag, east China sea basin, China. *Energies* 16 (4), 2013. doi:10.3390/en16042013

Gray, M. E., Daniel, R., Kaldi, J., and Kulikowski, D. (2021). Generating pseudo-capillary pressure curves from nuclear magnetic resonance (NMR) data: a case study from the Cooper Basin, Australia. *Aust. J. Earth Sci.* 68 (1), 83–98. doi:10.1080/08120099.2020.1750482

Guo, H. X., Cheng, L. S., Jia, P., and Cao, R. Y. (2023). An improved method for fitting relative permeability curve using nuclear magnetic resonance imaging. *Geoenergy Sci. Eng.* 227, 211812. doi:10.1016/j.geoen.2023.211812

Guo, X. B., Huang, Z. L., Zhao, L. B., Han, W., Ding, C., Sun, X. W., et al. (2019). Pore structure and multi-fractal analysis of tight sandstone using MIP, NMR and NMRC methods: a case study from the Kuqa depression, China. *J. Petroleum Sci. Eng.* 178, 544–558. doi:10.1016/j.petrol.2019.03.069

Hao, B., Ma, X. Y., Zhang, Q. F., Zhong, J. H., and Sun, N. L. (2020). Sedimentary facies model in the southwestern Part Of the Qaidam Basin, China. *Fresenius Environ. Bull.* 29 (4A), 3040–3047.

Ji, Y. K., Kneafsey, T. J., Hou, J., Zhao, J. L., Liu, C. L., Guo, T. K., et al. (2022). Relative permeability of gas and water flow in hydrate-bearing porous media: a micro-scale study by lattice Boltzmann simulation. *Fuel* 321, 124013. doi:10.1016/j.fuel.2022.124013

Jin, G. W., Xie, R. H., and Jin, B. C. (2024). New insight into data processing of nuclear magnetic resonance logging for pore structure characterization in tight sandstone reservoirs. *Ieee Trans. Geoscience Remote Sens.* 62, 1–10. doi:10.1109/tgrs.2024.3368096

Lai, J., Wang, G. W., Wang, Z. Y., Chen, J., Pang, X. J., Wang, S. C., et al. (2018). A review on pore structure characterization in tight sandstones. *Earth-Science Rev.* 177, 436–457. doi:10.1016/j.earscirev.2017.12.003

Li, C. L., Tan, M. J., Wang, Z. Z., Li, Y. J., and Xiao, L. Z. (2023). Nuclear magnetic resonance pore radius transformation method and fluid mobility characterization of shale oil reservoirs. *Geoenergy Sci. Eng.* 221, 211403. doi:10.1016/j.geoen.2022.211403

Li, S. J., Bian, H. Y., Zhang, D., Liu, Y. X., Liu, G. L., and Wang, F. (2024a). Research on pore structure and classification evaluation of tight oil reservoirs based on fractal theory. *Acta Geophys.* 72, 4079–4089. doi:10.1007/s11600-024-01299-2

Li, X., Wang, J. G., Long, G. H., Xu, L., Cui, J., Sun, X. J., et al. (2024b). Eocene lacustrine microbialites in the western Qaidam Basin, China: implication for the sedimentary record and hydrocarbon potential. *Carbonates Evaporites* 39 (1), 5. doi:10.1007/s13146-023-00911-8

Mo, C. P., Zhang, G. D., Tang, Y., and Zeng, D. F. (2024). Multi-parameter modeling for prediction of gas-water production in tight sandstone reservoirs. *J. Petroleum Explor. Prod. Technol.* 14 (8-9), 2459–2471. doi:10.1007/s13202-024-01822-7

Moodie, N., and McPherson, B. (2024). An integrated approach to derive relative permeability from capillary pressure. *Comput. Geosci.* 28 (4), 755–770. doi:10.1007/s10596-024-10297-8

Parvazdavani, M., Movaghar, M. R. K., and Dehghani, S. A. M. (2022). Low salinity water flooding: evaluating the effect of salinity on oil and water relative permeability curves using coupling of DLVO and geochemical reactions. *J. Petroleum Sci. Eng.* 215, 110677. doi:10.1016/j.petrol.2022.110677

Pei, J. Y., Zhang, Y. F., Hu, J., Zhang, J., Zhu, X. M., Wang, Q., et al. (2022). Experimental verification of reservoirs with different wettability using an oil-water relative permeability model. *Processes* 10 (6), 1211. doi:10.3390/pr10061211

Peng, S. (2020). Gas-water relative permeability of unconventional reservoir rocks: hysteresis and influence on production after shut-in. *J. Nat. Gas Sci. Eng.* 82, 103511. doi:10.1016/j.jngse.2020.103511

Su, H. B., Zhang, S. M., Sun, Y. H., Wang, X. H., Yu, B. M., Wang, Y., et al. (2020). A comprehensive model for oil-water relative permeabilities in low-permeability reservoirs by fractal theory. *Fractals-Complex Geometry Patterns Scaling Nat. Soc.* 28 (3), 2050055. doi:10.1142/s0218348x20500553

Tian, F., Wang, W. M., Liu, N. G., Jiang, J. Q., Niu, C. K., Zhang, Y. D., et al. (2018). Rock-type definition and pore characterization of tight carbonate rocks based on thin sections and MICP and NMR experiments. *Appl. Magn. Reson.* 49 (7), 631–652. doi:10.1007/s00723-018-0993-2

Wang, F. Y., Yang, K., and Cai, J. C. (2018). Fractal characterization of tight oil reservoir pore structure using nuclear magnetic resonance and mercury intrusion porosimetry. *Fractals-Complex Geometry Patterns Scaling Nat. Soc.* 26 (2), 1840017. doi:10.1142/s0218348x18400170

Wei, D., Gao, Z. Q., Zhang, C., Fan, T. L., Karubandika, G. M., and Meng, M. M. (2019). Pore characteristics of the carbonate shoal from fractal perspective. *J. Petroleum Sci. Eng.* 174, 1249–1260. doi:10.1016/j.petrol.2018.11.059

Wei, H. Y., Xie, R. H., Wang, Y. X., Xie, B., Lai, Q., and Guo, J. F. (2024). Nuclear magnetic resonance T_2 distribution-based gas-water relative permeability prediction in tight sandstone reservoirs: a case study on central sichuan basin, China. *Energy and Fuels* 38 (5), 3598–3608. doi:10.1021/acs.energyfuels.3c03972

Wenjie, F., and Ye, Z. (2024). Sedimentary characteristics and reservoir architecture of a lacustrine mixed carbonate/siliciclastic system: the lower member of the ShangGanchaigou Formation, Neogene, in the western Qaidam Basin, China. *Front. Earth Sci.* 12. doi:10.3389/feart.2024.1437205

Wu, J. T., Zhang, L., Liu, Y. X., Ma, K. Q., and Luo, X. B. (2024). Effect of displacement pressure gradient on oil-water relative permeability: experiment, correction method, and numerical simulation. *Processes* 12 (2), 330. doi:10.3390/pr12020330

Xiao, L., Mao, Z. Q., Zou, C. C., Jin, Y., and Zhu, J. C. (2016). A new methodology of constructing pseudo capillary pressure (P_c) curves from nuclear magnetic resonance (NMR) logs. *J. Petroleum Sci. Eng.* 147, 154–167. doi:10.1016/j.petrol.2016.05.015

Xie, W. B., Yin, Q. L., Wang, G. W., and Yu, Z. Y. (2021). Variable dimension fractal-based conversion method between the nuclear magnetic resonance T_2 spectrum and capillary pressure curve. *Energy and Fuels* 35 (1), 351–357. doi:10.1021/acs.energyfuels.0c02924

Yi, J., Qi, Z. L., Li, X. C. Z., Liu, H., and Zhou, W. (2024). Spatial correlation-based machine learning framework for evaluating shale gas production potential: a case study in southern Sichuan Basin, China. *Appl. Energy* 357, 122483. doi:10.1016/j.apenergy.2023.122483

Zhang, H. T., Li, G. R., Guo, H. P., Zhang, W. J., Wang, Y. M., Li, W. B., et al. (2020). Applications of nuclear magnetic resonance (NMR) logging in tight sandstone reservoir pore structure characterization. *Arabian J. Geosciences* 13 (13), 572. doi:10.1007/s12517-020-05590-6

Zhang, N., Wang, S. D., Xun, X. J., Wang, H. Y., Sun, X. M., and He, M. C. (2023). Pore structure and fractal characteristics of coal-measure sedimentary rocks using nuclear magnetic resonance (NMR) and mercury intrusion porosimetry (MIP). *Energies* 16 (9), 3812. doi:10.3390/en16093812

Zhao, X. L., Yang, Z. M., Zhou, S. B., Luo, Y. T., Liu, X. W., Zhang, Y. P., et al. (2021). Research on characterization and heterogeneity of microscopic pore throat structures in tight oil reservoirs. *Acs Omega* 6 (38), 24672–24682. doi:10.1021/acsomega.1c03382

Zhou, Y. Q., You, L. Z., Zi, H., Lan, Y. Y., Cui, Y. L., Xu, J., et al. (2022). Determination of pore size distribution in tight gas sandstones based on Bayesian regularization neural network with MICP, NMR and petrophysical logs. *J. Nat. Gas Sci. Eng.* 100, 104468. doi:10.1016/j.jngse.2022.104468

frontiers | Frontiers in Earth Science

TYPE Original Research
PUBLISHED 07 March 2025
DOI 10.3389/feart.2025.1493305

OPEN ACCESS

EDITED BY
Yihuai Zhang,
University of Glasgow, United Kingdom

REVIEWED BY
Jing Bi,
Guizhou University, China
Janez Perko,
Belgian Nuclear Research Centre (SCK CEN), Belgium
Weibiao Xie,
China University of Petroleum Beijing, China

*CORRESPONDENCE
Philippe Poncet,
philippe.poncet@univ-pau.fr

RECEIVED 08 September 2024
ACCEPTED 09 January 2025
PUBLISHED 07 March 2025

CITATION
Perez S, Etancelin J-M and Poncet P (2025) A semi-Lagrangian method for the direct numerical simulation of crystallization and precipitation at the pore scale.
Front. Earth Sci. 13:1493305.
doi: 10.3389/feart.2025.1493305

A semi-Lagrangian method for the direct numerical simulation of crystallization and precipitation at the pore scale

Sarah Perez[1,2], Jean-Matthieu Etancelin[1] and Philippe Poncet[1]*

[1]Universite de Pau et des Pays de l'Adour, Centre National de la Recherche Scientifique (CNRS), Laboratoire de Mathématiques et de leurs Applications (LMAP, UMR5412), Pau, France, [2]The Lyell Centre, Heriot-Watt University, Edinburgh, United Kingdom

This article introduces a new efficient particle method for the numerical simulation of crystallization and precipitation at the pore scale of real rock geometries extracted by X-Ray tomography. It is based on the coupling between superficial velocity models of porous media, Lagrangian description of chemistry using Transition-State-Theory, involving underlying grids. Its ability to successfully compute dissolution process has been established in the past, and is presently generalized to precipitation and crystallization by means of adsorption modeling. Numerical simulations of mineral CO_2 trapping are provided, showing evidence of clogging/non-clogging regimes, and one of the main results is the introduction of a new non-dimensional number needed for this characterization.

KEYWORDS

digital rock physics (DRP), crystallization, mineral trapping, CO_2 storage, precipitation, clogging, Lagrangian methods, superficial velocity

1 Introduction

Studying reactive flows in porous media is essential to manage the geochemical effects arising from CO_2 capture and storage in natural underground reservoirs. While long-term predictions are commonly modeled at the field scale (Class et al., 2009), pore-scale approaches meanwhile provide insights into local geochemical interactions between the injected CO_2 and the aquifer structure (Payton et al., 2022). Through mathematical homogenization of the sub-micrometer porous medium and appropriate modeling, one can simulate the reactive processes that occur at the pore scale and predict their impact on the macro-scale properties, as developed in Allaire and Hutridurga (2012); Allaire et al. (2010). Geochemical processes are critical components for understanding the mineral trapping mechanisms and local evolving interfaces within the porous environment, and investigating the impact of such reactive processes provides insights into reservoir safety submitted to chemical interactions that may compromise the aquifer structure. Pore-scale modeling of reactive flow hence appears as a complementary mean to field scale studies wherein homogenization theory bridges the gap between these scales.

In this context, several geochemical mechanisms play a critical role in the CO_2 sequestration process and mainly involve precipitation, crystallization, and dissolution phenomena. On one side, carbonate precipitation and crystallization ensure efficient capture of the injected CO_2 in the form of minerals such as calcite, aragonite, or dolomite: this is

referred to as mineral trapping, which informs about the storage capacities of the reservoir. These processes significantly impact the flow within the porous media at the pore scale, leading to restructuring of the flow path and morphological changes that alter, among other, the pore size distribution and the roughness of the interface due to partial or complete clogging of pore throats. Such alterations at the micro-scale subsequently alter the estimation of the macro-scale properties, namely, the porosity and permeability, and thereby require investigations to ensure wise management of the underground reservoir structures. On the other side, the reverse chemical process can also occur, resulting in carbonate mineral dissolution due to an acidification of the aqueous solution. This may compromise not only the efficiency of the trapping mechanisms, leading to an increase of both porosity and permeability, but also the integrity of the reservoir cap rock, and is, therefore, of great interest to prevent acute leakage issues. Consequently, one needs reliable estimations of the macro-properties changes due to these overall geochemical processes at the pore scale, to manage their impact on the reservoir scale modeling of CO_2 storage. This can be achieved through, first, efficient Direct Numerical Simulation (DNS) of reactive flows at the pore-scale and, subsequently, by embedding uncertainty concerns on the quantification of the petrophysical properties. In the present article, we address the first point with a focus on precipitation and crystallization modeling for CO_2 mineral storage into carbonate porous media.

Pore-scale investigation of reactive geochemical systems has garnered interest over the past decades based on imaging processes and laboratory experiments (Poonoosamy et al., 2023; Menke et al., 2015; Noiriel and Renard, 2022; Siena et al., 2021)), numerical simulations (Varzina et al., 2020; Patel et al., 2021; Payton et al., 2022; Soulaine et al., 2018), and a combination thereof (Molins et al., 2021; Noiriel and Soulaine, 2021). From this perspective, image-based DNS using microCT of a Representative Elementary Volume (REV) of a porous sample with efficient scientific computing and numerical method appears as a promising tool to query the impact of reactive processes on real rock geometries.

The present article focuses on the modeling aspects of CO_2 mineral trapping under the form of calcite crystal aggregates at the pore scale. Precipitation kinetics of calcite have been historically studied since the 1970s from the experimental and theoretical sides in Chou et al. (1989); Lasaga (1981); Plummer et al. (1978), and this has commonly established Transition State Theory (TST) as an efficient and straightforward way of predicting mineral reaction rate. Indeed, the deterministic TST is currently one of the most widely used models in reactive transport codes and DNS, detailed in Molins et al. (2012); Noiriel et al. (2021); Noiriel et al. (2016); Steefel et al. (2015). However, several doubts have risen in the research community about using such a deterministic approach for predicting crystal growth rates. In particular, comparison with experimentally determined growth rates has highlighted a wide range of discrepancies, querying the reliability of the TST model for overall crystallization processes, introduced in Hellevang et al. (2013); Pham et al. (2011). Meanwhile, probabilistic approaches, which find their origins in classical nucleation theory and the probabilistic nature of the precipitation and crystal growth mechanisms, have been developed in Masoudi et al. (2021); Nooraiepour et al. (2021a); Wolthers et al. (2012). These models make it possible to incorporate the effects of induction time characterizing the onset of the nucleation, the ionic affinities of the growing sites, and attachment frequencies of the ionic species involved in the reaction. Such attachment frequencies are, especially, significant for modeling surface adsorption and crystal aggregation that largely hinges on the surrounding porous structure in the sense that observable kinks and corners (above the voxel scale), for instance, are experimentally identified as preferential growing sites. However, such a geometrical dependency of the crystal aggregation is commonly neglected in most models, which makes it difficult to predict the spatial distribution of the new crystals.

Therefore, the main contribution of the present article is to build a novel numerical method dedicated to the precipitation and aggregation into crystal at the pore scale of microCT based geometry. Therefore, we formalize a two-step crystallization process wherein nuclei generation relies on a deterministic TST model before considering the probabilistic mineral aggregation—crystal growth—into the pore interface. The latter accounts for adsorption frequencies of the precipitate to the growth sites, which is weighted by a non-uniform probability of attachment rate depending on local mineral volume fraction. The current numerical method relies on a semi-Lagrangian approach, which handles a Lagrangian description of the chemistry with underlying grid methods for the hydrodynamic, based on the superficial velocity formalism introduced in the 1980s in Quintard and Whitaker (1988). The latter makes it possible to account for the involvement of the porous matrix in the overall flow process through a micro-continuum description of the medium. In this sense, one considers an intermediate state between the full resolution of each individual solid grain and the completely averaged continuum representation of the porous media at Darcy's scale. This establishes two-scale models that are widely used in hydrodynamics pore-scale modeling and μCT image-based DNS, as shown in Molins et al. (2021); Panga et al. (2005); Soulaine et al. (2017). The present semi-Lagrangian formalism has been successfully employed in the context of carbonate dissolution at the pore scale (Etancelin et al., 2020) and extensively benchmarked against state-of-the-art numerical alternatives, as detailed in Molins et al. (2021). The present work originality is to blend together the micro-continuum hydrodynamics and the two-step process involving precipitation with TST and aggregation with attachment probability. The result is an efficient numerical tool able to adress clogging studies in real geometries.

Moreover, this article investigates a case study involving a pure calcite sample in which alcalin solution saturated with calcium and dissolved CO_2 flow through, applying the numerical method developed here and allowing to compute whether this leads to material clogging or not. We show that the cohabitation of precipitation and aggregation define naturally two kinds of Damköhler numbers Da_{II}. This case study exhibits that as long as the precipitation Damköhler number is high enough, the crystallization Damköhler number drives whether there is clogging or not, for several Peclet numbers.

The present manuscript is structured as follows. The section 2 introduces reactive flow model at the pore-scale of rocks. First, the Darcy-Brinkman-Stokes model including to the Kozeny-Carman correlation terms in order to model highly heterogeneous medium at its pore scale, naturally meaningful for evolving fluid-solid

interface defining the pores structure. Second, the transport-reaction-diffusion of chemical species. In Section 3, we detail our particle method for highly heterogeneous diffusion arising from Archie's law in the two-scale description of the medium. The application of such models to the precipitation and the crystallization for the CO_2 mineral trapping is described in Section 4. It includes the implementation and its HPC features on hybrid architectures, *i.e.*, coupling CPU and GPU devices, for the present application, detailed in Section 4.4. The related numerical results are discussed in Section 5 in terms of clogging or non-clogging regimes of crystallization.

2 Models in reactive microfluidics

The present section focuses on the modeling of reactive hydrodynamics in the context of CO_2 mineral storage and presents the mathematical model used to simulate reactive processes at the pore scale. We first introduce the so-called Darcy-Brinkman-Stokes formulation for microfluidic flows based on superficial velocity formalism. We subsequently incorporate transport-reaction-diffusion equations modeling the geochemical interactions between the different species involved. Finally, we present an alternative formulation in velocity-vorticity for the hydrodynamics equation, which ensures the fluid incompressibility condition.

2.1 Darcy-Brinkman-Stokes: a superficial velocity formalism at the pore scale

We introduce a spatial domain $\Omega \subset \mathbb{R}^n$, $n = 1,2,3$ which corresponds to the porous medium described at its pore scale. This sample description involves a pure fluid region Ω_F, also called void-space and assumed to be a smooth connected open set, and a surrounding solid matrix Ω_S itself considered as a porous region. This region is seen as complementing the full domain Ω, which in practice represents the computational box of the numerical simulations such that $\Omega_F = \Omega \backslash \overline{\Omega}_S$, and the internal fluid/solid interface is denoted Σ. We denote the computational domain boundary by $\partial\Omega$ and use $\Gamma_F = \partial\Omega \cap \Omega_F$ and $\Gamma_S = \partial\Omega \cap \Omega_S$ to refer to the fluid and solid parts of the computational domain boundary, respectively, such that $\partial\Omega = \Gamma_F \cup \Gamma_S$ (see Figure 1 for instance).

The boundary conditions at the inlet and outlet faces, typically for a cubic computational domain $\Omega =]0, l[^3$ but not exclusively, either impose a prescribed flow rate $\overline{u}$ on the velocity or satisfy periodic boundary conditions for a prescribed driving force f. The boundary conditions on the other lateral faces are systematically periodic since rock samples are commonly constrained in an impermeable solid casing when μCT experiments are conducted. This ensures a consistent numerical representation of the sample compared to the experiments. This also guarantees $\mathcal{C}^\infty$ regularity on the boundary even if the domain exhibit corners, since the problem can be formalized by considering the equivalence relationship with the quotient space $\Omega \equiv \mathcal{Q}/G$ where $\mathcal{Q} = \mathbb{R}^2 \times]0, l[$ and $G = l\mathbb{Z}^2 \times \{0\}$ (*e.g.*, see Sanchez et al. (2019) for detailed configurations of acceptable domains).

From the μCT images, we can also characterize the static pore-space structure, corresponding to the sample's initial state before any geochemical interactions. we denote by $\varepsilon = \varepsilon_f = 1 - \varepsilon_s$ the micro-porosity field defined on Ω, given ε_f and ε_s respectively the volume fractions of void and solid according to usual notations from Soulaine et al. (2017). This defines a micro continuum description of the porous medium such that $\varepsilon = 1$ in the pure fluid region Ω_F and takes a small value in the surrounding matrix Ω_S. In fact, the local micro-porosity ε is assumed to have a strictly positive lower bound $\varepsilon(x,t) \geqslant \varepsilon_0 > 0$ for all (x,t) in the spatiotemporal domain $\Omega \times [0, T_f]$ for a final real-time $T_f > 0$ in the reactive process. This lower bound ε_0 characterizes the residual porosity of the porous matrix, potentially unresolved due to X-ray μCT imaging limitations (as discussed in Perez et al. (2022), see also Figure 1). In practice, we assume throughout this work $\varepsilon_0 = 5\%$, but this value can range from 1% to 10%.

Such a two-scale description of the local heterogeneities in the carbonate rocks is appropriate to simulate the pore-scale physics and establish the governing flow and transport equations in each distinct region. Indeed, although the hydrodynamic of a viscous flow in a pure fluid region is commonly quantified through the Navier-Stokes equation, we can formulate the problem on the whole domain Ω based on the two-scale micro continuum description of the medium. We, therefore, consider the model on the superficial velocity u introduced and derived rigorously by Quintard and Whitaker in the late 80 s (Quintard and Whitaker, 1988) and commonly used until nowadays (Molins et al., 2021; Soulaine et al., 2017; Wood et al., 2007):

$$\varepsilon^{-1}\frac{\partial \rho u}{\partial t} + \varepsilon^{-1}\mathrm{div}\left(\varepsilon^{-1}\rho u \otimes u\right) - \varepsilon^{-1}\mathrm{div}\left(2\mu D(u)\right) + \mu^* K_\varepsilon^{-1} u = f - \nabla p \tag{1}$$

along with the divergence-free condition $\mathrm{div}\, u := \nabla \cdot u = 0$. It is noticeable that this incompressibility condition should be changed when considering evolving porous structures to account for density variations, especially in the context of fast dissolution or nucleation (Soulaine et al., 2018). Indeed, this only depicts that crystal nucleation within a liquid volume, for instance, drastically increases the density and induces divergence effects in its neighborhood. Nevertheless, the divergence-free condition can be assumed to remain if the characteristic time of fluid/solid interface changes is way larger than the hydrodynamics time scale (Soulaine et al., 2017), which is the case for our study. In Equation 1, the notation $D(u)$ refers the shear-rate tensor $D(u) = (\nabla u + \nabla u^T)/2$, μ is the dynamic viscosity, p is the volumic pressure, f the volumic driving force and ρ the fluid density. The related viscosity μ^* usually coincides with the fluid viscosity μ but may be different in order to account for viscous deviations.

The quantities ρ, μ, μ^* and f are assumed to be constant. The quantities ε, ρ, μ and p are scalar fields; u, its rotational $\omega = \nabla \times u$, f and ∇p are vector fields, while $D(u)$ and K_ε are matrices.

The permeability K_ε refers to the micro-scale permeability and depends on the local micro-porosity field ε. This permeability of the micro-porous domain can be modeled by the empirical Kozeny-Carman relationship, historically introduced in Kozeny (1927) and Carman (1937), generalized in Quintard and Whitaker (1993) and now used meaningfully at the micrometer subscale (see Soulaine et al. (2017); Molins and Knabner (2019) and their next

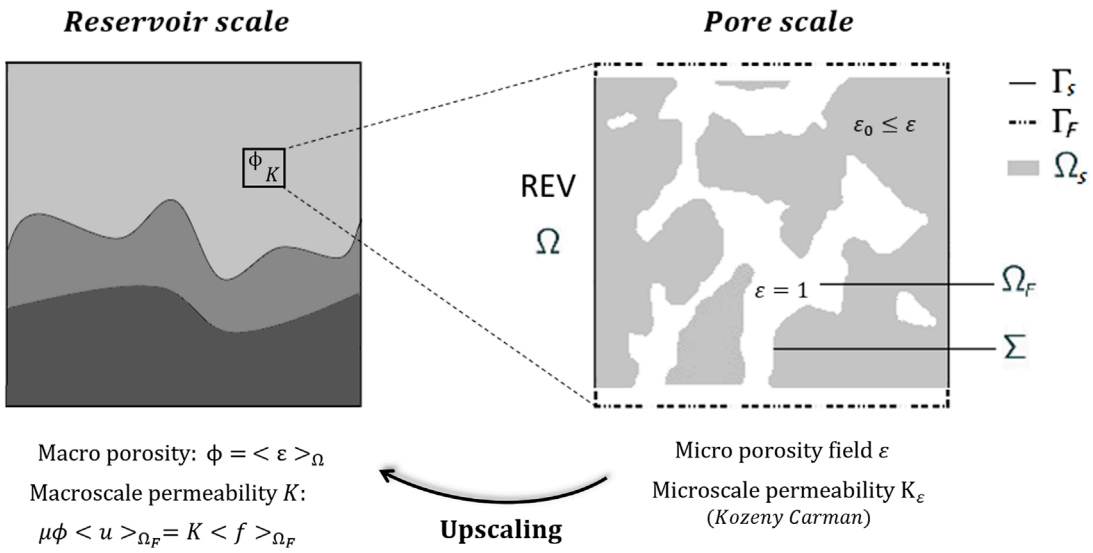

FIGURE 1
Upscaling from the pore-scale. Schematic representation of a reservoir or material scale structure, on the left, with its inherent averaged macro-properties ϕ and K computed on a representative elementary volume (REV). Local micro-continuum description of the pore-scale heterogeneity in this REV, on the right, along with its intrinsic micro-scale properties. These properties are the local micro porosity field ε and the micro-scale permeability K_ε, based on the Kozeny-Carman relationship developed in Equation 2.

publications). This relation is given by

$$K_\varepsilon^{-1} = \kappa_b^{-1} \frac{(1-\varepsilon)^2}{\varepsilon^3} \tag{2}$$

where κ_b is the bulk permeability, which can be taken as a coarse estimation of the reference macro-scale permeability κ_0. For instance, Soulaine et al. (2017) estimated that four orders of magnitude below the permeability are required for κ_b to ensure adherent boundary conditions at the pore interface. In this article, we consider both K_ε, κ_b and κ_0 as scalars, meaning we restrict ourselves to the isotropic case although this formalism can be extended to anisotropic porous media. Despite the validation of this correlation law for porous media at the sub-millimeter scale and its applicability to dissolution (Molins et al., 2021), we assume that it is also valid for crystal growth at pore walls as a reverse mechanism of dissolution. The dissolution-crystallization (whether it is one or two steps process) is not reversible since the resulting crystal may not reach the same tortuosity than the initial material (hence a different permability), but the similarity in the material is sufficiently strong to work with this assumption. The superficial velocity formulation Equation 1 defines a two-scale model that can be solved on the overall domain Ω — using, for instance, penalization principles—and retrieves the usual Navier-Stokes equation in the pure fluid region Ω_F (since $K_\varepsilon^{-1} = 0$ for $\varepsilon = 1$). Depending on the flow regime hypothesis, one can also encounter simplified versions of Equation 1 wherein some terms can be neglected. In the context of pore-scale simulations, in particular, the inertial effects become negligible compared to viscous forces due to low Reynolds number, denoted Re. The latter is a characteristic dimensionless number defined as:

$$\mathrm{Re} = \rho \overline{u} L / \mu,$$

where $\overline{u}$ and L are respectively the characteristic velocity and length of the sample. The characteristic length L can be related to average pore throat diameters and, therefore, we typically fall within the assumption $\mathrm{Re} \ll 1$ throughout this manuscript.

At low Reynolds numbers and for highly viscous Darcian flows, Equation 1 hence reduces to the following Darcy-Brinkman-Stokes (DBS) model:

$$-\mathrm{div}\left(2\mu D(u)\right) + \mu\kappa_b^{-1}\frac{(1-\varepsilon)^2}{\varepsilon^2}u = \varepsilon(f - \nabla p), \quad \text{in} \quad \Omega \tag{3}$$

where $\mu^* = \mu$ for sake of readability. In the present work, we consider this DBS Equation 3, which is adequate in the flow regime hypothesis of low Reynolds number representative in pore-scale modeling. The DBS equation based on the superficial velocity is an efficient formalism to model the hydrodynamic in multi-scale porous media, and account for heterogeneous porosity levels.

2.2 Reactive flow model: general formulation

The DBS flow model Equation 3 needs to be complemented by transport-reaction-diffusion equations of the different species involved in the geochemical processes. These equations are derived from the mass balance of the chemical species (Soulaine et al., 2017), and can be written under the form:

$$\frac{\partial \varepsilon \widetilde{C}_k}{\partial t} + \mathrm{div}\left(u\widetilde{C}_k\right) - \mathrm{div}\left(\alpha_k(\varepsilon)\varepsilon\nabla\widetilde{C}_k\right) = \dot{m}_k / M_k, \tag{4}$$

where $\widetilde{C}_k = \rho_f \overline{\omega}_{f,k}/M_k$ is a concentration per unit of fluid with M_k the molar mass and $\dot{m}_k$ the rate of mass transfer for the k^{th} species. We follow here the notations introduced by Quintard and Whitaker

in Quintard and Whitaker (1988), and afterward commonly used, where ρ_f is the fluid density and $\overline{\omega}_{f,k}$ is the mass fraction of the k^{th} component averaged on the fluid phase. The term $\alpha_k(\varepsilon)$ is a space-variable effective diffusion coefficient and accounts for a reduced diffusion in the surrounding porous matrix due to the tortuosity effect, which is usually quantified using Archie's law, historically introduced in Archie (1942):

$$\alpha_k(\varepsilon) = D_{m,k}\varepsilon^{\eta}.$$

In this empirical relationship, η refers to the tortuosity index and $D_{m,k}$ to the molecular diffusion of the k^{th} considered species, quantified at milimeter scale in Wakao and Smith (1962), generalized and downscaled in Coindreau and Vignoles (2005) and Glover (2016). We finally introduce $C_k = \varepsilon\widetilde{C}_k$, so that the Equation 4 is written:

$$\frac{\partial C_k}{\partial t} + \operatorname{div}\left(\varepsilon^{-1}uC_k\right) - \operatorname{div}\left(D_{m,k}\varepsilon^{1+\eta}\nabla\left(\varepsilon^{-1}C_k\right)\right) = R_k(\mathbf{C}), \qquad (5)$$

which is no more than a superficial modeling of the chemistry, that is to say C_k is the amount of moles per unit of volume while $\widetilde{C}_k$ is the amount of moles per unit of fluid volume. The notation $R_k(\mathbf{C})$ refers to a function (without differential operators) that models the rate contribution of the chemical reactions for the k^{th} component, where we denote by $\mathbf{C} \in \mathbb{R}^{N_s}$ the vector of the concentrations C_k of all the N_s chemical species. We distinguish N_m mobile species, and N_i immobile species such that $N_s = N_m + N_i$. The k^{th} rate contribution $R_k(\mathbf{C})$ is, practically, the balance of kinetics of all reactions involving the k^{th} species. The sign of individual reaction rates lies in the nature of the species k considered, either positive for a chemical product or negative for a reactant.

The model Equation 5 is the formalism that we retain for the aqueous species in the liquid phase. In particular, this model highlights a superficial gradient operator denoted $\nabla^{\epsilon} := \varepsilon\nabla\varepsilon^{-1}$ involved in the heterogeneous diffusion arising from the Archie's law. One should notice that the superficial gradient can become highly sensitive at the mineral boundary, mainly due to jumps in the porosity levels on either side of the interface, and thus will require special considerations to adequately manage evolving medium under reactive processes.

Concerning the solid phase of concentration $C_{(s)}$ (*e.g.*, the k^{th} component in vector $\mathbf{C}$), which we assume contains only one chemical species of molar volume v ($N_i = 1$), it is not subject to transport or diffusion, so that

$$\frac{\partial C_{(s)}}{\partial t} = R_k(\mathbf{C}). \qquad (6)$$

This solid concentration is subsequently linked to the micro-porosity ε by the relation $C_{(s)} = (1-\varepsilon)/v$, so one gets

$$\frac{\partial \varepsilon}{\partial t} = -vR_k(\mathbf{C}).$$

In the case of a typical reaction involving a unique solid X(s) of molar volume v, and two aqueous species Y and Z in the liquid phase, with their respective positive stoechiometric coefficients χ_i and following, for instance, the general chemical reaction:

$$\chi_1 \mathrm{X}_{(s)} + \chi_2 \mathrm{Y} \rightleftharpoons \chi_3 \mathrm{Z}, \qquad (7)$$

we define the vector of concentrations $\mathbf{C} := (C_1, C_2, C_3)^T = \left([\mathrm{X}_{(s)}], [\mathrm{Y}], [\mathrm{Z}]\right)^T \in \mathbb{R}^3$. Since there is only one reaction, one gets a unique kinetic balance written as $R_i(\mathbf{C}) = \pm\chi_i R(\mathbf{C})$, with $R(\mathbf{C})$ the kinetic rate. By default, we assume a positive sign for the solid species, so that one follows the convention $R(\mathbf{C}) < 0$ for the forward reaction corresponding to the solid $\mathrm{X}_{(s)}$ dissolution, while $R(\mathbf{C}) > 0$ for the reverse reaction, *e.g.*, precipitation and crystallization processes. The sign for the aqueous species subsequently depends on its interaction with the solid X(s): we get a positive sign for species Y, which is either consumed or produced in the same way as the solid, and a negative sign for species Z, which behaves oppositely. The reaction rate $R(\mathbf{C})$ can involve many concentrations, specific areas, chemical activities, equilibrium constants, etc. (see Section 4 thereafter for practical examples and further details).

Along with its boundary and initial conditions, the model for reaction (Equation 7) defines a set of partial differential equations modeling reactive flows at the pore scale:

$$\begin{cases} -\operatorname{div}\left(2\mu D(u)\right) + \mu\kappa_b^{-1}\dfrac{(1-\varepsilon)^2}{\varepsilon^2}u = \varepsilon(f - \nabla p), \quad \text{in } \Omega\times]0, T_f[\\ \dfrac{\partial C_1}{\partial t} = \chi_1 \ R(\mathbf{C}), \quad \text{in } \Omega\times]0, T_f[\\ \dfrac{\partial C_2}{\partial t} + \operatorname{div}\left(\varepsilon^{-1}uC_2\right) - \operatorname{div}\left(D_{m,2}\varepsilon^{1+\eta}\nabla\left(\varepsilon^{-1}C_2\right)\right) = \chi_2 R(\mathbf{C}), \quad \text{in } \Omega\times]0, T_f[\\ \dfrac{\partial C_3}{\partial t} + \operatorname{div}\left(\varepsilon^{-1}uC_3\right) - \operatorname{div}\left(D_{m,3}\varepsilon^{1+\eta}\nabla\left(\varepsilon^{-1}C_3\right)\right) = -\chi_3 R(\mathbf{C}), \quad \text{in } \Omega\times]0, T_f[\\ \varepsilon = 1 - vC_1, \quad \text{in } \Omega\times]0, T_f[\\ + \text{adequate boundary and initial conditions, along with div } u = 0 \end{cases} \qquad (8)$$

which is strongly coupled, since u and $\mathbf{C}$ depend on each other by means of the micro-porosity changes ε during the chemical process. It is also possible to straightforwardly substitute C_1 with ε in this system (Equation 8). Finally, one can notice that the reactive system is valid on the whole domain Ω, whether the local state is fluid or not. In the pure fluid region, this system indeed converges toward a Stokes hydrodynamic model coupled with a standard transport-diffusion equation. Mathematical modeling of reactive hydrodynamics at the pore-scale can be expressed under the general form of the PDE system (Equation 8) coupling DBS with transport-diffusion-reaction equations. It is noticeable that the micro-porosity ε remains in the range $[\varepsilon_0, 1]$ which provides a well-posed Darcy-Brinkman-Stokes equation for the flow due to the expressions of Kozeny-Carman term and reaction formula.

This can be extended naturally to systems of reactions involving as many aqueous species in the liquid phase as needed, and involving potentially several solids: in this case the porosity is a linear combination of solid species. Most of the configurations studied in this article involve solid calcite—or calcium carbonate—whose concentration is denoted $C_{\mathrm{CaCO}_{3(s)}}$ or $[\mathrm{CaCO}_3]$, and whose molar volume is given by $v = 36.93 \times 10^{-3}$ L.mol^{-1}.

2.3 A velocity-vorticity formulation

Two distinct approaches are successfully used in the literature to solve numerically the DBS Equation 3, namely, the velocity-pressure or velocity-vorticity formulations (Hume and Poncet, 2021; Lamichhane, 2013; Molins et al., 2021; Angot, 2018). The latter, inherited from vortex methods (Chatelain et al., 2008; Cottet et al.,

2000; El Ossmani and Poncet, 2010; Hejlesen et al., 2015) introduces the vorticity field ω which is intrinsically related to the fluid velocity u through the relation:

$$\omega = \nabla \times u.$$

Several advantages arise when considering the velocity-vorticity formulation that regards the PDE unknowns (u, ω) and can be interpreted as describing the local spinning motions generated by the flow constraints. First of all, one can benefit from the velocity projection on divergence-free fields, and thereby analytically ensures the incompressibility condition div $u = 0$. Secondly, this formalism can be effectively coupled with splitting strategies that sequentially separate the resolution of distinct physical phenomena, such as convection and diffusion. Finally, this also makes it possible to eliminate the pressure unknown from the momentum equation by applying the curl operator on the DBS equation, which reads as follows:

$$-\mu\Delta\omega + \mu\kappa_b^{-1}\nabla\times\left(\frac{(1-\varepsilon)^2}{\varepsilon^2}u\right) = \nabla\varepsilon\times(f-\nabla p) \tag{9}$$

given the assumption $\nabla \times f = 0$. Developing the curl of the Kozeny-Carman term, one gets the following expression:

$$\nabla\times\left(\frac{(1-\varepsilon)^2}{\varepsilon^2}u\right) = \frac{(1-\varepsilon)^2}{\varepsilon^2}\omega + 2(\varepsilon-1)\varepsilon^{-3}\nabla\varepsilon\times u$$

which, in practice, exhibits terms that become dominant compared to $\nabla\varepsilon\times(f-\nabla p)$. Consequently, the right-hand side in the vorticity formulation of the DBS Equation 9 is usually neglected (Etancelin et al., 2020; Molins et al., 2021).

Equation 9 is then supplemented with an equation that retrieves the velocity field from the related vorticity, and results in the relation:

$$-\Delta u = \nabla\times\omega \tag{10}$$

Based on the incompressibility condition. In practice, the previous Poisson Equation 10 is not straightforwardly considered, and one relies on an alternative using a stream function $\psi : \Omega \subset \mathbb{R}^3 \to \mathbb{R}^3$ (a vector potential) solution of:

$$\begin{cases} -\Delta\psi = \omega, \quad \text{in} \quad \Omega \\ +\text{boundary conditions such that div } \psi = 0 \text{ on } \partial\Omega. \end{cases}$$

The condition div $\psi = 0$ on $\partial\Omega$ is essential to ensure the overall incompressibility condition of the stream function on Ω and thereby identify $u = \nabla \times \psi$. This requires satisfying appropriate boundary conditions, namely, the following combination of homogeneous Dirichlet/Neumann conditions for a computational cubic domain $\Omega =]x_{\min}, x_{\max}[\times]y_{\min}, y_{\max}[\times]z_{\min}, z_{\max}[$:

$$\begin{cases} x = x_{\min} \text{ or } x = x_{\max} : \psi_y = \psi_z = \dfrac{\partial\psi_x}{\partial n} = 0, \\ y = y_{\min} \text{ or } y = y_{\max} : \psi_x = \psi_z = \dfrac{\partial\psi_y}{\partial n} = 0, \\ z = z_{\min} \text{ or } z = z_{\max} : \psi_x = \psi_y = \dfrac{\partial\psi_z}{\partial n} = 0. \end{cases}$$

Such boundary conditions ensure $(\nabla \times \psi) \cdot n = 0$, div $\psi = 0$ and $\psi \times n = 0$ at the same time, where n is the normal field at the interface, and consequently lead to a zero average velocity field lifted by a prescribed flow rate $\overline{u}$ oriented in the flow direction. Indeed, given $u = \overline{u} + \nabla \times \psi$, one gets:

$$< u >_\Omega = \frac{1}{|\Omega|}\int_\Omega u \ \mathrm{d}v = \overline{u} + \frac{1}{|\Omega|}\int_{\partial\Omega}\psi\times n \ \mathrm{d}s = \overline{u},$$

which replaces the setting of the driving force f by a prescribed flow rate, managed through the lifted vector $\overline{u}$.

Finally, using the stream function ψ analytically ensures the divergence-free condition on the velocity as div $u =$ div $(\nabla \times \psi) = 0$. Overall, the velocity-vorticity formulation (13) of the DBS equation is subsequently coupled with the transport-reaction-diffusion PDE system developed in Section 2.2 to model reactive hydrodynamics at the pore-scale.

3 Method: hybrid grid-particle scheme (semi-Lagrangian)

The present work relies on a semi-Lagrangian numerical method, mixing Eulerian and Lagrangian formalism, to tackle dynamically evolving porous media due to reactive micrometric processes. Such a semi-Lagrangian approach has been successfully used for simulations of calcite dissolution at the pore scale in Etancelin et al. (2020) and extensively benchmarked against state-of-the-art numerical alternatives in Molins et al. (2021).

A Lagrangian formalism consists of describing the flow motion through the observation along time of a large number of fluid particles, with their attached intrinsic properties and spatially varying positions (Cottet and Koumoutsakos, 2000). Each particle is then tracked throughout the evolving mechanism (transport, diffusion, …) to measure variations in the main properties (velocity, concentration, …). On the contrary, from the Eulerian point of view, the previous property changes are characterized on a predetermined spatial grid along the dynamical process. This section is dedicated to presenting this hybrid formalism, which is subsequently improved to account for the heterogeneous diffusion of the chemical reactants through the porous matrix.

The particle formulation is especially well-suited for transport-dominant phenomena as it avoids the explicit discretization of convective terms and alleviates the consideration of their related stability constraints—namely, the CFL conditions which constrains the time step for a given spatial discretization. The lack of regularity in the particle distributions throughout the dynamic process is, however, a recurring problem of Lagrangian methods. Indeed, as the particle positions move according to the flow field gradients, accumulation or scarcity issues in the particle distribution commonly occur. This, thereby, requires periodic remeshing steps to avoid this problem and not to lose information: namely, one proceeds two successive interpolations from the disorganized particle structure to a regular grid and subsequently from the grid to the new particle distribution (Cottet and Poncet, 2004; Magni and Cottet, 2012).

This is particularly suitable for hybrid approaches, wherein dedicated solvers can be straightforwardly implemented in the Eulerian context before performing the remeshing step. This also allows a representation of the quantities of interest on the grid, which can be coupled with domain decomposition or mesh adaptation methods. Hybrid grid-particle formalism has,

thereby, garnered considerable interest in addressing multiple complex phenomena in Computational fluid Dynamics (CFD) and geosciences (Beaugendre et al., 2012; Chatelain et al., 2008; Chatelin and Poncet, 2013; El Ossmani and Poncet, 2010; Hume and Poncet, 2021). Besides, incorporating high-order and compact support interpolation kernels makes it possible to reduce the overall computational complexity of the remeshing steps while keeping accurate predictions of the numerical solution. The choice of the interpolation kernels is, however, important to ensure a robust numerical method and guarantee properties such as mass conservation and sign-preservation of the interpolated quantities (Magni and Cottet, 2012). Improvements of the interpolation kernels, especially for applications to dissolution processes at the pore scale, have been investigated by Etancelin et al. (2020). Such improvements focused on sign preservation and accurate high-order interpolation through a correction step of the potential over-diffusive effects resulting from the remeshing step. This provides a well-established hybrid grid-particle framework that can robustly address pore-scale reactive flows.

In the present work, we aim to benefit from the main advantages of both approaches to model reactive hydrodynamics at the pore scale. We will, thereby, use a Lagrangian description for the chemical equations—including the heterogeneous diffusion operator and reactant transport—with an underlying regular grid for solving the DBS equation in its velocity-vorticity formulation. To do so, we describe in this sections this original numerical scheme, by detailing its components and how they are linked together:

- Section 3.1 describes the Lagrangian formalism of reaction-diffusion-transport equations and its resulting dynamical system (the particle formalism): it requires a velocity field to transport particles and the computation of a heterogeneous diffusion,
- Section 3.2 shows how this velocity, solution to the Darcy-Brinkman-Stokes, can be computed by an operator-splitting strategy using the algorithm 1/Brinkman penalization 2/Diffusion using improved PSE 3/Projection on divergence-free fields,
- Section 3.3 details the computational method for the required heterogeneous diffusion (that is to say space and time variable diffusion, including the space mapping based on the porosity field), and shows how its original formalism from Degond and Mas-Gallic (1989) is improved to become intrinsically second order.

3.1 Reactive dynamical system using Lagrangian formulation

In this section, we present the Lagrangian formulation dedicated to the resolution of the reactive dynamical system (Equation 8). detailed in Section 2.2, and more specifically to the transport-reaction-diffusion Equation 5.

We define a set of N_p fluid particles covering the computational domain Ω and characterize as triplets $(C_i,\ x_i,\ v_i)_{i=1..N_p}$ of species concentrations $C_{i,k}$ ($k = 1..N_m$ indexing the N_m chemical species), positions $x_i \in \Omega$ and volumes v_i, where i refers to the particle index. This mathematically introduces the particle description, denoted C^h, of the concentration fields as follows:

$$C^h(t) = \sum_{i=1}^{N_p} C_i(t)\ \ v_i(t)\ \ \delta_{x_i}(t) \tag{11}$$

which only depends on time t, and where δ refers to the Dirac function. The Lagrangian formulation of Equation 5 can then be written using the particle description Equation 11:

$$\begin{cases} \dfrac{\mathrm{d}C_{i,k}}{\mathrm{d}t} = R_k(\mathbf{C}_i(t)) + \left[\mathrm{div}\left(\alpha_k(\varepsilon)\nabla^\varepsilon C_k\right)\right]_{x_i(t)} & \forall k = 1..N_m \\ \dfrac{\mathrm{d}x_i}{\mathrm{d}t} = \left[\varepsilon^{-1}u\right]_{x_i(t)} \\ \dfrac{\mathrm{d}v_i}{\mathrm{d}t} = 0 \end{cases}$$

given the incompressibility condition div $u = 0$ and the notations introduced in Section 2.2. This results in a dynamical system over the particles whose positions are controlled by the field $\varepsilon^{-1}u$, and volumes remain constant under divergence-free conditions. The main advantage of such a Lagrangian formulation (20) is that the transport term $\mathrm{div}(\varepsilon^{-1}uC_k)$ vanishes along with its stability condition and, thereby, the method presents the ability to use arbitrary large time steps. This is, especially, of great interest when the Courant–Friedrichs–Lewy (CFL) condition on the transport term induces a stronger constraint on the time step compared to the diffusion stability condition.

The velocity field u in (20) arises from the solution of the DBS equation which is solved on an underlying Cartesian grid and coupled with the Lagrangian formulation of the chemical PDE system. Regarding such a strong coupling between these equations, one needs to interpolate on the grid the particle description of the solid chemical species—namely, $C^h_{\mathrm{CaCO_{3(s)}}}$ — which is related to the micro-porosity field ε and consequently involved in the DBS model. Similarly, the velocity field subsequently needs to be interpolated on the particles to solve the Lagrangian set of chemical equations. This requires a convolution with high-order remeshing kernels with compact supports (Etancelin et al., 2020; Magni and Cottet, 2012). The dynamical system (20) is finally integrated using standard numerical methods for Ordinary Differential Equations (ODE), such as explicit Runge-Kutta, while the diffusion term $\mathrm{div}(\alpha_k(\varepsilon)\nabla^\varepsilon C_k)$ is approximated through the Particle-Strength- Exchange (PSE) method, described in Section 3.3 and detailed in Supplementary Appendix.

In the present work, we incorporate in the semi-Lagrangian workflow the consideration of robustly estimating Archie's law term through such a particle-based PSE method. Thanks to this method, we make it possible to fully address the superficial gradient ∇^ε approximation with heterogeneous diffusion throughout the porous matrix.

3.2 Splitting operator strategy

The semi-Lagrangian formalism introduced in the previous Section 3.1 intrinsically relies on splitting strategies. Time-splitting methods, also known as fractional time-step algorithms, arise in many fields of computational science related to physics-based models and have been developed by Chorin (1973) in the context of vortex methods for the Navier-Stokes equation. Such methods

have been widely investigated afterward to separate the resolution of distinct physical phenomena and render more efficient algorithms (Beale and Majda, 1981; Hume and Poncet, 2021; Faragó, 2008). Indeed, one of the main advantages of splitting strategies is one can use different approaches for the distinct parts of the overall model, namely, either a Lagrangian or Eulerian formulation. This also straightforwardly extends to the choice of the numerical solver available for each component, allowing the use of the most efficient, accurate, and robust schemes independently.

The first natural splitting arising in workflow, thereby, lies in the semi-Lagrangian formalism itself, wherein we do not consider solving the overall Partial Differential Equation (PDE) system at once. We rather separate the transport-diffusion-reaction dynamics in its Lagrangian formulation from the pore-scale hydrodynamic resolved on the underlying Cartesian grid. The hydrodynamic part, composed of the DBS equation in the velocity-vorticity formulation, is also solved through a time-splitting method. Indeed, we approximate the solution of Equation 9 by the limit in time of the evolution equation

$$\frac{\partial \omega}{\partial t} - \mu\Delta\omega \; + \; \mu\kappa_b^{-1}\nabla\times\left(\frac{(1-\varepsilon)^2}{\varepsilon^2}u\right) = 0,$$

together with $\omega = \nabla \times u$, using a three-step operator splitting strategy coupled with a fixed-point algorithm. This means that considering a sequence (u_m, ω_m) of velocity-vorticity we aim to successively perform, over a time interval $[t_m, t_{m+1}]$ with $t_m = m\delta t$, Brinkman penalization, diffusion, and projection on divergence-free fields. The latter is achieved through the reconstruction of the velocity field u based on the stream function ψ (see Section 2.3). In practice, these three steps are specifically defined as:

- The Brinkman iteration given by the ordinary differential equation $\frac{\partial u}{\partial t} + \mu\lambda(\varepsilon)(u+\overline{u}) = 0$ with prescribed flow rate $\overline{u}$ and $\lambda(\varepsilon) \coloneqq \kappa_b^{-1}(1-\varepsilon)^2\varepsilon^{-2}$, whose exact solution after a δt is generated by

$$\Lambda(u) \coloneqq e^{-\mu\lambda(\varepsilon)\delta t}\left(u+\overline{u}\right) - \overline{u}$$

- The vorticity diffusion iteration, $\frac{\partial \omega}{\partial t} - \mu\Delta\omega = 0$, solved using an implicit Euler scheme given by the operator

$$\mathcal{D}_\omega(u) \coloneqq \left[I - \mu\delta t\Delta\right]^{-1}(\nabla\times u)$$

- The projection step $\Pi(\zeta) = \nabla\times\left((-\Delta^{-1})\zeta\right)$ which takes as ζ the right-hand side of the Poisson equation $-\Delta\psi = \zeta$ satisfying the boundary conditions (17), and followed by $u = \nabla\times\psi$.

Overall, this leads to the full iteration of the Brinkman-Diffusion-Projection splitting $\Pi\circ\mathcal{D}_\omega\circ\Lambda$ over a time step $[t_m, t_{m+1}]$, which reads as follows:

$$u_{m+1} = \Pi\circ\mathcal{D}_\omega\circ\Lambda\left(u_m\right)$$

and whose consistency has been theoretically discussed in Hume and Poncet (2021). One should notice that this projection step is not a projection by pressure gradient correction as in Chatelin and Poncet (2013), but an operator that takes the vorticity field ω and retrieves a divergence-free velocity field whose mean velocity is zero. The final velocity field is subsequently given by

$$u = \overline{u} + \lim_{m\to\infty} u_m$$

whose average is $\overline{u}$ and satisfies the Kozeny-Carman relation inside the solid region.

From a numerical perspective, we consider the exact treatment of the Brinkman term, a fourth-order finite difference scheme for the discrete curl operator, and FFT solvers for the vorticity diffusion and stream function recovery. Using FFT avoids matrix assembly procedure and, therefore, consists of efficient solvers in terms of computational time and memory storage requirements. Besides, the complexity of such algorithm scales as $\mathcal{O}(N_p\log(N_p))$, where N_p is recalled to refer to the number of particles. Finally, a stopping criterion on this fixed point algorithm is also defined based on the relative residual norm on the velocity, which manages the convergence of the pore-scale hydrodynamics toward a stationary state.

The updated velocity u_{m+1} is subsequently interpolated from the grid to the particles and used for solving the Lagrangian reactive system, which is split into convective/remeshing and diffusive/reactive steps. Regarding the convection, the particle trajectories are pushed to the next step through a directional advection, given the field $\varepsilon^{-1}u$ according to the Lagrangian formulation (20), and are then remeshed to avoid stagnation issues. The purpose of such a directional splitting is to reduce the dimensionality of the overall advection problem by considering several one-dimensional equations, and is developed in Cottet et al. (2014); Magni and Cottet (2012). The particle remeshing is also addressed using directional treatment of the multidimensional convolution. This means that within a time step $[t_m, t_{m+1}]$, the joint step of advection/remeshing of the particles is successively performed by alternating the spatial directions (Etancelin, 2014; Keck, 2019). This presents the advantage of significantly improving the computational efficiency of the method and allows the use of high-order remeshing kernels with large stencils while maintaining a minimal cost compared to multidimensional cases. This is also well-suited to parallel implementation on GPU architecture. The dimensional splitting is addressed, in practice, by a second-order Strang formula (Strang, 1968) and coupled with a second-order Runge-Kutta for time integration. The diffusion/reaction step is finally solved by means of a second-order explicit Runge-Kutta scheme along with PSE approximation of the heterogeneous diffusion operator. Once the Lagrangian formulation of the chemistry has been fully updated and remeshed on the underlying grid, one starts pushing the DBS hydrodynamics to the next sequential step of these temporal iterations.

Such an operator splitting strategy, in the context of a semi-Lagrangian approach, has been applied to the modeling of dissolution processes on a 2D synthetic calcite core and validated against state-of-the-art alternatives and experiments in Molins et al. (2021). This has also been used in Etancelin et al. (2020) on real porous media structures at the pore scale to investigate the dissolution of 3D carbonate rocks arising from μCT scans. Nonetheless, these previous works assumed that the superficial gradient ∇^ε involved in the heterogeneous diffusion could be approximated by the gradient operator, and subsequently

addressed this Archie's law term with standard finite differences schemes. In Section 3.3, we intend to alleviate this assumption and, therefore, improve the semi-Lagrangian method by incorporating in the workflow a PSE approximation of the heterogeneous diffusion.

3.3 Particle-strength-exchange method and Archie's law approximation

The PSE method consists in the approximation of a diffusion operator $\mathrm{div}(\mathbf{L}\nabla f)(x)$ with $x \in \Omega \subset \mathbb{R}^d$ and $\mathbf{L}$ a positive symmetric matrix, accounting for heterogeneous diffusion for instance. The main idea is then to approximate the diffusion by an integral operator, more suitable for particle methods:

$$Q^\xi \cdot f(x) = \int_\Omega \sigma^\xi(x,y)\,(f(y)-f(x))\,dy$$

where the kernel σ^ξ is supposed to be symmetric and satisfies some moment conditions, described thereafter and detailed in Supplementary Appendix. In the Lagrangian formulation, a particle approximation of the function f, denoted f^h, is also introduced based on the particle triplet $(f_i,\ x_i,\ v_i)$, such that:

$$f^h = \sum_{i=1}^{N_p} f_i\ v_i\ \delta_{x_i} \quad \text{where} \quad f_i = f(x_i)$$

where x_i and v_i are respectively the particle positions and volumes, while δ_{x_i} refers to the Dirac measure at position x_i. With such a N_p-particle representation of the function f, a discrete version of the operator Q^ξ is obtained by using the particles as quadrature points where h refers to the characteristic distance between particles. This results in the following quadrature expression, called Particle-Strength-Exchanges:

$$Q^\xi \cdot f^h(x_k) = \sum_{x_l \in \mathcal{S}(x_k)} \sigma^\xi(x_k,x_l)\,(f_l - f_k)\ v_l.$$

where $\mathcal{S}(x_k) \coloneqq \mathrm{Supp}\left(\sigma^\xi(x_k,\cdot)\right)$ refers to the set of points in the support of the kernel function σ^ξ.

In Supplementary Appendix, we detail that we can explicitly compute two constants γ_1 and γ_2 based on a given scale ξ and a given function Θ (named stencil generator) such as

$$\sigma^\xi(x,y) = \frac{1}{\xi^{d+4}}\Theta\left(\frac{y-x}{\xi}\right)\frac{\mathbf{m}(x)+\mathbf{m}(y)}{2} : (x-y)^{\otimes 2}$$

with

$$\mathbf{m} = c_0\ \mathbf{L} - c_1\ \mathrm{Tr}(\mathbf{L})\,\mathbf{Id_3} + \mathbf{H}$$

$$c_0 = \frac{2(\gamma_1+2\gamma_2)}{\gamma_1^2+\gamma_1\gamma_2-2\gamma_2^2},\ c_1 = \frac{2\gamma_2}{\gamma_1^2+\gamma_1\gamma_2-2\gamma_2^2},$$
$$H_{ij} = \left(\frac{\gamma_1^2-\gamma_1\gamma_2-6\gamma_2^2}{\gamma_2(\gamma_1^2+\gamma_1\gamma_2+2\gamma_2^2)}\right)(1-\delta_{ij})L_{ij}$$

In Supplementary Appendix, we detail that we can explicitly compute two constants γ_1 and γ_2 based on a given scale ξ and a given function Θ (named stencil generator) such as

$$\sigma^\xi(x,y) = \frac{1}{\xi^{d+4}}\Theta\left(\frac{y-x}{\xi}\right)\frac{\mathbf{m}(x)+\mathbf{m}(y)}{2} : (x-y)^{\otimes 2}$$

with

$$\mathbf{m} = c_0\ \mathbf{L} - c_1\ \mathrm{Tr}(\mathbf{L})\,\mathbf{Id_3} + \mathbf{H}$$

and

$$c_0 = \frac{2(\gamma_1+2\gamma_2)}{\gamma_1^2+\gamma_1\gamma_2-2\gamma_2^2},\ c_1 = \frac{2\gamma_2}{\gamma_1^2+\gamma_1\gamma_2-2\gamma_2^2},\ \text{and}$$
$$H_{ij} = \left(\frac{\gamma_1^2-\gamma_1\gamma_2-6\gamma_2^2}{\gamma_2(\gamma_1^2+\gamma_1\gamma_2+2\gamma_2^2)}\right)(1-\delta_{ij})L_{ij}$$

where δ_{ij} is the Kronecker symbol, γ_1, and γ_2 are the coefficients based on the fourth moments of Θ defined in 3D by

$$\gamma_1 = \sum_{x\in\mathbb{J}} x_k^4\Theta(x)\,h^3, \quad k \in [1,3]$$
$$\gamma_2 = \sum_{x\in\mathbb{J}} x_k^2x_l^2\Theta(x)\,h^3, \quad k \neq l \in [1,3]$$

for $\mathbb{J} \subset h\mathbb{Z}^3$ a three-dimensional lattice, including at least one neighborhood of the current mesh point. The convergence of the original PSE method introduced in Degond and Mas-Gallic (1989) depends on the scale ξ as $\mathcal{O}[(h/\xi)^2]$, which becomes $\mathcal{O}(1)$ when ξ is adapted linearly to h. The present discrete corrected version developed in Poncet (2006) and Schrader et al. (2010) is intrinsically second order convergence $\mathcal{O}(h^2)$ and is detailed in Supplementary Appendix.

This computational method of diffusion is used to compute the Archie's law, involving a tortuosity index η in the heterogeneous diffusion operator

$$\mathcal{D}(\varepsilon, C) \coloneqq \mathrm{div}\left(\varepsilon^{1+\eta}\nabla\left(\varepsilon^{-1}C\right)\right)$$

Involved in the PDE system (11). In this case, one gets a particular expression for the diffusion matrix $\mathbf{L} = \varepsilon^{1+\eta}\ \mathbf{I}_3$ with $\mathbf{I}_3$ the identity matrix in $\mathbb{R}^3$. This finally leads to the following discretized Archie's law diffusion operator (30) using the renormalized PSE scheme:

$$Q^\xi \cdot f^h(x_k) = \frac{1}{\xi^7}\sum_{l\sim k}(f_l-f_k)\,\Theta\left(\frac{x_l-x_k}{\xi}\right)\frac{(c_0-3c_1)}{2} \times\left(\varepsilon^{1+\eta}(x_k)+\varepsilon^{1+\eta}(x_l)\right)|x_l-x_k|^2 v_l \tag{12}$$

where $|.|$ is the Euclidean norm in $\mathbb{R}^3$ and $f_\bullet \coloneqq \varepsilon^{-1}(x_\bullet)C(x_\bullet)$. The overall Formula 12 accounts for the heterogeneous diffusion and ensures the accurate management of the chemical reactant penetration, given by its concentration field C, within the porous matrix. Indeed, one of the main advantages of the PSE scheme is that it includes all the lattice neighborhoods in the computation of the heterogenous diffusion, unlike crossed finite differences scheme. Finally, this guarantees the strict conservation of the reactant exchanges between the fluid portion and the porous matrix, and is numerically validated at the second order in Section 4 of Supplementary Appendix.

4 Application to precipitation and crystallization

CO_2 mineral storage in natural underground reservoirs, such as saline aquifers, involves competing geochemical phenomena

occurring at a large variety of scales. Among them, mineral dissolution and precipitation play crucial roles. On one side, studying the dissolution of native carbonate species, already present in the aquifers, provides insight into potential leakage issues and queries the reservoir safety. On the other side, CO_2 trapping under the form of carbonate precipitates and crystals informs on the storage capacities of the reservoir. These geochemical processes also induce changes in the macro-scale properties of the subsurface material, including permeability and porosity evolutions, that need to be investigated to ensure sustainable management of the reservoir structures.

In this section, we develop mathematical models for calcite precipitation and crystallization at the pore scale, with special considerations on the reaction rate expressions arising in the PDE system (11). Numerical simulations are performed within the HySoP platform (Etancelin et al., 2022) along with PSE treatment of the heterogeneous diffusion on accelerated GPU devices and address porous sample arising from X-ray μCT observations. This enables the investigations of macro-scale property changes along the CO_2 mineral trapping on real 3D rock geometries, which is an important component in the overall study of CO_2 storage.

4.1 The transition state theory: from dissolution to precipitation modeling

Dissolution of the injected CO_2 in the aqueous phase of deep underground reservoirs will affect the pH of the formation water through the following series of chemical reactions:

$$CO_{2\,(g)} \rightleftharpoons CO_{2\,(aq)} \tag{13a}$$

$$H_2O + CO_{2}\,(aq) \rightleftharpoons H_2CO_3 \tag{13b}$$

$$H_2CO_3 \rightleftharpoons H^+ + HCO_3^- \tag{13c}$$

$$HCO_3^- - \rightleftharpoons H^+ + CO_3^{2-}. \tag{13d}$$

Indeed, once the CO_2 has dissolved into water and established a first equilibrium under the form of the weak acid H_2CO_3, the H_2CO_3 species dissociates successively to bicarbonate HCO_3^- and carbonate CO_3^{2-} ions as the pH increases. These chemical reactions are pH-dependent, and the distribution evolutions of all these carbonate species are displayed in Figure 2 against the pH of the solution. In alkaline media, the chemical reactions (Equation 13c) and (Equation 13d) can, therefore, join together to read as follows:

$$H_2CO_3 + 2OH^- \rightleftharpoons CO_3^{2-} + 2H_2O$$

such that carbonate ions are the main carbonate species present in the solution. Such transformations in the ionic species composition of the aquifer water will considerably impact the original mineral structure through chemical rock-water interactions such as carbonate dissolution and precipitation.

Historically, the dissolution and precipitation kinetics of calcite in the context of CO_2 injection have been studied since the 1970s, both from the experimental and theoretical sides.

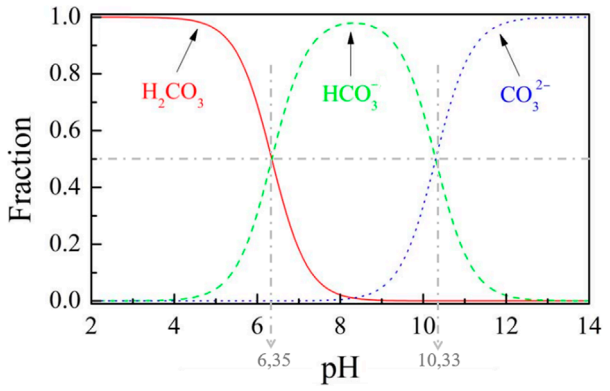

FIGURE 2
Distribution diagram of aqueous carbonate species against pH solution from Bohn et al. (1980) and Turk et al. (2015). Species distributions are represented as a fraction of total dissolved carbonate. The grey dotted lines highlight the transition pH of the chemical equilibria from (Equation 13).

Plummer et al. (1978) investigated the influence of several parameters on the forward reaction rates of calcite dissolution under far-from-equilibrium conditions. Among these parameters, one finds the partial pressure of CO_2 denoted P_{CO_2}, the hydrogen ions activities denoted a_{H^+} — directly related to the pH — and the temperature. Their experimental work was subsequently extended by Chou et al. (1989) using a fluidized bed reactor to compare the dissolution kinetics mechanisms between various carbonate minerals—involving *inter alia* calcite, aragonite, and dolomite—at 25°C. One should notice that these experiments were conducted under laboratory conditions in terms of pressures and temperatures, in opposition to the current abilities of *in situ* experiments to manage realistic reservoir conditions (Andrew et al., 2013; Wigand et al., 2008). Nonetheless, these experimental studies have highlighted three kinetic mechanisms occurring simultaneously in the process of calcite dissolution due to CO_2 injection. Such mechanisms are given by the following chemical reactions:

$$CaCO_{3(s)} + H^+ \overset{K_1}{\rightleftharpoons} Ca^{2+} + HCO_3^- \tag{14a}$$

$$CaCO_{3(s)} + H_2CO_3 \overset{K_2}{\rightleftharpoons} Ca^{2+} + 2HCO_3^- \tag{14b}$$

$$CaCO_{3(s)} \underset{K_{-3}}{\overset{K_3}{\rightleftharpoons}} Ca^{2+} + CO_3^{2-} \tag{14c}$$

where the notations K_i, $i = 1\ldots3$ refer to forward reaction rate constants, depending on the temperature (Busenberg and Plummer, 1986; Plummer et al., 1978; Plummer and Busenberg, 1982), and K_{-3} is the backward reaction rate corresponding to the reverse calcite precipitation process in Equation 14c. They experimentally identified both the forward and backward reaction rates and established the validity of kinetic models for carbonate dissolution and precipitation in comparison to thermodynamics theoretical considerations. In the present study, we assume the production of pure calcite without any of its polymorphs like aragonite or vaterite.

Meanwhile, mineral reaction rates were, indeed, theoretically investigated by Lasaga (1981) using the Transition State Theory

(TST), originally formulated by Eyring (1935). Since then, this formalism has successfully been extended (Aagaard and Helgeson, 1982; Lasaga, 1984; Steefel and Lasaga, 1994) and widely accepted in current kinetic geochemical models (Etancelin et al., 2020; Molins et al., 2012; Steefel et al., 2015). In this context, the reaction rates are commonly expressed as the product of far-from-equilibrium terms, involving the activities of the chemical species in solution, with an affinity term written as a function of the Gibbs free energy change ΔG for close to the equilibrium conditions. Considering the chemical model of calcite dissolution (34) suggested by Plummer et al. (1978) and Chou et al. (1989) and the vector of concentrations $\mathbf{C}$, the reaction rate arising from TST writes:

$$R(\mathbf{C}) = A_s\left(K_1 a_{H^+} + K_2 a_{H_2CO_3} + K_3\right)\left(\frac{a_{Ca^{2+}}\ a_{CO_3^{2-}}}{K_{eq}} - 1\right) \tag{15}$$

where K_{eq} is the equilibrium constant of the reaction, also called the solubility product, A_s is the reactive surface area of the mineral—in m^{-1}. The notations $a_\bullet = \gamma_\bullet C_\bullet$ refer to the dimensionless species activities with $\gamma_\bullet$ and $C_\bullet$, respectively, their activity coefficients and molar concentrations—whose unit is $mol.m^{-3}$. It follows that the micro-porosity changes reads as:

$$\frac{\partial \varepsilon}{\partial t} = -\upsilon R(\mathbf{C}),$$

given Equation 6 from Section 2.2 and the relation $C_{CaCO_{3(s)}} = (1-\varepsilon)/\upsilon$. Denoting by $Q = a_{Ca^{2+}}\ \ a_{CO_3^{2-}}$ the ion activity product, one obtains the following relation between Q and the Gibbs energy change (Aagaard and Helgeson, 1982; Lasaga, 1984):

$$\Delta G = RT \ln\left(\frac{Q}{K_{eq}}\right)$$

with T the temperature in Kelvin K, and R the universal gas constant in $J.mol^{-1}.K^{-1}$. The sign of the reaction term $R(\mathbf{C})$ in (Equation 15) is driven by the sign of $\ln\left(Q/K_{eq}\right)$ that is negative for dissolution and positive for precipitation, which is consistent with the convention from Section 2.2.

From now on, we focus on the concern of calcite precipitation and crystallization resulting from CO_2 injection based on the series of homogeneous reactions (Equation 13) along with the mineral-solute interaction given by Equation 14c. In practice, we enforce a pH greater than 10.33 such that the carbonate ions CO_3^{2-} are the predominant species (see Figure 2). This enables the restriction of the overall set of chemical reactions (Equation 13) to merely consider the Equation 14c in the sense that we assume the intermediate reactions as instantaneous and conservative—without loss of quantity of matter. Such an assumption is acceptable, in practice, since fluid-mineral reaction rates are usually slower than intra-aqueous reaction rates. Therefore, the initial concentration of carbonate ions, denoted $C_{CO_3^{2-}}(x, t=0)$ for $(x,t) \in \Omega \times [0, T_f]$ following the notations introduced in Section 2, is directly related to the partial pressure of injected CO_2 by means of the Henry law. The latter states, at a constant temperature, the relation between the amount of dissolved gas in a solute and its partial pressure based on Henry's law constant denoted K_H, which depends on the gas and temperature, such that for the CO_2 at 25°C one gets:

$$C_{CO2(aq)} = \frac{P_{CO_2}}{K_H} \simeq C_{CO_3^{2-}}(x, t=0) \tag{16}$$

where $K_H = 29.41$ $L.atm.mol^{-1}$. Considering such an alkaline medium—with pH > 10.33 — also results in the treatment of the chemical reaction (Equation 14c) as completely irreversible which corresponds to far-from-equilibrium conditions modelling the calcite precipitation chemical reaction:

$$Ca^{2+} + CO_3^{2-} \xrightarrow{K_{-3}} CaCO_{3(p)} \tag{17}$$

where the subscript p here refers to the precipitate form of the calcite product. In this case, the rate constants $K_1 = K_2 = 0$ in (35) and the affinity term dependent on the Gibbs energy satisfies the condition $\ln\left(Q/K_{eq}\right) \gg 0$ — corresponding to a supersaturated solution—so that we obtain an overall reaction rate for the calcite precipitation which reads as:

$$R_{prec}(\mathbf{C}) = K_{-3}\ A_s\ a_{Ca^{2+}}\ a_{CO_3^{2-}} \tag{18}$$

where $K_{-3} = K_3/K_{eq}$, which theoretically results from the TST law in Equation 15 and has been experimentally validated, *inter alia*, by Chou et al. (1989).

Therefore, in the following, we rely on the kinetic formulation of the mineral precipitation given by Equation 18, considering the rate laws determined by laboratory experiments (Chou et al., 1989) and normalized by the reactive surface area of the mineral A_s (Plummer et al., 1978). As the geometry evolves, the micro-porosity ε and the reactive specific area A_s, associated with the porous structure, also change. These evolutions are taken into account in the reaction rates management and the hydrodynamic modeling of the reactive process (see the overall PDE system (Equation 8) in Section 2.2). The calcite precipitation reaction is subsequently supplemented with a crystallization model which is elaborated in the next Section 4.2.

4.2 Crystal growth modeling: a two-step process

Crystal growth kinetics involves complex mechanisms occurring simultaneously and depending, *inter alia*, on the concentration of the constituent ions in the solute, but also on attachment frequencies of the ions or precipitates to lattice growth sites (Nielsen and Toft, 1984; Wolthers et al., 2012). Indeed, the growth rate is first controlled by advection and diffusion of the Ca^{2+} and CO_3^{2-} ions to the crystal surface coupled with a surface adsorption process that largely hinges on the crystal lattice shape. For instance, the growth of crystal aggregates is more likely to occur near kinks or corners (Nielsen and Toft, 1984; Yoreo and Vekilov, 2003). Mineral heterogeneity of the pore interface is also an important factor that influences the crystal growth location and morphology, providing preferential sites (Lioliou et al., 2007). This first process is commonly called primary heterogeneous nucleation, for which the crystallization reaction is catalyzed by the solid surface of the porous medium. In the absence of solid interface, crystal clusters can also form spontaneously in the solute, which is known as primary homogeneous nucleation and is closely related to the supersaturation state of the solution in order to initiate the nucleation—namely, satisfying the condition $\ln\left(Q/K_{eq}\right) \gg 0$. Finally, secondary nucleation occurs in the presence of existing crystals and is more likely to generate large crystal aggregates at

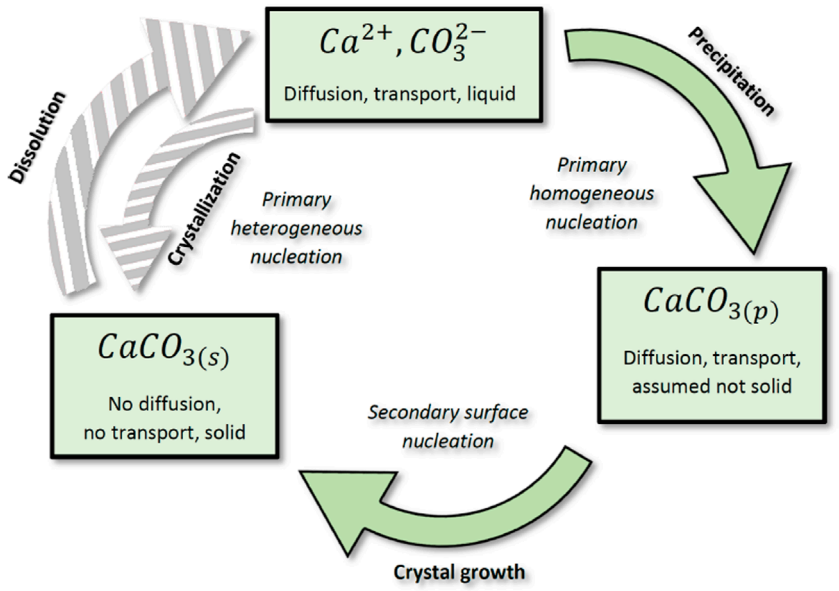

FIGURE 3
Overall reactive diagram of the reversible chemical Equation 14c and two-step calcite crystallization process. This diagram represents the chemical interactions between the different ionic species (Ca^{2+} and CO_3^{2-}), the calcium carbonate precipitate $CaCO_{3(p)}$ and mineral crystal $CaCO_{3(s)}$ and accounts for both dissolution, precipitation crystal growth processes. In the numerical applications (see Section 5), we mainly address the green part of this diagram that highlights the two-step modeling of the calcite crystallization process.

the mineral surface. Overall, calcite crystallization results from a combination of all these previous phenomena.

In this section, we consider a two-step crystallization process wherein calcite precipitates, also referred to as nuclei and denoted $CaCO_{3(p)}$, are first generated within the solute during the so-called nucleation stage according to the chemical Equation 17. These precipitates are subsequently aggregated at the mineral surface through adsorption phenomena during the crystal growth step. This sequential crystallization process is described in Figure 3, where the notation $CaCO_{3(s)}$ stands for the calcite crystal. In the applications developed in Section 5, we consider that the solid matrix of the 3D porous sample has a similar carbonate nature to the calcite crystal generated, though rock mineral heterogeneities can be integrated into the numerical framework as prospects. From now on, we refer to precipitation as the primary homogeneous nucleation and we investigate the surface attachment of the calcite precipitate, $CaCO_{3(p)}$, based on an autocatalytic process to model calcite crystal growth, referred to as the secondary surface nucleation in Figure 3. In the reaction scheme from Figure 3, we account for the precipitate diffusion and advection until the solid boundary where it leads to crystal growth through adsorption phenomena. Besides, we neglect the direct crystallization process induced by the solute diffusion to the solid matrix and the so-called primary heterogeneous nucleation.

In the literature, two distinct approaches are mainly developed when considering precipitation and crystal growth modeling altogether. The former can be regarded as "deterministic models" relying on the TST modeling developed in Section 4.1. Noiriel et al., for instance, investigated the effects of pore-scale precipitation on permeability through a combination of X-ray μCT experiments and "deterministic" modeling (Noiriel et al., 2021). They also derived crystal growth rates directly from the μCT through an imaging comparison between the beginning and end of the precipitation experiment. In this case, only two μCT scans were performed, and therefore, the process should be understood as distinct from 4D μCT experiments incorporating time dynamics. Such experimental identification of crystal growth rates can, however, be prone to intrinsic imaging limitations (Perez et al., 2022) and result in wide discrepancies in the reaction rate estimations. Nonetheless, their results showed satisfactory agreement between the experiments and numerical experiments for precipitation processes into fractures (Noiriel et al., 2021). Alternative modeling approaches lie in the probabilistic nature of nucleation or crystal growth and are referred to as "probabilistic models" (Fazeli et al., 2020; Masoudi et al., 2021; Nooraiepour et al., 2021a). Wolthers et al., for instance, developed a probabilistic approach for calcite crystal growth based on the nature of the kink sites depending on their ionic affinities and attachment frequencies of the constituent ions (Wolthers et al., 2012). Estimations of such adsorption frequency ranges can also be found in the literature (Christoffersen and Christoffersen, 1990; Nielsen, 1984). Finally, while it is commonly established experimentally that crystal growth occurs preferentially at kinks and corners of the surface lattice, few models incorporate the geometrical dependency of the crystal aggregation in the reaction rates (von Wolff et al., 2021).

In the present article, we propose a new approach coupling a deterministic model for the precipitation, which directly depends on the supersaturation ratio following the TST formalism, and a probabilistic formulation of the crystal growth process. The latter accounts for the adsorption frequencies of the precipitate to the growth sites with a coefficient, quantifying the physical probability of attachment rate, denoted P_{ad}, which relies on a locally averaged

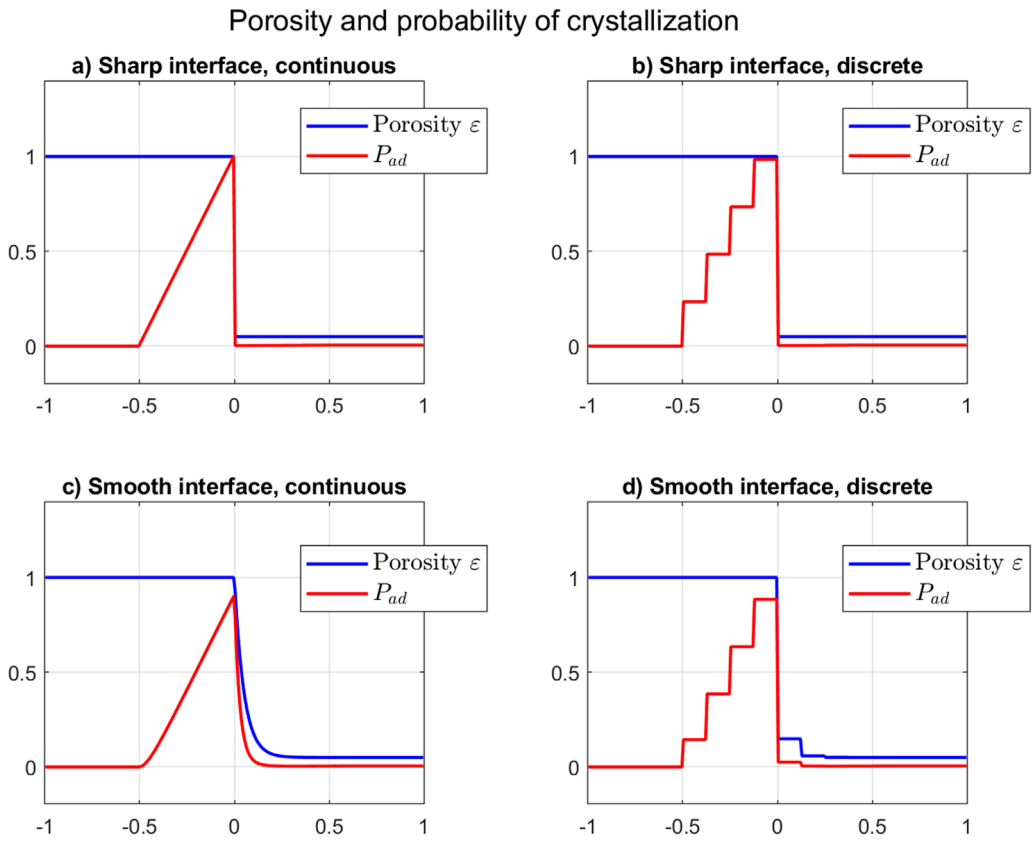

FIGURE 4
Probability of attachment rate $P_{ad} = C(1-\varepsilon^* W_h)\varepsilon^m$ for crystal growth modeling in 1D different contexts. Synthetic continuous and discrete (at the voxel size) representation of a 1D porous medium, with a residual micro-porosity in the porous matrix $\varepsilon_0 = 5\%$ for $x > 0$, for sharp and smooth interface. The probability values are computed based on Equation 20. **(A)** Sharp interface, continuous. **(B)** Sharp interface, discrete. **(C)** Smooth interface, continuous. **(D)** Smooth interface, discrete.

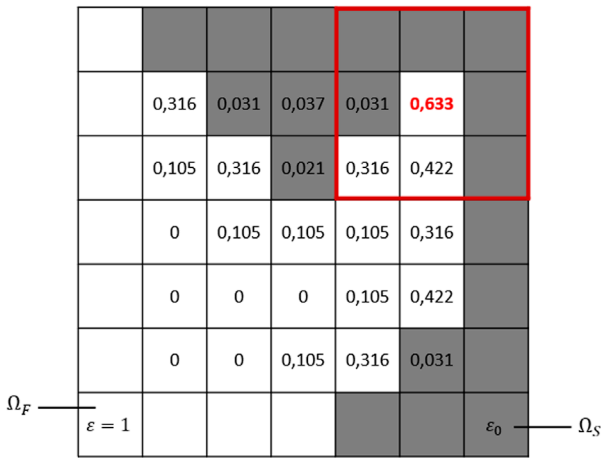

FIGURE 5
Impact of the probability of attachment rate P_{ad} for crystal growth modeling. Synthetic representation of a discrete (at the voxel size) porous medium with smooth interface (t be compared with Figure 4), with a rock matrix micro-porosity $\varepsilon_0 = 5\%$. The probability values are computed based on Equation 20 and include the one-neighborhood (*e.g.*, the red square).

mineral volume fraction. In this formalism, one obtains the crystal growth reaction rate, which is expressed as:

$$R_{\text{crys}}(\mathbf{C}) = K_c \; P_{\text{ad}} \; C_{\text{CaCO}_{3(p)}} \tag{19}$$

with K_c the adsorption frequency (expressed in s^{-1}). It possible then to include the geometrical dependency in the crystal growth reaction rate by means of involving the neighborhood of the solid using a convolution of the porosity (the size of the neighborhood is provided by the support of the convolution kernel). Practically, this leads to the relation

$$P_{\text{ad}} = C\left(1 - \varepsilon * W_h\right)\varepsilon^m, \tag{20}$$

where $W_h(x) = h^{-d} W^{\otimes d}(x/h)$ is the rescaled kernel based on a local averaging kernel W, so that $(1-\varepsilon^* W_h)\varepsilon$ is enhanced in the layer close to the fluid/solid interface and depending on the solid proportion in the neighborhood (see Figures 4, 5). The calibration of C and kernel support size h can be established by comparison with experiments (Poonoosamy et al., 2023) or numerical simulations in standardized geometry (Varzina et al., 2020; Patel et al., 2021), or estimated in the same spirit as the *crystallites* used in the LBM schemes in Masoudi et al. (2024).

In the case of K_c being a production of crystal volume per unit of volume and time, then the normalization coefficient C satisfies $1/C = \langle (1-\varepsilon^* W_h)\varepsilon^m \rangle_\Omega$ so that P_{ad} is a probability distribution, and the index m describes the ability to decrease strongly the reaction rate inside the solid in the spirit of the Archie's law (in practice $m = 2$ is suitable). In the case of K_c being the local production of crystal at the fluid/solid interface, which is the case considered in the present study, then C satisfies

$$1/C = (1-\varepsilon_0)/2$$

so that P_{ad} is a point-wise probability of capture by the crystal. This is based on the jump between ε_0 and 1 through a sharp interface, with a factor 1/2 (half the integral of the kernel W, which can be slightly adjusted for concave interface as shown in Poncet (2007)). This convolution-based formulation is appropriate for a crystallization process and is inspired by the gradient-based technique from Luo et al. (2012) and Soulaine et al. (2017) that locates the first layer on the solid side and is suitable for dissolution processes. In practice, the local averaging kernel W can be as simple as $W = 1_{[-1,1]}/2$ or Gaussian in a continuous description, or approximated by its discrete formulation $W = (\delta_{-1} + \delta_0 + \delta_1)/3$, or even with weighting in order to modulate the length of capture with respect to the grid size.

The Figure 4 shows different probability distributions in 1D with a residual micro-porosity of $\varepsilon_0 = 5\%$ (in the area $x > 0$), for sharp and smooth fluid/solid interface, and for the continuous and discrete formulations described above. The resulting probability values in 2D are represented in Figure 5 for a synthetic example with smooth interface and discrete formulation (to be compared to the 1D version of Figure 4D), where the residual micro-porosity in Ω_S is estimated to $\varepsilon_0 = 5\%$ as well.

4.3 Final system of PDEs

Finally, we define the vector of concentrations

$$\mathbf{C} = \left(C_{CaCO_{3(s)}}, C_{CaCO_{3(p)}}, \ C_{CO_3^{2-}}, \ C_{Ca^{2+}} \right)$$

and consider the reactions rates $R_{prec}(\mathbf{C})$ and $R_{crys}(\mathbf{C})$ respectively given by Formula 40, 41. Overall, the calcite crystallization modeled as a two-step process of precipitation and crystal growth, according to the reaction scheme from Figure 3, writes:

$$\begin{cases} -\mathrm{div}\left(2\mu D(u)\right) + \mu\kappa_b^{-1}\dfrac{(1-\varepsilon)^2}{\varepsilon^2}u = \varepsilon(f - \nabla p), \quad \text{in } \Omega\times]0,T_f[\\ \dfrac{\partial C_{CO_3^{2-}}}{\partial t} + \mathrm{div}\left(F\left(C_{CO_3^{2-}}\right)\right) = -R_{prec}(\mathbf{C}), \quad \text{in } \Omega\times]0,T_f[\\ \dfrac{\partial C_{Ca^{2+}}}{\partial t} + \mathrm{div}\left(F\left(C_{Ca^{2+}}\right)\right) = -R_{prec}(\mathbf{C}), \quad \text{in } \Omega\times]0,T_f[\\ \dfrac{\partial C_{CaCO_{3(p)}}}{\partial t} + \mathrm{div}\left(F\left(C_{CaCO_{3(p)}}\right)\right) = R_{prec}(\mathbf{C}) - R_{crys}(\mathbf{C}), \quad \text{in } \Omega\times]0,T_f[\\ \dfrac{\partial C_{CaCO_{3(s)}}}{\partial t} = R_{crys}(\mathbf{C}), \quad \text{in } \Omega\times]0,T_f[\\ \varepsilon = 1 - \nu C_{CaCO_{3(s)}}, \quad \text{in } \Omega\times]0,T_f[\\ F(C_\bullet) = \varepsilon^{-1}uC_\bullet - \alpha_\bullet(\varepsilon)\nabla^\varepsilon C_\bullet, \ \alpha_\bullet(\varepsilon) = \varepsilon^\eta D_{m,\bullet} \quad \text{in } \Omega\times]0,T_f[\\ + \text{adequate boundary and initial conditions, along with div } u = 0 \end{cases} \tag{21}$$

where the advective and diffusive flux $F(C_\bullet)$ is taken from expressions in Section 2.2, using the lifted gradient $\nabla^\varepsilon(\cdot) = \varepsilon\nabla(\varepsilon^{-1}\cdot)$.

The reactive hydrodynamic model (44) ensures that part of the precipitate, generated in the solute through homogeneous nucleation, is transferred to the mineral surface by adsorption. One should notice that in this model the precipitate $C_{CaCO_{3(p)}}$ is both advected and diffused. Such diffusion enables to account for the interaction of the precipitates with potential unresolved roughness or features in the porous matrix Ω_S.

In the next Section 5, we apply this two-step crystallization model to DNS of CO_2 mineral trapping into a real rock geometry at the pore-scale. We investigate the morphological changes in the porous matrix structure, the clogging of pore throats, and the evolution of the macro-scale properties, namely, the porosity and permeability.

4.4 High-performance-computing aspects

One of the major constraints when dealing with a semi-Lagrangian formulation lies in the ability of the computational framework to handle an overall hybrid approach in terms of grid-particle formalism, numerical methods, multi-grid resolutions, and hardware devices. Indeed, Cottet et al. (2009) suggested a semi-Lagrangian method coupled with hybrid grid resolutions to address a multi-scale transport problem of a passive scalar. The scalar is discretized on a sub-grid compared to the velocity and vorticity fields and enables the accurate prediction of the small-scale effects. Finally, considering hybrid computing methodologies makes it possible to distribute the distinct parts of an overall problem to different types of hardware architectures. This formalism, therefore, exploits the advantages of each method individually according to the characteristics of the problem.

Nonetheless, implementing such a hybrid approach requires a highly flexible computational framework that gathers a wide range of numerical methods and, therefore, benefits from their intrinsic strengths. One also needs libraries incorporating effective parallel computing tools and able to address, *inter alia*, hybrid CPU-GPU programming. In this section, we present the HPC framework considered to address this DNS of pore-scale reactive flows for CO_2 mineral trapping into carbonate rocks.

The library HySoP is a high-performance computing platform (Etancelin et al., 2022), jointly developed at LMAP (Laboratoire de Mathématiques et de leurs Applications, UMR 5142 CNRS, UPPA), LJK (Laboratoire Jean Kuntzmann, Alpes-Grenoble University, UMR 5224 CNRS), and M2N (Laboratoire Modélisation mathématique et numérique, Conservatoire National des Arts et Métiers–CNAM, Paris, EA 7340 CNRS). The library, originally developed to address flow simulations based on remeshed particle methods on hybrid muti-CPU and multi-GPU architectures, was initiated by the work of Etancelin (2014) and has been successfully extended to a larger scope of HPC applications including dissolution at pore-scale (Etancelin et al., 2020).

The entire code is structured around the operator splitting strategy that defines the different operators involved in a problem (at a high level of abstraction), and afterward, enables the discretization of these operators, which are solved using the most appropriate numerical method (at a lower level of abstraction). The overall problem is formally described through an acyclic graph that expresses the operators interactions in the

splitting formulation through data dependencies (Etancelin, 2014; Etancelin et al., 2020; Keck, 2019). Even if the code is mainly written in Python, the numerical methods are either implemented using compiled language that enables threads parallelism (using OpenMP on CPU and OpenCL on accelerators) or taken from external libraries. User interface enables building together both numerical methods provided with HySoP on cartesian grid and user defined Python functions. In the latter, performances are obtained provided the usage of interfaces to compiled language (*i.e.*, among others f2py, swig, cython, numba, …). A complementary distributed parallelism is naturally available using domain decomposition implemented with a Message Passing Interface library (MPI).

One of the core features of HySoP is to target hybrid computing using both CPU and GPU. The latter was made possible by the emergence, in the 2000s, of the so-called GPGPU concept, which integrates the GPU as a CPU co-processing partner targeting accelerated performances. The choice of OpenCL was made to cope with portability of the performances as a generic multicore artichecture programming standard (Stone et al., 2010). The initial GPU computing feature was latter enhanced with code generation from templates or symbolic mathematical expressions together with auto-tuning tanks to micro-benchmarks at run time (Keck, 2019). *Just-in-time* compiling is extensively used to achieve performance portability and lazy specification of kernel parameters which known as challenging problem widely dependent on the hardware architecture (Dolbeau et al., 2013).

The previous numerical method have been implemented on a hybrid computing strategy. Darcy-Brinkmann-Stokes equation is solved on CPU architecture using full MPI parallelization technique while all the reactive and transport part is computed using OpenCL on GPUs.

Overall profiling is represented on Figure 6 for two cases of the next section. Results are showing that recent hardware is capable of better performances without any changes in the code. We benefit here from OpenCL code generation and micro-benchmarks on accelerator and usual compiler optimizations for CPU part. Significant variation appears in computational time associated to flow steps because larger $\mathrm{Da}_{\mathrm{II}}^{\mathrm{crys}}$ implies more intense geometrical changes and then reorganization of main flowpath, as described later in Section 5. One can notice the quite large proportion of computational time spend in data management specially for reactive transport part. It corresponds to ghosts layers that handle boundary conditions and whole data transposition in order to get the first varying index identical to the current direction of directional splitted advection and remeshing operator. Ghosts layer widths are quite large due to large CFL numbers handled here. Data management on GPU has been identified as a known bottleneck of the code and would be investigated in future high performance computing engineering efforts.

5 Results and discussion on clogging/non-clogging regimes

5.1 Pore-scale and reactive setup

The present section focuses on the effects of calcite crystallization on changes in the pore geometry, macro-properties, and flow at the pore scale in the context of CO_2 mineral trapping. We consider a pore-scale geometry obtained by microtomography measurements from Sheppard and Prodanovic (2015) and freely available on the Digital Rocks data portal, which includes μCT datasets of limestone, glass bead pack, and Castlegate sandstone. The numerical simulations are performed on the Castlegate geometry at a resolution of 128^3 with a voxel size of 5.6 μm, which represents a numerical sub-sample of about $L = 0.7168$mm. We assume, as previously introduced in Section 4.2, that the porous matrix is of identical mineral nature as the crystal generated along the reactive process and, thereby, consider that the sub-sample is composed of calcite. While including mineral heterogeneities as perspectives, we here hypothesize the homogeneity of the mineral structure within the sample. Finally, the specific area is numerically estimated for this sample to get, at the initial state, $A_s = 8300$ m^{-1}, and is afterward updated along the reactive process.

Numerical simulations are performed under atmospheric conditions in terms of pressure and temperature and rely on the experimental identification of the reaction rate constants, arising from the literature (Chou et al., 1989). We consider isothermal conditions with a temperature of $T = 25°$C and an injection of CO_2 with a partial pressure of $P_{CO_2} = 3.15 \times 10^{-2}$ bar $= 2.96 \times 10^{-2}$ atm — which is about 100 times greater than the partial pressure of CO_2 in the atmosphere. Given Henry's law constant for the CO_2 at 25°C, and under the assumption of a highly alkaline medium—with pH > 10.33 — we estimate from Equation (16) that the initial concentration of carbonate ions is given by $C_{CO_3^{2-}}(x, t = 0) = 10^{-3}$ mol.L^{-1}.

The calcium initial concentration is subsequently determined based on the equilibrium constant $K_{eq} = 10^{-8.48}$ (Chou et al., 1989; Plummer and Busenberg, 1982) to ensure a far-from-equilibrium precipitation regime given by the supersaturation condition $Q \gg K_{eq}$. We assume that the medium pore space is initially filled with a saturated solution wherein the initial concentration of calcium ions is $C_{Ca^{2+}}(x, t = 0) = 0.1$ mol.L^{-1}. Therefore, in our case, the saturation in calcium ions Ca^{2+} initially present in the domain is not a limiting factor of the precipitation reaction, and we consider a continuous calcium injection that maintains the supersaturation constraint. Actually, in order to maintain this supersaturation, we will assume that the concentration in Ca^{2+} remains constant at its initial value. Comparable initial conditions and assumptions have been employed in investigating dissolution experiments by Maes et al. (2022), wherein the sample core was initially flooded with a brine solution that had previously reached equilibrium with supercritical CO_2.

Regarding the reaction rate constant for the precipitation, we rely on the experimental identification from Chou et al. (1989) such that:

$$K_{-3} = \frac{K_3}{K_{eq}} = \frac{6.6 \cdot 10^{-7}}{10^{-8.48}} = 199 \ \text{mol.m}^{-2}.\text{s}^{-1}$$

while adsorption frequencies K_c commonly encountered in the literature range from 10^3 to 10^8 s^{-1} (Christoffersen and Christoffersen, 1990; Nielsen, 1984; von Wolff et al., 2021; Wolthers et al., 2012). In practice, we set for the numerical simulations $K_c = 10^3$ s^{-1}, the molecular diffusion $D_m = 10^{-9}$ m^2.s^{-1} for all the species and the prescribed flow rate $\overline{u} = 1.10^{-3}$ m.s^{-1}.

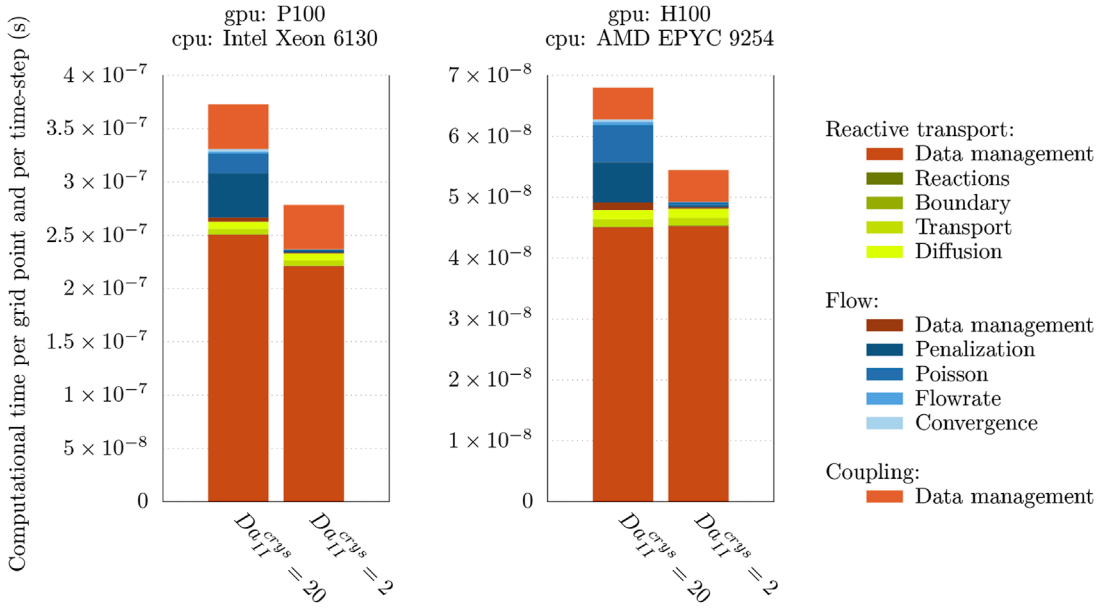

FIGURE 6
Performances in various hardware configuration and discretization: The considered hardware is NVIDIA P100 and H100 GPUs and 16-cores Intel Xeon 6130 cpus and 24-cores AMD EPYC 9254. The computational time is splitted according to the algorithm steps, including operator splitting and data management. Both cases where run with $Pe = 4.47$ (see Section 5 for details).

5.2 Pertinent non-dimensional numbers

Investigating the different precipitation patterns and regimes relies on the definition of well-established characteristic dimensionless numbers, namely, the Peclet and (second or catalytic) Damköhler numbers respectively denoted Pe and Da_{II} (Noiriel et al., 2021; Soulaine et al., 2017; Steefel and Lasaga, 1990). However, in the context of the joint precipitation and crystal growth modeling, we define two distinct Damköhler numbers characterizing each process and respectively denoted Da_{II}^{prec} and Da_{II}^{crys}. These dimensionless numbers are subsequently defined as:

$$\mathrm{Pe} = \frac{\overline{u}L}{D_m},\quad \mathrm{Da}_{II}^{prec} = \frac{K_{-3}\gamma_{CO_3^{2-}}A_s L^2}{D_m} \quad \text{and} \quad \mathrm{Da}_{II}^{crys} = \frac{K_c L^2}{D_m}$$

where $\overline{u}$ and L are respectively the characteristic velocity and length of the sample, and the activity coefficient of the carbonate ions is $\gamma CO_3^{2-} = 10^{-3}$ $m^3.mol^{-1}$. The characteristic length L can be related to pore size (Steefel and Lasaga, 1990), though it is commonly set as $L = \sqrt{\kappa_0}$ provided an experimental or numerical estimation of κ_0 (Soulaine et al., 2017). The latter alternative is applied here, with an estimation of $\kappa_0 = 2 \times 10^{-11}$ m^2 for the porous sample considered.

5.3 Evidence of two clogging regimes at same Da_{II}^{prec} and two different Da_{II}^{crys}

The first crystallization regime we investigate is characterized by the following dimensionless numbers Pe = 4.47, $Da_{II}^{prec} = 33.034$ and $Da_{II}^{crys} = 20$. Precipitation and crystallization of calcite lead to a significant decrease in the macro-scale permeability and porosity, resulting from flow path disruptions at the micro-scale through partial or complete clogging of pore throats. This can also affect the roughness of the mineral interface and the pore-size distribution of the sample and, thereby, contribute to influencing the sample hydrodynamics properties. In particular, we observe these effects at the pore scale in Figure 7 along the reactive process and for several physical times t going from 2h45 to $T_f = 6h56$. On the right side of Figure 7, we depict partial views of the porous sample's morphology, illustrating the changes in pore structure over the reaction time, along with the micro-porosity field ε within the porous matrix Ω_S. On the left side, we represent along a slice in the main flow direction (taken at $z = -0.0168$mm), the local variations on the micro-porosity with respect to the initial state—before the reaction process—given by $\varepsilon(t) - \varepsilon(0)$. Initially, we notice that higher micro-porosity variations are more likely localized at the mineral interfaces but also near thin pore throats.

These variations subsequently lead to pore-clogging and reorganization of the main flow pathway (see Figure 7C). In Figure 8B, we investigate the effects of such micro-scale changes on the evolution of the petrophysical properties at the macro-scale, namely, the porosity ϕ and permeability κ_0 (upscaled quantities from Figure 1). The results are consistent with the expected decrease along the CO_2 mineral trapping process but also highlight sharp permeability drops, which characterize the pore-clogging phenomena. Finally, in order to identify more clearly the crystallization pattern in this particular regime, we display in Figure 8A an isosurface of the micro-porosity variation between the final and initial times. This illustrates that micro-scale variations occur preferentially in a compact and non-uniform manner in the first inlet part of the domain while following the individual ramifications in the pore structure.

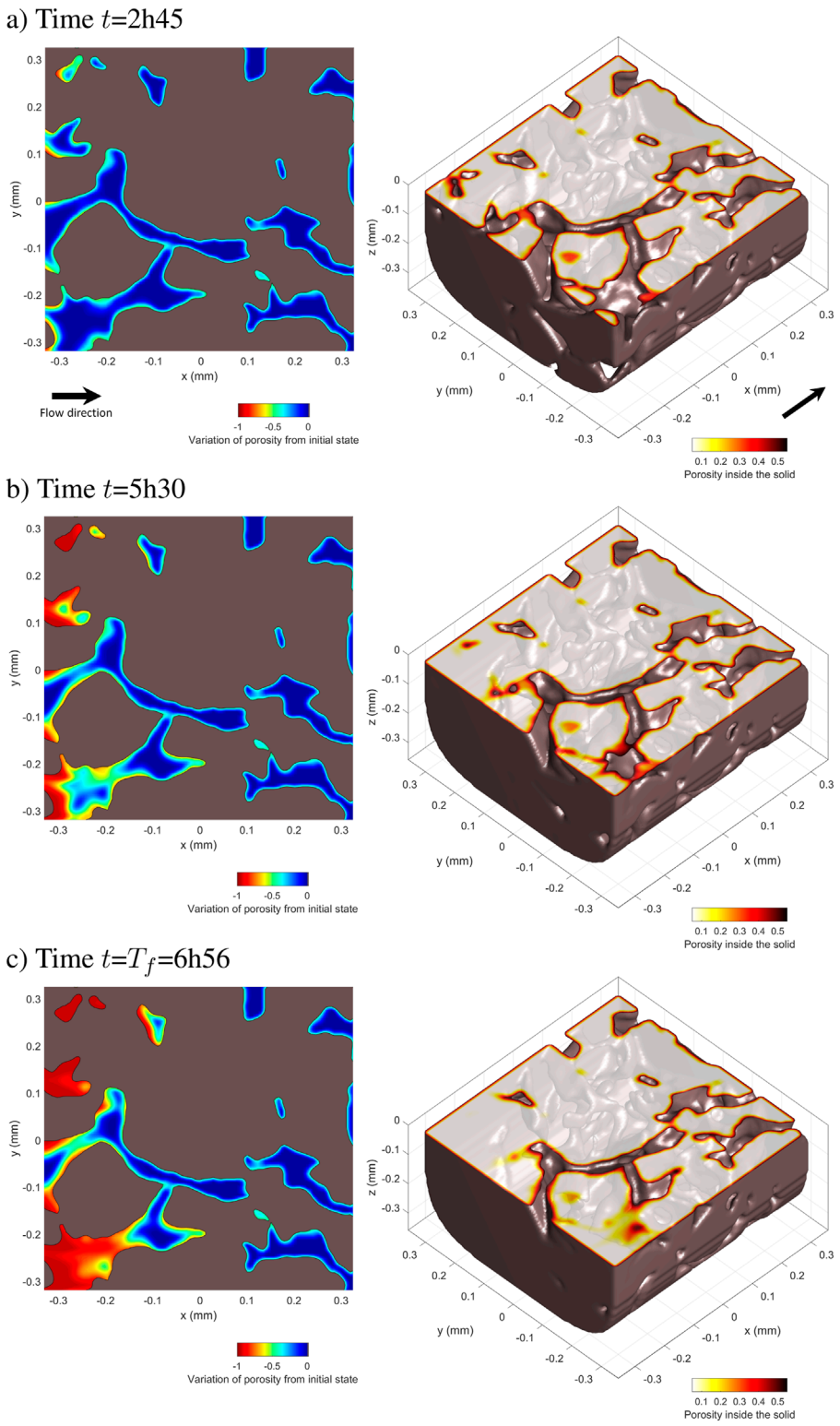

FIGURE 7
Time evolution of the sample geometry and micro-porosity at the pore scale, illustrating pore-clogging effects. Slice at $z = -16.8\mu$m of the porosity variations $\varepsilon(t) - \varepsilon(0)$ in the fluid region of the pore space for various times t, on the left. Partial view of the pore space structure as an isosurface of $\varepsilon(t)$ for several times t, on the right. The clogging occurs in the red areas, mainly upstream (flow direction is given by the arrow on picture **(A)** Time t = 2h45. **(B)** Time t = 5h30. **(C)** Time $t = T_f$ = 6h56.

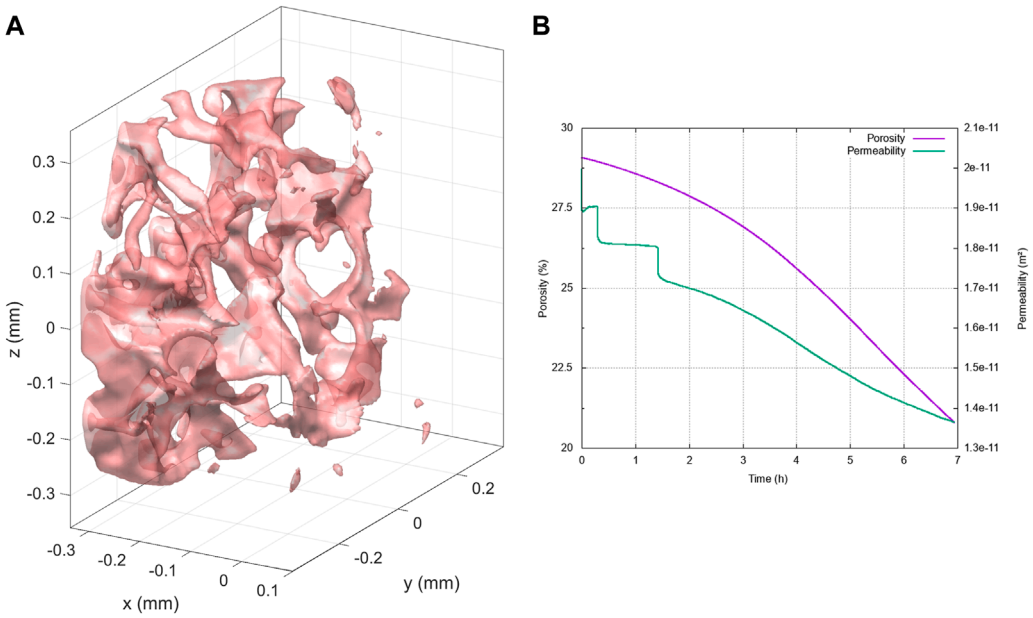

FIGURE 8
Evolution of the sample properties along the reactive process: **(A)** Micro-porosity evolution represented by an isosurface of the porosity variation $\varepsilon(T_f) - \varepsilon(0)$ at half of its maximum value. Results after nearly 7 h of precipitation and crystal growth, illustrating a non-uniform compact regime following the natural ramification of the sample. **(B)** Evolution of the macro-scale properties, porosity ϕ and permeability κ_0, along the two-step crystallization process from Figure 3.

We subsequently investigate the impact of different dominant regimes on the overall two-step crystallization process. To do so, we consider both transport dominant cases with Pe = 4.47 > 1 and diffusion dominant cases with Pe = 0.447 < 1, coupled with two different crystal growth regimes characterized by $\mathrm{Da}_{\mathrm{II}}^{\mathrm{crys}} = 2$ and $\mathrm{Da}_{\mathrm{II}}^{\mathrm{crys}} = 20$. One should notice that the effect of precipitation Damköhler $\mathrm{Da}_{\mathrm{II}}^{\mathrm{prec}}$ changes are not analyzed since this number, characterizing the first homogeneous nucleation regime, is a limiting factor of the crystallization process from Figure 3. Here, we assume in all the previous cases that $\mathrm{Da}_{\mathrm{II}}^{\mathrm{crys}} < \mathrm{Da}_{\mathrm{II}}^{\mathrm{prec}}$ which guarantees a supersaturation state suitable to the development of crystal aggregates on the mineral surface.

To the best of our knowledge, considering that the crystallization regime can be driven by three distinct dimensionless numbers is one of the contributions of the present article. Indeed, most of the regime diagrams presented in the literature mainly characterize precipitation patterns according to the Pe and $\mathrm{Da}_{\mathrm{II}}^{\mathrm{prec}}$ dimensionless numbers, which implies neglecting the effects of nuclei adsorption at the mineral surface in the different regime configurations (Tartakovsky et al., 2007; Yang et al., 2021). However, our results indicate that both homogeneous calcite nucleation (the precipitation step in Figure 3) and growth stages are important in the development of precipitation and crystallization patterns. In particular, we establish that the crystal growth Damköhler number $\mathrm{Da}_{\mathrm{II}}^{\mathrm{crys}}$ has a non-negligible impact on precipitation pattern and porosity variations along the reactive process, regardless of the other dimensionless numbers Pe and $\mathrm{Da}_{\mathrm{II}}^{\mathrm{prec}}$ commonly investigated.

Indeed, Figures 9B, 10B highlight two distinct crystallization regimes at similar Pe and $\mathrm{Da}_{\mathrm{II}}^{\mathrm{prec}}$, but with a ten times smaller adsorption frequency K_c in Figure 9B which impact the $\mathrm{Da}_{\mathrm{II}}^{\mathrm{crys}}$. Figure 9B shows that, for a small adsorption frequency K_c, the calcite precipitate is uniformly generated and advected along the main flow path direction (due to the transport dominant regime with Pe > 1) while the micro-porosity changes are minimal. This illustrates that the main flow path is maintained since few calcite nuclei aggregate to the mineral surface. By increasing the adsorption frequency in Figure 10B, the precipitate formation concentrates on the inlet of the domain and is less subject to advection, while the micro-porosity changes become significant. On the one hand, this highlights pore-clogging that prevents further transport of the calcite nuclei. On the other hand, we also notice a backward increase in calcite precipitates that accumulate behind the clogging after some time. The same analysis holds for Figures 9A, 10A, except we consider a diffusion dominant regime with Pe < 1, which means that the precipitate transport is reduced so that the nuclei formation and micro-porosity changes are even more constrained to the inlet boundary of the domain. The results presented in Figures 7 and 8 correspond to the crystallization regime identified by Pe > 1 and $\mathrm{Da}_{\mathrm{II}}^{\mathrm{crys}} = 20$ in Figure 10B. This confirms that the permeability drops observed in Figure 8B are characteristics of pore-clogging effects.

To conclude, at $\mathrm{Da}_{\mathrm{II}}^{\mathrm{crys}} = 2$, $\mathrm{Da}_{\mathrm{II}}^{\mathrm{prec}} = 33$ and for Pe = 0.447 < 1 as well as for Pe = 4.47 > 1, Figure 9 shows that there is no clogging measured. At $\mathrm{Da}_{\mathrm{II}}^{\mathrm{crys}} = 20$, $\mathrm{Da}_{\mathrm{II}}^{\mathrm{prec}} = 33$ and for the two same Peclet numbers, Figure 10 displays evidence of pore-clogging. The clogging is consequently driven principally by the non-dimensional number $\mathrm{Da}_{\mathrm{II}}^{\mathrm{crys}}$ in this case study, the Peclet number affecting the depth of the clogging effect. This is valid as long as the $\mathrm{Da}_{\mathrm{II}}^{\mathrm{prec}}$ is sufficiently high in order to provide precipitate able to turn into crystal.

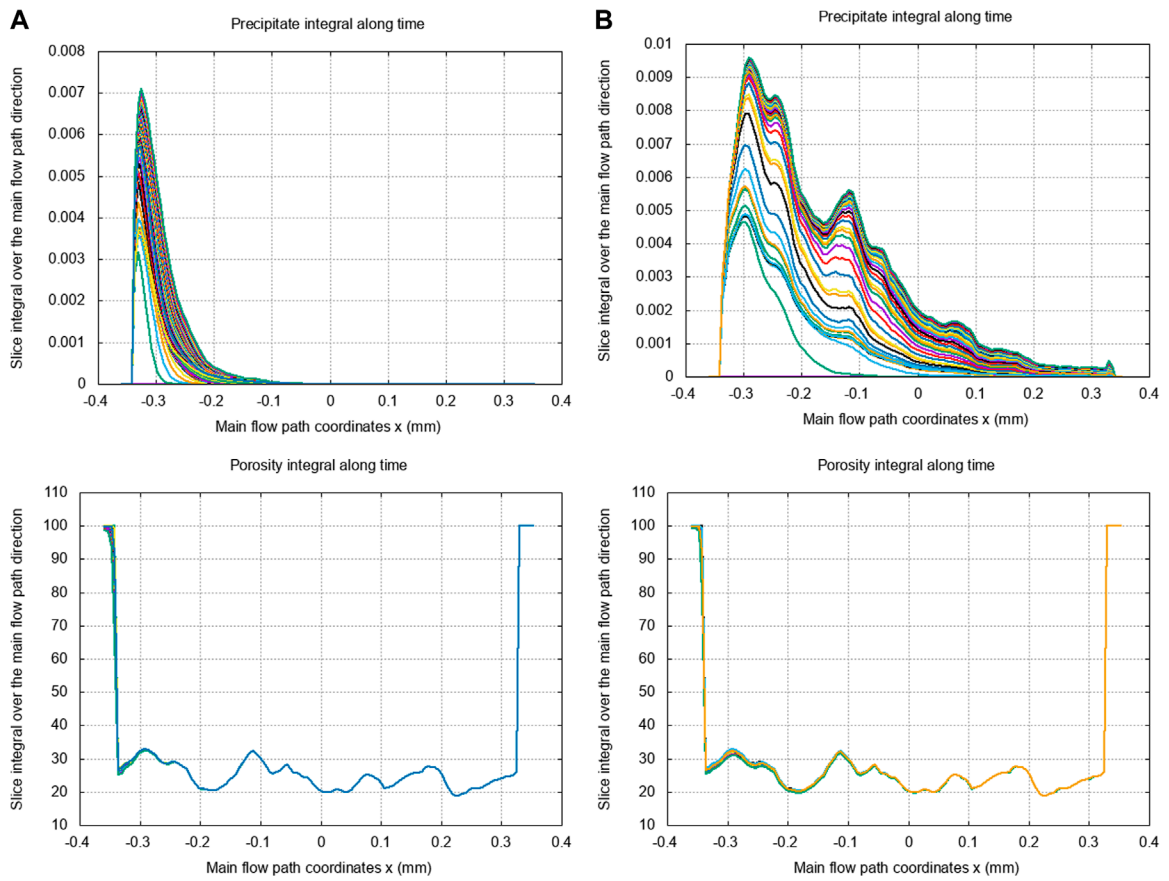

FIGURE 9
Crystallization regimes at $Da_{II}^{crys} = 2$ and $Da_{II}^{prec} = 33$ for Peclet numbers below 1 **(A)** and above 1 **(B)**: no clogging. Slice integrals of the precipitates and macro-porosity—computed over 2D YZ directional slices—plotted with respect to the main flow path direction coordinates x (in mm mm) and where each curve (using segmented colors) represents a distinct time in the reactive process. The porosity integral remains close to its initial value, which shows that pores remain open with the same flow, hence no clogging effect.

5.4 Discussion

This section aims at positioning the final set of Equation 21 with the existing literature on nucleation. These models involve the physics of fluid precipitation (homogeneous nucleation) and its subsequent crystallization (heterogeneous nucleation), while as shown on Figure 3, the direct crystallization from reactants is also another possible kind of nucleation. The later direct crystallization is not considered in the present study, but can be compared to our two-step modeling as long as $Da_{II}^{prec} \gg Da_{II}^{crys}$ since we don't model the precipitate rheology.

Moreover, the existing literature considers either internal flows (porous medium as a pore collection) or external flows (porous medium as a grain collection, also referred to as pore-scale). Every study has its own configuration and Dahmköhler/Peclet setup that we cannot investigate one by one in this study.

More in detail concerning recent literature, confined internal flows have been studied experimentally in Poonoosamy et al. (2023); Noiriel et al. (2021) and numerically in Molins and Knabner (2019), but most geometries of porous media described at their pore-scale for systematic analysis are grain-shaped and involve the hydrodynamics of low Reynolds external flow. Such external flow analysis are numerical (Starchenko, 2022; Nooraiepour et al., 2021b; Yang et al., 2021; Varzina et al., 2020; Fazeli et al., 2020) or experimental (Nooraiepour et al., 2021a), some of them focusing on the wall as an initially flat fluid/solid interface Deng et al. (2022). Also, some configuration are in between confined and grain-shaped geometries (Masoudi et al., 2024), with some focus on cement material (Tong et al., 2024; Patel et al., 2021).

Among these studies, qualitative comparison with Yang et al. (2021), and quantitative comparison with Masoudi et al. (2024) are of direct interest for the present investigation.

First, in Yang et al. (2021), a diagram showing the expected nucleation regime with respect to Da_{II} and *Pe* is available on their Figure 13. They consider crystal growth around a grain, studying the hydrodynamic and reaction balance and the resulting grain shape. Their model rely on Kozeny-Carman correlation law and TST so only the numerical method significantly differs (they use LBM while we use semi-Lagrangian with PSE method). Their results are compatible to ours, as for $1 \leqslant Da_{II} \leqslant 100$ and $Pe \leqslant 10$ we don't observe dendrite formation nor uniform distribution of crystallization.

Second, the article Masoudi et al. (2024) considers only heterogeneous nucleation with both spherical grains and pore

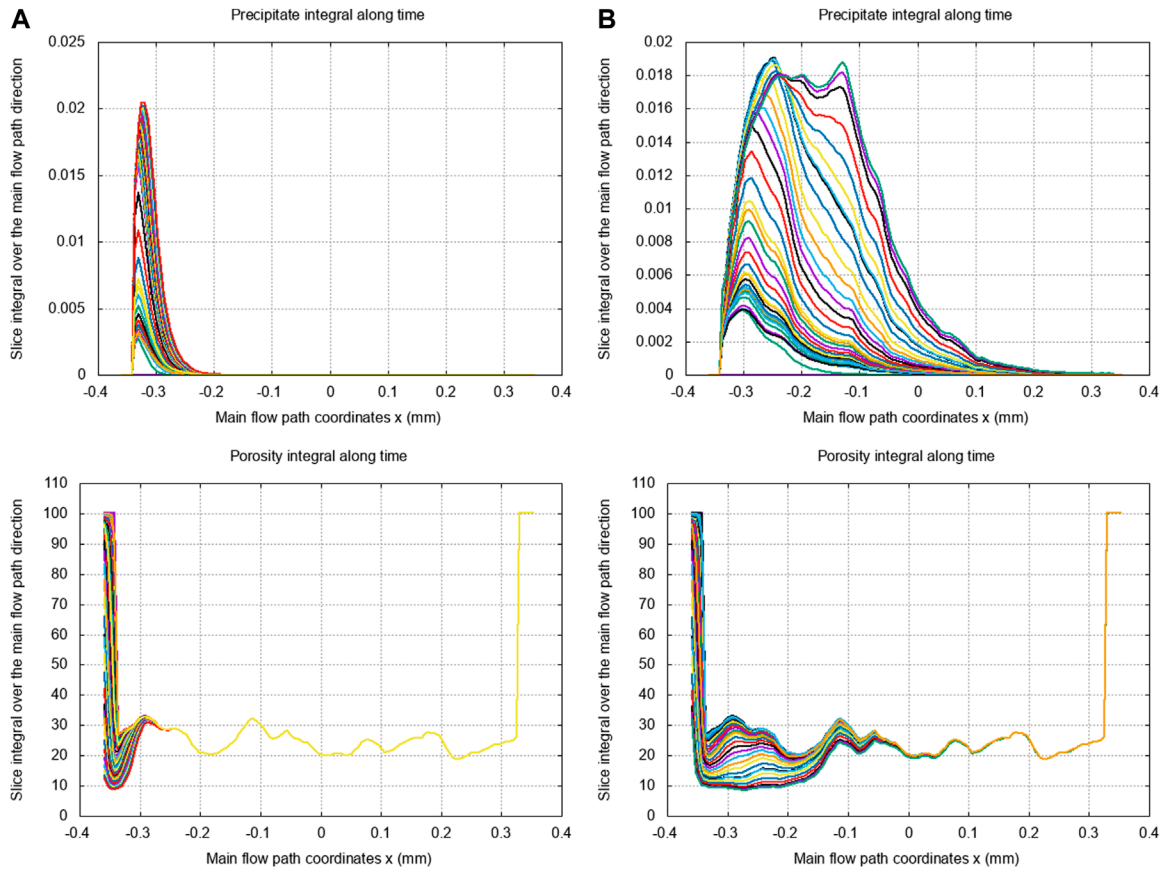

FIGURE 10
Crystallization regimes at $Da_{II}^{crys} = 20$ and $Da_{II}^{prec} = 33$ for Peclet numbers below 1 **(A)** and above 1 **(B)**: pore-clogging. Slice integrals of the precipitates and macro-porosity—computed over 2D YZ directional slices—plotted with respect to the main flow path direction coordinates x (in mm mm) and where each curve represents a distinct time in the reactive process. The porosity integral goes from 30% to 10% (close to the cristal porosity at 5%) in the upstream part of the sample, which shows a pore-clogging effect.

structures at several crystallites levels and links porosity and permeability during crystallization process. They consider Lattice Boltzmann simulations of crystal growth from aqueous material with a rate $R_G = k_G S$ in mol/s which is no more than our relation (41). Despite the formulation of crystallites events fitting well to LBM expression of reaction formula but far from our deterministic PDE formulation, we are comparable to their heterogeneous geometry with high crystallite level. Our configuration at $Da_{II}^{crys} = 20$ contains region of high crystallization rate and some not reached by reactants so the comparison is pertinent to the cases B and D of the Figure 3 from Masoudi et al. (2024). On Figure 11 we plot the similar petro-physical diagram showing the renormalized permeability K/K_0 with respect to renormalized global porosity ϕ/ϕ_0. In order to get a pertinent measurement of the crystallization process, we restrict the computation of K and ϕ to the upstream quarter of the computational domain, so that the porosity displayed on Figure 10 for Pe > 1 evolves from 30% to 13.9% in 3h40, that is to say $\phi/\phi_0 =$ 46.5% of the initial porosity remains.

With this setup, the renormalized $K-\phi$ diagram is displayed on the Figure 11A, along with the power laws $K/K_0 = (\phi/\phi_0)^n$ for $n = 2, 3, 8, 64$, the case $n = 3$ being related to the Kozeny-Carman correlation far from $\phi = 1$. We exhibits on this diagram our 4 configurations (two different Dahmköhler and Peclet number) for the whole simulation and for the strongest crystallization events, corresponding to individual pore clogging time window and identified by a sharp decrease of the permeability (see Figure 8 for instance). At a global level we observe clogging events with exponents n between 64 and 8 as expected [see Figure 3D in Masoudi et al. (2024)], but a lower exponent around 1.5 at long time scale [2–4 was expected from Figure 3B in Masoudi et al. (2024)]. Concerning the time evolution of our regime, the Figure 11B shows a zoom at high K and ϕ values, exhibiting short time scale (the maximum renormalized values 1 corresponding to the initial condition). We can then read that for short time scale at $Da_{II}^{crys} = 20$, the Kozeny-Carman law is quite well followed but deviates strongly after the last individual pore clogging ($t = 1h25$). Moreover, the low Dahmköhler case $Da_{II}^{crys} = 2$ that exhibits no clogging (see Figure 9 for instance) has very limited effect on permeability and porosity (see Figure 11B), but shows nevertheless a small crystallization event at low Pecler number that is also coherent in term of exponent.

Moreover, to conclude with this comparison, such a $K-\phi$ criterion can be applied only when the full sample is involved in the crystallization process, otherwise the porosity will reach

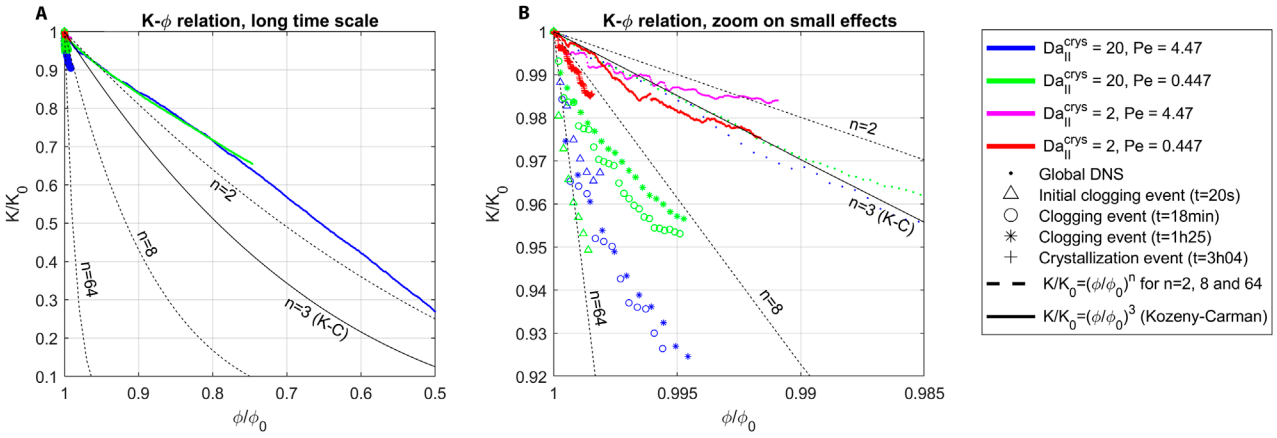

FIGURE 11
Renormalized $K-\phi$ comparison with Masoudi et al. (2024) indicators for the regimes displayed on Figures 9, 10. Kozeny-Carman relationship developed in Equation 2. **(A)** K-ϕ relation, long time scale. **(B)** K-ϕ relation, zoom on small effects

a limit and the permeability will still decrease, which is not compatible with a power-law. Consequently, a special care has to be taken for the computational domain of this criterion when considering a preferential spot of cristallization (such as our case of upstream furring).

Finally, in Starchenko (2022), nucleations occur around a single grain but can be compared to our model (Equation 21) if reduced to 1D (our Da_{II}^{prec} values are similar, 34 and 33 respectively). Deng et al. (2022) shows growth on a wall, also comparable if reduced to 1D. These two growth rates at wall scale will be the topic of future investigation, but are currently too far, at a geometrical level, from our pore-scale configuration.

6 Concluding remarks

This article focused on developing an efficient DNS framework to address reactive flows at the pore scale in the context of CO_2 mineral storage. Indeed, the injected CO_2 will interact with the aquifer structure and eventually lead to mineral trapping in the form of calcite precipitates and crystals. These processes are interesting to study at the pore scale to ensure a comprehensive analysis of the local rock-fluid interactions and evolving pore structures. This can subsequently translate into meaningful estimations of the macro-scale properties changes and measure the impact of the geochemical processes on the natural underground reservoirs. In particular, precipitation and crystallization lead to a significant reduction in the macro-scale permeability and porosity, which result from partial or complete pore clogging and thus from a reorganization of the flow path at the micro-scale.

From a conceptual perspective, we developed a new crystallization model that efficiently combines a classical deterministic TST approach of the nucleation process with a probabilistic view of the crystal aggregation to the pore surface. This enables us to account for spatial and geometrical dependency in the crystal growth modeling through a probabilistic attachment rate depending on local mineral volume fraction. In this sense, we integrate the modeling of preferential growing sites that largely hinge on the surrounding pore arrangement. To the best of our knowledge, such considerations are here accounted for the first time to model crystallization processes in complex 3D geometries at the pore scale. Investigating probabilistic attachment rates based on the surrounding pore structure also ensures reliable prediction of pore-clogging at the pore scale. Finally, we demonstrate that the proper characterization of crystallization regimes both depends on the nucleation process and crystal aggregation. Indeed, we exhibit that the two commonly considered dimensionless numbers, Pe and Da_{II}^{prec}, are not sufficient to explain clogging effects and precipitation patterns. A novelty of the present manuscript is, therefore, that the crystallization regimes are characterized by three dimensionless numbers that include the effects of nuclei adsorption to the pore surface.

This reactive hydrodynamic model consistently couples a Lagrangian formulation for the reaction equations with a grid-based approach for the flow using the DBS equation with the superficial velocity formalism. This semi-Lagrangian method is addressed through a splitting operator strategy coupled with high-order remeshing steps for grid-particle interpolations. This original numerical method introduced to solve this coupled model has been efficiently incorporated into the hybrid numerical framework HySoP and results in a CPU-GPU implementation of the method. It includes a robust estimation of the heterogeneous diffusion operator arising from Archie's law term in the reactive system.

At the same time, this article also demonstrated strong implications in the overall reactive system of several parameters that can be subject to a wide range of discrepancies. In particular, morphological features and kinetic parameters, such as the micro-porosity ε, specific area A_s, rate constants K_i, and adsorption frequencies K_c, have a significant impact on the reaction rates and the dynamical patterns.

Experimental determination of these parameters can range over several orders of magnitude and result in highly different

regimes that drastically affect the estimation of the macro-scale properties: the adsorption frequencies K_c commonly found in the literature can range from 10^3 to 10^8 s^{-1} as shown in Christoffersen and Christoffersen (1990); Nielsen (1984); von Wolff et al. (2021); Wolthers et al. (2012). Our present method has been shown to compute accurately the phenomena of crystallization and precipitation in different regimes, and will be used intensively in future works for inverse problems in order to get a robust and accurate estimation of such adsorption frequencies from experiments imaging. New methods relying of AI and BPINNs for the estimation of reaction rates at the pore scale are already available for dissolution (Perez and Poncet, 2024) and could be adapted to nucleation process in the near future.

Data availability statement

The raw data supporting the conclusions of this article will be made available by the authors, without undue reservation.

Author contributions

SP: Conceptualization, Formal Analysis, Investigation, Methodology, Resources, Software, Validation, Writing–original draft, Writing–review and editing. J-ME: Investigation, Resources, Software, Validation, Visualization, Writing–original draft, Writing–review and editing. PP: Conceptualization, Funding acquisition, Investigation, Methodology, Project administration, Supervision, Visualization, Writing–original draft, Writing–review and editing.

Funding

The author(s) declare that financial support was received for the research, authorship, and/or publication of this article. This work was partially supported by ANR Grant ANR-20-CE45-0022, Carnot Institute ISIFoR Grant P450902ISI and E2S-UPPA project MicroMineral.

Conflict of interest

The authors declare that the research was conducted in the absence of any commercial or financial relationships that could be construed as a potential conflict of interest.

Publisher's note

All claims expressed in this article are solely those of the authors and do not necessarily represent those of their affiliated organizations, or those of the publisher, the editors and the reviewers. Any product that may be evaluated in this article, or claim that may be made by its manufacturer, is not guaranteed or endorsed by the publisher.

Supplementary material

The Supplementary Material for this article can be found online at: https://www.frontiersin.org/articles/10.3389/feart.2025.1493305/full#supplementary-material

References

Aagaard, P., and Helgeson, H. C. (1982). Thermodynamic and kinetic constraints on reaction rates among minerals and aqueous solutions; I, Theoretical considerations. *Am. J. Sci.* 282, 237–285. doi:10.2475/ajs.282.3.237

Allaire, G., Brizzi, R., Mikelić, A., and Piatnitski, A. (2010). Two-scale expansion with drift approach to the Taylor dispersion for reactive transport through porous media. *Chem. Eng. Sci.* 65, 2292–2300. doi:10.1016/j.ces.2009.09.010

Allaire, G., and Hutridurga, H. (2012). Homogenization of reactive flows in porous media and competition between bulk and surface diffusion. *IMA J. Appl. Math.* 77, 788–815. doi:10.1093/imamat/hxs049

Andrew, M., Bijeljic, B., and Blunt, M. J. (2013). Pore-scale imaging of geological carbon dioxide storage under *in situ* conditions. *Geophys. Res. Lett.* 40, 3915–3918. doi:10.1002/grl.50771

Angot, P. (2018). Well-posed Stokes/Brinkman and Stokes/Darcy coupling revisited with new jump interface conditions. *ESAIM M2AN* 52, 1875–1911. doi:10.1051/m2an/2017060

Archie, G. E. (1942). The electrical resistivity log as an aid in determining some reservoir characteristics. *Petroleum Trans. AIME* 146, 54–62. doi:10.2118/942054-g

Beale, J. T., and Majda, A. J. (1981). Rates of convergence for viscous splitting of the Navier-Stokes equations. *Math. Comput.* 37, 243–259. doi:10.1090/s0025-5718-1981-0628693-0

Beaugendre, H., Huberson, S., and Mortazavi, I. (2012). Coupling particle sets of contours and streamline methods for solving convection problems. *Appl. Math. Lett.* 25, 11–19. doi:10.1016/j.aml.2011.06.031

Bohn, H., McNeal, B., and O'Connor, G. (1980). Soil chemistry. *Soil Chem. Soil Sci.* 129, 389. doi:10.1097/00010694-198006000-00010

Busenberg, E., and Plummer, L. N. (1986). A comparative study of the dissolution and crystal growth kinetics of calcite and aragonite. *Stud. diagenesis* 1578, 139–168. doi:10.3133/b1578

Carman, P. C. (1937). Fluid flow through granular beds. *Trans. Institution Chem. Eng.* 15, 150–166.

Chatelain, P., Curioni, A., Bergdorf, M., Rossinelli, D., Andreoni, W., and Koumoutsakos, P. (2008). Billion vortex particle direct numerical simulations of aircraft wakes. *Comput. Methods Appl. Mech. Eng.* 197, 1296–1304. doi:10.1016/j.cma.2007.11.016

Chatelin, R., and Poncet, P. (2013). A hybrid grid-particle method for moving bodies in 3D Stokes flow with variable viscosity. *SIAM J. Sci. Comput.* 35, B925–B949. doi:10.1137/120892921

Chorin, A. J. (1973). Numerical study of slightly viscous flow. *J. Fluid Mech.* 57, 785–796. doi:10.1017/S0022112073002016

Chou, L., Garrels, R. M., and Wollast, R. (1989). Comparative study of the kinetics and mechanisms of dissolution of carbonate minerals. *Chem. Geol.* 78, 269–282. doi:10.1016/0009-2541(89)90063-6

Christoffersen, J., and Christoffersen, M. R. (1990). Kinetics of spiral growth of calcite crystals and determination of the absolute rate constant. *J. Cryst. Growth* 100, 203–211. doi:10.1016/0022-0248(90)90623-S

Class, H., Ebigbo, A., Helmig, R., Dahle, H. K., Nordbotten, J. M., Celia, M. A., et al. (2009). A benchmark study on problems related to CO2 storage in geologic formations. *Comput. Geosci.* 13, 409–434. doi:10.1007/s10596-009-9146-x

Coindreau, O., and Vignoles, G. L. (2005). Assessment of geometrical and transport properties of a fibrous c/c composite preform using x-ray computerized micro-tomography: Part i. image acquisition and geometrical properties. *J. Mater. Res.* 20, 2328–2339. doi:10.1557/jmr.2005.0311

Cottet, G.-H., Balarac, G., and Coquerelle, M. (2009). Subgrid particle resolution for the turbulent transport of a passive scalar. *Adv. Turbul.* XII, 779–782. doi:10.1007/978-3-642-03085-7_188

Cottet, G.-H., Etancelin, J.-M., Pérignon, F., and Picard, C. (2014). High order Semi-Lagrangian particle methods for transport equations: numerical analysis and implementation issues. *ESAIM Math. Model. Numer. Analysis* 48, 1029–1060. doi:10.1051/m2an/2014009

Cottet, G.-H., and Koumoutsakos, P. (2000). *Vortex methods: theory and practice*. Cambridge University Press. doi:10.1017/CBO9780511526442

Cottet, G.-H., Koumoutsakos, P., and Salihi, M. L. O. (2000). Vortex Methods with spatially varying cores. *J. Comput. Phys.* 162, 164–185. doi:10.1006/jcph.2000.6531

Cottet, G.-H., and Poncet, P. (2004). Advances in direct numerical simulations of 3d wall-bounded flows by vortex-in-cell methods. *J. Comput. Phys.* 193, 136–158. doi:10.1016/j.jcp.2003.08.025

Degond, P., and Mas-Gallic, S. (1989). The weighted particle method for convection-diffusion equations. *Math. Comput.* 53, 485–526. doi:10.2307/2008716

Deng, H., Poonoosamy, J., and Molins, S. (2022). A reactive transport modeling perspective on the dynamics of interface-coupled dissolution-precipitation. *Appl. Geochem.* 137, 105207. doi:10.1016/j.apgeochem.2022.105207

Dolbeau, R., Bodin, F., and de Verdière, G. C. (2013). "One OpenCL to rule them all?," in *2013 IEEE 6th international workshop on multi-/many-core computing systems (MuCoCoS)*, 1–6. doi:10.1109/MuCoCoS.2013.6633603

El Ossmani, M., and Poncet, P. (2010). Efficiency of multiscale hybrid grid-particle vortex methods. *Multiscale Model. and Simul.* 8, 1671–1690. doi:10.1137/090765006

Etancelin, J.-M. (2014). *Couplage de modèles, algorithmes multi-échelles et calcul hybride*. Grenoble, France: Université de Grenoble. Ph.D. thesis.

Etancelin, J.-M., Moonen, P., and Poncet, P. (2020). Improvement of remeshed Lagrangian methods for the simulation of dissolution processes at pore-scale. *Adv. Water Resour.* 146, 103780. doi:10.1016/j.advwatres.2020.103780

[Dataset] Etancelin, J.-M., Mimeau, C., Keck, J.-B., Picard, C., Cottet, G.-H., Perignon, F., et al. (2022). HySoP: hybrid simulation with particles. Available at: https://hal.science/hal-04606382.

Eyring, H. (1935). The activated complex in chemical reactions. *J. Chem. Phys.* 3, 107–115. doi:10.1063/1.1749604

Faragó, I. (2008). A modified iterated operator splitting method. *Appl. Math. Model.* 32, 1542–1551. doi:10.1016/j.apm.2007.04.018

Fazeli, H., Masoudi, M., Patel, R. A., Aagaard, P., and Hellevang, H. (2020). Pore-scale modeling of nucleation and growth in porous media. *ACS Earth Space Chem.* 4, 249–260. doi:10.1021/acsearthspacechem.9b00290

Glover, P. W. J. (2016). Archie's law – a reappraisal. *Solid earth.* 7, 1157–1169. doi:10.5194/se-7-1157-2016

Hejlesen, M. M., Koumoutsakos, P., Leonard, A., and Walther, J. H. (2015). Iterative brinkman penalization for remeshed vortex methods. *J. Comput. Phys.* 280, 547–562. doi:10.1016/j.jcp.2014.09.029

Hellevang, H., Pham, V. T., and Aagaard, P. (2013). Kinetic modelling of CO2–water–rock interactions. *Int. J. Greenh. Gas Control* 15, 3–15. doi:10.1016/j.ijggc.2013.01.027

Hume, L., and Poncet, P. (2021). A velocity-vorticity method for highly viscous 3D flows with application to digital rock physics. *J. Comput. Phys.* 425, 109910. doi:10.1016/j.jcp.2020.109910

Keck, J.-B. (2019). Numerical modelling and high performance computing for sediment flows. *Theses*.

Kozeny, J. (1927). Umber kapillare Leitung des Wassers im Boden. *Sitzungsber Akad. Wiss., Wien* 136, 271–306.

Lamichhane, B. P. (2013). A new Finite Element method for Darcy-Stokes-Brinkman equations. *ISRN Comput. Math.* 2013, 1–4. doi:10.1155/2013/798059

Lasaga, A. C. (1981). Transition state theory. *Rev. Mineral.* 8.

Lasaga, A. C. (1984). Chemical kinetics of water-rock interactions. *J. Geophys. Res. Solid Earth* 89, 4009–4025. doi:10.1029/JB089iB06p04009

Lioliou, M. G., Paraskeva, C. A., Koutsoukos, P. G., and Payatakes, A. C. (2007). Heterogeneous nucleation and growth of calcium carbonate on calcite and quartz. *J. Colloid Interface Sci.* 308, 421–428. doi:10.1016/j.jcis.2006.12.045

Luo, H., Quintard, M., Debenest, G., and Laouafa, F. (2012). Properties of a diffuse interface model based on a porous medium theory for solid–liquid dissolution problems. *Comput. Geosci.* 16, 913–932. doi:10.1007/s10596-012-9295-1

Maes, J., Soulaine, C., and Menke, H. P. (2022). Improved volume-of-solid formulations for micro-continuum simulation of mineral dissolution at the pore-scale. *Front. Earth Sci.* 10. doi:10.3389/feart.2022.917931

Magni, A., and Cottet, G.-H. (2012). Accurate, non-oscillatory, remeshing schemes for particle methods. *J. Comput. Phys.* 231, 152–172. doi:10.1016/j.jcp.2011.09.005

Masoudi, M., Fazeli, H., Miri, R., and Hellevang, H. (2021). Pore scale modeling and evaluation of clogging behavior of salt crystal aggregates in CO2-rich phase during carbon storage. *Int. J. Greenh. Gas Control* 111, 103475. doi:10.1016/j.ijggc.2021.103475

Masoudi, M., Nooraiepour, M., Deng, H., and Hellevang, H. (2024). Mineral precipitation and geometry alteration in porous structures: how to upscale variations in permeability–porosity relationship? *Energy and Fuels* 38, 9988–10001. doi:10.1021/acs.energyfuels.4c01432

Menke, H. P., Bijeljic, B., Andrew, M. G., and Blunt, M. J. (2015). Dynamic three-dimensional pore-scale imaging of reaction in a carbonate at reservoir conditions. *Environ. Sci. and Technol.* 49, 4407–4414. doi:10.1021/es505789f

Molins, S., and Knabner, P. (2019). Multiscale approaches in reactive transport modeling. *Rev. Mineralogy Geochem.* 85, 27–48. doi:10.2138/rmg.2019.85.2

Molins, S., Soulaine, C., Prasianakis, N. I., Abbasi, A., Poncet, P., Ladd, A. J. C., et al. (2021). Simulation of mineral dissolution at the pore scale with evolving fluid-solid interfaces: review of approaches and benchmark problem set. *Comput. Geosci.* 25, 1285–1318. doi:10.1007/s10596-019-09903-x

Molins, S., Trebotich, D., Steefel, C. I., and Shen, C. (2012). An investigation of the effect of pore scale flow on average geochemical reaction rates using direct numerical simulation. *Water Resour. Res.* 48. doi:10.1029/2011WR011404

Nielsen, A. E. (1984). Electrolyte crystal growth mechanisms. *J. Cryst. Growth* 67, 289–310. doi:10.1016/0022-0248(84)90189-1

Nielsen, A. E., and Toft, J. M. (1984). Electrolyte crystal growth kinetics. *J. Cryst. Growth* 67, 278–288. doi:10.1016/0022-0248(84)90188-X

Noiriel, C., and Renard, F. (2022). Four-dimensional X-ray micro-tomography imaging of dynamic processes in geosciences. *Comptes Rendus. Géoscience* 354, 255–280. doi:10.5802/crgeos.137

Noiriel, C., Seigneur, N., Le Guern, P., and Lagneau, V. (2021). Geometry and mineral heterogeneity controls on precipitation in fractures: an X-ray micro-tomography and reactive transport modeling study. *Adv. Water Resour.* 152, 103916. doi:10.1016/j.advwatres.2021.103916

Noiriel, C., and Soulaine, C. (2021). Pore-scale imaging and modelling of reactive flow in evolving porous media: tracking the dynamics of the fluid–rock interface. *Transp. Porous Media* 140, 181–213. doi:10.1007/s11242-021-01613-2

Noiriel, C., Steefel, C. I., Yang, L., and Bernard, D. (2016). Effects of pore-scale precipitation on permeability and flow. *Adv. Water Resour.* 95, 125–137. doi:10.1016/j.advwatres.2015.11.013

Nooraiepour, M., Masoudi, M., and Hellevang, H. (2021a). Probabilistic nucleation governs time, amount, and location of mineral precipitation and geometry evolution in the porous medium. *Sci. Rep.* 11, 16397. doi:10.1038/s41598-021-95237-7

Nooraiepour, M., Masoudi, M., Shokri, N., and Hellevang, H. (2021b). Probabilistic nucleation and crystal growth in porous medium: new insights from calcium carbonate precipitation on primary and secondary substrates. *ACS Omega* 6, 28072–28083. doi:10.1021/acsomega.1c04147

Panga, M. K. R., Ziauddin, M., and Balakotaiah, V. (2005). Two-scale continuum model for simulation of wormholes in carbonate acidization. *AIChE J.* 51, 3231–3248. doi:10.1002/aic.10574

Patel, R. A., Churakov, S. V., and Prasianakis, N. I. (2021). A multi-level pore scale reactive transport model for the investigation of combined leaching and carbonation of cement paste. *Cem. Concr. Compos.* 115, 103831. doi:10.1016/j.cemconcomp.2020.103831

Payton, R. L., Sun, Y., Chiarella, D., and Kingdon, A. (2022). Pore scale numerical modelling of geological carbon storage through mineral trapping using true pore geometries. *Transp. Porous Media* 141, 667–693. doi:10.1007/s11242-021-01741-9

Perez, S., Moonen, P., and Poncet, P. (2022). On the deviation of computed permeability induced by unresolved morphological features of the pore space. *Transp. Porous Media* 141, 151–184. doi:10.1007/s11242-021-01713-z

Perez, S., and Poncet, P. (2024). Auto-weighted Bayesian physics-informed neural networks and robust estimations for multitask inverse problems in pore-scale imaging of dissolution. *Comput. Geosci.* 28, 1175–1215. doi:10.1007/s10596-024-10313-x

Pham, V. T., Lu, P., Aagaard, P., Zhu, C., and Hellevang, H. (2011). On the potential of CO2–water–rock interactions for CO2 storage using a modified kinetic model. *Int. J. Greenh. Gas Control* 5, 1002–1015. doi:10.1016/j.ijggc.2010.12.002

Plummer, L. N., and Busenberg, E. (1982). The solubilities of calcite, aragonite and vaterite in CO2-H2O solutions between 0 and 90°C, and an evaluation of the aqueous model for the system CaCO3-CO2-H2O. *Geochimica Cosmochimica Acta* 46, 1011–1040. doi:10.1016/0016-7037(82)90056-4

Plummer, L. N., Wigley, T. M. L., and Parkhurst, D. L. (1978). The kinetics of calcite dissolution in CO2-water systems at 5 degrees to 60 degrees C and 0.0 to 1.0 atm CO2. *Am. J. Sci.* 278, 179–216. doi:10.2475/ajs.278.2.179

Poncet, P. (2006). Finite difference stencils based on particle strength exchange schemes for improvement of vortex methods. *J. Turbul.* 7, N23. doi:10.1080/14685240600595586

Poncet, P. (2007). Analysis of direct three-dimensional parabolic panel methods. *SIAM J. Numer. Analysis* 45, 2259–2297. doi:10.1137/050625849

Poonoosamy, J., Obaied, A., Deissmann, G., Prasianakis, N. I., Kindelmann, M., Wollenhaupt, B., et al. (2023). Microfluidic investigation of pore-size dependency of barite nucleation. *Commun. Chem.* 6, 250. doi:10.1038/s42004-023-01049-3

Quintard, M., and Whitaker, S. (1988). Two-phase flow in heterogeneous porous media: the method of large-scale averaging. *Transp. Porous Media* 3, 357–413. doi:10.1007/BF00233177

Quintard, M., and Whitaker, S. (1993). Transport in ordered and disordered porous media: volume-averaged equations, closure problems, and comparison with experiment. *Chem. Eng. Sci.* 48, 2537–2564. doi:10.1016/0009-2509(93)80266-S

Sanchez, D., Hume, L., Chatelin, R., and Poncet, P. (2019). Analysis of the 3D non-linear Stokes problem coupled to transport-diffusion for shear-thinning heterogeneous microscale flows, applications to digital rock physics and mucociliary clearance. *ESAIM Math. Model. Numer. Analysis* 53, 1083–1124. doi:10.1051/m2an/2019013

Schrader, B., Reboux, S., and Sbalzarini, I. F. (2010). Discretization correction of general integral PSE Operators for particle methods. *J. Comput. Phys.* 229, 4159–4182. doi:10.1016/j.jcp.2010.02.004

[Dataset] Sheppard, A., and Prodanovic, M. (2015). Network generation comparison forum. doi:10.17612/P7059V

Siena, M., Bussetti, G., Recalcati, C., Riva, M., Duò, L., and Guadagnini, A. (2021). Statistical characterization of heterogeneous dissolution rates of calcite from *in situ* and real-time AFM imaging. *Transp. Porous Media* 140, 291–312. doi:10.1007/s11242-021-01624-z

Soulaine, C., Roman, S., Kovscek, A., and Tchelepi, H. A. (2017). Mineral dissolution and wormholing from a pore-scale perspective. *J. Fluid Mech.* 827, 457–483. doi:10.1017/jfm.2017.499

Soulaine, C., Roman, S., Kovscek, A., and Tchelepi, H. A. (2018). Pore-scale modelling of multiphase reactive flow: application to mineral dissolution with production of CO_2. *J. Fluid Mech.* 855, 616–645. doi:10.1017/jfm.2018.655

Starchenko, V. (2022). Pore-scale modeling of mineral growth and nucleation in reactive flow. *Front. Water* 3. doi:10.3389/frwa.2021.800944

Steefel, C. I., Appelo, C. A. J., Arora, B., Jacques, D., Kalbacher, T., Kolditz, O., et al. (2015). Reactive transport codes for subsurface environmental simulation. *Comput. Geosci.* 19, 445–478. doi:10.1007/s10596-014-9443-x

Steefel, C. I., and Lasaga, A. C. (1990). "Evolution of dissolution patterns," in *Chemical Modeling of aqueous systems II (American chemical society), vol. 416 of ACS symposium series*, 212–225. doi:10.1021/bk-1990-0416.ch016

Steefel, C. I., and Lasaga, A. C. (1994). A coupled model for transport of multiple chemical species and kinetic precipitation/dissolution reactions with application to reactive flow in single phase hydrothermal systems. *Am. J. Sci.* 294, 529–592. doi:10.2475/ajs.294.5.529

Stone, J. E., Gohara, D., and Shi, G. (2010). OpenCL: a parallel programming standard for heterogeneous computing systems. *Comput. Sci. and Eng.* 12, 66–73. doi:10.1109/MCSE.2010.69

Strang, G. (1968). On the construction and comparison of difference schemes. *SIAM J. Numer. Analysis* 5, 506–517. doi:10.1137/0705041

Tartakovsky, A. M., Meakin, P., Scheibe, T. D., and Wood, B. D. (2007). A smoothed particle hydrodynamics model for reactive transport and mineral precipitation in porous and fractured porous media. *Water Resour. Res.* 43. doi:10.1029/2005WR004770

Tong, L.-y., Cai, Y., and Liu, Q.-f. (2024). Carbonation modelling of hardened cementitious materials considering pore structure characteristics: a review. *J. Build. Eng.* 96, 110547. doi:10.1016/j.jobe.2024.110547

Turk, M. C., Shi, X., Gonyer, D. A. J., and Roy, D. (2015). Chemical and mechanical aspects of a Co-Cu planarization scheme based on an alkaline slurry formulation. *ECS J. Solid State Sci. Technol.* 5, P88–P99. doi:10.1149/2.0271602jss

Varzina, A., Cizer, O., Yu, L., Liu, S., Jacques, D., and Perko, J. (2020). A new concept for pore-scale precipitation-dissolution modelling in a lattice Boltzmann framework – application to portlandite carbonation. *Appl. Geochem.* 123, 104786. doi:10.1016/j.apgeochem.2020.104786

von Wolff, L., Weinhardt, F., Class, H., Hommel, J., and Rohde, C. (2021). Investigation of crystal growth in enzymatically induced calcite precipitation by micro-fluidic experimental methods and comparison with mathematical modeling. *Transp. Porous Media* 137, 327–343. doi:10.1007/s11242-021-01560-y

Wakao, N., and Smith, J. M. (1962). Diffusion in catalyst pellets. *Chem. Eng. Sci.* 17, 825–834. doi:10.1016/0009-2509(62)87015-8

Wigand, M., Carey, J. W., Schütt, H., Spangenberg, E., and Erzinger, J. (2008). Geochemical effects of CO2 sequestration in sandstones under simulated *in situ* conditions of deep saline aquifers. *Appl. Geochem.* 23, 2735–2745. doi:10.1016/j.apgeochem.2008.06.006

Wolthers, M., Nehrke, G., Gustafsson, J. P., and Van Cappellen, P. (2012). Calcite growth kinetics: modeling the effect of solution stoichiometry. *Geochimica Cosmochimica Acta* 77, 121–134. doi:10.1016/j.gca.2011.11.003

Wood, B. D., Radakovich, K., and Golfier, F. (2007). Effective reaction at a fluid-solid interface: applications to biotransformation in porous media. *Adv. water Resour.* 30, 1630–1647. doi:10.1016/j.advwatres.2006.05.032

Yang, F., Stack, A. G., and Starchenko, V. (2021). Micro-continuum approach for mineral precipitation. *Sci. Rep.* 11, 3495. doi:10.1038/s41598-021-82807-y

Yoreo, J. J. D., and Vekilov, P. G. (2003). *Principles of crystal nucleation and growth*. Berlin: De Gruyter. doi:10.1515/9781501509346-008

frontiers | Frontiers in Earth Science

TYPE Original Research
PUBLISHED 26 March 2025
DOI 10.3389/feart.2025.1516970

OPEN ACCESS

EDITED BY
Weichao Yan,
Ocean University of China, China

REVIEWED BY
Qibin Lin,
University of South China, China
Gang Cheng,
North China Institute of Science and Technology, China

*CORRESPONDENCE
Wulin Lei,
xakjdxwl@163.com

RECEIVED 25 October 2024
ACCEPTED 20 February 2025
PUBLISHED 26 March 2025

CITATION
Lei W, Chai J, Zheng C, Zhao J, Wang S, Liu G, Zhang J and Yang R (2025) Research on the spatiotemporal evolution of deformation and unloading mechanical effects in underlying coal and rock during upper protective layer mining.
Front. Earth Sci. 13:1516970.
doi: 10.3389/feart.2025.1516970

Research on the spatiotemporal evolution of deformation and unloading mechanical effects in underlying coal and rock during upper protective layer mining

Wulin Lei[1]*, Jing Chai[2], Chao Zheng[1], Jian Zhao[1], Siyang Wang[1], Guixian Liu[3], Jufeng Zhang[1] and Rili Yang[1]

[1]School of New Energy, Longdong University, Qingyang, Gansu, China, [2]College of Energy Engineering, Xi'an University of Science and Technology, Xi'an, China, [3]School of Literature and History, Longdong University, Qingyang, Gansu, China

The spatiotemporal rule of pressure release in rock–coal strata within the mining zone serves as the theoretical basis for the prevention and control of dynamic disasters during the mining of the stress-concentration stratum. Taking the mining of the upper protective layer of the Hulusu coal mine located in Ordos City, Inner Mongolia Autonomous Region, China, as the engineering background, this study, based on the theory of elastic–plastic mechanics, investigates the pressure relief mechanics of the underlying coal and rock during the upper protective layer mining. The research is conducted across different scales through rock mechanics experiments, numerical simulations, and on-site industrial experiments. The spatiotemporal evolution of the stress and displacement fields in the underlying coal and rock strata during the upper protective layer mining was simulated and analyzed using the 3-Dimensional Distinct Element Code. Brillouin optical time-domain analysis distributed fiber-optic sensing technology was used to monitor the deformation and unloading dynamic process of different rock–coal strata under the mining floor in real-time. The results indicate that the stress changes in the underlying rock–coal strata during the mining of the upper stress-concentration stratum can be divided into four phases, namely, *in situ* stress, stress concentration, stress release, and stress restoration. Due to the uneven distribution of the waste rock collapse in the mined-out area, stress is alternately distributed in the unloading stable zone, unloading recovery zone, and boosting zone. The mining-induced stress distribution curve in the protected coal seam changes from a U-shape to a W-shape and then to a "WWW"-shape. The stress-relieving effect of upper stress-concentration stratum mining is significant, but the stress-relieving parameters vary depending on time and spatial factors. The research results have important theoretical and practical significance for guiding the layout and key parameter design of stress-concentration stratum mining.

KEYWORDS

upper stress-concentration stratum, stress-relieving effect, rock mechanics tests, numerical simulation, field monitoring

1 Introduction

With the shallow coal resources being depleted, deep coal development has become the norm (Li et al., 2020; Kang et al., 2023; Zhu et al., 2021). However, deep coal resources are affected by high *in situ* stress, which leads to frequent mine dynamic disasters. Thus, the complex stratum environment becomes difficult to predict and control, posing challenges to the safety of working in many mines (Yu et al., 2018; Xu L. et al., 2019; Xie et al., 2019). Mining stress-concentration strata is one of the most economically effective measures for preventing and controlling mining-induced dynamic disasters in many coal seams. It has a wide range of applications in several mines across China (Lei et al., 2024; Liu et al., 2022; Liu et al., 2023). The mining of stress-concentration strata can change the stress distribution within the rock–coal structure, release the elastic energy from strata extrusion, and damage the wall rock structure, effectively preventing and controlling the intensity of dynamic disasters at the source (Shen et al., 2017; Xiao et al., 2019; Li et al., 2021).

In recent years, the frequent occurrence of rockburst disasters in mines has attracted widespread attention from scholars both at home and abroad. Yuan et al. (2024) introduced cloud model theory for the prediction of rockburst intensity levels and ultimately established a comprehensive evaluation model for rockburst intensity based on the BO-XGBoost cloud model. Wang et al. (2024) proposed a backpropagation neural network (BPNN) prediction model based on surface subsidence data to address the frequent occurrence of high-energy microseismic events in coal mines, providing a basis for safe and effective prediction of coal mine disasters. Lv et al. (2024) proposed a new prevention and control method based on hydraulic fracturing and conducted a sensitivity analysis on key parameters such as geostress, roof solidity coefficient, flow increment, and borehole spacing to evaluate their impact on the hydraulic fracturing effect. Yang (2024) successfully used random forest and Mann–Kendall trend testing methods to identify and predict precursor characteristic signals of coal mine rockburst. Mu et al. (2024) used FLAC3D's dynamic module to simulate and analyze the effects of propagation distance, overburden structure in multi-seam mining, and interlayer plastic zones on vibration wave attenuation. Sitao et al. (2021) analyzed the stress changes and energy release laws of the working face advancement and fault zone, revealing the rockburst mechanism under the coupling effect of square and regional structural stresses in the working face. Stress-concentration stratum mining technology was first applied to coal or gas outburst control in France, Germany, Poland, and other countries in 1930 (Cundall PA, 1976; Banerjee, 1987; Blair and Cook, 1998), and it was not until 1980 that it was gradually adopted for controlling the intensity of dynamic disasters such as rockburst (Lan et al., 2016; Jiang and Zhao, 2015). Most scholars believe that the mechanism of stress-concentration stratum mining for controlling dynamic disasters is closely related to factors such as rock–coal structure, rock–coal strata migration, stress distribution in the mining zone, and spatiotemporal effects (Cao et al., 2018; Xuanhong et al., 2024). Li et al. (1997) analyzed the anti-erosion effect and protection parameters of stress-concentration stratum mining in the Huafeng coal mine. Guan et al. (2002) studied the displacement, stress, and other changes in the rock–coal mass during the mining of steeply inclined stress-concentration coal stratum, as well as the extent of the protection range. Zhu et al. (2003) studied the dynamic process and stress-relief range of the development of fracture zones while mining the steeply inclined stress-concentration stratum in the Datai well. Tu et al. (2007) studied the stress distribution characteristics and pressure relief range of the protected layer during long-distance underground mining. Shen et al. (2011) analyzed the feature of stress transfer from lower stress-concentration stratum mining to the deep coal body. Sun et al. (2013) studied the stress variation trait of the rock body on the mining floor using the stress–strain test method. Xiong et al. (2014) divided the protected layer into five zones along the strike direction, namely, compression zone, depressurization expansion zone, depressurization expansion stable zone, depressurization expansion zone, and compression zone. Pang et al. (2016) numerically simulated and studied the elastic zone, velocity, stress, and plastic zone under the influence of the dynamic load disturbance stress of the same strength when the upper protection layer was not mined and after mining. Zhang et al. (2017) researched the development of cracks, stress state, expansion deformation, and changes in permeability characteristics in the protected coal seam. Jiang et al. (2019) proposed stress criteria for impact and large deformation boundaries under different widths of local stress-concentration strata. Tian et al. (2014), Li et al. (2012), Guan et al. (2008), and Gong et al. (2005) studied the dynamic change feature of stress in the rock–coal strata of the bottom plate during the mining process of the stress-concentration stratum through physical simulation experiments and obtained a W-shaped curve characteristic of stress distribution in the protected coal seam along the strike direction under the influence of mining. Xu G. et al. (2019), Chen et al. (2013), and Dai et al. (2013) used numerical simulation software to construct a large three-dimensional ore body. Their findings indicate that the vertical stress in the middle of the mined-out area is superimposed in multiple V-shapes, while the horizontal stress is superimposed in multiple A-shapes. Yuan et al. (2019) used multiple regression analysis to study the protective effect of stress-concentration stratum mining at different interlayer intervals. Fang et al. (2020) researched the stress-relieving range of stress-concentration stratum mining under different dip angles using similarity simulation research methods. Lin et al. (2021) studied that the failure mechanism of the sample is mainly caused by crack propagation in the low-strength layer. Shi et al. (2022) analyzed the relationship between mining height and the stress-relieving effect of the protected coal seam. Chen et al. (2024) researched the impact of long-distance mining of residual coal pillars in the stress-concentration stratum on the recovery of the protected coal seam. Liu et al. (2023) utilized numerical simulation methods to study the stress distribution and evolution rule of wall rock after the mining of upper and lower stress-concentration strata. For a long time, research on stress-concentration stratum mining has mainly focused on the qualitative analysis of coal seam stress relief, gas extraction, and stress changes in the protected coal seam, without considering the dynamic relationship between mining-induced stress in time and space and rarely involving quantitative research on pressure relief parameters.

Therefore, with the Hulusu mine as the research background, by combining 3DEC simulation with BOTDA monitoring, the advantages of both can be fully utilized to achieve complementarity between numerical simulation and real-time monitoring. 3DEC

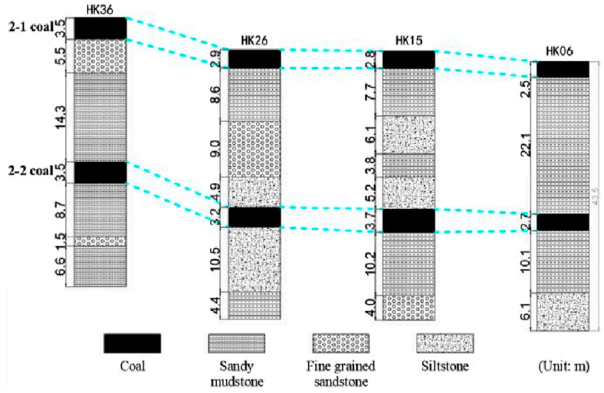

FIGURE 1
Schematic diagram of changes in the distribution of roof and floor rock properties of coal seams 2-2 and 2-1.

simulation can provide theoretical predictions of coal rock deformation and stress distribution, while BOTDA monitoring can verify these predictions and provide real-time deformation data. This combination can significantly improve the accuracy and reliability of coal and rock deformation monitoring, providing a more accurate scientific basis for engineering practice. The spatiotemporal evolution feature of the stress zone and displacement field of the underlying rock–coal strata during upper stress-concentration stratum mining is studied. On this basis, the spatiotemporal relationship of the stress-relieving effect of the protected coal seam is explored. Parameters such as pressure relief angle, depth, and range are obtained. The research results contribute to a systematical understanding the influence of coal seam occurrence conditions on the protective effect of protective layer mining, providing a theoretical and scientific basis and technical guidance for the scientific and reasonable development layout design of close-range coal seam groups in rockburst-induced mines. It is of great significance for improving the safety of protective layer mining design and refining the theory of protective layer mining, and preventing and controlling rockburst disasters in the Hulusu mine and surrounding areas.

2 Overview of mines

The Hulusu coal mine in Inner Mongolia is selected as the experimental mine. The 2-1 coal seam and 2-2 coal seam in this mine have a strong impact tendency, with average thicknesses of 2.5 m and 3.9 m, respectively, average burial depths of approximately 639 m and 658 m, respectively, and an average inclination angle of 2°. The interlayer lithology of the two layers of coal is mainly composed of sandy mudstone, fine-grained sandstone, and siltstone, all of which have a weak impact tendency, with a spacing range of 19.19 m–23.73 m, as shown in Figure 1. The upper 2-1 coal seam was mined first, followed by the lower 2-2 coal seam. Therefore, mining the 2-1 coal seam would release some concentrated stress above the 2-2 coal seam, allowing us to define the 2-1 coal seam as the stress-concentration stratum for the 2-2 coal seam.

The experimental work zone mainly mines the 2-1 coal seam, with a strike length of 3,015 m, a dip length of 320 m, and a mining height of 3.9 m. The work zone advances eight times a day, with each cut of 0.8 m and a daily pushing progress of 6.4 m. The monthly effective working days are 27.5 days, and the monthly pushing progress is 190.3 m. The service life is 17.4 months. The mining method is the longwall backward mining method. In addition, the entire collapse method is used to treat the roof of the mined-out area.

3 Rock–coal stratum physical and mechanical parameter testing

The coal samples used in the test were taken from the heading face of the 2-2 coal seam in the Hulusu coal mine, with a buried depth of approximately 660 m and a coal seam thickness of approximately 3.86 m. The collected coal samples were sealed with plastic film and plastic foam to prevent the coal and rock from breaking during transportation. The coal sample is black in color, with brownish-black stripes, stepped fractures, and layered structures. The macroscopic coal rock composition is mainly composed of bright coal, followed by dark coal and visible filamentous coal. The organic microscopic components of coal samples are mainly composed of inertinite and vitrinite, with a small amount of shell.

According to the "method for determining the physical and mechanical properties of coal and rock," the test specimens are processed into standard cylindrical specimens with a diameter of 50 mm and a height of 100 mm after drilling, sawing, and grinding processes. The test piece must ensure that both ends are parallel, smooth, and free of significant scratches. The parallelism of the two end faces should be less than 0.02 mm, the flatness should be less than 0.5 mm, and the diameter deviation should be less than 0.02 mm. The processing accuracy of the test piece must meet the requirements of the national standard for rock mechanics testing. The apparent density of rock–coal mass was measured using electronic tray scales, Vernier calipers, and other equipment, with the average value obtained from multiple measurements. A microcomputer-controlled electronic universal testing machine was used to determine mechanical parameters such as rock and coal strength, friction angle, cohesion, and Poisson's ratio. The parameters are shown in Table 1.

4 Model establishment and excavation

The numerical simulation software 3DEC is a three-dimensional discrete element method program that can simulate the discontinuous discrete characteristics of surrounding rocks in goaf areas. It can realistically achieve failure phenomena such as mutual shear and displacement or detachment of overlying rocks in goaf areas, making the collapse of gangue in goaf areas cause discontinuous deformation of the underlying coal rock mass under stress, and can more realistically simulate the stress recovery process of the underlying coal rock mass in goaf areas. However, 3DEC needs to simplify the complex coal rock geological structure into a collection of blocks and assume the interaction relationships

10.3389/feart.2025.1516970

TABLE 1 Physical and mechanical parameters of rock and coal.

Category	Bulk density /kg·m^{-3}	Unidirectional compressive strength/MPa	Unidirectional tensile strength/MPa	Elastic modulus /GPa	Poisson's ratio	Adhesive strength /MPa	Internal friction angle/°
2–1 coal roof	2,386	33.73	4.24	9.81	0.18	5.5	38
2-1 coal	1,260	12.97	1.22	2.29	0.29	2.3	40
2-1 coal floor	2,501	38.31	6.15	15.05	0.24	10.9	25
2–2 coal roof	2,297	15.87	2.42	7.91	0.25	3.0	40
2-2 coal	1,269	14.67	1.21	2.63	0.259	3.1	38
2-2 coal floor	2,500	28.42	7.43	24.3	0.26	7.2	36

between blocks during numerical simulation calculations. The dynamic transmission mode of stress between the collapsed gangue and the top and bottom shale layers in the goaf is also different from that in the field, which will have a certain impact on the research results. Therefore, by taking measures such as optimizing model construction, setting reasonable physical and mechanical parameters of coal and rock masses, and optimizing calculation settings, the accuracy and reliability of 3DEC simulation can be significantly improved.

Therefore, this article adopts 3DEC simulation to simulate the full cycle process of pressure relief of the protected 2-2 coal seam under the influence of upper stress-concentration stratum (2-1 coal seam) mining. The two coal mining faces of 2-1 seam are named 1# and 2#, respectively. Based on the boundary effect of the model and a reasonable calculation time, the model dimensions are 1,200 m long, 600 m wide, and 325 m high. A coal pillar of 100 m is left at each boundary, with an excavation length of 10,000 m. A total of 30 layers of rock are formed, with a cumulative thickness of 325 m, as shown in Figure 2. Model displacement boundary conditions: displacement boundaries are used in the x-direction of the model to restrict displacement in the x-direction. Displacement boundaries are used in the y-direction to limit the displacement in the y-direction. Displacement boundaries at the bottom boundary of the model are used to limit the displacement in the z-direction. The upper boundary of the model adopts a free boundary, first simulating some overlying rock layers and then simplifying the overlying rock mass of the mined coal seam into a uniformly distributed load applied to the upper boundary instead of the gravity of the overlying rock, resulting in vertical stress. A certain gradient of horizontal stress on both sides of the model is applied, and fixed boundaries are used. The maximum initial vertical principal stress is 17.58 Mpa in the model, and the maximum initial horizontal principal stress is 21.09 Mpa. In addition, the stress coefficient is 1.1–1.3. Before excavating the model, all node displacements were reset to 0. The work zone is 320 m long, with a mining height of 7.5 m. Each excavation is 5 m, with a total of 200 excavations and a total advance length of 1,000 m.

5 Analysis of the deformation rule of rock–coal strata in the mining zone

5.1 Stress variation rule

According to the simulation results, a profile was taken along the strike direction of advancement in the middle of the 1# coal mining face of the upper stress-concentration stratum (2-1 coal seam). In addition, the stress distribution rule of the wall rock in the mining zone was obtained, as shown in Figure 3. When the moving forward distance of the work zone is between 30 m and 90 m, stress-concentration occurs in the rock–coal strata before and after the mining zone, and the distribution position is relatively fixed. There is a phenomenon of stress reduction in the mined-out area, and as the work zone advances, the range of stress reduction continues to expand and gradually decreases toward the middle of the mined-out area. When the moving forward distance of the work zone is 120 m, stress recovery occurs in the unloading zone. As the degree and range of stress recovery continue to increase, some

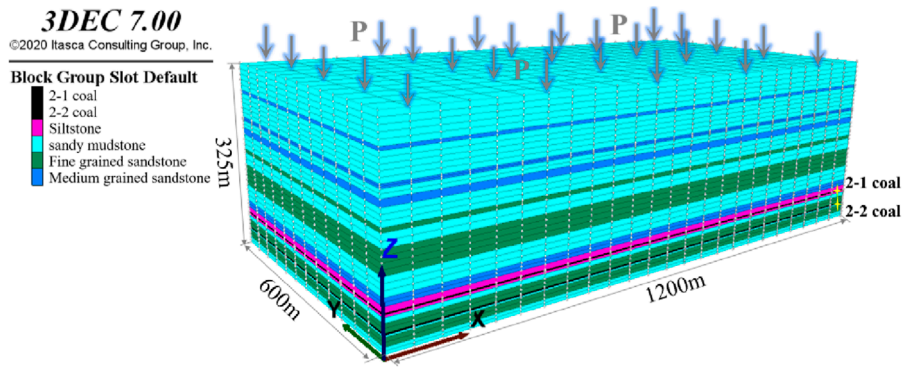

FIGURE 2
Schematic diagram of the numerical model of three-dimensional geological structure of a mine.

zones begin to change from the unloading zone to the boosting zone. When the moving forward distance of the work zone is 200 m, the stress-relieving zone is completely separated, transforming from one pressure relief zone to two pressure relief zones and one pressure relief zone. This is due to the uneven collapse of the mined-out area, which results in the formation of compacted and non-compacted waste rock zones, indicating that the stress relief effect of mining the stress-concentration stratum (2-1 coal seam) mining is time-dependent. When the moving forward distance of the work zone is 240 m, the mining reaches a fully mined state. In addition, the vertical influence range of the stress-relieving zone reaches its maximum value. At this time, the maximum depth of pressure relief reaches 32.8 m, and the distance between the maximum depth of the stress-relief zone and the work zone is 35.5 m. When the moving forward distance of the work zone is 280 m, a total of four pressure relief zones and three pressure-boosting zones are formed in the mined-out area, and they are alternately distributed.

Along the variation of the strike, after the mining of the work zone is completed, a total of 16 pressure relief zones and 17 pressure-boosting zones are formed in the mining zone. The maximum range and degree of pressure relief are located on both sides of the mined-out area, with the lowest degree of pressure relief in the middle of the mined-out area. The range and degree of pressure relief of the roof strata are larger than those of the floor strata. In addition, the stress-relieving effect gradually weakens from the mined-out area in both upward and downward directions, as shown in Figure 4A. In the dip direction, there are a total of five unloading zones and six boosting zones formed in the 1# coal mining face and four unloading zones and five boosting zones formed in the 2# coal mining face. This is because the stress-relieving zone on the coal pillar side of the 1# coal mining face is affected by the mining of the 2# coal mining face. In addition, the stress in the stress-relieving zone is restored, transforming from one pressure relief zone to two pressure relief zones and one pressure-boosting zone. The 30-m width of the coal pillar between the two working faces causes the maximum compressive stress peak to appear at the position of the coal pillar. In addition, the stress is significantly concentrated. The compressive stress is transmitted to the lower part of the bottom plate, causing the 2-2 protected coal seam below the coal pillar to become a pressurized zone. The risk of dynamic disasters in this zone is relatively high, as shown in Figure 4B.

5.2 Displacement variation rule

The displacement variation rule of the rock–coal strata in the mining zone along the strike direction is shown in Figure 5A. The roof collapse of the mined-out area is uneven, with the alternating distribution of fully collapsed and compacted zones and non-fully collapsed zones, resulting in different compression deformation effects of collapsed waste rock on the bottom plate, which leads to inconsistent recovery of bottom plate deformation within the mined-out area range. The maximum sinking amount of the mined-out area roof is 2.51 m. In addition, the maximum floor heave is 0.258 m. The bottom plate in the fully collapsed zone is subjected to significant compression deformation. The deformation of the floor bulge in the intermediate position of the mined-out area is significantly restored. The bottom plate in the zone with insufficient collapse is less affected by compression deformation, and the deformation recovery of the bottom bulge on both sides of the mined-out area is weaker. The displacement variation rule of rock–coal strata in the dip direction mining zone is shown in Figure 5B. The displacement changes in the mined-out area are symmetrically distributed, with a small sinking amount of displacement of the roof on both sides and a large sinking amount of the middle roof. The displacement characteristics of the roof and floor of the two working faces are basically the same, but the displacement of the roof and floor of the 2# coal mining face is significantly larger than that of the 1# coal mining face after mining. In addition, the 30-m-wide coal pillar undergoes compression and deformation, causing regional stress concentration and the propagation of compressive stress to the bottom plate. This, in turn, results in stress concentration in the protected coal seam directly beneath the coal pillar.

6 Mechanical analysis of the rule of pressure relief under protection

To quantitatively analyze the stress variation rule of the 2-2 protected coal seam after stress-concentration stratum mining (2-1 coal seam), 241 measuring points were set up along the strike direction of the protected coal seam to quantitatively analyze the

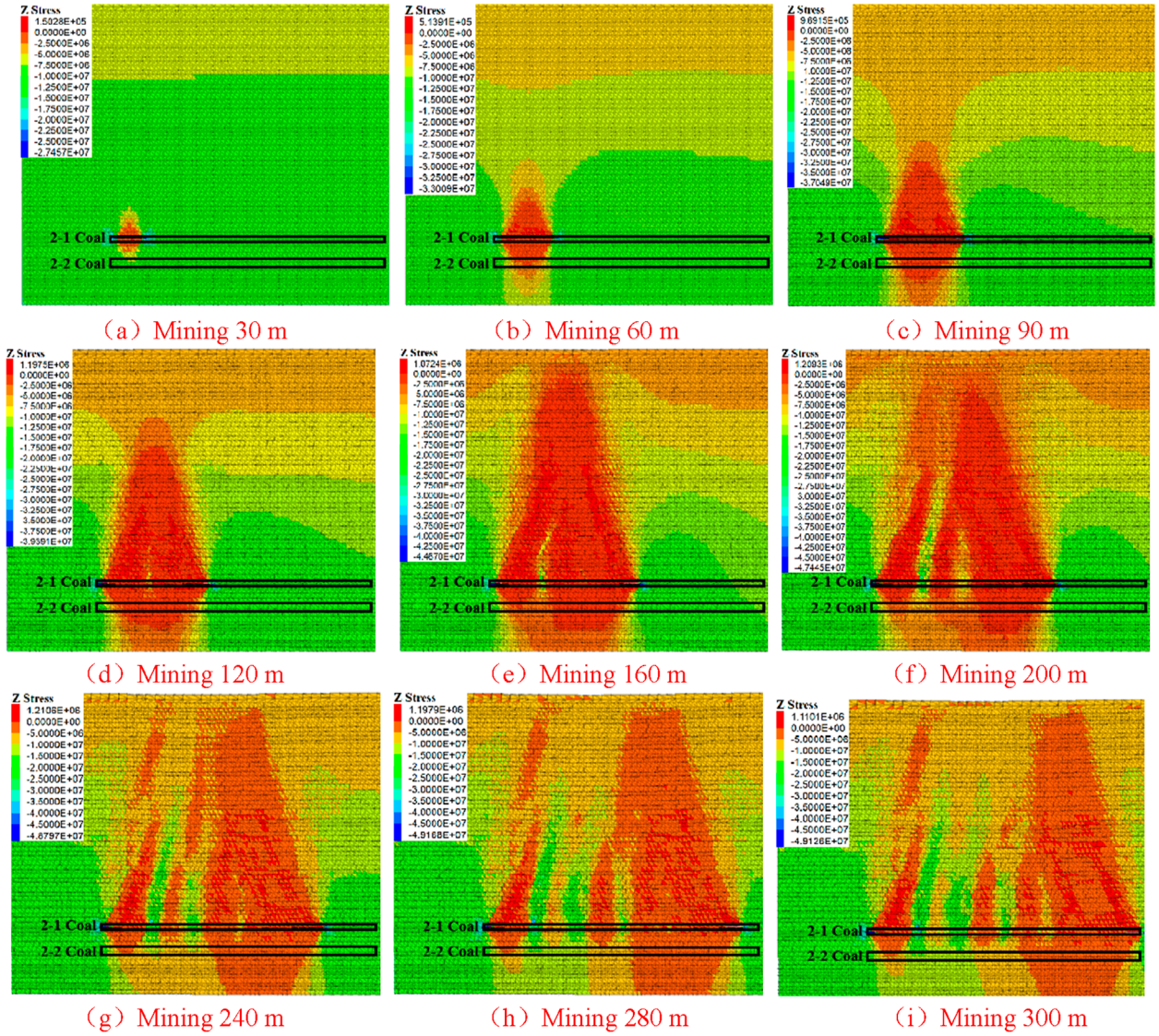

FIGURE 3
Stress distribution in the mining area during the mining process of the upper protective layer 2-1 coal and stress variation cloud map of the protected 2-2 coal: **(A)** mining 30 m, **(B)** mining 60 m **(C)** mining 90 m, **(D)** mining 120 m, **(E)** mining 160 m, **(F)** mining 200 m, **(G)** mining 240 m, **(H)** mining 280 m, and **(I)** mining 300 m.

stress variation rule of the 2-2 coal seam during the 2-1 coal seam mining process. The vertical compressive stress is positive, while the tensile stress is negative. The compression deformation of vertical displacement is negative, while the expansion deformation is positive.

6.1 Distribution rule of induced stress

With the mining of the upper stress-concentration stratum (2-1 coal seam), the strain change curve of the protected coal seam (2-2 coal seam) can be divided into three parts, namely, the stress increase zone, the stress decrease zone, and the *in situ* stress zone. When the moving forward distance of the work zone is 10 m, the stress-relieving effect of the protected coal seam begins to emerge, and as the work zone advances, the stress-relieving effect becomes more and more significant. When the moving forward distance of the work zone is 80 m, the first minimum stress peak of the protected coal seam is 1.29 MPa, and the step distance of the first unloading peak is 80 m. As the work zone continues to advance, the peak value of the minimum stress moves forward along the strike direction and begins to increase. This is because the stress in the unloading zone gradually recovers due to the stress disturbance of the collapse of the overburden in the mined-out area, indicating that the unloading of the stress-concentration stratum is time-dependent. When the moving forward distance of the work zone is 140 m, some stress in the unloading zone has been restored to the *in situ* stress or high-stress state, and the unloading zone has transformed into a stable or pressurized unloading zone. The initial unloading recovery step distance is 140 m. When the moving

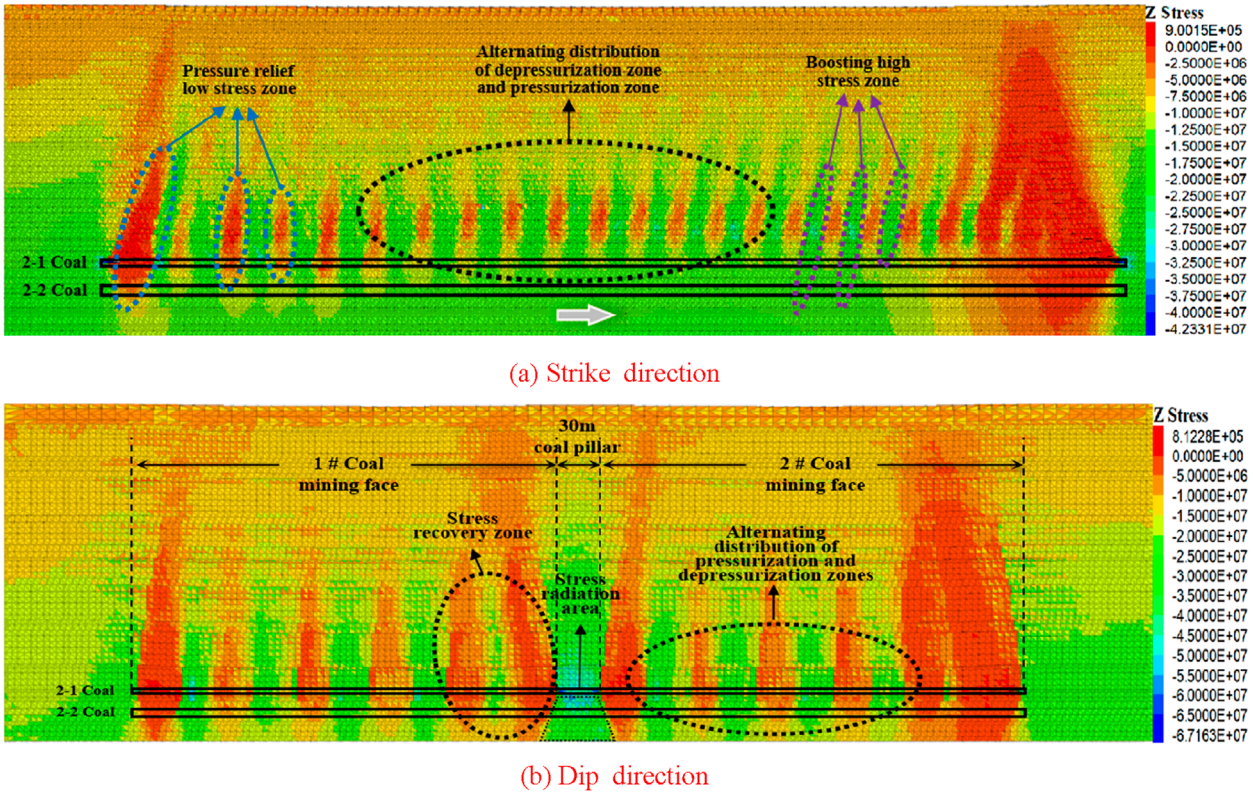

FIGURE 4
Visualization cloud diagram of stress distribution in the mining area after the completion of the mining of the 1 # and 2 # working faces of the upper protective layer 2-1 coal: **(A)** strike direction and **(B)** dip direction.

forward distance of the work zone is 200 m, the third minimum stress peak appears in the protected coal seam, and the step distance of the unloading peak is 60 m. When the moving forward distance of the work zone is 210 m, the distance from the unloading zone to the boosting zone for the second time is 70 m, and the recovery distances for the two unloading zones are 140 m and 70 m, respectively. Therefore, the reasonable unloading distance should be less than 70 m, and the unloading protection effect is most significant. As the work zone moves forward, the stress-relieving zone continuously moves forward along the strike direction of advancement, and the stress in the protected coal seam undergoes dynamic processes of initial increasing, gradually decreasing, then increasing, and recovering. When the mining range of the stress-concentration stratum is small, the vertical stress distribution curve of the protected coal seam takes on a U-shape. As the mining range of the stress-concentration stratum gradually increases, the vertical stress distribution curve gradually changes from a U-shape to a W-shape. As the mining space further increases, the vertical stress distribution curve changes from a W-shape to a "WWW"-shape, as shown in Figure 6.

According to the stress variation rule of coal in the 2-2 protected coal seam, parameters such as the initial unloading peak step distance, periodic unloading peak step distance, and unloading recovery step distance can be obtained when the protection layer mining reaches the maximum unloading effect. For details, please refer to Table 2.

The quantitative analysis of the stress changes of the protected coal seam (2-2 coal seam) is shown in Figure 7. The red zone in the figure represents the pressurization zone, the green zone represents the depressurization zone, and the blue zone represents the fully depressurized zone. If the stress release rate exceeds 10%, serving as the unloading index, the unloading angles of the protected coal seam along the direction of the strike are 79.1° and 80.2°, and the cumulative range of the unloading zone of the protected coal seam is 555 m, accounting for 55.4% of the mined-out area range. The unloading angles of the protected coal seam in the dip-inclined direction after mining at the 1# coal mining face are 59.5° and 70.3°, and the cumulative range of the unloading zone is 112.8 m, accounting for 35.2% of the mined-out area range. The stress-relieving angles of the protected coal seam in the dip direction after mining at the 2# coal mining face are 73.6° and 69.7°, and the cumulative pressure relief range in the mined-out area is 147.9 m, accounting for 46.1% of the mined-out area range.

6.2 Mining-induced stress path effect

Through an in-depth analysis of the mining stress rule of the protected coal seam, the mining stress can be divided into two categories. The first category is any point on the boundary of the mined-out area, and the entire process of stress change at that point can be divided into four phases, as shown in Figure 8A. The

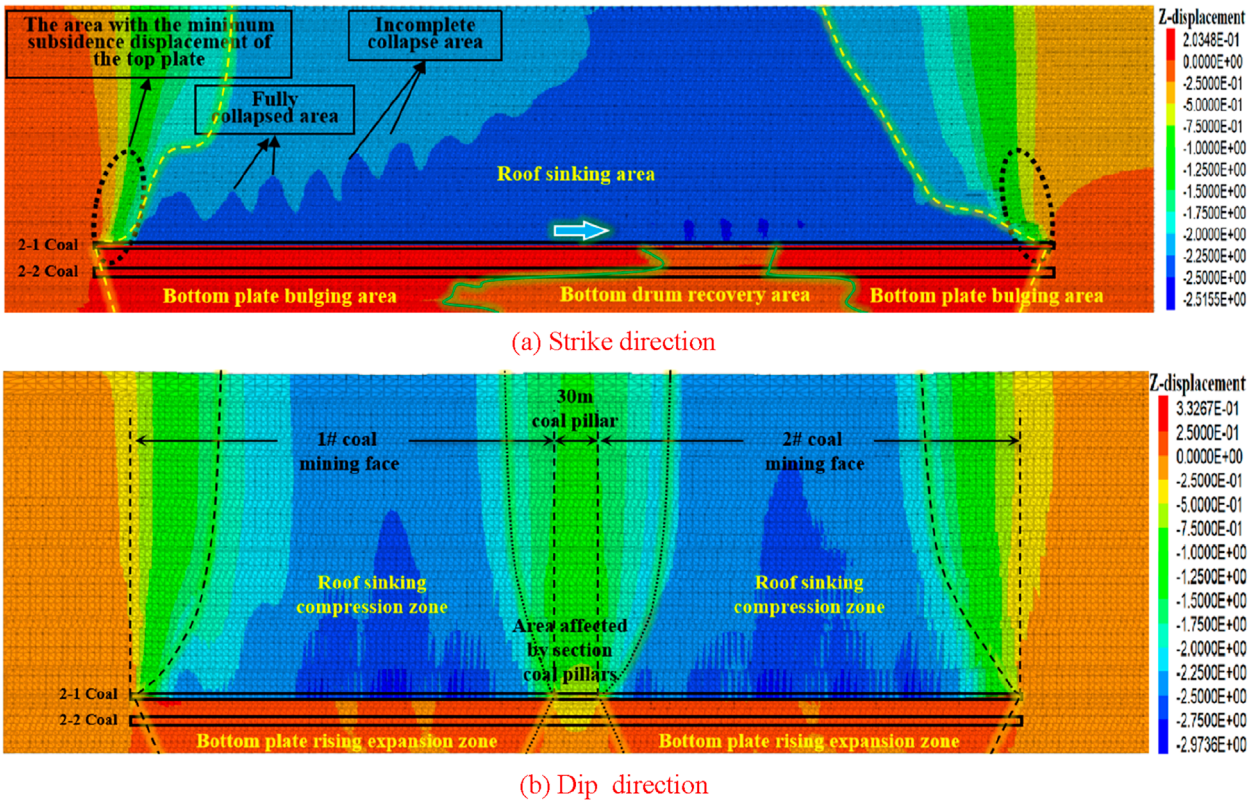

FIGURE 5
Visualization cloud diagram of displacement distribution in the mining area after the completion of the mining of the 1 # and 2 # working faces of the upper protective layer 2-1 coal: **(A)** strike direction and **(B)** dip direction.

OB area is a low-stress phase, located below the coal wall of the work zone in the early phase of mining. Due to the short mining distance, the stress concentration in the mining zone is low, and the stress transmitted to the 2-2 coal seam (the protected coal seam) is also low. Point A is the maximum stress peak. The BC area is in the phase of stress relief development. After the work zone passes through this point, it is located below the mined-out area. As the work zone moves forward, the stress continuously decreases. Point C is the minimum stress peak, indicating the most optimal time and space state for stress relief. Due to its location at the boundary of the mined-out area, the roof collapse of the mined-out area is insufficient, and the degree of stress relief recovery is relatively low. The DE area is the phase of stress relief and stability. Due to the stable deformation of the wall rock in the mined-out area, the stress at this point remains basically stable as the work zone advances. As shown in Figure 8B, the second type is any point in the middle of the mined-out area, and the entire process of stress change at that point can also be divided into four phases. Stage OB is the phase of high stress, and mining is more thorough due to the distance from the cutting eye. Therefore, the changing process of stress can be divided into three parts, namely, unaffected in the initial phase, slow growth in the middle phase, and rapid decline in the later phase. The BC area is in the phase of stress relief development, so the stress in the mining zone transfers to both sides of the mined-out area, resulting in a continuous decrease. The CD area is in the phase of full stress recovery, characterized by a large mining space and significant collapse of the overlying strata. The mined-out area is gradually filled and compacted by waste rock, so the basic top rotation deformation contacts the waste rock. The geostatic stress of the overburden is applied to the bottom rock stratum, and the stress of the protected coal seam is fully restored. At point D, the vertical stress foundation quickly recovers to the level of the *in situ* stress, or at point D1, the vertical stress exceeds the *in situ* stress. The DE phase is the stable phase of stress relief.

6.3 Evolution rule of mining-induced stress and displacement

There are some internal relationships between displacement field variation and stress field characteristics of the protected coal seam (2-2 coal seam) during the mining process of the upper stress-concentration stratum (2-1 coal seam). Along the variation of the strike, the peak position of the displacement curve can correspond to the valley position of the stress curve, and the valley position of the displacement curve can correspond to the peak position of the stress curve, indicating that the greater the displacement of the protected coal seam, the more severe its expansion deformation, so the better the stress-relieving effect. The smaller the displacement of the protected coal seam, the smoother its expansion deformation, resulting in a weaker stress-relieving effect, as shown in Figure 9A. In dip inclination, the relationship

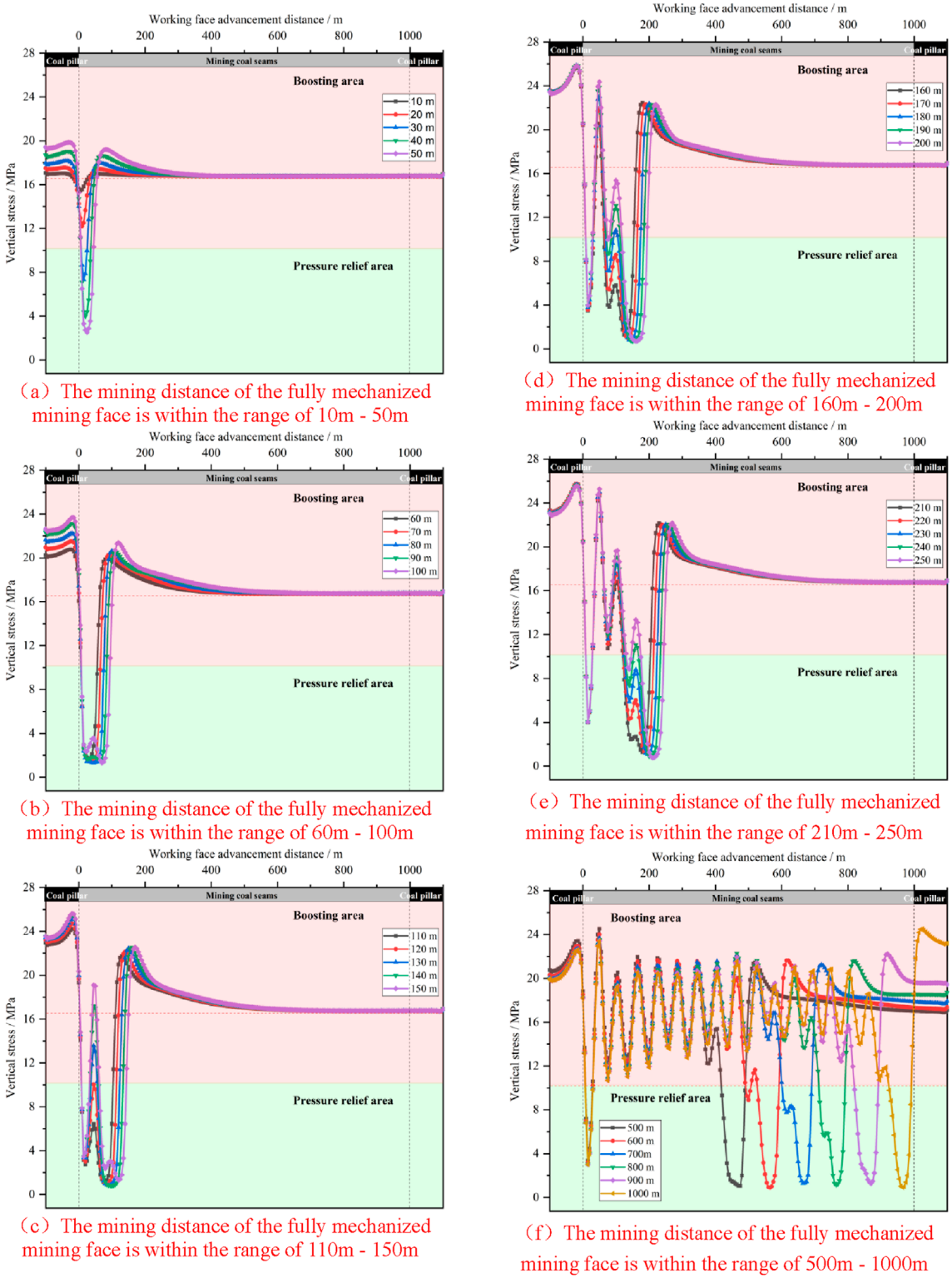

FIGURE 6
Stress variation pattern of coal in the lower protective layer 2-2 during the mining process of the upper protective layer 2-1. **(A)** The mining distance of the fully mechanized mining face is within the range of 10 m–50 m. **(B)** The mining distance of the fully mechanized mining face is within the range of 60 m–100 m. **(C)** The mining distance of the fully mechanized mining face is within the range of 110 m–150 m. **(D)** The mining distance of the fully mechanized mining face is within the range of 160 m–200 m. **(E)** The mining distance of the fully mechanized mining face is within the range of 210 m–250 m. **(F)** The mining distance of the fully mechanized mining face is within the range of 500 m–1,000 m.

TABLE 2 Parameters related to the pressure relief of stress-concentration stratum.

Classification	Parameter/m
Peak step distance for initial pressure relief	80
Peak step distance for periodic pressure relief	60~80
Recovery step distance for initial pressure relief	140
Recovery step distance for periodic pressure relief	70~80

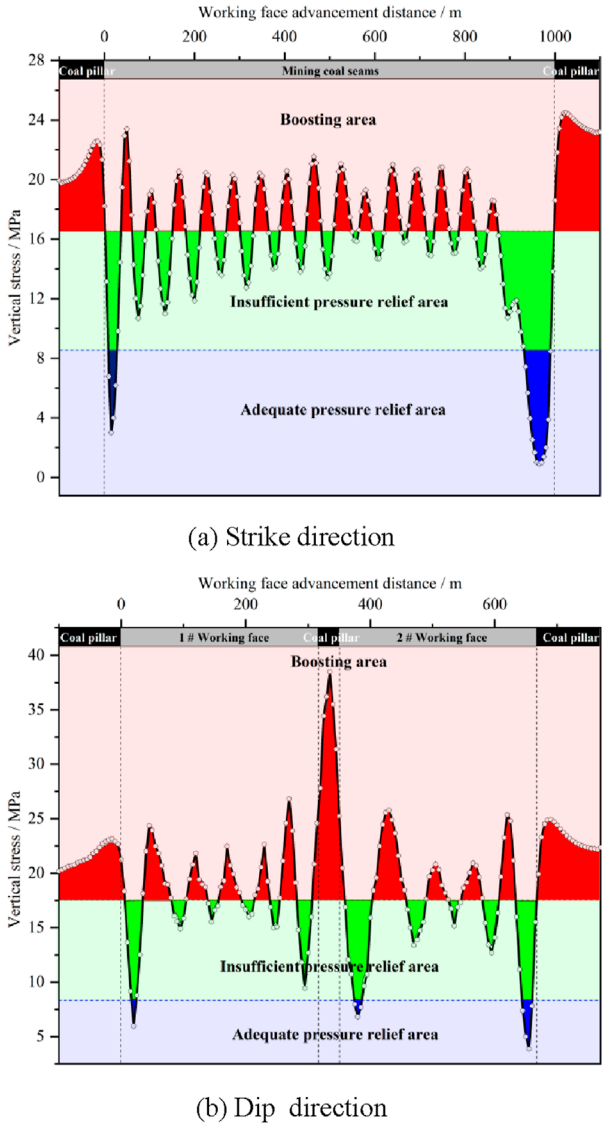

FIGURE 7
Distribution pattern of the depressurization and pressurization zones of 2-2 coal in the protected layer during the mining process of the upper protective layer: **(A)** strike direction and **(B)** dip direction.

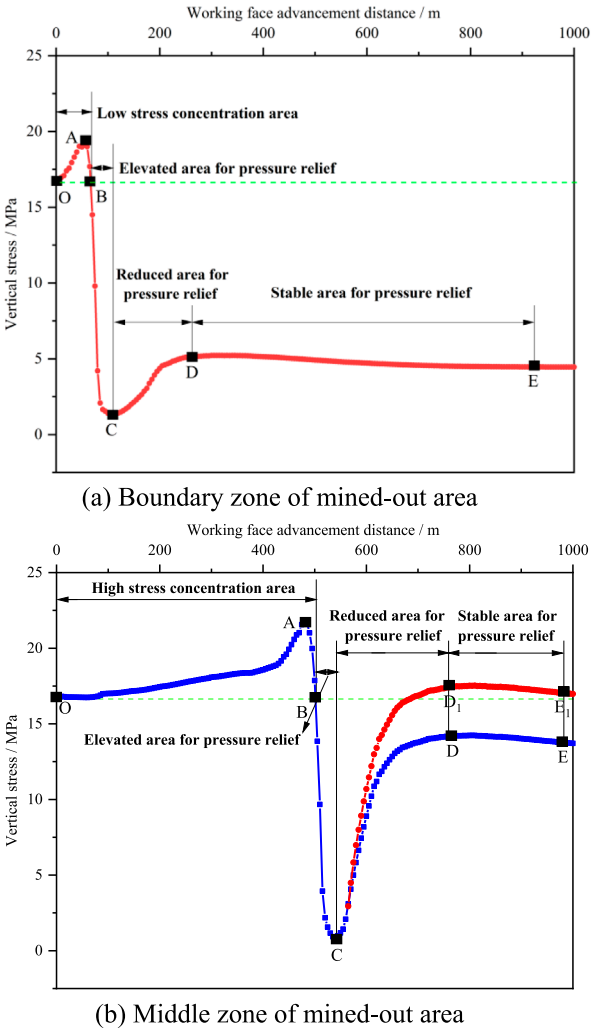

FIGURE 8
Schematic diagram of the entire process curve of mining stress for the protected layer 2-2 coal: **(A)** boundary zone of mine and **(B)** middle zone of the mined-out area.

between the displacement field and stress field changes is basically consistent with the direction of the strike. The displacement at the coal pillar reaches its minimum peak, while the stress reaches its maximum peak. The stress field and displacement field change amplitude are the largest in the zone affected by the coal pillar, as shown in Figure 9B.

7 Engineering measurement

The on-site monitoring of the mine adopts distributed fiber-optic sensing technology and Brillouin optical time-domain analysis technology based on stimulated Brillouin scattering. The spatial resolution is 5 cm, the sampling interval is 1 cm, and the testing range is 95.37 m in direction, 128.47 m in inclination, and 36.94 m in vertical direction. Three boreholes, namely, 1 #, 2 #, and 3 #, were drilled toward the bottom plate of the main transportation roadway in the 21104 working face. The azimuth angle of borehole

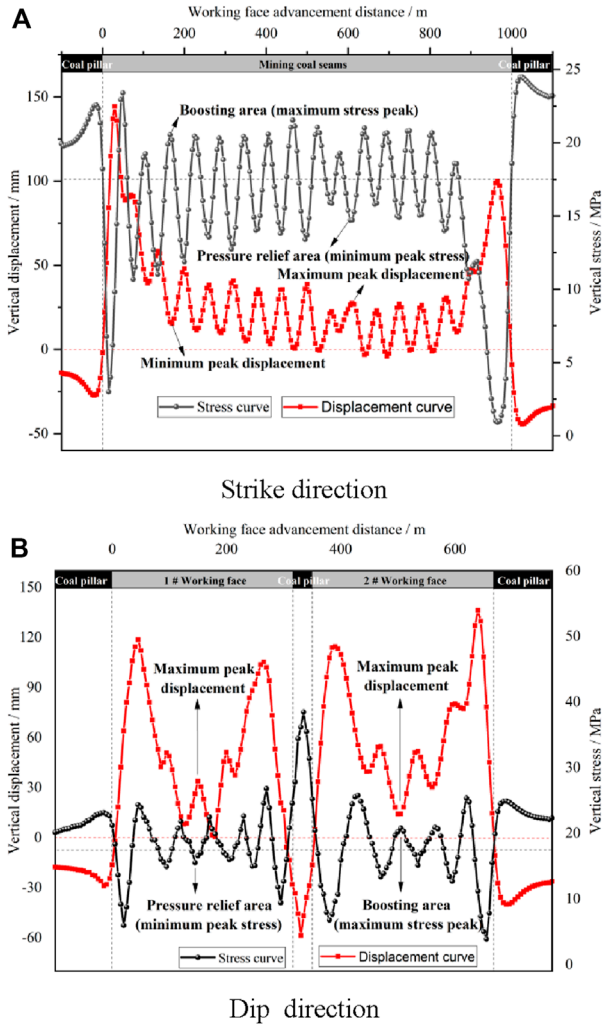

FIGURE 9
Comparison diagram of the changes in the mining stress and displacement of the protected layer 2-2 coal during the mining process of the upper protective layer. **(A)** Strike direction. **(B)** Dip direction.

1 # is 270°, the inclination angle is 15°, and the borehole length is 133.00 m. The azimuth angle of hole 2 is 270°, the inclination angle is 45°, and the hole length is 37.00 m. The azimuth angle of hole 3 is 200°, the inclination angle is 20°, and the hole length is 108.00 m. Fiber optic cables are implanted in the borehole, and metal-based cable-shaped optical cables are used as fiber optic sensors, which have superior tensile performance and good coupling with rock layers. The installation process of the fiber optic monitoring system consists of four steps, namely, fiber optic hole positioning and construction, fiber optic sensor implantation drilling, fiber optic hole grouting, and monitoring system connection. The fiber optic implantation method adopts the coupling method of drilling and grouting throughout the entire section, the spatial positioning adopts the micro-bending event method, and the data denoising processing adopts the wavelet threshold method. As the working face advances, data are continuously collected and analyzed until the mining impact range moves beyond the fiber-optic sensor or the deformation of the surrounding rock stabilizes. In other words, the fiber-optic sensor strain data remain stable and unchanged, marking the end of monitoring. (Figure 10)

Lei et al. (2022) conducted a real-time analysis on the stress data of the underlying rock–coal strata during the mining process of the upper stress-concentration stratum (2-1 coal seam) in the Hulusu mine. The results show that the maximum unloading depth along the direction of the strike is 28.4 m, and the length between the maximum unloading depth location and the horizontal distance of the work zone is approximately 38.5 m–40.5 m. The unloading lag distance of the protected coal seam is 14.3 m. The unloading angle of the protected coal seam along the direction of the strike is 63.6°, which is 58.7° in the dip direction. The unloading ratio of the protected coal seam along the direction of the strike is 63.4%–84.7%, which is 43.5%–63.4% in the dip direction. The numerical calculation and engineering measurement results of the stress-relieving parameters for the upper stress-concentration stratum mining are shown in Table 3, and the trend of parameter changes is basically consistent. However, the numerical simulation analysis shows a larger stress-relieving angle than that of engineering measurements, and the results of the stress-relieving ratio and pressure relief lag distance are smaller than those measured in engineering. This discrepancy arises because numerical simulations account for the deformation of the rock–coal strata in the mining zone more comprehensively.

8 Discussion

In order to compare and observe the stress change pattern of 2-2 coal throughout the whole mining process, 20 stress change curves were plotted at intervals of 50 m for different advance distances, with the trough representing the pressure relief area and the peak representing the pressure increase area, as shown in Figure 11. As shown in the figure, the depressurization and pressurization zones are alternately distributed in the goaf, and the depressurization zone shows an uneven distribution pattern. As the working face advances along the direction of the strike, the pressure relief zone continuously moves forward along the direction of the strike, and the pressurization zone in front of the coal wall gradually transforms into the pressure relief zone. The working face continues to advance, with a portion of the pressure relief zone transforming into a pressure-boosting zone, while the degree of pressure relief in the other portion decreases. The pressure relief range of the entire mining process continues to increase, and the maximum pressure relief zone is always located on the side of the goaf near the coal wall.

A comparative analysis was performed to study the stress and strain changes during the 2-2 coal and 2-1 coal mining process. During the mining of 2-2 coal, the large cycle weighting step distance of the working face is shorter than that of 2-1 coal, which indicates that the mining of the 2-2 coal working face is affected by the pressure relief of 2-1 coal. Furthermore, the mining of 2-1 coal has weakened the overburden structure, reducing the limit span of the suspended roof in the key thick sandstone stratum. The large period weighting strength of the working face during the mining of the 2-2 coal seam is lower than that of the 2-1 coal seam, which indicates that 2-2 coal is located in the lower part of the goaf

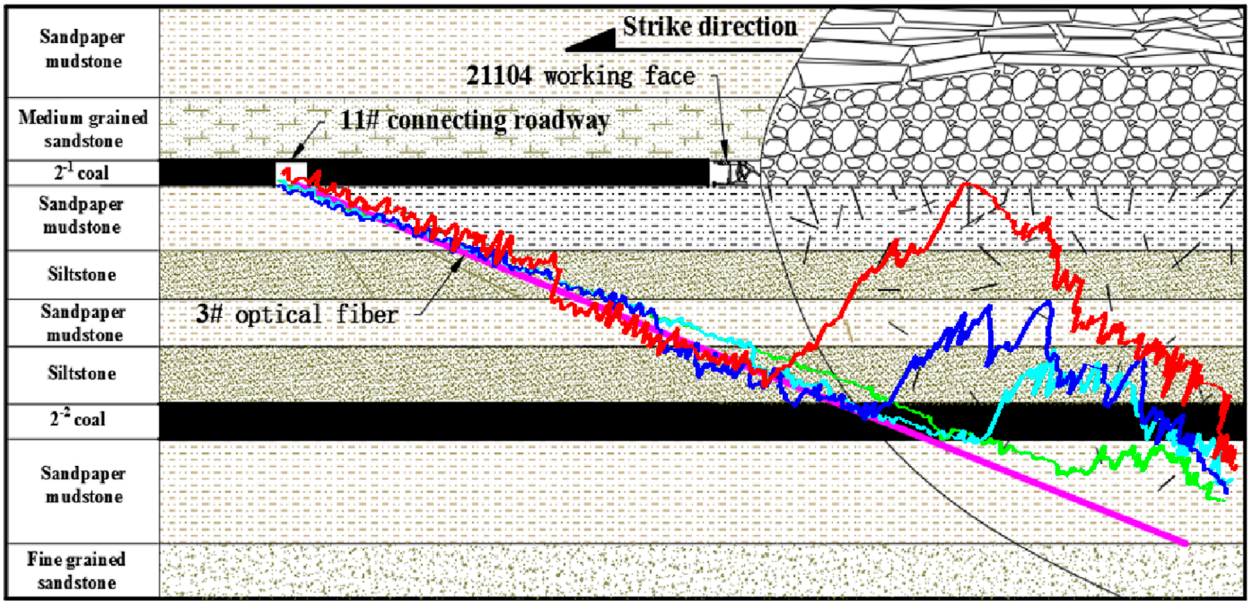

FIGURE 10
Schematic diagram of changes in the lower coal and rock mass during the mining process of the upper protective layer monitored by distributed fiber-optic sensing technology.

TABLE 3 Comparison of pressure relief parameters during upper stress-concentration stratum mining.

Classification	Numerical calculation	Engineering measurement
Stress-relieving angle of the protected coal seam along the direction of the strike/°	79.1–80.2	63.6
Stress-relieving angle of the protected coal seam in the dip direction/°	59.5–70.3	58.7
Proportion of the pressure relief of the protected coal seam along the direction of the strike/%	55.4	63.4–84.7
Proportion of the pressure relief of the protected coal seam in the dip direction/%	35.2–46.1	43.5–63.4
Stress-relieving hysteresis distance of the protected coal seam/m	10.0	14.3
Maximum depth of stress relief/m	32.8	28.4
Maximum depth of stress relief and distance from the work zone/m	35.5	38.5–40.5

during mining, making it easier for the goaf to be quickly filled. The breaking rotation space of the key thick sandstone stratum is reduced, and the breaking distance is shortened, so the energy released during the weighting of the working face is weakened. The results show that during the mining process of the protected layer, the degree of deformation caused by the collapse of the overlying rock is reduced, and the distance of the overlying rock roof and key thick sandstone layers from the hanging roof is reduced. The cyclic compression step distance and strength of the working face are also reduced, indicating that is the energy released by the rock layer fracture is reduced. Due to the uneven collapse of gangue in the goaf after the mining of the upper protective layer, the fully collapsed compacted area and the partially collapsed compacted area are alternately distributed, resulting in inconsistent strain recovery in the goaf and uneven distribution of underlying coal and rock unloading pressure. The unloading zone, stress recovery zone, and pressure-boosting zone are alternately distributed in the goaf. The research results provide a certain theoretical and scientific basis and technical guidance for the scientific and rational development and layout of close-range coal seam groups in mines, which has

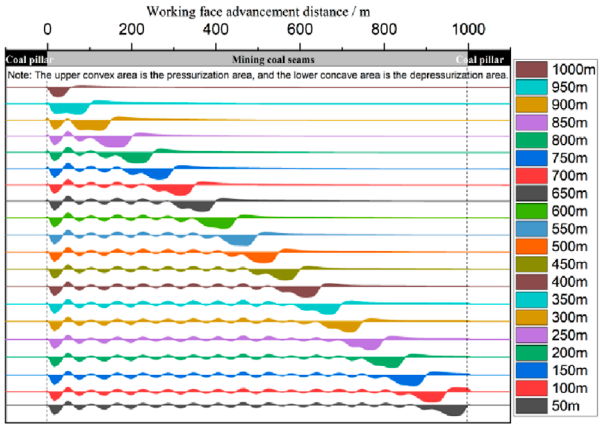

FIGURE 11
Schematic diagram of the dynamic evolution law of the vertical stress distribution in the direction of the protected layer 2-2 coal during the mining process of the upper protective layer.

important practical significance for the prevention and control of rockburst disasters in protective layer mining.

Fiber-optic sensing technology has enabled real-time monitoring of the pressure relief patterns and range of the underlying coal and rock mass during the mining process of the protective layer. The fiber-optic monitoring data reflect the dynamic process of stress increase, compression deformation, stress reduction, expansion deformation, and stress recovery, as well as tensile deformation reduction in the underlying coal rock mass during the mining process of the protective layer. Based on the fluctuation amplitude of the fiber-optic strain increment to characterize the pressure relief effect, the pressure relief process is divided into three stages, namely, the pressure relief start stage, the pressure relief active stage, and the pressure relief decay stage. This study aims to provide technical support for implementing pressure relief and anti-collision strategies in the mining of protective layers and explore the reliability of using fiber-optic sensing technology to monitor the pressure relief effect in protective layer mining. These findings are significant for the promotion and application of fiber optic sensing technology in the field of mining engineering.

According to the abovementioned research, when implementing protective layer mining to prevent and control rockburst disasters, the following issues should be emphasized:

(1) Selection and development layout of protective layer: When mining coal seams with the risk of rockburst, the protective layer should be first mined to prevent rockburst, and coal seams with no or weak rockburst risk should be selected as the protective layer as much as possible, with priority given to the upper protective layer. When dividing mining areas, it is necessary to ensure a reasonable mining sequence and minimize the formation of stress concentration areas such as coal pillars. The mining of the protective layer should be ahead of the mining of the protected layer to ensure that the protected layer is in a depressurized state.
(2) Mining technology and process optimization: When mining the protective layer, the longwall mining method should be used as much as possible, and the full collapse method should be used to manage the roof of the goaf. During the mining process of the protective layer, coal pillar-free mining technology should be adopted as much as possible to avoid leaving coal pillars in the goaf and reduce stress concentration.

9 Conclusion

(1) The stress changes in the underlying rock–coal strata during the mining of the upper stress-concentration stratum can be divided into four phases, namely, *in situ* stress, stress concentration, stress release, and stress recovery. At the same time, the strata undergo dynamic processes such as "pressure boosting, unloading development, unloading recovery, and unloading stability."
(2) After mining of the upper protective layer, the distribution of the gangue collapse in the goaf is divided into fully collapsed and compacted areas and partially collapsed areas. The stress in the goaf alternates between the stable unloading area, the recovery unloading area, and the pressure-increasing area. The stress distribution curve of the protected layer changes from a "U"-shape to a "W"-shape and then to a "WWW"-shape.
(3) The initial pressure relief peak step distance for the upper protective layer mining is 80 m, the periodic pressure relief peak step distance is 60 m, the initial pressure relief recovery step distance is 140 m, and the periodic pressure relief recovery step distance is 70 m. The pressure relief ratio in the goaf direction is 55.5%, and the pressure relief ratio in the dip range is 35.3%–46.2%.
(4) The numerical simulation calculation results of the stress-relieving parameters for the upper stress-concentration stratum mining are basically consistent with the engineering measurement results. This indicates that using the 2-1 coal seam as a stress-concentration stratum for mining in the Hulusu mine can have a pressure relief effect on the 2-2 coal seam. Thus, the stress-relieving effect of the stress-concentration stratum opening has significant time and space effects.

Data availability statement

The original contributions presented in the study are included in the article/Supplementary Material; further inquiries can be directed to the corresponding author.

Author contributions

WL: conceptualization, formal analysis, writing–original draft, and writing–review and editing. JC: project administration and writing–review and editing. CZ: data curation, formal analysis, and writing–review and editing. JZ: data curation, formal analysis, and writing–review and editing. SW: writing–review and editing. GL: writing–review and editing. JZ: methodology and writing–review and editing. RY: methodology and writing–review and editing.

Funding

The author(s) declare that financial support was received for the research, authorship, and/or publication of this article. This work is supported by the National Natural Science Foundation of China (No. 52264007), the Longyuan Youth Innovation and Entrepreneurship Talent (Team) Project, the Youth Doctoral Support Project for Universities in Gansu Province (2025QB-093), and Enterprise Research Projects (No. HXZK2344).

Conflict of interest

The authors declare that the research was conducted in the absence of any commercial or financial relationships that could be construed as a potential conflict of interest.

Generative AI statement

The author(s) declare that no Generative AI was used in the creation of this manuscript.

Publisher's note

References

Banerjee, B. D. (1987). A new approach to the determination of methane content of coal seams. *Geotechnical Geol. Eng.* 5 (4), 369–376. doi:10.1007/bf01552751

Blair, S. C., and Cook, N. G. W. (1998). Analysis of compressive fracture in rock using statistical techniques: Part II. Effect of microscale heterogeneity on macroscopic deformation. *Int. J. Rock Mech. Min. Sci.* 35 (7), 849–861. doi:10.1016/s0148-9062(98)00009-6

Cao, Z., He, X., Wang, E., and Kong, B. (2018). Protection scope and gas extraction of the low-protective layer in a thin coal seam: lessons from the DaHe coalfield, China. *Geosciences J.* 22 (3), 487–499. doi:10.1007/s12303-017-0061-1

Chen, S., Shi, B., Mu, C., and Lu, Z. (2013). Study on seam permeability - increased effects and pressure - relaxed range during protective seam mining. *Coal Sci. Technol.* 41 (04), 45–49.

Chen, X., Sheng, G., and Gao, Z. (2024). Study on the influence of coal pillar left by long-distance mining of protected layer on the mining of protected layer. *Saf. Coal Mines* 55 (3), 46–52.

Cundall, P. A. (1976). Explicit finite-difference methods in geomechanics. *Numer. Methods Geomechanics* 1, 132–150.

Dai, G., Guo, L., and Zhang, S. (2013). Numerical simulation of haizi mine upper protective layer mining's protection scope. *China Saf. Sci. J.* 23 (07), 13–18.

Fang, F., Shu, C., and Wang, H. (2020). Physical simulation of upper protective coal layer mining with different coal seam inclinations. *Energy Sci. & Eng.* 8 (9), 3103–3116. doi:10.1002/ese3.740

Gong, P., Hu, Y., Zhao, Y., and Yang, D. (2005). Three dimensional simulation study on law of deformation and breakage of coal floor on mining above aquifer. *Chin. J. Rock Mech. Eng.* 24 (12), 4396–4402.

Guan, J., Sun, K., and Zhu, Y. (2002). Study of rockburst prevention and its numerical simulation in slant coalbed. *J. Liaoning Tech. Univ. Sci.*, 411–413.

Guan, Y., Li, H., and Fan, Z. (2008). Similar material simulation of the failure law of coal seam floor. *Saf. Coal Mines* 2, 67–69.

Jiang, F., Liu, Y., Liu, J., Zhang, M., Du, J., Sun, W., et al. (2019). Pressure-releasing mechanism of local protective layer in coal seam with rock burst. *Chin. J. Geotechnical Eng.* 41 (02), 368–375.

Jiang, Y., and Zhao, Y. (2015). State of the art:investigation on mechanism, forecast and control of coal bumps in China. *Chin. J. Rock Mech. Eng.* 34 (11), 2188–2204.

Kang, H., Gao Fuqiang, Xu Gang, Ren Huaiwei, (2023). Mechanical behaviors of coal measures and ground control technologies for China's deep coal mines - a review. *J. Rock Mech. Geotechnical Eng.* 15 (1), 37–65. doi:10.1016/j.jrmge.2022.11.004

Lan, H., Chen, D., and Mao, D. (2016). Current status of deep mining and disaster prevention in China. *Coal Sci. Technol.* 44 (01), 39–46.

Lei, W., Chai, J., Ding, G., Zhang, Y., Yao, R., and Wang, L. (2024). Industrial experimental study on fiber optic sensing of pressure relief effect in coal and rock mining with upper urotective layer. *Min. Res. Dev.* 44 (4), 130–137.

Lei, W., Chai, J., Zhang, Y., Ding, G., Yao, R., Chen, Y., et al. (2022). Study on pressure relief effect of upper protective coal seam mining based on distributed optical fiber sensing monitoring. *Opt. Fiber Technol.* 68, 102830–102915. doi:10.1016/j.yofte.2022.102830

Li, J., Tian, Y., Yan, X., Xie, K., Wang, Y., Xu, W., et al. (2020). Approach and potential of replacing oil and natural gas with coal in China. *Front. Energy* 14 (2), 419–431. doi:10.1007/s11708-020-0802-0

Li, P., Chen, Y., Wang, L., and Ren, W. (2012). Similar simulation experiment of the released range of upper protective seam mining. *Saf. Coal Mines* 43 (12), 32–36.

Li, X., Chen, S., Wang, S., Zhao, M., and Liu, H. (2021). Study on *in situ* stress distribution law of the deep mine: taking linyi mining area as an example. *Adv. Mater. Sci. Eng.* 2021, 1–11. doi:10.1155/2021/5594181

Li, X., Chen, S., and Zhang, X. (1997). Research on the application of protective layer mining to prevent and control rockburst. *J. Min. And Strata Control Eng.*, 18–20.

Lin, Q., Cao, P., Wen, G., Meng, J., Cao, R., and Zhao, Z. (2021). Crack coalescence in rock-like specimens with two dissimilar layers and pre-existing double parallel joints under uniaxial compression. *Int. J. Rock Mech. Min. Sci.* 139, 104621–104714. doi:10.1016/j.ijrmms.2021.104621

Liu, H., Hao, C., Wang, Z., Li, C., Guo, L., Liang, J., et al. (2022). Study on stability of underlying room and pillar old goaf in close coal seam and mining of the upper coal seam. *Front. Earth Sci.* 10, 1–14. doi:10.3389/feart.2022.1071250

Liu, J., Zhang, X., and Zhang, X. (2023). Study on spatial and temporal evolution law of surrounding rock stress in mining of upper and lower protective layers of coal seams group and its application. *J. Saf. Sci. Technol.* 19 (6), 66–73.

Lv, H., Cheng, Z., Xie, F., Pan, J., and Liu, F. (2024). Study on hydraulic fracturing prevention and control of rock burst in roof of deep extra-thick coal seam roadway group. *Sci. Rep.* 14 (1), 29537. doi:10.1038/s41598-024-77363-0

Mu, H., Zhang, Y., Gao, M., Zhu, Q., Li, J., Cao, J., et al. (2024). Research on the attenuation characteristics of seismic energy in multicoal seam mining and the warning method of rock burst. *Energy Sci. & Eng.* 12 (11), 4932–4949. doi:10.1002/ese3.1904

Pang, L., Xu, X., Si, L., Zhang, H., and Li, Z. (2016). Analysis of prevention mechanism of upper protective seam mining on rock rockburst induced by thick conglomerate. *Rock Soil Mech.* 37 (S2), 120–128.

Shen, R., Wang, E., Liu, Z., and Li, Z. (2011). Rockburst prevention mechanism and technique of close-distance lower protective seam mining. *J. China Coal Soc.* 36 (S1), 63–67.

Shen, W., Dou, L., He, H., and Zhu, G. (2017). Rock burst assessment in multi-seam mining: a case study. *Arabian J. Geoences* 10 (8), 196–211. doi:10.1007/s12517-017-2979-z

Shi, Z., Ye, D., Qin, B., Hao, J., Sun, W., and Fang, S. (2022). Mining height effect and application of upper protected layer mining pressure relief. *Sustainability* 14 (16), 10119–10218. doi:10.3390/su141610119

Sitao, Z., Decheng, G., Fuxing, J., Wang, C., Li, D., Shang, X., et al. (2021). Rock burst mechanism under coupling action of working face square and regional Tectonic stress. *Shock Vib.* 2021, 21–11. doi:10.1155/2021/5538179

Sun, R., Jiang, Z., Li, X., Yao, H., and Sun, Q. (2013). Study on the failure depth of thick seam floor in deep mining. *J. China Coal Soc.* 38 (1), 67–72.

Tian, K., Tang, X., Liu, Z., and Zheng, J. (2014). Analysis on protection effect of upper protective seam mining and fractured zone. *Coal Eng.* 46 (04), 71–73.

Tu, M., Huang, N., and Liu, B. (2007). Research on pressure - relief effect of overlying coal rock body using far distance lower protective seam Exploitation method. *J. Min. & Saf. Eng.*, 418–421.

Wang, H., Xu, L., Yu, H., and Zhang, J. (2024). Research on prediction of high energy microseismic events in rock burst mines based on BP neural network. *Sci. Rep.* 14 (1), 29934. doi:10.1038/s41598-024-81614-5

Xiao, Z., Liu, J., Gu, S., Liu, M., Zhao, F., Wang, Y., et al. (2019). A control method of rock burst for dynamic roadway floor in deep mining mine. *Shock Vib.* 2019, 1–16. doi:10.1155/2019/7938491

Xie, H., Gao, M., Zhang, R., Peng, G., Wang, W., and Li, A. (2019). Study on the mechanical properties and mechanical Response of coal mining at 1000m or deeper. *Rock Mech. Rock Eng.* 52 (05), 1475–1490. doi:10.1007/s00603-018-1509-y

Xiong, Z., Tao, G., and Yuan, G. (2014). Pressure relief boundary of protected seam mining with subhorizontal long-distance. *J. Xi'an Univ. Sci. Technol.* 34 (02), 147–151.

Xu, G., Wang, L., Jin, H., and Wang, Q. (2019). Study on movement deformation laws and protection effect of lower ultra-thick coal seam affected by upper protective layer mining. *J. Saf. Sci. Technol.* 15 (06), 36–41.

Xu, L., Lu, K., Pan, Y., and Qin, Z. (2019). Study on rock burst characteristics of coal mine roadway in China. *Energy Sources Part A Recovery Util. Environ. Eff.* 44, 3016–3035. doi:10.1080/15567036.2019.1655114

Xuanhong, D., Junhua, X., Lan, Y., Wulin, L., Hengfei, M., Chen-Rui, C., et al. (2024). Coal damage and energy characteristics during shallow mining to deep mining. *Energy* 291, 1–13.

Yang, T. (2024). Recognition and prediction of precursory feature signals of coal mine rock burst based on random forest and MK trend test. *Front. Comput. Intelligent Syst.* 8 (3), 1–5. doi:10.54097/5xwgxa77

Yu, Y., Geng, D., Tong, L., Zhao, X., Diao, X., and Huang, L. (2018). Time fractal behavior of microseismic events for different intensities of immediate rock bursts. *Int. J. Geomechanics* 18 (7), 1–11. doi:10.1061/(asce)gm.1943-5622.0001221

Yuan, H., Ji, S., Li, H., Zhu, C., Zou, Y., Ni, B., et al. (2024). Classification forecasting research of rock burst intensity based on the BO-XGBoost-Cloud model. *Earth Sci. Inf.* 18 (1), 95. doi:10.1007/s12145-024-01596-w

Yuan, Z. G., Shao, Y. H., and Zhu, Z. H. (2019). Similar material simulation study on protection effect of steeply inclined upper protective layer mining with varying interlayer distances. *Adv. Civ. Eng.* 2019, 1–14. doi:10.1155/2019/9849635

Zhang, H., Fu, X., Huo, B., Lu, Y., and Zhou, K. (2017). On preparing the materials as close as possible in the experimental ratio and mechanical properties with those gained from mining. *J. Saf. Environ.* 17 (06), 2134–2139.

Zhu, Y., Zhang, Y., and Pan, Y. (2003). Feasible research on prevention of rock-burst in dip-slopping coal seam. *J. Liaoning Tech. Univ. Sci.*, 332–333.

Zhu, Z., Wu, Y., and Han, J. (2021). A prediction method of coal burst based on analytic hierarchy process and fuzzy comprehensive evaluation. *Front. Earth Sci.* 9, 1–12. doi:10.3389/feart.2021.834958

frontiers | Frontiers in Earth Science

TYPE Original Research
PUBLISHED 03 April 2025
DOI 10.3389/feart.2025.1512811

OPEN ACCESS

EDITED BY
Yihuai Zhang,
University of Glasgow, United Kingdom

REVIEWED BY
Umar Ashraf,
Yunnan University, China
Zhishui Liu,
Chang'an University, China
Liu Lifeng,
China University of Petroleum, China

*CORRESPONDENCE
Yingwei Li,
liyw17@CNOOC.com.cn

RECEIVED 17 October 2024
ACCEPTED 07 March 2025
PUBLISHED 03 April 2025

CITATION
Li Y, Zhu Y, Li Z, Zhang X and Cai G (2025) Reservoir parameter prediction technology based on deep learning and its application in the Panyu 4 Sag, Pearl river mouth Bain. *Front. Earth Sci.* 13:1512811. doi: 10.3389/feart.2025.1512811

Reservoir parameter prediction technology based on deep learning and its application in the Panyu 4 Sag, Pearl river mouth Bain

Yingwei Li*, Yanhui Zhu, Zhenshen Li, Xiaozhao Zhang and Guofu Cai

Shenzhen Branch of CNOOC Ltd., Shenzhen, Guangdong, China

The continental deep strata in the Panyu 4 Sag of the Pearl River Mouth Basin in the South China Sea are characterized by complex lithology and tight sandstone reservoirs with low porosity and low permeability. Predicting porosity and lithology in this area has long been a challenge in seismic reservoir prediction. Traditional methods, which rely on linear mapping based on well data or probabilistic mapping through multi-attribute fusion, struggle to capture the complex nonlinear relationships between reservoir parameters and seismic attributes. To address this issue, this paper proposes a method using a convolutional neural network for predicting porosity and facies distribution. Based on rock physics analysis and pre-stack elastic impedance inversion data, this approach first takes the effective porosity and shale content (VCL) from well-log interpretation as training targets. It then constructs training samples by simulating different lithologies and extracting the corresponding elastic parameters from well-log data. Through optimal evaluation, the model parameters of the deep learning network are determined, and a nonlinear mapping relationship between elastic parameters and reservoir parameters, such as porosity, is established. Finally, the trained deep learning model is applied to the elastic parameter bodies to obtain predictions of effective porosity and VCL, thereby achieving a quantitative characterization of high-quality deep sandstone reservoirs. The application of this method in the deltaic sediments of the Panyu 4 Sag in the Pearl River Mouth Basin shows that the deep learning-based predictions of facies distribution and porosity are consistent with well data and geological understanding. The fractured well, designed on the basis of the prediction results, achieved significant productivity enhancement following drilling, thereby demonstrating the efficacy of this method as a reservoir parameter prediction tool.

KEYWORDS

deep learn, reservoir evaluation, rock physics, porosity prediction, shale content prediction

1 Introduction

The Paleogene continental deep sandstone reservoirs in the Pearl River Mouth Basin are characterized by significant burial depth, poor physical properties, and pronounced reservoir heterogeneity. These tight sandstone reservoirs typically exhibit porosity ranging from 8% to 14%, permeability between 0.1 and 5 mD, and natural productivity often below the economic production threshold. In hydrocarbon exploration and development, sandstone distribution and porosity are routinely employed for reserve evaluation and stimulation strategy optimization (Ehsan et al., 2018; Yasin et al., 2019; Ali et al., 2021; Ashraf et al., 2021). Consequently, the prediction of reservoir parameters such as porosity and lithofacies distribution has become a research priority for geophysicists, petrophysicists, and petroleum engineers (Ehsan et al., 2018; Ashraf et al., 2019; Radwan, 2020; Vo Thanh et al., 2020; Ashraf et al., 2021; Kassem et al., 2021; Ullah et al., 2022; Anees et al., 2022).

Seismic inversion serves as a key technology for the identification of the reservoir's porosity and lithofacies distribution (Saussus and Sams, 2012; Sa et al., 2015). The post-stack inversion, while operationally convenient through direct utilization of well-log data, frequently compromises the effective information contained in amplitude *versus* offset (AVO) responses (Downton, 2005; Gan et al., 2005). In contrast, pre-stack AVO inversion, grounded in the Zoeppritz equations, employs various algorithms to derive multiple elastic parameters that quantitatively characterize lithology and fluid properties in target formations (Sheuey, 1985; Connolly, 1999; Hampson et al., 2005). Rock physics analysis as an essential bridge connecting petrophysical parameters (e.g., lithofacies and porosity) with reservoir elastic properties (Li et al., 2007; Yan et al., 2002; Yin et al., 2015; Abdolahi et al., 2022). This methodology establishes linear functional relationships between porosity, clay content, and sensitive elastic parameters, thereby enabling the derivation of critical reservoir parameters. However, for continental deep formations characterized by substantial spatial variability and strong heterogeneity, it remains challenging to identify linearly correlated and effective elastic parameters. The application of Bayesian statistical principles to convert elastic parameters into maximum probability volumes of sandstone-shale distributions and corresponding porosity volumesnecessitates large sample sizes, resulting in limited accuracy for offshore exploration with sparse well control (Mavko et al., 1988; Mukerji et al., 2001; Hu et al., 2017). Alternatively, nonlinear approaches employing multi-attribute fusion or neural networks exhibit enhanced prediction accuracy but impose stringent requirements on seismic attributes (Wu et al., 2008; Zhang et al., 2014). Conventional network architectures (e.g., Back Propagation (BP) networks (Saffarzadeh and Shadizadeh 2012; Huang et al., 2016))suffer from structural simplicity, constrained computational units, and limited learning capacity, hindering their ability to precisely characterize the complex nonlinear mapping relationships between seismic attributes and porosity in tight sandstone reservoirs. Furthermore, operational instability and significant variability in inversion results restrict their large-scale implementation.

Recent advancements in machine learning have driven the widespread adoption of deep learning across domains including image processing, natural language processing, and industrial design. Geophysicists have begun integrating deep learning algorithms with enhanced hidden layers, advanced architectures, and superior computational efficiency to address complex geological challenges (Hu Ying et al., 2013). Among these, Convolutional Neural Networks (CNNs), as a rapidly evolving artificial neural network paradigm, demonstrate exceptional capabilities in modeling nonlinear mapping relationships of complex functions. Their inherent advantages in solving large-scale nonlinear inversion problems have fostered extensive applications in geophysics (Gao et al., 2020; Hinton et al., 2006; Liu et al., 2020; Li et al., 2023).

The study area is located in the Panyu 4 Sag of the Pearl River Mouth Basin in the South China Sea. Panyu 4 Sag has been explored for nearly 4 decades for hydrocarbon resources, but Paleogene Wenchang Formation exploration began only 5 years ago. To date, significant hydrocarbon discoveries have been made in the Paleogene Enping and Wenchang formations, highlighting the exploration potential of these strata. However, multiple drilled wells reveal that the Wenchang Formation reservoirs exhibit poor physical properties and strong heterogeneity, with the distribution of high-quality porouszones remaining unclear. Recent studies on the Paleogene strata in the Panyu 4 Sag have focused on geological aspects such as hydrocarbon migration, sedimentary facies classification, and tectonic evolution. Geophysical research has predominantly addressed seismic interpretation and post-stack inversion, with limited attention to porosity estimation and lithofacies identification.

This study attempts to investigate lithofacies distribution and porosity estimation in the Paleogene Wenchang Formation (FM.WC) of the Panyu 4 Sag. Based on rock physical analysis and pre-stack AVO inversion, we establish a nonlinear mapping relationship among porosity, VCL, and elastic parameters using the CNN deep learning model. This approach enables the conversion of elastic parameters into reservoir characterization parameters, thereby obtaining more accurate sandstone distribution and porosity characterization. Our methodology aims to facilitate reserve estimation and optimize stimulation strategies through the prediction of high-porous zones, which will be helpful for the future oil exploration in the Paleogene strata of the Panyu 4 Sag.

2 Geological characteristics of the study area

The Panyu 4 Subsag is located in the southern margin of the Xijiang Sag within the Zhu I Depression of the Pearl River Mouth Basin, South China Sea. Its structural framework manifests as a composite dustpan-shaped subsag characterized by northwestern overlap and southeastern faulting (Cai et al., 2022). It connects to the Xijiang Mid-Low Uplift and Xijiang 36 Subsag structural belt to the north, abuts the Xi'en Low Uplift to the west, and adjoins the Dongsha Uplift and Panyu Low Uplift to the east and south, respectively. Inheriting the basin's tectonic evolution characterized by "lower faulting and upper depression, terrestrial followed by marine phases," its stratigraphic development is dominated by Cenozoic sequences: the basement comprises Mesozoic granite overlain by Paleogene Wenchang, Enping, and Zhuhai formations,

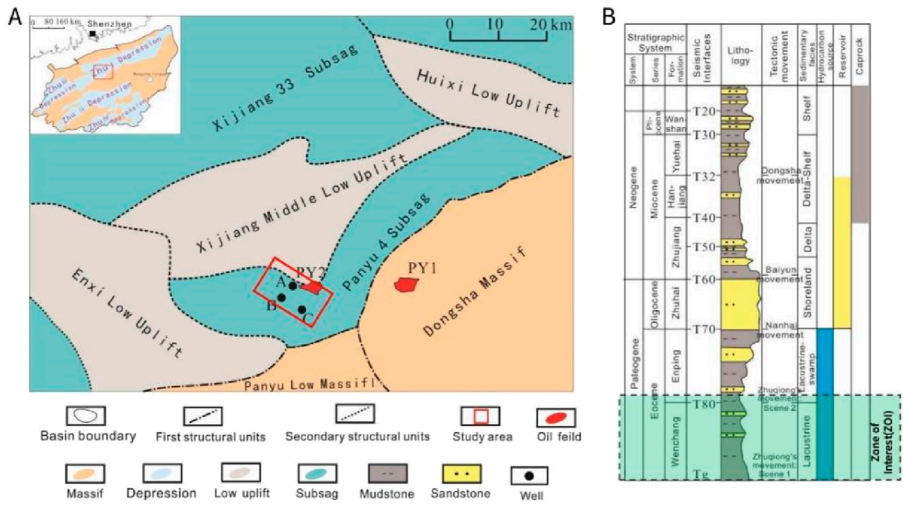

FIGURE 1
Location **(A)** and stratigraphic column **(B)** of Panyu 4 Sag in Pearl River Mouth Basin. The highlighted region shows the targeted reservoir formations and ZOI.

along with Neogene Zhujiang, Hanjiang, and Yuehai formations (Figure 1) (Ma et al., 2021).

The Paleogene Wenchang Formation features lacustrine-fluvial depositional systems with high-organic-matter source rocks exhibiting robust hydrocarbon generation potential. Reservoir systems primarily occur in transitional marine-terrestrial to marine sandstones within the Zhuhai, Zhujiang, and Hanjiang formations (Zhang et al., 2021). Current exploration data indicate that although over 80% of proven hydrocarbon resources are concentrated in Neogene strata, research emphasis has shifted to the Paleogene Wenchang Formation as Neogene structural traps approach exploration maturity (Peng et al., 2022).

This study focuses on critical blocks along the northern margin of Panyu 4 Subsag adjacent to the Xijiang Mid-Low Uplift provenance area. The Zone of Interest (ZOI) contains hydrocarbon reservoirs within the Wenchang Formation. Sequence stratigraphic analysis reveals three third-order sequences developed during the FM. WC depositional period (Zhang et al., 2022). Wenchang IV Member (FM.WC4) is characterized by fan-delta facies, hosting thick, box-shaped sandstone reservoirs with poor physical properties due to significant burial depth. Wenchang III Member (FM.WC3) consists of shallow lacustrine mudstones, serving as a regional effective seal layer. Wenchang II Member (FM.WC2), dominated by braided river delta facies, contains multiple thin sandstone layers with relatively favorable reservoir quality, though notable lateral variations in lithology and sandbody thickness are observed (Li et al., 2024). The transitional depositional features between the braided delta front and shore-shallow lake facies in FM. WC2 create favorable conditions for lithologic trap development, while the vertical stacking of sandstone-mudstone sequences establishes effective reservoir-caprock configurations. This stratigraphic architecture provides critical geological prerequisites for hydrocarbon accumulation in the study area.

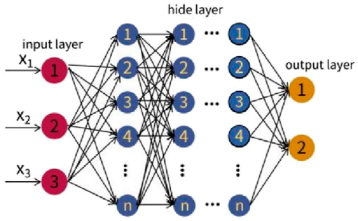

FIGURE 2
Deep learning network.

3 Data and methods

3.1 Theoretical foundation

Deep learning is a type of multi-layer neural network that includes three or more hidden layers, capable of gradually extracting higher-level features from raw data. Compared to traditional BP neural networks, deep learning has a stronger ability to simulate complex nonlinear relationships with higher precision. There are various mainstream neural network algorithms in deep learning, with Convolutional Neural Networks (CNNs) being one of the most representative (Figure 2).

The working principle of CNNs is similar to that of BP neural networks, where features are extracted layer by layer during forward propagation, and in backward propagation, the gradient descent algorithm is used to minimize the loss function error, adjusting the training parameters to complete the weight update. CNNs essentially perform a nonlinear mapping from input to output and do not require precise mathematical expressions. With simple model training, CNNs can complete complex classification tasks and exhibit strong "feature learning" capabilities (Di et al., 2021).

A CNN network typically consists of input layers, convolutional layers, pooling layers, and fully connected layers. The input layer serves as the entry point for training data, and the input can be a one-dimensional, two-dimensional, or three-dimensional vector. The convolutional layer is the feature mapping layer, where each feature map consists of multiple neurons, and the input features are extracted using convolution filters. The mathematical expression for convolution is as follows Equation 1:

$$Y_{\mathrm{P}}^{k} = f\left(\left(\sum_{m\in R\mathrm{p}} X_{\mathrm{P}}^{k-1}\right) \times k_{mp}^{k} + b_{p}^{k}\right) \tag{1}$$

In the equation: Y_p^k and X_p^{k-1} denote the *pth* feature map values at the *kth* and *(k-1)-th* layers, respectively; k_{mp}^k represents the convolutional filter weight values; b_p^k indicates the bias term for the *pth* feature map in the *kth* layer; R_p corresponds to the number of convolutional filters; f denotes the activation function, commonly implemented as the Rectified Linear Unit (ReLU) function (Wang et al., 2022).

The convolutional layer is sequentially connected to a pooling layer, which performs local averaging and subsampling operations to achieve feature selection and information filtering, thereby reducing the dimensionality of feature maps. The mathematical formulation of the pooling layer is presented below Equation 2:

$$y_{p}^{k} = P\left(N_{ij}^{k} * Y_{p}^{k-1}\right) \tag{2}$$

where P is the pooling function.

The fully connected layer typically consists of 1-3 layers and is responsible for converting the features output by the convolutional and pooling layers into a one-dimensional feature map, which is then mapped to the sample label space for classification.

3.2 Establishing the reservoir parameter prediction model

The CNN-based reservoir parameter prediction model consists of four main components: data preparation, sample set construction, model training, and model application.

1. Data preparation: This consists of two parts. First, a suitable rock physics model is established based on logging data. Second, pre-stack elastic parameter inversion is performed, predicting P-wave impedance (PI), S-wave impedance (SI), and density as low-frequency models, followed by pre-stack AVO inversion to obtain the elastic parameter volumes.
2. Sample set construction: Constructing the sample set is key to establishing the deep learning model. The sample set must be complete, encompassing all data types. In offshore exploration, due to the sparse distribution of well locations, random sampling may result in missing rare lithology types. In this study, elastic parameters predicted by the rock physics model are selected as sample inputs, which not only clarify the relationship between reservoir parameters and elastic parameters but also reduce data randomness, enhancing the sample set's rationality.
3. Model training: The elastic parameters predicted by the rock physics model are used as inputs, and VCL and porosity are chosen as training targets. By combining the conjugate gradient method with the steepest descent method, the deep learning network parameters are optimized, establishing a nonlinear mapping between elastic parameters and reservoir parameters.
4. Model application: The trained deep learning model is applied to the elastic parameter volumes obtained from pre-stack AVO inversion, predicting VCL and effective porosity to guide well placement and optimize design.

4 Application case and results

The study area encompasses 300 km^{2}of full-fold 3D seismic coverage with the following acquisition parameters: streamer length of 6,000 m, bin dimensions of 12.5 m × 25 m, and 80-fold coverage. The water depth averages 100 m with minimal variations. Three wells (Well A, B, and C) are located within the ZOI. Wells A and C provide comprehensive logging suites including acoustic slowness (DT) (μs/m), density (DEN) (g/cm^3), deep resistivity (LLD) (ohmm), shallow resistivity (LLS) (ohmm), compensated neutron porosity (CNL) (%), and gamma ray (GR) (API). Additionally, Well A contains S-wave slowness (DTS) measurements. Well B, a high-angle sidetrack of Well A, only offers limited logging data (GR and DEN) acquired during drilling operations.

In the initial phase, seismic stratigraphic and structural interpretation identified four key horizons: T80, T82, T83, and the basement Tg. Reservoir intervals are primarily developed in the FM. WC 2 (between T80-T82) and FM. WC 4 (between T83-Tg).

4.1 Rock physics modeling

S-wave velocity prediction is the foundation for pre-stack AVO inversion and petrophysical analysis. Establishing an appropriate petrophysical model enables the characterization of relationships among reservoir lithology, physical property parameters, and elastic parameters, thereby predicting acoustic and shear wave velocities (Han, 1986; Haas and Dubrule, 1994; Hinton et al., 2006). In the study area, only Well A within the WC. FM contains measured shear wave velocity data, which serves as critical validation for the model. The Wenchang Formation primarily comprises mudstone, siltstone, sandstone, and minor carbonaceous mudstone. By applying the Xu-White sand-mudstone petrophysical model theory, input parameters including mineral volume fractions, porosity, and fluid saturation were utilized to predict both acoustic and shear wave velocities. This approach successfully established the petrophysical framework for the study area (Mavko et al., 1988; Xu and White, 1995; Xu and White, 1996; Keys and Xu, 2002; Li et al., 2007).

As shown in Figure 3, the cross-plot results of the three parameters PI, density, and Vp/Vs) between the model data and the measured data (logging points) show good consistency, indicating the reliability of the model. Mudstone has lower PI and higher Vp/Vs, while sandstone and siltstone exhibit higher PI and lower Vp/Vs.

Based on prediction data from the rock physical model, polynomial regression analysis was employed to establish functional relationships between porosity and PI for sandstone (clay content

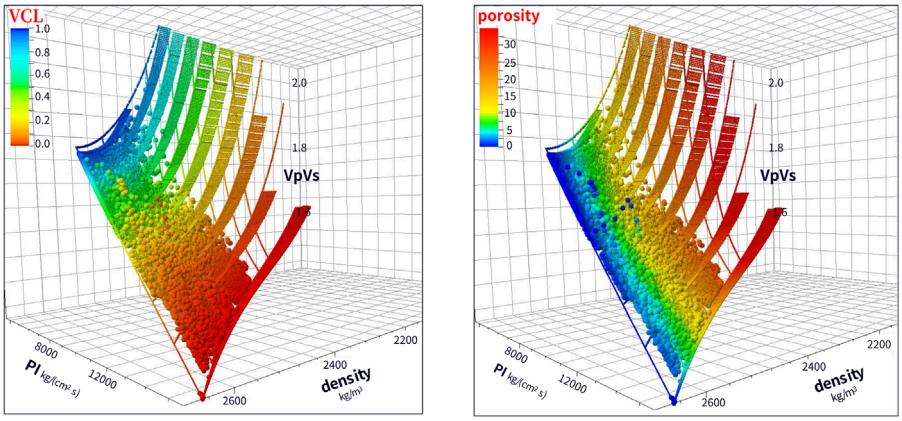

FIGURE 3
Cross plots of PI, Vp/Vs, and Density.

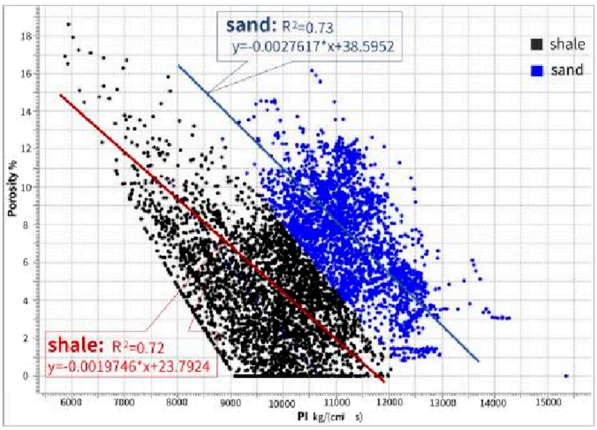

FIGURE 4
A cross plot between the PI and porosity shows a negative slope trend line.

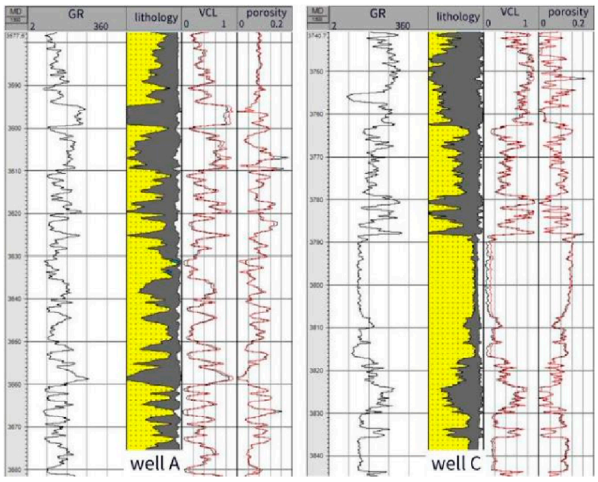

FIGURE 5
Comparison between predicted curves and logging interpreted curves. Red curves are predicted data, and black curves are logging interpretations.

<35%) and mudstone (clay content ≥35%), respectively (Figure 4). The analysis reveals a negative correlation between PI and porosity in sandstone, where high-porosity sandstone exhibits relatively low PI. With accurate lithological differentiation between sandstone and mudstone, the sandstone fitting relationship demonstrates a correlation coefficient of 0.73 and a relative error of 0.18.

4.2 Construction of the deep learning model

Based on the lithology encountered by drilled wells, logging data were divided into three rock types: sandstone, mudstone, and carbonaceous mudstone. Sample points were extracted, with 200 points each for sandstone and mudstone and 30 points for carbonaceous mudstone, forming a sample set. Effective porosity and VCL curves, obtained through detailed logging interpretation, were used as target samples for learning. The selection of input variables needs to have strong correlations with reservoir parameters. Based on comprehensive rock physics analysis and pre-stack inversion results, PI and Vp/Vs were selected as input variables for the training samples.

After extensive testing, the optimal hidden layer and node numbers were determined, and a nonlinear mapping relationship between elastic parameters and reservoir parameters was established. The test results show that when here are four hidden layers and 12 nodes, the correlation coefficient is the highest, and the root mean square error is the smallest, indicating the best prediction performance. The trained deep learning model was applied to the well section data. In Figure 5, the predicted VCL and porosity showed very small errors compared to the actual logging interpretation.

Figure 6 presents a comparative analysis of well-log porosity predictions derived from the fitting formula method and the CNN

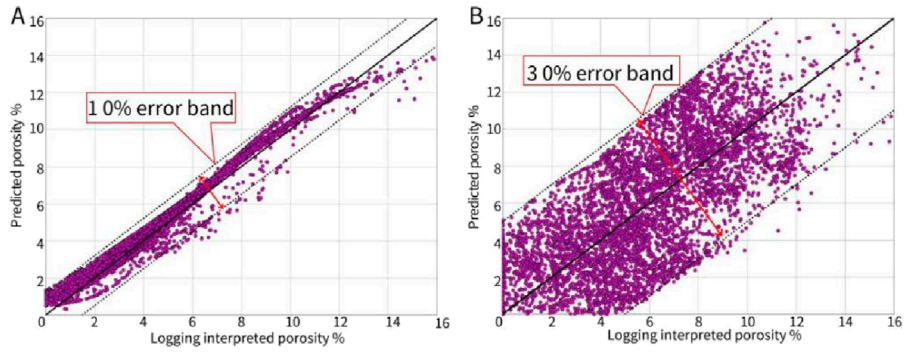

FIGURE 6
(A) A cross plot of logging interpreted porosity and deep learning model predicted porosity. **(B)** A cross plot of logging interpreted porosity and deep learning model predicted porosity.

deep learning model. The results demonstrate that over 90% of the porosity values predicted by the CNN model fall within a ±10% error margin. In contrast, the fitting formula method exhibits significantly larger prediction errors, exceeding those of the deep learning model by more than threefold.

4.3 Pre-stack AVO inversion

Seismic data, as the core input for pre-stack inversion, critically determines inversion accuracy through its quality and fidelity (Nickel and Sonneland, 1999; Zhang et al., 2013). In the study area, the primary target zone exhibits two-way travel times between 2.3–3 s with deep burial depth. The original seismic data shows notable interbed noise, severe energy attenuation, and low resolution. To enhance signal-to-noise ratio, broaden effective frequency bandwidth, and establish high-quality data foundations for pre-stack inversion and reservoir prediction, we implemented advanced reprocessing techniques including Adaptive Deghosting technology and Fault-Controlled velocity modeling (Shi et al., 2024). An integrated interactive workflow was established to iteratively optimize seismic processing and inversion parameter (Liu et al., 2019).

To achieve optimal inversion results, this study conducted over 30 iterations of integrated seismic processing-inversion tests, with particular focus on the Wenchang Formation sandstone reservoirs. Through detailed analysis of angle-dependent amplitude responses, the optimal angle ranges for pre-stack inversion were determined as 3°–13°, 13°–23°, and 23°–33° based on comprehensive angle gather testing (Liu et al., 2020).

Wavelet extraction was performed using the optimized seismic data. By integrating three angle-stacks and conducting refined well-to-seismic calibration, wavelets were extracted from the T80-Tg interval. The synthetic seismograms exhibited strong correlation (≥80%) with actual seismic data across all angle stacks (Figures 7A–C). A composite wavelet derived from three key wells was ultimately selected as the final wavelet (Figure 7D).

For the target interval (2,300–3,000 ms), spectral analysis revealed low energy below 4 Hz and weak signal between 4–6 Hz. A low-frequency prior model was constructed using well data (0–6 Hz) and seismic velocity trends as constraints. The AVO inversion employed simulated annealing global optimization to maximize resolution, yielding high-quality inversion volumes for PI, Vp/Vs, and density.

The elastic parameters obtained from the inversion were compared with the measured values (filtered at 60 Hz) for two wells, and the results showed a high degree of agreement (Figure 8A). Figure 8B shows the profiles of PI and Vp/Vs obtained from the inversion. In Well B, the thick sandstone reservoir at the top of the FM. WC4, with relatively good physical properties, shows a clear response of high PI and low Vp/Vs on the inversion profile, while Well C encountered a clayey sandstone layer with high clay content, and the dry layer shows low PI and high Vp/Vs. This indicates that the elastic parameters derived from pre-stack AVO inversion are feasible as input for predicting effective porosity and clay content in the study area.

5 Discussion

The trained deep learning model was applied to the elastic parameter volume in the study area. Figure 9 shows a cross-sectional view of the prediction results, where the well curves represent the 60 Hz low-pass filtered density-modulated display of corresponding logging interpretation curves. In Figure 9, the predicted clay content and porosity generally align with the logging interpretation results, with minor errors. In the FM. WC 2, Wells A and B are located in the same sedimentary delta lobe, and the predicted sandstone bodies are clearly delineated, with porosity ranging from 10% to 14%. Well C is located at the delta front, where VCL is higher, and porosity is lower. At the top of the FM. WC4, Well A encountered a dense dry sandstone layer, while Well B encountered a thick sandstone layer with good physical properties. The prediction results match the drilling findings.

Based on the clay content volume, we delineated the sandstone bodies within the T80-T82 interval of the FM. WC2, generating a sandstone time-thickness map. Subsequently, the sandstone depth-thickness distribution was calculated using average velocity

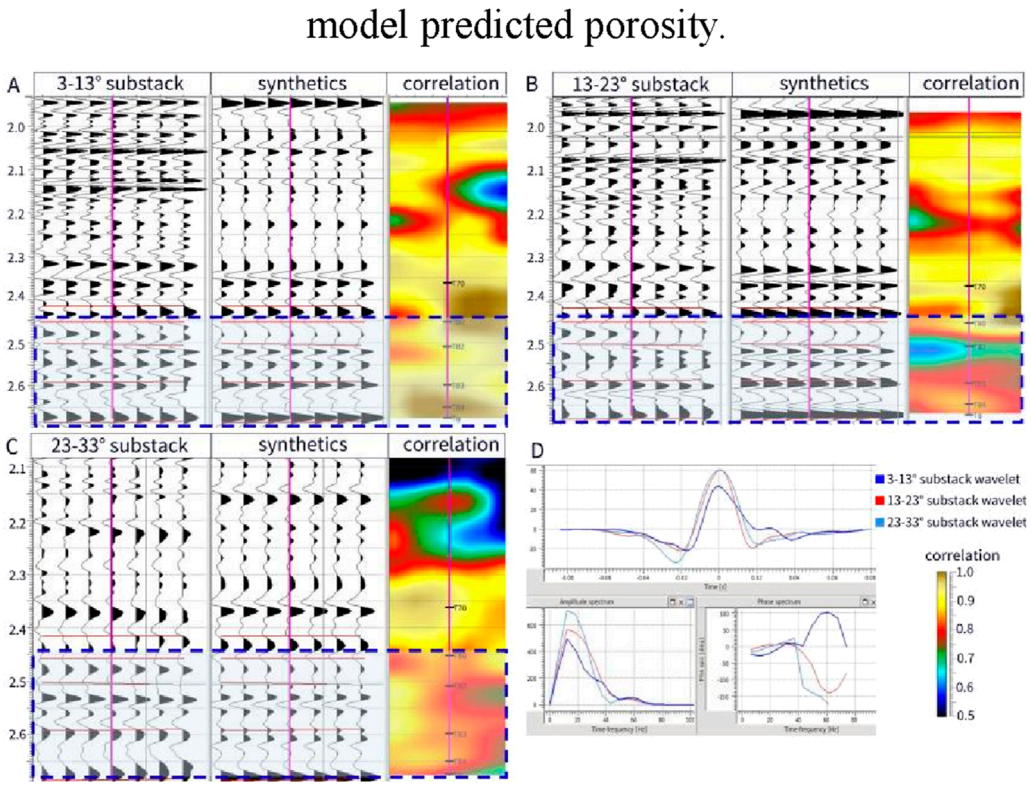

FIGURE 7
The well editing windows for the near-angle **(A)**, mid-angle **(B)**, and far-angle **(C)** substacks display the synthetic seismogram derived from Well **(C)**. The first panel shows seismic data from well traces. The second panel show synthetics, and third shows the correlation between the seismic and synthetics. The highlighted region delineates the ZOI. **(D)** An average wavelet along with amplitude and phase spectrums were made by utilizing the wavelets of all the studied wells.

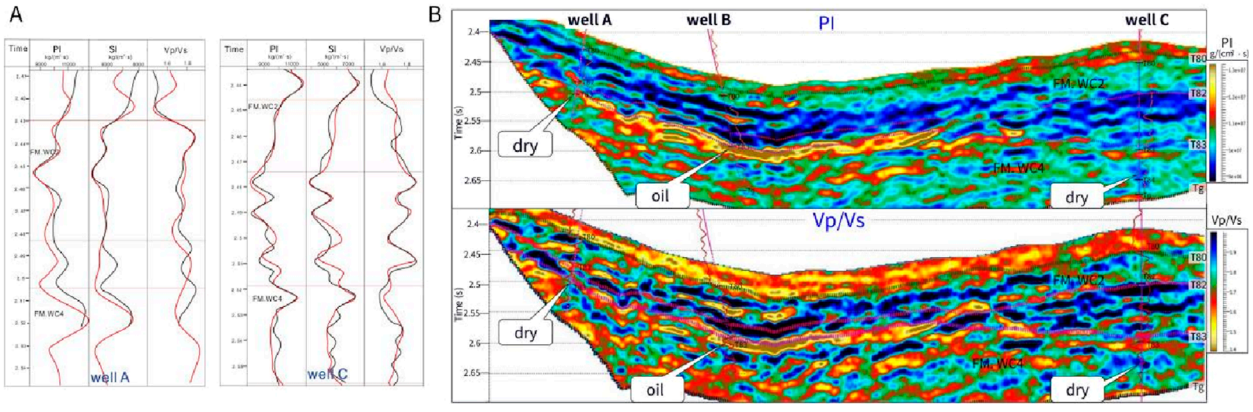

FIGURE 8
(A) 1D QC plot of AVO inversion result. Red curves are inverted data extracted along well, and black curves are measured logs with 60 Hz low pass filter **(B)** Inverted PI and Vp/Vs section with GR at well location with 60 Hz low pass filter.

conversion. As shown in Figure 10, the predicted sandstone thickness map (Figures 10A, B) exhibits strong consistency with regional sedimentary facies interpretations (Figure 10C), demonstrating the geological rationality of our sandstone predictions. Current drilling operations have primarily targeted the margins of braided river delta lobes, where encountered sand layers are relatively thin. Notably, the central zone within the polygon demonstrates thickened sandstone accumulations, representing high-priority exploration targets for future well placement.

In the upper FM. WC4, thick sandstone packages were encountered with poor reservoir quality. Integrating predicted

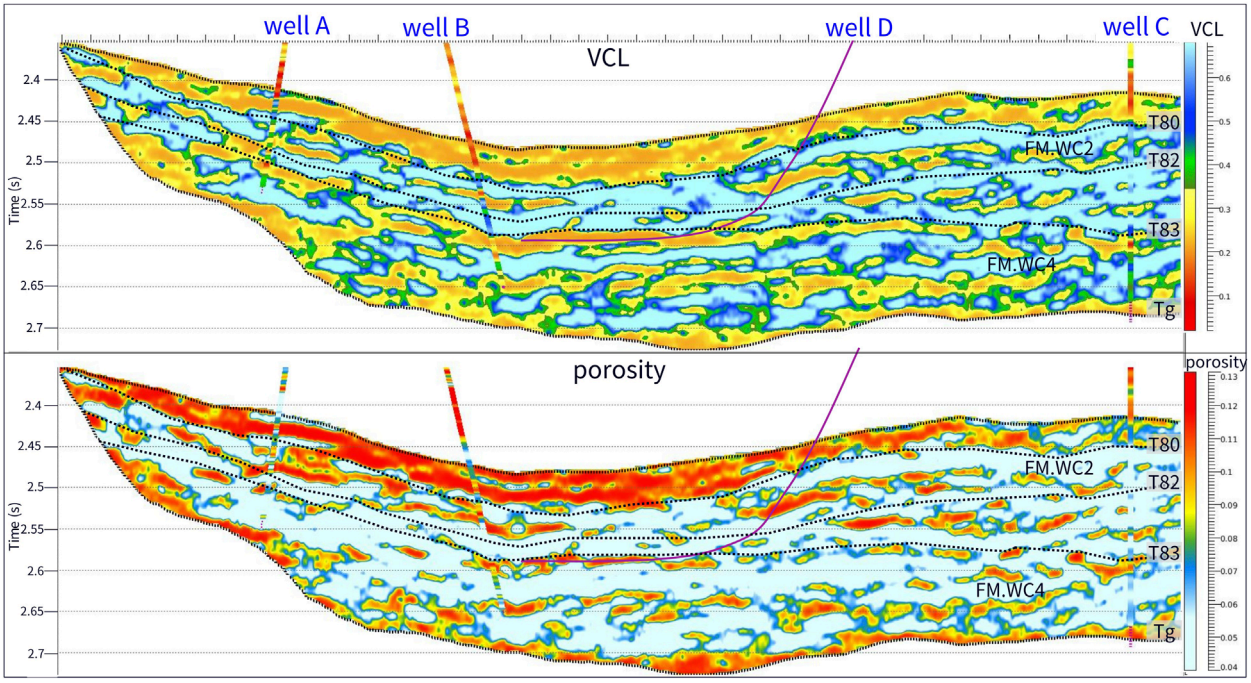

FIGURE 9
Predicted shale content section with VCL log at well location and porosity section with porosity log at well location.

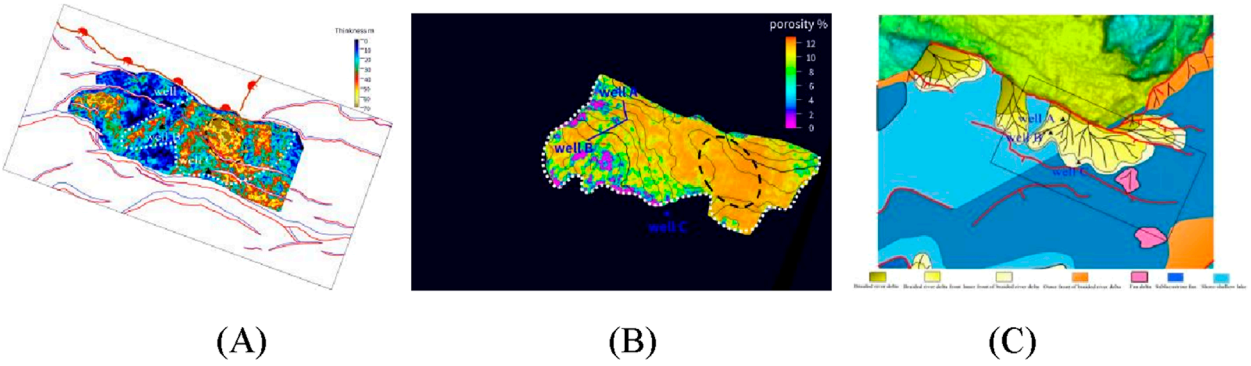

FIGURE 10
Sand thinkness **(A)**, porosity map of characterized sand bodies **(B)** and sedimentary facies **(C)** of FM. WC2.

sandstone thickness and porosity distributions (Figure 11), we recalculated reserves and conducted economic viability assessments. This analysis guided the deployment of a horizontal fracturing well (Well D) within a stable, high-porosity thick sand zone, achieving significant production enhancement through post-drilling stimulation.

The study has achieved favorable application results, and we will promote the application of this methodology throughout the Wenchang Formation in the Panyu 4 Subsag. For futuret research, we will further integrate geological research findings with methods such as seismic forward modeling and sedimentary facies-controlled inversion to enhance the accuracy of predictive results.

6 Limitations and conclusion

The CNN deep learning method for reservoir parameter prediction demonstrates significant advantages in predicting complex lithologies and porosity. The specific benefits are as follows:

1. The CNN deep learning method uses a deep network structure with multiple hidden layers, allowing it to extract effective information from logging data and establish nonlinear relationships with lithology and porosity. When applied to pre-stack AVO inversion results, it achieves higher prediction accuracy compared to traditional linear and probabilistic mapping methods.

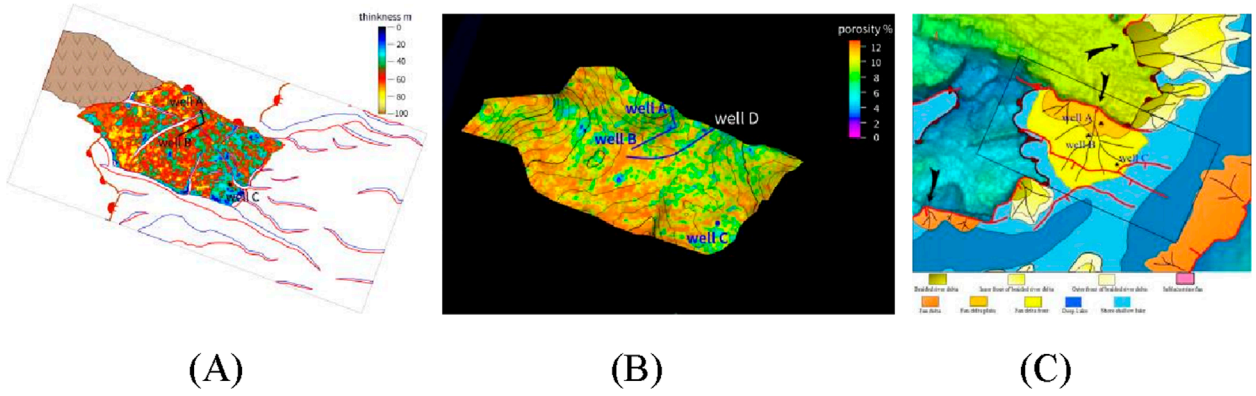

FIGURE 11
Sand thinkness **(A)**, porosity map of characterized sand bodies **(B)** and sedimentary facies **(C)** of the upper FM. WC4.

2. Deep learning has strong nonlinear representation capabilities, and CNN excel at handling classification problems. As a result, they perform well in identifying different lithologies and predicting porosity. The practical application results show that the prediction errors are small, and the accuracy is high.

However, the method also has some limitations, primarily relying on the quality of pre-stack AVO inversion results. Nevertheless, the method has been successfully applied to the low-porosity, low-permeability sand-mudstone reservoirs of the Paleogene in the Panyu 4 Sag of the Pearl River Mouth Basin. The fractured well designed based on the prediction results, achieved significant productivity improvement after drilling and has been put into production, proving that this method is suitable for lithology identification and porosity prediction in low-porosity, low-permeability sandstone reservoirs.

Data availability statement

The datasets presented in this article are not readily available because just for reading. Requests to access the datasets should be directed to YL, liyw17@cnooc.com.cn.

Author contributions

YL: Data curation, Investigation, Methodology, Writing–original draft, Writing–review and editing. YZ: Formal Analysis, Methodology, Writing–review and editing. ZL: Project administration, Writing–review and editing. XZ: Data curation, Formal Analysis, Software, Writing–review and editing. GC: Conceptualization, Data curation, Formal Analysis, Writing–review and editing.

Funding

The author(s) declare that financial support was received for the research and/or publication of this article. This research was supported by CNOOC Major Exploration and Production Research Project: 3D Seismic Data Reprocessing for the Enping 17 Sag South (Grant Nos. SCKY-2025-SZ-YJYKT-13) and 3D Seismic Data Reprocessing for the Buried Hill in Panyu 4 Sag (Grant Nos. SCKY-2025-SZ-YJYKT-14).

Acknowledgments

YL and YZ are grateful to the project manager ZL for providing essential support to this research, including data, equipment, funding, and other resources. We also extend our gratitude to Shenzhen Branch of CNOOC Ltd. for their financial sponsorship of this project.

Conflict of interest

Authors YL, YZ, ZL, XZ, and GC were employed by Shenzhen Branch of CNOOC Ltd.

The authors declare that this study received funding from CNOOC. The funder had the following involvement in the study: study design.

Generative AI statement

The author(s) declare that no Generative AI was used in the creation of this manuscript.

Publisher's note

References

Abdolahi, A., Chehrazi, A., Kadkhodaie, A., and Babasafari, A. A. (2022). Seismic inversion as a reliable technique for anticipating of porosity and facies delineation, a case study on Asmari Formation in Hendijan field, southwest part of Iran. *J. Pet. Explor. Prod. Technol.*, 1–14. doi:10.1007/s13202-022-01497-y

Ali, M., Jiang, R., Ma, H., Pan, H., Abbas, K., Ashraf, U., et al. (2021). Machine learning-A novel approach of well logs similarity based on synchronization measures to predict shear sonic logs. *J. Pet. Sci. Eng.* 203, 108602. doi:10.1016/j.petrol.2021.108602

Anees, A., Zhang, H., Ashraf, U., Wang, R., Liu, K., Abbas, A., et al. (2022). Sedimentary facies controls for reservoir quality prediction of lower Shihezi member-1 of the Hangjinqi area, Ordos Basin. *Minerals* 12, 126. doi:10.3390/min12020126

Ashraf, U., Zhang, H., Anees, A., Mangi, H. N., Ali, M., Zhang, X., et al. (2021). A core logging, machine learning and geostatistical modeling interactive approach for subsurface imaging of lenticular geobodies in a clastic depositional system, SE Pakistan. *Nat. Resour. Res.* 30 (3), 2807–2830. doi:10.1007/s11053-021-09849-x

Ashraf, U., Zhu, P., Yasin, Q., Anees, A., Imraz, M., Mangi, H. N., et al. (2019). Classification of reservoir facies using well log and 3D seismic attributes for prospect evaluation and field development: a case study of sawan gas field, Pakistan. *J. Pet. Sci. Eng.* 175, 338–351. doi:10.1016/j.petrol.2018.12.060

Cai, G., Peng, G., Wu, J., Bai, H., Li, Y., Xu, X., et al. (2022). Sedimentary filling response to detachment structural deformation in Shallow-Water continental shelf of Pearl River Mouth basin: a case study of enping sag. *Chin. J. Earth Sci.* 47 (7), 2391–2409. doi:10.3799/dqkx.2022.215

Connolly, P. (1999). Elastic impedance. *Lead. Edge* 18 (4), 438–452. doi:10.1190/1.1438307

Downton, J. (2005). "Seismic parameter estimation from AVO inversion," in *Department of geology and geophysics*. Calgary,Canada: University of Calgary.

Ehsan, M., Gu, H., Akhtar, M. M., Abbasi, S. S., and Ullah, Z. (2018). Identification of hydrocarbon potential of Talhar shale: member of lower Goru Formation using well logs derived parameters, southern lower Indus basin, Pakistan. *J. Earth Sci.* 29, 587–593. doi:10.1007/s12583-016-0910-2

Ehsan, M., Gu, H., Akhtar, M. M., Abbasi, S. S., and Ullah, Z. (2018). Identification of hydrocarbon potential of Talhar shale: member of lower Goru Formation using well logs derived parameters, southern lower Indus basin, Pakistan. *J. Earth Sci.* 29 (3), 587–593. doi:10.1007/s12583-016-0910-2

Gan, L., Zhao, B., Du, W., and Li, L. (2005). The potential analysis of elastic impedance in the lithology and fluid prediction. *Geo-physical Prospect. Petroleum.* 44 (5), 504-508.

Gao, J., Song, Z., Gui, J., and Yuan, S. (2020). Gas-bearing prediction using transfer learning and CNNs: an application to a deep tight dolomite reservoir. *IEEE Geoscience Remote Sens. Lett.* 19 (99), 1–5. doi:10.1109/LGRS.2020.3035568

Hampson, D. P., Russell, B. H., and Bankhead, B. (2005). "Simul-taneous inversion of pre-stack seismic data," in *SEG annual meeting*. Houston, 1635-1638.

Han, D. H., Nur, A., and Morgan, D. (1986). Effects of porosity and clay content on wave velocities in sandstones. *Geophysics* 51 (11), 2093–2107. doi:10.1190/1.1442062

Hinton, G. E., Osindero, S., and Then, Y. (2006). A faset learning algorithm for deep belief nets. *Neural Omputation* 18 (7), 1527–1554. doi:10.1162/neco.2006.18.7.1527

Hu, Y., Chen, H., He, Z., Huang, D., and Wen, X. (2017). Seismic facies classification based on seismic texture attributes and fuzzy clustering. *Oil Geothysical Prospeting* 48 (1), 114–120. doi:10.13810/j.cnki.issn.1000-7210.2013.01.018

Huang, F., Xia, Z., Gui, H., Zhang, M., Gui, Z., and Wang, Y. (2016). The application of BP neural network to DMT Hill metamorphic fracture prediction. *Chin. J. Eng. Geophys.* 13 (4), 483–490. doi:10.3969/j.issn.1672-7940.2016.04014

Kassem, A. A., Hussein, W. S., Radwan, A. E., Anani, N., Abioui, M., Jain, S., et al. (2021). Petrographic and diagenetic study of siliciclastic Jurassic sediments from the Northeastern Margin of Africa: implication for reservoir quality. *J. Pet. Sci. Eng.* 200, 108340. doi:10.1016/j.petrol.2020.108340

Keys, R. G., and Xu, S. (2002). An approximation for the Xu-White velocity model. *Geophysics* 67 (5), 1406–1414. doi:10.1190/1.1512786

Li, K., Wang, T., Zhao, H., Tang, X., Tian, D., Zheng, X., et al. (2023). Porosity prediction of tight sandstone reservoir based on deep feedforward neural network. *Petroleum Geol. Oilfield Dev. Daqing.* 202212004. doi:10.19597/J.ISSN.1000-3754

Li, W., Shi, G., Wang, H., and Yao, Z. (2007). The study on the relation-ships of elastic properties of rock physics. *Prog. Geophys.* 22 (5), 1380-1385. doi:10.3969/j.issn.1004-2903.2007.05.007

Li, Z., Peng, G., Chen, W., Cai, G., Zhang, L., and Huang, R. (2024). Coupling relationship between structure and sedimentary of the Paleogene Wenchang Formation in Panyu 4 sag, Pearl River Mouth basin. *Chin. J. Mar. Geol. Front.* 40 (2), 50–58. doi:10.16028/j.1009-2722.2023.032

Lin, N., Zang, D., Zhang, K., Wang, S., Fu, C., and Zhang, J. (2018). Prediction distribution of hydrocarbon reservoirs with seismic data based on learning of the small-sample convolution neural network. *Chin. J. Geophys.* 61 (10), 4110–4125. doi:10.038/cjg2018j0775

Liu, L., Liang, D., Peng, G., Ruan, X., Li, Y., Xu, J., et al. (2020). Seismic integrated study for offshore deep- and thin-stratum characterization: a case study from the Enping sag within the Pearl River Mouth Basin. *Lead. Edge* 39 (3), 176–181. doi:10.1190/tle39030176.1

Liu, L., Lu, R., and Yang, W. (2019). Seismic lithofacies inversion based on deep learning. *Geophys. Prospect. Petrolum.* 58 (1), 123–129. doi:10.3969/j.issn.1000-1441.2019.01.014

Ma, X., Liu, J., Zhu, D., Li, S., Li, Y., Suo, Y., et al. (2021). Sedimentary response of multi-stage pull-apart basin: insights from the Pearl River Mouth Basin in the northern south China Sea margin. *Chin. J. Geotect. Metallogenia* 45 (1), 64–78. doi:10.16539/j.ddgzyckx.2021.01.006

Mavko, G., Mukerji, T., and Dvorikin, J. (1988). *The rock physics handbook: tools for seismic analysis in porous media*. United Kingdom: Cambridge University Press.

Mukerji, T., Jorstad, A., and Avseth, P. (2001). Mapping lithofacies and pore-fluid probabilities in the North Sea reservoir: seismic inversions and statistical rock physics. *Geophysics* 66 (4), 998–1001. doi:10.1190/1.1487078

Nickel, m., and Sonneland, L. (1999). "Non-rigid matching of migrated timelapse seismic," in *69th SEG annual international meeting*. SEG, Expanded Abstracts, 872–875. doi:10.1190/1.1821191

Peng, G., Pang, X., Xu, Z., Luo, R., Yu, S., Li, H., et al. (2022). Characteristics of Paleogene whole petroleum system and orderly distribution of oil and gas reservoirs in south lufeng depression, Pearl River Mouth basin. *Chin. J. Earth Sci.* 47 (7), 2494–2508. doi:10.3799/dqkx.2022.253

Radwan, A. E. (2020). *Hydrocarbon type estimation using the synthetic logs: a case study in baba member*. Gulf of Suez, Egypt: AAPG/datapages search and discovery.

Sa, L., Yang, W., Yao, F., Yin, X., and Yong, X. (2015). Past present and future of geophysical inversion. *Oil Geophys. Prospcting* 50 (1), 184-202. doi:10.13810/j.cnki.issn.1000-7210.2015.01.028

Saffarzadeh, S., and Shadizadeh, S. R. (2012). Reservoir rock permeability prediction using support vector regression in an Iranian oil field. *J. Geophys. Eng.* 9 (3), 336–344. doi:10.1088/1742-2132/9/3/336

Saussus, D., and Sams, M. (2012). Facies as the key to using seismic inversion for modelling reservoir properties. *First Break* 30, 45–52. doi:10.3997/1365-2397.2012009

Shi, Y., Chen, R., Xu, Y., Yang, J., Li, Y., and Huang, N., (2024). Key technologies for improving the imaging of Paleogene interior structure: a case study on the gentle slope zone in Panyu 4 sag, the Pearl River Mouth Basin. 63 (2):357–369.

Shuey, R. T. (1985). A simplification of the zoeppritz equations. *Geophysics* 50 (4), 609–614. doi:10.1190/1.1441936

Spikes, K., Mukerji, T., Dvorkin, J., and Mavko, G. (2007). Probabilistic seismic inversion based on rock-physics models. *Geophysics* 72 (5), 87–97. doi:10.1190/1.2760162

Ullah, J., Luo, M., Ashraf, U., Pan, H., Anees, A., Li, D., et al. (2022). Evaluation of the geothermal parameters to decipher the thermal structure of the upper crust of the Longmenshan fault zone derived from borehole data. *Geothermics* 98, 102268. doi:10.1016/j.geothermics.2021.102268

Vo Thanh, H., Sugai, Y., and Sasaki, K. (2020). Impact of a new geological modelling method on the enhancement of the CO_2 storage assessment of E sequence of Nam Vang field, offshore Vietnam. *Util. Environ. Eff.* 42, 1499–1512. doi:10.1080/15567036.2019.1604865

Wang, H., Qu, Y., and Zhang, Q. (2017). Tight sandstone reservoir prediction of the deep shahe-zi Formation in songliao basin. *Pet. Geophys. Prospect.* 52 (2), 129–134. doi:10.13810/.cnki.issn.1000-7210.2017.s2.022

Wang, J., Wen, X., He, Y., Lan, Y., and Zhang, C. (2022). Logging curve prediction based on a CNN-GRU neural network. *Geophys. Prospect. Peltroleum.* 61 (2), 276–285. doi:10.3969/j.cnki.issn.1000-1441.2022.02.009

Wu, M., Fu, L., and Li, W. (2008). Inversion method and application of high-resolution nonlinear reservoir physical parameters. *Chin. J. Geophys.* 51 (2), 546–557.

Xu, S., and White, R. E. (1995). A new velocity model for clay-sand mixtures. *Geophys. Prospect.* 43 (1), 91–118. doi:10.1111/j.1365-2478.1995.tb00126.x

Xu, S., and White, R. E. (1996). A physical model for shear-wave velocity prediction. *Geophys. Prospect.* 44 (4), 687–717. doi:10.1111/j.1365-2478.1996.tb00170.x

Yan, J., Li, X., and Liu, E. (2002). Effects of pore aspect ratios on velocity prediction from well-log data. *Geophys. Prospect.* 50 (3), 289–300. doi:10.1046/j.1365-2478.2002.00313.x

Yasin, Q., Du, Q., Ismail, A., and Shaikh, A. (2019). A new integrated workflow for improving permeability estimation in a highly heterogeneous reservoir of Sawan Gas Field from well logs data. *Geomech. Geophys. Geo. Energy. Ge. Resour.* 5 (2), 121–142. doi:10.1007/s40948-018-0101-y

Yin, X., Zong, Z., and Wu, G. (2015). Research on seismic fluid identification driven by rock physics. *Sci. China(Earth Sci.)* 45 (1), 8-21. doi:10.1007/s11430-014-4992-3

Zhang, F., Liu, H., and Niu, X. (2014). High-resolution seismic inversion of convolutional neural network. *Pet. Geophys. Prospect.* 49 (6), 1165–1169. doi:10.13810/j.cnki.issn.1000-7210.2014.06.019

Zhang, L., Wu, J., Cai, G., Li, Z., and Chen, S. (2022). Resrvoir characteristics and main controlling factors of wencghang formation in PY4 depresddion, Pearl River mouth basin. *Mineralogy Petrology* 42 (4), 116–127. doi:10.19719/j.cnki.1001-6872.2022.04.11

Zhang, W., Liu, J., Liu, L., Zhang, X., Bai, H., and Yang, D. (2022). Lithology prediction technology and its application of Paleogene Wenchang Formation in Panyu 4 depression, Pearl River Mouth basin. *Lithol. Reserv.* 34 (6), 118–125. doi:10.12108/yxyqc.20220610

Zhang, X., Liu, P., Wang, W., Du, J., and Chen, W. (2021). Controlling effect of tectonic transformation in Paleogene Wenchang Formation on oil and gas accumulation in Zhu I depression. *Chin. J. Earth Sci.* 46 (5), 1797–1813. doi:10.3799/dqkx.2020.106

Zhang, Y., Sun, S., Tang, Z., and Li, Y. (2013). Caved carbonate reservoir prediction based on AVO inversion. *Chin. J. Oil Geophys. Prospect.* 48 (1), 109–120. doi:10.13810/j.cnki.issn.1000-7210.2013.01.017

frontiers | Frontiers in Earth Science

TYPE Original Research
PUBLISHED 03 April 2025
DOI 10.3389/feart.2025.1456257

OPEN ACCESS

EDITED BY
Yihuai Zhang,
University of Glasgow, United Kingdom

REVIEWED BY
Lin Ma,
The University of Manchester, United Kingdom
Weichao Yan,
Ocean University of China, China
Xuefeng Liu,
China University of Petroleum (East China), China
Filip Košek,
Faculty of Science, Charles University, Czechia

*CORRESPONDENCE
Jianfeng Zhu,
zhujf.dbsj@sinopec.com

RECEIVED 28 June 2024
ACCEPTED 06 March 2025
PUBLISHED 03 April 2025

CITATION
Zhu J, Liu Y and Hu Z (2025) Multi-scale CT imaging technique characterization of volcanic rock reservoirs: a study case from the Changling fault depression of the southern Songliao Basin.
Front. Earth Sci. 13:1456257.
doi: 10.3389/feart.2025.1456257

Multi-scale CT imaging technique characterization of volcanic rock reservoirs: a study case from the Changling fault depression of the southern Songliao Basin

Jianfeng Zhu[1]*, Yuhu Liu[1,2] and Zhiwei Hu[3]

[1]Sinopec Northeast Oil and Gas Branch, Changchun, China, [2]College of Earth Sciences, Jilin University, Changchun, China, [3]Sanya Offshore Oil and Gas Research Institute, Northeast Petroleum University, Sanya, China

The Changling fault depression in the southern Songliao Basin hosts volcanic rock reservoirs with significant oil and gas potential, yet their complex pore structures require advanced characterization to optimize resource exploration. To address this, we employed multi-scale computed tomography (CT) imaging combined with mercury intrusion porosimetry (MIP) to analyze three representative volcanic rock samples through three-tier micrometer CT scanning. This integrated approach enabled the construction of a multi-scale digital rock model, facilitating qualitative and quantitative evaluations of pore-throat structures across diverse storage spaces. Results revealed detailed three-dimensional distributions of porosity, connectivity, and pore-throat radii, demonstrating pronounced heterogeneity in reservoir properties. The results demonstrate that integrating multi-scale CT scanning with mercury intrusion data provides a robust method for characterizing the three-dimensional pore distribution effectively. This research provides an in-depth understanding of the microscopic characteristics of volcanic rock reservoirs and establishes a scientific and technical foundation for advancing the exploration and development of oil and gas resources.

KEYWORDS

volcanic rock reservoir, multi-scale CT imaging, microscopic characterization, pore network model, oil and gas exploration

1 Introduction

Reservoir characterization has traditionally relied on methods such as core observation, thin section identification, mercury intrusion porosimetry (MIP), and scanning electron microscopy (SEM) (Anovitz and Cole, 2015; Dong et al., 2024). Each of these techniques, however, has inherent limitations. Core observation is restricted to external features and lacks the capability to investigate the internal pore structures. Thin section identification, while valuable for detailed mineralogical and textural analysis, is confined to two-dimensional assessments and cannot capture the three-dimensional pore architecture

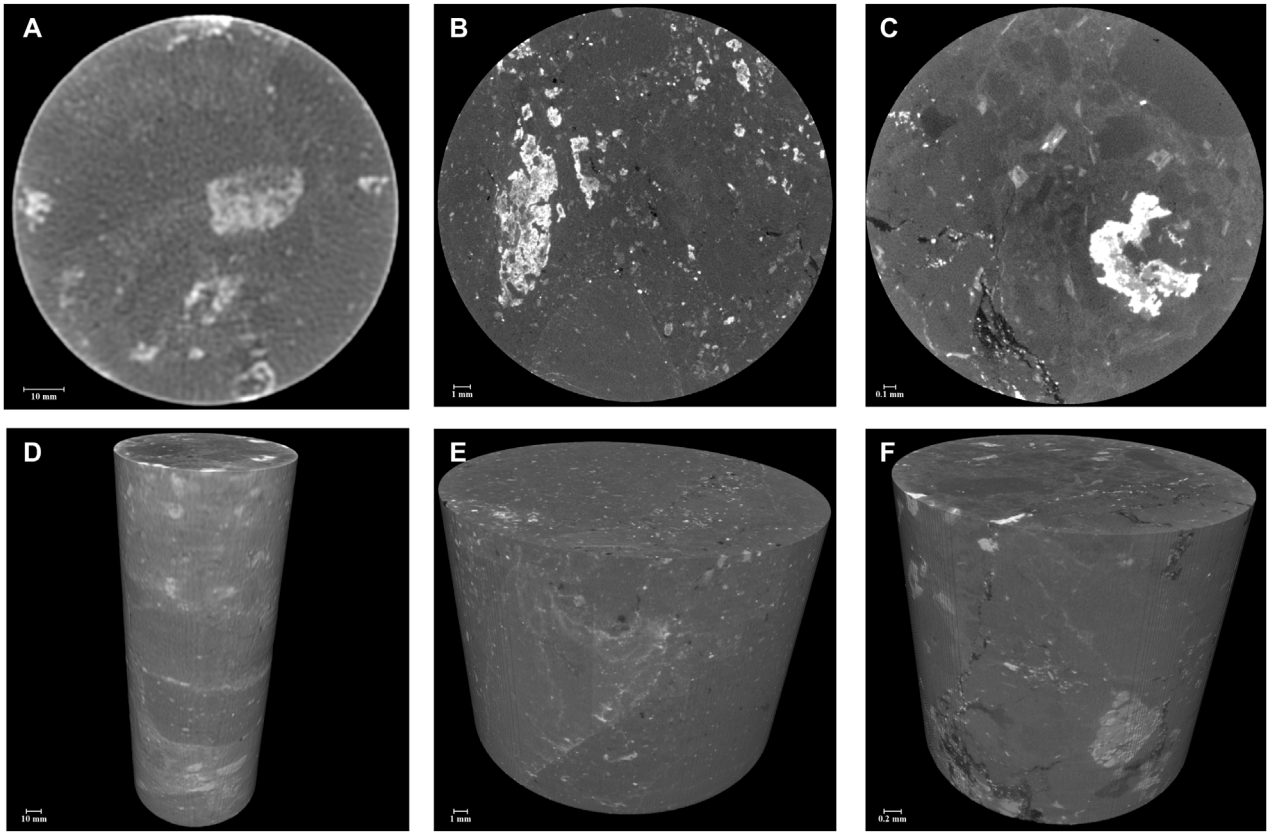

FIGURE 1
Three-scale CT scan images of rhyolitic volcanic breccia **(A, D)**: show the large-scale structure of the full diameter sample; **(B, E)**: show the mineral and part of the pore structure of centimeter plug sample; **(C, F)**: show finer mineral and pore structure of millimeter plug sample.

(Bai et al., 2013; Liu et al., 2020). Similarly, SEM provides high-resolution imagery of micropore morphology and dimensions but is also limited to two-dimensional analysis (Bera and Shah, 2021; Chalmers et al., 2012). MIP quantifies accessible porosity and pore-throat sizes through mercury penetration under pressure, but only addresses interconnected pore spaces, neglecting isolated pores (Kuila, 2013; Njiekak et al., 2018; Qajar and Arns, 2022). In contrast, computed tomography (CT) imaging represents a significant advancement in reservoir characterization by enabling non-destructive, three-dimensional visualization of rock samples (Dong et al., 2019; Cnudde and Boone, 2013; Ma et al., 2016; Mees et al., 2003). CT imaging allows for the extraction of detailed microstructural pore-throat parameters across a continuum of scales (Ma and Liu, 2011; Bai et al., 2013; Ma et al., 2016; Li et al., 2016; Liu X. F. et al., 2021). This facilitates a comprehensive spatial and quantitative evaluation of reservoir quality, critical for accurate reservoir characterization (Ma et al., 2017; Remeysen and Swennen, 2008; Dong et al., 2018). However, due to the heterogeneity in pore sizes within core samples, ranging from nanometers to millimeters, capturing the full spectrum of pore characteristics requires multiple resolutions during CT scanning.

The Changling fault depression of the Southern Songliao Basin holds immense potential for oil and gas resources, with multiple volcanic gas reservoirs already discovered in the Yingcheng and Huoshiling formations (Zou et al., 2012; Wang et al., 2015; Miao et al., 2020; Li et al., 2023). Despite the promising resource potential, complex geological structures and uncertainties in reservoir microscopic features pose substantial obstacles to oil and gas exploration and development in the region (Zheng et al., 2021; Qu et al., 2022; Li et al., 2023). Hence, advancing reservoir studies, particularly on pore structure characteristics, is essential for effectively evaluating and predicting reservoirs (Liu et al., 2017; Liu B. et al., 2021). This is vital for achieving breakthroughs in the exploration of volcanic oil and gas resources in the Songliao Basin. The Flint Ridge Formation, studied herein, developed in the early stage of fault basin formation and was filled during the fault's initial stages. It lies in unconformity contact with the underlying strata and exhibits deposition thicknesses exceeding 800 m. The lithology is predominantly gray-black mudstone interspersed with gray fine sandstone in the lower part, transitioning to volcanic breccia, andesite, and tuff in the upper part. While multi-scale CT imaging has been successfully applied to sedimentary reservoirs (Dong et al., 2019; Ma et al., 2017), its integration with mercury intrusion data for characterizing volcanic rock reservoirs—particularly in the Songliao Basin—remains underexplored. This study represents the first systematic application of this approach to address the unique challenges posed by the

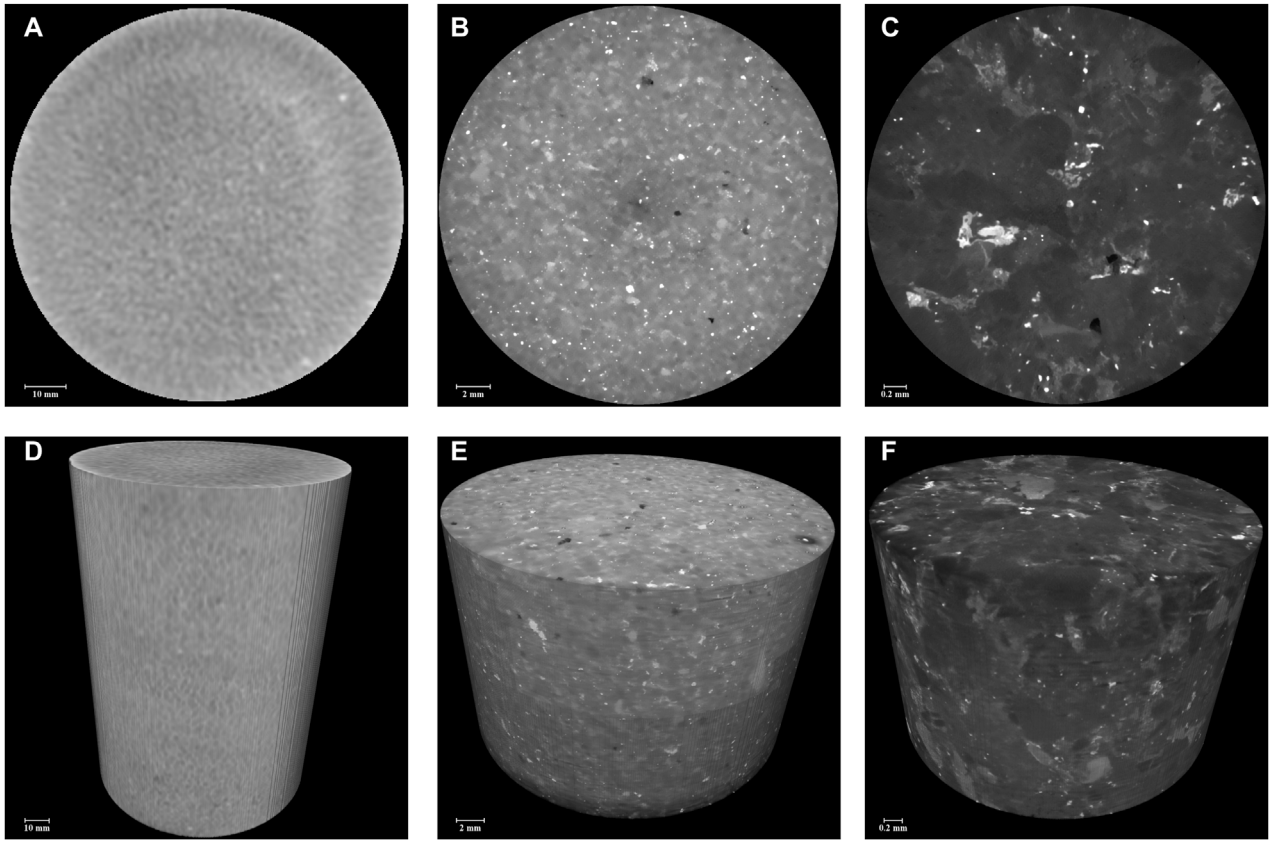

FIGURE 2
Three-scale CT scan images of crystal tuff. **(A, D)**: show the large-scale structure of the full diameter sample; **(B, E)**: show the mineral and part of the pore structure of centimeter plug sample; **(C, F)**: show finer mineral and pore structure of millimeter plug sample.

heterogeneity of volcanic pore networks in the Changling fault depression.

To address the complex exploration challenges in the Changling fault depression, this study employed a three-scale micrometer-resolution CT scanning protocol on three representative volcanic rock reservoir samples. By integrating CT imaging with MIP, a multi-scale pore network digital core model was developed, significantly enhancing understanding of the reservoir's microstructural characteristics.

Qualitative analyses provided a detailed description of the three-dimensional pore-throat structures across various types of storage spaces within these volcanic rocks. Quantitative evaluations calculated critical parameters such as porosity, connectivity, and pore-throat radii distribution. This combined approach enabled a comprehensive characterization of the microscopic features of volcanic rock reservoirs.

This study not only advances the understanding of microstructural attributes influencing fluid flow and trapping mechanisms in volcanic reservoirs but also provides a scientific and technical basis for optimizing exploration and development strategies in the Changling fault depression. Moreover, it demonstrates the value of integrating multi-scale imaging and analytical techniques to gain critical insights into reservoir quality and performance, offering a robust foundation for oil and gas exploration and development.

2 Samples and methods

2.1 Samples

In this study, 64 core samples were obtained from 11 wells drilled in the Huoshiling Formation of the Changling fault depression. These cores encompass lithologies such as tuff, tuffite, breccia, and andesite. Three representative samples—rhyolitic volcanic breccia, crystal tuff, and tuffite—were selected based on (1) lithological abundance (>60% of the Huoshiling Formation's volcanic sequences), (2) distinct pore structure characteristics, and (3) resource significance. Although andesite is present in the formation, it was excluded due to its limited abundance (<15%) and low porosity (<2% in preliminary helium tests). Samples were drilled from texturally homogeneous zones to minimize intra-lithology variability.

The analysis began with a macroscopic examination of the full-diameter samples via initial CT scanning. This step provided an overview of the structural composition and facilitated preliminary identification of heterogeneities within the samples. Subsequently,

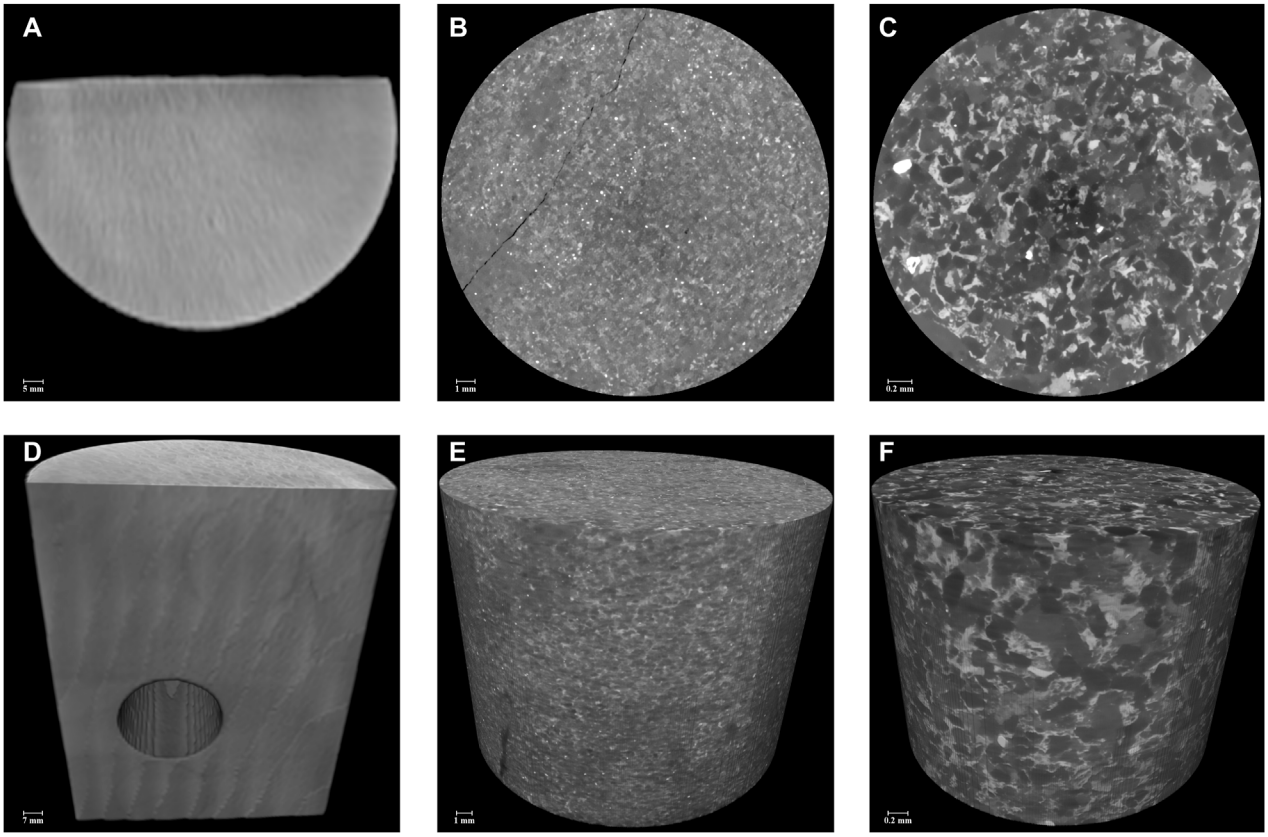

FIGURE 3
Three-scale CT scan images of tuffite. **(A, D)**: show the large-scale structure of the full diameter sample; **(B, E)**: show the mineral and part of the pore structure of centimeter plug sample; **(C, F)**: show finer mineral and pore structure of millimeter plug sample.

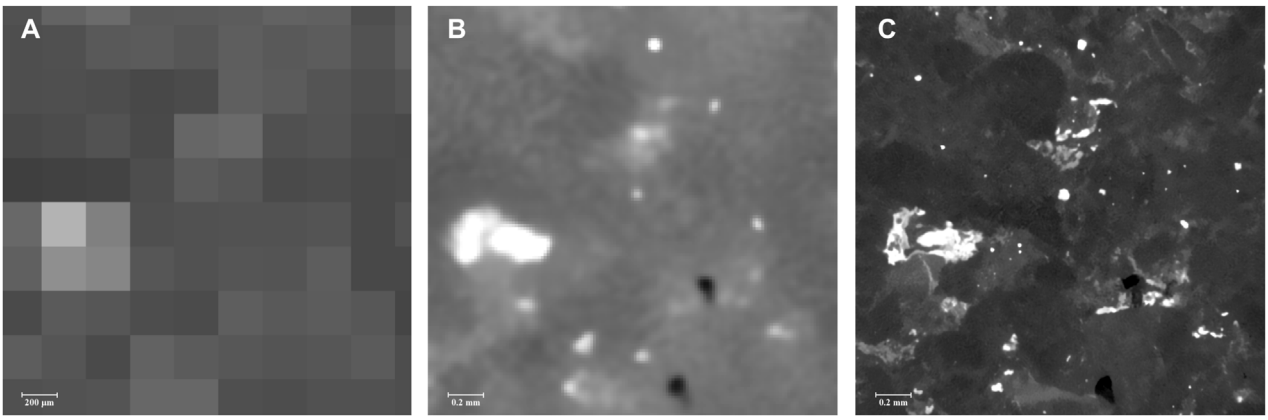

FIGURE 4
Registration results of CT images of crystal tuff. The same view of **(A)**: Full diameter sample; **(B)**: Centimeter plug sample; **(C)**: Millimeter plug sample.

thin sections were prepared to aid in accurate rock typing and the identification of pore types, further refining the geological characterization of the reservoirs.

Following these macroscopic and microscopic assessments, centimeter plugs were drilled from the primary samples for quantitative evaluation. Helium porosity measurements were performed on centimeter plugs (samples ①–③) using a ECK-III porosimeter following GB/T 29172-2012. Helium porosity measurements conducted on these plugs revealed porosities of 8.21%, 3.57%, and 0.34% for samples ①, ②, and ③, respectively.

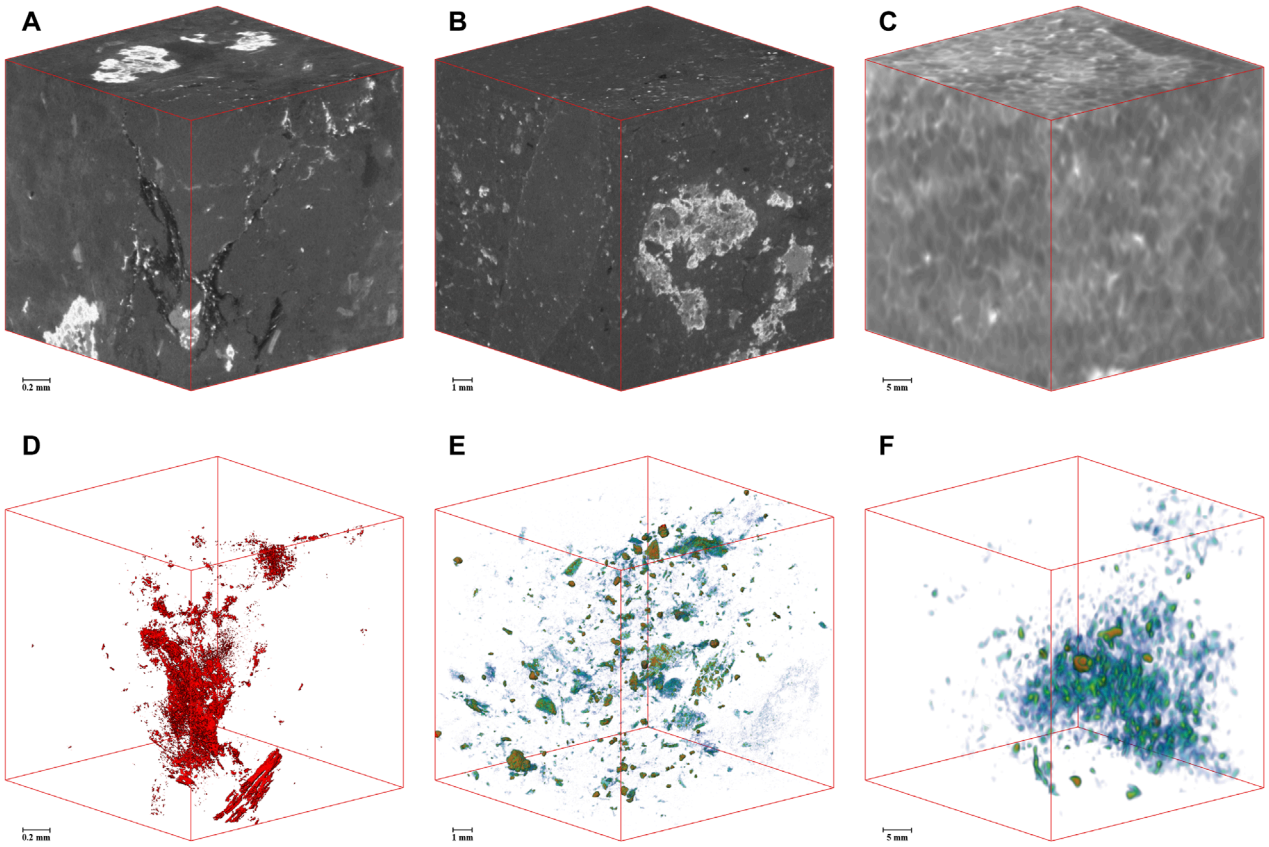

FIGURE 5
CT grayscale images and pore segmentation results of rhyolitic volcanic breccia at three scales **(A, D)**: Full diameter sample; **(B, E)**: Centimeter plug sample; **(C, F)**: Millimeter plug sample.

These values highlight the significant variability in porosity among the samples, which reflects their distinct textural and compositional properties.

To further explore pore-throat size distributions and connectivity, high-pressure mercury intrusion tests were performed. High-pressure mercury intrusion tests utilized a Micromeritics AutoPore IV 9505 on subsamples from the CT-scanned plugs, with pore-throat radii calculated via the Washburn equation.

2.2 Methods

This study employed a comprehensive methodology to characterize volcanic rock features at multiple scales using advanced imaging techniques. The workflow included multi-scale core CT imaging, precise image registration, multi-scale image segmentation, and multi-scale pore network modeling and analysis.

2.2.1 CT imaging and sample preparation

The primary equipment utilized in this study is the nanoVoxel-3502E CT scanner, manufactured by Tianjin Sanying Precision Instruments Co., Ltd., China. This state-of-the-art scanner has a maximum spatial resolution of 0.5 μm and can hold sample diameters of up to 30 cm. This equipment can carry out a multi-scale CT scanning across a diverse range of sample sizes, thereby enabling detailed and accurate visualization of geological samples from the macro to the micro scale.

Each sample undertook an initial CT scanning at a resolution of 80 μm. This scanning provided a comprehensive view of the entire core, capturing macroscopic features that were essential for initial assessments and further detailed studies. Following the full diameter scanning, a standard plug of 2.5 cm diameter was extracted from the core for higher resolution scanning at 16 μm. This step was essential for examining finer structural details that were not discernible at lower resolutions. To get even greater details, particularly focusing on the microporosity of the core, a 4 mm diameter millimeter plug sample was drilled using a precision millimeter drill bit. These smaller samples were scanned at an ultra-high resolution of 2.6 μm, enhancing the visibility of the smaller scale pore structures. This level of detail is pivotal for accurately characterizing the microporosity and determining the connectivity and distribution of pore-throats within the volcanic rock.

2.2.2 Image registration across scales

To align CT images across three distinct scales—millimeter plugs, centimeter plugs, and full diameter cores—a hybrid registration method is utilized. This method combines algorithms

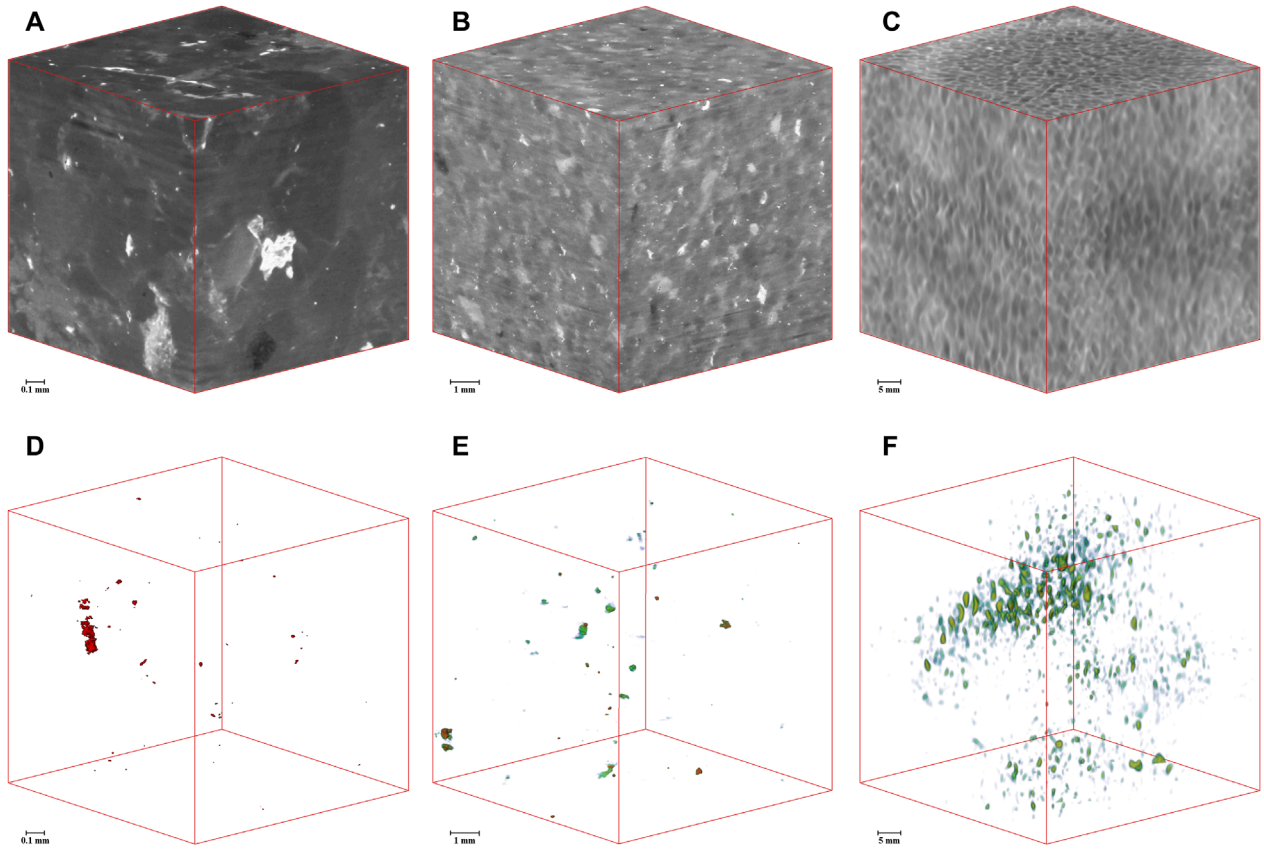

FIGURE 6
CT grayscale images and pore segmentation results of crystal tuff at three scales. **(A, D)**: Full diameter sample; **(B, E)**: Centimeter plug sample; **(C, F)**: Millimeter plug sample.

of image features and grayscale information to optimize the accuracy of alignment (Cui et al., 2017; Cui et al., 2020). This dual approach allows for effective handling of the different resolutions and complexities encountered in multi-scale imaging, ensuring that features across scales are accurately matched and the continuity of geological features is maintained. Image registration was implemented with MATLAB R2021a (MathWorks) using custom scripts based on the hybrid registration method. Image processing and analysis were performed using Avizo 9.0 (Thermo Fisher Scientific) for 3D visualization.

2.2.3 Image segmentation

Multi-scale image segmentation plays a crucial role in the multi-scale characterization process, allowing for a detailed analysis of porosity and structural features across different scales. This step ensures that corresponding features across the scales are accurately matched, facilitating a coherent analysis across different resolutions. To simplify the computational process and optimize the analysis, the largest square area within the cylindrical scanned data is extracted for segmentation. This approach focuses the segmentation process on the core area of the sample, minimizing edge effects and ensuring the most representative data is analyzed. Segmentation is performed sequentially, starting from the smallest scale (millimeter plug) to the largest (full diameter core). This hierarchical approach allows for detailed analysis at smaller scales to inform the broader, more generalized segmentation at larger scales.

The segmentation process is structured in several steps to effectively differentiate between various rock components such as pores and minerals: (1) Initially, threshold segmentation was applied to high-resolution images using Otsu's method (Otsu, 1979) to distinguish pores from the matrix; (2) In the registered overlapping image regions, a low-resolution voxel corresponds to N^3 voxels at a higher resolution (where N is the resolution ratio). By analyzing the proportion of components within these regions, the grayscale values of the low-resolution images are calibrated against a curve that represents the average distribution of the grayscale-component proportion. This calibration is crucial for accurately scaling up detailed pore and mineral information to larger voxel scales; (3) Utilizing the established grayscale-porosity distribution curve, porosity values are assigned to each voxel in the low-resolution images, ranging from 0 to 1, to depict the distribution of porosity accurately; (4) Following the methodology used for porosity, grayscale values are similarly used to assign values to different mineral components across the scales. These steps are applied progressively to achieve multi-scale image segmentation from millimeter plugs to centimeter plugs to full diameter cores.

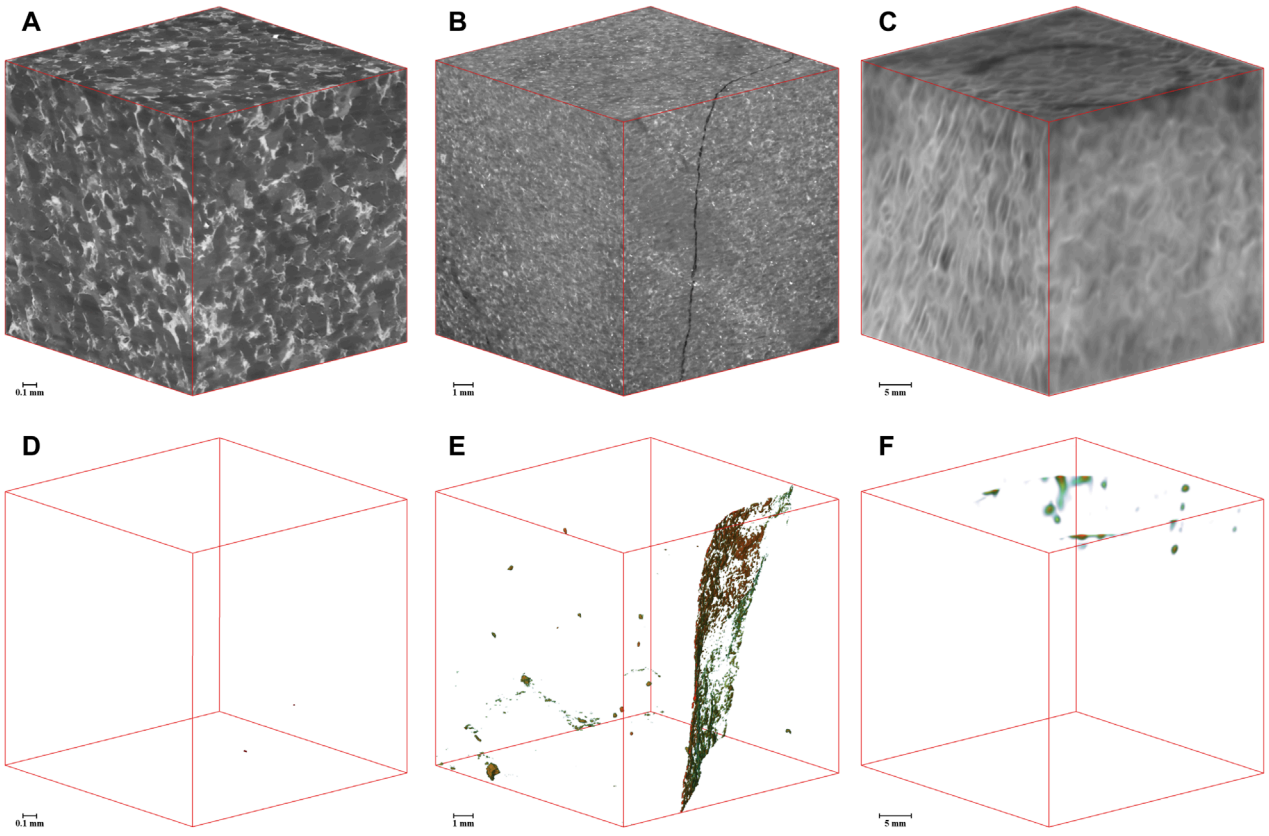

FIGURE 7
CT grayscale images and pore segmentation results of tuffite at three scales. **(A, D)**: Full diameter sample; **(B, E)**: Centimeter plug sample; **(C, F)**: Millimeter plug sample.

TABLE 1 Distribution of pore proportions at different scales.

Samples	Porosity (%)			
	<0.1 um	0.1–1 um	1–10 um	>10 um
Rhyolitic volcanic breccia	61.07	8.68	25.68	4.57
Crystal tuff	87.79	1.09	7.98	3.14
Tuffite	75.22	21.72	1.16	1.93

2.2.4 Pore network modeling

The modeling of the pore network also follows a structured multi-scale approach (Jiang et al., 2012; Jiang et al., 2013; Ma et al., 2017), which was implemented through the following steps: (1) Multi-scale model extraction. Pore network models were extracted at each scale using the maximal ball algorithm (Dong and Blunt, 2009). This algorithm identifies pores as maximal spheres fitting within void spaces and connects them via throats (narrowest constrictions between pores). At each resolution, the extracted networks captured pore-throat radii distributions, coordination numbers, and spatial connectivity specific to their scale. (2) Fine-scale model generation. For sub-resolution pores below the CT detection limit, a stochastic modeling approach was adopted. Based on MIP data, we generated synthetic pore networks, matching the cumulative pore size distribution derived from MIP curves. This hybrid approach ensured representation of both resolved and unresolved porosity. (3) Cross-scale model coupling. Statistical distributions of throat properties from finer-scale models are used to bridge coarse scale pores and fine scale pores.

3 Results

3.1 Imaging scanning results

The multi-scale scale CT imaging of the rhyolitic volcanic breccia reveal significant insights into the internal structure and porosity of the rock at varying scales (Figure 1).

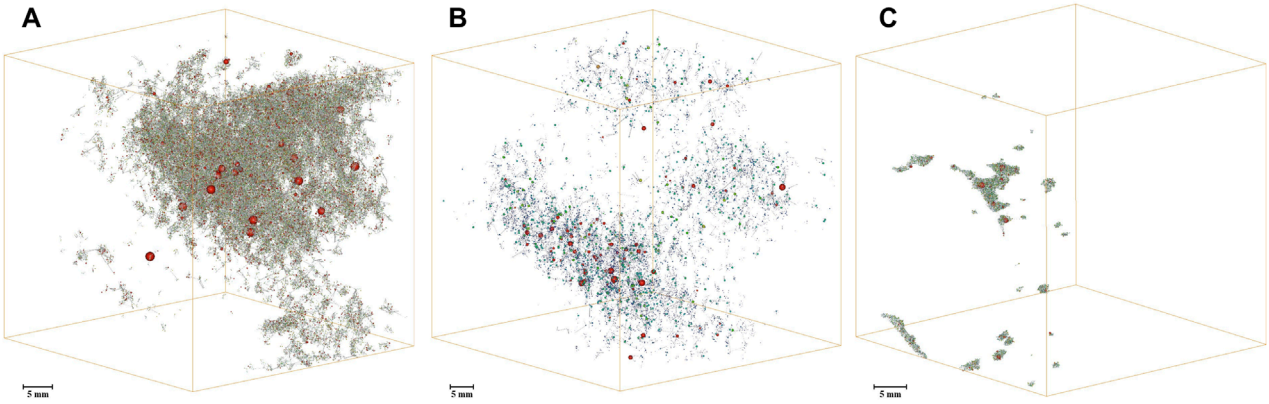

FIGURE 8
Multi-scale integrated pore network model **(A)** Rhyolitic volcanic breccia **(B)** Crystal tuff **(C)** Tuffite.

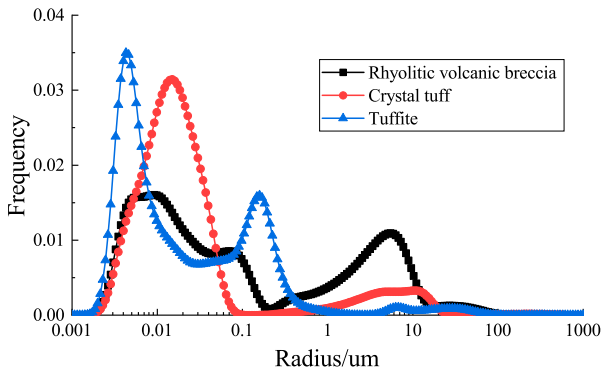

FIGURE 9
Multi-scale integrated pore radius distribution for three sample groups.

The initial full diameter scanning at 80 μm resolution provides a broad view of the rhyolitic volcanic breccia, showcasing its clastic lava structure. The largest observable clasts measure approximately 3 cm, indicating a heterogeneously distributed coarser grain structure typical of breccia. At this scale, some areas of pore development are visible, offering initial insights into the porosity of the sample. However, due to the relatively coarse resolution, finer details of pore structures are not discernible, which may underrepresent the total porosity and complexity of the pore network.

The increase in resolution in the centimeter plug scanning allows for a better identification of larger pores. This mid-scale imaging provides a more detailed view of the porosity that was only partially visible in the full diameter core scans. These images are critical for assessing the connectivity and size distribution of the larger pores, which are essential factors in evaluating the potential fluid flow and storage capacity of the reservoir.

The highest resolution imaging of the millimeter plugs reveals the finest details of the rock's internal structure. This level of detail is crucial for understanding the micro-scale features that influence the overall properties of volcanic rocks. The scans clearly display the distribution of cracks and smaller-sized pores. These features significantly impact the mechanical properties of the rock, including its permeability and structural integrity. At this scale, the shapes and boundaries of clastic structures become more distinct.

The results from the three-scale CT imaging of the crystal tuff provide detailed insights into the structural and porosity characteristics of the rock, revealing significant variations at different scales (Figure 2).

The CT images of the full diameter core indicate that the crystal tuff exhibits a good level of homogeneity, with no large or clearly visible pores. This suggests a dense matrix with potentially minor macroscopic porosity, which could imply limited macroscopic fluid flow paths within this scale. The lack of large pores might indicate a relatively intact rock structure, which is beneficial for certain types of structural stability but might limit reservoir capacity at this scale.

At this intermediate scale of the centimeter plug CT scanning, the emergence of some large pores becomes evident. These features were not visible at the lower resolution of the full diameter scan, showcasing the importance of examining different scales to capture varying pore sizes. The presence of these larger pores could enhance the potential fluid storage and permeability of the rock, indicating more favorable reservoir properties than initially suggested by the full diameter core scan.

The highest resolution scan of the millimeter plug reveals the development of micropores, predominantly characterized as intracrystalline dissolution pores. These types of pores are typically formed by the chemical alteration of minerals, particularly feldspar, within the rock matrix. The clear visibility of angular feldspar grains within the matrix underscores the mineralogical composition of the tuff. Feldspar, being a primary component, plays a significant role in the rock's overall behavior, including its reaction to geochemical processes and its mechanical properties.

The CT imaging results from the three-scale examination of the Tuffite provide critical insights into the structural integrity and porosity characteristics of this type of volcanic rock (Figure 3).

The full diameter core CT images reveal a high degree of homogeneity with a notable absence of large pores. This suggests a compact rock matrix with limited macroscopic porosity, which

TABLE 2 Multi-scale digital rock core pore-throat parameters results.

Samples			Rhyolitic volcanic breccia	Crystal tuff	Tuffite
	Porosity/%		8.21	3.57	0.34
	Connected Volume/%		62.3	48.2	31.7
Porosity	Number		174,536	27,928	15,453
	Radius/um	Maximum	887	741.5	320.4
		Minimum	0.002	0.002	0.002
		Average	2.36	1.69	0.74
Throat	Number		147,218	9,490	4,240
	Radius/um	Maximum	293.2	244.7	103.9
		Minimum	0.001	0.001	0.001
		Average	0.83	0.27	0.11

could imply restricted large-scale fluid flow within this sample at this resolution.

The centimeter plug images uncover the development of horizontal fractures, which appear as vertical fractures in the CT images. The presence of these fractures is crucial as they could represent potential pathways for fluid flow despite the overall low porosity observed. The same images display hardly any visible pores, emphasizing the rock's structural density and the likely reliance on fractures for any significant permeability.

The millimeter plug CT imaging suggest pores are not developed, reinforcing the findings from larger scales regarding the compact nature of the rock. However, the detailed imaging reveals mineral debris particles, predominantly quartz and feldspar, with varying degrees of rounding. A significant portion of the rock matrix is bound by clay cement, with clay content constituting about 30% of the composition. This high clay content could significantly impact the mechanical properties of the rock, potentially influencing its brittleness and reducing permeability.

3.2 Multi-scale images segmentation

The CT images of the crystal tuff sample at different scales (full diameter, centimeter plug, and millimeter plug) are aligned using image registration techniques as an example (Figure 4). After the imaging process, we get the CT grayscale images and pore segmentation results of rhyolitic volcanic breccia, crystal tuff, and Tuffite at three scales (Figures 5–7). The segmentation at the millimeter scale is precise, capturing detailed pore structures and microporosity. This high-resolution segmentation provides crucial insights into the finest porosity features, which are essential for understanding fluid flow at the microscopic level. At the centimeter scale, the segmentation is probabilistic, reflecting the variation and distribution of pores as observed in the higher resolution data. This intermediate scale bridges the detailed microporosity and the more general macroscopic features, offering a balanced view of porosity distribution. The largest scale employs a probabilistic segmentation approach as well, which captures the overall three-dimensional distribution of porosity. While this scale provides less detail, it is crucial for understanding the general porosity trends and guiding macroscopic analyses and interpretations.

3.3 Multi-scale integrated models in reservoir evaluation

In order to construct a multi-scale integrated digital rock core model, it is necessary to calculate the porosity proportions at different pore sizes. Using gas-measured porosity as the standard for total porosity, the porosity proportions of three sample groups are statistically analyzed across four intervals: less than 0.1 μm, 0.1–1 μm, 1–10 μm, and greater than 10 μm, in terms of their contribution to the total porosity (Table 1).

The digital rock core pore network model is progressively integrated across different scales. In the millimeter pore network digital rock core model, nanoscale pores reflected by mercury intrusion data are filled using a random filling method. This model serves as the input to fill the centimeter pore network digital rock core model, and ultimately the full diameter model. The final multi-scale pore network digital rock core model integrates mercury intrusion and three different CT scale pore data (Figure 8), aligning the digital rock core porosity with the gas-measured porosity.

Based on the integrated multi-scale pore network model, the full-scale pore radius distribution is calculated (Figure 9). The pore radius here represents equivalent spherical radius, calculated using the maximal inscribed sphere algorithm (Dong and Blunt, 2009). The pore radius distributions of the three sample groups all show a multimodal distribution, with detailed pore and throat parameters presented in Table 2. The integrated model provides parameters such as connected porosity, number of pores, pore radius distribution, number of throats, and throat radius distribution. Based on this model, the effectiveness and distribution of porosity can be accurately assessed. Combined with the frequency distribution

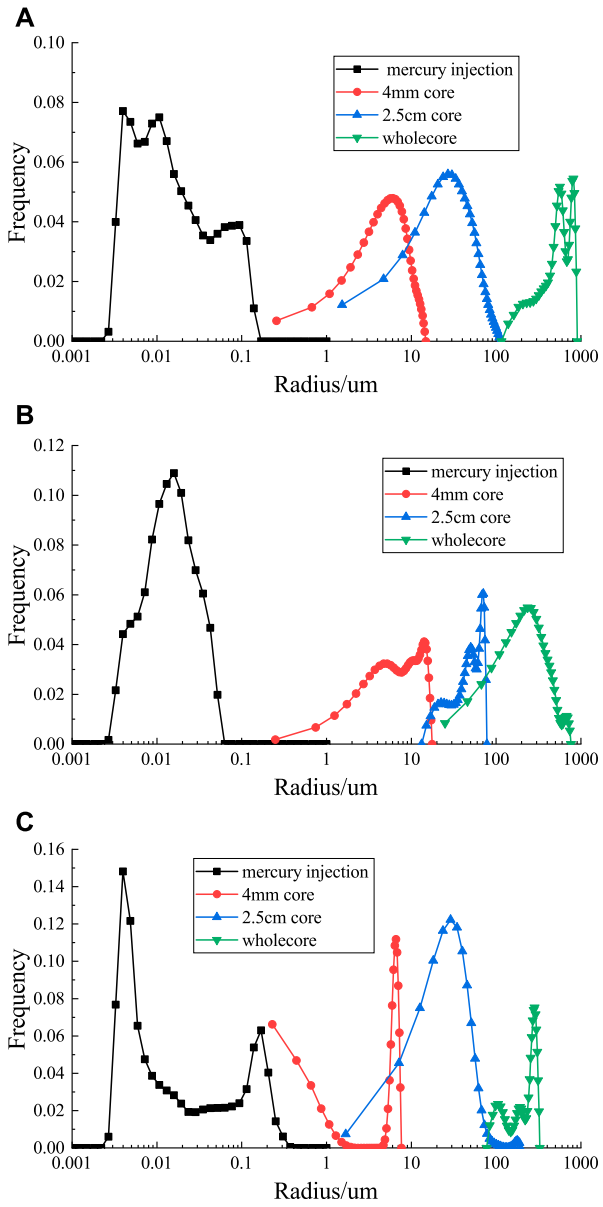

FIGURE 10
Pore radius distribution based on mercury intrusion and CT imaging. **(A)** Rhyolitic volcanic breccia **(B)** Crystal tuff **(C)** Tuffite.

of storage spaces, this can provide a robust basis for reservoir identification and prediction.

4 Discussion

4.1 Relationship between reservoir lithology and its pore distribution

The segmentation results and subsequent analyses of the three sample groups reveal intricate details about the relationship between reservoir lithology and pore distribution. Each type of volcanic tuff exhibits unique pore characteristics that significantly affect the reservoir's storage capacity and flow dynamics.

4.1.1 Rhyolitic volcanic tuff

This sample predominantly exhibits intergranular, fissure, and dissolution pores. Porosity measurements across scales (2.1%–2.4%) indicate a relatively uniform micrometer-scale pore distribution. However, these account for only 30% of the gas-measured porosity, suggesting that significant nanometer-scale pores remain undetected by CT imaging. The pore distribution is unimodal and skewed, with micrometer-scale pores significantly larger than nanometer-scale ones, as depicted by the normalized pore radius distribution curve (Figure 10A).

4.1.2 Crystal tuff

The primary storage spaces in this sample are devitrification and dissolution pores (Figure 10B). The core porosity is extremely low (0.4%) compared to gas-measured porosity, indicating a substantial presence of nanometer-scale pores. The unimodal and skewed distribution curve reveals a wide range of pore sizes, with devitrification and dissolution processes playing critical roles in pore formation.

4.1.3 Tuffite

This sample is characterized by sparse development of storage spaces, primarily interstitial pores among clay minerals, with occasional fractures (Figure 10C). The very low porosity (0.01%) accounts for only 3% of the gas-measured porosity, highlighting the dominance of nanometer-scale pores. The multimodal, skewed distribution reflects a complex interplay between minimal interstitial porosity and sporadic larger fractures.

The lithological differences among rhyolitic, crystal tuffs, and tuffite significantly influence pore characteristics and reservoir behavior. Rhyolitic tuffs feature relatively higher micrometer-scale porosity, while crystal tuff and tuffite exhibit predominantly nanometer-scale pores and limited macroscopic porosity. These variations are critical for reservoir modeling and fluid flow predictions.

The presence of substantial nanometer-scale pores across all samples emphasizes the importance of using complementary techniques, such as MIP, alongside CT imaging. This dual approach captures both micrometer- and nanometer-scale porosity, enabling a comprehensive understanding of reservoir properties. Effective reservoir management must incorporate these insights to optimize fluid flow modeling and recovery strategies.

In conclusion, integrating CT imaging with MIP provides a robust framework for assessing volcanic rock reservoirs. The lithological control on pore distribution is a key factor in defining reservoir quality, performance, and potential exploitation strategies.

4.2 Application of multi-scale integrated models in reservoir evaluation

4.2.1 Multi-scale imaging technique application

The application of multi-scale CT imaging provides a comprehensive view of volcanic rock structural and porosity characteristics, from macroscopic to microscopic scales. Such as, the presence of micropores and intracrystalline dissolution pores indicates significant secondary porosity, which is crucial for evaluating reservoirs where primary porosity is limited. These features are often critical in volcanic rocks where primary porosity is limited. The lack of significant pore development and high clay

content in tuffite samples limit its natural porosity. However, the presence of fractures could offset these limitations by offering alternative fluid flow pathways.

This approach offers critical insights into the interplay between rock texture, porosity development, and reservoir potential. It enhances the geological and petrophysical characterization of volcanic rock reservoirs, aiding in the development of more effective exploration and extraction strategies. By providing a detailed understanding of reservoir architecture, multi-scale imaging improves predictions of fluid flow behavior and reservoir quality, particularly in complex volcanic formations.

4.2.2 Applications of multi-scale integrated models

The integration of high-resolution imaging techniques, such as CT scans, MIP, and nanoscale imaging, enables detailed characterization of reservoir pore and throat networks across various scales. Multi-scale models offer a precise depiction of porosity, permeability, and structural integrity, facilitating reliable simulations of fluid dynamics within reservoirs. Understanding fluid movement across interconnected pore networks enables the prediction of hydrocarbon behavior during extraction, essential for optimizing recovery techniques.

Comprehensive models guide well placement, production rates, and enhanced recovery strategies. By identifying high-permeability and high-porosity zones, these models support targeted resource deployment, improving yield potential.

The detailed spatial and quantitative analysis provided by multi-scale models significantly reduces the uncertainties traditionally associated with reservoir evaluations. This improved predictive capability is crucial for both upstream exploration decisions and ongoing reservoir management, helping to minimize financial risks and optimize operational strategies.

Multi-scale models are particularly valuable for evaluating unconventional reservoirs, such as shale and tight gas formations, where pore structures are highly heterogeneous. The models aid in tailoring hydraulic fracturing and other recovery methods to the unique characteristics of each reservoir.

The complex datasets generated by multi-scale models are ideal for machine learning and artificial intelligence applications. These technologies enhance data interpretation, automate trend detection, and refine predictive reservoir behavior models under various operational scenarios.

In conclusion, multi-scale integrated models represent a paradigm shift in reservoir evaluation. By offering a detailed understanding of pore structures and fluid dynamics, these models enhance the efficiency, sustainability, and profitability of hydrocarbon extraction projects. They provide a foundation for informed decision-making, robust resource management, and improved recovery strategies, transforming the approach to exploring and managing volcanic rock reservoirs.

5 Conclusion

(1) Multi-scale scanning technology enables the detailed three-dimensional characterization of pore distribution across scales, from millimeter-sized samples to full-diameter cores. However, in tight reservoirs, a significant portion of pores, particularly at the nanometer scale, may remain undetected, necessitating complementary methods for a comprehensive analysis.

(2) Among the three analyzed volcanic rock types—rhyolitic volcanic breccia, crystal tuff, and tuffite—the rhyolitic volcanic breccia exhibits the best physical properties and the highest pore connectivity, making it the most favorable reservoir. Crystal tuff ranks second in reservoir quality, while tuffite demonstrates the poorest characteristics, with limited porosity and connectivity.

(3) The integration of multi-scale CT scanning with MIP and nanoscale imaging facilitates the construction of a full-scale digital pore network model. This model provides a visual representation of the morphology and spatial distribution of pores in three dimensions, enabling the quantitative analysis of pore and throat characteristics. Key parameters, including pore count, radius distribution, connectivity, and throat dimensions, are quantitatively evaluated, offering a robust foundation for assessing reservoir effectiveness and guiding exploration and development strategies.

Data availability statement

The original contributions presented in the study are included in the article/supplementary material, further inquiries can be directed to the corresponding author.

Author contributions

JZ: Writing–original draft, Writing–review and editing. YL: Writing–review and editing. ZH: Writing–original draft.

Funding

The author(s) declare financial support was received for the research, authorship, and/or publication of this article. This study was supported by the Hainan Province Science and Technology Special Fund (ZDYF2023GXJS009) and the SINOPEC Key Science and Technology Project 'Integrated Technology Research and Application for the Volcanic Gas Reservoirs in the Songnan Fault Depression' (P21104) and the Open fund of SINOPEC Key Laboratory of Geophysics (33550006-22-FW0399-0017). The authors declare that this study received funding from SINOPEC. The funder was not involved in the study design, collection, analysis, interpretation of data, the writing of this article, or the decision to submit it for publication.

Conflict of interest

Authors JZ and YL were employed by Sinopec Northeast Oil and Gas Branch.

The remaining author declares that the research was conducted in the absence of any commercial or financial relationships that could be construed as a potential conflict of interest.

Publisher's note

References

Anovitz, L. M., and Cole, D. R. (2015). Characterization and analysis of porosity and pore structures. *Rev. Mineralogy Geochem.* 80, 61–164. doi:10.2138/rmg.2015.80.04

Bai, B., Zhu, R. K., Wu, S. T., Yang, W. J., Jeff, G., Allen, G., et al. (2013). Multi-scale method of nano(micro)-CT study on microscopic pore structure of tight sandstone of yanchang formation, ordos basin. *Petroleum Explor. Dev.* 40 (3), 354–358. doi:10.1016/S1876-3804(13)60042-7

Bera, A., and Shah, S. (2021). A review on modern imaging techniques for characterization of nanoporous unconventional reservoirs: challenges and prospects. *Mar. Petroleum Geol.* 133, 105287. doi:10.1016/j.marpetgeo.2021.105287

Chalmers, G. R., Bustin, R. M., and Power, I. M. (2012). Characterization of gas shale pore systems by porosimetry, pycnometry, surface area, and field emission scanning electron microscopy/transmission electron microscopy image analyses: examples from the Barnett, Woodford, Haynesville, Marcellus, and Doig units. *AAPG Bull.* 96, 1099–1119. doi:10.1306/10171111052

Cnudde, V., and Boone, M. N. (2013). High-resolution X-ray computed tomography in geosciences: a review of the current technology and applications. *Earth-Science Rev.* 123, 1–17. doi:10.1016/j.earscirev.2013.04.003

Cui, L. K., Sun, J. M., Yan, W. C., and Dong, H. M. (2020). Multi-scale and multi-component digital core construction and elastic property simulation. *Appl. Geophys.* 17 (1), 26–36. doi:10.1007/s11770-019-0789-7

Cui, L. K., Sun, J. M., Yan, W. C., Gao, Y. S., Wang, H. J., and Song, L. Y. (2017). Construction of multi-scale and -component digital cores based on fusion of different resolution core images. *J. Jilin Univ. Sci. Ed.* 47 (6), 1904–1912. doi:10.13278/j.cnki.jjuese.201706307

Dong, H., and Blunt, M. J. (2009). Pore-network extraction from micro-computerized-tomography images. *Phys. Rev. E* 80 (3), 036307. doi:10.1103/PhysRevE.80.036307

Dong, H. M., Luo, B., Dang, C. Y., Xu, S., Wang, F., and Chi, P. (2024). Quantitative characterization of the carbonate rock microstructure considering topological features: a case study from the gaoshiti–moxi block of the sichuan basin. *Front. Earth Sci.* 12 (March), 1375637. doi:10.3389/feart.2024.1375637

Dong, H. M., Sun, J. M., Cui, L. K., Naser, G., and Yan, W. C. (2019). Characteristics of the pore structure of natural gas hydrate reservoir in the qilian mountain permafrost, northwest China. *J. Appl. Geophys.* 164 (May), 153–159. doi:10.1016/j.jappgeo.2019.03.005

Dong, H. M., Sun, J. M., Naser, G., Cui, L. K., Jiang, L. M., Yan, G. L., et al. (2018). A method to construct high-precision complex pore digital rock. *J. Geophys. Eng.* 15 (6), 2695–2703. doi:10.1088/1742-2140/aae04e

Jiang, Z., Van Dijke, M. I. J., Sorbie, K. S., and Couples, G. D. (2013). Representation of multiscale heterogeneity via multiscale pore networks: representation of multiscale heterogeneity. *Water Resour. Res.* 49 (9), 5437–5449. doi:10.1002/wrcr.20304

Jiang, Z., van Dijke, M. I. J., Wu, K., Couples, G. D., Sorbie, K. S., and Ma, J. (2012). Stochastic pore network generation from 3D rock images. *Transp. Porous Media* 94 (2), 571–593. doi:10.1007/s11242-011-9792-z

Kuila, U. (2013). *Measurement and interpretation of porosity and pore-size distribution in mudrocks: the hole story of shales*. Colorado School of Mines: Colorado, United States.

Li, R. L., Yang, L. Y., Zhu, J. F., Liu, Y. H., Xu, W., Li, Z. B., et al. (2023). Volcanic reservoir characteristics and hydrocarbon accumulation control factors of rift depressions in southern Songliao Basin. *Earth Sci. Front.* 30 (4), 100. doi:10.13745/j.esf.sf.2022.10.24

Li, Y. L., Zhang, Y. F., Cong, L., Xie, Z., Yan, M., and Tian, X. X. (2016). Application of X-CT scanning technique in the characterization of micro pore structure of tight sandstone reservoir: an example from fuyu oil layer in daan oilfield. *J. Jilin Univ. Sci. Ed.* 46 (2), 379–387. doi:10.13278/j.cnki.jjuese.201602107

Liu, B., He, S. L., Wang, H. X., Fu, X., and Gong, L. (2021). Sealing mechanisms in volcanic faulted reservoirs in xujiaweizi extension, northern Songliao Basin, northeastern China. *AAPG Bull.* 105 (8), 1721–1743. doi:10.1306/03122119048

Liu, B., Yang, Y. Q., Li, J. T., Chi, Y. A., Li, J. H., and Fu, X. F. (2020). Stress sensitivity of tight reservoirs and its effect on oil saturation: a case study of lower cretaceous tight clastic reservoirs in the hailar basin, northeast China. *J. Petroleum Sci. Eng.* 184 (January), 106484. doi:10.1016/j.petrol.2019.106484

Liu, X. F., Wang, J. F., Ge, L., Hu, F. L., Li, C. L., Li, X., et al. (2017). Pore-scale characterization of tight sandstone in Yanchang Formation Ordos Basin China using micro-CT and SEM imaging from nm-to cm-scale. *Fuel* 209, 254–264. doi:10.1016/j.fuel.2017.07.068

Liu, X. F., Yan, J. X., Zhang, X. W., Zhang, L. T., Ni, H., Zhou, W., et al. (2021). Numerical upscaling of multi-mineral digital rocks: electrical conductivities of tight sandstones. *J. Petroleum Sci. Eng.* 201, 108530. doi:10.1016/j.petrol.2021.108530

Ma, L., Fauchille, A. L., Patrick, J. D., Fernando, F. P., Loic, C., Kevin, G. T., et al. (2017). *Correlative multi-scale imaging of shales: a review and future perspectives*, 454. London: Geological Society, 175–199. Special Publications.

Ma, L., Kevin, G. T., Peter, D. L., Katherine, J. D., Patrick, J. D., and Loic, C. (2016). Novel 3D centimetre-to nano-scale quantification of an organic-rich mudstone: the carboniferous bowland shale, northern england. *Mar. Petroleum Geol.* 72 (April), 193–205. doi:10.1016/j.marpetgeo.2016.02.008

Ma, W. G., and Liu, A. X. (2011). The study of the pore structure parameters in rocks by CT scanning technology. *Sino-Global Energy* 16 (7), 54–56.

Mees, F., Swennen, R., Geet, M. V., and Jacobs, P. (2003). *Applications of X-ray computed tomography in the geosciences*, 215. London: Geological Society, 1–6. Special Publications.

Miao, C. S., Wen, X., Liu, Y. H., and Xie, R. X. (2020). Characteristics of volcanic reservoirs in southern Songliao Basin. *J. Jilin Univ. Sci. Ed.* 50 (2), 635–643. doi:10.13278/j.cnki.jjuese.20190253

Njiekak, G., Schmitt, D. R., and Kofman, R. S. (2018). Pore systems in carbonate formations, Weyburn field, Saskatchewan, Canada: micro-tomography, helium porosimetry and mercury intrusion porosimetry characterization. *J. Petroleum Sci. Eng.* 171, 1496–1513. doi:10.1016/j.petrol.2018.08.029

Otsu, N. (1979). A threshold selection method from gray-level histograms. *IEEE Transactions on Systems, Man, and Cybernetics* 1 (9), 62–66. doi:10.1109/TSMC.1979.4310076

Qajar, J., and Arns, C. H. (2022). A comparative study of micro-CT and mercury intrusion techniques for predicting permeability and surface area evolution during chemical dissolution. *Adv. Water Resour.* 168, 104301. doi:10.1016/j.advwatres.2022.104301

Qu, X. Y., Miao, C. S., Li, R. L., Zhu, J. F., Xu, W., and Liu, Y. N. (2022). Influencing factors of tight clastic reservoir physical properties and main controlling factors of high-quality reservoirs:taking the Yingcheng Formation of longfengshan sub-sag in changling fault depression of Songliao Basin as an example. *Nat. Gas. Geosci.* 33 (7), 1036–1048. doi:10.11764/j.issn.1672-1926.2022.02.005

Remeysen, K., and Swennen, R. (2008). Application of microfocus computed tomography in carbonate reservoir characterization: possibilities and limitations. *Mar. Petroleum Geol.* 25, 486–499. doi:10.1016/j.marpetgeo.2007.07.008

Wang, P. J., Chen, C. Y., Zhang, Y., Gao, Y. F., Qu, X. J., and Yi, J. (2015). Characteristics of volcanic reservoirs and distribution rules of effective reservoirs in the changling fault depression, Songliao Basin. *Nat. Gas. Ind. B* 2 (5), 440–448. doi:10.1016/j.ngib.2015.09.020

Zheng, J., Wang, P. J., Zhu, J. F., Bian, W. H., Hong, Y. M., Cheng, Z. Y., et al. (2021). Characteristics and main controlling factors of pyroclastic reservoirs: a case study in longfengshan area, changling fault depression, southern Songliao Basin. *World Geol.* 40, 399–407.

Zou, C. N., Tao, S. Z., Yang, Z., Yuan, X. J., Zhu, R. K., Hou, L. H., et al. (2012). New advance in unconventional Petroleum exploration and research in China. *Bull. Mineralogy, Petrology Geochem.* 31 (4), 312–322. doi:10.0000/BMPG.1007-2802.2012-i4-02

frontiers | Frontiers in Earth Science

TYPE Original Research
PUBLISHED 11 April 2025
DOI 10.3389/feart.2025.1539368

OPEN ACCESS

EDITED BY
Huaimin Dong,
Chang'an University, China

REVIEWED BY
Kesai Li,
Chengdu University of Technology, China
Zhen Qin,
East China University of Technology, China

*CORRESPONDENCE
Zhenguan Wu,
wuzg2014@163.com

RECEIVED 04 December 2024
ACCEPTED 25 March 2025
PUBLISHED 11 April 2025

CITATION
Li F, Wu Z, Ni W, Li X, Liao X, Xiao H and Zeng Y (2025) A simplified 3D finite difference method for electromagnetic logging while drilling simulation in symmetrical models. *Front. Earth Sci.* 13:1539368. doi: 10.3389/feart.2025.1539368

A simplified 3D finite difference method for electromagnetic logging while drilling simulation in symmetrical models

Fengbo Li[1,2,3], Zhenguan Wu[4]*, Weining Ni[1,2,3], Xin Li[1,2,3], Xiaoqiao Liao[4], Hong Xiao[4] and Yunxin Zeng[4]

[1]State Energy Key Laboratory for Carbonate Oil and Gas, Beijing, China, [2]Sinopec Key Laboratory of Well Logging, Beijing, China, [3]Sinopec Research Institute of Petroleum Engineering Co., Ltd., Beijing, China, [4]School of Geoscience and Technology, Southwest Petroleum University, Chengdu, China

Electromagnetic (EM) Logging While Drilling (LWD) plays an increasingly significant role in oil and gas exploration and development. Fast and accurate simulation of EM LWD is essential for optimizing tool parameters and data processing. As the depth of investigation increases, EM LWD simulation and inversion in complex geological structures become more important, while the computational cost of three-dimensional (3D) simulations remains a major challenge. In this paper, we present a simplified 3D finite-difference frequency domain method for symmetric geological models. In such models, the electromagnetic field generated by a magnetic dipole source exhibits symmetry in all directions. Leveraging this symmetry, we reduce the computational domain by half, centering it on the symmetry plane, and impose new boundary conditions based on the symmetry of the electric field. Compared to conventional methods, the proposed approach reduces the number of unknowns by half, significantly improving computational efficiency. Numerical simulations show that the results from the proposed method agree well with both analytical solutions and finite element simulations. We further apply the method to analyze borehole effects, mud invasion, and near-wellbore anomalies. The numerical results indicate that in a 12-inch diameter borehole, EM LWD apparent resistivity curves are influenced by borehole effects, deviating from those obtained under borehole-free conditions. The impact of the borehole and mud invasion varies with tool frequency and transmitter-receiver (TR) spacing: shorter TR spacings and higher frequencies are more susceptible to these effects, whereas longer TR spacings and lower frequencies exhibit greater stability.

KEYWORDS

electromagnetic, logging while drilling, 3d finite difference method, half-space computational domain, borehole effects

1 Introduction

With the increasing number of high angle and horizontal wells, Electromagnetic Logging While Drilling (EM LWD) is widely applied in oil and gas exploration

and development (Qin et al., 2017). EM LWD can measure the formation's electrical properties in real time, allowing for inversion-based determination of formation structures (Pardo and Torres-Verdín, 2015; Li H. et al., 2020). Consequently, it plays a crucial role in horizontal well landing and real-time geosteering (Bittar et al., 2009; Wu B. et al., 2022; Yue et al., 2022). Over the past decades, EM LWD technology has continuously evolved in its applications (Tian et al., 2023). From the perspective of tool structure and detection capabilities, EM LWD has developed from single-frequency and single transmitter-receiver spacing to multi-frequency and multi-spacing configurations (Bittar et al., 1993). Measurement components have expanded from a single coaxial component to multiple components, and the detection depth has increased from several inches to several tens of meters (Bazara et al., 2016; Clegg et al., 2022). In this process, numerical simulation technology has also played an important role (Gao et al., 2010; Qin et al., 2021).

Numerical simulation serves as the foundational basis for the optimization of EM LWD tool parameters, analysis of logging response characteristics, investigation of influencing factors, and data inversion (Wei et al., 2024). To achieve this, a variety of numerical simulation methods have been employed to calculate EM LWD responses (Liu et al., 2015). Depending on the specific requirements, different methods are employed for EM LWD simulation. For conventional EM LWD measurements, the mapping relationship between formation resistivity and phase shift or amplitude ratio can be simulated using the analytical expression of the electromagnetic field generated by a dipole source in a homogenous medium. To further analyze the impact of formation boundaries on the logging response, a pseudo-analytical algorithm in a one-dimensional (1D) model is required (Hong et al., 2016; Li Y. et al., 2020; Wang L. et al., 2020). By combining specific tool signals and inversion algorithms, it becomes possible to obtain formation resistivity and delineate formation boundaries (Wang et al., 2018; Xu et al., 2023). To address the analysis of more complex formation properties, Davydycheva et al. derived a pseudo-analytical algorithm for biaxial anisotropic media (Davydycheva et al., 2014; Fan et al., 2019). As the tool's detection depth increases, using only a 1D model becomes insufficient to describe the actual formation environment. Therefore, 2.5D algorithms for two-dimensional formation models have been widely applied (Wu et al., 2020b). Chen et al. introduced the 2.5D algorithm into EM LWD simulation and analyzed the impact of faults on the azimuthal EM LWD responses (Chen et al., 2011; Noh et al., 2022). Tool responses in anisotropic and complex scenarios are also discussed with 2.5D algorithms (Zeng et al., 2018; Wu et al., 2020a; Wu Z. et al., 2022).

Recently, to more accurately characterize reservoir structures, 3D inversion has been incorporated into EM LWD measurements and has gradually emerged as a new trend. Consequently, 3D numerical forward modeling has become increasingly essential. In fact, the application of 3D numerical algorithm techniques in EM LWD forward modeling has a long history (Wang and Fang, 2001; Davydycheva et al., 2003). In 3D numerical simulation algorithms, the finite difference method, including the finite difference time domain (FDTD) and finite difference frequency domain (FDFD) methods, is among the most widely used (Lee and Teixeira, 2010; Yuan et al., 2011; Sun and Hu, 2022). It is often applied to simulate and analyze the eccentric response of azimuthal EM LWD tools (Hue et al., 2005; Li and Wang, 2016). As another important numerical simulation method, the finite element method (FEM) offers significant advantages in simulating complex structural models due to its flexible mesh discretization (Jaysaval et al., 2016). In recent years, the discontinuous Galerkin (DG) finite element techniques have also been applied to EM logging simulations (Sun et al., 2017; Zhang et al., 2020). In addition, the finite volume method (FVM) is widely used for simulating the responses of extra-deep EM LWD tools and plays an important role in 3D inversion (Clegg et al., 2019; Wang H. et al., 2020; Wang et al., 2023). Overall, 3D numerical simulation techniques have been effectively applied in EM LWD modeling. This paper focuses on improving the traditional finite difference algorithm for a specific symmetric model to enhance computational efficiency.

In this paper, we apply the 3D finite difference frequency domain method to EM LWD simulation. For symmetric models, a simplified 3D simulation scheme is obtained by applying appropriate boundary conditions. The remainder of this paper is organized as follows. In Section 2, we briefly introduce the physics of EM LWD tools. In Section 3, the 3D finite difference algorithm with symmetric boundary conditions and the difference scheme are presented. In Section 4, the algorithm is validated through comparison with results from other methods. In Section 5, we apply the algorithm to Electromagnetic Logging While Drilling modeling and analyze the effects of borehole and mud invasion on the logging response.

2 Physics of the EM LWD tools

Electromagnetic Logging While Drilling tools were initially designed with a single-transmitter, dual-receiver configuration, using the phase shift and amplitude ratio of the induced electromotive force between two receiver coils to measure formation resistivity. The latest generation of EM LWD tools measures multi-component magnetic fields and employs low frequencies and extended transmitter-receiver spacing to enable formation detection over distances of several tens of meters (Li et al., 2020). Figure 1 shows the basic structure of EM LWD tools. The figure illustrates the tri-axial configuration for both transmitter and receiver. However, in practice, the actual tools may only use a subset of these coil systems, depending on the specific requirements, measuring only a few components. For example, traditional EM LWD tools typically use coaxial coils to measure the H_{zz} component, while azimuthal EM LWD tools also measure the H_{xz}/H_{zx} components. Additionally, some tools utilize tilted coils instead of orthogonal coils to obtain cross-coupling components. It is important to note that actual tools may incorporate additional coil systems and employ multiple frequencies for measurement.

For traditional EM LWD tools, the basic structure consists of an axial transmitter and two axial receivers. The phase shift (PS) and amplitude ratio (AR) between the dual receiver coils are formally defined by Equations 1, 2, respectively:

$$PS = atan\left(\frac{Imag(V2)}{Real(V2)}\right) - atan\left(\frac{Imag(V1)}{Real(V1)}\right) \tag{1}$$

$$AR = 20\,lg\left(\frac{Imag(V1)^2 + Real(V1)^2}{Imag(V2)^2 + Real(V2)^2}\right)^{1/2} \tag{2}$$

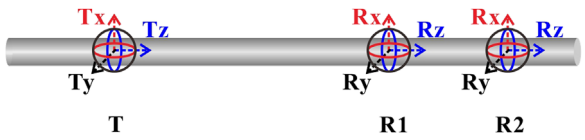

FIGURE 1
Configuration of typical EM LWD tools.

where *PS* and *AR* represent the phase shift and amplitude ratio between the two receivers, respectively. $V1$ and $V2$ are the induced electromotive forces on receiver coil 1 (R1) and receiver coil 2 (R2), respectively. Imag (·) and Real(·) are functions that extract the imaginary and real parts of a complex number, respectively. For azimuthal EM LWD tools, the basic structure is typically single-transmitter, single-receiver. When different tool configurations are used, the definition of the geosignal may vary. For instance, when an orthogonal coil system is employed, the geosignal can be defined as V_{zx} or V_{xz}. In contrast, when a tilted coil system is used (Bittar, 2000), the geosignal is defined as the phase shift geosignal (*GeoP*) and the amplitude ratio geosignal (*GeoA*). The definitions of *GeoP* (*GeoA*) are analogous to those of *PS* (*AR*), with the distinction that $V1$ and $V2$ no longer represent the induced electromotive forces from the two receiver coils. Instead, $V1$ and $V2$ correspond to the induced electromotive forces at tool rotation angles of 0° and 180°, respectively. For extra-deep EM LWD tools, the basic unit is typically a single-transmitter, single-receiver configuration. The measured coaxial, coplanar, and cross components are then used for signal synthesis. Taking Schlumberger's Geosphere service as an example, its synthesized signals include eight modes: *USDA*, *USDP*, *UADA*, *UADP*, *UHRA*, *UHRP*, *UHAA*, and *UHRP* (Seydoux et al., 2014; Wu et al., 2018; Zhang et al., 2021).

3 3D finite difference algorithm

3.1 Governing equation and boundary condition

In EM LWD measurements, fixed frequencies are typically used. In this paper, the time convention of $e^{-i\omega t}$ is assumed, and the variation in rock magnetic permeability is ignored. The Maxwell equations in the frequency domain for inhomogeneous medium can be expressed as

$$\nabla \times \mathbf{E} = i\omega\mu_0 \mathbf{H} \tag{3}$$

$$\nabla \times \mathbf{H} = \mathbf{J}_s + (\sigma - i\omega\varepsilon)\mathbf{E} \tag{4}$$

where, $\mathbf{E}$ is the Electric field, V; $\mathbf{H}$ is the magnetic fields, $A{\cdot}m^{-1}$; ω is the angular frequency, $rad{\cdot}s^{-1}$; $\mathbf{J}_s$ is the current source, $A{\cdot}m^{-2}$; $\boldsymbol{\sigma}$ is the conductivity tensor, $S{\cdot}m^{-1}$; μ_0 is the permeability of vacuum, $4\pi{\cdot}10^{-7}$ $H{\cdot}m^{-1}$; $\boldsymbol{\varepsilon}$ is the dielectric constant, $F{\cdot}m^{-1}$. By combining Equations 3, 4, the wave equation of electric field can be obtained as shown in Equation 5. Moreover, the conductivity-permittivity coupling term $(\sigma - i\omega\varepsilon)$ can exhibit anisotropic properties, as characterized in Equation 7.

$$\nabla \times \nabla \times \mathbf{E} = i\omega\mu_0 \mathbf{J}_s + i\omega\mu_0(\sigma - i\omega\varepsilon)\mathbf{E} \tag{5}$$

The electromagnetic fields generated in the formation is the superposition of the incident field produced by a magnetic dipole source and the scattered field. Specifically, in a homogeneous isotropic formation, only the incident field, denoted as $\mathbf{E}^i$, exists. The scattered field, denoted as $\mathbf{E}^s$, is due to the heterogeneity of the formation. Therefore, the total field can be expressed as the sum of $\mathbf{E}^i$ and $\mathbf{E}^s$. Substitute the total field $\mathbf{E}$ and the incident field $\mathbf{E}^i$ into Equation 3 and take the difference to obtain Equation 6:

$$\nabla \times \nabla \times \mathbf{E}^s - i\omega\mu_0 \hat{\sigma}\mathbf{E}^s = i\omega\mu_0(\hat{\sigma} - \hat{\sigma}_0)\mathbf{E}^i \tag{6}$$

where

$$\sigma - i\omega\varepsilon = \begin{bmatrix} \sigma_{xx} - i\omega\varepsilon_{xx} & \sigma_{xy} - i\omega\varepsilon_{xy} & \sigma_{xz} - i\omega\varepsilon_{xz} \\ \sigma_{yx} - i\omega\varepsilon_{yx} & \sigma_{yy} - i\omega\varepsilon_{yy} & \sigma_{yz} - i\omega\varepsilon_{yz} \\ \sigma_{zx} - i\omega\varepsilon_{zx} & \sigma_{zy} - i\omega\varepsilon_{zy} & \sigma_{zz} - i\omega\varepsilon_{zz} \end{bmatrix} \tag{7}$$

Since subsurface rocks are often lossy media, the electromagnetic field will decay to zero far from the source. Therefore, the boundary condition of the EM LWD modeling problem becomes Equation 8:

$$\boldsymbol{E}|_{(x\to\infty,or,y\to\infty,or,z\to\infty)} = 0 \tag{8}$$

In fact, considering the exponential decay of the electromagnetic field, using a Perfect Electric Conductor (PEC) boundary at a distance greater than 2.3 times the skin depth from the magnetic dipole source ensures that the boundary's influence on the simulation results is less than 1%.

3.2 Model construction and conductivity equivalence

Taking into account factors such as the borehole condition, mud invasion and formation structure, a three-dimensional model as shown in Figure 2 is established. For the three-dimensional simulation of EM LWD, we typically need to focus on factors such as mud resistivity, wellbore dimensions, mud invasion, and the environment of deviated or horizontal wells. The dashed lines in Figure 2 represent the finite difference grid, which divides the formation model into a series of small cells. By assigning corresponding electrical parameters to each cell, further difference simulations can be conducted. The figure shows a vertical well model under inclined formation conditions. By rotating the coordinates, it can also be used to simulate inclined well conditions in horizontal formations.

It should be noted that formation conductivity is usually expressed in the formation coordinate system. In EM LWD modeling, it is necessary to rotate the formation coordinate system to the tool coordinate system as expressed in Equation 9:

$$\sigma_t = \mathbf{R}^{-1}\sigma_f\mathbf{R} \tag{9}$$

where, $\boldsymbol{\sigma}_t$ and $\boldsymbol{\sigma}_f$ are the conductivity matrices in the tool coordinate system and the formation coordinate system, respectively. $\mathbf{R}$ is the rotation matrix, which is shown in Equation 10.

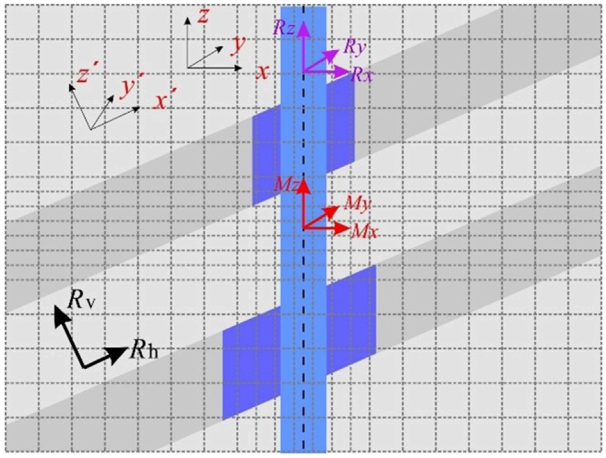

FIGURE 2
A three-dimensional formation model for EM LWD modeling.

$$\mathrm{R}=\begin{bmatrix}\cos\theta\cos\varphi\cos\gamma-\sin\varphi\sin\gamma & -\cos\theta\cos\varphi\sin\gamma-\sin\varphi\cos\gamma & \sin\theta\cos\varphi\\ \cos\theta\sin\varphi\cos\gamma+\cos\varphi\sin\gamma & -\cos\theta\sin\varphi\sin\gamma+\cos\varphi\cos\gamma & \sin\theta\sin\varphi\\ -\sin\theta\cos\gamma & \sin\theta\sin\gamma & \cos\theta\end{bmatrix} \tag{10}$$

where θ, φ and γ are the three Euler angles.

3.3 Finite difference scheme

To apply the finite difference method, the electric field wave equation is first expanded into a scalar equation:

$$\begin{aligned}
&\left(\frac{\partial^2 E_y^s}{\partial x\partial y}+\frac{\partial^2 E_z^s}{\partial x\partial z}-\frac{\partial^2 E_x^s}{\partial y^2}-\frac{\partial^2 E_x^s}{\partial z^2}\right)-\mathrm{i}\omega\mu_0\left(\sigma_{xx}E_x^s+\sigma_{xy}E_y^s+\sigma_{xz}E_z^s\right)\\
&\quad=\mathrm{i}\omega\mu_0\left[(\sigma_{xx}-\sigma_0)E_x^i+\sigma_{xy}E_y^i+\sigma_{xz}E_z^i\right]\\
&\left(\frac{\partial^2 E_x^s}{\partial x\partial y}+\frac{\partial^2 E_z^s}{\partial y\partial z}-\frac{\partial^2 E_y^s}{\partial x^2}-\frac{\partial^2 E_y^s}{\partial z^2}\right)-\mathrm{i}\omega\mu_0\left(\sigma_{yx}E_x^s+\sigma_{yy}E_y^s+\sigma_{yz}E_z^s\right)\\
&\quad=\mathrm{i}\omega\mu_0\left[\sigma_{yx}E_x^i+(\sigma_{yy}-\sigma_0)E_y^i+\sigma_{yz}E_z^i\right]\\
&\left(\frac{\partial^2 E_x^s}{\partial x\partial z}+\frac{\partial^2 E_y^s}{\partial y\partial z}-\frac{\partial^2 E_z^s}{\partial x^2}-\frac{\partial^2 E_z^s}{\partial y^2}\right)-\mathrm{i}\omega\mu_0\left(\sigma_{zx}E_x^s+\sigma_{zy}E_y^s+\sigma_{zz}E_z^s\right)\\
&\quad=\mathrm{i}\omega\mu_0\left[\sigma_{zx}E_x^i+\sigma_{yz}E_y^i+(\sigma_{zz}-\sigma_0)E_z^i\right]
\end{aligned} \tag{11}$$

It can be observed that the incident and scattered fields of the electric field are separated to the left and right sides of the equation, respectively. The scattered field is the unknown to be solved, while the incident field can be obtained through an analytical solution. Therefore, a linear system of equations can be formed by Equation 11. By using the finite difference method, the differential on the left side of the equation is converted into a difference, thereby obtaining the coefficient matrix for the linear system of equations. For the second-order difference, the coordinates at node (i, j, k) are defined as (x_i, y_j, z_k). The coordinates $x_{i+1/2}$, $y_{j+1/2}$, and $z_{k+1/2}$ correspond to the positions at the midpoints of the cell edges between nodes in the x, y, and z directions, respectively. The distances between two nodes in the x, y, and z directions are $\Delta x_i = x_{i+1}\text{-}x_i, \Delta y_j = y_{j+1}\text{-}y_j, \Delta z_k = z_{k+1}\text{-}z_k$. The distances from the node centers are $\Delta x_{i\text{-}1/2} = x_{i+1/2}\text{-}x_{i\text{-}1/2}, \Delta y_{j\text{-}1/2} = y_{j+1/2}\text{-}y_{j\text{-}1/2}, \Delta z_{k\text{-}1/2} = z_{k+1/2}\text{-}z_{k\text{-}1/2}$. The derivation of finite difference schemes is a nontrivial process. Without loss of generality, we take the first term on the left side of Equation 11 as an example. Its finite difference scheme is formulated in Equation 12:

$$\begin{aligned}
\frac{\partial^2 E_y^s}{\partial x\partial y}&=\frac{\partial}{\partial y}\left(\frac{E^s_{y(i+1,j,k)}-E^s_{y(i,j,k)}}{\Delta x_i}\right)=\frac{1}{\Delta x_i\Delta y_{j-\frac{1}{2}}}\\
&\times\left[\left(E^s_{y\left(i+1,j+\frac{1}{2},k\right)}-E^s_{y\left(i,j+\frac{1}{2},k\right)}\right)-\left(E^s_{y\left(i+1,j-\frac{1}{2},k\right)}-E^s_{y\left(i,j-\frac{1}{2},k\right)}\right)\right]
\end{aligned} \tag{12}$$

The other terms on the left side of the equation can be obtained using the same method. For the terms on the right side, we only need to calculate the incident field at the corresponding nodes using an analytical solution. Another issue in constructing the linear system of equations is the assignment of conductivity values. Since the electric field is located on the edge of a cell and there are four cells surrounding that edge, it is necessary to use the properties of the four cells to equivalently assign the conductivity of the electric field at that location. Here, we use the xx component as an example to derive the equivalent conductivity. Assume that the electric field within any cell is uniform and equal to the electric field at $(i+1/2, j, k)$. For the electric field in the x-direction, the current generated in the x-direction is given by

$$\begin{aligned}
&J_{xx(i,j-1,k-1)}S_{(i,j-1,k-1)}+J_{xx(i,j,k-1)}S_{(i,j,k-1)}+J_{xx(i,j-1,k)}S_{(i,j-1,k)}\\
&\quad+J_{xx(i,j,k)}S_{(i,j,k)}=J_{xx\left(i+\frac{1}{2},j,k\right)}S
\end{aligned} \tag{13}$$

where S represents the cross-sectional area. By combining the differential form of Ohm's law with Equation 13, we obtain the equivalent conductivity as expressed in Equation 14.

$$\begin{aligned}
\sigma_{xx\left(i+\frac{1}{2},j,k\right)}&=\frac{\Delta z_{k-\frac{1}{2}}\left(\Delta y_{j-1}\sigma_{xx(i,j-1,k-1)}+\Delta y_j\sigma_{xx(i,j,k-1)}\right)}{4\Delta y_{j-\frac{1}{2}}\Delta z_{k-\frac{1}{2}}}\\
&+\frac{\Delta z_k\left(\Delta y_{j-1}\sigma_{xx(i,j-1,k)}+\Delta y_j\sigma_{xx(i,j,k)}\right)}{4\Delta y_{j-\frac{1}{2}}\Delta z_{k-\frac{1}{2}}}
\end{aligned} \tag{14}$$

The equivalent conductivity for other components can be derived in a similar manner and will not be repeated here.

3.4 Symmetric fields-based half-space modeling method

Typically, due to the complex formation structures and measurement environments, the electromagnetic field distribution generated by the EM LWD tools is quite intricate. However, when the complexity of the formation structure is reduced, and only horizontal layered formations are considered, the electromagnetic field distribution will exhibit certain symmetric or antisymmetric properties. Consider a deviated borehole model within a horizontally layered formation. The top and bottom shoulder beds are modeled as semi-infinite, isotropic formations, with resistivities of 3 Ω·m and 4 Ω·m, respectively. The middle layer is characterized by anisotropic properties, with a horizontal resistivity of 10 Ω·m and a vertical resistivity of 40 Ω·m. The

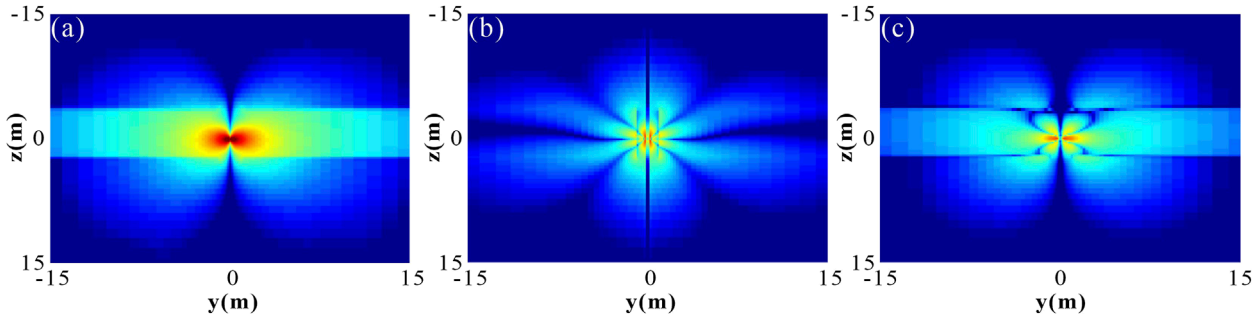

FIGURE 3
Cross-sectional view of the electric field generated by a magnetic dipole source in the z-direction on YOZ plane: **(a)** *Ex* component; **(b)** *Ey* component; **(c)** *Ez* component.

wellbore deviates at an angle of 60° relative to the formation normal, with a radius of 4.25 inches (10.8 cm), and is filled with drilling mud of resistivity 0.1 Ω·m. Mud invasion occurs within the middle layer, extending to a depth of 0.5 m. The invaded zone exhibits a horizontal resistivity of 1 Ω·m and a vertical resistivity of 4 Ω·m. Figure 3 illustrates the cross-sectional view of the electric field in the YOZ plane generated by a magnetic dipole source oriented in the z-direction. It is evident that all components of the electric field are symmetric about the $y = 0$ plane. Much more numerical simulations indicate that similar results can be observed for magnetic dipole sources oriented in other directions. This symmetry arises from the fact that, although the current model is three-dimensional, it is symmetric about the $y = 0$ plane. Therefore, the symmetry of the field is an inherent property of the model.

To further validate the symmetry of the electromagnetic field, a three-dimensional model is established. Specifically, a vertical well is embedded in a homogeneous formation with a resistivity of 10 Ω·m. The borehole has a diameter of 8.5 inches and is filled with mud of resistivity 0.1 Ω·m. The transmitter coil is positioned at the center of the well axis at a relative depth of 0 m, with coordinates (0, 0, 0). A low-resistivity anomaly, characterized by a resistivity of 1 Ω·m and a side length of 2 m, is placed adjacent to the well, with its center located at coordinates (2 m, 0 m, 0 m). Figure 4 presents the cross-sectional distribution of the Ez component on the XOY plane (z = 0.5) generated by different directional dipole sources. The results indicate that the electric field maintains symmetry with respect to the y = 0 plane.

Since the electromagnetic field exhibits symmetrical properties, we can simplify the simulations by computing the field in half of the space. Figure 5a presents a schematic of the electric field nodes on the YOZ plane within a full-space computation domain, while Figure 5b illustrates the corresponding electric field node distribution on the YOZ plane in a half-space computation domain. In this case, we assume the midpoint of the y-axis coordinates $y\left(\frac{Ny+1}{2}\right)$ and $y\left(\frac{Ny+1}{2}+1\right)$ of the symmetry plane. In half-space modeling, a crucial consideration is that by eliminating half of the spatial domain, the boundary conditions of the computational model are consequently altered. Specifically, in the full-space 3D finite difference simulation of EM LWD, PEC boundary conditions are used. However, in the case of half-space modeling, one of the boundaries is transformed into a symmetry plane (i.e., the YOZ plane). On this symmetry plane, the electric field cannot be treated with PEC boundary conditions. In contrast, we can leverage the symmetry of the field to establish new boundary conditions. Assuming the number of grid points in the x, y, and z directions are denoted as Nx, Ny, and Nz, respectively, with each being an odd number. The boundary conditions on the symmetry plane can be set according to Equation 15:

$$\begin{cases} E_{x\left(i+\frac{1}{2},\frac{Ny+1}{2},k\right)} = sgn(M)\cdot E_{x\left(i+\frac{1}{2},\frac{Ny+1}{2}+1,k\right)} \\ E_{z\left(i,\frac{Ny+1}{2},k+\frac{1}{2}\right)} = sgn(M)\cdot E_{z\left(i,\frac{Ny+1}{2}+1,k+\frac{1}{2}\right)} \end{cases} \tag{15}$$

where sgn (·) is a function of the magnetic dipole moment. For magnetic dipole sources oriented in the x and z directions, sgn (·) equals −1, while for those oriented in the y direction, sgn (·) equals +1. The relative position relationship of the electric field in the equation can be seen in Figure 4B. It should be noted that on the YOZ plane, only electric field components in the x and z directions are present. Therefore, boundary conditions need only be considered for E_x and E_z. Since the computational domain has been reduced to half of its original size, the number of electric field nodes to be solved is similarly halved. Consequently, the computational efficiency can be significantly improved.

4 Algorithm validation

To validate the accuracy of the algorithm, three models were designed: a homogenous anisotropic formation, a horizontally layered formation, and a mud invasion model. The 3D finite difference simulation results were compared with analytical solutions and results from 3D finite element method. For the homogeneous model, the horizontal and vertical resistivity are set to 5 Ω·m and 20 Ω·m, respectively. The well deviation ranges from 0° to 90°, with the tool operating at a frequency of 100 kHz and a transmitter-receiver spacing of 96 inches. Figure 6a illustrates the variation of the H_{xx} component of the magnetic field at the receiver as a function of the borehole dip angle. In the figure, the black solid line represents the analytical solution, while the red scattered points indicate the results from the 3D finite difference simulation.

For the horizontally layered formation, the model consists of three layers: the top and bottom shoulder beds are both semi-infinite

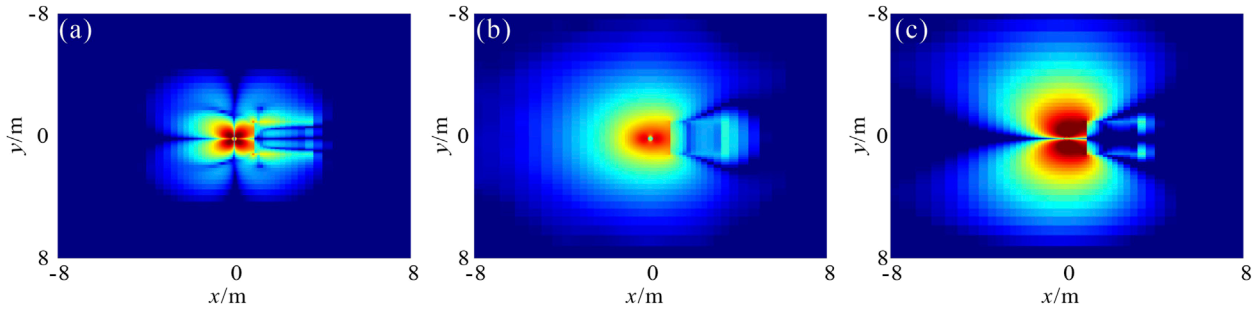

FIGURE 4
Cross-sectional view of *Ez* component on XOY plane (z = 0.5m) generated by: **(a)** *x*-oriented dipole; **(b)** *y*-oriented dipole; **(c)** *z*-oriented dipole.

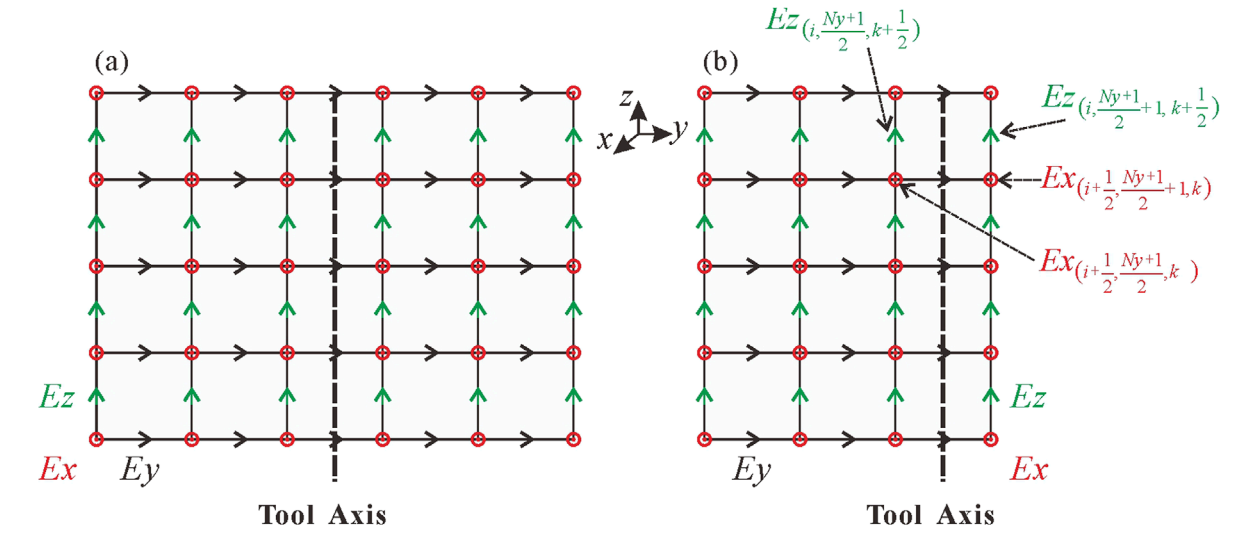

FIGURE 5
Finite difference grids and electric field nodes. **(a)** full-space; **(b)** half-space.

with a resistivity of 1 Ω·m, and the middle layer is a 2-m thick anisotropic layer with horizontal and vertical resistivities of 10 Ω·m and 40 Ω·m, respectively. The tool frequency is set to 100 kHz, with a transmitter-receiver spacing of 96 inches, and the well deviation angle is 0°. Figure 6b shows the variation of the imaginary part of H_{xx} component with true vertical depth (Tvd). In the figure, the black solid line represents the analytical solution, while the red scattered points denote the 3D finite difference results. For the mud invasion model, the borehole radius is assumed to be 4.25 inches, filled with mud having a resistivity of 0.5 Ω·m. The resistivities of the invaded zone and the virgin zone are 1 Ω·m and 10 Ω·m, respectively. Figure 6c shows the variation of the imaginary part of H_{xx} with the invasion radius, where the invasion radius refers to the distance from the boundary of the invaded zone to the wellbore wall. In the figure, the black solid line represents the 3D finite element method results, while the red scattered points denote the 3D finite difference results. It can be observed that in all three tested models, the 3D finite difference simulation results closely match the reference solutions, with relative errors of less than 1%, thereby validating the accuracy of the algorithm.

5 Numerical examples

In this section, we apply the 3D finite difference algorithm to simulate the EM LWD responses and analyze the effects of borehole environment and mud invasion on the responses of different types of EM LWD tools.

5.1 Borehole effects

During the drilling process, the wellbore is typically filled with drilling mud. As a result, the electromagnetic waves generated by EM LWD tools are inevitably influenced by the borehole environment. In this section, we take the *Hzz* (coaxial component) and *Hzx* (cross-coupling component) components as examples to analyze the effects of the borehole on the tool response. Consider a three-layer formation model, where the middle resistive layer exhibits a resistivity of 10 Ω·m and a thickness of 3 m. The top and bottom layers are infinitely thick with a resistivity of 1 Ω·m. The formation is penetrated by a vertical borehole. In the first scenario, we ignore

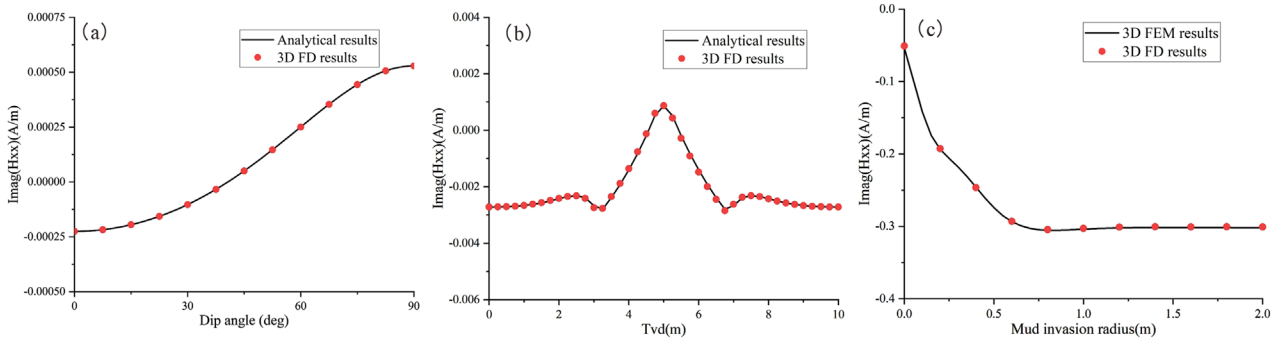

FIGURE 6
Comparison of 3D finite difference results with the analytical solution and 3D finite element method. **(a)** Homogeneous Formation Model; **(b)** Horizontally Layered Formation Model; **(c)** Mud Invasion Model.

the influence of the borehole and consider only the variation in formation resistivity. In the second scenario, we take the borehole effects into account, with a borehole radius of 6 inches and a mud resistivity of 0.2 Ω·m. In this case, we assume a one-transmitter, one-receiver configuration, with an operating frequency of 20 kHz and a transmitter-receiver spacing of 40 inches. Figure 7 illustrates the variation of the imaginary part of the *Hzz* component with depth in the formation. In Figure 7a, the comparison between the FDFD results and the analytical solutions demonstrates a good agreement, confirming the validity of the 3D finite difference algorithm. Figure 7b compares the response results with and without the presence of a borehole, revealing that the existence of the borehole leads to deviations in the *Hzz* curve. Since the *Hzz* component is typically used for measuring apparent resistivity in formations, it is important to appropriately consider the borehole environment during apparent resistivity analysis. Figure 8 illustrates the variation of the *Hxz* component with depth (in this case, the formation dip angle is 45°, and the other parameters are the same as in Figure 7). Separation of the curves can be observed as the tool approaches the formation boundary. The *Hxz* component is commonly used for detecting bed boundaries, and significant borehole effects may lead to errors in determining the distance to the boundary. It should be noted that, in most cases, a borehole radius of 4.25 inches is typically used rather than 6 inches. However, in this example, our primary goal is to demonstrate the validity of the method and the overall impact of the borehole on the curves. Therefore, slight variations in borehole size will not affect the conclusions.

When discussing borehole effects, it is essential to consider the influence of mud resistivity. The resistivity of drilling mud can vary significantly; for instance, saline-based muds exhibit very low resistivity, while freshwater and oil-based muds demonstrate much higher resistivity. Consider a homogeneous formation with a resistivity of 10 Ω·m, penetrated by a wellbore with a radius of 4.25 inches. The resistivity of the mud within the wellbore varies from 0.002 to 100 Ω·m. Here, we focus on examining the impact of wellbore mud on the apparent resistivity curve. Figure 9 illustrates the variation in amplitude ratio and phase shift with mud resistivity for electromagnetic logging-while-drilling (LWD) configurations of 2 MHz–28 in and 400 kHz-40 in. As shown in Figure 9a, the amplitude ratio for the 2 MHz-28 in configuration decreases rapidly with increasing mud resistivity, eventually leveling off, indicating the response of a homogeneous medium. In particular, when the mud resistivity is as low as 0.002 Ω·m, the amplitude ratio of the 400 kHz-40 in configuration remains approximately equal to that of a homogeneous formation. In contrast, when the mud resistivity falls below 0.01 Ω·m, the amplitude ratio of the 2 MHz-28 in configuration is significantly affected by the borehole. In Figure 9b, the two curves exhibit singularities in the low-resistivity (high-conductivity) mud region, which may be attributed to the nonlinear phase shift induced by the presence of highly conductive mud. For the 400 kHz-40 in phase difference, the measurement results remain largely unaffected by borehole conditions when the mud resistivity exceeds 0.05 Ω·m. In contrast, the 2 MHz-28 in phase difference remains susceptible to borehole effects unless the mud resistivity exceeds 0.2 Ω·m. Overall, high-frequency phase difference signals exhibit greater sensitivity to low-resistivity mud conditions, whereas low-frequency amplitude ratio signals demonstrate higher robustness against such influences.

5.2 Mud invasion

In the process of oil and gas well drilling, overbalanced drilling is commonly employed, where the wellbore pressure exceeds the formation pressure, leading to drilling mud invasion into the formation. Considering that logging-while-drilling (LWD) incorporates real-time measurement during the drilling process, the effects of mud invasion are typically neglected. In this paper, we utilize numerical simulation to rigorously investigate the impact of mud invasion on the response characteristics of various logging tools.

First, we consider the impact of mud invasion on apparent resistivity measurements obtained from a conventional EM LWD tool. Two mud invasion models are established as follows: (1) Conductive invasion model: The wellbore radius is 4.25 in, with a mud resistivity of 0.5 Ω·m, a formation resistivity of 10 Ω·m, and an invasion zone resistivity of 1 Ω·m. (2) Resistive invasion model: The wellbore radius is 4.25 in, with a mud resistivity of 1,000 Ω·m, a formation resistivity of 1 Ω·m, and an invasion zone resistivity of 10 Ω·m. Figure 10 illustrates the variation of A28H, P28H, A40L,

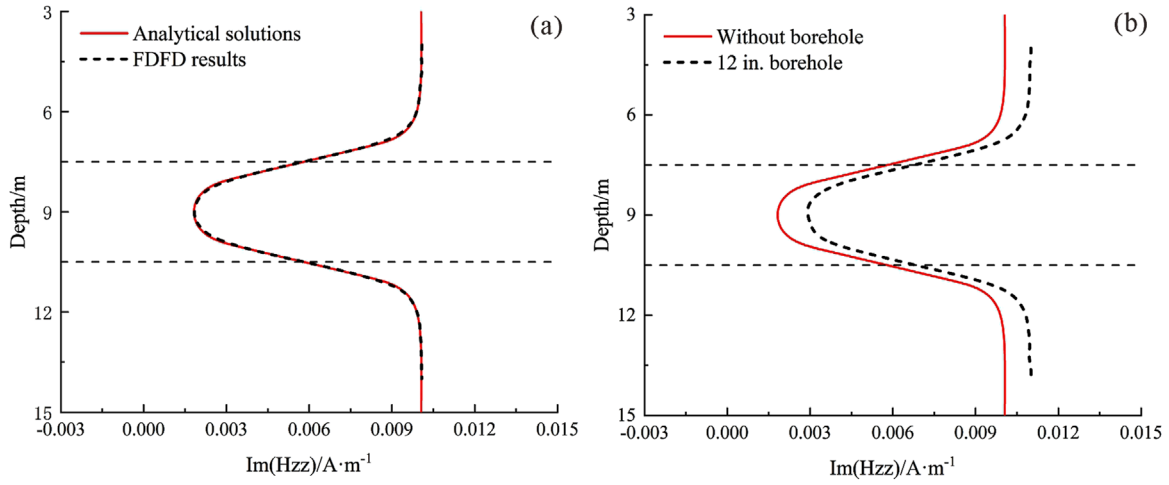

FIGURE 7
Variation of the imaginary part of the *Hzz* component with depth. **(a)** Comparison of FDFD results and analytical solutions in 1D model; **(b)** Comparison of responses with and without borehole.

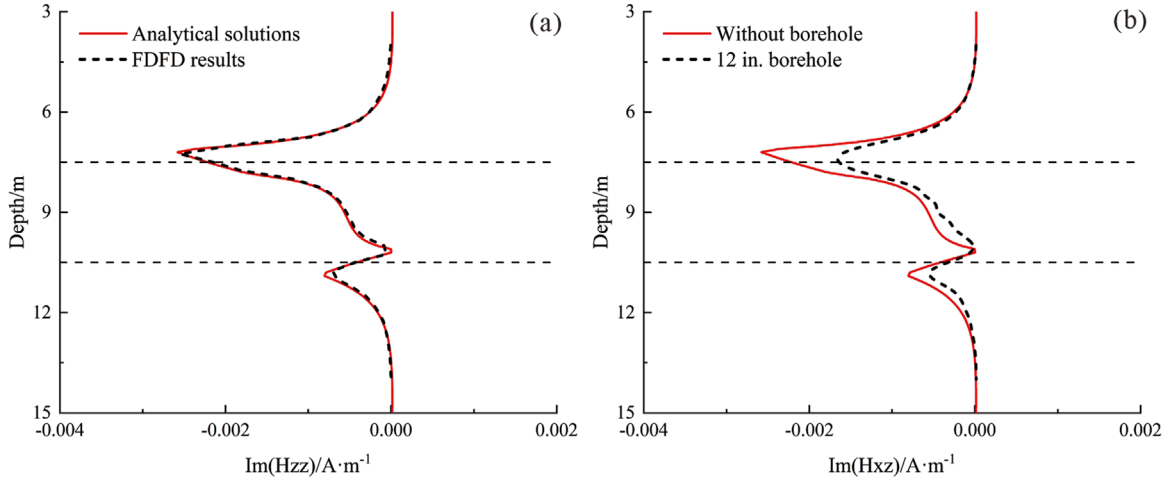

FIGURE 8
Variation of the imaginary part of the *Hxz* component with depth. **(a)** Comparison of FDFD results and analytical solutions in 1D model; **(b)** Comparison of responses with and without borehole.

and P40L with respect to the invasion depth. In this context, A28H and P28H represent the amplitude ratio and phase shift signals from the 2 MHz-28 in configuration, while A40L and P40L represent the amplitude ratio and phase shift signals from the 400 kHz-40 in configuration, respectively. Here, 'A' and 'P' denote the amplitude ratio and phase shift, respectively, to distinguish the types of signals, while 'H' and 'L' stand for high frequency and low frequency, respectively, to differentiate between the 2 MHz and 400 kHz signals. It can be observed that conductive invasion increases both the amplitude ratio and phase shift, while resistive invasion results in a decrease in both parameters. The amplitude ratio shows the most significant variation at invasion depths between 0.5 and 1.0 m, while the phase shift exhibits the most pronounced variation between 0 and 0.5 m. When the invasion depth exceeds 1.0 m, neither the amplitude ratio nor phase shift undergoes significant changes with further increases in invasion depth, primarily because the invasion zone extends beyond the detection range of the EM LWD tools.

Using the same mud invasion models as previously described, we further analyze the variation in the responses of an extra-deep EM LWD tool with different measurement modes as a function of invasion depth, taking the 24 kHz-13 m coil configuration as an example. The numerical simulation results are shown in Figure 11.

The figure demonstrates that mud invasion does not significantly affect the responses of *USDA*, *USDP*, *UADA*, *UADP*, *UHAA*, and *UHAP*. Although mud invasion causes a slight variation in the values of UHRA and UHRP, the effect is minimal, especially when the invasion depth is less than 1 m, where the influence can be considered negligible.

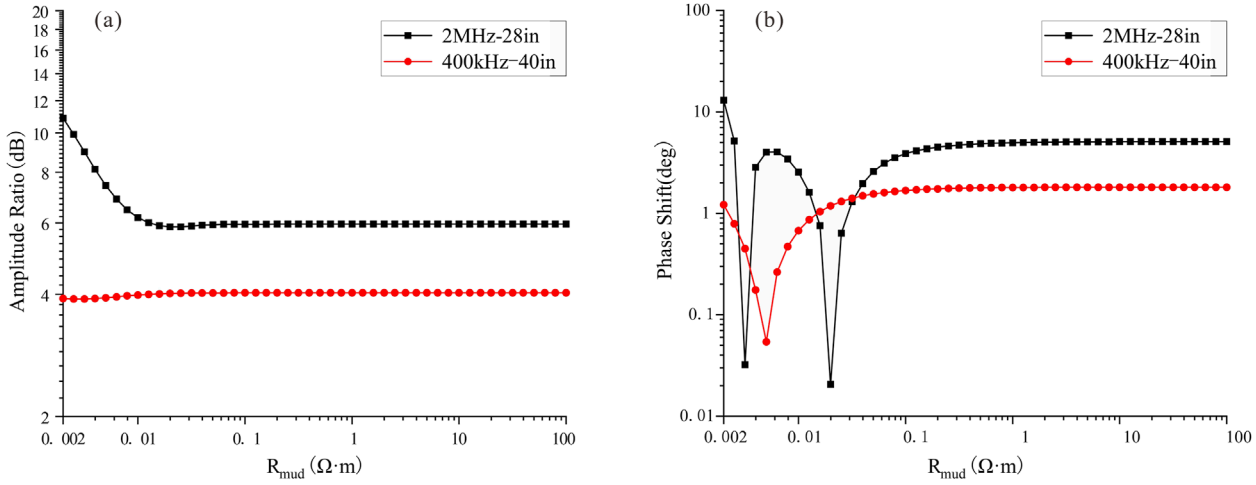

FIGURE 9
Amplitude ratio and phase shift vary with mud resistivity. **(a)** Amplitude ratio; **(b)** Phase shift.

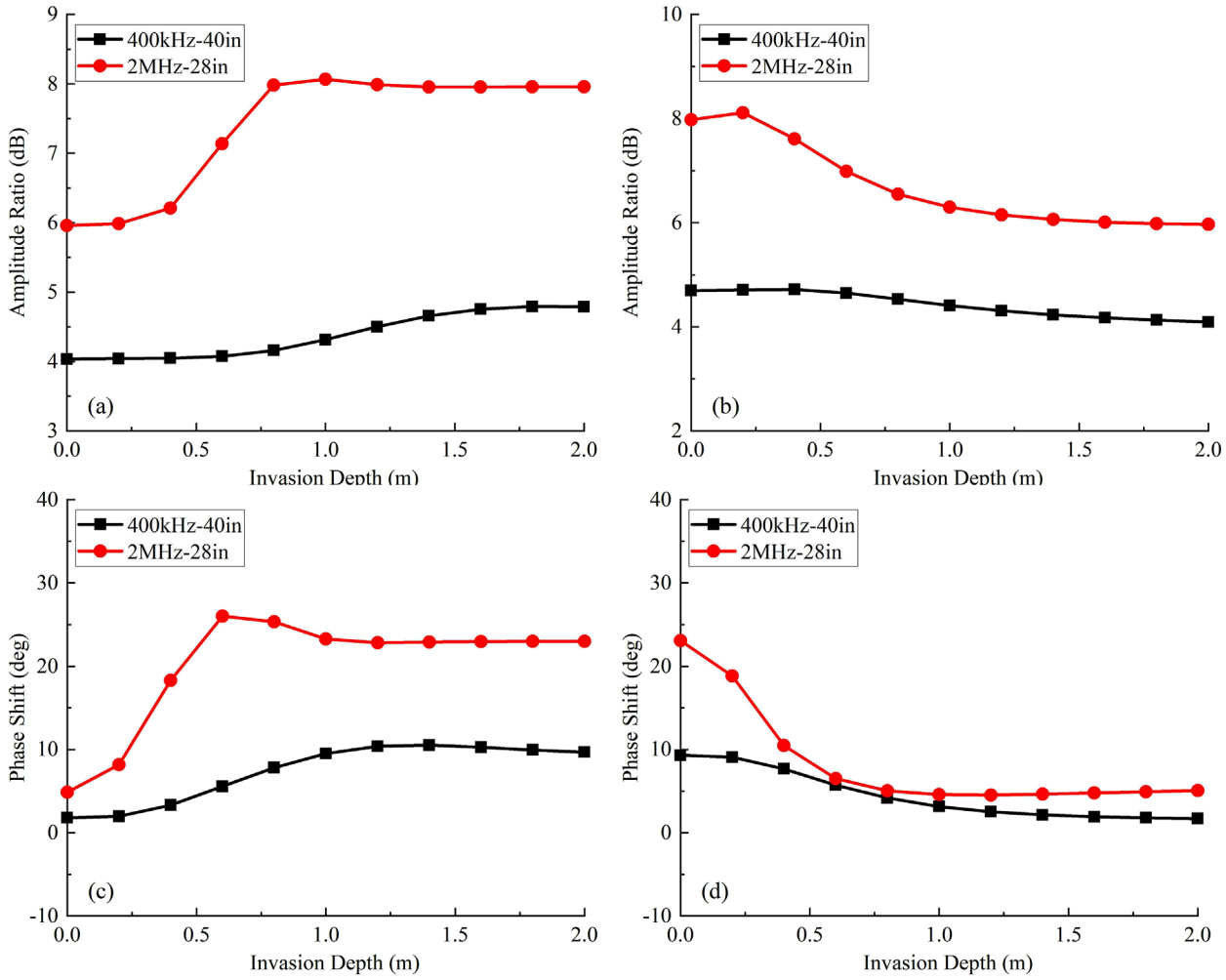

FIGURE 10
Amplitude ratio and phase shift vary with invasion depth. **(a)** Amplitude ratio with conductive invasion model; **(b)** Amplitude ratio with resistive invasion model; **(c)** Phase shift with conductive invasion model; **(d)** Phase shift with resistive invasion model.

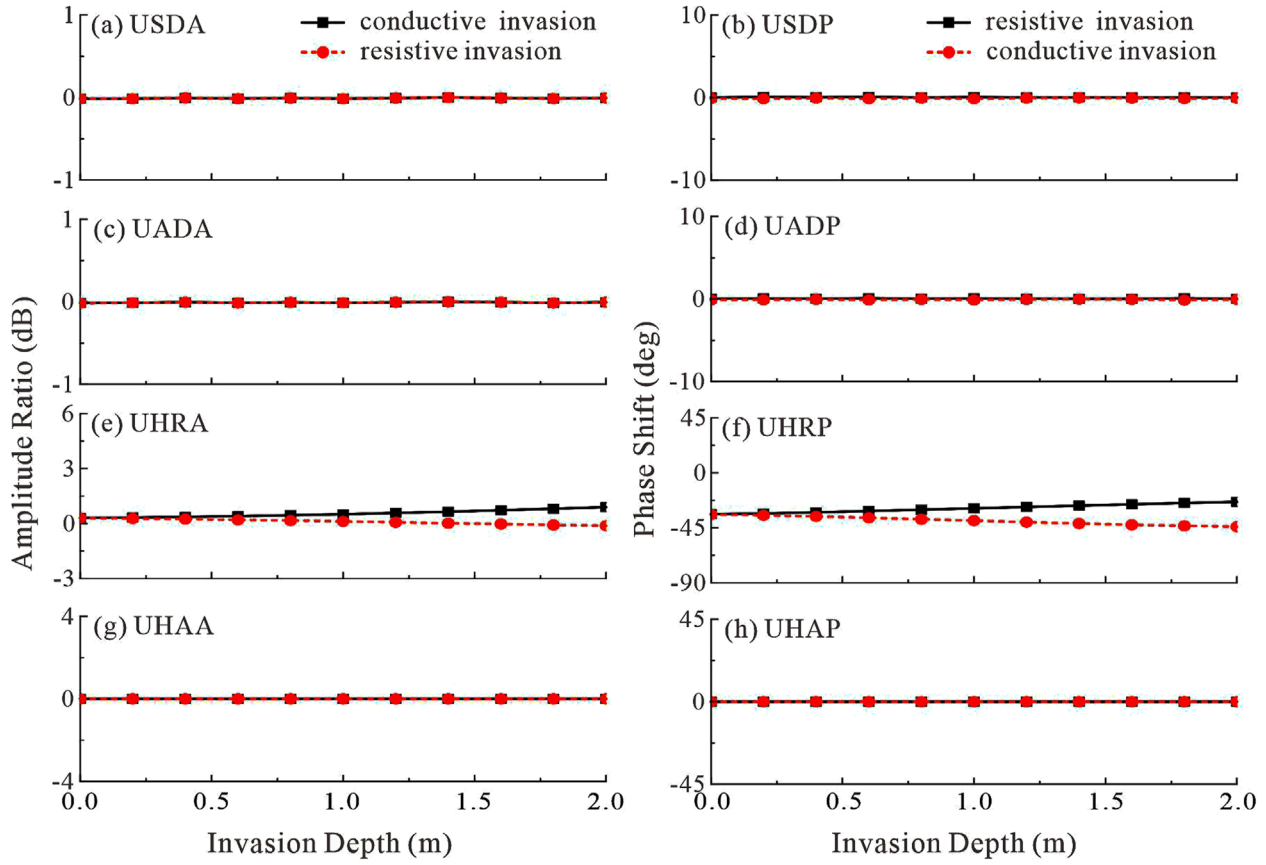

FIGURE 11
Extra-deep EM LWD responses vary with invasion depth. **(a)** USDA; **(b)** USDP; **(c)** UADA; **(d)** UADP; **(e)** UHRA; **(f)** UHRP; **(g)** UHAA; **(h)** UHAP.

Numerical simulations indicate that the effect of mud invasion on tool responses is strongly dependent on the tool parameters and the type of invasion. For high-frequency, short-spacing signals, mud invasion leads to a deviation of the apparent resistivity from the true formation resistivity. In contrast, for low-frequency, long-spacing signals, the impact of mud invasion is minimal and can generally be disregarded in well logging analysis.

5.3 Resistivity anomaly near the borehole

To further illustrate the applicability of the proposed method, we developed the model presented in Figure 12 to investigate the effect of a resistivity anomalous body adjacent to the borehole on EM LWD responses. In this model, a homogeneous sandstone formation with a resistivity of 10 Ω·m is assumed, incorporating an infinitely long, low-resistivity shale inclusion with a cross-sectional dimension of 2 m × 2 m. A horizontal well traverses beneath the shale, with the borehole positioned at a distance D2A of 1 m from the lower boundary of the shale.

Figure 13 illustrates the tool responses obtained from EM LWD, where GA96L and GA96M denote the amplitude ratio signals at 96 in-100 kHz and 96 in-400 kHz, respectively, while GP96L and GP96M represent the phase shift signals at 96 in-100 kHz and 96 in-400 kHz, respectively. It is well established that when the tool operates in a homogeneous formation, geosignals are equal to zero. The detection capability of the tool is typically defined by threshold values of 0.25 dB for the amplitude ratio and 1.5° for the phase shift. As shown in Figure 13a, when adopting 0.25 dB as the threshold, GA96L can detect the presence of the anomalous body at a distance of 2.5 m from its left boundary, whereas GA96M can only detect it within 1.5 m of the left boundary. This observation indicates that lower-frequency signals exhibit greater detection depth. In Figure 13b, due to the relatively small magnitude of the phase shift signal, GP96L fails to detect the anomalous body when using 1.5° as the threshold, while GP96M is capable of detecting it only when the distance to the left boundary is reduced to 0.5 m. These results demonstrate that the amplitude ratio signal provides superior detection capability compared to the phase shift signal.

6 Discussion

Three-dimensional (3D) numerical modeling is the most robust approach for simulating well-logging responses in subsurface formations (Weiss and Newman, 2002; Ma et al., 2014), as these responses are inherently controlled by the synergistic effects of multiple geological factors, including lithological heterogeneity, borehole geometry, and fluid saturation dynamics (Grayver and Bürg, 2014; Kang et al., 2023). However, the substantial memory requirements and computational complexity of 3D numerical modeling significantly

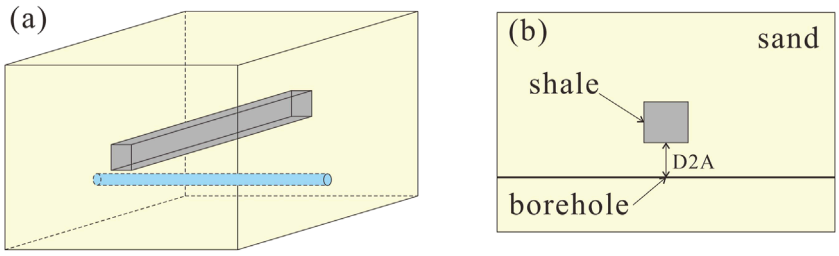

FIGURE 12
Model of the anomalous body adjacent to the borehole. **(a)** Three-dimensional model; **(b)** Two-dimensional cross-sectional view.

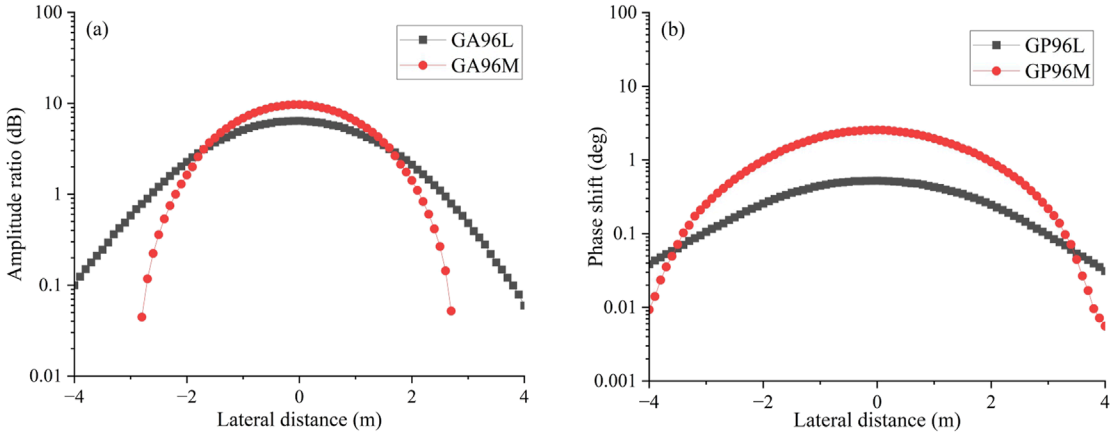

FIGURE 13
EM LWD geosignals responses: **(a)** Amplitude ratio; **(b)** Phase shift.

constrain its practical application, particularly in data processing workflows where it fails to meet the efficiency demands of interpretation engineers (Zhou et al., 2016). To mitigate these limitations, researchers have developed simplified approaches tailored to specific logging instruments and methodologies. Among these, the sliding window method is the most widely adopted, as it reduces computational costs by incrementally approximating complex 3D models through sequential 2D and 1D representations (Wang et al., 2018). This dimensionality reduction approach is highly effective in improving computational efficiency (Abubakar et al., 2008; Auken and Christiansen, 2004; Lovell and Chew, 1987). However, it remains a simplification method that inherently involves neglecting certain factors, leading to inherent limitations. For instance, when the simultaneous effects of mud invasion and borehole inclination must be considered, a 3D model cannot be adequately reduced to a 2D model.

The fundamental principle of our computational simplification is based on the symmetry of the electromagnetic field. Through theoretical analysis and numerical experiments, we rigorously demonstrate that the electromagnetic field generated in a symmetric formation model also exhibits symmetry. Leveraging this property, we reduce computational complexity by solving for the field in only half of the domain, while the other half is reconstructed using symmetry. The accuracy of the proposed method is further validated through numerical simulations. Moreover, several case studies are presented to illustrate the applicability of the simplified algorithm under various conditions. With the increasing application of extra-deep EM LWD tools, the demand for 3D simulations is expected to grow rapidly. The method proposed in this study holds significant potential for broader applications in this context.

As with all simplification algorithms, the method presented in this study has its limitations. Specifically, it requires that the model being simulated exhibit symmetry. In other words, this method is not universally applicable to all 3D problems. Nonetheless, it is crucial to highlight the advantages of this method and its potential future applications: (a) Our method improves upon traditional 3D algorithms, making it highly cost-effective for researchers or institutions already utilizing 3D simulation programs. (b) When analyzing the impact of individual factors, such as borehole mud, instrument eccentricity, or mud invasion, this algorithm offers a significant advantage by reducing computation time compared to conventional 3D methods. (c) Although the algorithm requires symmetry in the model, it can still serve as an approximate solution for asymmetric models, providing a near solution at a substantially lower computational cost.

7 Conclusion

In this paper, we propose a three-dimensional finite-difference frequency-domain method for electromagnetic (EM) modeling, specifically designed for symmetric geological models. The

method is applied to simulate EM Logging-While-Drilling (LWD) tool responses and analyze key influencing factors. Numerical simulations demonstrate that the proposed approach achieves high accuracy in modeling EM LWD responses while significantly reducing computational costs. A detailed analysis of borehole effects reveals that the influence of the borehole environment on apparent resistivity curves is primarily governed by mud resistivity and tool parameters. Generally, tools operating at higher frequencies and with shorter transmitter-receiver (TR) spacings are more susceptible to borehole effects. However, when the mud resistivity exceeds a certain threshold- 0.2 Ω·m in the examples presented in this study—the impact of the borehole can be considered negligible. The effect of mud invasion on logging responses is found to be highly dependent on tool parameters. Specifically, tools operating at higher frequencies and with shorter transmitter-receiver (TR) spacings exhibit greater sensitivity to invasion-induced resistivity contrasts. Conversely, extra-deep EM LWD tools, which typically operate at lower frequencies and employ longer TR spacings, show minimal sensitivity to invasion effects. Given that the invasion depth during logging-while-drilling is generally shallow, the impact of mud invasion on extra-deep EM LWD measurements can be considered negligible in most practical scenarios.

It is important to note that the method proposed in this study is fundamentally a simplified simulation approach tailored for symmetric models. While the current implementation is based on a 3D finite-difference formulation in Cartesian coordinates, the underlying methodology can be extended to cylindrical coordinates, broadening its applicability to a wider range of wellbore and formation geometries. Future research will focus on extending this approach to more complex anisotropic formations and integrating it with inversion algorithms to improve subsurface characterization in challenging geological environments.

Data availability statement

The original contributions presented in the study are included in the article/supplementary material, further inquiries can be directed to the corresponding author.

Author contributions

FL: Funding acquisition, Methodology, Writing – original draft. ZW: Funding acquisition, Investigation, Methodology, Writing – original draft, Writing – review and editing. WN: Funding acquisition, Investigation, Writing – review and editing. XL (4th author): Methodology, Writing – review and editing. XL (5th author): Methodology, Writing – review and editing. HX: Validation, Writing – review and editing. YZ: Validation, Writing – review and editing.

Funding

The author(s) declare that financial support was received for the research and/or publication of this article. We are indebted to the financial support from the National Key R&D Program of China (2019YFA0708301), National Natural Science Foundation of China (42304140), Natural Science Foundation of China (No.U24B6001), and Natural Science Foundation of Sichuan, China (2023NSFSC0771).

Conflict of interest

Authors FL, WN, and XL (4th author) were employed by Sinopec Key Laboratory of Well Logging and Sinopec Research Institute of Petroleum Engineering Co., Ltd.

The remaining authors declare that the research was conducted in the absence of any commercial or financial relationships that could be construed as a potential conflict of interest.

Generative AI statement

The author(s) declare that no Generative AI was used in the creation of this manuscript.

Publisher's note

References

Abubakar, A., Habashy, T. M., Druskin, V. L., Knizhnerman, L., and Alumbaugh, D. (2008). 2.5D forward and inverse modeling for interpreting low-frequency electromagnetic measurements. *Geophysics* 73 (4), F165–F177. doi:10.1190/1.2937466

Auken, E., and Christiansen, A. V. (2004). Layered and laterally constrained 2D inversion of resistivity data. *Geophysics* 69 (3), 752–761. doi:10.1190/1.1759461

Bazara, M., Abdelwahid, D. K., and Popov, T. (2016). "Ultra-deep directional resistivity measurements and the way of revealing formation tops ahead of time," in *Abu dhabi international petroleum exhibition and conference*.

Bittar, M. (2000). Electromagnetic wave resistivity tool having a tilted antenna for determining the horizontal and vertical resistivities and relative dip angle in anisotropic earth formations. *U.S. Pat. Appl. no.* 6 (163)–155.

Bittar, M., Klein, J., Beste, R., Hu, G., Wu, M., Pitcher, J., et al. (2009). A new azimuthal deep-reading resistivity tool for geosteering and advanced formation evaluation. *SPE Reserv. Eval. and Eng.* 12 (02), 270–279. doi:10.2118/109971-pa

Bittar, M., Rodney, P., Mack, S., and Bartel, R. (1993). A multiple-depth-of-investigation electromagnetic wave resistivity sensor: theory, experiment, and field test results. *SPE Form. Eval.* 8 (03), 171–176. doi:10.2118/22705-pa

Chen, Y., Omeragic, D., Druskin, V., Kuo, C., Habashy, T., Abubakar, A., et al. (2011). "2.5D FD modeling of EM directional propagation tools in high-angle and horizontal wells," in *81th annual international meeting, SEG*, 422–426.

Clegg, N., Parker, T., Djefel, B., Monteilhet, L., and Marchant, D. (2019). "The final piece of the puzzle: 3-D inversion of ultra-deep azimuthal resistivity lwd data," in *SPWLA 60th annual logging symposium*. D043S010R003.

Clegg, N., Sinha, S., Rodriguez, K. R., Walmsely, A., Sviland-Østre, S., Lien, T., et al. (2022). "Ultra-deep 3D electromagnetic inversion for anisotropy, a guide to understanding complex fluid boundaries in a turbidite reservoir," in *SPWLA 63rd annual logging symposium*.

Davydycheva, S., Druskin, V., and Habashy, T. (2003). An efficient finite-difference scheme for electromagnetic logging in 3D anisotropic inhomogeneous media. *Geophysics* 68 (5), 1525–1536. doi:10.1190/1.1620626

Davydycheva, S., Zhou, M., and Liu, R. (2014). "Triaxial induction tool response in 1D layered biaxial anisotropic formation," in *SEG annual meeting*.

Fan, Y., Hu, X., Deng, S., Yuan, X., and Li, H. (2019). Logging while drilling electromagnetic wave responses in inclined bedding formation. *Petroleum Explor. Dev.* 46 (4), 711–719. doi:10.1016/S1876-3804(19)60228-4

Gao, J., Ke, S., Wei, B., and Tan, M. (2010). Introduction to numerical simulation of electrical logging and its development trend. *Well Logging Technol.* 34 (01), 1–5. doi:10.16489/j.issn.1004-1338.2010.01.002

Grayver, A. V., and Bürg, M. (2014). Robust and scalable 3-D geo-electromagnetic modelling approach using the finite element method. *Geophys. J. Int.* 198 (1), 110–125. doi:10.1093/gji/ggu119

Hong, D., Huang, W., and Liu, Q. (2016). Radiation of arbitrary magnetic dipoles in a cylindrically layered anisotropic medium for well-logging applications. *IEEE Trans. Geoscience Remote Sens.* 54 (11), 6362–6370. doi:10.1109/TGRS.2016.2582535

Hue, Y.-K., Teixeira, F., Martin, L., and Bittar, M. (2005). Three-dimensional simulation of eccentric LWD tool response in boreholes through dipping formations. *IEEE Trans. Geoscience Remote Sens.* 43 (2), 257–268. doi:10.1109/TGRS.2004.841354

Jaysaval, P., Shantsev, D. V., de la Kethulle de Ryhove, S., and Bratteland, T. (2016). Fully anisotropic 3-D EM modelling on a Lebedev grid with a multigrid pre-conditioner. *Geophys. J. Int.* 207 (3), 1554–1572. doi:10.1093/gji/ggw352

Kang, Z., Qin, H., Zhang, Y., Hou, B. B., Hao, X. L., and Chen, G. (2023). Coil optimization of ultra-deep azimuthal electromagnetic resistivity logging while drilling tool based on numerical simulation. *J. Petroleum Explor. Prod. Technol.* 13 (3), 787–801. doi:10.1007/s13202-022-01575-1

Lee, H., and Teixeira, F. (2010). Locally-conformal FDTD for anisotropic conductive interfaces. *IEEE Trans. Antennas Propag.* 58 (11), 3658–3665. doi:10.1109/TAP.2010.2071362

Li, H., and Wang, H. (2016). Investigation of eccentricity effects and depth of investigation of azimuthal resistivity LWD tools using 3D finite difference method. *J. Petroleum Sci. Eng.* 143, 211–225. doi:10.1016/j.petrol.2016.02.032

Li, H., Wang, H., Wang, L., and Zhou, X. (2020a). A modified Boltzmann Annealing Differential Evolution algorithm for inversion of directional resistivity logging-while-drilling measurements. *J. Petroleum Sci. Eng.* 188, 106916. doi:10.1016/j.petrol.2020.106916

Li, K., Gao, J., and Zhao, X. (2020). Tool design of look-ahead electromagnetic resistivity LWD for boundary identification in anisotropic formation. *J. Petroleum Sci. Eng.* 184, 106537. doi:10.1016/j.petrol.2019.106537

Li, Y., Sun, X., Wang, M., and Li, R. (2020b). Numerical simulation and analysis of multicomponent induction logging response in anisotropic formation. *IEEE Access* 8, 149345–149361. doi:10.1109/ACCESS.2020.3015722

Liu, N., Wang, Z., and Liu, C. (2015). The simulations of formation resistivity imaging by applying directional resistivity tool with a joint-coil antenna while drilling. *Prog. Geophys. (in Chinese)* 30 (6), 2897–2905. doi:10.6038/pg20150659

Lovell, J. R., and Chew, W. C. (1987). Response of a point source in a multicylindrcally layered medium. *IEEE Transactions on Geoscience and Remote Sensing GE-* 25 (6), 850–858. doi:10.1109/TGRS.1987.289757

Ma, J., Nie, Z., and Sun, X. (2014). Efficient modeling of large-scale electromagnetic well-logging problems using an improved nonconformal FEM-DDM. *IEEE Transactions on Geoscience and Remote Sensing* 52 (3), 1825–1833. doi:10.1109/tgrs.2013.2255298

Noh, K., Pardo, D., and Torres-Verdín, C. (2022). 2.5-D Deep learning inversion of LWD and deep-sensing EM measurements across formations with dipping faults. *IEEE Geoscience and Remote Sensing Letters* 19, 1–5. doi:10.1109/LGRS.2021.3128965

Pardo, D., and Torres-Verdín, C. (2015). Fast 1D inversion of logging-while-drilling resistivity measurements for improved estimation of formation resistivity in high-angle and horizontal wells. *Geophysics* 80 (2), E111–E124. doi:10.1190/geo2014-0211.1

Qin, Z., Pan, H., Wu, A., Yang, H., Hu, T., Hou, M., et al. (2017). Application of conventional propagation resistivity logging for formation boundary identification in geosteering. *Journal of Geophysics and Engineering* 14 (5), 1233–1241. doi:10.1088/1742-2140/aa80a0

Qin, Z., Tang, B., Wu, D., Luo, S. C., Ma, X. G., Huang, K., et al. (2021). A qualitative characteristic scheme and a fast distance prediction method of multi-probe azimuthal gamma-ray logging in geosteering. *Journal of Petroleum Science and Engineering* 199, 108244–1-10. doi:10.1016/j.petrol.2020.108244

Seydoux, J., Legendre, E., Mirto, E., Dupuis, C., Denichou, J.-M., Bennett, N., et al. (2014). "Full 3D deep directional resistivity measurements optimize well placement and provide reservoir-scale imaging while drilling," in *SPWLA 55th annual logging symposium* (Abu Dhabi, UAE: SPWLA-2014-LLLL).

Sun, Q., and Hu, Y. (2022). Fast geometric multigrid preconditioned finite-difference frequency-domain method for borehole electromagnetic sensing. *IEEE Geoscience and Remote Sensing Letters* 19, 1–4. doi:10.1109/LGRS.2021.3053590

Sun, Q., Ren, Q., Zhan, Q., and Liu, Q. (2017). 3-D Domain decomposition based hybrid finite-difference time-domain/finite-element time-domain method with nonconformal meshes. *IEEE Transactions on Microwave Theory and Techniques* 65 (10), 3682–3688. doi:10.1109/TMTT.2017.2686386

Tian, Y., Zhu, J., Die, Y., Liu, L., Yue, C., Wang, X., et al. (2023). Boundary detection capability and influencing factors of electromagnetic resistivity while using drilling tools in a horizontal well. *Frontiers in Earth Science* 10. doi:10.3389/feart.2022.1042353

Wang, H., Wang, H., Yang, S., and Yin, C. (2020a). Efficient finite-volume simulation of the LWD orthogonal azimuth electromagnetic response in a three-dimensional anisotropic formation using potentials on cylindrical meshes. *Applied Geophysics* 17 (2), 192–207. doi:10.1007/s11770-020-0818-6

Wang, L., Fan, Y., Yuan, C., Wu, Z., Deng, S., and Zhao, W. (2018). Selection criteria and feasibility of the inversion model for azimuthal electromagnetic logging while drilling (LWD). *Petroleum Exploration and Development* 45 (5), 974–982. doi:10.1016/S1876-3804(18)30101-0

Wang, L., Wu, Z., Fan, Y., and Huo, L. (2020b). Fast anisotropic resistivities inversion of logging-while-drilling resistivity measurements in high-angle and horizontal wells. *Applied Geophysics* 17 (3), 390–400. doi:10.1007/s11770-020-0830-x

Wang, T., and Fang, S. (2001). 3-D electromagnetic anisotropy modeling using finite differences. *Geophysics* 66 (5), 1386–1398. doi:10.1190/1.1486779

Wang, Y., Wang, H., Kang, Z., and Yin, C. (2023). Efficient computation of nonlinear Born approximation of the LWD ultra-deep look ahead resistivity measurement using coupled potentials 3D finite-volume method and differential operator expansion. *Chinese Journal of Geophysics (in Chinese)VL* - 66 (7), 3102–3114. doi:10.6038/cjg2022Q0650

Wei, K., Qin, Z., Wang, C., Zhang, Z., Su, K., Wang, G., et al. (2024). Response characteristics and novel understandings of dual induction logging of horizontal wells in fractured reservoirs. *Journal of Applied Geophysics* 225, 105393, 1–10. doi:10.1016/j.jappgeo.2024.105393

Weiss, C. J., and Newman, G. A. (2002). Electromagnetic induction in a fully 3-D anisotropic earth. *Geophysics* 67 (4), 1104–1114. doi:10.1190/1.1500371

Wu, B., Yang, Z., Guo, T., and Yuan, X. (2022a). Response characteristics of logging while drilling system with multi-scale azimuthal electromagnetic waves. *Petroleum Drilling Techniques* 50 (6), 7–13. doi:10.11911/syztjs.2022107

Wu, H.-H., Golla, C., Parker, T., Clegg, N., and Monteilhet, L. (2018). "A new ultra-deep azimuthal electromagnetic LWD sensor for reservoir insight," in *SPWLA 59th annual logging symposium*.

Wu, Z., Deng, S., He, X., Zhang, R., Fan, Y., Yuan, X., et al. (2020a). Numerical simulation and dimension reduction analysis of electromagnetic logging while drilling of horizontal wells in complex structures. *Petroleum Science* 17 (3), 645–657. doi:10.1007/s12182-020-00444-y

Wu, Z., Fan, Y., Wang, J., Zhang, R., and Liu, Q. (2020b). Application of 2.5-D Finite difference method in Logging-While-Drilling electromagnetic measurements for complex scenarios. *IEEE Geoscience and Remote Sensing Letters* 17 (4), 577–581. doi:10.1109/LGRS.2019.2926740

Wu, Z., Li, H., Han, Y., Zhang, R., Zhao, J., and Lai, Q. (2022b). Effects of formation structure on directional electromagnetic logging while drilling measurements. *Journal of Petroleum Science and Engineering* 211, 110118. doi:10.1016/j.petrol.2022.110118

Xu, L., Zhang, R., Sun, S., Sun, J., and Shi, J. (2023). Modified levenberg–marquardt inversion for high-resolution resistivity distribution reconstruction of multilayered formation. *IEEE Transactions on Instrumentation and Measurement* 72, 1–10. doi:10.1109/TIM.2022.3224519

Yuan, N., Liu, R., and Nie, X. (2011). "Electromagnetic field of arbitrarily oriented coil antennas in complicated underground environment," in *2011 IEEE international symposium on antennas and propagation (APSURSI)*, 1658–1661.

Yue, X., Liu, T., Li, G., Nie, Z., Ma, M., and Sun, X. (2022). An analytically fast forward method of LWD azimuthal electromagnetic measurement and its geo-steering application. *Chinese Journal of Geophysics (in Chinese)VL* - 65 (5), 1909–1920. doi:10.6038/cjg2022P0233

Zeng, S., Chen, F., Li, D., Chen, J., and Chen, J. (2018). A novel 2.5D finite difference scheme for simulations of resistivity logging in anisotropic media. *Journal of Applied Geophysics* 150, 144–152. doi:10.1016/j.jappgeo.2018.01.021

Zhang, P., Deng, S., Hu, X., Wang, L., Wang, Z., Yuan, X., et al. (2021). Detection performance and sensitivity of logging-while-drilling extra-deep azimuthal resistivity measurement. *Chinese Journal of Geophysics (in Chinese)VL* - 64 (6), 2210–2219. doi:10.6038/cjg2021O0087

Zhang, R., Wu, Z., Sun, Q., Zhuang, M., Cai, Q., Wang, D., et al. (2020). Memory-Efficient 3-D LWD solver with the flipped total field/scattered field-based DGFD method. *IEEE Geoscience and Remote Sensing Letters* 17 (9), 1498–1502. doi:10.1109/LGRS.2019.2950659

Zhou, J., Li, H., Rabinovich, M., and D'Arcy, B. (2016). "Interpretation of azimuthal propagation resistivity measurements: modeling, inversion, application and discussion," in *SPWLA 57th annual logging symposium* (Reykjavik, Iceland: SPWLA-2016-HHHH).

frontiers | Frontiers in Earth Science

TYPE Original Research
PUBLISHED 16 April 2025
DOI 10.3389/feart.2025.1477727

OPEN ACCESS

EDITED BY
Jeroen van Hunen,
Durham University, United Kingdom

REVIEWED BY
Qibin Lin,
University of South China, China
Changshuo Wang,
Ningbo University, China
Pengju An,
Ningbo University, China
Nagessa Zerihun Jilo,
Wuhan University of Technology, China

*CORRESPONDENCE
Wen-Ling Tian,
tianwenling3@163.com

RECEIVED 08 August 2024
ACCEPTED 03 April 2025
PUBLISHED 16 April 2025

CITATION
Zhao J, Tian W-L, Zhang B-Q and Yang S-Q (2025) Experimental study on deformation and failure mechanism of the double-arch tunnel without a middle pilot.
Front. Earth Sci. 13:1477727.
doi: 10.3389/feart.2025.1477727

Experimental study on deformation and failure mechanism of the double-arch tunnel without a middle pilot

Jiang Zhao[1,2], Wen-Ling Tian[1]*, Ben-Qing Zhang[1] and Sheng-Qi Yang[1]

[1]School of Mechanics and Civil Engineering, China University of Mining and Technology, Xuzhou, China, [2]Bureau of Transport of Zhaotong Municipal, Zhaotong, China

To explore the deformation and failure mechanism of multi-arch tunnel without a middle pilot tunnel, taking the Sanyanjing tunnel of Qiuyan Expressway in Yunnan province as the research object. The stress evolution and the associated deformation and failure mechanisms of the surrounding rock, composed of class IV limestone, were studied using a physical model test during the excavation process. The results show that tangential stress attenuation occurs within a distance equal to the diameter of the tunnel wall, while stress concentration occurs beyond this range in the unsupported tunnel. However, the supporting structure, forms a stable pressure arch within the surrounding rock, which makes the elastic zone extend to the surrounding and deep of the tunnel. The surrounding rock at the top of the middle wall in the unsupported tunnel shows the trend of linear decrease of horizontal stress and rapid linear increase of vertical stress. Meanwhile, vertical stress remains relatively stable, whereas horizontal stress exhibits a pronounced "bias effect." The tunnel invert and the outer arch foot are identified as vulnerable structural components, necessitating close attention to lining strength and construction quality.

KEYWORDS

multi-arch tunnel, without a middle pilot tunnel, physical experiment, mechanical behavior, deformation and failure mechanism

Highlights

- The evolution process of radial stress and tangential stress of surrounding rock of tunnel during excavation is analyzed, and the influence of lining on the stability of surrounding rock during the construction of multi-arch tunnel without a middle pilot tunnel is revealed.
- The strain field of surrounding rock in physical model test was obtained by using XTDIC three-dimensional digital speckle full-field strain measurement and analysis system.

1 Introduction

A type of highly efficient tunnel, double-connected arch tunnel, is widely used in mountainous road projects, urban expressways, and engineering projects that require saving land and optimizing the layout of routes in China (Wu et al., 2020; Liu et al., 2022).

At present, the middle pilot tunnel method is used mostly in the construction of double-arch tunnels (Ambika and Neelima, 2020), as shown in Figure 1a. Due to the steel arch, the position of the shared middle wall have twice the bias action, which laid the groundwork for the secondary ling cracking of the double-arch tunnel (Zhang et al., 2019), thus the method without a middle pilot tunnel was proposed (Min, et al., 2020; Sui et al., 2021), as shown in Figure 1b. Compared with the traditional tunnel with middle pilot and the three-tunnel method, this method has the advantages of high construction efficiency, low cost, environmental friendliness, and strong safety (Tang et al., 2022).

The construction technology without pilot tunnel represents a development trend in the construction of multi-arch tunnel, and the construction technology has gradually matured (Bi et al., 2024). It is used in the construction of some tunnels such as the Baiyun Mountain double-arch tunnel, Beijing Tianwaitian underground shopping mall, Huangyan high-speed Yangquangou Tunnel (Jian et al., 2024). When this kind of tunnel structure is adopted, the rock and soil body in the upper part of one tunnel is excavated firstly, and then the lower rock and soil excavation is carried out near the middle partition wall, and the rock and soil excavation in the middle partition wall area is completed simultaneously. Then the temporary support is arranged, followed by the casting of the partition wall is carried out. After the completion of the middle partition wall, the other side of the tunnel will be excavated, and the temporary support structure will be removed in time. The core of non-center pilot tunnel construction is to use appropriate temporary support methods to ensure the stability of the middle partition wall in the construction process. Therefore, in the face of different strata and geological conditions, it is usually required to use a variety of pre-strengthening technical methods such as advanced small conduit and advanced anchor rod to stabilize (Zeng et al., 2019).

Physical model tests in a laboratory using a small-scale model are a common method to investigate the stability of large-scale geotechnical engineering, which is an intuitive and efficient research method (Xiao et al., 2005; Meguid et al., 2008; Wang et al., 2023). Physical model testing originated in Italy in the 1960s, then Heuer and Hendron et al. (1971) selected an underground cavern as the research entity and conducted a series of model tests to discuss the excavation process under static load, focusing on the changes of the mechanical properties of the surrounding rock of the underground cavern with time under different conditions with or without lining structure and with different rock integrity (including intact rock mass and fractured rock mass). Fumagalli conducted an in-depth study of the Vajont arch dam through a series of model tests, covering from the elastic response of materials to plastic deformation to the ultimate failure of the structure (Fumagalli, 1979; Sterpi and Cividini, 2004 conducted a series of physical simulation experiments on shallow-buried tunnels under soft soil layers, supplemented by two-dimensional and three-dimensional finite element numerical simulation analysis. Based on a series of tunnel physical model experiments carried out in the environment of soft soil layer, Meguid et al. (2008) conducted an in-depth discussion on the deformation and fracture mechanism of soft soil induced during tunnel excavation. Xie et al. (2022) conducted model tests and numerical simulations to study the time-varying response regularity of surrounding rock construction mechanics in a double-arch tunnel without a middle pilot tunnel.

After years of research, Chinese scholars have made a series of achievements in the field of physical model test (Li et al., 2016; Liu et al., 2006; Lin et al., 2021, 2024). Since 1973, team of Gu has carried out model test research on anchor support and reinforcement mechanism research on prestressed anchor cable with underground caverns. It is the first in China to propose and successfully implement the test scheme of tunnel model under plane strain conditions and the innovative test scheme of "loading first, excavating later". This greatly enhanced the consistency of model test results with real engineering situations, and thus achieved a series of important academic achievements (Gu et al., 1994). Based on the engineering background of Baziling bifurcated tunnel, Li and Zhang et al. (2007) conducted a series of large-scale physical model tests for the transition from small arch section to large arch section and from multiple arch section to small clear distance section, and deeply explored the law of stress and displacement variation around the bifurcated tunnel, as well as the failure mechanism of surrounding rock of the bifurcated tunnel. Li et al. (2012) relying on the Changcheng multi-arch tunnel project as the engineering background, focused on the changes in the mechanical characteristics of the surrounding rock during the construction of the extremely shallow buried multi-arch tunnel, and used physical model test methods to simulate the tunnel excavation process.

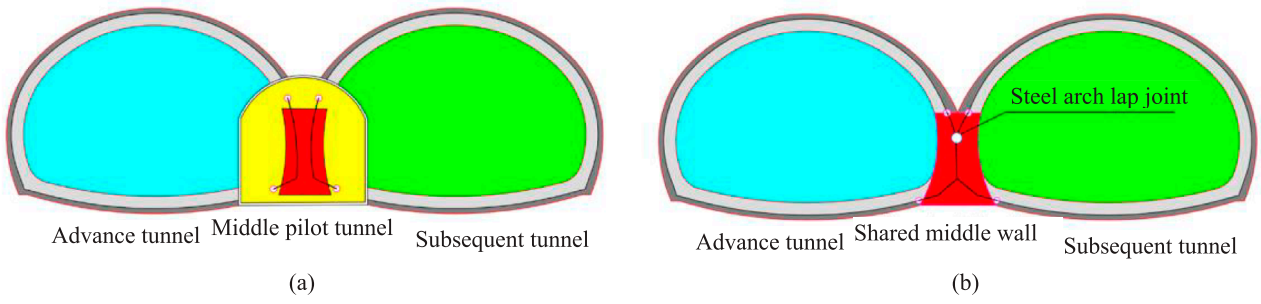

FIGURE 1
Two construction methods for double-connected arch tunnels. **(a)** Conventional double-arch tunnel. **(b)** Double-arch tunnel without a middle pilot tunnel (Jiang et al., 2021).

He et al. (2018) made an in-depth analysis of the mechanical properties and failure processes of the surrounding rock and lining of the asymmetric multi-arch tunnel under different load conditions by using a large-scale experimental device. Li et al. (2021) set up a large three-dimensional physical model of the Letuan tunnel in Binlai high-speed, and conducted an overload test on the ultra-large tunnel, and studied its stress and displacement changes and the overall stability of surrounding rock. Jiang et al. (2021) designed a large-scale shaking model with 1:20 scale to study the dynamic characteristics of double-arch tunnel slope under earthquake action.

In recent years, many scholars have carried out numerous model tests of multi-arch tunnels relying on various large-scale loading equipment and new measurement technologies. Most of these studies adopt the middle pilot tunnel method, where the tunnel structure is primarily characterized by an integral middle wall and a compound middle wall. However, there has been relatively little systematic research on model tests of multi-arch tunnels without a middle pilot tunnel. Therefore, a physical model test and XTDIC three-dimensional digital speckle full-field strain measurement and analysis system were used to explore the stress evolution and the associated deformation and failure mechanisms of the surrounding rock, and the vulnerable structural components can be identified, which provided theoretical support for similar projects.

2 Physical experimental and numerical methodology

2.1 Engineering geological condition

The Sanyanjing tunnel, located at 1.5 km north of Nuoyi Village, Yanshan, is part of the 3rd section of Yunnan Qiuyan Expressway. The maximum buried depth of the tunnel is 64 m. The surrounding rock of this tunnel area is dominated by red clay and medium-weathered limestone, with weak to medium water richness. The length of the IV level surrounding rock section accounts for 55% of the tunnel length (210 m), as shown in Figure 2a. The tunnel is designed as a multi-arch tunnel without a middle pilot tunnel, and the cross-section of the tunnel lining is shown in Figure 2b.

2.2 Physical experimental design

2.2.1 Similarity ratio and similar material

The key of a geotechnical model tests depends on whether it can be based on engineering and geological conditions and the three fundamental theorems of similarity (Lin et al., 2020), ensuring that the prototype and model systems achieve mechanical similarity within the elastic range. In practical operation, although it is necessary to meet the requirements of the equilibrium equation, geometric equation, physical equation, boundary conditions, and compatibility conditions, the limitations of the experimental equipment scale and the complexity and variability of geological conditions and stress environments often make it difficult to ensure all the mechanical parameters of similar materials satisfied the requirements of the similarity ratio. Based on previous research, geotechnical prototype and model can achieve most of the experimental objectives by satisfying the similarity of stress and geometry, and the Equation 1 needs to be satisfied:

$$f[P, E, L, R, \sigma, \varepsilon, \gamma, \delta, \mu] = 0 \tag{1}$$

where, P represents the external load on the rock mass, MPa; E represents the elastic modulus of rock, GPa; L represents the geometric size of the tunnel, m; R represents the strength of the surrounding rock, MPa; σ represents the stress of the surrounding rock, MPa; ε represents the deformation of the surrounding rock; γ represents the material weight of the surrounding rock, kN/m^3; δ represents the deformation of the surrounding rock, m; and μ represents the Poisson's ratio of the surrounding rock.

Considering the test equipment and tunnel size, the test similarity ratio was determined: the geometric similarity ratio is 70, the material weight similarity ratio is 1.2, and the similarity ratios of the tensile strength, elastic modulus and uniaxial compression is 84. According to the physical and mechanical parameters of limestone in the engineering geological exploration report, the parameters of the surrounding rock and similar materials are compared as shown in Table 1.

The vertical principal stress (σ_v) generated by the overlying strata of the tunnel can be obtained by Equation 2:

$$\sigma_v = \gamma H = 23.5\,\text{kN/m}^3 \times 64\,\text{m} = 1504\,\text{kPa} \tag{2}$$

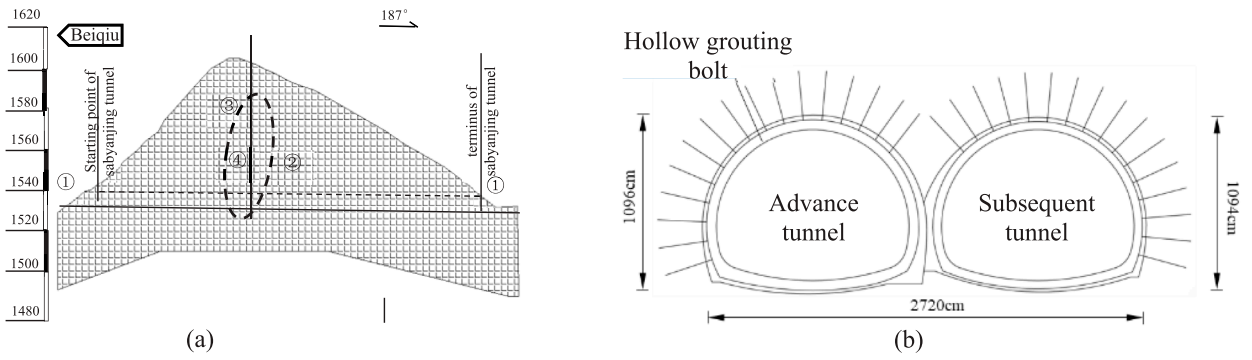

FIGURE 2
The **(a)** longitudinal section diagram and **(b)** Cross section diagram of the Sanyanjing tunnel.

TABLE 1 Mechanical parameters of prototype surrounding rock and model similar materials.

Material type		Material weight γ (KN/m^3)	Elastic modulus E (GPa)	Tensile strength σ_t (MPa)
Surrounding rock	prototype	24	10	78.6
	similar material	19.6	0.12	1.4
C25 shotcrete	prototype	—	20	25
	similar material	—	0.048	0.246

Then, the vertical principal stress (σ_v') in similarity model can be obtained by Equation 3:

$$\sigma_V' = \frac{\sigma_V}{84} = 1504\frac{\text{kPa}}{84} = 17.9\,\text{kPa} \tag{3}$$

where, γ is average unit weight of overlying strata, and H is burial depth.

At present, many scholars have conducted relevant studies on limestone similar materials. However, due to different grades and qualities of cementing materials, as well as differences in particle size and grading of aggregates, direct use of the existing ratio may lead to large test errors. According to the mechanical properties of the limestone with high hardness and brittleness, and as close as possible to the geological environment of the original rock, and referring to the research results of model test on similar materials by Wu et al. (2013), the similar materials were determined. The similar materials for surrounding rock were prepared using 325-grade composite Portland cement and building gypsum as cement, and river sand with particle size less than 2 mm as aggregate. Based on the results of similar materials under uniaxial compression, as shown in Figure 2, the elastic modulus increases from 95.5 MPa to 235.26 MPa, and peak strength increases from 1.03 MPa to 2.52 MPa with increasing cement content. The group of similar materials that best meets the requirements has a mass ratio of river sand, gypsum, cement and water is 100:6:9:11.5. The main consideration of the bolt is to meet the geometric similarity requirements while allowing some deviation in stiffness similarity. Therefore, aluminum wire with a diameter of 2 mm and a length of 43 mm was used to simulate the bolt body, and iron sheet with a size of 10 mm × 10 mm was used to simulate the bolt tray, as shown in Figure 3a. Referring to the research of model tests of multi-arch tunnel by Tian et al. (2013), the initial tunnel support was constituted by water, gypsum and barite powder, and the mass ratio of them is 0.65:1:0.06.

Given the challenge of simultaneously employing excavation and support methods to simulate the construction of a multi-arch tunnel without a middle pilot tunnel, this experiment utilizes the internal mold casting technique to create the tunnel support structure. Additionally, anchor bolts are strategically placed at corresponding positions, and after being positioned at their designated burial points using the embedment method, the rock mass material is cast together. The production process of the shotcrete anchor supporting structure primarily involves utilizing a high-strength foam board to create a mold, pre-arranging the anchor bolt in its designated position, and subsequently pouring layers of evenly mixed gypsum mixture into the mold. Each layer is vibration on a shaking table to ensure material consistency. Following a 2-day curing period following the pouring, the resulting shotcrete anchor supporting structure, formed by releasing the mold is depicted in Figure 4b. Before the test, the left and right apertures were joined together using a gypsum mixture in the same proportions to create a cohesive structure, thereby simulating the overlapping effect between the advanced tunnel and the subsequent tunnel.

2.2.2 Monitoring system

The monitoring system is composed of strain bricks, static strain data acquisition instruments and digital photographic measurement system. The static strain acquisition system (Figure 5) includes a strain brick and a static strain data acquisition instrument. Polyurethane was selected as the matrix of strain brick, cut into a cube with a side length of 15 mm. Two resistance strain gauges (BF120-5AA) were pasted in the center of any surface to form a 90° strain flower, and the surface was coated with silicone rubber for protection. By connecting the strain gauge with the static strain data acquisition instrument, the horizontal and vertical strain values of the measuring points in the surrounding rock during tunnel excavation can be monitored, and the horizontal and vertical stresses of the measuring points can be calculated according to the elastic mechanics equation:

$$\begin{aligned}\sigma_1 &= \frac{E(\varepsilon_0 + \mu\varepsilon_{90})}{1-\mu^2}\\ \sigma_2 &= \frac{E(\varepsilon_{90} + \mu\varepsilon_0)}{1-\mu^2}\end{aligned} \tag{4}$$

where, ε_0 and ε_{90} represent horizontal and vertical strain, σ_1 and σ_2 represent horizontal and vertical stress.

According to the size of the model box and the purpose of the experiment, 27 strain gauges were arranged. Of these 4 were arranged in the crown, waist, and inverted arch of the tunnel in the same manner, and 3 were arranged at the top of the intercalation, enabling the monitoring of the strain state of the surrounding rock within twice the diameter of the tunnel. The position of the measurement points is shown in Figure 6, where A-F represent the 6 strain measurement zones on both sides of the tunnel, and 4 measurement points are arranged at increasing distances from the tunnel wall in each measurement zone.

The digital photogrammetry method is widely used in the study of rock deformation and destruction. The XTDIC three-dimensional digital speckle field strain measurement and analysis system (Figure 7) was used to analyses the strain and displacement of the tunnel surface, consisting of a camera system and a software analysis system. The equipment can achieve a

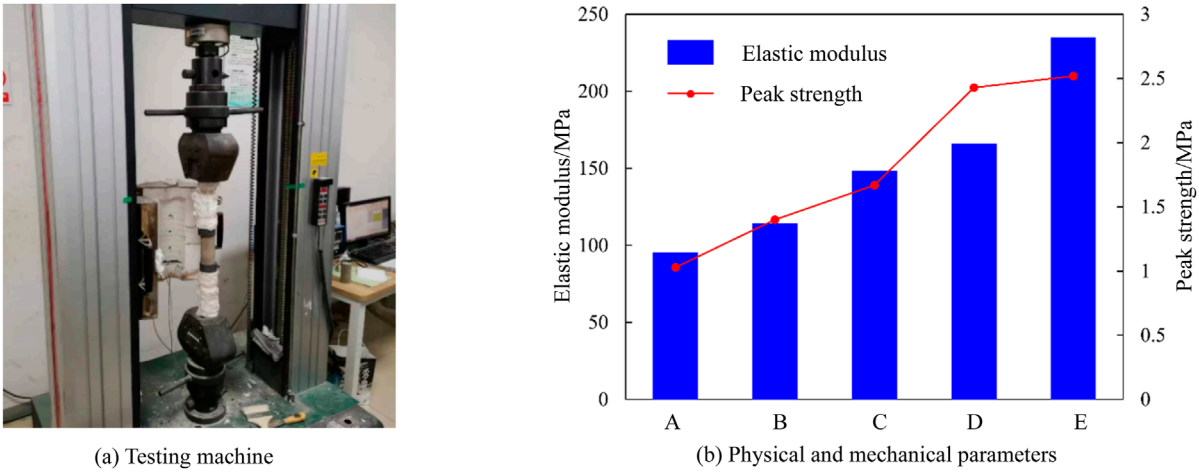

FIGURE 3
Results of similar materials for the surrounding rock under uniaxial compression. **(a)** Testing machine **(b)** Physical and mechanical parameters.

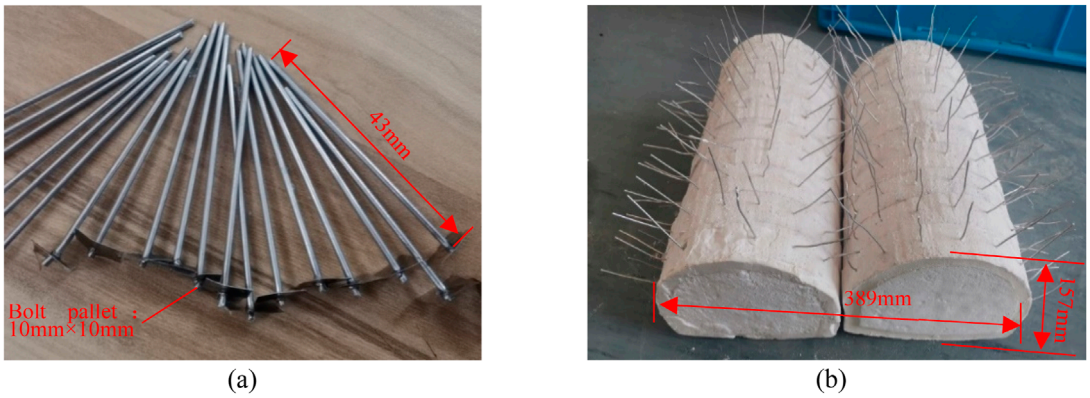

FIGURE 4
Similar material for the support material. **(a)** anchor bolt, **(b)** Spray anchor support structure.

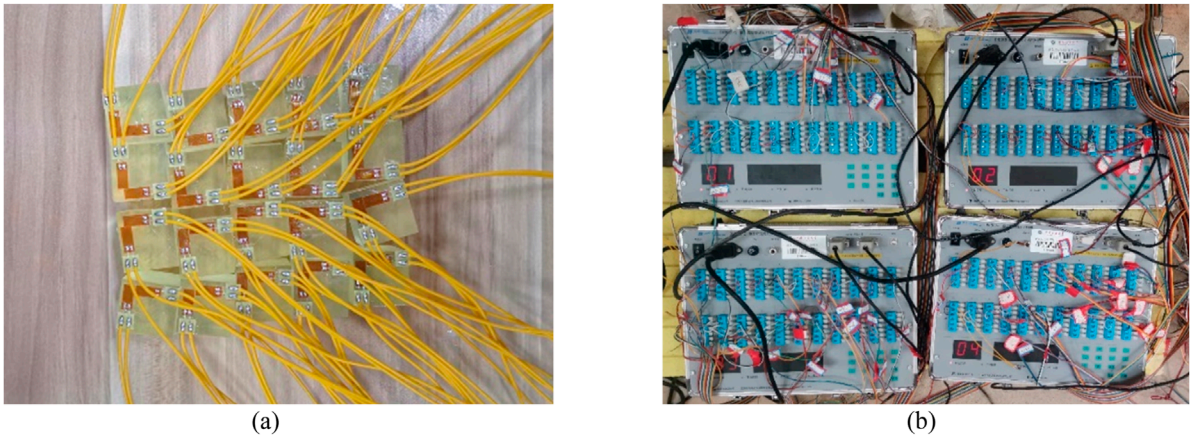

FIGURE 5
Static strain acquisition system, which can be monitored the stress variation during loading process. **(a)** strain brick, **(b)** DH3818 strain data acquisition instrument.

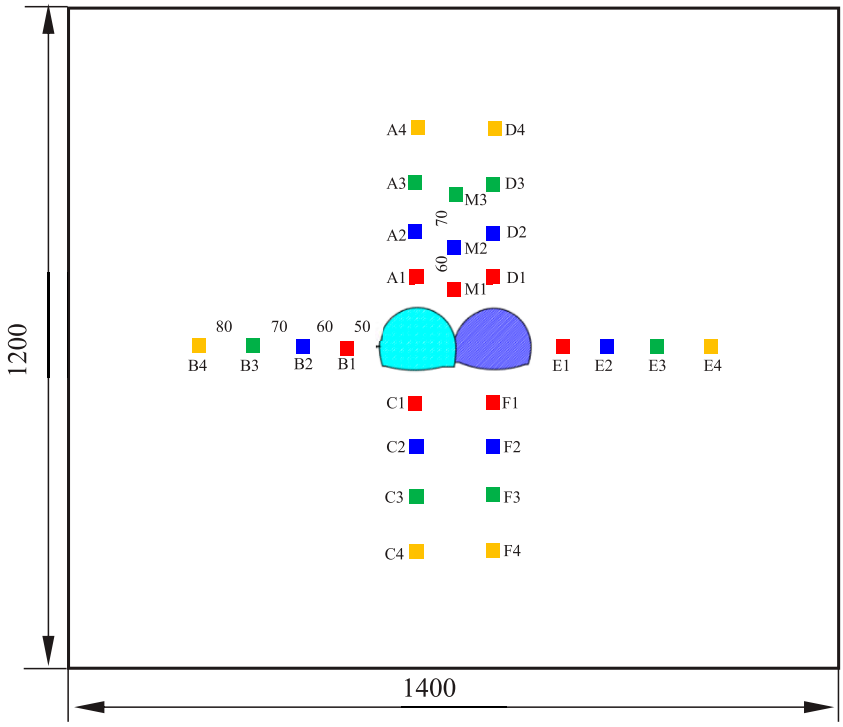

FIGURE 6
Schematic diagram of measurement point layout (unit: millimeters).

FIGURE 7
XTDIC digital image correlation system, which can be monitored the strain field during the whole failure process. **(a)** Picture pick-up system, **(b)** Analysis system.

maximum capture rate of 1,000 frames/s and can measure effective strains ranging from 0.01% to 1,000%. The captured photos were imported into the software analysis system, where digital image correlation algorithms were used to identify speckle points on the object surface. Based on the algorithm, the evolution of the rock strain field could be obtained, reflecting the progressive instability and failure process of the rock.

2.3 Experimental procedure

The model test was conducted independently in a model box composed of channel steel, high-strength bolts, and acrylic plates. And, the sides of the physical model were constrained by the side panels. Therefore, the horizontal field stress can be generated by the Poisson effect under axial loading process. The size of the model test

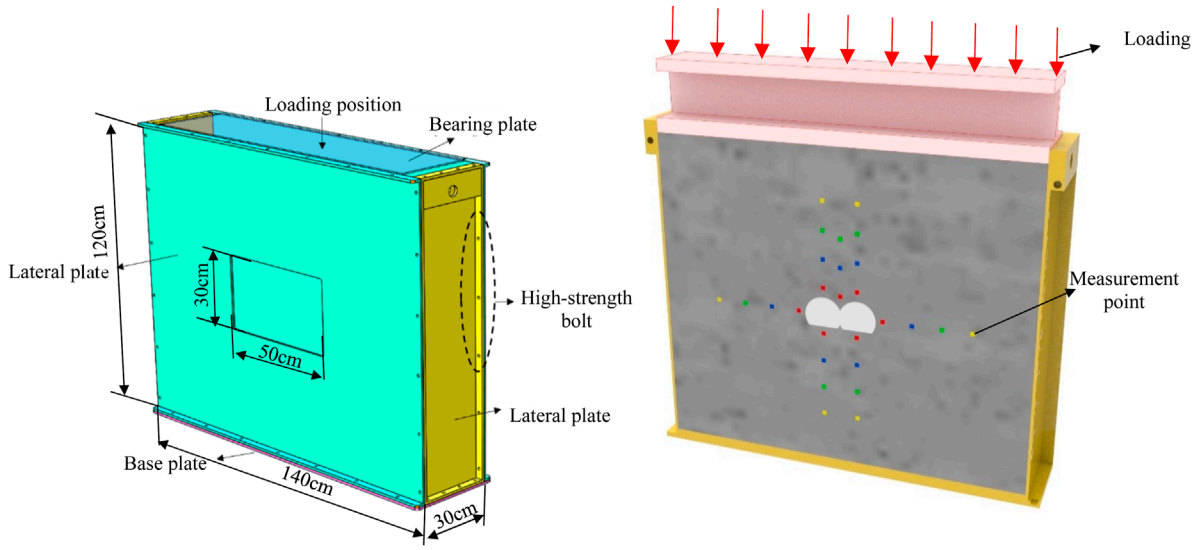

FIGURE 8
Model Test System, composed of channel steel, high-strength bolts, and acrylic plates.

box was 140 cm × 30 cm×120 cm (length × width × height), and an observation window was reserved on one side of the box with a size of 50 cm × 30 cm. The side panels were connected with high-strength bolts, facilitating the adhesion of anti-friction paper and ensuring sufficient box strength. An independent pressure plate was used at the top, allowing the upper load to be uniformly applied to the upper surface of the model. Figure 8 shows the schematic diagram of each component of the model box. The main purpose of this test was to study the deformation and failure mechanism of surrounding rock. The influence of tunnel longitudinal excavation footage on the stability of the surrounding rock was not considered, so the plane strain model test with this model box can meet the test requirements. According to the Saint-Venant principle, to eliminate the influence of boundary effect on the model test, the distance between the tunnel entrance and the model boundary should be more than twice the hole diameter. In the test, the length of the physical model specimen poured is 140 cm, the total width of the left and right holes of the tunnel supporting model is 38 cm, and the ratio of model length to hole diameter is about 4:1, which can eliminate the influence of boundary effect.

The physical model was constructed by layered pouring. The main production steps are as follows: (1) Paste tin foil on the inside of the mold to make anti-friction paper, and mark the layer thickness of each layer of material, the buried point of strain brick and the position of supporting structure on one side of the anti-friction paper; (2) prepared the material referring to the Section 2.2.1, and stirred with a mixer for 15–20 min; (3) Layering and tamping the material from bottom to top, and then gouging to avoid obvious layering; (4) The measuring device and shotcrete anchor support model were buried at the marked points, and the location of the anchor rod needs to be compactor with a small rammer.

The model test adopts the test method of first loading and then excavation. First, the vertical stress is loaded step by step to 17.90 kPa, corresponding to an 8 kN force exerted by the jack, with each stage increment being 2 kN. Then the pressure is stabilized for about 2 h until the strain data is relatively stable. Subsequently, the left cavity was excavated sectional. The test excavation took 6 cm as a footage driving cycle until the tunnel was cut through. After each section of excavation, the pressure was maintained for about 30 min. After the completion of tunnel excavation, the pressure of the model was stabilized for 2 h, and then the overload test was carried out through the stress control mode. Each stage of load increments of 8 kN is loaded every 5 min until no further loading is possible or the tunnel collapses.

3 Experimental results

To facilitate the analysis and comparison of the cumulative quantity and dynamic quantity during stress adjustment, the stress release ratio (k_σ), stress release rate (v_σ) and the stress release average ratio ($\overline{k_\sigma}$) are defined as Equation 5. When k_σ >0, the surrounding rock is in the plastic zone, and the surrounding rock is in the original rock stress zone or elastic zone when $k_\sigma \leq 0$. v_σ reflects the intensity of stress change of surrounding rock disturbed by excavation.

$$k_\sigma = \frac{\sigma_0 - \sigma_1}{\sigma_0} \times 100\% \tag{5}$$

$$v_\sigma = \left| \frac{k_\sigma}{\Delta t} \right|$$

$$\overline{k_\sigma} = \frac{\sum_{i=1}^{n} k_\sigma}{n}$$

where, σ_0 and σ_1 are the initial stress value and real-time stress value of the measuring point, respectively. n indicates the number of measurement points.

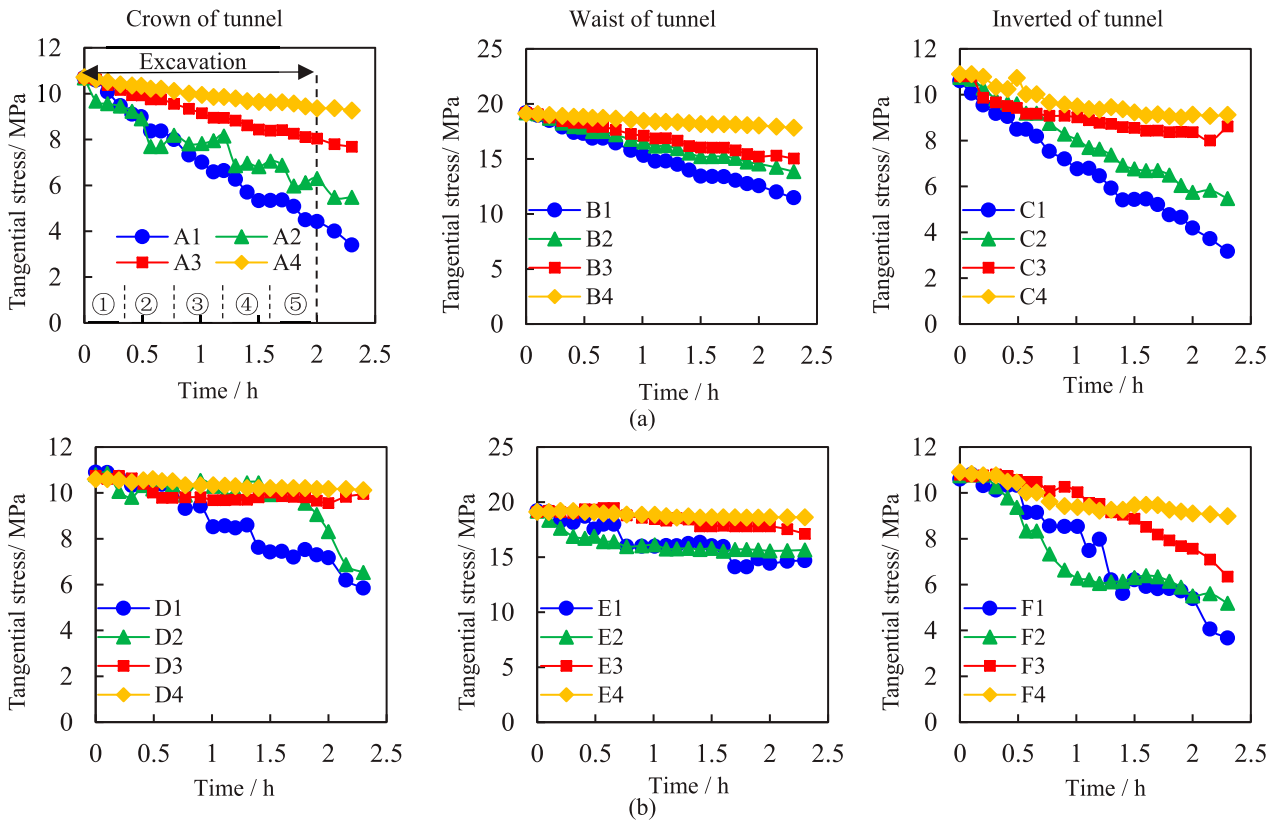

FIGURE 9
Tangential stress evolution of unsupported tunnel during the loading process. **(a)** Advance tunnel, **(b)** Subsequent tunnel.

3.1 Tangential stress evolution

During tunnel excavation, the change of tangential stress reflects the internal adjustment of surrounding rock to resist the deformation caused by unloading (Nagessa et al., 2024). From Figure 9, tangential stress decreases overall, with different locations exhibiting varying magnitudes and rates of stress release throughout the excavation process. The stress release ratio of the left hole (about 68%) is higher than that of the right hole (about 46%), but the variation between the maximum and minimum stress release ratios is greater in the right hole. The reason for this phenomenon is that the advanced tunnel excavation can be regarded as a conventional single tunnel excavation, which disrupts the geo-stress balance of the top and bottom rock mass of the composite tunnel, causing the initial adjustment of stresses. Therefore, the secondary release of stresses caused by the subsequent tunnel excavation is lower than that of the advanced tunnel excavation. Moreover, due to the small spacing between the two tunnel sections, the stress environment and redistribution process in the subsequent tunnel are more complex, resulting in greater variability in stress attenuation across different locations within the tunnel. This ultimately leads to a relatively larger difference in the stress release ratio of the subsequent tunnel.

It also can be seen that the stress attenuation of the 4 measuring points located at the invert of the two holes is obvious, and the measuring points of the surrounding rock are all in the plastic zone. Whereas, the tangential stress at the waist and crown of the two holes either remains undisturbed or exhibits minimal linear attenuation. This shows that the stability and self-adjustment ability of surrounding rock at invert are poor during tunnel excavation. In contrast, at the waist and crown, the surrounding rock is extruded with each other under the influence of excavation and unloading, which imparts a certain degree of self-stabilizing ability. However, due to the lack of external support, no stable and reliable pressure arch is formed, and the tangential stress of the surrounding rock is still released obviously near the inner wall of the tunnel.

Figure 10 shows the tangential stress evolution of supported tunnel, compared with Figure 9 it can be seen that the evolution of tangential stress is different on the unsupported and supported tunnel on the whole. The different evolutionary pattern arises from the pre-embedding of sprayed anchor support structures prior, with completion of the support structure following tunnel excavation. This approach effectively constrains rock mass deformation and mitigates excavation disturbance influence. Consequently, both left and right tunnels exhibit comparable stress evolution patterns. Additionally, due to the proximity of the tunnel-surrounding rock mass to the surface, despite limited support structure, it experiences swelling deformation. As a result, a stress attenuation zone of 9 cm in diameter near the tunnel wall while a stress concentration zone emerges at its farther end, creating a stable pressure arch bearing area.

After the initial excavation, the tangential stress of A3 and A4 gradually increased to 11.8 kPa and 11.4 kPa, respectively, while the

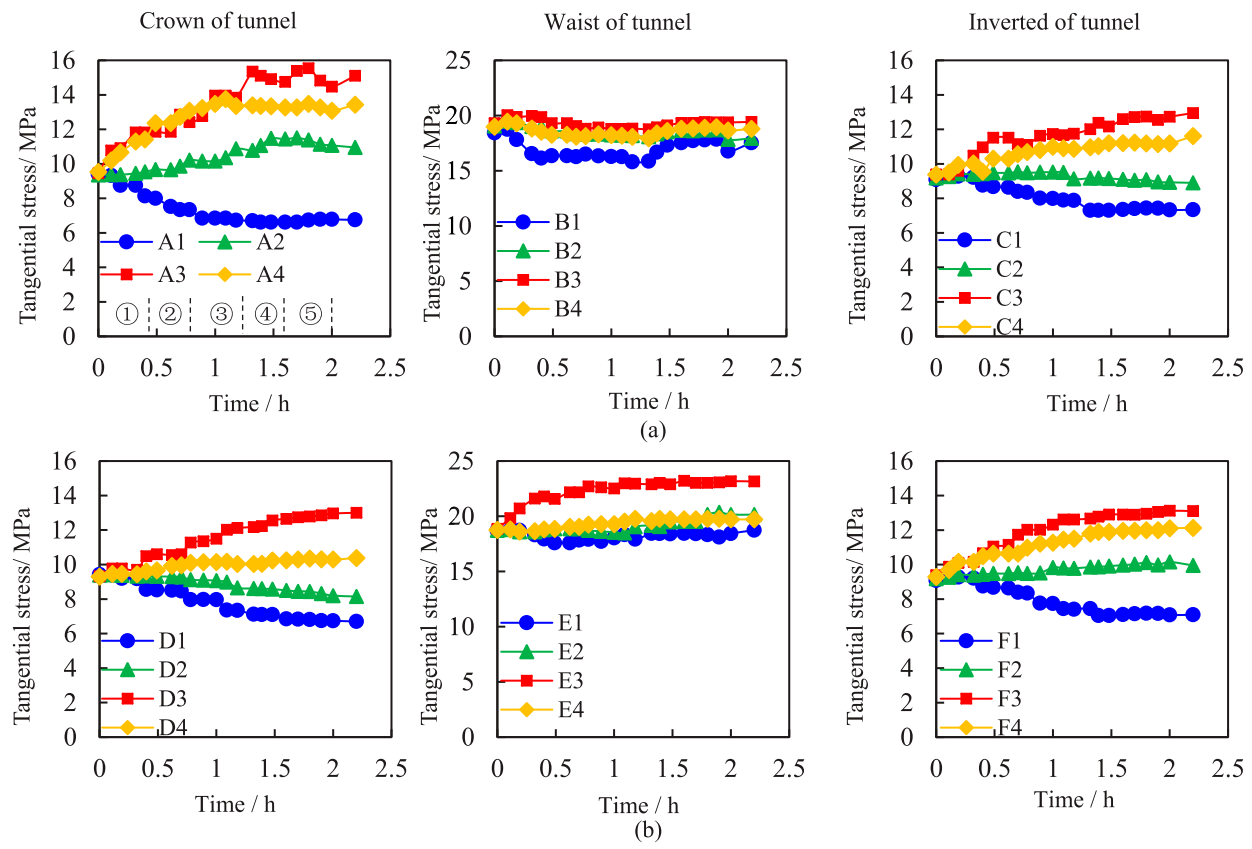

FIGURE 10
Tangential stress evolution of supported tunnel during the loading process. **(a)** Advanced tunnel, **(b)** Subsequent tunnel.

stress of other measuring points remained unchanged. After the second and third excavation, the tangential stress release ratio of measuring points A1 and D1 reaches 27.2% and 15.4%, respectively, resulting in obvious stepped attenuation. In the subsequent excavation stages, the tangential stress of measuring point No. 1 remained relatively stable. The stress evolution at measuring point No.2 of the two holes showed the greatest difference. The tangential stress at measuring point A2 increased to 10.2 kPa and the stress release ratio was −8.7%, while the tangential stress at measuring point D2 decreased to 9.1 kPa and the stress release ratio was 2.9%. This indicates that the surrounding rock at the advanced hole had formed a pressure arch and had the bearing capacity, but the surrounding rock at the subsequent hole was still in the plastic zone. The tangential stress at measuring points A3 and D3 continuously increased with excavation, reaching 13.8 kPa and 12.1 kPa, and the stress release ratios are −46.4% and −30%, respectively. Among the 4 measuring points, the tangential stress concentration phenomenon of surrounding rock is the most obvious, and the tangential stress release ratios at A4 and D4 measuring points are −40% and −7.8%, respectively. The tangential stress at these points was lower than that at No. 3 measuring point. It can be concluded that the surrounding rock of the measuring point A3 is in the core area of the elastic zone, the measuring point A4 is out of the core area of elastic zone, and the tangential stress of the measuring point D4 remained in the zone without significant fluctuation during the whole excavation process. After the fourth and fifth excavation, the tangential stress at measuring point A3 increased incrementally, while at measuring point D3, it increased linearly. The tangential stress of surrounding rock at other measuring points is relatively stable or changes slightly along the original trend, and the influence of excavation disturbance is not obvious.

The process of tangential stress redistribution of surrounding rock at the waist is relatively simple. The supporting structure significantly improves the stability of surrounding rock at the waist, with excavation disturbance having minimal impact on the tangential stress in this area. It can be seen that the tangential stress of the advanced hole presents a regular “step” increase with the step of excavation, while that of the subsequent hole is relatively insignificant. The three initial steps of excavation have a significant impact on the crown and waist of the tunnel. In the tangential stress concentration area, the stress release ratio changes greatly; in the tangential stress attenuation area, the supporting structure simultaneously reduces its decay ratio. The surrounding rock can fully realize its self-stability and load-bearing capacity in a long time.

As shown in Figure 11, the adoption of shotcrete anchor support resulted in a significant reduction in the average tangential stress release ratio of the rock mass. The tangential stress release ratios of the crown, waist, and invert of the left tunnel were −22.4%, 2.77%, and −9.92%, respectively, while those of the right tunnel were −2.28%, −8.9%, and −14.18%. Compared with the tangential stress

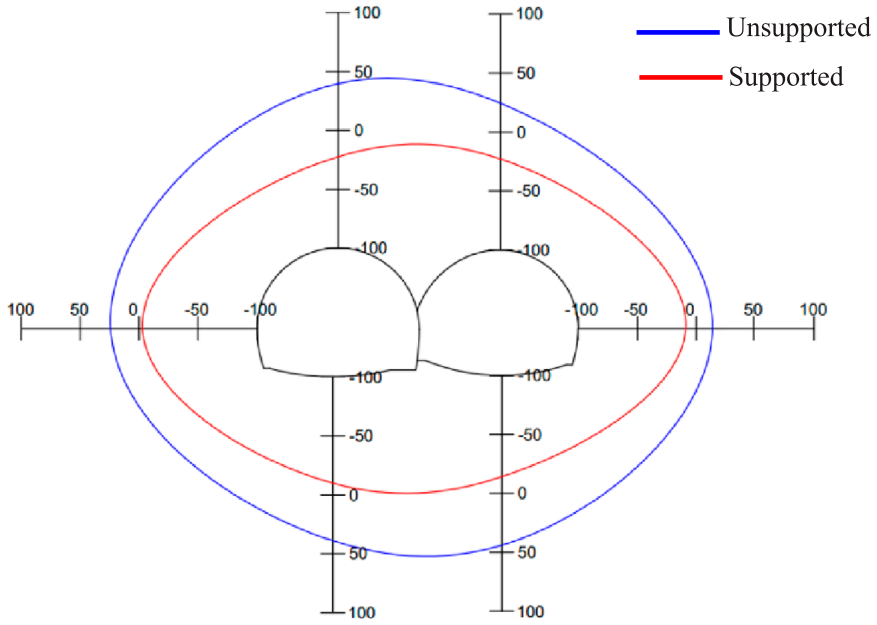

FIGURE 11
Comparison of stress release average ratio in surrounding rock before and after support.

release average ratio of the rock mass without support, the reduction in the same location of the two tunnel sections with support was similar. However, the average tangential stress release ratio in the left tunnel was lower when the two sections were compared with each other, indicating that the range of the rock mass pressure arch in the advanced tunnel was larger, and the self-stability and bearing capacity of the rock mass were stronger.

Overall, the stress in the subsequent tunnel tends to decay, whereas the stress in the advanced tunnel tends to concentrate. This phenomenon can also be explained by the characteristics of this construction method. When the multi-arch tunnel is constructed without a central guide tunnel, it is excavated and formed in two stages, leading to a two-phase stress release in the surrounding rock due to the absence of additional supporting structures. In the process of excavation, the surrounding rock of the subsequent tunnel experiences continuous disturbance, so the overall stress release ratio of the advanced tunnel is usually higher than that of the subsequent tunnel. If the embedded support structure is used, stress redistribution will occur at the top and bottom of the surrounding rock of the subsequent tunnel during the excavation stage of the advanced tunnel, and the elastic zone will be formed in the surrounding rock within a certain range, resulting in the stress concentration in the first tunnel.

3.2 Stress evolution at the middle wall

The multi-arch tunnel differs from the separate tunnel or the small clear distance tunnel in that it relies on the middle wall to bear most of the surrounding rock load. Therefore, the stability of the middle wall is very important to the overall stability of the tunnel structure. Figure 12a shows the stress evolution at the middle wall of tunnel without support, it can be seen that the horizontal stress of measuring points M1 and M2 decreases linearly, with the stress decay rate remaining nearly constant during excavation. Finally, the horizontal stress of the two measuring points decreases to 5.4 kPa and 6.9 kPa, and the stress decay ratios are 43.1% and 26.5%, respectively. Due to the distance from the middle partition wall, the horizontal stress of measuring point M3 remains consistent with the original rock stress. The corresponding vertical stress of surrounding rock showed a completely opposite variation. The vertical stress of surrounding rock at the top of the middle wall increased linearly and the stress release rate remained relatively constant. Additionally, the change amplitude of the vertical stress was also significantly greater than that of the horizontal stress. Finally, the vertical stress at the measuring point M1 and M2 increased to 34.2 kPa and 29.8 kPa respectively. The stress release ratios are −86.3% and −62.1%, representing the largest stress variations among all measuring points, which led to a pronounced stress concentration phenomenon. Meanwhile, the stress of measuring point M3 is also relatively stable. This phenomenon can be explained by the Figure 13, the double-arch tunnel can be regarded as a large single hole with a large single-hole collapse arch at the top. Individually, the double-arch tunnel can be regarded as two independent single holes with two independent pressure arches at the top, resulting in a crossed pressure arch is formed at the top of the middle wall. At the same time, due to the high stress release rate of the tunnel surrounding rock in the test without support, the vertical compression state of the surrounding rock is more obvious and the stress increases greatly.

Figure 12b shows the stress evolution at the middle wall of tunnel with support, the shotcrete anchor support structure obviously changes the stress evolution at the top of the middle wall.

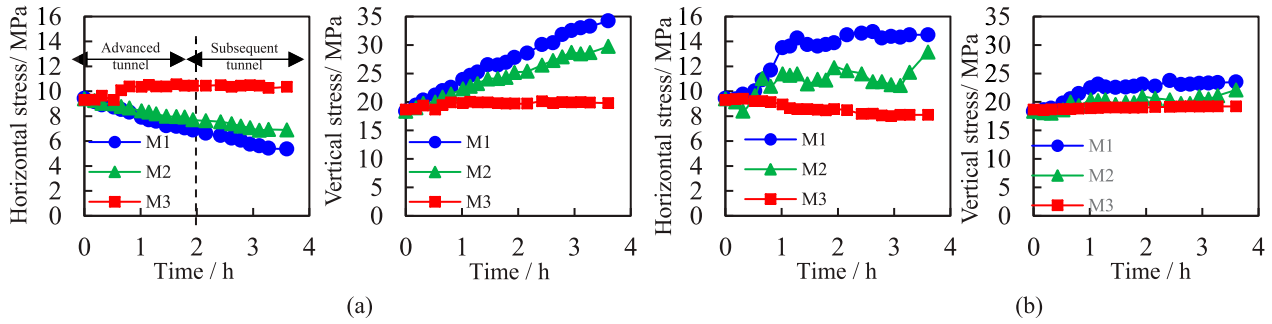

FIGURE 12
Stress evolution of surrounding rock at the top of the middle wall during the loading process. **(a)** Unsupported tunnel, **(b)** Supported tunnel.

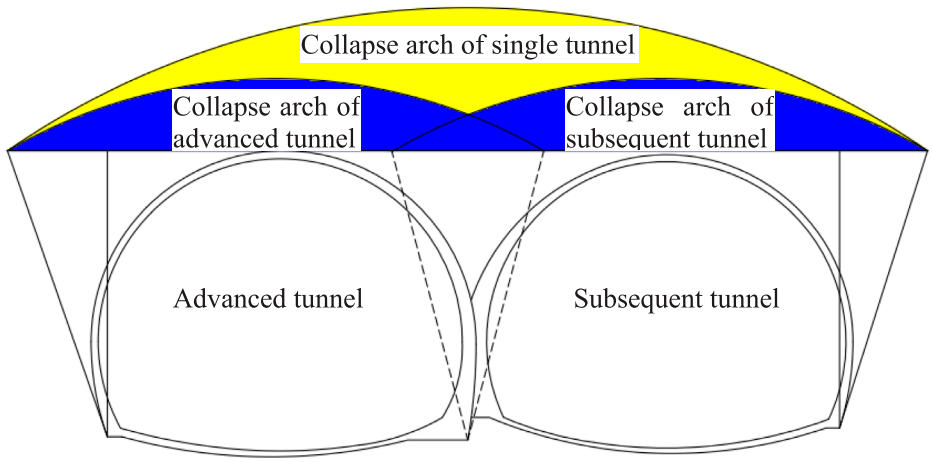

FIGURE 13
Schematic diagram of collapse arch for multi arch tunnel.

The horizontal stress increases greatly during the whole excavation process of the two tunnel holes, and the stress release ratio is also difference obviously in each stage. The excavation disturbance of the left hole has a greater influence on the change of horizontal stress, while the horizontal stress of the right hole increases slightly during the excavation process. Finally, the stress at the measuring point M1 and M2 reach 14.5 kPa and 13.1 kPa, and the stress release ratios are −54.1% and −40.1%, respectively, while M3 measurement point is also still under the original rock stress due to the long distance. The variation trend of the vertical stress in the surrounding rock at the measuring point is the same as that in the test without support. The vertical stress at the measuring points M1 and M2 reach to 23.5 kPa and 22.1 kPa, and the stress release ratios are −28% and −20.4%, respectively. The original rock stress at the measuring point M3 is maintained, indicating that the variation of stress at the measuring point M1 and M2 is significantly reduced.

3.3 Strain field evolution

After the pressure was stabilized for 2 h after excavation, and 8 kN was pressed every 5 min according to the design scheme, continuing until the surrounding rock of the tunnel was completely compromised. In this process, the DIC measuring system was used to analyze the deformation and failure process of tunnel. As shown in Figure 14a, when the overload test is carried out in the unsupported tunnel, the upper surrounding rock of the back tunnel penetrates the advanced tunnel, and part of the surrounding rock of the middle wall has a counterclockwise rotational tendency in the plane, and the stable middle wall can transfer the displacement load to the bottom surrounding rock. At this stage, the left side of the surrounding rock of the middle wall is under compressive and the right side is under tensile, while the lower part is on the contrary. This leads to the tensile failure of the arch foot of the advanced tunnel and the vault of the subsequent tunnel in different programs. The failure develops rapidly at the initial stage of loading, but as the damage degree of the middle wall intensifies, the ability of transferring load is gradually lost, and the stress on the top of the two holes converges. Consequently, the crack propagation speed slows down, and the final failure mode can be seen in Figure 15a.

During the overload test of the support tunnel, as shown in Figure 14b, the damage degree of surrounding rock and support in the lower part of the tunnel is higher than that in the upper part of the

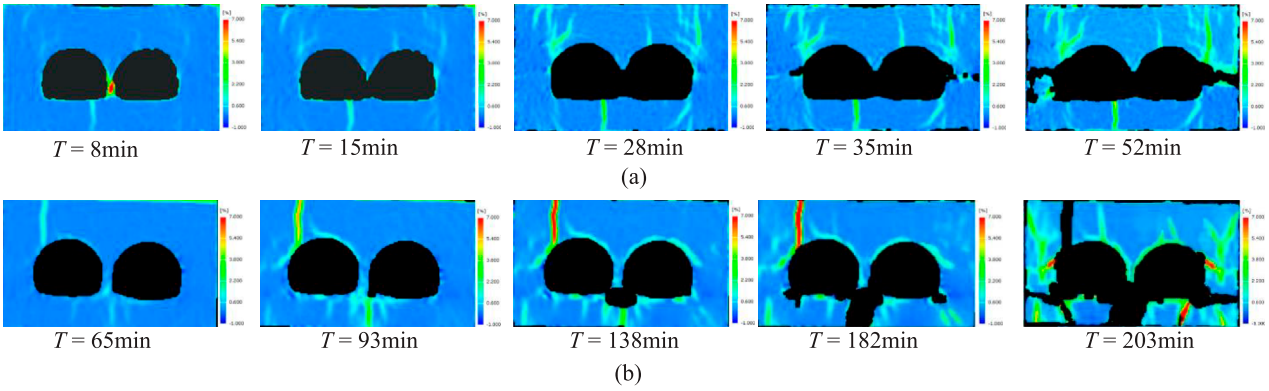

FIGURE 14
Strain field evolution in surrounding rock of tunnel. **(a)** unsupported tunnel, **(b)** supported tunnel.

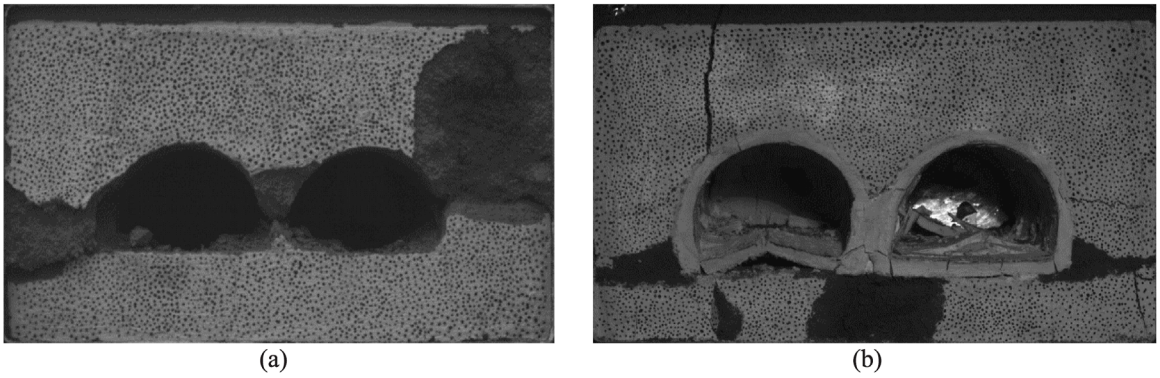

FIGURE 15
Final failure of tunnel. **(a)** unsupported tunnel, **(b)** supported tunnel.

tunnel. The deformation and failure of the tunnel are mainly due to that the surrounding rock at the bottom is subjected to tensile action, resulting in upward uplift deformation. The arch foot of the tunnel, located at the junction of the arch waist and invert, has low structural strength and exhibits significant stress concentration. When the compressive load of surrounding rock on the supporting structure exceeds its bearing capacity, the supporting structure will cause large deformation and even failure. The surrounding rock on both sides of the tunnel is squeezed into the bottom of the invert under the action of pressure, and shear failure occurs in the surrounding rock at the arch foot. This results in horizontal and vertical macroscopic cracks, and the final failure mode can be seen in Figure 15b.

3.4 Verification of the model test results

To verify the validity of the model test, Figure 16 shows the comparison of the surrounding rock failure process of the unsupported tunnel model test and the numerical simulation results. It can be seen that as the vertical pressure at the top is applied, the failure process of the surrounding rock in the numerical simulation is similar to that of the model test, both showing severe damage in the middle wall area, with the surrounding rock first experiencing shear failure. As the pressure increases, the failure area expands from the free face at the arch waist to both sides. In the test, due to the lack of constraints on the observation surface, the surrounding rock surface begins to peel off. It can also be seen that the tunnel excavation face is significantly flattened, and the inverted arch is pressed to a horizontal position. With the further increase of the top pressure, the failure zone of the surrounding rock expands in the upper and lower directions outside the arch waist. It can also be seen from the test that a vertical through crack appears at the arch shoulder of the trailing tunnel, and with the loading, a large area of the surrounding rock eventually peels off at this location. In summary, the failure process of surrounding rock in the numerical simulation is in good agreement with the model test, which indicates the validity of the test.

4 Discussion

Scholars have conducted extensive experiments, theoretical analyses, and numerical simulations on the stability of surrounding

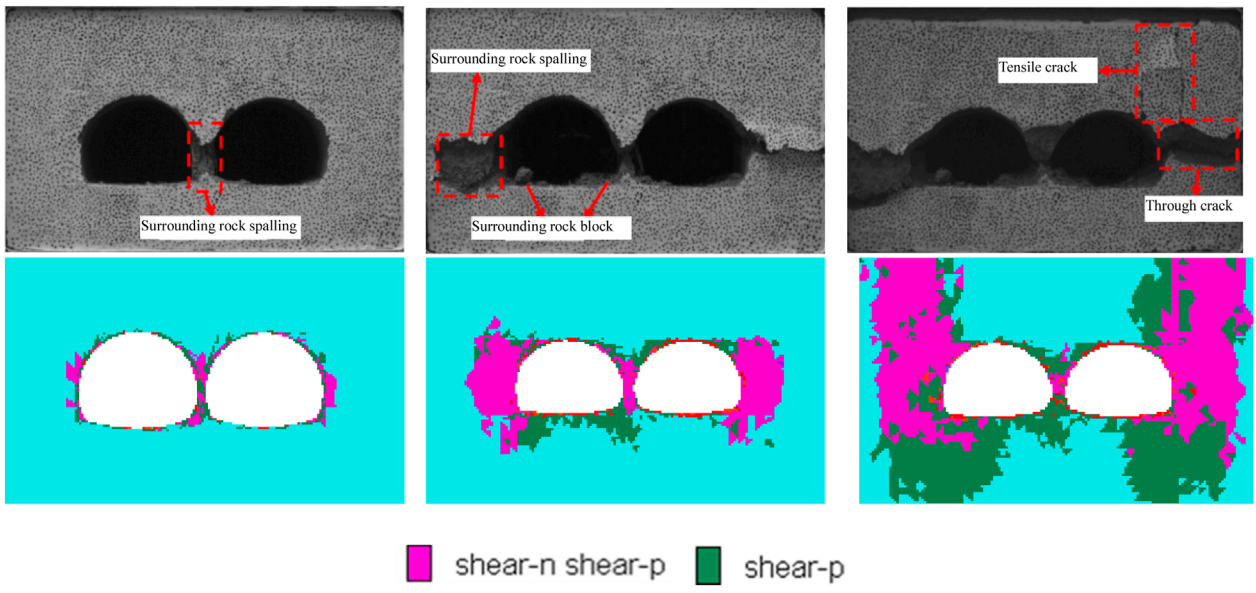

FIGURE 16
Comparison of model test and numerical simulation of surrounding rock damage process.

rock in the double-arch tunnel without a middle pilot. Regarding non-symmetric double-arch tunnels, Min et al. (2020) explored the impact of voids behind the tunnel lining on the structural safety of the tunnel and investigated the real three-dimensional response of non-symmetric double-arch tunnels caused by voids. In terms of theoretical analysis, Sui et al. (2021) studied the continuous strain distribution of damaged linings in double-arch tunnels using distributed optical fiber sensing (DFOS) technology and analyzed their deformation patterns. Based on the fiber strain data, an inverse analysis method based on the curved beam theory to determine the deformation and stress state of the arch structure was proposed. In numerical research, Tang et al. (2022) verified the feasibility of the theoretical method through numerical analysis, studied the dynamic evolution and spatial distribution characteristics of surrounding rock pressure during tunnel excavation, and analyzed the influence of tunnel depth and surrounding rock properties on pressure distribution. However, the study on the fracture characteristics of surrounding rock and the influence of support on the excavation of the double-arch tunnel without a middle pilot is insufficient, so this work carried out the relevant research through the model test. The evolution process of radial stress and tangential stress of surrounding rock of tunnel during excavation was analyzed, and the influence of lining on the stability of surrounding rock during the construction of multi-arch tunnel without a middle pilot tunnel is revealed. And, the strain field of surrounding rock in physical model test was obtained by using XTDIC three-dimensional digital speckle full-field strain measurement and analysis system. Through the related research, the stress concentration location and corresponding fracture characteristics of the tunnel are determined, which can guide the design of support scheme.

5 Conclusion

In this paper, the model test of multi-arch tunnel without support and with shotcrete anchor support is designed to solve the engineering problem of multi-arch tunnel construction without a middle pilot tunnel under Class IV limestone stratum. Using the limestone similar materials and test equipment, the corresponding physical model tests were carried out, and the following conclusions are drawn:

(1) In the multi-step excavation of unsupported tunnel, the stress release ratio and damage degree in the advanced tunnel are higher. However, the stress redistribution process of the subsequent tunnel is more complex and more sensitive to the excavation response. The surrounding rock at the top of the middle wall shows the trend of linear decrease of horizontal stress and rapid linear increase of vertical stress, and the decay rate of both remains constant, reflecting the obvious anisotropic response characteristics.

(2) The supporting structure forms a stable pressure arch in the surrounding rock, extending the elastic zone both laterally and deeper into the tunnel. The variation of stress in the area of arch waist is relatively small. The stress at a distance of one tunnel diameter outside the tunnel wall decays rapidly, while a stress concentration area tends to form beyond this distance, where the stress release ratio is greater than in the stress decay area. The surrounding rock at the top of the middle wall remains relatively stable in the vertical direction, and presents obvious "bias effect" in the horizontal direction, and the stability of the surrounding rock of the middle wall is reduced by the excavation of the subsequent tunnel.

(3) When the overload test is carried out in the unsupported tunnel, the upper surrounding rock of the subsequent tunnel

intrudes into the advanced tunnel, and some surrounding rock of the middle wall exhibits a counterclockwise rotational tendency in the plane. The damage degree of surrounding rock and support in the lower part of the tunnel is higher than that in the upper part of the tunnel with support.

However, the physical result is not verified by the field data and the numerical simulation result. Therefore, the numerical simulation should be done in future. And, the field data will be collected to verify the reasonability of the physical result.

Data availability statement

The raw data supporting the conclusions of this article will be made available by the authors, without undue reservation.

Author contributions

JZ: Writing – original draft, Writing – review and editing, Investigation. W-LT: Writing – original draft, Writing – review and editing, Software. B-QZ: Writing – original draft, Investigation. S-QY: Writing – review and editing, Software.

Funding

The author(s) declare that no financial support was received for the research and/or publication of this article.

Conflict of interest

The authors declare that the research was conducted in the absence of any commercial or financial relationships that could be construed as a potential conflict of interest.

Publisher's note

All claims expressed in this article are solely those of the authors and do not necessarily represent those of their affiliated organizations, or those of the publisher, the editors and the reviewers. Any product that may be evaluated in this article, or claim that may be made by its manufacturer, is not guaranteed or endorsed by the publisher.

References

Ambika, S., and Neelima, S. (2020). Understanding the impact of the arthquake on circular tunnels in different rock mass: a numerical approach. *Innov. Infrastruct. So.* 5 (8), 15–20.

Bi, T. J., Deng, Q., Tang, H., Jiang, C. Y., and Qin, Y. Q. (2024). Analytical solution of stress and displacement of double-arch tunnel without middle drift based on functions of complex variables. *Rock Soil Mech.* 45 (03), 777–787. doi:10.16285/j.rsm.2023.0380

Fumagalli, E. (1979). "Geomechanical models of dam foundation," in *Proceedings of the international colloquium on physical geomechanical models*. Bergamo, Italy: ISRM.

Gu, J. C., Zheng, Q. P., Shen, J., and Ming, Z. Q. (1994). Model test study on the reinforcement effects of prestressed cable on homogenous rock mass. *J. North China Inst. Water Conservancy Hydroelectr. Power* 3, 69–76. doi:10.19760/j.ncwu.zk.1994.03.011

He, J., Zhang, C. P., Yang, G. B., and Wang, M. S. (2018). Experimental study on mechanical behavior of nonsymmetric multi-arch tunnel in sand-cobble ground. *China Civ. Eng. J.* 50 (4), 116–124. doi:10.15951/j.tmgcxb.2017.04.014

Heuer, R. E., and Hendron, A. J. (1971). "Geomechanical model study of the behavior of underground openings in rock subjected to static loads," in *Report 2. Tests on Unlined Openings in Intack Rock. ergebnisse der anatomie und entwicklungsgeschichte*. doi:10.1063/1.468654

Jian, B. X., Tao, T. J., Song, S., Xie, C. J., Tian, X. C., Li, G. Q., et al. (2024). Damage and reliability analysis of double-arch tunnel without a middle pilot tunnel under blast load. *Sci. Rep.* 14, 9246. doi:10.1038/s41598-024-59681-5

Jiang, X., Liu, W., Yang, H., Shi, H. T., and Yu, L. (2021). Study on dynamic response characteristics of slope with double-arch tunnel under seismic action. *Geotechnical Geol. Eng.* 39 (8), 1349–1363. doi:10.1007/s10706-020-01562-5

Li, L. P., Shang, C. S., Chu, K. W., Zhou, Z. Q., Song, S. G., Liu, Z. H., et al. (2021). Large-scale geo-mechanical model tests for stability assessment of super-large cross-section tunnel. *Tunn. Undergr. Sp. Tech.* 109, 103756. doi:10.1016/j.tust.2020.103756

Li, S. C., Yuan, C., Feng, X. D., and Li, S. C. (2016). Mechanical behaviour of a large-span double-arch tunnel. *Ksce J. Civ. Eng.* 20 (7), 2737–2745. doi:10.1007/s12205-016-0456-y

Li, S. C., Yuan, C., Li, S. C., Feng, X. D., and Li, W. T. (2012). Model test study on mechanical behavior of extremely shallow double-arch tunnel during excavation. *J. China Coal Soc.* 37 (5), 713–718. doi:10.13225/j.cnki.jccs.2012.05.010

Lin, Q. B., Cao, P., Meng, J. J., Cao, R. H., and Zhao, Z. Y. (2020). Strength and failure characteristics of jointed rock mass with double circular holes under uniaxial compression: insights from discrete element method modelling. *Theor. Appl. Fract. Mec.* 109, 102692. doi:10.1016/j.tafmec.2020.102692

Lin, Q. B., Cao, P., Wen, G. P., Meng, J. J., Cao, R. H., and Zhao, Z. Y. (2021). Crack coalescence in rock-like specimens with two dissimilar layers and pre-existing double parallel joints under uniaxial compression. *Int. J. Rock. Mech. Min.* 139, 104621. doi:10.1016/j.ijrmms.2021.104621

Lin, Q. B., Zhang, S. C., Liu, H., and Shao, Z. L. (2024). Water saturation effects on the fracturing mechanism of sandstone excavating by TBM disc cutters. *Arch. Civ. Mech. Eng.* 24, 154. doi:10.1007/s43452-024-00964-z

Liu, B., Xu, F., Zhao, W. G., and Gao, Y. (2022). Review and prospect of model test system for tunnel engineering structure. *Rock Soil Mech.* 43 (S1), 452–468. doi:10.16285/j.rsm.2021.0737

Liu, T., Shen, M. R., Tao, L. B., He, Z. M., and Yuan, Y. (2006). Model test and 3D numerical simulation study on excavation of double-arch tunnel. *Chin. J. Rock Mech. Eng.* 25 (09), 1802–1808.

Meguid, M. A., Saada, O., Nunes, M. A., and Mattar, J. (2008). Physical modeling of tunnels in soft ground: a review. *Tunn. Undergr. Sp. Tech.* 23 (2), 185–198. doi:10.1016/j.tust.2007.02.003

Min, B., Zhang, C., Zhang, X., Wang, H. L., Li, P. F., and Zhang, D. L. (2020). Cracking performance of asymmetric double-arch tunnels due to the voids behind linings. *Thin. Wall. Struc.* 154, 106856. doi:10.1016/j.tws.2020.106856

Nagessa, Z. J., Siraj, M. A., and Eleyas, A. (2024). Numerical analysis of underground tunnel deformation: a case study of Midroc Lega-Dembi gold mine. *Sci. Rep.* 14, 7964. doi:10.1038/s41598-024-57621-x

Sterpi, D., and Cividini, A. (2004). A physical and numerical investigation on the stability of shallow tunnels in strain softening media. *Rock Mech. Rock Eng.* 37 (4), 277–298. doi:10.1007/s00603-003-0021-0

Sui, Y., Cheng, X. H., and Wei, J. X. (2021). Distributed fibre optic monitoring of damaged lining in double-arch tunnel and analysis of its deformation mode. *Tunn. Undergr. Sp. Tech.* 110, 103812. doi:10.1016/j.tust.2021.103812

Tang, H., Jiang, C. Y., Deng, Q., Bi, T. J., and Cha, Z. Y. (2022). Calculation of pressure on the shallow-buried double-arch tunnel without middle drift. *Ksce J. Civ. Eng.* 26 (11), 4805–4814. doi:10.1007/s12205-022-1958-4

Tian, L. G., Duan, Q. M., Xu, Q. W., and Cai, Y. C. (2013). Analysis and research on laboratory model test for twin-tunnel under unsymmetrical pressure. *Chin. J. Undergr. Space Eng.* 9 (1), 119–125.

Wang, C. S., Yong, R., Luo, Z. Y., Du, S. G., Karakus, M., and Huang, C. X. (2023). A novel method for determining the three-dimensional roughness of rock joints based on profile slices. *Rock Mech. Rock Eng.* 56, 4303–4327. doi:10.1007/s00603-023-03274-7

Wu, B., Lu, M., Huang, W., Lan, Y. B., Wu, Y. F., and Huang, Z. H. (2020). A case study on the construction optimization decision scheme of urban subway tunnel based on the TOPSIS method. *Ksce J. Civ. Eng.* 24 (11), 3488–3500. doi:10.1007/s12205-020-1290-9

Wu, B. T., Zhu, H. H., and Xu, Q. W. M. J. (2013). Experimental study of similar material for weak surrounding rock mass of class IV. *Rock Soil Mech.* 34 (S1), 109–116. doi:10.16285/j.rsm.2013.s1.044

Xiao, L. P., Zhao, Y. G., and Shen, Y. S. (2005). Model experimental study on style of structural internal force and stability of surrounding rock in double-arch tunnel. *Chin. J. Rock Mech. Eng.* 24 (23), 4346–4351.

Xie, G. J., Tao, T. J., and Rao, J. Y. (2022). Time-varying response analysis of surrounding rock construction mechanics of a double-arch tunnel without a middle pilot tunnel and suggestions for tunnel construction. *Lithosphere* 2022, 6306861. doi:10.2113/2022/6306861

Zeng, W. C., Zhou, Y. X., Zhai, J. L., and Xie, X. Y. (2019). Construction technology without middle drift and monitoring analysis of double-arch tunnel. *Chin. J. Undergr. Space Eng.* 15 (S1), 361–366.

Zhang, Q. Y., Li, S. C., Li, Y., and Wang, H. P. (2007). 3D geomechanical model test research on stability and supporting for surrounding rock mass of a large-scale diversion tunnel. *Chin. J. Rock Mech. Eng.* 26 (S2), 4051–4059.

Zhang, X., Ye, Z. J., Min, B., and Xu, Y. J. (2019). Effect of voids behind lining on the failure behavior of symmetrical double-arch tunnels. *Symmetry* 11 (10), 1321. doi:10.3390/sym11101321

Frontiers in Earth Science

Investigates the processes operating within the major spheres of our planet

Advances our understanding across the earth sciences, providing a theoretical background for better use of our planet's resources and equipping us to face major environmental challenges.

Discover the latest Research Topics

See more →

Frontiers

Avenue du Tribunal-Fédéral 34
1005 Lausanne, Switzerland
frontiersin.org

Contact us

+41 (0)21 510 17 00
frontiersin.org/about/contact